

1-1-2016

# New Chemistry For The Growth Of First-Row Transition Metal Films By Atomic Layer Deposition

Joseph Peter Klesko  
*Wayne State University,*

Follow this and additional works at: [http://digitalcommons.wayne.edu/oa\\_dissertations](http://digitalcommons.wayne.edu/oa_dissertations)

 Part of the [Chemical Engineering Commons](#), [Chemistry Commons](#), and the [Materials Science and Engineering Commons](#)

---

## Recommended Citation

Klesko, Joseph Peter, "New Chemistry For The Growth Of First-Row Transition Metal Films By Atomic Layer Deposition" (2016). *Wayne State University Dissertations*. Paper 1401.

This Open Access Dissertation is brought to you for free and open access by DigitalCommons@WayneState. It has been accepted for inclusion in Wayne State University Dissertations by an authorized administrator of DigitalCommons@WayneState.

**NEW CHEMISTRY FOR THE GROWTH OF FIRST-ROW TRANSITION METAL FILMS  
BY ATOMIC LAYER DEPOSITION**

by

**JOSEPH PETER KLESKO**

**DISSERTATION**

Submitted to the Graduate School

of Wayne State University,

Detroit, Michigan

in partial fulfillment of the requirements

for the degree of

**DOCTOR OF PHILOSOPHY**

2015

MAJOR: CHEMISTRY (Physical)

Approved By:

\_\_\_\_\_  
Advisor

\_\_\_\_\_  
Date

\_\_\_\_\_  
\_\_\_\_\_  
\_\_\_\_\_  
\_\_\_\_\_

**© COPYRIGHT BY**  
**JOSEPH PETER KLESKO**  
**2015**  
**All Rights Reserved**

## DEDICATION

I dedicate this dissertation to Lauren Elizabeth Hopper  
and to my parents, Joseph Daniel and Barbara Klesko.

My accomplishments are a testament to your sacrifice, support, and understanding.  
You have my eternal love and gratitude.

*“People who say it cannot be done should not interrupt those who are doing it.”*

- George Bernard Shaw

## ACKNOWLEDGMENTS

The pursuit of my doctorate has been an experience like none other; the tedium of failed experiments and long nights in the lab punctuated by the occasional small step forward. In short, it has been a difficult, yet rewarding journey, the completion of which was only realized by the generosity and counsel of others. As I reflect upon the fond memories of the past several years, I acknowledge those whose advocacy and tutelage were pertinent to my success in this program.

First and foremost, I thank my advisor, Prof. Charles H. Winter, for introducing me to the fascinating field of atomic layer deposition (ALD). Prof. Winter has been an outstanding mentor, and it has been a privilege to learn from someone of his talent and character. He challenged me, encouraged my creativity, and believed in my potential. For all of this, I remain in his debt.

My committee members, Prof. Claudio N. Verani, Prof. G. Andrés Cisneros, and Dr. Charles L. Dezelah are gratefully acknowledged for their careful review of my thesis. Dr. Dezelah is additionally thanked for lending his time and acumen toward troubleshooting periodic problems with our ALD reactors. His advice and assistance were truly indispensable to my completion of this degree.

I thank the professionals within the ALD community whose mentorship has enhanced my doctoral experience. Dr. Thomas J. Knisley guided me through my first depositions and taught me the fundamentals of thin film characterization. Dr. Ravi Kanjolia facilitated my internship at SAFC-Hitech and made valuable contributions as a research collaborator. Dr. Mark J. Saly was a tremendous asset while at SAFC-Hitech, managing my projects while teaching me elements of ALD precursor design and process development.

I appreciate the wealth of technological resources made available by Wayne State University and the Department of Chemistry. I thank the personnel at the Lumigen Instrument Center, Wayne State University Grid, Science and Engineering Library, and Science Storeroom for their technical assistance, especially Dr. Yuriy Danylyuk, Dr. Bashar Ksehati, Dr. Zhi "Mike" Mei, Dr. Phil Martin, Christopher M. Thrush, and Nestor Ocampo. I also thank my friends and colleagues whose fruitful discussions have contributed to my research endeavors and overall knowledge of chemistry, namely, Dr. Brian T. Psciuk, Dr. Caleb Ryder, Dr. Dong Fang, Dr. Yuan-Wei "David" Nei, Dr. Amarnath Bheemaraju, Lucas Hamlow, and Derak James.

I am especially indebted to Lauren Elizabeth Hopper, who helped me navigate the travails of graduate school, both technical and personal. Our countless discussions were an important component to my development as a chemist, broadening my knowledge of organic spectroscopy and providing fresh perspectives toward research-related problems. Most of all, her love and encouragement gave me the strength needed to surpass every obstacle en route to this degree.

Finally, I am thankful for my family. I am grateful to my grandparents, Joseph Andrew and Helen Klesko, and George and Sally Romanowski, for sharing their wisdom and encouraging my pursuit of higher education. I appreciate the love and support of my sister, Pamela Marie Klesko. Lastly, my sincerest gratitude is reserved for my parents, Joseph Daniel and Barbara Klesko, whose hard work and sacrifice afforded a quality education for my sister and me. Their commitment to my professional development is the cornerstone upon which this degree was built.

Thank you all for standing by me.

## TABLE OF CONTENTS

Dedication .....	i
Acknowledgements.....	ii
List of Tables .....	vii
List of Figures .....	ix
List of Charts.....	xxii
List of Abbreviations .....	xxiii
CHAPTER 1: Introduction	
1.1 Miniaturization of Microelectronic Devices .....	1
1.2 Materials Containing Transition Metal Thin Films .....	2
1.3 Deposition Methods .....	6
1.3.1 Physical Vapor Deposition .....	7
1.3.2 Chemical Vapor Deposition.....	8
1.3.3 Atomic Layer Deposition.....	9
1.4 ALD Fundamentals.....	13
1.5 First-row Transition Metal ALD Precursors and Processes	
1.5.1 Titanium.....	18
1.5.2 Vanadium.....	20
1.5.3 Chromium .....	21
1.5.4 Manganese .....	22
1.5.5 Iron.....	24
1.5.6 Cobalt.....	26

1.5.7	Nickel .....	29
1.5.8	Copper .....	32
1.5.9	Zinc .....	40
1.6	Reducing Coreagents .....	42
1.7	Thesis Problem.....	43
<b>CHAPTER 2: Thermal Atomic Layer Deposition of Titanium and Antimony Films Using 2-Methyl-1,4-bis(trimethylsilyl)-2,5-cyclohexadiene or 1,4-Bis(trimethylsilyl)-1,4-dihydropyrazine</b>		
2.1	Introduction.....	45
2.2	Results and Discussion	
2.2.1	Computational Assessment of Six-membered Rings Containing Two Trimethylsilyl Groups.....	46
2.2.2	Titanium Films from $TiCl_4$ and 2-Methyl-1,4-bis(trimethylsilyl)-2,5-cyclohexadiene .....	48
2.2.3	Titanium Films from $TiCl_4$ and 1,4-Bis(trimethylsilyl)-1,4-dihydropyrazine .....	74
2.2.4	Antimony Films from $SbCl_3$ and 1,4-Bis(trimethylsilyl)-1,4-dihydropyrazine .....	92
2.3	Conclusions.....	96
2.4	Experimental .....	98
<b>CHAPTER 3: Low Temperature Thermal Atomic Layer Deposition of Cobalt and Other Metal Films Using Formic Acid</b>		
3.1	Introduction.....	103
3.2	Results and Discussion .....	105
3.2.1	Cobalt Films by a Three-step Process.....	108
3.2.2	Cobalt Films by a Two-step Process.....	110
3.2.3	Other Metal-containing Films by Three-step Processes .....	133



3.3	Conclusions.....	149
3.4	Experimental.....	150
CHAPTER 4: Evaluation of Mg(II), Al(III), Ti(IV), Zn(II), and Zr(IV) Bis(1,4-di- <i>tert</i> -butyl-1,3-diazabutadienyl) Complexes as Precursors for Atomic Layer Deposition		
4.1	Introduction.....	152
4.2	Results and Discussion .....	153
4.3	Conclusions.....	158
4.4	Experimental.....	159
CHAPTER 5: Unusual Stoichiometry Control in the Atomic Layer Deposition of Manganese Borate Films from Manganese Bis(tris(pyrazolyl)borate) and Ozone		
5.1	Introduction.....	163
5.2	Results and Discussion	
5.2.1	Mn <sub>3</sub> (BO <sub>3</sub> ) <sub>2</sub> Films from Bis(tris(pyrazolyl)borate)Mn(II) and Ozone.....	164
5.2.2	CoB <sub>2</sub> O <sub>4</sub> Films from Bis(tris(pyrazolyl)borate)Co(II) and Ozone.....	176
5.2.3	Other Films from Bis(tris(pyrazolyl)borate) Precursors and Ozone.....	182
5.3	Conclusions.....	190
5.4	Experimental.....	192
CHAPTER 6: Conclusions.....		
Appendix A: Thermal Analysis of (2- <i>tert</i> -Butylallyl)Co(CO) <sub>3</sub> .....		198
Appendix B: Permissions.....		200
References.....		202
Abstract.....		236
Autobiographical Statement.....		239

## LIST OF TABLES

<b>Table 1.</b>	Electrochemical potentials of first-row transition metals .....	16
<b>Table 2.</b>	NICS(1) <sub>iso</sub> and NICS(1) <sub>zz</sub> values for <b>1</b> , <b>2</b> , and a benzene analogue.....	48
<b>Table 3.</b>	Solution reactions of metal complexes with <b>1</b> .....	49
<b>Table 4.</b>	Surface roughnesses measured by AFM of films grown using TiCl <sub>4</sub> and <b>1</b> at 140 and 180 °C on Si(100) and SiO <sub>2</sub> substrates.....	58
<b>Table 5.</b>	EDS element mapping of films grown on Si(100) and SiO <sub>2</sub> substrates from TiCl <sub>4</sub> and <b>1</b> at 180 °C .....	62
<b>Table 6.</b>	Solution reactions of metal complexes with <b>2</b> .....	75
<b>Table 7.</b>	Surface roughnesses measured by AFM of films grown using TiCl <sub>4</sub> and <b>2</b> at 100 °C on Si(100) and SiO <sub>2</sub> substrates .....	84
<b>Table 8.</b>	Reported thermal properties of M( <sup>t</sup> Bu <sub>2</sub> DAD) <sub>2</sub> complexes .....	104
<b>Table 9.</b>	Surface roughnesses measured by AFM of a 105 nm thick film grown on Ru from <b>3</b> and formic acid at 180 °C. Measurements were taken from 2 and 5 μm <sup>2</sup> areas .....	127
<b>Table 10.</b>	Resistivity data for bare substrates and cobalt films deposited at 180 °C after 1,000 cycles .....	129
<b>Table 11.</b>	Crystal data, collection parameters, bond lengths (Å) and angles (°) for <b>13</b> .....	156
<b>Table 12.</b>	Electrochemical potentials of metals used in <b>8–13</b> .....	157
<b>Table 13.</b>	Preparative sublimation data, melting point, solid state decomposition temperature, and magnetic moment data for <b>8–13</b> .....	158
<b>Table 14.</b>	Surface roughnesses measured by AFM of films grown from <b>14</b> and ozone at 300, 325, and 350 °C for 2,000 cycles. Measurements were taken from 3 and 5 μm <sup>2</sup> areas .....	169
<b>Table 15.</b>	XPS atomic concentrations (at.%) of 35–36 nm thick films grown from <b>14</b> and ozone on Si(100) after 2 minutes of sputtering .....	171

<b>Table 16.</b>	TOF-ERDA atomic concentrations (at.%) of 35–36 nm thick films grown from <b>14</b> and ozone on Si(100) .....	173
<b>Table 17.</b>	Crystal data, collection parameters, bond lengths (Å) and angles (°) for <b>20</b> .....	187
<b>Table 18.</b>	Crystal data, collection parameters, bond lengths (Å) and angles (°) for <b>21</b> .....	189

## LIST OF FIGURES

<b>Figure 1.</b>	N-channel MOSFET structure .....	3
<b>Figure 2.</b>	PVD of a Cu/Mn alloy for $MnSi_xO_y$ diffusion barrier formation .....	5
<b>Figure 3.</b>	Comparison of film coverage and conformality by (a) CVD, PVD, (b) ALD processes .....	6
<b>Figure 4.</b>	Film growth by (a) evaporative PVD, (b) sputter PVD .....	7
<b>Figure 5.</b>	Film growth by CVD .....	8
<b>Figure 6.</b>	Number of ALD publications per year from 2000–2014, per SciFinder .....	9
<b>Figure 7.</b>	A typical ALD process: $TiCl_4$ reacts with $H_2O$ toward the growth of $TiO_2$ films.....	10
<b>Figure 8.</b>	Growth rate versus precursor pulse length. Region <b>A</b> indicates sub-saturative growth, while region <b>B</b> indicates saturative growth.....	11
<b>Figure 9.</b>	Growth rate versus deposition temperature, illustrating regions <b>A</b> : insufficient precursor reactivity, <b>B</b> : precursor condensation, <b>C</b> : ALD window, <b>D</b> : precursor decomposition, and <b>E</b> : desorption of precursor from the substrate or surface site deactivation.....	12
<b>Figure 10.</b>	Proposed mechanism for the reduction of $TiCl_4$ by <b>2</b> to afford Ti metal .....	47
<b>Figure 11.</b>	Powder XRD of $CuCl$ ; reduction of $CuCl_2$ and $CuCl_2 \cdot 2H_2O$ by <b>1</b> in THF .....	50
<b>Figure 12.</b>	Powder XRD of Cu metal; reduction of $CuCl_2 \cdot DME$ by <b>1</b> and en in DME .....	50
<b>Figure 13.</b>	Powder XRD spectrum of Ti metal; reduction of $TiCl_4$ by <b>1</b> in toluene .....	51
<b>Figure 14.</b>	$^1H$ NMR spectra of <b>1</b> and the reaction product of $TiCl_4$ and <b>1</b> in $C_6D_6$ .....	51
<b>Figure 15.</b>	Cyclic voltammogram of toluene relative to ferrocene.....	52
<b>Figure 16.</b>	Saturation plot of $TiCl_4$ using 0.2 s pulses of <b>1</b> at 180 °C .....	53
<b>Figure 17.</b>	Saturation plot of <b>1</b> using 0.3 s pulses of $TiCl_4$ at 180 °C. The secondary axis shows the consumption rate of <b>1</b> as a function of the pulse length of <b>1</b> .....	54

<b>Figure 18.</b>	Plot of growth rate versus temperature using 0.3 s pulses of TiCl <sub>4</sub> and 0.2 s pulses of <b>1</b> for 3,000 cycles .....	54
<b>Figure 19.</b>	Plot of film thickness versus number of ALD cycles using TiCl <sub>4</sub> and <b>1</b> at 180 °C .....	55
<b>Figure 20.</b>	Cross-sectional SEM images of films deposited on thermal SiO <sub>2</sub> using TiCl <sub>4</sub> and <b>1</b> at 110, 130, 160, and 180 °C .....	56
<b>Figure 21.</b>	Cross-sectional SEM images of films deposited on thermal SiO <sub>2</sub> using TiCl <sub>4</sub> and <b>1</b> at 200, 220, 240, and 260 °C .....	57
<b>Figure 22.</b>	Cross-sectional SEM images of films deposited on Si(100) and Pt substrates using TiCl <sub>4</sub> and <b>1</b> at 140 °C.....	58
<b>Figure 23.</b>	AFM image of a 2 μm <sup>2</sup> region of a film grown using TiCl <sub>4</sub> and <b>1</b> . The film was deposited on Si(100) with native oxide at 140 °C .....	59
<b>Figure 24.</b>	AFM image of a 5 μm <sup>2</sup> region of a film grown using TiCl <sub>4</sub> and <b>1</b> . The film was deposited on Si(100) with native oxide at 140 °C .....	59
<b>Figure 25.</b>	AFM image of a 2 μm <sup>2</sup> region of a film grown using TiCl <sub>4</sub> and <b>1</b> . The film was deposited on thermal SiO <sub>2</sub> at 140 °C .....	60
<b>Figure 26.</b>	AFM image of a 5 μm <sup>2</sup> region of a film grown using TiCl <sub>4</sub> and <b>1</b> . The film was deposited on thermal SiO <sub>2</sub> at 140 °C .....	60
<b>Figure 27.</b>	Top-down SEM images of films grown on Si(100) (a, b) and SiO <sub>2</sub> (c, d) substrates from TiCl <sub>4</sub> and <b>1</b> at 180 °C. EDS analyses were performed in tandem on areas with and without nanoparticulate growth .....	61
<b>Figure 28.</b>	XPS survey scans of an 82 nm thick film grown on Si(100) from TiCl <sub>4</sub> and <b>1</b> at 140 °C.....	64
<b>Figure 29.</b>	XPS O 1s ionization region of an 82 nm thick film grown on Si(100) from TiCl <sub>4</sub> and <b>1</b> at 140 °C .....	64
<b>Figure 30.</b>	XPS Ti 2p ionization region of an 82 nm thick film grown on Si(100) from TiCl <sub>4</sub> and <b>1</b> at 140 °C .....	65
<b>Figure 31.</b>	XPS Si 2p ionization region of an 82 nm thick film grown on Si(100) from TiCl <sub>4</sub> and <b>1</b> at 140 °C .....	65
<b>Figure 32.</b>	XPS depth profile of an 82 nm thick film grown from TiCl <sub>4</sub> and <b>1</b> on Si(100) at 140 °C .....	66

<b>Figure 33.</b>	Relative abundance of Ti(IV), Ti(III), Ti(II), and Ti(0) oxidation states versus sputter time for an 82 nm thick film grown from TiCl <sub>4</sub> and <b>1</b> on Si(100) at 140 °C .....	66
<b>Figure 34.</b>	XPS survey scans of a 76 nm thick film grown from TiCl <sub>4</sub> and <b>1</b> on Si(100) at 180 °C .....	67
<b>Figure 35.</b>	XPS O 1s ionization region of a 76 nm thick film grown from TiCl <sub>4</sub> and <b>1</b> on Si(100) at 180 °C.....	67
<b>Figure 36.</b>	XPS Si 2p ionization region of a 76 nm thick film grown from TiCl <sub>4</sub> and <b>1</b> on Si(100) at 180 °C.....	68
<b>Figure 37.</b>	XPS Ti 2p ionization region of a 76 nm thick film grown from TiCl <sub>4</sub> and <b>1</b> on Si(100) at 180 °C.....	68
<b>Figure 38.</b>	XPS depth profile of a 76 nm thick film grown from TiCl <sub>4</sub> and <b>1</b> on Si(100) at 180 °C .....	69
<b>Figure 39.</b>	XPS survey scans of a 35 nm thick film grown from TiCl <sub>4</sub> and <b>1</b> on Pt/SiO <sub>2</sub> /Si at 140 °C.....	70
<b>Figure 40.</b>	XPS O 2p ionization region of a 35 nm thick film grown from TiCl <sub>4</sub> and <b>1</b> on Pt/SiO <sub>2</sub> /Si at 140 °C .....	70
<b>Figure 41.</b>	XPS Pt 4f ionization region of a 35 nm thick film grown from TiCl <sub>4</sub> and <b>1</b> on Pt/SiO <sub>2</sub> /Si at 140 °C .....	71
<b>Figure 42.</b>	XPS Si 2p ionization region of a 35 nm thick film grown from TiCl <sub>4</sub> and <b>1</b> on Pt/SiO <sub>2</sub> /Si at 140 °C .....	71
<b>Figure 43.</b>	XPS Ti 2p ionization region of a 35 nm thick film grown from TiCl <sub>4</sub> and <b>1</b> on Pt/SiO <sub>2</sub> /Si at 140 °C .....	72
<b>Figure 44.</b>	XPS depth profile of a 35 nm thick film grown from TiCl <sub>4</sub> and <b>1</b> on Pt/SiO <sub>2</sub> /Si at 140 °C .....	72
<b>Figure 45.</b>	XPS survey scans of a 99.7% pure 0.127 mm thick titanium foil .....	73
<b>Figure 46.</b>	XPS Ti 2p ionization region of a 99.7% pure 0.127 mm thick titanium foil.....	73
<b>Figure 47.</b>	TGA analysis of <b>2</b> performed under inert atmosphere.....	74
<b>Figure 48.</b>	Solution reduction products of Cu(thmd) <sub>2</sub> , CoCl <sub>2</sub> , FeCl <sub>2</sub> , and SiCl <sub>4</sub> from <b>2</b> .....	76

<b>Figure 49.</b>	Powder XRD spectrum showing Cu metal; reduction of Cu(tmhd) <sub>2</sub> by <b>2</b> in THF .....	76
<b>Figure 50.</b>	Cyclic voltammagram of pyrazine relative to ferrocene.....	77
<b>Figure 51.</b>	Saturation plot of TiCl <sub>4</sub> using 0.1 s pulses of <b>2</b> at 100 °C .....	78
<b>Figure 52.</b>	Saturation plot of <b>2</b> using 0.3 s pulses of TiCl <sub>4</sub> at 100 °C. The secondary axis shows the consumption rate of <b>2</b> as a function of the pulse length of <b>2</b> .....	79
<b>Figure 53.</b>	Plot of growth rate versus TiCl <sub>4</sub> purge length using 0.3 s pulses of TiCl <sub>4</sub> and 0.2 s pulses of <b>2</b> at 100 °C.....	79
<b>Figure 54.</b>	Plot of growth rate versus temperature using 0.3 s pulses of TiCl <sub>4</sub> and 0.1 s pulses of <b>2</b> for 3,000 cycles .....	80
<b>Figure 55.</b>	Plot of film thickness versus number of ALD cycles using TiCl <sub>4</sub> and <b>2</b> at 100 °C.....	80
<b>Figure 56.</b>	Cross-sectional SEM images of films deposited on Si(100) and SiO <sub>2</sub> substrates using TiCl <sub>4</sub> and <b>2</b> within the 90–100 °C ALD window .....	81
<b>Figure 57.</b>	AFM image of a 2 μm <sup>2</sup> region of a film grown using TiCl <sub>4</sub> and <b>2</b> .....	82
<b>Figure 58.</b>	AFM image of a 5 μm <sup>2</sup> region of a film grown using TiCl <sub>4</sub> and <b>2</b> .....	82
<b>Figure 59.</b>	AFM image of a 2 μm <sup>2</sup> region of a film grown using TiCl <sub>4</sub> and <b>2</b> .....	83
<b>Figure 60.</b>	AFM image of a 5 μm <sup>2</sup> region of a film grown using TiCl <sub>4</sub> and <b>2</b> .....	83
<b>Figure 61.</b>	XPS survey scans of a 95 nm thick film grown from TiCl <sub>4</sub> and <b>2</b> on Si(100) at 100 °C .....	85
<b>Figure 62.</b>	XPS O 1s ionization region of a 95 nm thick film grown from TiCl <sub>4</sub> and <b>2</b> on Si(100) at 100 °C.....	85
<b>Figure 63.</b>	XPS Si 2p ionization region of a 95 nm thick film grown from TiCl <sub>4</sub> and <b>2</b> on Si(100) at 100 °C.....	86
<b>Figure 64.</b>	XPS Ti 2p ionization region of a 95 nm thick film grown from TiCl <sub>4</sub> and <b>2</b> on Si(100) at 100 °C.....	86
<b>Figure 65.</b>	XPS depth profile of a 95 nm thick film grown from TiCl <sub>4</sub> and <b>2</b> on Si(100) at 100 °C .....	87

<b>Figure 66.</b>	Relative abundance of Ti(IV), Ti(III), Ti(II), and Ti(0) oxidation states versus sputter time for a 95 nm thick film grown from TiCl <sub>4</sub> and <b>2</b> on Si(100) at 100 °C .....	87
<b>Figure 67.</b>	AES depth profile of a 95 nm thick film grown from TiCl <sub>4</sub> and <b>2</b> on Si(100) at 100 °C .....	88
<b>Figure 68.</b>	Cross-sectional SEM image of a film deposited on thermal SiO <sub>2</sub> using TiCl <sub>4</sub> and <b>2</b> , then overcoated with Co metal by a CVD process .....	89
<b>Figure 69.</b>	XPS survey scans of a 97 nm thick film grown from TiCl <sub>4</sub> and <b>2</b> on Si(100) at 100 °C and overcoated with Co by a CVD process .....	90
<b>Figure 70.</b>	XPS Co 2p ionization region of a 97 nm thick film grown from TiCl <sub>4</sub> and <b>2</b> on Si(100) at 100 °C and overcoated with Co by a CVD process .....	90
<b>Figure 71.</b>	XPS Ti 2p ionization region of a 97 nm thick film grown from TiCl <sub>4</sub> and <b>2</b> on Si(100) at 100 °C and overcoated with Co by a CVD process .....	91
<b>Figure 72.</b>	XPS depth profile of a 97 nm thick film grown from TiCl <sub>4</sub> and <b>2</b> on Si(100) at 100 °C and overcoated with Co by a CVD process .....	91
<b>Figure 73.</b>	AES depth profile of a 97 nm thick film grown from TiCl <sub>4</sub> and <b>2</b> on Si(100) at 100 °C and overcoated with Co by a CVD process .....	92
<b>Figure 74.</b>	Cross-sectional SEM image of a 20 nm thick film grown on Pt from SbCl <sub>3</sub> and <b>2</b> for 1,000 cycles at 180 °C.....	93
<b>Figure 75.</b>	Top-down SEM image of a 20 nm thick film grown on Pt from SbCl <sub>3</sub> and <b>2</b> for 1,000 cycles at 180 °C.....	93
<b>Figure 76.</b>	Cross-sectional SEM image of material grown on Pd from SbCl <sub>3</sub> and <b>2</b> for 1,000 cycles at 180 °C.....	94
<b>Figure 77.</b>	Top-down SEM image of material grown on Pd from SbCl <sub>3</sub> and <b>2</b> for 1,000 cycles at 180 °C.....	94
<b>Figure 78.</b>	XPS survey scans of a 20 nm thick film grown from SbCl <sub>3</sub> and <b>2</b> on Pt at 180 °C .....	95
<b>Figure 79.</b>	XPS Sb 3d ionization region of a 20 nm thick film grown from SbCl <sub>3</sub> and <b>2</b> on Pt at 180 °C .....	96
<b>Figure 80.</b>	Cyclic voltammogram of <b>3</b> relative to ferrocene .....	105
<b>Figure 81.</b>	Cyclic voltammogram of <b>4</b> relative to ferrocene .....	105



<b>Figure 82.</b>	Powder XRD spectrum of the product obtained by reacting <b>1</b> and formic acid. Major reflections for $\text{Co}(\text{OCHO})_2 \cdot \text{H}_2\text{O}$ <21–0257> are shown by vertical lines.....	106
<b>Figure 83.</b>	Powder XRD spectrum of the product obtained by reacting <b>1</b> and formic acid. Known reflections for the hexagonal <05–0727> and cubic <15–0806> phases of cobalt metal are shown by vertical lines.....	107
<b>Figure 84.</b>	Powder XRD spectrum of the product obtained by reacting <b>1</b> and formic acid. Known reflections for the cubic phases of $\text{Co}_3\text{O}_4$ <43–1003> and $\text{CoO}$ <48–1719> are shown by vertical lines.....	107
<b>Figure 85.</b>	Cross-sectional and top-down SEM images of an 84 nm thick film grown on $\text{SiO}_2$ from <b>3</b> , formic acid, and <b>2</b> for 1,000 cycles at 180 °C.....	108
<b>Figure 86.</b>	XPS survey scans of a 24 nm thick film grown from <b>3</b> , formic acid, and <b>2</b> on Ru at 180 °C.....	109
<b>Figure 87.</b>	XPS Co 2p ionization region of a 24 nm thick film grown from <b>3</b> , formic acid, and <b>2</b> on Ru at 180 °C.....	109
<b>Figure 88.</b>	Powder XRD spectrum of an 84 nm thick cobalt film grown on $\text{SiO}_2$ from <b>3</b> , formic acid, and <b>2</b> for 1,000 cycles at 180 °C.....	110
<b>Figure 89.</b>	Saturation plot of <b>3</b> using 0.2 s pulses of formic acid at 180 °C. The secondary axis shows the consumption rate of <b>3</b> as a function of the pulse length of <b>3</b> .....	112
<b>Figure 90.</b>	Saturation plot of formic acid using 5.0 s pulses of <b>3</b> at 180 °C.....	112
<b>Figure 91.</b>	Plot of growth rate versus temperature using 5.0 s pulses of <b>3</b> and 0.2 s pulses of formic acid for 1,000 cycles. The secondary axis shows the bulk resistivity of the film as a function of temperature.....	113
<b>Figure 92.</b>	Plot of film thickness versus number of ALD cycles using <b>3</b> and formic acid at 180 °C. The secondary axis shows the bulk resistivity of the film as a function of the number of ALD cycles.....	113
<b>Figure 93.</b>	Cross-sectional SEM image of a 24 nm thick film grown on Ru from <b>3</b> and formic acid for 1,000 cycles at 140 °C.....	115
<b>Figure 94.</b>	Top-down SEM image of a 24 nm thick film grown on Ru from <b>3</b> and formic acid for 1,000 cycles at 140 °C.....	115
<b>Figure 95.</b>	Cross-sectional SEM image of a 57 nm thick film grown on Ru from <b>3</b> and formic acid for 1,000 cycles at 160 °C.....	116

<b>Figure 96.</b>	Top-down SEM image of a 57 nm thick film grown on Ru from <b>3</b> and formic acid for 1,000 cycles at 160 °C .....	116
<b>Figure 97.</b>	Cross-sectional SEM image of a 98 nm thick film grown on Ru from <b>3</b> and formic acid for 1,000 cycles at 170 °C.....	117
<b>Figure 98.</b>	Top-down SEM image of a 98 nm thick film grown on Ru from <b>3</b> and formic acid for 1,000 cycles at 170 °C .....	117
<b>Figure 99.</b>	Cross-sectional SEM image of a 132 nm thick film grown on Ru from <b>3</b> and formic acid for 1,000 cycles at 200 °C.....	118
<b>Figure 100.</b>	Top-down SEM image of a 132 nm thick film grown on Ru from <b>3</b> and formic acid for 1,000 cycles at 200 °C.....	118
<b>Figure 101.</b>	Cross-sectional SEM image of a film grown on Ru from <b>3</b> and formic acid for 1,000 cycles at 240 °C .....	119
<b>Figure 102.</b>	Top-down SEM image of a film grown on Ru from <b>3</b> and formic acid for 1,000 cycles at 240 °C.....	119
<b>Figure 103.</b>	SEM image at a 5-degree tilt showing nanoparticulate grown on Ru from <b>3</b> and formic acid for 100 cycles at 180 °C.....	120
<b>Figure 104.</b>	SEM image at a 5-degree tilt showing a continuous film grown on Ru from <b>3</b> and formic acid for 250 cycles at 180 °C.....	120
<b>Figure 105.</b>	Cross-sectional SEM image of a 24 nm thick film grown on Ru from <b>3</b> and formic acid for 250 cycles at 180 °C.....	121
<b>Figure 106.</b>	Top-down SEM image of a 24 nm thick film grown on Ru from <b>3</b> and formic acid for 250 cycles at 180 °C .....	121
<b>Figure 107.</b>	Cross-sectional SEM image of a 50 nm thick film grown on Ru from <b>3</b> and formic acid for 500 cycles at 180 °C.....	122
<b>Figure 108.</b>	Top-down SEM image of a 50 nm thick film grown on Ru from <b>3</b> and formic acid for 500 cycles at 180 °C .....	122
<b>Figure 109.</b>	Cross-sectional SEM image of a 93 nm thick film grown on Ru from <b>3</b> and formic acid for 1,000 cycles at 180 °C.....	123
<b>Figure 110.</b>	Top-down SEM image of a 93 nm thick film grown on Ru from <b>3</b> and formic acid for 1,000 cycles at 180 °C .....	123

<b>Figure 111.</b>	Cross-sectional SEM image of a 196 nm thick film grown on Ru from <b>3</b> and formic acid for 2,000 cycles at 180 °C.....	124
<b>Figure 112.</b>	Top-down SEM image of a 196 nm thick film grown on Ru from <b>3</b> and formic acid for 2,000 cycles at 180 °C; 130,000 magnification .....	124
<b>Figure 113.</b>	Top-down SEM image of a 196 nm thick film grown on Ru from <b>3</b> and formic acid for 2,000 cycles at 180 °C; 90,000 magnification .....	125
<b>Figure 114.</b>	Cross-sectional SEM image of a 92 nm thick film grown on Cu from <b>3</b> and formic acid for 1,000 cycles at 180 °C.....	125
<b>Figure 115.</b>	Cross-sectional SEM image of a 122 nm thick film grown on Pd from <b>3</b> and formic acid for 1,000 cycles at 180 °C.....	126
<b>Figure 116.</b>	Cross-sectional SEM image of a 97 nm thick film grown on Pt from <b>3</b> and formic acid for 1,000 cycles at 180 °C.....	126
<b>Figure 117.</b>	AFM images of a 105 nm thick film grown on Ru from <b>3</b> and formic acid at 180 °C: (a) 2 $\mu\text{m}^2$ region, (b) 5 $\mu\text{m}^2$ region.....	127
<b>Figure 118.</b>	TEM image of Co metal grown from <b>3</b> and formic acid on a TEM grid at 180 °C .....	128
<b>Figure 119.</b>	Powder XRD spectrum of a 93 nm thick film grown from <b>3</b> and formic acid on Ru for 1,000 cycles at 180 °C.....	128
<b>Figure 120.</b>	Sheet resistivity data for cobalt films grown from <b>3</b> and formic acid for 1,000 cycles.....	130
<b>Figure 121.</b>	XPS survey scans of a 95 nm thick film grown from <b>3</b> and formic acid on Ru at 180 °C.....	131
<b>Figure 122.</b>	XPS Co 2p ionization region of a 95 nm thick film grown from <b>3</b> and formic acid on Ru at 180 °C .....	131
<b>Figure 123.</b>	Cross-sectional SEM image of a 30 nm thick film grown on a 5 nm thick Ru substrate from Ni(dmamp) <sub>2</sub> , formic acid, and <b>2</b> for 1,000 cycles at 150 °C .....	134
<b>Figure 124.</b>	Cross-sectional SEM image of a 20 nm thick film grown on a 5 nm thick Co substrate from Ni(dmamp) <sub>2</sub> , formic acid, and <b>2</b> for 1,000 cycles at 150 °C .....	134
<b>Figure 125.</b>	XPS survey scans of a 32 nm thick film grown from Ni(dmamp) <sub>2</sub> , formic acid, and <b>2</b> on Pd at 150 °C .....	135

<b>Figure 126.</b>	XPS Ni 2p ionization region of a 32 nm thick film grown from Ni(dmamp) <sub>2</sub> , formic acid, and <b>2</b> on Pd at 150 °C .....	136
<b>Figure 127.</b>	Cross-sectional SEM image of a 32 nm thick film grown on a 5 nm thick Ru substrate from <b>4</b> , formic acid, and <b>2</b> for 1,000 cycles at 180 °C .....	137
<b>Figure 128.</b>	Top-down SEM image of a 35 nm thick film grown on Cu from <b>4</b> , formic acid, and <b>2</b> for 1,000 cycles at 180 °C.....	137
<b>Figure 129.</b>	XPS survey scans of a 32 nm thick film grown from <b>4</b> , formic acid, and <b>2</b> on Ru at 180 °C.....	138
<b>Figure 130.</b>	XPS Ni 2p ionization region of a 32 nm thick film grown from <b>4</b> , formic acid, and <b>2</b> on Ru at 180 °C.....	138
<b>Figure 131.</b>	Cross-sectional SEM image of a 30 nm thick film grown on a 5 nm thick Ru substrate from <b>5</b> , formic acid, and <b>2</b> for 1,000 cycles at 225 °C .....	139
<b>Figure 132.</b>	Cross-sectional SEM image of a 32 nm thick film grown on SiO <sub>2</sub> from <b>5</b> , formic acid, and <b>2</b> for 1,000 cycles at 225 °C.....	140
<b>Figure 133.</b>	XPS survey scans of a 30 nm thick film grown from <b>5</b> , formic acid, and <b>2</b> on Ru at 225 °C.....	140
<b>Figure 134.</b>	XPS Fe 2p ionization region of a 30 nm thick film grown from <b>5</b> , formic acid, and <b>2</b> on Ru at 225 °C after 2 min of sputtering.....	141
<b>Figure 135.</b>	Cross-sectional SEM image of a 38 nm thick film grown on a 5 nm thick Ru substrate from <b>6</b> , formic acid, and <b>2</b> for 1,000 cycles at 225 °C .....	142
<b>Figure 136.</b>	Cross-sectional SEM image of a 129 nm thick film grown on SiO <sub>2</sub> from <b>6</b> , formic acid, and <b>2</b> for 1,000 cycles at 225 °C.....	142
<b>Figure 137.</b>	XPS survey scans of a 129 nm thick film grown from <b>6</b> , formic acid, and <b>2</b> on SiO <sub>2</sub> at 225 °C.....	143
<b>Figure 138.</b>	XPS Cr 2p ionization region of a 129 nm thick film grown from <b>6</b> , formic acid, and <b>2</b> on SiO <sub>2</sub> at 225 °C after 2 min of sputtering.....	143
<b>Figure 139.</b>	Cross-sectional SEM image of nanoparticulate growth on SiO <sub>2</sub> from <b>7</b> , formic acid, and <b>2</b> for 1,000 cycles at 225 °C.....	144

<b>Figure 140.</b>	Top-down SEM image of nanoparticulate growth on a 5 nm thick Ru substrate from <b>7</b> , formic acid, and <b>2</b> for 1,000 cycles at 225 °C.....	145
<b>Figure 141.</b>	XPS survey scans of nanoparticulate growth from <b>7</b> , formic acid, and <b>2</b> on SiO <sub>2</sub> at 225 °C.....	145
<b>Figure 142.</b>	XPS Mn 2p ionization region of nanoparticulate growth from <b>7</b> , formic acid, and <b>2</b> on SiO <sub>2</sub> at 225 °C after 2 min of sputtering.....	146
<b>Figure 143.</b>	Cross-sectional SEM image of nanoparticles grown on a 5 nm thick Co substrate from Cu(dmap) <sub>2</sub> , formic acid, and <b>2</b> for 1,000 cycles at 150 °C.....	147
<b>Figure 144.</b>	Top-down SEM image of nanoparticles grown on a 5 nm thick Co substrate from Cu(dmap) <sub>2</sub> , formic acid, and <b>2</b> for 1,000 cycles at 150 °C.....	147
<b>Figure 145.</b>	XPS survey scans of nanoparticulate growth from Cu(dmap) <sub>2</sub> , formic acid, and <b>2</b> on Si-H at 150 °C.....	148
<b>Figure 146.</b>	XPS Cu 2p ionization region of nanoparticulate growth from Cu(dmap) <sub>2</sub> , formic acid, and <b>2</b> on Si-H at 150 °C after 2 min of sputtering.....	148
<b>Figure 147.</b>	Synthesis of metal diazadienyl complexes.....	153
<b>Figure 148.</b>	<sup>1</sup> H NMR spectra of the ligand backbone (imine) proton for diamagnetic <sup>t</sup> Bu <sub>2</sub> DAD complexes.....	154
<b>Figure 149.</b>	<sup>1</sup> H NMR spectra of the <i>tert</i> -butyl proton for diamagnetic <sup>t</sup> Bu <sub>2</sub> DAD complexes.....	154
<b>Figure 150.</b>	Perspective view of <b>13</b> with thermal ellipsoids at the 50% probability level.....	155
<b>Figure 151.</b>	TGA/DTA analyses of <b>14</b> .....	165
<b>Figure 152.</b>	Saturation plot of <b>14</b> using 5.0 s pulses of ozone at 325 °C. The secondary axis shows the consumption rate of <b>14</b> as a function of the pulse length of <b>14</b> .....	166
<b>Figure 153.</b>	Saturation plot of ozone using 5.0 s pulses of <b>14</b> at 325 °C.....	166
<b>Figure 154.</b>	Plot of growth rate versus temperature using 5.0 s pulses of <b>14</b> and 5.0 s pulses of ozone for 2,000 cycles.....	167

<b>Figure 155.</b>	Plot of film thickness versus number of ALD cycles using <b>14</b> and ozone at 325 °C.....	167
<b>Figure 156.</b>	Cross-sectional SEM image of a 56 nm thick film grown on Si(100) from <b>14</b> and ozone for 3,000 cycles at 325 °C.....	168
<b>Figure 157.</b>	AFM images of 3 $\mu\text{m}^2$ regions of films grown from <b>14</b> and ozone on Si(100) for 2,000 cycles: (a) 300 °C, (b) 325 °C, (c) 350 °C .....	168
<b>Figure 158.</b>	Powder XRD spectra of a 36 nm thick film grown from <b>14</b> and ozone on Si(100) for 2,000 cycles at 325 °C. The film was annealed under an N <sub>2</sub> atmosphere .....	169
<b>Figure 159.</b>	Powder XRD spectra of a 36 nm thick film grown from <b>14</b> and ozone on Si(100) for 2,000 cycles at 325 °C. The film was annealed under an O <sub>2</sub> atmosphere .....	170
<b>Figure 160.</b>	XPS survey scans of a 35 nm thick film grown from <b>14</b> and ozone on Si(100) at 300 °C .....	171
<b>Figure 161.</b>	XPS survey scans of a 36 nm thick film grown from <b>14</b> and ozone on Si(100) at 325 °C .....	172
<b>Figure 162.</b>	XPS survey scans of a 36 nm thick film grown from <b>14</b> and ozone on Si(100) at 350 °C .....	172
<b>Figure 163.</b>	XPS B 1s ionization region of 35–36 nm thick films grown from <b>14</b> and ozone on Si(100) after 2 min of sputtering .....	173
<b>Figure 164.</b>	XPS Mn 2p ionization region of 35–36 nm films grown from <b>14</b> and ozone on Si(100) after 2 min of sputtering .....	173
<b>Figure 165.</b>	TOF-ERDA depth profile of a 35 nm thick film grown from <b>14</b> and ozone on Si(100) at 300 °C.....	174
<b>Figure 166.</b>	TOF-ERDA depth profile of a 35 nm thick film grown from <b>14</b> and ozone on Si(100) at 325 °C.....	174
<b>Figure 167.</b>	TOF-ERDA depth profile of a 35 nm thick film grown from <b>14</b> and ozone on Si(100) at 350 °C.....	174
<b>Figure 168.</b>	Plot of reflectance versus wavelength of films grown from <b>14</b> and ozone on Si(100) at 325 °C. The pulse of <b>14</b> was varied with a constant 5.0 s ozone pulse.....	175

<b>Figure 169.</b>	Plot of reflectance versus wavelength of films grown from <b>14</b> and ozone on Si(100) at 325 °C. The pulse of ozone was varied with a constant 5.0 s <b>14</b> pulse .....	175
<b>Figure 170.</b>	TGA/DTA analyses of <b>16</b> .....	176
<b>Figure 171.</b>	Saturation plot of <b>16</b> using 5.0 s pulses of ozone at 325 °C. The secondary axis shows the consumption rate of <b>16</b> as a function of the pulse length of <b>16</b> .....	177
<b>Figure 172.</b>	Saturation plot of ozone using 6.0 s pulses of <b>16</b> at 325 °C .....	177
<b>Figure 173.</b>	Plot of film thickness versus number of ALD cycles using <b>16</b> and ozone at 325 °C .....	178
<b>Figure 174.</b>	Cross-sectional SEM image of a 78 nm thick film grown on Si(100) from <b>16</b> and ozone for 2,000 cycles at 325 °C .....	178
<b>Figure 175.</b>	XPS survey scans of a 78 nm thick film grown from <b>16</b> and ozone on Si(100) at 325 °C .....	179
<b>Figure 176.</b>	XPS B 1s ionization region of a 78 nm thick film grown from <b>16</b> and ozone on Si(100) after 2 min of sputtering .....	180
<b>Figure 177.</b>	XPS Co 2p ionization region of a 78 nm thick film grown from <b>16</b> and ozone on Si(100) after 2 min of sputtering .....	180
<b>Figure 178.</b>	TOF-ERDA depth profile of a 78 nm thick film grown from <b>16</b> and ozone on Si(100) at 325 °C .....	181
<b>Figure 179.</b>	Plot of reflectance versus wavelength of a 78 nm thick film grown from <b>16</b> and ozone on Si(100) at 325 °C. The applied pulses of <b>16</b> and ozone were 6.0 and 5.0 s, respectively .....	181
<b>Figure 180.</b>	Cross-sectional SEM image of a 76 nm thick film grown on Si(100) from <b>15</b> and ozone for 4,000 cycles at 325 °C .....	182
<b>Figure 181.</b>	TGA/DTA analyses of <b>17</b> .....	183
<b>Figure 182.</b>	Cross-sectional SEM image of a 56 nm thick film grown on Si(100) from <b>17</b> and ozone for 4,000 cycles at 325 °C .....	184
<b>Figure 183.</b>	Perspective view of <b>20</b> with thermal ellipsoids at the 50% probability level .....	186

<b>Figure 184.</b>	Perspective views of the two half-molecules comprising the asymmetric unit of <b>21</b> with thermal ellipsoids at the 50% probability level.....	188
<b>Figure A1.</b>	Thermal analysis of (2- <i>tert</i> -butylallyl)Co(CO) <sub>3</sub> after heating to various temperatures .....	199



## LIST OF CHARTS

<b>Chart 1.</b>	Monoanionic ligands used for vapor deposition precursors .....	15
<b>Chart 2.</b>	Titanium precursors used for vapor deposition processes .....	19
<b>Chart 3.</b>	Vanadium precursors used for vapor deposition processes .....	21
<b>Chart 4.</b>	Chromium precursors used for vapor deposition processes .....	22
<b>Chart 5.</b>	Manganese precursors used for vapor deposition processes.....	24
<b>Chart 6.</b>	Iron precursors used for vapor deposition processes .....	25
<b>Chart 7.</b>	Cobalt precursors used for vapor deposition processes .....	28
<b>Chart 8.</b>	Nickel precursors used for vapor deposition processes .....	32
<b>Chart 9.</b>	Copper precursors used for vapor deposition processes .....	40
<b>Chart 10.</b>	Zinc precursors used for vapor deposition processes .....	42
<b>Chart 11.</b>	Structures of <b>1</b> and <b>2</b> .....	46
<b>Chart 12.</b>	Three forms of the redox non-innocent $\alpha$ -diimine ligand: (a) neutral ligand, (b) radical monoanion, (c) dianion .....	152

## LIST OF ABBREVIATIONS

<u>ABBREVIATION</u>	<u>LONG FORM</u>
AACVD .....	Aerosol-Assisted Chemical Vapor Deposition
acac .....	Acetylacetonate ( $\beta$ -Diketonate)
acnac .....	$\beta$ -Ketiminate
AES .....	Auger Electron Spectroscopy
AFM .....	Atomic Force Microscopy
ALD .....	Atomic Layer Deposition
APCVD .....	Atmospheric Pressure Chemical Vapor Deposition
at.....	Atoms
at.% .....	Atomic %
ATR.....	Attenuated Total Reflectance
BTMSA.....	Bis(trimethylsilyl)acetylene
CCTBA .....	$\mu^2$ - $\eta^2$ -( <i>tert</i> -Butylacetylene)-dicobalthexacarbonyl
CHD .....	2-Methyl-1,4-bis(trimethylsilyl)-2,5-cyclohexadiene
CIGS .....	Copper Indium Gallium Diselenide
CIS .....	Copper Indium Diselenide
CMOS .....	Complimentary Metal-Oxide Semiconductor
CMP .....	Chemical Mechanical Planarization
COD .....	1,5-Cyclooctadiene
Cp.....	Cyclopentadienyl
Cp* .....	1,2,3,4,5-Pentamethylcyclopentadienyl

CV.....	Cyclic Voltammetry
CVD.....	Chemical Vapor Deposition
CZTS.....	Copper Zinc Tin Sulfide
deacam.....	N,N-diethylacetoacetamide
DFT.....	Density Functional Theory
DHP.....	1,4-Bis(trimethylsilyl)-1,4-dihydropyrazine
DLI.....	Direct Liquid Injection
dmamb.....	1-Dimethylamino-2-methyl-2-butoxide
dmamp.....	1-Dimethylamino-2-methyl-2-propoxide
dmap.....	1-Dimethylamino-2-propoxide
DME.....	Dimethoxyethane
DMF.....	Dimethylformamide
DRAM.....	Dynamic Random Access Memory
DTA.....	Differential Thermal Analysis
DVTMSO.....	1,2-Divinyltetramethyl-disiloxane
ECD.....	Electrochemical Deposition
ECP.....	Electrochemical Plating
EDS.....	Energy-Dispersive X-ray Spectroscopy
en.....	Ethylenediamine
ERDA.....	Elastic Recoil Detection Analysis
EtCp.....	Ethylcyclopentadienyl
EUV.....	Extreme Ultraviolet
FWHM.....	Full Width at Half Maximum

G2.....	Gaussian-2 Composite Method
hfac.....	1,1,1,5,5,5-Hexafluoro-2,4-pentanedionate
hfip.....	N <sup>2</sup> -hydroxyhexafluoroisopropyl-N <sup>1</sup>
hfod.....	2,2-Dimethyl-6,6,7,7,8,8,8-heptafluoro-3,5-octanedionate
HVM.....	High-Volume Manufacturing
<sup>i</sup> Pr <sub>2</sub> DAD.....	1,4-Di-isopropyl-1,3-diazabutadienyl
IR.....	Infrared Spectroscopy
Ktfaa.....	2-Imino-pen-en-trifluoro-acetate
LCVD.....	Laser-Assisted Chemical Vapor Deposition
MeCp.....	Methylcyclopentadienyl
MHY.....	2-Methyl-1-hexene-3-yne
MOSFET.....	Metal Organic Semiconducting Field Effect Transistor
MP.....	Møller-Plesset Perturbation Theory
MPTMS.....	(3-Mercaptopropyl)trimethoxysilane
MRAM.....	Magneto-resistive Random Access Memory
nacnac.....	β-Diketiminate
NHC.....	N-Heterocyclic Carbene
NICS.....	Nucleus-Independent Chemical Shift
ohapim.....	2-(1-Iminoethyl)phenoxide
ohppim.....	2-(1-Iminopropyl)phenoxide
O <sup>t</sup> Bu.....	<i>tert</i> -Butoxy
OTS.....	Octadecyltrichlorosilane
PEALD.....	Plasma-Enhanced Atomic Layer Deposition
PECVD.....	Plasma-Enhanced Chemical Vapor Deposition

PMe <sub>3</sub> .....	Trimethylphospine
PVD.....	Physical Vapor Deposition
PyrIm <sup>Et</sup> .....	N-ethyl-2-pyrrolylaldiminate
PyrIm <sup>iPr</sup> .....	N-isopropyl-2-pyrrolylaldiminate
Pz.....	Pyrazolate
RBS.....	Rutherford Backscattering Spectrometry
RF.....	Radio Frequency
RMS.....	Root Mean Square
rt.....	Room Temperature
RTA.....	Rapid Thermal Annealing
S-NHC-CuH.....	1,3-Diphenyl-4,5-imidazolidinedithione Copper Hydride
SAM.....	Self-Assembled Monolayer
SEM.....	Scanning Electron Microscopy
SHG.....	Second Harmonic Generating
SiV.....	Stress-Induced Voiding
<sup>t</sup> Bu <sub>2</sub> DAD.....	1,4-Di- <i>tert</i> -butyl-1,3-diazabutadienyl
TEM.....	Transmission Electron Microscopy
TFAA.....	Trifluoroacetic Acid
TGA.....	Thermogravimetric Analysis
THF.....	Tetrahydrofuran
TMEDA.....	Tetramethylethylenediamine
tmhd.....	2,2,6,6-Tetramethyl-3,5-heptanedionate
TMS.....	Trimethylsilyl

TOF.....	Time-of-Flight
Trp.....	Tris(pyrazolyl)borate
Trz.....	Triazolate
TTA.....	2-Thenoyltrifluoroacetate
UV.....	Ultraviolet
UV-Vis.....	Ultraviolet-Visible Spectroscopy
UV/VIS/NIR.....	Ultraviolet/Visible/Near Infrared
VTMS.....	Vinyltrimethylsilane
wt.%.....	Weight %
XPS.....	X-ray Photoelectron Spectroscopy
XRD.....	X-ray Diffractometry
XRF.....	X-ray Fluorescence Spectroscopy
ZTO.....	Zinc Tin Oxide
1.....	2-Methyl-1,4-bis(trimethylsilyl)-2,5-cyclohexadiene
2.....	1,4-Bis(trimethylsilyl)-1,4-dihydropyrazine
3.....	Bis(1,4-di- <i>tert</i> -butyl-1,3-diazabutadienyl)cobalt(II)
4.....	Bis(1,4-di- <i>tert</i> -butyl-1,3-diazabutadienyl)nickel(II)
5.....	Bis(1,4-di- <i>tert</i> -butyl-1,3-diazabutadienyl)iron(II)
6.....	Bis(1,4-di- <i>tert</i> -butyl-1,3-diazabutadienyl)chromium(II)
7.....	Bis(1,4-di- <i>tert</i> -butyl-1,3-diazabutadienyl)manganese(II)
8.....	Bis(1,4-di- <i>tert</i> -butyl-1,3-diazabutadienyl)magnesium(II)
9.....	Bis(1,4-di- <i>tert</i> -butyl-1,3-diazabutadienyl)titanium(IV)
10.....	Bis(1,4-di- <i>tert</i> -butyl-1,3-diazabutadienyl)zinc(II)

- 11.....Bis(1,4-di-*tert*-butyl-1,3-diazabutadienyl)zirconium(IV)
- 12.....Bis(1,4-di-*tert*-butyl-1,3-diazabutadienyl)aluminum(III)
- 13.....1,4-Di-*tert*-butyl-1,3-diazabutadienyldichloroaluminum(III)
- 14.....Bis(tris(pyrazolyl)borate)manganese(II)
- 15..... Bis(tris(pyrazolyl)borate)iron(II)
- 16.....Bis(tris(pyrazolyl)borate)cobalt(II)
- 17.....Bis(tris(pyrazolyl)borate)nickel(II)
- 18..... Bis(tris(pyrazolyl)borate)copper(II)
- 19.....Bis(tris(pyrazolyl)borate)zinc(II)
- 20.....Bis(tris(pyrazolyl)borate)vanadium(II)
- 21..... Bis(tris(pyrazolyl)borate)chromium(II)

## CHAPTER 1

### Introduction

#### 1.1 Miniaturization of Microelectronic Devices

Since its development in 1947, the transistor has been a fundamental component of modern electronics. In 1965, co-founder of Intel Corporation, Gordon E. Moore, predicted that the number of transistors on an integrated circuit would double every 18–24 months.<sup>1</sup> Keeping pace with this assertion, known as “Moore’s Law”, has supported the exponential growth of transistor density in microelectronic architecture, leading to smaller, faster, and more power-efficient devices. Many of today’s logic devices have gate lengths of 22 nm, a space allowing only 50 silicon atoms between the source and drain. Some commercially-available chips contain features as small as 14 nm.<sup>2</sup> By 2016, transistors are expected to shrink to the 10 nm node.<sup>3</sup> However, continuation of this trend presents formidable challenges. The need to increase photolithographic resolution has motivated the refinement of numerical aperture to compensate for the intrinsic birefringence of lenses,<sup>4</sup> and has spawned new techniques such as multiple patterning, directed self-assembly, and the use of extreme ultraviolet (EUV) light ( $\lambda = 13.5$  nm).<sup>2</sup> Secondly, undesirable topographical effects during chemical mechanical planarization (CMP), such as dishing, scratching, and the propensity to leave remnant particles, become increasingly problematic at smaller scales, requiring continuous improvements to polishing pads and slurries.<sup>2</sup> Finally, conventional materials often fail to support optimal device performance at reduced dimensions and the growth of thin films with absolute thickness control in very high aspect ratio features is limited by traditional methods.<sup>2</sup> Consequently, new precursors and deposition processes must be developed to drive device miniaturization beyond the 10 nm node.<sup>2</sup>



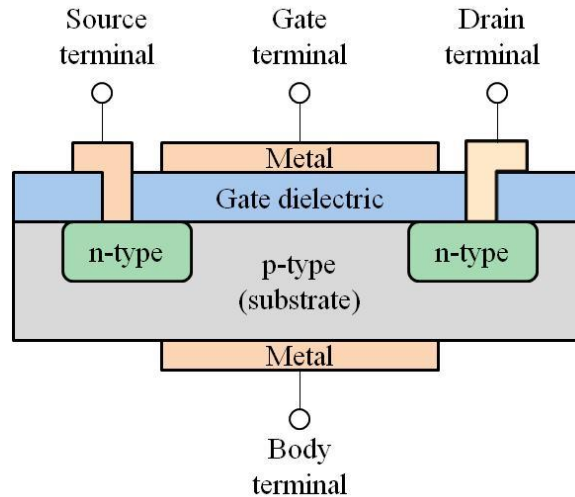
## 1.2 Materials Containing Transition Metal Thin Films

Thin films are ubiquitous in nanotechnology, finding use in magnetic, catalytic, optical, and electrical applications. In microelectronic devices, metallic films are employed as conductors (transistor gates, electrodes, interconnects) and seed/capping layers, while metal oxides and nitrides are used for high- $\kappa$  applications and diffusion barriers, respectively. Transition metal borides are used as hard, refractory, and electrically-conductive materials,<sup>5</sup> while borates demonstrate nonlinear optical behavior,<sup>6</sup> finding use in devices such as frequency converters, waveguides, and switches.<sup>7</sup>

Modern processors employ billions of transistors as electrically-driven switches for parallel computation. The MOSFET is manufactured in a silicon substrate (Figure 1). The conductivity can be altered by the controlled addition of impurity atoms, which support the presence of charged particles (n-type: electrons, p-type: holes). Structures are manufactured with discrete n-type and p-type regions, isolating domains of negative and positive charges through the formation of barriers that prevent the flow of current. The gate is made of a highly-conductive material, separated from the semiconductor by a dielectric. Applying a suitable voltage at the gate attracts electrical charge from the source, lowering the barrier and allowing the formation of a conductive channel between the source and drain. CMOS technology uses both N-channel and P-channel MOSFETS; the basic cell behaving as a pair of switches acting in complementary fashion. However, as the size of the transistor (distance between source and drain) is reduced, quantum tunneling effects prevent sufficient charge separation, requiring the replacement of traditional SiO<sub>2</sub>-based dielectrics with materials more resilient to leakage current (e.g. HfO<sub>2</sub>, ZrO<sub>2</sub>, and TiO<sub>2</sub>).<sup>8</sup> As the interlayer of the gate stack, these high- $\kappa$  dielectrics must

resist diffusion of dopants (e.g. boron, phosphorus) and display adequate capacitance, thermal stability (high recrystallization temperature), and interface properties.

**Figure 1.** N-channel MOSFET structure.



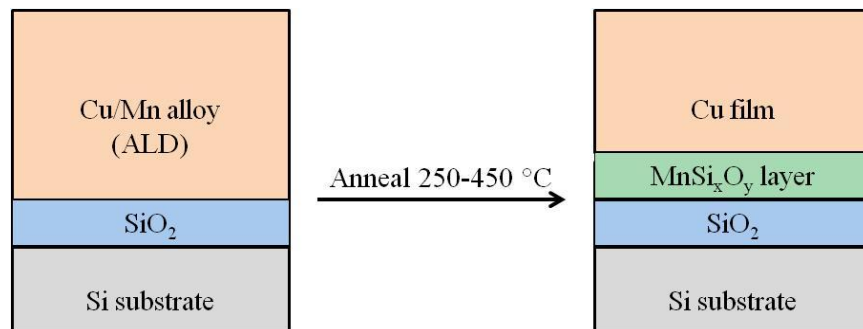
Copper has replaced aluminum as the preferred material for conductive interconnect structures due to its comparatively-low resistivity and relative resistance to electromigration. Metallic Cu is applied to the trenches and vias of circuit elements by a two-step process entailing the growth of a thin seed layer by physical vapor deposition (PVD), followed by bulk-fill electrodeposition.<sup>9</sup> However, Cu demonstrates poor nucleation to insulating substrates, preventing the formation of a continuous seed layer. Additionally, the diffusion of Cu into Si and SiO<sub>2</sub> substrates at the elevated temperatures encountered during device fabrication can result in short circuits. Mitigating these effects requires the use of inert, refractory materials with good adhesion to both Cu and the insulating substrate. Seed layers of metals such as Cr, Co, and Ru have been used to enhance Cu nucleation.<sup>10</sup> Metallization barriers are used to prevent interdiffusion, and optimally consist of highly-dense, amorphous films free of grain boundaries and defects<sup>11</sup> that are resistant to stress-induced voiding (SiV) and electromigration.<sup>12</sup> Nitride-based films such as TaN and WN<sub>x</sub> (x = 0.5–1.0), as well as ternary compositions of these

materials containing carbon or silicon have been investigated as advanced barriers,<sup>13</sup> but may fail at thicknesses of  $\leq 5$  nm.<sup>9</sup> Traditionally, PVD TaN has been used for Cu/Ta/TaN/SiO<sub>2</sub> architectures.<sup>12,14</sup> However, at trench widths  $< 100$  nm, uniform coverage by this method becomes difficult.<sup>12</sup> CVD TiSiN was subsequently proposed, however, SiV in lower-level interconnects and vias resulted from the requisite higher deposition temperatures and poor adhesion to Cu, respectively.<sup>12</sup> WC<sub>x</sub>N<sub>y</sub> films also proved unreliable due to their poor adhesion to Cu.<sup>15</sup> Since future liners may require amorphous layers of only 1–3 sequential atoms with sub-monolayer control,<sup>11</sup> very thin films ( $\leq 5$  nm) of Mn,<sup>12,14,16</sup> Cr, and Ru<sup>17</sup> have emerged as potential Cu diffusion barrier materials.<sup>18</sup>

Although necessary to the interconnect framework, the volume occupied by these seed, barrier, and capping layers decreases the Cu content in trenches and vias, reducing the operating frequency of the circuit through increased electrical resistance.<sup>11</sup> As feature sizes contract, these ancillary layers comprise a greater fraction of available volume at the expense of device performance. The concept of a “self-forming” Cu barrier offers an alternative to the traditional approach. Deposition of a Cu alloy film directly onto SiO<sub>2</sub>, followed by annealing, enables the migration of the alloying element to the alloy/SiO<sub>2</sub> interface, forming a thin barrier layer via reaction with SiO<sub>2</sub>.<sup>14</sup> Exploiting the strength of metal-oxide bonds led to the formation of a self-forming MgO layer from a Cu/Mg alloy after annealing at 600 °C.<sup>19</sup> However, the concurrent reduction of SiO<sub>2</sub> led to free Si atoms that diffused into the Cu interior.<sup>14</sup> The resultant increase in resistivity coupled with the unacceptable thickness (20 nm) of the barrier ruled out Cu/Mg from further consideration.<sup>14</sup> In contrast to Mg and Al, which strongly interact with Cu, Mn has an activity coefficient greater than one, and is easily expelled from Cu to participate in energetically-favorable reactions.<sup>14</sup> The diffusivity of Mn in Cu is faster than the self-diffusivity

of Cu by an order of magnitude at 450 °C.<sup>14</sup> Finally, the  $\Delta G^\circ$  of MnO is slightly larger than that of SiO<sub>2</sub>, therefore, the reduction of SiO<sub>2</sub> was not expected as with MgO formation.<sup>14</sup> Consequently, it was proposed that Mn atoms would quickly migrate to the interface and form a stable oxide before Cu and Si atoms had time to react. Annealing a 150 nm thick 90/10 Cu/Mn alloy film on SiO<sub>2</sub> at 250–450 °C led to migration of the Mn atoms towards the SiO<sub>2</sub> interface, forming a 2–8 nm amorphous MnSi<sub>x</sub>O<sub>y</sub> layer between the SiO<sub>2</sub> and Cu layers (Figure 2),<sup>16</sup> with no Mn present in the SiO<sub>2</sub> layer or Cu interior.<sup>14</sup> The barrier layer resisted Cu diffusion during annealing at 450 °C for up to 100 h.<sup>16</sup> Films annealed at temperatures above 300 °C showed good adhesion and rapid resistivity reduction, suggestive of reaction at the interface and depletion of Mn from the Cu/Mn alloy layer.<sup>14</sup> In addition to thickness reduction, the MnSi<sub>x</sub>O<sub>y</sub> barrier showed leakage current values slightly less than those for a 15 nm PVD Ta layer.<sup>12</sup>

**Figure 2.** PVD of a Cu/Mn alloy for MnSi<sub>x</sub>O<sub>y</sub> diffusion barrier formation.



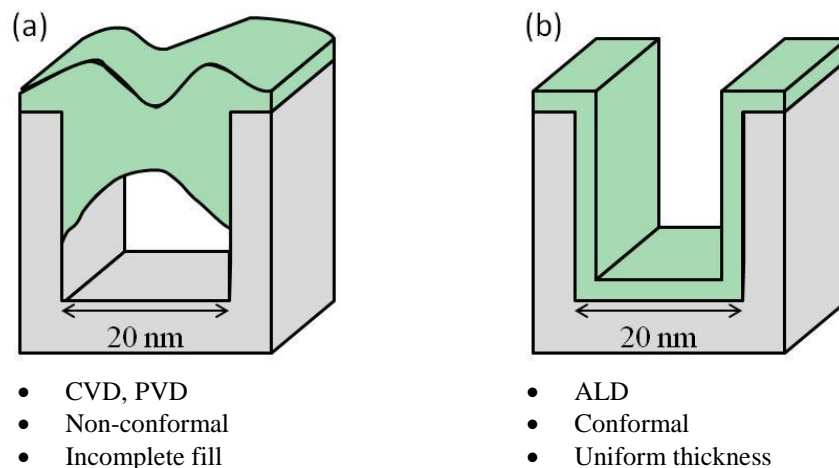
Although MnSi<sub>x</sub>O<sub>y</sub> self-forming barrier layers have proven effective in Cu dual damascene interconnect structures, PVD is incapable of producing conformal Cu/Mn alloy films in high aspect ratio features.<sup>20</sup> More recently, a low-temperature, plasma-enhanced atomic layer deposition (PEALD) process demonstrated control of Mn content from 0–10 at.%, with subsequent annealing affording a 3 nm thick barrier of MnSi<sub>x</sub>O<sub>y</sub>.<sup>20</sup> However, radical

recombination resulting in film nonuniformity may limit this approach to the 30 nm node.<sup>20</sup> Last year, Winter and coworkers developed novel precursors toward the ALD of Cu/Mn/Cu/SiO<sub>2</sub> stacks, which showed migration of Mn to the Si layer, diagnostic of a self-forming barrier.<sup>21</sup> This development has significant implications for the widespread use of Cu/Mn self-forming barrier layers in future microelectronic devices.

### 1.3 Deposition Methods

Improving device complexity while lowering cost requires increasing the quantity and efficiency of transistors on an integrated circuit. This objective has driven the evolution of thin film deposition processes. Established methods, such as physical vapor deposition (PVD)<sup>22</sup> and chemical vapor deposition (CVD),<sup>23</sup> are typically less expensive, but lack the thickness control and conformality required for future applications. By contrast, atomic layer deposition (ALD) offers sub-nm thickness control of conformal films in high aspect ratio features and on 3D architectures (Figure 3).<sup>24</sup>

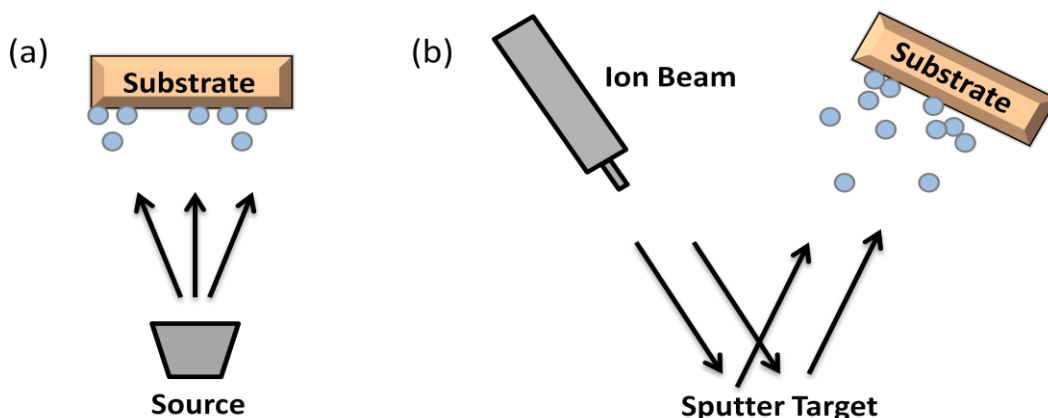
**Figure 3.** Comparison of film coverage and conformality by (a) CVD, PVD, (b) ALD processes.



### 1.3.1 Physical Vapor Deposition

PVD encompasses numerous techniques, including laser-ablation deposition, vacuum-arc-based deposition, evaporation, and sputter deposition. These methods involve the removal of atoms from a source material for deposition on a substrate, either by evaporation or by high-energy particle bombardment by photons, electrons, atoms, ions, or molecules in a vacuum system.<sup>22</sup> For evaporative deposition, atoms are thermally emitted by heating a region of the source material beyond its melting point, with the sample in the direct line-of-sight to the source (Figure 4a).<sup>22</sup> The distance between the sample and source is typically 10–100 cm, with the deposition rate roughly scaling as the inverse of the distance squared.<sup>22</sup> The evaporated flux can sustain very high deposition rates (~100 nm/min), supporting the efficient coating of large objects such as mirrors, windows, telescope reflectors, and rolls of plastic film.<sup>22</sup> By contrast, sputter deposition uses energetic particles (50–2000 eV) to bombard a surface (known as a target).<sup>22</sup> During these collisions, near-surface atoms dislodged with sufficient energy to overcome the surface binding energy are emitted from the target (Figure 4b).

**Figure 4.** Film growth by (a) evaporative PVD, (b) sputter PVD.



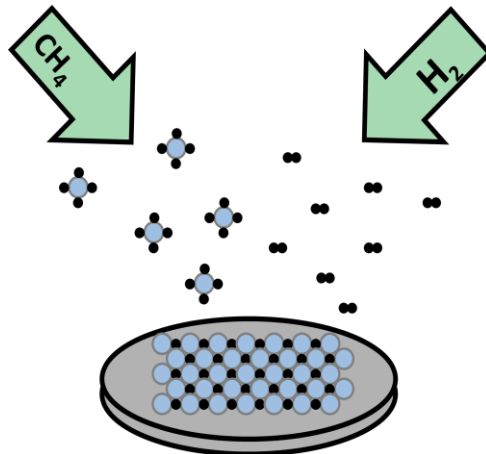
However, despite its widespread use in manufacturing, the directional nature of sputtering restricts the number of atoms entering a trench or via, typically limiting its application to features

with aspect ratios of  $< 5:1$ .<sup>11</sup> Sputter-coating features of higher aspect ratio often necessitates improved control of the depositing trajectories through the use of collimators or in-flight ionization.<sup>11</sup>

### 1.3.2 Chemical Vapor Deposition

CVD is a technique whereby the substrate is simultaneously exposed to one or more gaseous precursors in a vacuum chamber typically heated to  $> 600\text{ }^\circ\text{C}$  (Figure 5).<sup>24e</sup> Gas-phase and surface reactions result in film growth. Particle formation from gas-phase reactions often produces non-conformal, granular films<sup>24e</sup> and can be reduced by decreasing the pressure in the deposition chamber, resulting in fewer collisions between gaseous molecules.<sup>23c</sup> CVD obviates the step coverage limitations inherent to PVD at feature sizes  $< 0.25\text{ }\mu\text{m}$ .<sup>25</sup> However, thermal decomposition of precursors often results in uncontrolled growth leading to morphology degradation and impurity incorporation in the film. These factors render CVD inappropriate for many high aspect ratio applications. Also, high temperature processes require longer preheating and cool-down times and are incompatible with polymer-based low- $\kappa$  dielectrics, which are often limited to temperatures  $< 200\text{ }^\circ\text{C}$ .<sup>11</sup>

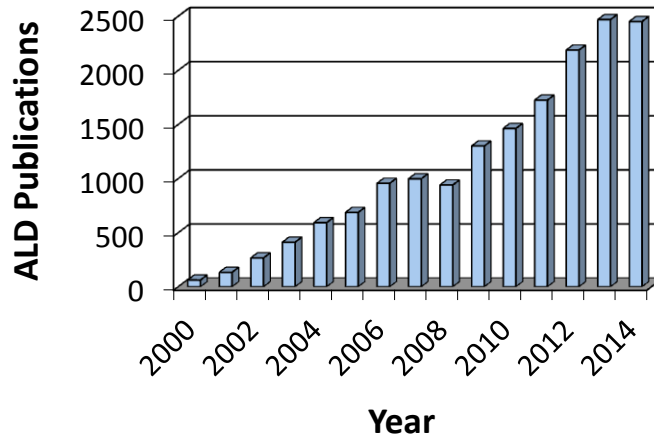
**Figure 5.** Film growth by CVD.



### 1.3.3 Atomic Layer Deposition

The concept of ALD was first proposed in 1952, in the Ph.D. thesis of V. B. Aleskovskii.<sup>26</sup> Working in Finland in the mid-1970s, Tuomo Suntola later developed the technology (originally referred to as atomic layer epitaxy), toward the manufacturing of thin film electroluminescent flat-panel displays.<sup>27–28</sup> In 1989, advances in alkyl precursor development and III–V compounds led to the discovery of the most widely-studied ALD process to date, Al<sub>2</sub>O<sub>3</sub> films from trimethylaluminum and water.<sup>29</sup> By offering atomic-level thickness control and uniform coverage of high aspect ratio features,<sup>24</sup> ALD supports the precision demands required of next-generation devices.<sup>2,9–10</sup> Consequently, interest in ALD continues to increase, as evidenced by the rise in the number of annual ALD publications (Figure 6).

**Figure 6.** Number of ALD publications per year from 2000–2014, per SciFinder.

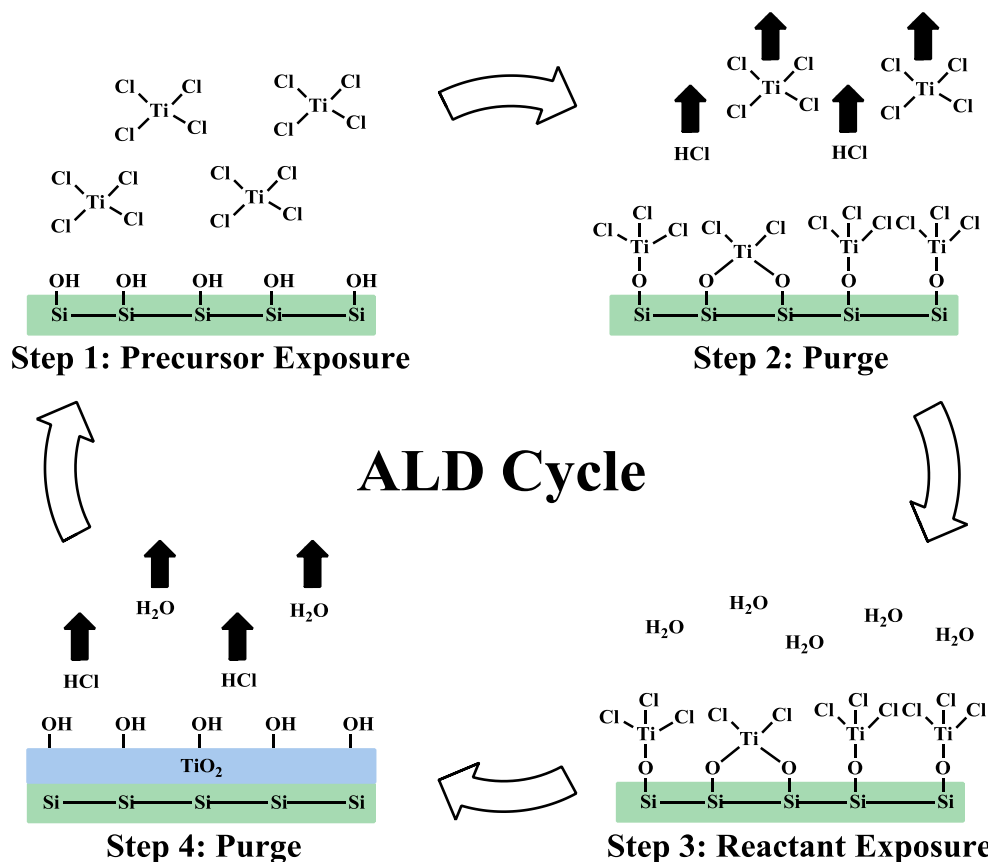


In essence, ALD is an advanced variant of CVD, whereby precursor vapors are delivered to the substrate surface by alternating pulses, typically in a four-step sequence.<sup>24a–b</sup> The metal precursor is transported as a vapor by an inert gas to the reactor, where it adsorbs to, or reacts with surface sites on the substrate. Once the surface is saturated, an inert gas purge removes residual precursor and reaction byproducts. A coreagent is then pulsed into the reactor, where it



reacts with the adsorbed metal precursor, affording a portion of the film. A final inert gas purge removes excess coreagent and byproducts, concluding one growth cycle (Figure 7).<sup>24</sup> Surface saturation supports self-limited growth, and exact reagent stoichiometries are unnecessary.<sup>24</sup> This stepwise process is repeated a plurality of times until the desired film thickness is achieved.<sup>24b</sup>

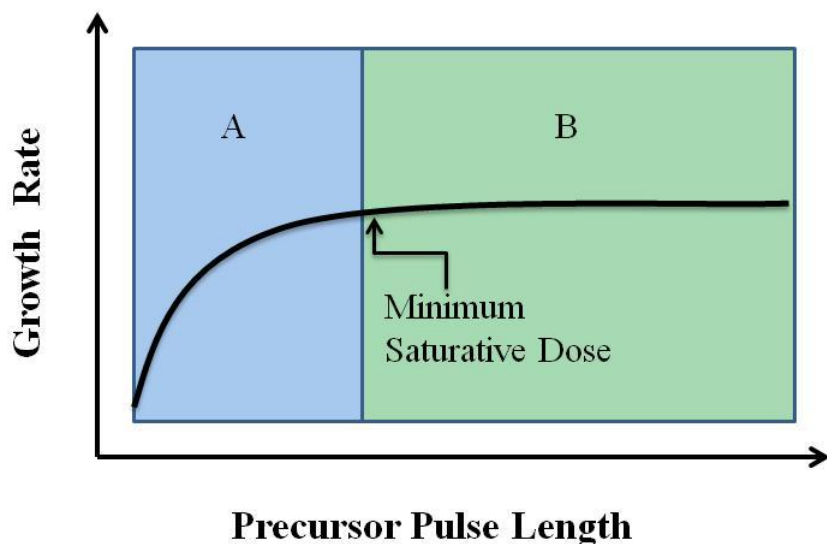
**Figure 7.** A typical ALD process:  $\text{TiCl}_4$  reacts with  $\text{H}_2\text{O}$  toward the growth of  $\text{TiO}_2$  films.



Unlike CVD, where high temperatures often result in uncontrolled growth by precursor decomposition, ALD processes are defined by a self-limited growth mechanism, at temperatures precluding thermal decomposition of the precursors. Reactions are driven by the formation of strong chemical bonds (e.g. metal-oxygen, silicon-halogen, etc.) and the formation of

entropically-favorable gaseous byproducts. Although PVD and CVD offer higher growth rates, the conformality and level of control offered by ALD is of greater relevance for many applications. The hallmark of an ALD process is a region of constant growth on a plot of growth rate versus precursor pulse length (Figure 8).<sup>24</sup> Delivery of a minimum saturative dose is required for the reaction of all available surface sites. For a thermally-stable precursor, this self-limited mechanism prevents additional growth beyond this dose.

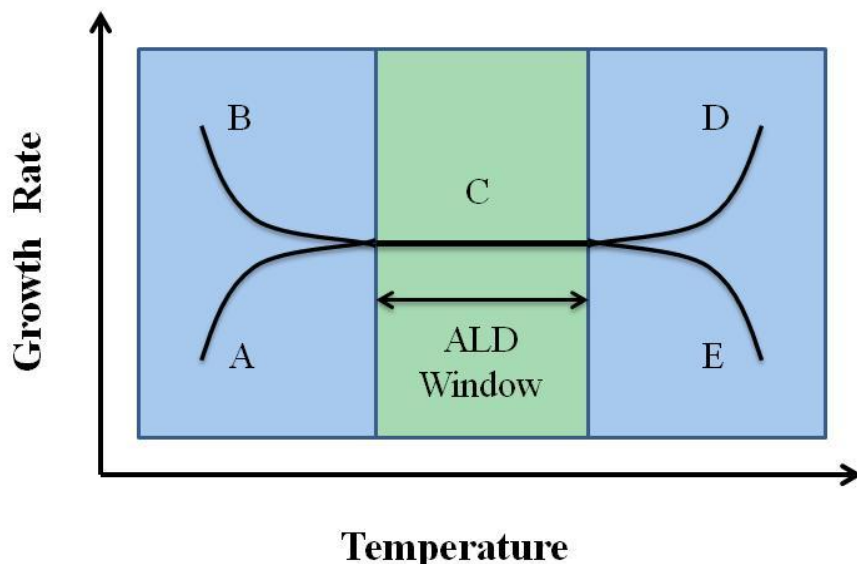
**Figure 8.** Growth rate versus precursor pulse length. Region **A** indicates sub-saturative growth, while region **B** indicates saturative growth.



The thermal behavior of an ALD process is reported as the dependence of growth rate on deposition temperature. An “ALD window” is defined as the region where the growth rate is independent of temperature.<sup>24</sup> The width of the window depends on the physical properties of the precursors and the nature of the chemistry between them. Figure 9 depicts an ALD window (**C**) along with areas corresponding to increased growth rate due to precursor condensation (**B**) and thermal decomposition (**D**, CVD-type growth), and decreased growth rate due to insufficient precursor reactivity (**A**) and desorption of the substrate-bound precursor or loss of surface

reactive sites (**E**). The presence of an ALD window is typical of most ALD processes, though not required for self-limited growth. A wide ALD window allows for a fixed growth rate during temperature fluctuations<sup>24</sup> and overlapping ALD windows enable the deposition of different materials (e.g. multilayer films, metal alloys, etc.) at a constant substrate temperature.

**Figure 9.** Growth rate versus deposition temperature, illustrating regions **A**: insufficient precursor reactivity, **B**: precursor condensation, **C**: ALD window, **D**: precursor decomposition, and **E**: desorption of precursor from the substrate or surface site deactivation.



A plot of film thickness versus the number of cycles should be linear when saturative precursor doses are applied.<sup>24e</sup> The slope of this line indicates the saturative growth rate, while the extrapolated y-intercept gives insight to potential nucleation issues and crosses the origin for ideal processes. Typically, material is deposited by ALD at a rate of 0.1–3.0 Å/cycle.<sup>24a</sup>

The growth temperature of an ALD process depends on the thermal behavior and chemical reactivity of the precursors and the desired qualities of the film. Elevated temperatures may be used to increase the density of certain metallic films or induce crystallinity. The

crystalline structure of a film is often temperature dependent, and strongly affects the properties of oxide films.<sup>30</sup> Lower temperatures characteristic of many ALD processes curtail the agglomeration of highly surface-mobile species (e.g. Cu). Surface migration of metal atoms can result in island-type growth, rough films, or void formation, all of which can compromise device performance. ALD processes  $\leq 100$  °C tend to avoid these deleterious effects.

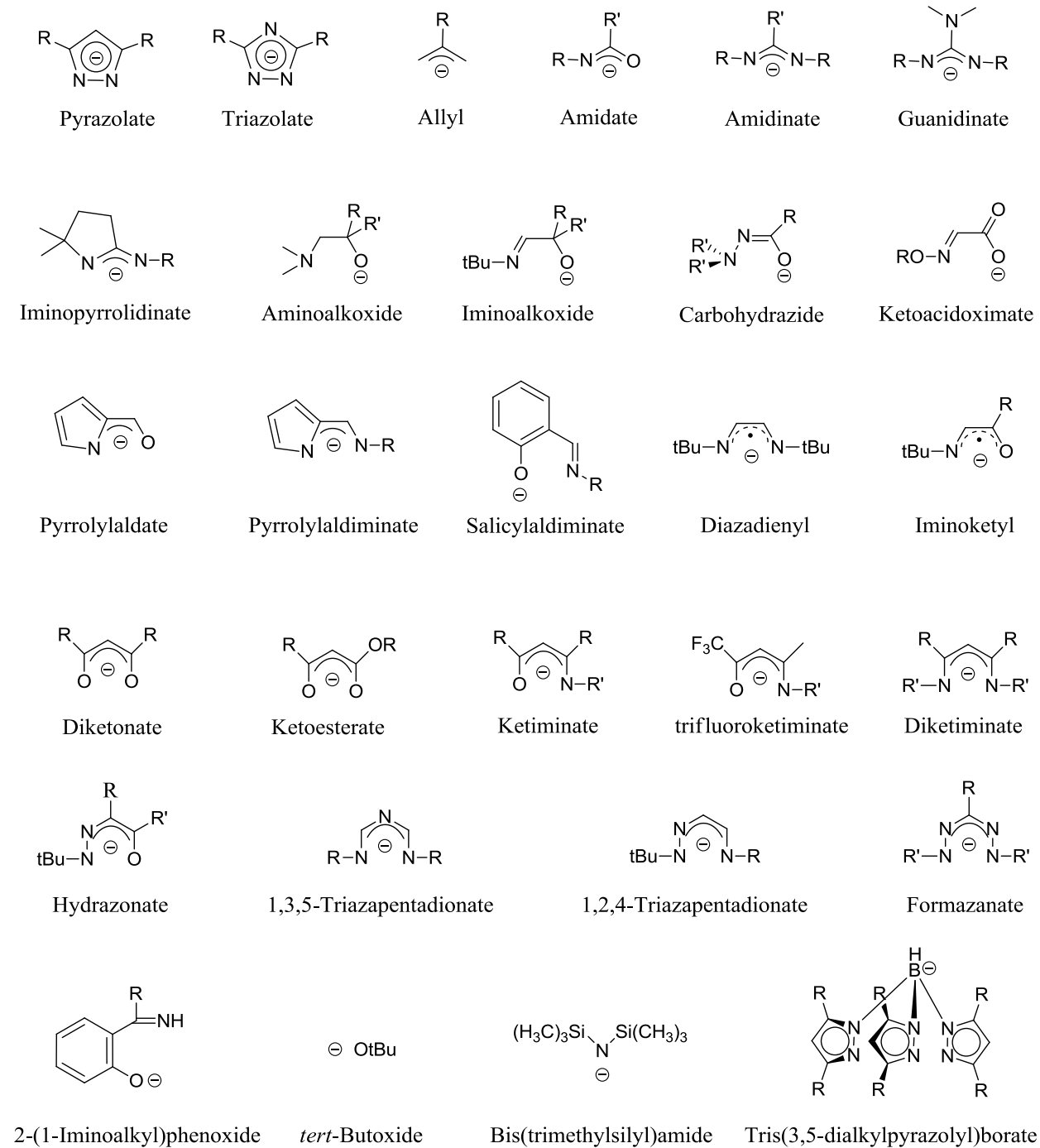
#### 1.4 ALD Fundamentals

ALD precursors must possess adequate volatility, thermal stability, and chemical reactivity toward coreagents to facilitate film growth.<sup>24a-b</sup> The structure of the ligand has a strong effect on the properties of the metal precursor. Ligands can be categorized as either anionic or neutral. Some anionic ligands that have been used for vapor deposition precursors include alkoxides,  $\beta$ -diketonates, amidinates, carbohydrazides, diazadienes, hydrazonates, triazapentadienes, pyrrolylaldiminates,  $\beta$ -diketiminates, cyclopentadienes, and halides (Chart 1). Neutral ligands that have been used for precursors include phosphines, vinyltrimethylsilanes, and carbonyls.

Sufficient volatility (high vapor pressure) is required for effective mass transport of the precursor, enabling surface saturation. Highly-volatile precursors are typically monomers comprised of low molecular weight ligands. First-row transition metal compounds containing many  $\beta$ -diketonate ligands are oligometric due to insufficient saturation of the metal coordination sphere. While adding bulky substituents to the ligand backbone has afforded monomeric  $\beta$ -diketonate complexes, these also display low volatilities due to increased molecular weight.<sup>31</sup> The sterics and electronic structure of the ligand can also effect the volatility of the metal precursor. The addition of alkyl groups to a ligand can lower the symmetry of the metal precursor, reducing the binding energy of the crystalline lattice, resulting in increased volatility.

Ligands containing aromatic moieties may sublime at higher temperatures due to  $\pi$ -stacking interactions in the solid state. Also, ligands containing NMe<sub>2</sub> groups may sublime at lower temperatures than analogues containing *tert*-butyl groups due to the intermolecular repulsions of the nitrogen lone pairs.<sup>32</sup> Finally, the rotational entropy of a ligand can affect the melting point of the precursor, and thus, its volatility. However, as a general rule, the steric bulk of the ligands should be minimized to maximize the density of precursor molecules adsorbed to the substrate.

Thermal stability of the precursor is required to prevent the incorporation of contaminating elements (e.g. H, C, N, O) into the film by decomposition pathways (CVD-type growth). Precursors that are thermally-stable above 200 °C are often preferred, as these tend to avoid decomposition over extended periods of heating in bubblers and support processes with wider ALD windows.<sup>31</sup> Chelating anionic ligands generally afford higher thermal stabilities, and consequently, higher upper temperature limits for self-limited growth, while neutral ligands typically have low thermal stabilities, as neutral ligand loss often provides a low-temperature decomposition pathway. Precursors with carbonyl ligands are often very volatile; however, facile ligand loss may result in CVD growth contributions in ALD processes at higher temperatures. Conjugated ligands lacking  $\beta$ -hydrogen atoms are desirable, as resonance and the absence of  $\beta$ -hydrogen elimination pathways contribute to greater thermal stability. Alkoxide ligands such as *dmamp* and *dmamp* have been used for Cu and Ni complexes with high volatilities, however, the presence of  $\beta$ -hydrogen atoms impart low thermal stabilities to these precursors.  $\beta$ -diketiminates<sup>33–34</sup> and some amidinates<sup>35–38</sup> are monomeric but may also display low thermal stabilities.  $\alpha$ -Imino alkoxide ligands do not contain  $\beta$ -hydrogen atoms and have been used for precursors containing Co(II), Fe(II), Mn(II), and Cr(II) ions.<sup>39</sup>

**Chart 1.** Monoanionic ligands used for vapor deposition precursors.

Precursors must also demonstrate adsorption or reaction with surface sites and sufficient reactivity toward coreagents to support an acceptable growth rate at the deposition temperature.<sup>40</sup> Consequently, metal ALD is best developed for Mo, W, Cu, Sb and the noble metals. The positive reduction potentials of these metal ions enable the reduction of M(II) precursors to the zero valent state by low-temperature ALD processes.<sup>31</sup> In contrast, cations of electropositive metals have negative reduction potentials,<sup>41</sup> and thus, typically require high temperatures or the use of plasma to facilitate film growth (Table 1).<sup>31</sup> A general lack of strongly-reducing coreagents has greatly limited the ALD of first-row transition metal and other electropositive element films. New chemistry capable of facilitating the low-temperature reduction of first-row transition metal cations is in high demand. A recent report described a set of first-row transition metal complexes using the <sup>t</sup>Bu<sub>2</sub>DAD radical anion ligand which sublime at 85–115 °C/0.05 Torr and are thermally stable to  $\geq 230$  °C.<sup>42</sup> These precursors decompose to metal foils at elevated temperatures by ligand-to-metal electron transfer due to the redox non-innocent nature of the ligand, and thus, offer an interesting route to metal film growth by ALD or CVD.<sup>42</sup>

**Table 1.** Electrochemical potentials of first-row transition metals.<sup>41</sup>

Reaction	E° (V)
Ti(II) + 2e <sup>-</sup> ↔ Ti(0)	-1.630
V(II) + 2e <sup>-</sup> ↔ V(0)	-1.175
Cr(II) + 2e <sup>-</sup> ↔ Cr(0)	-0.913
Mn(II) + 2e <sup>-</sup> ↔ Mn(0)	-1.185
Fe(II) + 2e <sup>-</sup> ↔ Fe(0)	-0.447
Co(II) + 2e <sup>-</sup> ↔ Co(0)	-0.280
Ni(II) + 2e <sup>-</sup> ↔ Ni(0)	-0.257
Cu(II) + 2e <sup>-</sup> ↔ Cu(0)	0.3419
Zn(II) + 2e <sup>-</sup> ↔ Zn(0)	-0.7618

Precursor reactivity may be augmented by the use of an additional energy source such as plasma. PEALD employs the use of high-energy radicals which can increase fragmentation of the surface-bound precursor molecules or enhance the removal of byproducts, offering higher growth rates akin to CVD at reduced temperatures.<sup>11</sup> Plasma sources include O<sub>2</sub>, N<sub>2</sub>, NH<sub>3</sub>, H<sub>2</sub>, and H<sub>2</sub>O vapor. PEALD processes have been reported for numerous metal and metal alloy films, including Ti,<sup>11</sup> Mn,<sup>20</sup> Co,<sup>43-45</sup> Ni,<sup>45-47</sup> and Cu.<sup>20,48</sup> However, plasma species can damage substrates and engage in radical recombination reactions, limiting their availability for conformal surface coverage in high aspect ratio features.<sup>31,49</sup>

Precursor selection typically requires compromise with regard to volatility, thermal stability, and reactivity, highlighting the need for new classes of ligands. Still, other considerations are also important when selecting a precursor or designing an ALD process. In general, liquid precursors are preferred, due to their constant, high vapor pressures and ease of handling. By contrast, the sublimation rate of a solid depends on its particle size, and some solid particles may be inadvertently transported into the deposition zone. Byproducts of the film growth process must be volatile, lest they become incorporated into the growing film. Finally, the chemistry supporting an ALD process is ideally non-toxic, scalable, and cost-effective (relatively simple, high-yield syntheses) for use in high volume manufacturing. Failure to meet these criteria has limited or prevented the ALD of many materials.

The following sections describe the current status of first-row transition metal precursors and vapor deposition processes.



## 1.5 First-row Transition Metal ALD Precursors and Processes

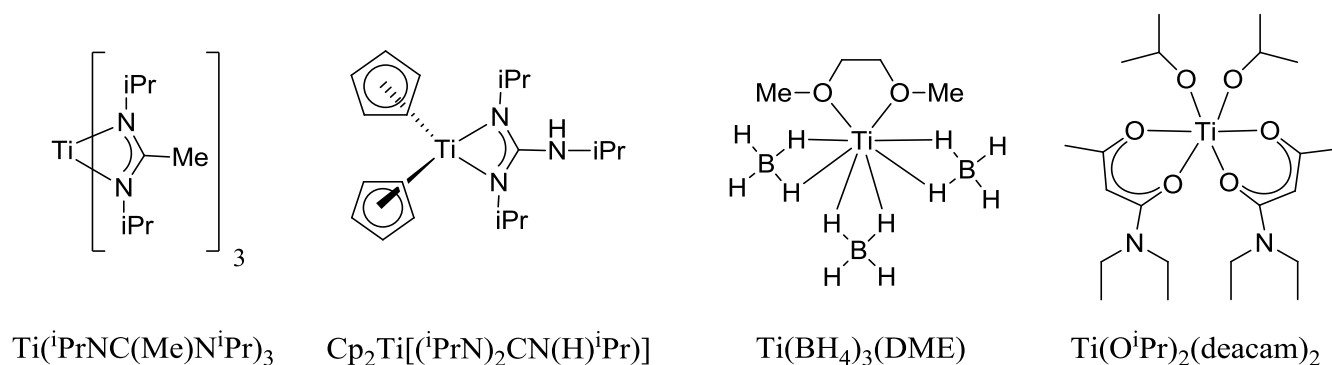
### 1.5.1 Titanium

TiO<sub>2</sub> is a wide-bandgap (3.3 eV) semiconductor used for reflective optical coatings. Films of TiO<sub>2</sub> are used to protect the native oxide layer on titanium surfaces,<sup>50</sup> while films of Ti/TiN serve as liners for dielectric trenches, preventing the diffusion of copper into the dielectric.<sup>11</sup> TiC and TiB<sub>2</sub><sup>51</sup> are metallic ceramics while TiCN is used as a metal coating to increase hardness or reduce friction. Titanium metal films have numerous applications in microelectronic devices, including recent reports of Ti/Al alloy liners for advanced transistor structures.<sup>52–54</sup>

There is an abundance of commercially-available titanium precursors, and numerous examples of non-metallic Ti-containing films have been reported. TiO<sub>2</sub> films were grown by CVD<sup>55</sup> and PEALD<sup>56</sup> using Ti(O<sup>i</sup>Pr)<sub>4</sub>, and by CVD using Ti(O<sup>i</sup>Pr)<sub>2</sub>(deacam)<sub>2</sub>.<sup>57</sup> TiO<sub>2</sub> films were grown by ALD using TiCl<sub>4</sub>,<sup>58</sup> Ti(OMe)<sub>4</sub>,<sup>59–60</sup> Ti(OEt)<sub>4</sub>,<sup>61</sup> Ti(O<sup>i</sup>Pr)<sub>4</sub>,<sup>62</sup> Ti(NMe<sub>2</sub>)<sub>4</sub>,<sup>63–64</sup> Ti(NEt<sub>2</sub>)<sub>4</sub>,<sup>63</sup> and Ti(NMeEt)<sub>4</sub>.<sup>63</sup> Annealing of TiO<sub>2</sub> co-deposited with other metal oxides produced mixed-oxide crystalline species, e.g. Ho<sub>2</sub>Ti<sub>2</sub>O<sub>7</sub>,<sup>62b,65</sup> CoTiO<sub>3</sub>,<sup>60</sup> or CoTi<sub>2</sub>O<sub>5</sub>.<sup>60</sup> TiN films were grown by PECVD using Ti(OEt)<sub>4</sub> with N<sub>2</sub> plasma<sup>66</sup> and by PEALD using Ti(NMe<sub>2</sub>)<sub>4</sub> with NH<sub>3</sub> plasma.<sup>67</sup> Titanium carbide films were grown by low-pressure CVD from Ti(NEt<sub>2</sub>)<sub>4</sub> and NH<sub>3</sub> at 500–700 °C, affording a TiC<sub>x</sub>N<sub>y</sub>O<sub>z</sub> composition,<sup>68</sup> and TiB<sub>2</sub> films were grown by CVD using a single-source precursor, Ti(BH<sub>4</sub>)<sub>3</sub>(MeOCH<sub>2</sub>CH<sub>2</sub>OMe), at temperatures ≥ 170 °C.<sup>51</sup> Novel titanium precursors suited for ALD include a trivalent amidinate complex<sup>37</sup> and a set of heteroleptic guanidates, Cp<sub>2</sub>Ti[(<sup>i</sup>PrN)<sub>2</sub>CNRR'] (R = R' = Me<sub>2</sub>; R = R' = Et<sub>2</sub>; R = H, R' = <sup>i</sup>Pr; R = R' = <sup>i</sup>Pr<sub>2</sub>).<sup>69</sup> However, titanium has a very negative electrochemical potential (Ti(II) → Ti(O), E° = -1.631 V),<sup>41</sup> thus, reports of titanium metal film growth from chemical precursors are scarce.

CVD of Ti/Al alloy films was demonstrated using  $\text{AlH}_3(\text{NMe}_3)$  and  $\text{TiX}_4$  ( $X = \text{Cl}, \text{Br}$ ) at temperatures of 65–127 °C.<sup>70</sup> The aluminum content resulted from the competitive thermal decomposition of  $\text{AlH}_3(\text{NMe}_3)$  to aluminum metal during the reduction of  $\text{TiX}_4$  to titanium metal.<sup>70</sup> Varying the  $\text{AlH}_3(\text{NMe}_3)/\text{TiX}_4$  ratio enabled the tuning of the  $\text{Ti}_x\text{Al}_{1-x}$  film composition by favoring one of the two competing processes (Al co-deposition or  $\text{AlH}_3(\text{NMe}_3)$  reduction of  $\text{TiX}_4$ ).<sup>70</sup> Although carbon, nitrogen, and oxygen impurities were < 1 at.% for conformal films grown at 127 °C, a critical ratio of  $\text{AlH}_3(\text{NMe}_3)/\text{TiCl}_x$  was required to prevent significant halide contamination, likely by removal of chlorine through the formation of  $\text{AlCl}_3$  as a volatile byproduct.<sup>70</sup> An alternate CVD approach to titanium films used  $\text{TiCl}_4$  and sodium vapor, which afforded films that were contaminated with  $\text{NaCl}$ .<sup>71</sup> The lone report of ALD titanium films employed  $\text{TiCl}_4$  and  $\text{H}_2$  plasma at 20–200 °C.<sup>11</sup> Amorphous films were grown at a rate of 1.5–1.7 Å/cycle at substrate temperatures of ~250–400 °C and oxidized immediately upon air exposure.<sup>11</sup> The development of a low-temperature, plasma-free ALD process for the growth of metallic titanium is a presently-intractable problem requiring new chemistry to address the difficult chemical reduction of the titanium cation.

**Chart 2.** Titanium precursors used for vapor deposition processes.



### 1.5.2 Vanadium

Vanadium oxides find numerous applications in catalysis, solid-state batteries, electrochromic devices, and infrared modulators.<sup>72</sup> VO<sub>2</sub> undergoes a reversible thermochromic transition at 68 °C, suggesting its application as a smart window coating,<sup>73–75</sup> while V<sub>2</sub>O<sub>3</sub> displays a crossover in transmission and reflection curves, suggesting its use in solar control applications.<sup>76</sup>

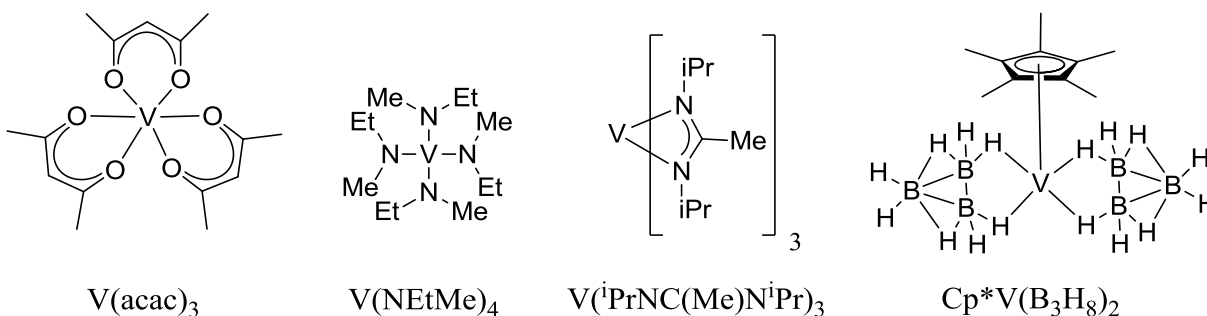
Various methods are known for the preparation of vanadium oxides, including sol-gel, sputtering, vacuum evaporation, spin coating, thermal oxidation of metallic vanadium substrates, and CVD.<sup>77–79</sup> CVD precursors include vanadium chlorides such as VCl<sub>4</sub> and VOCl<sub>3</sub>,<sup>77e,78</sup> vanadium alkoxides such as VO(O<sup>i</sup>Pr)<sub>3</sub>,<sup>72b,80</sup> VO(OC<sub>2</sub>H<sub>5</sub>)<sub>3</sub>,<sup>81</sup> and V(OCMe<sub>2</sub>CH<sub>2</sub>OMe)<sub>3</sub>,<sup>82</sup> vanadium β-diketonates such as V(acac)<sub>3</sub>,<sup>76</sup> VO(acac)<sub>2</sub>,<sup>76,83–84</sup> VO(hfac)<sub>2</sub>(H<sub>2</sub>O),<sup>84</sup> VO(tmhd)<sub>2</sub>,<sup>84</sup> and VO(hfod)<sub>2</sub>,<sup>84</sup> along with nitrogen-containing compounds such as V(NMe<sub>2</sub>)<sub>4</sub><sup>85</sup> and VO(NO<sub>3</sub>)<sub>3</sub>.<sup>80</sup>

The phase of vanadium oxide grown by CVD is dependent on several factors, including substrate temperature,<sup>78</sup> reagent concentration,<sup>78</sup> solvent (for AACVD),<sup>76</sup> and carrier gas flow rate.<sup>76</sup> Additionally, the orientation (dominant growth face) and morphology of the deposited film can significantly depend on the precursor and the growth temperature, respectively.<sup>80</sup> APCVD of V<sub>2</sub>O<sub>5</sub>, VO<sub>2</sub>, VO<sub>x</sub> (x ~2.00–2.50) and V<sub>6</sub>O<sub>13</sub> on glass used VCl<sub>4</sub> and water at 400–550 °C.<sup>78</sup> AACVD of V<sub>2</sub>O<sub>3</sub>, VO<sub>2</sub>, and V<sub>2</sub>O<sub>5</sub> on glass used VO(acac)<sub>2</sub> or V(acac)<sub>3</sub> at 500–600 °C.<sup>76</sup> Doping can modify the properties of these films. Use of VO(acac)<sub>2</sub> and W(V)-ethoxide in ethanol afforded the AACVD of W-doped VO<sub>2</sub> films with lower transition temperatures and improved optical properties.<sup>86</sup> Use of VO(acac)<sub>2</sub> and TFAA in ethanol afforded fluorine-doped

VO<sub>2</sub> films with improved aesthetics when grown by AACVD on glass at 525 °C.<sup>87</sup> Finally, VSe<sub>2</sub> films were grown by APCVD using V(NMe<sub>2</sub>)<sub>4</sub> and <sup>t</sup>Bu<sub>2</sub>Se.<sup>85</sup>

The ALD of VO<sub>2</sub> films was reported using V(NEtMe)<sub>4</sub> and ozone at 150 °C.<sup>88</sup> Other volatile vanadium compounds include a trivalent amidinate complex, V(<sup>i</sup>PrNC(Me)N<sup>i</sup>Pr)<sub>3</sub> (subl. 70 °C/0.045 Torr),<sup>37</sup> and an octahydrotriborate complex, Cp\*V(B<sub>3</sub>H<sub>8</sub>)<sub>2</sub> (subl. 70 °C/0.05 Torr),<sup>89</sup> however, these have not yet been evaluated as vapor deposition precursors. To date, vanadium metal film growth has not been reported by CVD or ALD.

**Chart 3.** Vanadium precursors used for vapor deposition processes.

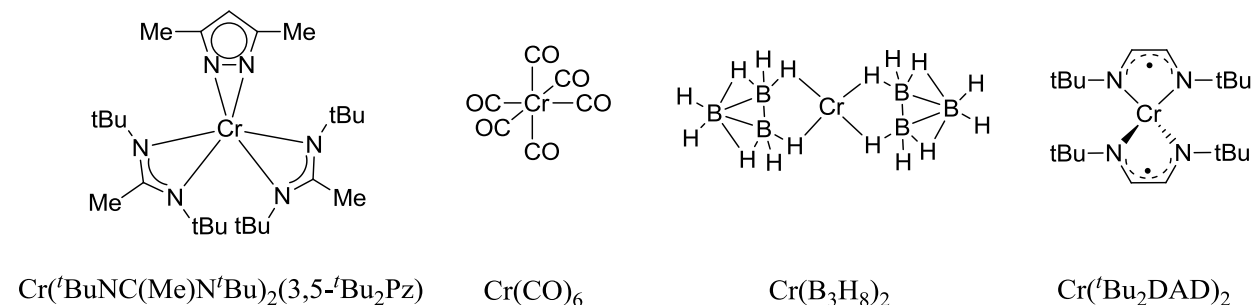


### 1.5.3 Chromium

Recently, non-stoichiometric chromium oxide-based thin film cathodes were used in rechargeable and primary lithium batteries,<sup>90</sup> while chromium metal has been proposed as a seed layer for copper.<sup>10</sup> CVD of chromium oxide films has employed the use of Cr(acac)<sub>3</sub>, Cr(tmhd)<sub>3</sub>,<sup>91</sup> Cr(CO)<sub>6</sub>, CrO<sub>2</sub>Cl<sub>2</sub>, CrO<sub>3</sub>, and other volatile chromium oxides,<sup>92–93</sup> whereby the oxide-containing compounds function as single source precursors while the organometallic compounds require a coreagent (e.g. H<sub>2</sub>O, O<sub>2</sub>, etc).<sup>94</sup> More recently, Cr<sub>2</sub>O<sub>3</sub> films were deposited using Cr(CO)<sub>6</sub> and O<sub>2</sub>, by low-pressure photolytic LCVD at room temperature.<sup>95</sup> Cr(CO)<sub>6</sub> was also decomposed to Cr<sub>2</sub>O<sub>3</sub> by CVD, then carburized under CH<sub>4</sub>/H<sub>2</sub> at 700–850 °C, leading to a metastable Cr<sub>3</sub>C<sub>2–x</sub> phase and a stable Cr<sub>3</sub>C<sub>2</sub> phase.<sup>96</sup> Finally, Cr(B<sub>3</sub>H<sub>8</sub>)<sub>2</sub><sup>97a–b</sup> was used as a single-source precursor for the CVD of CrB<sub>2</sub> at temperatures ≥ 200 °C.<sup>97c</sup>

Other chromium precursors with sufficient volatility and thermal stability for ALD include the amidinate ( $\text{Cr}(\text{}^i\text{PrNC}(\text{Me})\text{N}^i\text{Pr})_3$ ),<sup>94</sup> diazadienyl ( $\text{Cr}(\text{}^t\text{Bu}_2\text{DAD})_2$ ),<sup>42</sup> hydrazonate ( $\text{Cr}(\text{}^t\text{BuNNCHC}^t\text{BuO})_2$ ),<sup>98</sup> and 1,2,5-triazapentadienyl ( $\text{Cr}(\text{}^t\text{BuNNCHCHN}^t\text{Bu})_2$ )<sup>32</sup> complexes, along with complexes containing the pyrazolate/triazolate ( $\text{Cr}(\text{}^t\text{BuNC}(\text{Me})\text{N}^t\text{Bu})_2(\text{X})$ ) ( $\text{X} = \text{Pz}^{3,5-\text{Me}2}$ ,  $\text{Pz}^{3,5-t\text{Bu}2}$ ,  $1,2,4\text{-Trz}^{3,5-\text{Me}2}$ ,  $1,2,4\text{-Trz}^{3,5-i\text{Pr}2}$ )<sup>94</sup> and  $\alpha$ -imino alkoxide ( $\text{Cr}(\text{RR}'\text{COCN}^t\text{Bu})_2$ ) ( $\text{R} = \text{Me}$ ,  $\text{R}' = {}^t\text{Bu}$ ;  $\text{R} = \text{R}' = {}^t\text{Bu}$ )<sup>39</sup> ligand systems. The lone report of Cr metal ALD used  $\text{Cr}(\text{Me}^t\text{BuCOCN}^t\text{Bu})_2$  and  $\text{BH}_3(\text{NHMe}_2)$ , demonstrating a growth rate of 0.08 Å/cycle within the 170–185 °C temperature range.<sup>39</sup> However, growth only occurred on a Ru substrate and required a nucleation step. Growth was linear up to 1,000 ALD cycles, beyond which a plateauing effect suggested the catalytic function of the Ru substrate.<sup>39</sup>

**Chart 4.** Chromium precursors used for vapor deposition processes.



#### 1.5.4 Manganese

All manganese oxides are semiconductors.<sup>99</sup>  $\text{MnO}_2$  films have numerous applications, including use in batteries and as a layer material in Ta thin film capacitors.<sup>99</sup>  $\text{MnO}$  films also have applications for batteries,<sup>100</sup> while Mn metal films are of interest for self-forming Cu/Mn barrier layers.<sup>12,14,16</sup>

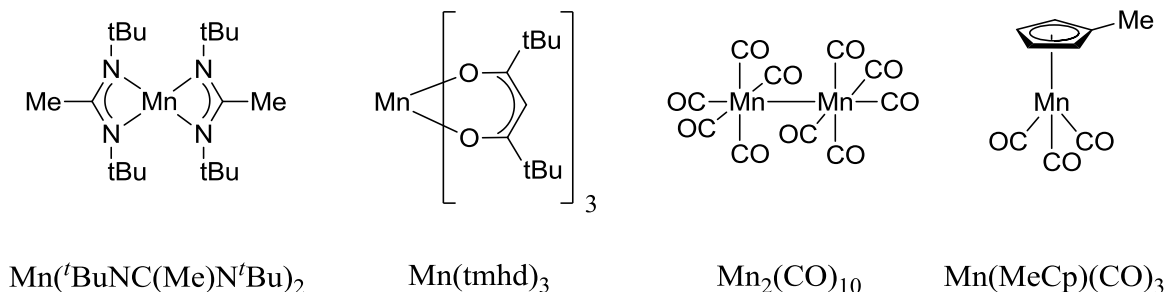
A CVD process using  $\text{Mn}_2(\text{CO})_{10}/\text{H}_2\text{O}$  afforded the epitaxial growth of  $\text{MnO}$  nanoparticles on Pt(111) substrates;<sup>101</sup> subsequent work probed the surface chemistry of this

precursor on SiO<sub>2</sub>/Si(100) and Cu surfaces.<sup>102</sup> Mn(tmhd)<sub>3</sub> is a useful precursor for CVD and PEALD.<sup>91</sup> A CVD process using Mn(tmhd)<sub>3</sub>/O<sub>2</sub> yielded carbon-free manganese oxide films at 360–480 °C; high resolution XRF analysis suggested that the oxidation state of the Mn(III) ion remained unchanged from the precursor to the deposited oxide film.<sup>103</sup> ALD of β-MnO<sub>2</sub> films was achieved from Mn(tmhd)<sub>3</sub>/ozone.<sup>99</sup> This process was later used to show the dependence of the MnO<sub>2</sub> phase on the substrate, growing films of α-MnO<sub>2</sub>, β-MnO<sub>2</sub>, β'-MnO<sub>2</sub>, and ε-MnO<sub>2</sub>.<sup>104</sup> ALD of MnO films was demonstrated using (Mn(CpEt)<sub>2</sub>)/H<sub>2</sub>O.<sup>105</sup> Subsequent work probed the surface chemistry<sup>106</sup> of this precursor on Si/SiO<sub>2</sub> substrates and the use of gas-phase electron-impact ionization toward enhanced dissociative adsorption on silicon surfaces with the formation of very thin layers of Mn metal.<sup>107</sup>

The amidinate precursor, Mn(<sup>i</sup>PrNC(<sup>n</sup>Bu)N<sup>i</sup>Pr)<sub>2</sub>, was used with H<sub>2</sub> toward the selective CVD of Mn metal on Cu to strengthen the interface between Cu and dielectric insulators.<sup>108</sup> Mn(tmhd)<sub>3</sub> was used for the PEALD of Cu/Mn metal alloy films, whereby the Mn content was controlled from 0–10 at.%.<sup>20</sup> A growth rate of 0.65 Å/cycle was observed within the 100–180 °C temperature range with < 3% of C, O, and N impurities observed by XPS.<sup>20</sup> Subsequent annealing of these films afforded a 3 nm barrier of MnSi<sub>x</sub>O<sub>y</sub>.<sup>20</sup> Thermal ALD growth of Mn metal was demonstrated using the α-imino alkoxide dimer, [Mn(Me<sup>t</sup>BuCOCN<sup>t</sup>Bu)<sub>2</sub>]<sub>2</sub>, and BH<sub>3</sub>(NHMe<sub>2</sub>) at 225 °C (0.10 Å/cycle), however, growth only occurred on a Ru substrate and required a nucleation step.<sup>39</sup> Film thickness plateaued after 1,000 ALD cycles, suggesting the catalytic function of the Ru substrate.<sup>39</sup> Subsequently, this precursor was used with Cu(dmap)<sub>2</sub> and BH<sub>3</sub>(NHMe<sub>2</sub>) for the ALD of 70/30 Cu/Mn alloy films (0.09 Å/cycle) and Cu/Mn/Cu film stacks over-coated with SiO<sub>2</sub>.<sup>21</sup> Stacks grown on Pd and Pt substrates showed diffusion of Mn atoms to the SiO<sub>2</sub>/Cu interface, diagnostic of self-forming Cu/Mn barrier layers.<sup>21</sup>

Other compounds with the requisite volatility and thermal stability for ALD include the amidinate ( $\text{Mn}(\text{tBuNC}(\text{Me})\text{N}^t\text{Bu})_2$ ),<sup>36-37</sup> diazadienyl ( $\text{Mn}(\text{tBu}_2\text{DAD})_2$ ),<sup>42</sup> and hydrazonate ( $\text{Mn}(\text{tBuNNCHC}(\text{tBu})\text{O})_2$ )<sup>98</sup> complexes, along with complexes containing the 1,2,5-triazapentadienyl ( $\text{Mn}(\text{tBuNNCHCHNR})_2$  ( $\text{R} = \text{tBu}, \text{NMe}_2$ ))<sup>32</sup> and  $\alpha$ -imino alkoxide ( $[\text{Mn}(\text{RR}'\text{COCN}^t\text{Bu})_2]_2$  ( $\text{R} = \text{Me}, \text{R}' = \text{tBu}; \text{R} = \text{R}' = \text{tBu}$ ))<sup>39</sup> ligand systems.

**Chart 5.** Manganese precursors used for vapor deposition processes.



### 1.5.5 Iron

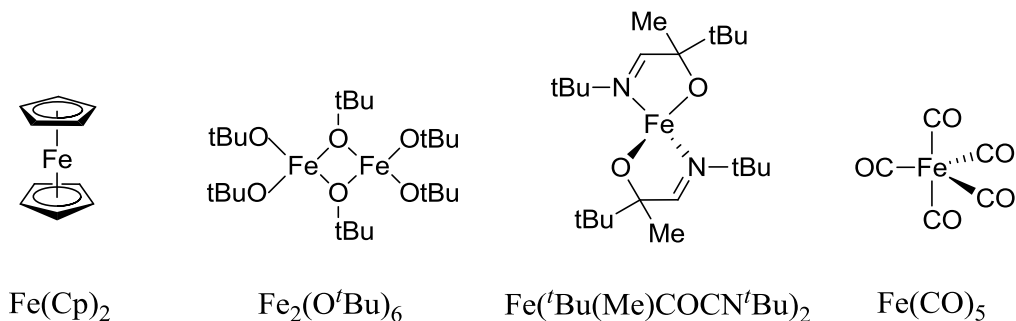
Iron oxides find numerous applications as pigments, coatings, and catalysts. Specifically,  $\alpha$ - $\text{Fe}_2\text{O}_3$  serves as an energy-efficient paint coating, enhancing near infrared reflectance, thereby reducing solar absorption.<sup>109</sup> Hematite ( $\alpha$ - $\text{Fe}_2\text{O}_3$ ) and magnetite ( $\text{Fe}_3\text{O}_4$ )<sup>110</sup> have useful magnetic and optical properties that may be exploited in transparent magnetic oxide films.<sup>111</sup> Finally, metallic Fe is used for MRAM device applications.<sup>112</sup>

Phase-selective deposition of  $\alpha$ - $\text{Fe}_2\text{O}_3$  and  $\text{Fe}_3\text{O}_4$  was achieved by CVD using  $[\text{Fe}(\text{O}^t\text{Bu})_3]_2$ .<sup>111</sup> ALD processes using  $[\text{Fe}(\text{O}^t\text{Bu})_3]_2$  and water enabled the growth of Mg-doped  $\text{Fe}_2\text{O}_3$  films<sup>113</sup> and  $\text{Fe}_2\text{O}_3$  nanotube arrays.<sup>114</sup>  $\text{Fe}(\text{tmhd})_3$ <sup>91</sup> was used with ozone for the ALD of spinel phase  $\text{Fe}_2\text{CoO}_4$  films.<sup>115</sup>  $\text{Fe}(\text{Cp})_2$  was used with  $\text{O}_2$  for the ALD of  $\alpha$ - $\text{Fe}_2\text{O}_3$  on zirconia nanoparticles.<sup>116</sup>  $\text{Fe}(\text{Cp})_2$  was also used with ozone for the ALD of  $\alpha$ - $\text{Fe}_2\text{O}_3$  on Si(100),<sup>117</sup>  $\text{Fe}_2\text{O}_3/\text{Fe}_3\text{O}_4$  on 3D substrates with  $\text{SnO}_2$  nanoparticles,<sup>118</sup> and Ti-doped  $\alpha$ - $\text{Fe}_2\text{O}_3$  electrodes for

water oxidation.<sup>119</sup> Finally, FeO films were grown by ALD from  $\text{Fe}(\text{}^t\text{BuNC}(\text{Me})\text{N}^t\text{Bu})_2/\text{H}_2\text{O}$  at 250 °C.<sup>36</sup>

CVD of Fe metal was demonstrated by the pyrolysis of  $\text{Fe}(\text{Cp})_2$  on thin Ni strips at 490–600 °C,<sup>120</sup> and by the selective decomposition of  $\text{Fe}(\text{CO})_5$  on patterned  $\text{SiO}_2$  substrates at 250–400 °C.<sup>121</sup> Claims of Fe metal ALD are scarce, and require the use of higher temperatures<sup>36</sup> or a catalytic substrate.<sup>39</sup> Amidinate ligands were used to synthesize monomeric and dimeric Fe(II) compounds;<sup>37</sup> a process using  $\text{Fe}(\text{}^t\text{BuNC}(\text{Me})\text{N}^t\text{Bu})_2/\text{H}_2$  afforded Fe films at 250 °C with a growth rate of 0.08 Å/cycle.<sup>36</sup> Self-limited behavior was claimed, however, the solid state decomposition temperature of this precursor was not reported, suggesting the possibility of a CVD contribution toward film growth.

**Chart 6.** Iron precursors used for vapor deposition processes.



Other compounds with the requisite volatility and thermal stability for ALD include a diazadienyl ( $\text{Fe}(\text{}^t\text{Bu}_2\text{DAD})_2$ ) complex,<sup>42</sup> along with complexes containing the hydrazone ( $\text{Fe}(\text{}^t\text{BuNNCHC}(\text{R})\text{O})_2$  ( $\text{R} = \text{}^t\text{Bu}, \text{}^i\text{Pr}$ ) and  $\text{Fe}(\text{}^t\text{BuNNCMeCMeO})_2$ ),<sup>98</sup> 1,2,5-triazapentadienyl ( $\text{Fe}(\text{}^t\text{BuNNCHCHNR})_2$  ( $\text{R} = \text{}^t\text{Bu}, \text{NMe}_2$ )),<sup>32</sup> and  $\alpha$ -imino alkoxide ( $\text{Fe}(\text{RR}'\text{COCN}^t\text{Bu})_2$  ( $\text{R} = \text{Me}, \text{R}' = \text{}^t\text{Bu}; \text{R} = \text{R}' = \text{}^t\text{Bu}$ ))<sup>39</sup> ligand systems. Of these, self-limited growth was demonstrated using  $\text{Fe}(\text{Me}^t\text{BuCOCN}^t\text{Bu})_2$  and  $\text{BH}_3(\text{NHMe}_2)$  at 180 °C (0.07 Å/cycle), however, growth only



occurred on a Ru substrate and required a nucleation step.<sup>39</sup> Film thickness plateaued after 1,000 ALD cycles, suggesting the catalytic function of the Ru substrate.<sup>39</sup>

### 1.5.6 Cobalt

Cobalt-containing materials are used in lithium ion batteries and magnetoresistive devices, while cobalt metal films are employed in DRAM and MRAM applications. Additionally, cobalt metal films serve as magnetic materials, CoSi<sub>2</sub> contact materials, liners for copper seed layers, and caps for selective deposition over copper circuit lines (functioning as both a diffusion barrier and an adhesion layer for SiC).<sup>122</sup>

Co<sub>3</sub>O<sub>4</sub> films have been grown from Co(tmhd)<sub>2</sub> by PECVD<sup>123a</sup> and pulsed liquid-injection CVD.<sup>123b</sup> A PEALD process for Co<sub>3</sub>O<sub>4</sub> was reported using CoCp<sub>2</sub> and remote O<sub>2</sub> plasma, with a growth rate of 0.50 Å/cycle within the 100–400 °C temperature range. ALD Co<sub>3</sub>O<sub>4</sub> films were subsequently described using Co(<sup>i</sup>Pr<sub>2</sub>DAD)<sub>2</sub> and ozone, with a growth rate of 1.20 Å/cycle within the 120–250 °C window.<sup>125</sup> ALD processes employing Co(tmhd)<sub>2</sub> and ozone were used for the growth of Co<sub>3</sub>O<sub>4</sub>,<sup>126</sup> spinel phase Fe<sub>2</sub>CoO<sub>4</sub>,<sup>115</sup> and a p-type thermoelectric material, [Ca<sub>2</sub>CoO<sub>3</sub>]<sub>0.62</sub>[CoO<sub>2</sub>].<sup>127</sup> ALD CoO films were claimed using Co(<sup>i</sup>PrNC(Me)N<sup>i</sup>Pr)<sub>2</sub> and H<sub>2</sub>O at 250 °C.<sup>36</sup>

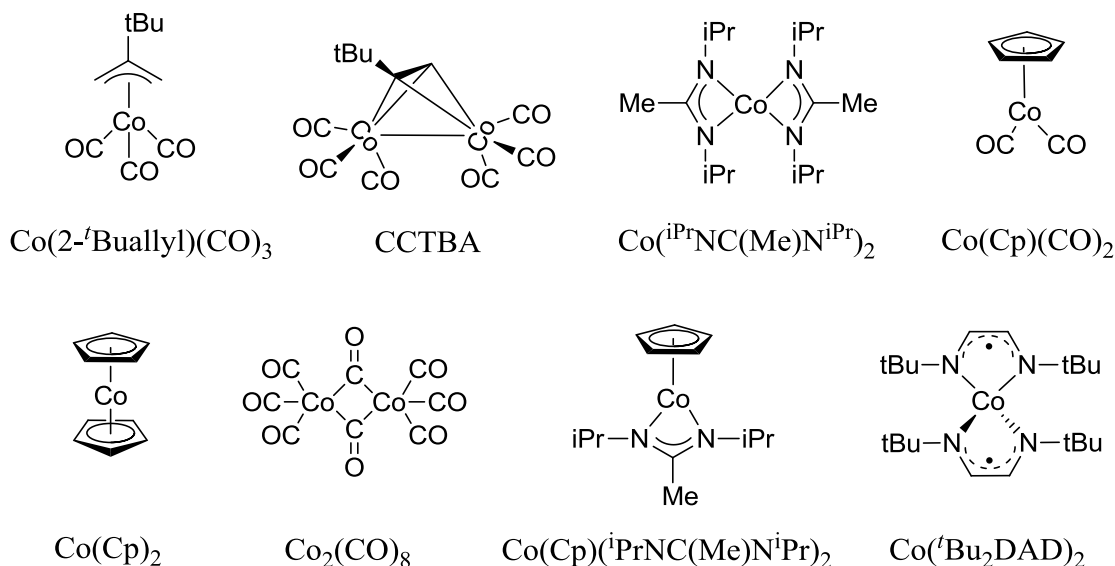
CVD of cobalt metal from the liquid precursor μ<sup>2</sup>-η<sup>2</sup>-(<sup>t</sup>Bu-acetylene)Co<sub>2</sub>(CO)<sub>6</sub> (CCTBA) and H<sub>2</sub> at 150 °C afforded conformal, high-purity films on 15:1 aspect ratio patterned wafers.<sup>128</sup> Rapid thermal annealing (RTA) produced CoSi at 500 °C, while CoSi<sub>2</sub> was observed at 600 °C.<sup>128</sup> CCTBA was subsequently used for the PEALD of continuous cobalt films at 150 °C.<sup>129</sup> Application of a plasma pretreatment improved nucleation density by increasing the number of active sites, while the use of H<sub>2</sub> as the carrier gas decreased film resistivity by improving the efficiency of organic ligand removal; resultant films were sufficient for copper

electrochemical plating (ECP).<sup>129</sup> PEALD cobalt films were also reported using  $\text{CoCp}(\text{CO})_2$ ,<sup>130–131</sup>  $\text{CoCp}_2$ ,<sup>130a,132–133</sup>  $\text{Co}(\text{MeCp})_2$ ,<sup>134</sup>  $\text{Co}_2(\text{CO})_8$ ,<sup>43,131</sup> and  $\text{CoCp}(\text{iPrNC}(\text{Me})\text{N}^{\text{iPr}})$ .<sup>44</sup> Films from  $\text{CoCp}_2$  or  $\text{CoCp}(\text{CO})_2$  with  $\text{NH}_3$  plasma resulted in  $\text{CoSi}$  and  $\text{CoSi}_2$  phases after RTA due to the presence of a  $\text{SiN}_x$  interlayer.<sup>130,132</sup> PEALD cobalt nanorods were subsequently grown on Si and  $\text{SiO}_2$  substrates using  $\text{CoCp}_2$  with a mixture of  $\text{NH}_3$  plasma/ $\text{SiH}_4$  plasma.<sup>45</sup> Two indirect methods were reported for the thermal ALD of cobalt metal nanotubes in alumina membranes:  $\text{CoCp}_2/\text{H}_2\text{O}/\text{H}_2$  and  $\text{CoCp}_2/\text{ozone}$  followed by a 400 °C anneal under forming gas.<sup>135</sup>

Claims of direct thermal ALD for cobalt metal include multiple processes where the deposition temperature exceeded the thermal stability of the precursor. Several amidinate complexes were synthesized with good volatilities for vapor deposition processes.<sup>37–38</sup>  $\text{Co}(\text{iPrNC}(\text{Me})\text{N}^{\text{iPr}})_2$  was used with and  $\text{H}_2$  gas at 350 °C for the growth of cobalt metal at a rate of 0.12 Å/cycle.<sup>36</sup> This precursor was subsequently used for area-selective ALD with an octadecyltrichlorosilane (OTS) self-assembled monolayer (SAM) blocking layer at 300–340 °C ( $\text{H}_2$  gas)<sup>136</sup> and 350 °C ( $\text{H}_2$  gas,<sup>137</sup>  $\text{NH}_3$  gas,<sup>137–138</sup> and  $\text{NH}_3$  plasma).<sup>138</sup> Although self-limited behavior was demonstrated,<sup>36</sup> the temperatures used for these studies were significantly higher than the decomposition temperature of  $\text{Co}(\text{iPrNC}(\text{Me})\text{N}^{\text{iPr}})_2$  (215–225 °C),<sup>139</sup> suggesting a considerable CVD component toward film growth. Theoretical studies showed the thermal decomposition of cobalt amidinate complexes may be due to metal activation of  $\beta$ -C-H bonds of N- and C-bound alkyl groups in the amidinate ligand cores.<sup>140–141</sup> The cyclic exposure of CCTBA at 140 °C followed by a 300 °C anneal yielded cobalt metal films on  $\text{SiO}_2$  and Si-H substrates; the stability of the carbonyl groups on Si-H lead to lower growth rates.<sup>142</sup> The subsequent ALD of cobalt metal from a similar liquid compound, (2-*tert*-butylallyl) $\text{Co}(\text{CO})_3$ , with 1,1-dimethylhydrazine was claimed at 140 °C, however, self-limited growth was not

demonstrated.<sup>143</sup> Additionally, the onset of thermal decomposition for this precursor appears to be ~90 °C in the liquid state (Appendix A), implying a CVD component to the film growth process at 140 °C. However, this process displayed impressive selectivity, favoring growth on Si-H over OH-terminated oxide surfaces on Si(111) substrates.<sup>143</sup> This precursor was later used with trisilane for the ALD growth of CoSi<sub>2</sub> films.<sup>144</sup>

**Chart 7.** Cobalt precursors used for vapor deposition processes.



Other cobalt compounds with the requisite volatility and thermal stability for ALD include the diazadienyl (Co(<sup>t</sup>Bu<sub>2</sub>DAD)<sub>2</sub>)<sup>42</sup> and carbonylhydrazide (Co(Me<sub>2</sub>NN=C(<sup>t</sup>Bu)O)<sub>2</sub>)<sup>145</sup> complexes, along with complexes containing hydrazonate (Co(<sup>t</sup>BuNNCHCRO)<sub>2</sub> (R = <sup>t</sup>Bu, <sup>i</sup>Pr) and Co(<sup>t</sup>BuNNCMeCMeO)<sub>2</sub>)<sup>98</sup> 1,2,5-triazapentadienyl (Co(<sup>t</sup>BuNNCHCHNR)<sub>2</sub> (R = <sup>t</sup>Bu, NMe<sub>2</sub>)),<sup>32</sup> and α-imino alkoxide (Co(RR'COCN<sup>t</sup>Bu)<sub>2</sub> (R = Me, R' = <sup>i</sup>Pr; R = Me, R' = <sup>t</sup>Bu; R = R' = <sup>t</sup>Bu))<sup>39</sup> ligand systems. Self-limited growth was demonstrated using Co(Me<sup>i</sup>PrCOCN<sup>t</sup>Bu)<sub>2</sub> and BH<sub>3</sub>(NHMe<sub>2</sub>) at 180 °C (0.07 Å/cycle), however, growth only occurred on a Ru substrate and required a nucleation step.<sup>39</sup> Film thickness plateaued after 1,000 ALD cycles, suggesting the catalytic function of the Ru substrate.<sup>39</sup>

### 1.5.7 Nickel

$\text{Ni}_3\text{N}$  is used for negative electrodes for lithium ion batteries<sup>146</sup> and as an intermediate material for the formation of nickel metal and  $\text{NiSi}$ .<sup>147</sup>  $\text{NiO}$  is a p-type semiconductor with a bandgap of 3.5–4.0 eV<sup>148</sup> with applications for non-volatile memory devices<sup>149–151</sup> and photocatalytic water splitting.<sup>152–153</sup> Nickel metal thin films are used as electrodes and contacts in MOSFETs.<sup>154</sup>

$\text{Ni}_3\text{N}$  has been grown by both CVD and ALD. A direct liquid injection (DLI) CVD process for  $\text{NiN}_x$  films was described using  $\text{Ni}(\text{tBuNC}(\text{Me})\text{N}^t\text{Bu})_2$  and  $\text{NH}_3$  on H-terminated  $\text{Si}(100)$  and highly-doped polysilicon substrates; RTA in forming gas at  $\geq 440$  °C resulted in  $\text{NiSi}$  films with resistivities of 15  $\mu\Omega\cdot\text{cm}$ .<sup>147</sup> CVD  $\text{Ni}_3\text{N}$  films were also reported from  $\text{Ni}(\text{tmhd})_2$ <sup>91</sup> with  $\text{NH}_3$  or  $\text{H}_2$  gas.<sup>155–156</sup> An ALD process for  $\text{Ni}_3\text{N}$  was demonstrated from  $\text{Ni}(\text{tBu}_2\text{DAD})_2$  and anhydrous 1,1-dimethylhydrazine, with a growth rate of 0.70 Å/cycle within the 225–240 °C temperature range.<sup>157</sup>

Nickel oxide deposition has been well-documented.  $\text{NiCp}_2$  was used with  $\text{O}_2$  for the CVD of  $\text{NiO}$ <sup>158</sup> and  $\text{NiO}/\text{Ni}_2\text{O}_3$ .<sup>159</sup>  $\text{NiO}$  films were also grown by CVD from  $\text{Ni}(\text{dmamb})_2/\text{O}_2$ <sup>149</sup> and  $\text{Ni}(\text{TTA})_2\cdot\text{TMEDA}/\text{O}_2$ ,<sup>160</sup> and by PECVD from  $\text{Ni}(\text{acac})_2/\text{O}_2$ .<sup>161</sup> In some cases, the deposition temperature<sup>149,159</sup> and  $\text{O}_2$  flow rate<sup>161</sup> had an effect on the preferred crystal orientation. ALD processes for  $\text{NiO}$  have been reported from  $\text{NiCp}_2/\text{ozone}$ ,<sup>162–163</sup>  $\text{Ni}(\text{EtCp})_2/\text{ozone}$ ,<sup>162</sup>  $\text{Ni}(\text{tmhd})_2/\text{H}_2\text{O}$ ,<sup>155,164</sup>  $\text{Ni}(\text{dmamp})_2/\text{H}_2\text{O}$ ,<sup>165</sup> and  $\text{Ni}(\text{dmamb})_2/\text{ozone}$ <sup>166</sup> or water.<sup>151,167</sup> Of these, the final approach was applied at 140 °C to induce crystallization in amorphous silicon after annealing at 575 °C for 1 hr under forming gas.<sup>168</sup> The metal-induced crystallization may arise from the formation of nickel silicides, which act as seeds for nucleation in the growth of crystalline silicon.<sup>168</sup>

Nickel metal CVD was demonstrated from Ni(dmamp)<sub>2</sub> as a single-source precursor at  $\geq 250$  °C<sup>169</sup> and by the pyrolysis of Ni(Cp)<sub>2</sub> on stainless steel rods at temperatures  $\geq 550$  °C.<sup>120</sup> Other reported CVD processes include CpNi(allyl)/H<sub>2</sub><sup>170–171</sup> and Ni(ktfaa)<sub>2</sub>/H<sub>2</sub>.<sup>172</sup> Another CVD approach used Ni(MeCp)<sub>2</sub>/H<sub>2</sub> at 300 °C; subsequent reaction of the Ni film with the Si substrate resulted in NiSi and NiSi<sub>2</sub> formation.<sup>173</sup> A novel indirect route employed the CVD of Ni<sub>3</sub>N on NiO layers from Ni(tmhd)<sub>2</sub>/NH<sub>3</sub>, with subsequent decomposition of the metastable Ni<sub>3</sub>N layers by annealing under H<sub>2</sub> to afford a Ni/NiO product.<sup>155</sup> Ni<sub>3</sub>N decomposes to nickel metal at  $\sim 150$  °C under a reducing H<sub>2</sub> atmosphere and at  $\sim 300$  °C under vacuum.<sup>156,174</sup>

PEALD nickel metal films were demonstrated using Ni(dmamp)<sub>2</sub>/H<sub>2</sub> plasma at 220 °C, with a growth rate of 1.55 Å/cycle.<sup>175</sup> The as-deposited Ni film possessed a cubic structure and exhibited a very low sheet resistance of 3.10 Ω/□.<sup>175</sup> However, Ni(dmamp)<sub>2</sub> thermally decomposes at 180–185 °C,<sup>176</sup> suggesting growth enhancement by a CVD component. PEALD Ni nanorods were grown on SiO<sub>2</sub> substrates using Ni(dmamb)<sub>2</sub> with a mixture of NH<sub>3</sub> plasma and SiH<sub>4</sub> plasma.<sup>45</sup> Subsequent PEALD processes for Ni using Ni(dmamb)<sub>2</sub> at 250 °C afforded growth rates of 2.0 and 0.8 Å/cycle with NH<sub>3</sub> plasma and H<sub>2</sub> plasma, respectively.<sup>46</sup> The NH<sub>3</sub> process resulted in a higher growth rate, lower carbon content, and a 1–2 nm SiN<sub>x</sub> interface layer due to the catalytic effects of the NH<sub>3</sub> radicals.<sup>46</sup>

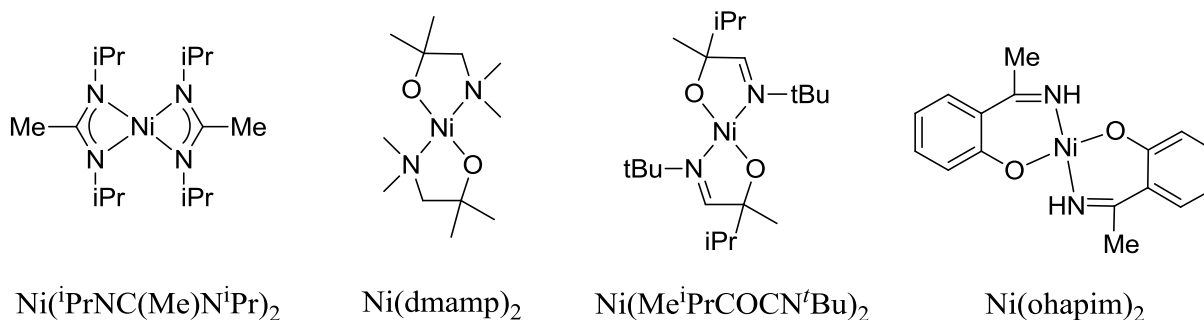
An indirect thermal ALD process for nickel metal entailed growing NiO from NiCp<sub>2</sub>/water at 165 °C, then reducing the resultant NiO film by H<sub>2</sub> plasma.<sup>47</sup> This process was used to grow continuous and conformal nickel films as seed layers for CVD Cu on TiN-coated Si wafers.<sup>47</sup> Two other indirect methods were subsequently reported for the thermal ALD of nickel metal nanotubes inside the pores of alumina membranes: NiCp<sub>2</sub>/H<sub>2</sub>O/H<sub>2</sub> and NiCp<sub>2</sub>/ozone followed by a 400 °C anneal under forming gas.<sup>135</sup>

Nickel metal films grown by direct thermal ALD processes include  $\text{Ni}(\text{}^i\text{PrNC}(\text{Me})\text{N}^i\text{Pr})_2/\text{H}_2$ <sup>37</sup> at 250 °C (0.04 Å/cycle).<sup>36</sup> Although self-limited behavior was reported,<sup>36</sup> the solid state decomposition temperature of this precursor is ~180 °C,<sup>37</sup> suggesting a strong CVD component to the growth. Theoretical studies suggested that the thermal decomposition of nickel amidinate complexes may be due to metal activation of  $\beta$ -C-H bonds of N- and C-bound alkyl groups in the amidinate ligand cores.<sup>140–141</sup> A second ALD nickel process using  $\text{Ni}(\text{dmamb})_2/\text{H}_2$  afforded a growth rate of 1.25 Å/cycle within the 200–250 °C temperature range.<sup>177</sup> The uniformly-distributed carbon content of a film deposited at 220 °C was proposed to promote the formation a  $\text{Ni}_3\text{C}$  phase which supported a low sheet resistance of 18  $\Omega/\square$  by eliminating other crystalline defects.<sup>177</sup> A  $\text{Ni}(\text{dmamb})_2/\text{NH}_3$  process was subsequently developed for area-selective ALD in conjunction with OTS SAM as a blocking layer at 300 °C.<sup>178</sup> Finally, the ALD of nickel films was reported using  $\text{Ni}(\text{hfip})_2/\text{H}_2$  at a deposition rate of 1.25 Å/cycle within the 200–250 °C window, whereby the formation of a  $\text{Ni}_3\text{C}$  phase was controlled by varying the flow rate of the  $\text{H}_2$  gas.<sup>179</sup> RTA of films grown on Si yielded NiSi.<sup>179</sup>

Other compounds with the requisite volatility and thermal stability for ALD include a diazadienyl complex  $(\text{Ni}(\text{}^t\text{Bu}_2\text{DAD})_2)$ <sup>42</sup> along with complexes containing carbohydrazide  $(\text{Ni}(\text{Me}_2\text{NN}=\text{C}(\text{R})\text{O})_2)$ , (R =  ${}^t\text{Bu}$ ,  ${}^i\text{Pr}$ , Me) and  $\text{Ni}((\text{CH}_2)_5\text{NN}=\text{C}(\text{}^t\text{Bu})\text{O})_2$ , (R =  ${}^t\text{Bu}$ ,  ${}^i\text{Pr}$ , Me),<sup>145</sup> hydrazonate  $(\text{Ni}(\text{}^t\text{BuNNCHC}(\text{R})\text{O})_2)$  (R =  ${}^t\text{Bu}$ ,  ${}^i\text{Pr}$ ) and  $\text{Ni}(\text{}^t\text{BuNNCMeCMeO})_2$ ,<sup>98</sup> 1,2,5-triazapentadienyl  $(\text{Ni}(\text{}^t\text{BuNNCHCHNR})_2)$ , (R =  ${}^t\text{Bu}$ ,  $\text{NMe}_2$ ),<sup>32</sup>  $\alpha$ -imino alkoxide  $(\text{Ni}(\text{RR}'\text{COCN}^t\text{Bu})_2)$  (R = Me, R' =  ${}^i\text{Pr}$ ; R = Me, R' =  ${}^t\text{Bu}$ ; R = R' =  ${}^t\text{Bu}$ ),<sup>39</sup> and 2-(1-iminoalkyl)phenoxide (ohapim, ohppim)  $(\text{Ni}(2\text{-O-1-(C}(\text{R})=\text{NH})\text{-C}_6\text{H}_4)_2)$  (R = Me, Et)<sup>180</sup> ligand systems. Self-limited growth was demonstrated using  $\text{Ni}(\text{Me}^i\text{PrCOCN}^t\text{Bu})_2$  and  $\text{BH}_3(\text{NHMe}_2)$  at 180 °C (0.09 Å/cycle), however, growth only occurred on a Ru substrate and required a

nucleation step.<sup>39</sup> Film thickness plateaued after 1,000 ALD cycles, suggesting the catalytic function of the Ru substrate.<sup>39</sup>

**Chart 8.** Nickel precursors used for vapor deposition processes.



### 1.5.8 Copper

Copper and copper-containing films have numerous uses in microelectronic and photovoltaic devices.  $\text{Cu}_3\text{N}$  is relevant to optical data storage and microelectronic applications.<sup>181</sup>  $\text{Cu}_3\text{N}$  decomposes to Cu metal at 250–450 °C<sup>182</sup> and reflects less infrared light than pure Cu.<sup>183</sup> These properties suggest its use in optical recording media, as laser heating can generate localized regions of Cu on  $\text{Cu}_3\text{N}$  films.<sup>183b</sup>  $\text{Cu}_2\text{O}$  is a p-type semiconductor maintaining a band gap of 2.3 eV with potential applications for sensors and solar cells due to its low toxicity, light absorption, and low production cost.<sup>184</sup> Recent interest has also focused on the potential use of  $\text{Cu}_2\text{O}$ -based semiconductor devices such as diodes, photovoltaics, and CMOS integrated devices.<sup>184a</sup> Copper metal has replaced aluminum metal as the primary interconnect material in microelectronic device manufacturing due to its lower resistivity and superior resistance to stress migration and electromigration.<sup>185</sup> Copper thin films are used as seed layers for the ECD of Cu interconnect lines on integrated circuits, improving adhesion and influencing the nucleation and texture of the ECD Cu.<sup>186</sup> Copper-containing semiconductors with ternary and quaternary

compositions (e.g. CIS, CIGS, CZTS) are used for solar cells.<sup>187</sup> Several precursors and methods for Cu ALD have been developed due to the positive electrochemical potentials of the Cu(I) and Cu(II) ions and their attendant ease of reduction.<sup>31,188–189</sup>

Cu(I) species often react at low temperatures by thermally-induced disproportionation to copper metal. Cu(I)  $\beta$ -diketonate derivatives display high vapor pressures and relatively low activation energies for film growth.<sup>190</sup> For compounds of the general formula Cu(hfac)L, the neutral ligand (L) significantly affects the precursor properties and the morphology and texture of the resultant Cu film.<sup>191</sup> Cu(hfac)L (L = VTMS, PMe<sub>3</sub>, 2-butyne, and COD) precursors have been especially useful for CVD processes.<sup>190</sup> Of these compounds, only Cu(hfac)VTMS is a liquid at room temperature;<sup>25</sup> marketed as Cupraselect,<sup>®</sup> it is the most widely used Cu precursor.<sup>192</sup> Subsequently, Cu(hfac)(MHY) was developed; marketed as GigaCopper,<sup>®</sup> it afforded lower resistivity films (without anneal) and a 50% higher growth rate at 190 °C relative to Cu(hfac)VTMS.<sup>193–194</sup> Cu(hfac)(MHY) exhibits weaker intermolecular interactions (affording a more homogenous gas phase) and better adsorption to the surface due to its free double bond, resulting in an improved disproportionation yield with fewer contaminating atoms incorporated into the film.<sup>194</sup> This compound was used to study the initial stages of Cu nucleation by CVD on irradiated SAMs of (3-mercaptopropyl)trimethoxysilane (MPTMS) on SiO<sub>2</sub> substrates.<sup>195</sup> Finally, a series of liquid, fluorine-free Cu(I)  $\beta$ -diketonate compounds employing bis(trimethylsilyl)acetylene (BTMSA) as the stabilizing ligand had improved thermal stability over GigaCopper<sup>®</sup>.<sup>196</sup> These asymmetric  $\beta$ -diketonate compounds displayed reduced melting points and increased volatilities relative to the symmetric acetylacetonone analogue, and were used for the CVD of high-purity Cu films on Ta/TaN substrates.<sup>196–197</sup> Phosphite trifluoroacetate Cu(I) complexes of composition  $[(\text{RO})_3\text{P}]_m\text{CuO}_2\text{CCF}_3$  ( $m = 1, 2, 3$ ; R = CH<sub>3</sub>, CH<sub>2</sub>CH<sub>3</sub>, CH<sub>2</sub>CF<sub>3</sub>)



were also reported as potential CVD precursors; the liquid compound  $((\text{MeO})_3\text{P})_3\text{CuO}_2\text{CCF}_3$  was used for the CVD of a pure Cu layer on TiN at 380 °C.<sup>198</sup> In contrast to the Cu(I)  $\beta$ -diketonates, these Lewis-base Cu(I) carboxylates do not require additional reducing agents (e.g.  $\text{H}_2$ ) for the growth of pure Cu layers.<sup>198</sup>

Ketoiminate compounds KI3 and KI5 (Chart 9) contain an olefin group tethered by a seven-membered ring, imparting high thermal stabilities by suppressing disproportionation initiated by loss of the olefin moiety; the CVD of pure Cu films was reported using formic acid as a coreagent<sup>199–200</sup> and the thermal chemistry of KI5 was later studied on a Cu surface.<sup>201</sup>  $[\text{Cu}(\text{hfac})]_2(\text{DVTMSO})$  and  $[\text{Cu}(\text{hfac})]_2(1,5\text{-hexadiene})$  contain two Cu(hfac) fragments coordinated by a bidentate neutral ligand; CVD processes afforded Cu nanoparticles on TiN at 100–225 °C.<sup>202</sup> Cu(I)  $\beta$ -diketiminato complexes of the general formula  $\text{Cu}(\text{nacnac})\text{L}$  ( $\text{L} = \text{VTMS}$ , 3,3-dimethyl-1-butene) are also volatile, thermally-stable precursors,<sup>33,203</sup> a pulsed-CVD process with diethylsilane was demonstrated.<sup>34</sup>

Several Cu(I) amidinate dimers have been synthesized as vapor deposition precursors,<sup>37,204</sup> and the surface chemistry of  $[\text{Cu}(\text{t}^i\text{BuNC}(\text{Me})\text{N}^t\text{Bu})]_2$  has been studied on polycrystalline cobalt,<sup>205</sup> Ni(100)<sup>205–206</sup> and Cu(110)<sup>207</sup> single-crystal surfaces, and  $\text{SiO}_2$  films.<sup>208</sup> Cu(I) guanidinate complexes<sup>209</sup> extend the  $\pi$  system of the amidinate chelate ring and have been used as single-source CVD precursors for Cu films at 225 °C.<sup>210</sup> However,  $\text{Cu}(\text{t}^i\text{PrNC}(\text{NMe}_2)\text{N}^t\text{Pr})_2$  undergoes decomposition at < 150 °C by carbodiimide elimination.<sup>210b</sup> A series of Cu(I) iminopyrrolidinate complexes<sup>211</sup> was subsequently designed to prevent the thermal decomposition by  $\beta$ -hydrogen abstraction and carbodiimide deinsertion that plagues the amidinate and guanidinate precursors, respectively. Guanidinate and iminopyrrolidinate complexes were shown to undergo dissociative adsorption to Cu(I) monomers on Ni(110) single-

crystal substrates.<sup>212</sup> Finally, an isoelectronic Cu(I) isoureate complex was used for the CVD of Cu on Ru under an H<sub>2</sub> atmosphere at 225–300 °C.<sup>213</sup>

The tendency for thermally-induced disproportionation of Cu(I) precursors on substrate surfaces generally precludes their use for thermal ALD processes.<sup>214</sup> Preservation of the self-limiting mechanism favors the use of Cu(II) compounds, however, the high surface mobility of Cu often results in Volmer-Weber (island-type) growth<sup>215</sup> at temperatures above 150 °C. Cu(dmap)<sub>2</sub> and Cu(dmamb)<sub>2</sub> have been used for the CVD of high-quality Cu seed layers.<sup>216</sup> Cu(dmap)<sub>2</sub> has also been used as a single-source CVD precursor for high-purity Cu metal films at 230–260 °C.<sup>217</sup> Numerous precursors have been used for PEALD processes with H<sub>2</sub> plasma, including Cu(acac)<sub>2</sub>,<sup>218–219</sup> Cu(tmhd)<sub>2</sub>,<sup>91,220</sup> Cu(dmamb)<sub>2</sub>,<sup>221</sup> NHC-Cu(N(SiMe<sub>3</sub>)<sub>2</sub>),<sup>48</sup> Cu(OCMeCHC(Me)NEt)<sub>2</sub> (sold as AbaCus) or structural analogues,<sup>222–223</sup> and a bis(aminoalkoxide)copper(II) precursor (CTA-1).<sup>223</sup> The chemistry of Cu(acac)<sub>2</sub> was subsequently studied on Ni(110) and Cu(110) single-crystal surfaces.<sup>224</sup>

Multiple indirect routes for thermal ALD Cu films have been reported whereby Cu<sub>2</sub>O is reduced to Cu metal. Cu(hfac)<sub>2</sub> was delivered by H<sub>2</sub> gas bubbled through water at 300 °C; subsequent decomposition and oxidation of the resultant Cu(hfac)<sub>2</sub>·xH<sub>2</sub>O yielded Cu<sub>2</sub>O and adsorbed hfac.<sup>225</sup> Reduction to Cu was achieved using methanol, ethanol, isopropanol, formalin or CO. High-purity films were grown using isopropanol (260 °C) or formalin (300 °C) with good conformal coverage in high aspect ratio features and resistivities near that of bulk Cu.<sup>225</sup> A variant of this approach used Cu(acac)(<sup>t</sup>Bu<sub>3</sub>P)<sub>2</sub>, a liquid precursor, with wet O<sub>2</sub> for the ALD of Cu<sub>2</sub>O on Ru, TaN, and SiO<sub>2</sub> substrates<sup>226–227</sup> and on multi-walled carbon nanotubes.<sup>228</sup> *In-situ* XPS analysis of films grown on SiO<sub>2</sub> showed that most of the <sup>t</sup>Bu<sub>3</sub>P ligands were released during or prior to adsorption, with no disproportionation of the precursor within the 22–145 °C

temperature range.<sup>229</sup> Cu<sub>2</sub>O films were grown on SiO<sub>2</sub> at 0.05 Å/cycle at 145 °C and contained 24.1% carbon.<sup>229</sup> Cu<sub>2</sub>O grown on Ru by this process was subsequently reduced by formic acid, affording Cu films at 110–120 °C, where the underlying Ru layer enabled the catalytic decomposition of formic acid to H<sub>2</sub> and CO<sub>2</sub>.<sup>227</sup> This ALD-grown Cu was superior to PVD Cu for seed layer growth on Ru, as evidenced by smaller grain sizes and lower values of specific resistivity and RMS roughness.<sup>227</sup>

A second indirect approach employed Cu(hfac)<sub>2</sub> and H<sub>2</sub> with the catalytic addition of pyridine; 15 nm thick films grown within the 25–100 °C ALD window had resistivity values of 19 μΩ·cm.<sup>214</sup> DFT calculations confirmed that Cu-O bond length elongation (2.01 Å) occurs from the combined effects of pyridine interacting with the Cu metal atom and the asymmetric interactions between pyridine and a hydrogen atom on the surface-bound Cu(hfac)<sub>2</sub>.<sup>214</sup> However, precursors containing fluorine are typically not desirable, since the hydrofluoric acid byproduct can result in fluorine contamination, reduced adhesion, or etching of substrates.

Multiple indirect routes have also focused on the ALD of Cu<sub>3</sub>N, with subsequent reduction to Cu metal. One method used a Cu(I) amidinate dimer, [Cu(<sup>t</sup>BuNC(Me)N<sup>t</sup>Bu)]<sub>2</sub>, with NH<sub>3</sub> to grow Cu<sub>3</sub>N on Ru substrates at 160 °C.<sup>181</sup> Subsequent annealing under forming gas (RTA, 225 °C) or H<sub>2</sub> (160–185 °C) resulted in highly-conductive Cu films that displayed conformal coverage at an aspect ratio of 42:1.<sup>181</sup> Saturation of the amidinate precursor was not demonstrated, however, Cu films grown by this process were smoother than those from a binary ALD process using the same precursor with H<sub>2</sub> at 160 °C.<sup>181</sup> A similar approach used Cu(dmamb)<sub>2</sub> and NH<sub>3</sub> at 100–140 °C for the ALD of Cu<sub>3</sub>N, followed by annealing at 200–250 °C to afford Cu metal.<sup>230</sup>

A final indirect method employed  $\text{Cu}(\text{dmap})_2$ , formic acid, and hydrazine for the low-temperature ALD of high-purity Cu metal films on Si(100) substrates.<sup>231</sup> This process entailed the reduction of intermediate Cu(II) formate layers by hydrazine, enabling Cu metal film growth at  $\geq 80$  °C with a growth rate of 0.50 Å/cycle within the 100–160 °C ALD window.<sup>231</sup>

Direct “ALD” processes for Cu metal include  $\text{CuCl}/\text{H}_2$  at 360–410 °C<sup>232</sup> and  $\text{CuCl}/\text{Zn}$  at 440–500 °C.<sup>233</sup> However, self-limited growth was not achieved for these extremely high-temperature processes and the latter approach suffered from reversible dissolution of Zn into the Cu films, resulting in 3 at.% Zn impurities for films grown at 500 °C.<sup>233</sup> Subsequently, ALD film growth was reported using  $\text{Cu}(\text{hfac})_2 \cdot x\text{H}_2\text{O}$  with methanol, ethanol, and formalin at 300 °C.<sup>234</sup>  $\text{Cu}(\text{tmhd})_2/\text{H}_2$  also afforded films on Si(100) and glass at 350 °C<sup>235–236</sup> and selective film growth on Pd-seeded regions over oxide surfaces at 190–260 °C.<sup>237</sup> A series of unfluorinated ketoimine and diimine compounds with a tethered olefin moiety was used for Cu film growth at 130–200 °C, although saturative behavior was not demonstrated.<sup>238</sup>  $\text{Cu}(\text{ethylketoiminate})_2/\text{H}_2$  was subsequently employed for the ALD of high-purity Cu films on Ru.<sup>239</sup> Although this process supports a growth rate of 1.2 Å/cycle, films grown at 140 °C had a relatively high resistivity of 18  $\mu\Omega\cdot\text{cm}$ .<sup>239</sup>  $\text{Cu}(\text{dmamb})_2$  was used with  $\text{H}_2$  for both CVD and ALD Cu films; the latter suffered from either low nucleation and growth rates (120–140 °C), yielding islands of Cu, or thermal decomposition of the precursor (160–200 °C), leading to CVD-type growth.<sup>230</sup> Recently, the carbene-stabilized Cu(I) silylamide,  $\text{NHC-Cu}(\text{N}(\text{SiMe}_3)_2)$ , was used with  $\text{H}_2$  for Cu ALD on Pd substrates, maintaining a growth rate of 0.4 Å/cycle within the 190–250 °C ALD window.<sup>240</sup> Subsequently, 1,3-diphenyl-4,5-imidazolidinedithione copper hydride (S-NHC-CuH) was studied theoretically as a Cu(I) carbene hydride that functions as both the precursor and reducing

agent for low-temperature Cu ALD, whereby the electron withdrawing groups on the heterocycle support easy accessibility to the hydride.<sup>241</sup>

Copper ALD processes using amidinate precursors include  $[\text{Cu}(\text{iPrNC}(\text{Me})\text{N}^{\text{iPr}})]_2/\text{H}_2$  at 280 °C<sup>36</sup> and  $[\text{Cu}(\text{sBuNC}(\text{Me})\text{N}^{\text{sBu}})]_2/\text{H}_2$  at 150–190 °C.<sup>242–244</sup> The initial reaction of  $[\text{Cu}(\text{sBuNC}(\text{Me})\text{N}^{\text{sBu}})]_2$  and surface Si-OH groups was shown to occur by displacement of one protonated amidinate ligand and formation of a Si-O-Cu-amidinate surface species.<sup>243</sup> Subsequent exposure to molecular H<sub>2</sub> produces neutral amidine and mobile Cu atoms that agglomerate on the SiO<sub>2</sub> surface.<sup>243</sup> Surface-bound ligand rearrangement from a bridging to a monodentate structure occurs at > 220 °C on the SiO<sub>2</sub> surface and 185 °C on the growing Cu surface.<sup>243</sup>  $[\text{Cu}(\text{sBuNC}(\text{Me})\text{N}^{\text{sBu}})]_2$  was also used to grow Cu top contact electrodes on carboxylic acid-terminated SAM films as a protective layer that did not alter the Si/SAM interface.<sup>244</sup> During this process, the Cu precursor first interacts with the carboxyl groups to form an acid salt structure, with the intact ligands still linked to the Cu ions.<sup>244</sup> A subsequent pulse of H<sub>2</sub> releases the ligands while regenerating the COOH groups on top of the SAM.<sup>244</sup> The resulting free Cu atoms agglomerate into 40–80 nm nanoparticles after only 20 cycles.<sup>244</sup> Finally,  $[\text{Cu}(\text{sBuNC}(\text{Me})\text{N}^{\text{sBu}})]_2$  was used for the ALD of Cu and Cu<sub>3</sub>N on low-density silica aerogel substrates, using H<sub>2</sub> and NH<sub>3</sub> as respective coreagents.<sup>245</sup>

Most Cu ALD processes require higher temperatures to promote reactivity or prevent condensation of the precursors. However, a breakthrough discovery was made in 2009, with an ALD process employing a ligand exchange reaction using  $\text{Cu}(\text{dmap})_2/\text{Et}_2\text{Zn}$ ; high-purity, low-resistivity (2.78 μΩ·cm) Cu films were obtained within the 100–120 °C ALD window.<sup>246</sup> A theoretical study of this process proposed disproportionation of  $\text{Cu}(\text{dmap})_2$  to a Cu(I)dmap intermediate, followed by ligand exchange and reductive elimination to Cu metal.<sup>247</sup> A related

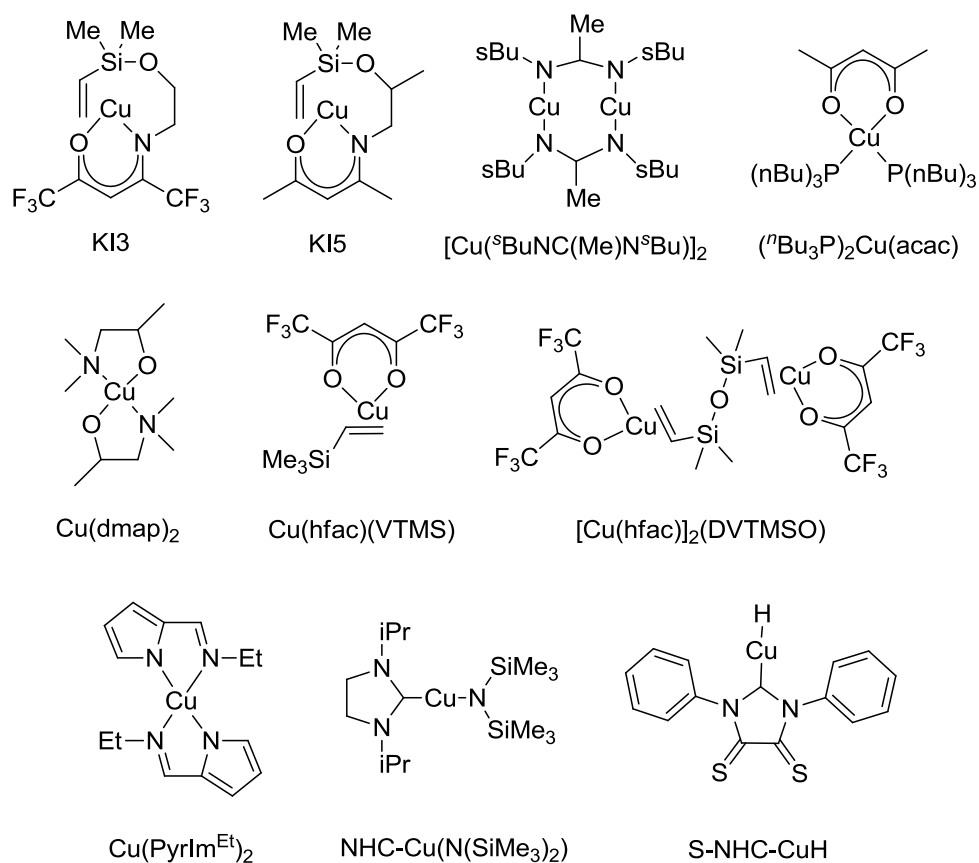
pulsed-CVD study reported copper-containing films from N-ethyl-2-pyrrolyaldimine (Cu(PyrIm<sup>Et</sup>)<sub>2</sub>) and either AlMe<sub>3</sub> or ZnEt<sub>2</sub> as coreagents at 120–150 °C.<sup>248</sup> The former process yielded nonconductive films with significant Al<sub>2</sub>O<sub>3</sub> incorporation, while the latter process afforded metallic Cu films with 8–15% Zn impurities, which were attributed to the self-decomposition of ZnEt<sub>2</sub> to zinc metal.<sup>248</sup> Solution reactions of Cu(PyrIm<sup>iPr</sup>)<sub>2</sub> with AlMe<sub>3</sub>, BEt<sub>3</sub>, and ZnEt<sub>2</sub> suggested that reduction occurs in two stages by way of a stable dinuclear Cu(I) pyrrolyaldimine complex.<sup>249</sup>

Recently, Cu(dmap)<sub>2</sub> was used with BH<sub>3</sub>(NHMe<sub>2</sub>) for the growth of Cu films on Ru substrates at a rate of 0.13 Å/cycle within the 130–160 °C ALD window.<sup>250</sup> A seed layer was required for the growth, leading to porous, rough films. A subsequent ternary process using formic acid supported the growth of smooth, low-resistivity films on Pt and Pd substrates without the need of a seed layer.<sup>250</sup> A growth rate of 0.20 Å/cycle was observed on both substrates within the 135–165 °C ALD window. In all cases, growth was proposed to occur by catalytic decomposition of BH<sub>3</sub>(NHMe<sub>2</sub>) by noble metal sites on the surface. The growth rate on Pt was reduced after 500 cycles while remaining unchanged on Pd up to 2000 cycles, likely due to the formation of a Cu/Pd alloy resulting from the rapid diffusion of Pd in Cu.<sup>250</sup> Cu(dmap)<sub>2</sub> was later used with an α-imino alkoxide dimer, [Mn(Me<sup>t</sup>BuCOCN<sup>t</sup>Bu)<sub>2</sub>]<sub>2</sub>, and BH<sub>3</sub>(NHMe<sub>2</sub>) for the ALD of 70/30 Cu/Mn alloy films (0.09 Å/cycle) and Cu/Mn/Cu film stacks over-coated with SiO<sub>2</sub>.<sup>21</sup> Stacks grown on Pt and Pd substrates showed diffusion of Mn atoms to the SiO<sub>2</sub>/Cu interface, diagnostic of self-forming Cu/Mn barrier layers.<sup>21</sup>

Other Cu compounds with the requisite volatility and thermal stability for ALD include complexes containing carbonylhydrazide (Cu(Me<sub>2</sub>NN=C(R)O)<sub>2</sub> (R = <sup>t</sup>Bu, <sup>i</sup>Pr, Me)),<sup>145</sup> α-imino

alkoxide ( $\text{Cu}(\text{RR}'\text{COCN}^t\text{Bu})_2$  ( $\text{R} = \text{Me}$ ,  $\text{R}' = \text{}^i\text{Pr}$ ;  $\text{R} = \text{Me}$ ,  $\text{R}' = \text{}^t\text{Bu}$ ;  $\text{R} = \text{R}' = \text{}^t\text{Bu}$ ),<sup>39</sup>  $\beta$ -ketoesterate,<sup>251</sup> guanidinate,<sup>209–210,212</sup> and iminopyrrolidinate<sup>211–212</sup> ligand systems.

**Chart 9.** Copper precursors used for vapor deposition processes.



### 1.5.9 Zinc

ZnO is an abundant, nontoxic transparent conducting oxide with a large band gap (3.37 eV),<sup>252</sup> finding use in window coatings, flat panel displays, and photovoltaic devices. Materials such as zinc tin oxide (ZTO) are used in solar cells<sup>253</sup> and thin film transistors.<sup>254</sup> ZnS has been a recent substitute for CdS as a buffer layer in photovoltaic devices due to its larger band gap (~3.8 eV)<sup>255</sup> along with its greater natural abundance and the less-toxic nature of zinc over

cadmium.<sup>256</sup> Other zinc-containing semiconducting materials include ZnSe, ZnTe, Zn<sub>3</sub>P<sub>2</sub>, Zn<sub>3</sub>As<sub>2</sub>, Zn<sub>3</sub>Sb<sub>2</sub>, ZnSiP<sub>2</sub>, Cu<sub>2</sub>ZnSnS<sub>4</sub>, Cu<sub>1.18</sub>Zn<sub>0.40</sub>Sb<sub>1.90</sub>S<sub>7.2</sub>, CdZnTe, HgZnTe, and HgZnSe.

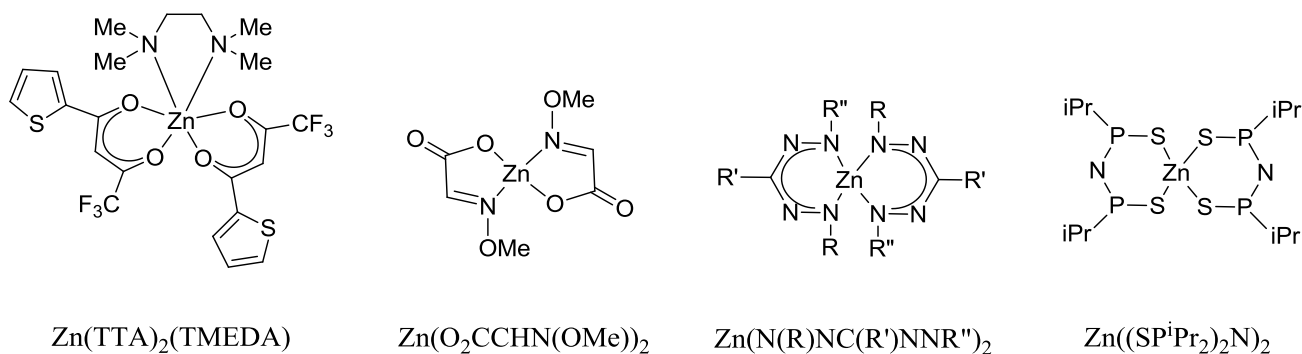
ZnO has been deposited by numerous techniques, including chemical spray pyrolysis,<sup>257</sup> sputtering,<sup>258</sup> reactive plasma deposition,<sup>259</sup> CVD,<sup>260</sup> radical source molecular beam epitaxy,<sup>261</sup> and sol-gel processes.<sup>262</sup> Zn(tmhd)<sub>2</sub>/O<sub>2</sub> was used for the CVD of ZnO films<sup>263–264</sup> and nanowire arrays.<sup>265</sup> Zn(TTA)<sub>2</sub>·TMEDA/O<sub>2</sub> was also used for ZnO films by CVD and PECVD processes.<sup>266</sup> The zinc ketoacidoximate complex, (Zn(O<sub>2</sub>CCHN(OMe))<sub>2</sub>·2H<sub>2</sub>O),<sup>267</sup> along with two fluorine-free β-diketiminate complexes,<sup>268</sup> have desirable thermal properties for CVD applications. One of the latter was used with O<sub>2</sub> for the CVD of ZnO films at 450–700 °C.<sup>268</sup> ZnEt<sub>2</sub> is a common precursor for the PEALD and thermal ALD of ZnO;<sup>269–270</sup> thermal ALD applications include the growth of Al-doped ZnO films<sup>271</sup> and the growth of ZnO on CdSe quantum-dot films.<sup>272</sup>

ZnS has traditionally been deposited by RF sputtering,<sup>273</sup> evaporation,<sup>274</sup> and CVD.<sup>275</sup> For CVD, use of single-source precursors circumvents the need for toxic, highly-reactive compounds (e.g. ZnEt<sub>2</sub> and H<sub>2</sub>S) and the challenge of controlling their gas-phase reactions. The dithiocarbamates Zn(S<sub>2</sub>CNMe<sub>2</sub>)<sub>2</sub><sup>255</sup> and Zn(S<sub>2</sub>CN(C<sub>2</sub>H<sub>5</sub>)<sub>2</sub>)<sub>2</sub><sup>276</sup> were respectively used as single-source precursors for the CVD of high-purity crystalline ZnS films and ordered ZnS nanotube arrays. Zn(S<sub>2</sub>CO<sup>i</sup>Pr)<sub>2</sub> was used as a single-source precursor for the CVD of ZnS,<sup>277</sup> and as the zinc precursor for the CVD of homogenous Zn<sub>x</sub>Cd<sub>1-x</sub>S<sup>278</sup> (0 ≤ x ≤ 1). Other single-source precursors used for the CVD of ZnS include Zn((SP<sup>i</sup>Pr<sub>2</sub>)<sub>2</sub>N)<sub>2</sub><sup>279</sup> and the dithiocarbamates<sup>280</sup> Zn(S<sub>2</sub>CNEtBu)<sub>2</sub> and Zn(S<sub>2</sub>CN(CH<sub>2</sub>)<sub>5</sub>Et)<sub>2</sub>. Finally, Zn(tmhd)<sub>2</sub> and *in situ* generated H<sub>2</sub>S were used for the ALD of ZnS films<sup>256</sup> and multilayer film stacks consisting of ZnS and Cu<sub>x</sub>S (x ~2).<sup>281</sup>



Numerous zinc-containing binary and ternary films have been reported. Zinc antimonide films were grown by ion beam sputter deposition.<sup>282</sup>  $Zn_2SiO_4$  films were grown by APCVD from homoleptic zinc amide compounds and  $O_2$ .<sup>283</sup> The use of  $Zn(N(SiMe_3)_2)_2/O_2$  gave amorphous films at 400–550 °C with stoichiometries close to  $ZnSiO_3$ , while the use of  $Zn(tBuN(SiMe_3))_2/O_2$  gave amorphous films at 350–550 °C with stoichiometries of  $Zn_2Si_{0.8\pm 1.4}O_{3.7\pm 4.8}$ ; subsequent annealing under  $N_2$  produced crystalline zinc orthosilicate,  $Zn_2SiO_4$ , in both cases.<sup>283</sup> Zn/Mg heterobimetallic carbamates have properties appropriate for use as single-source precursors for the CVD of  $Zn_xMg_{1-x}O$  films.<sup>284</sup> Finally, a series of tetrahedral zinc formazanate complexes,  $(Zn(N(R)NC(R')NNR''))_2$ , was recently synthesized as nitrogen-rich  $\beta$ -diketiminato analogues, however, these compounds have not yet been evaluated as vapor deposition precursors.<sup>285</sup>

**Chart 10.** Zinc precursors used for vapor deposition processes.



## 1.6 Reducing Coreagents

Reports of Cu ALD are numerous due to the positive reduction potentials of the Cu(I) and Cu(II) cations. Reducing coreagents used for Cu ALD include  $H_2$ ,<sup>36,242-244</sup> isopropanol,<sup>225</sup> formalin,<sup>225</sup> Zn,<sup>233</sup>  $ZnEt_2$ ,<sup>246</sup> hydrazine,<sup>231</sup>  $BH_3(NHMe_2)$ ,<sup>250</sup> and formic acid.<sup>199-200,227,231</sup> With the exception of Cu, thermal ALD of first-row transition metals is very challenging due to the negative reduction potentials of their cations and a general lack of strongly-reducing coreagents.

Main group element hydrides are promising reducing coreagents that should facilitate the transfer of a hydride from the main group element to the transition metal.<sup>31</sup> Transition metal hydrides are unstable, and once formed, should reduce to the metal with the elimination of H<sub>2</sub>.<sup>286</sup> Several neutral polyhedral boranes and borane adducts BH<sub>3</sub>(L) (L = THF, amines, other donor ligands) are volatile, commercially available, and have been previously used for the growth of transition metal nanoparticles.<sup>287</sup> BH<sub>3</sub>(NHMe<sub>2</sub>) was used for the ALD of high-purity Cu,<sup>250</sup> Cu/Mn alloys,<sup>21</sup> and films of Cr, Fe, Co, Ni, and MnO<sub>x</sub>.<sup>39</sup> To date, no thermal ALD processes have been reported for Ti metal, and no ALD processes whatsoever have been reported for V or Zn metal. New strongly-reducing coreagents are distinctly lacking for the thermal ALD of high-purity first-row transition metal films.

## 1.7 Thesis Problem

Thin films containing first-row transition metals are widely used in microelectronic, photovoltaic, catalytic, and surface-coating applications. In particular, metal films are essential for interconnects and seed, barrier, and capping layers in integrated circuitry. Traditional vapor deposition methods for film growth include PVD, CVD, or the use of plasma. However, these techniques cannot afford sub-nm thickness control, and thus, are inadequate for many current and future applications. By contrast, ALD enables absolute surface conformality and thickness control on 3D architectures and in high aspect ratio features.<sup>31</sup> However, the low-temperature chemical reduction of most first-row transition metal cations to their zero-valent state is very challenging due to their negative electrochemical potentials.<sup>41</sup> The general lack of strongly-reducing coreagents has rendered the thermal ALD of metal films an intractable problem for many elements. Additionally, many established processes for metal film growth are plagued by

low growth rates, impurity incorporation, poor nucleation, high surface roughness, or the need for hazardous coreagents.<sup>31</sup> Additionally, new ALD methods offering precise stoichiometric control are in demand for ternary films, such as first-row transition metal borates, as these materials have emerging applications as cathode materials in lithium-ion batteries.<sup>288</sup>

The research herein seeks to develop new ALD processes for the broader application of metal, metal oxide, and metal borate films to future nanoscale technologies. These processes should display the self-limited growth mechanism and support the facile nucleation of smooth, continuous, high-purity films at the lowest possible temperatures to satisfy future microelectronic demands and other manufacturing requirements.<sup>31</sup> Focus will be given to the development of strongly-reducing coreagents for the ALD of very electropositive metal films, such as titanium. Additionally, new processes will be considered for the growth of cobalt and nickel metal films and for the stoichiometric control of first-row transition metal borate films.

Computational techniques such as density functional theory (DFT) using nucleus-independent chemical shift (NICS) will be used to determine the electronic structure and predict the relative reducing power of organic coreagents. Potential ALD precursors will be analyzed by  $^1\text{H}$  and  $^{13}\text{C}$  NMR, thermogravimetric and differential thermal analyses (TGA/DTA), melting point and solid state decomposition measurements, preparative sublimation studies, and solution-screening reactions. Deposition parameters will be optimized for successful ALD processes. The resultant films will be studied by scanning electron microscopy (SEM), tunneling electron microscopy (TEM), atomic force microscopy (AFM), X-ray photoelectron spectroscopy (XPS), auger electron spectroscopy (AES), powder X-ray diffractometry (XRD), time-of-flight elastic recoil detection analysis (TOF-ERDA), ultraviolet-visible spectroscopy (UV-Vis), energy-dispersive X-ray spectroscopy (EDS), and four-point probe resistivity measurements.

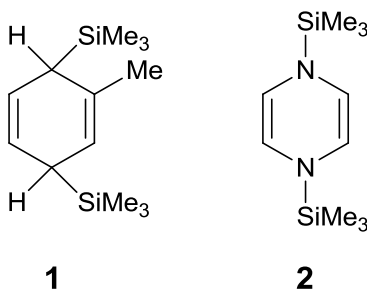
## CHAPTER 2

### Thermal Atomic Layer Deposition of Titanium and Antimony Films Using 2-Methyl-1,4-bis(trimethylsilyl)-2,5-cyclohexadiene or 1,4-Bis(trimethylsilyl)-1,4-dihydropyrazine

#### 2.1 Introduction

Metallic titanium films have numerous applications in microelectronic devices, including recent reports of Ti/Al alloy liners for advanced transistor structures.<sup>52–54</sup> However, the growth of Ti and other electropositive metal films from chemical precursors is extremely challenging due to the difficult reductions of the precursor metal ions and the lack of powerful reducing coreagents that can transform the metal ions to the metals rapidly.<sup>24g,31,39,289–290</sup> Titanium is a typical electropositive metal and has a very negative electrochemical potential ( $\text{Ti(II)} \leftrightarrow \text{Ti(O)}$ ,  $E^0 = -1.631 \text{ V}^{41}$ ). Consequently, reports of Ti deposition from chemical precursors have been scarce and limited to CVD<sup>70–71</sup> and plasma-based<sup>11</sup> approaches. However, due to the very small feature sizes and 3D architectures of future transistors, Ti metal must be deposited by ALD to meet thickness uniformity and conformality requirements.<sup>52–54</sup> Thus, new strongly-reducing coreagents are required to facilitate the low-temperature ALD of Ti films.

In a series of recent papers, Mashima and coworkers described the use of 2-methyl-1,4-bis(trimethylsilyl)-2,5-cyclohexadiene (**1**, Chart 11) and 1,4-bis(trimethylsilyl)-1,4-dihydropyrazine (**2**, Chart 11) and as salt-free reagents for the reduction of early transition metal halide complexes from their highest oxidation states to lower oxidation states.<sup>291–294</sup> Mashima's use of **1** to reduce  $\text{TaCl}_5$  to  $\text{TaCl}_3$  afforded a highly-efficient process for 1-hexene production without the need for organic supporting ligands, salt contact, or cocatalysts.<sup>294</sup> Compound **1** was also used to reduce  $\text{TiCl}_4$  to surface-bound  $\text{TiCl}_2$ .<sup>295</sup> Herein, we describe the low-temperature ALD of metallic Ti films using  $\text{TiCl}_4$  and **1** or **2** as precursors.

**Chart 11.** Structures of **1** and **2**.

## 2.2 Results and Discussion

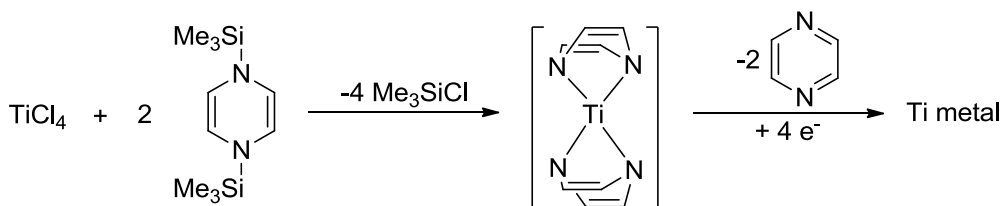
### 2.2.1 Computational Assessment of Six-membered Rings Containing Two Trimethylsilyl Groups

1,4-Dihydropyrazine is the unsubstituted analogue of **2** and has been studied theoretically. Using the high-level G2 method implemented in the Gaussian 03 suite, Vashchenko showed that 1,4-dihydropyrazine adopts a boat conformation with a relative population of conformers of 79% *syn* versus 21% *anti*.<sup>296</sup> Using MP2/6-311++G(d,p), an analysis of the potential energy surface for *syn-anti* transition showed a barrier to inversion on the nitrogen atom of 3 kcal/mol.<sup>296</sup> The electronic structures of **1**, **2**, and similar compounds are compared herein in an attempt to predict their relative reducing power.

Mashima demonstrated that **1** and **2** react with metal halides with the elimination of  $\text{ClSiMe}_3$ ,<sup>291-294</sup> so it is likely that intermediate 2-methyl 1,4-cyclohexadienyl or 1,4-dihydropyrazinyl complexes are formed, which then eliminate aromatic toluene or pyrazine to reduce the metal center by two electrons per ligand (Figure 10). During this double desilylation process, non-conjugated **1** or antiaromatic **2** may be transformed to dianions coordinated to a Ti(IV) cation. Strong Si-Cl bond formation coupled with the elimination of an aromatic byproduct are the proposed driving forces for this reduction. Thus, quantifying the change in

aromaticity from the parent compound to the aromatic byproduct may provide a useful metric for predicting the relative reducing power of **1**, **2**, and structural analogues.

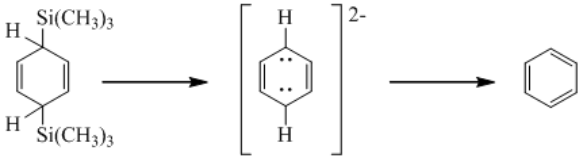
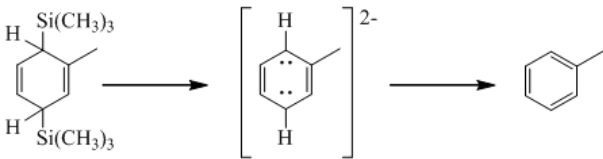
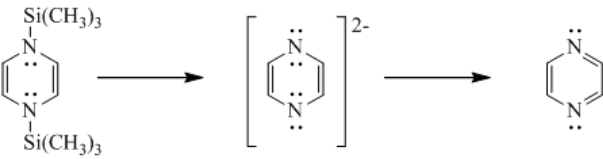
**Figure 10.** Proposed mechanism for the reduction of  $\text{TiCl}_4$  by **2** to afford Ti metal.



A magnetic field directed perpendicular to the plane of an aromatic ring will induce a current in the conjugated  $\pi$  system, which itself creates a second magnetic field, in accordance with Ampere's law. The induced magnetic field has the same direction as the applied magnetic field outside of the ring, while the two fields oppose one another inside of the ring. Consequently, protons located outside of the ring are deshielded, while protons located inside of the ring are shielded. Nucleus-independent chemical shift (NICS) is a technique to calculate this magnetic shielding; negative values indicate aromaticity, while positive values indicate antiaromaticity.<sup>297</sup>

Geometry optimizations were performed at the B3LYP/6-311G(d,p) level of theory using Gaussian 09. The total isotropic chemical shift ( $\sigma_{\text{iso}}$ ) and the chemical shift tensor component orthogonal to the plane of the ring ( $\sigma_{\text{zz}}$ ) were calculated by placing a ghost atom (Bq) 1 Å above the geometric center of the ring, defined as the NICS(1) position.<sup>297d</sup> NICS(1) is affected by  $\pi$ -electron density only, and thus, NICS(1)<sub>iso</sub> and NICS(1)<sub>zz</sub> are reliable measures of the relative aromaticity of these systems. The differences between the NICS values of the parent compound and its aromatic counterpart were used to quantify the relative reducing power of **1**, **2**, and a benzene analogue. The transformation of **2** to pyrazine produced the greatest changes in NICS values (Table 2).

**Table 2.** NICS(1)<sub>iso</sub> and NICS(1)<sub>zz</sub> values for **1**, **2**, and a benzene analogue.

	<p>NICS(1)<sub>iso</sub>    <b>+1.125</b></p> <p>NICS(1)<sub>zz</sub>    <b>+6.232</b></p>	<p>-10.207</p> <p>-29.243</p>	<p><math>\Delta = -11.332</math></p> <p><math>\Delta = -35.475</math></p>
	<p>NICS(1)<sub>iso</sub>    <b>+0.141</b></p> <p>NICS(1)<sub>zz</sub>    <b>+3.942</b></p>	<p>-10.096</p> <p>-28.035</p>	<p><math>\Delta = -10.237</math></p> <p><math>\Delta = -31.977</math></p>
	<p>NICS(1)<sub>iso</sub>    <b>+7.858</b></p> <p>NICS(1)<sub>zz</sub>    <b>+26.563</b></p>	<p>-10.235</p> <p>-28.359</p>	<p><math>\Delta = -18.093</math></p> <p><math>\Delta = -54.922</math></p>

Thus, NICS calculations suggest that the transition from an 8  $\pi$  electron antiaromatic ring (**2**) to aromatic pyrazine provides a stronger driving force than that from a non-conjugated cyclohexadiene ring (**1**) to aromatic toluene. Previously-reported experimental results for **2** demonstrate distinct paratropism and an exceptionally low ionization potential.<sup>298</sup>

### 2.2.2 Titanium Films from TiCl<sub>4</sub> and 2-Methyl-1,4-bis(trimethylsilyl)-2,5-cyclohexadiene

**Synthesis.** 2-Methyl-1,4-bis(trimethylsilyl)-2,5-cyclohexadiene (**1**) was synthesized by reductive silylation of toluene with lithium and ClMe<sub>3</sub>Si.<sup>299</sup> The crude product was distilled at 90–100 °C/0.05 Torr, yielding a pure mixture of two diastereomers by <sup>1</sup>H NMR analysis. Compound **1** boils at 70–72 °C/0.12 Torr,<sup>299</sup> and was found to be thermally stable to > 300 °C. Exposure to air at 23 °C resulted in the formation of a hazy-white suspension that was increasingly cloudy after approximately 20 minutes.

**Solution Reactivity.** Solution reductions were attempted with a variety of metal complexes, using five molar equivalents of **1** (Table 3). Analyses by powder XRD confirmed that  $\text{CuCl}_2$  and  $\text{CuCl}_2 \cdot \text{H}_2\text{O}$  were each reduced to  $\text{CuCl}$ . (Figure 11). Compound **1** reacted with  $\text{CuBr}_2$  to afford a milky-white precipitate, likely  $\text{CuBr}$ . Compound **1** also reduced  $\text{CuCl}_2 \cdot \text{DME}$  to  $\text{CuCl}$ ; subsequent addition of ethylenediamine (en) facilitated the disproportionation to Cu metal, with a crystallite size of  $35.9 \pm 1.6$  nm (Figure 12). Compound **1** (6.8 mmol) was dissolved in 60 mL of dry toluene. Upon direct addition of  $\text{TiCl}_4$  (2.7 mmol), the solution instantly turned a very dark brown/rust color with a precipitate that was dark brown/black in color. Analysis by powder XRD showed the  $\langle 110 \rangle$  reflection at  $38.48^\circ$  corresponding to Ti metal (Figure 13). Reactivity of **1** with other compounds may be limited by slow reaction kinetics.

**Table 3.** Solution reactions of metal complexes with **1**.

ML <sub>2</sub>	Sol	Reaction		Reflux		Solution Reaction
		Temp (°C)	Time (min)	Temp (°C)	Time (min)	
$\text{CuCl}_2$	THF	rt	60	66	60	milky white $\rightarrow$ $\text{CuCl}$ (insoluble)
$\text{CuCl}_2 \cdot 2\text{H}_2\text{O}$	THF	rt	60	-	-	milky white $\rightarrow$ likely $\text{CuCl}$ (insoluble)
$\text{CuCl}_2 \cdot 2\text{H}_2\text{O}$	THF	0	5	66	65	milky white $\rightarrow$ $\text{CuCl}$ (insoluble)
$\text{CuCl}_2 \cdot \text{DME}$	DME	rt	20	85	75	milky white $\rightarrow$ add en $\rightarrow$ Cu metal
$\text{CuBr}_2$	THF	rt	60	-	-	milky white $\rightarrow$ likely $\text{CuBr}$ (insoluble)
$\text{Cu}(\text{dmap})_2$	THF	rt	80	66	60	none
$\text{Cu}(\text{hfac})_2 \cdot x\text{H}_2\text{O}$	THF	rt	35	66	60	none
$\text{Cu}(\text{tmhd})_2$	THF	rt	60	66	60	none
$\text{Cu}(\text{OCHO})_2 \cdot 4\text{H}_2\text{O}$	THF	0	5	66	60	none
$\text{CoCl}_2$	THF	rt	60	66	60	none
$\text{ZnCl}_2$	THF	rt	105	66	60	none
$\text{TiCl}_4$	toluene	rt	< 1	-	-	brown precipitate
$\text{SiCl}_4$	toluene	rt	600	-	-	none



**Figure 11.** Powder XRD spectra of CuCl; reduction of CuCl<sub>2</sub> and CuCl<sub>2</sub>·2H<sub>2</sub>O by **1** in THF.

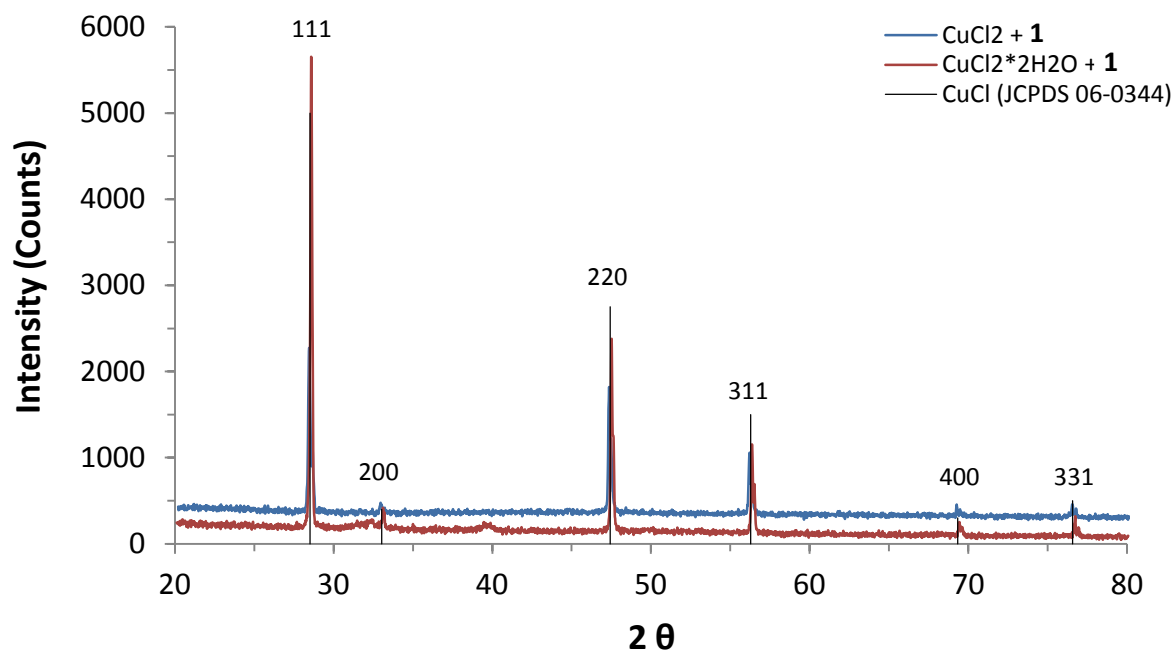


**Figure 12.** Powder XRD spectrum of Cu metal; reduction of CuCl<sub>2</sub>·DME by **1** and en in DME.

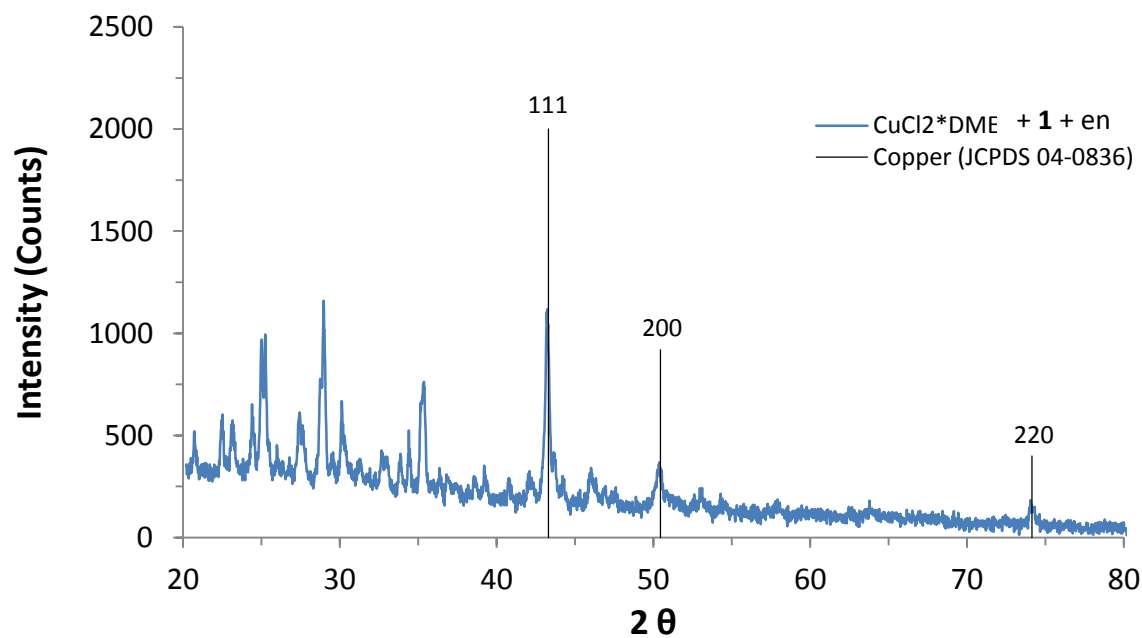


**Figure 13.** Powder XRD spectrum of Ti metal; reduction of  $\text{TiCl}_4$  by **1** in toluene.

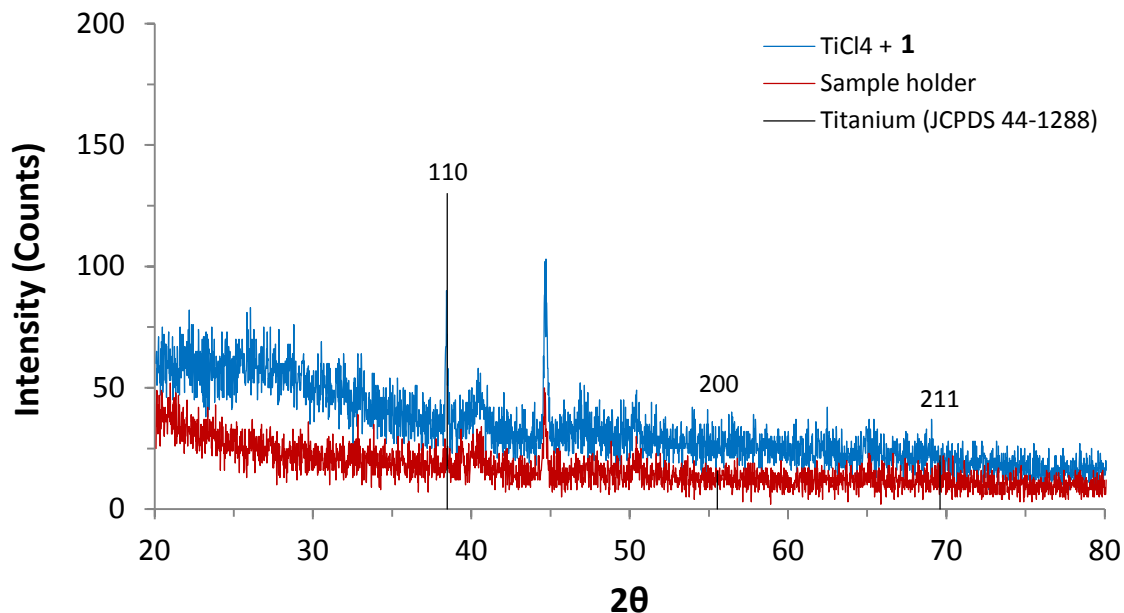
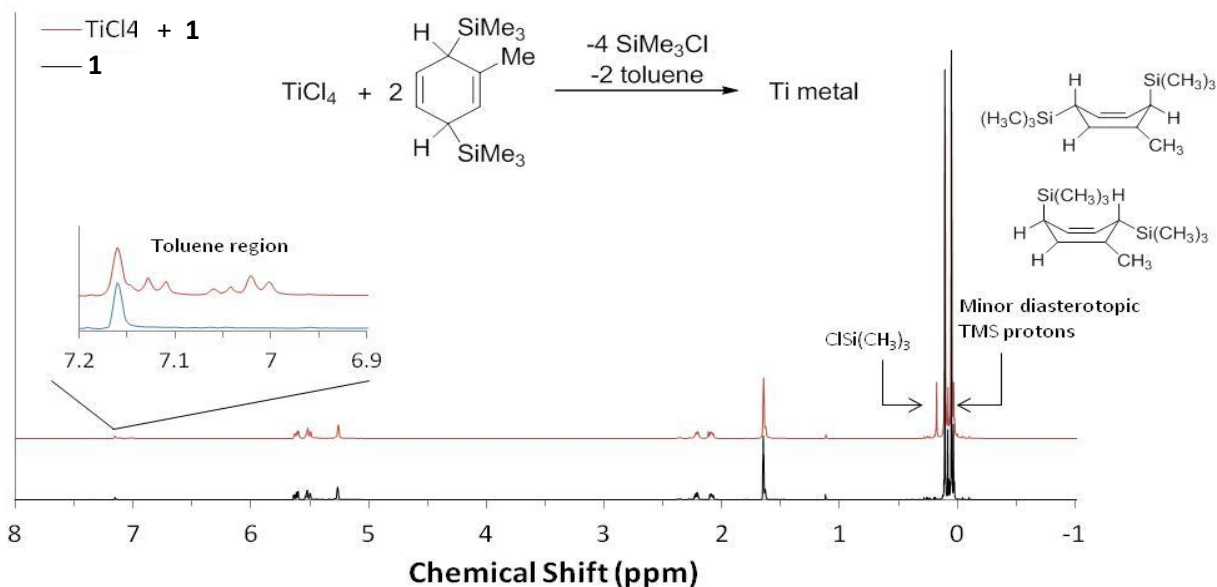


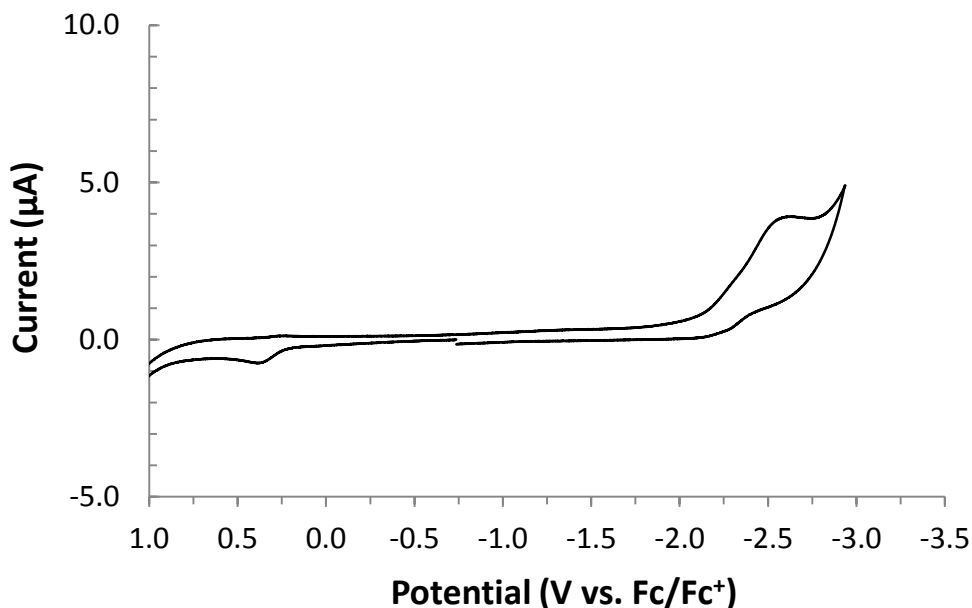
Figure 14 shows the  $^1\text{H}$  NMR spectrum of the two diastereomers comprising **1**. Direct addition of  $\text{TiCl}_4$  to a solution of **1** in  $\text{C}_6\text{D}_6$  in an NMR tube resulted in the immediate formation of a black precipitate. The  $^1\text{H}$  NMR spectrum of the reaction product shows the expected formation of  $\text{ClSiMe}_3$  and toluene.

**Figure 14.**  $^1\text{H}$  NMR spectra of **1** and the reaction product of  $\text{TiCl}_4$  and **1** in  $\text{C}_6\text{D}_6$ .



**Cyclic Voltammetry.** To quantify the reducing power of the toluene dianion, CV experiments were performed in DMF, using 0.1 M  $\text{NBu}_4\text{ClO}_4$  as the supporting electrolyte. Reported data are relative to ferrocene (referenced to 0.31 V), using  $\text{Ag}/\text{AgNO}_3$  as the reference electrode. Toluene showed a reduction at  $E_{1/2} = -2.46$  V. (Figure 15).

**Figure 15.** Cyclic voltammogram of toluene relative to ferrocene ( $\text{Fc}/\text{Fc}^+$ ,  $E^\circ = 0.31$  V).



**Film Deposition Data.** Encouraged by the reducing capability of **1**, film depositions were explored using  $\text{TiCl}_4$  and **1** as precursors. The growth rate was probed as a function of the pulse lengths of  $\text{TiCl}_4$  and **1** at 180 °C, using 3,000 cycles and 5.0 and 10.0 s  $\text{N}_2$  purges after the pulses of  $\text{TiCl}_4$  and **1**, respectively. Similar growth rates were observed on Si(100) with native oxide, 100 nm thermal  $\text{SiO}_2/\text{Si}$ , and 15 nm Pt/100 nm  $\text{SiO}_2/\text{Si}$ . The ALD study was conducted using  $\text{SiO}_2$  substrates. Microscopic analyses were performed on films grown on Si(100),  $\text{SiO}_2$ , and Pt, while XPS analyses were performed on films grown on Si(100) and Pt. All films were exposed to ambient atmosphere prior to analyses, which led to rapid oxidation. X-ray diffraction spectra of all films showed no reflections, suggesting either amorphous films or oxidation of the

Ti before the analyses could be performed. Films measured within 30 s of removal from the reactor were electrically nonconductive by four-point probe analysis, consistent with the rapid oxidation of the surface. Films grown on SiO<sub>2</sub> and Si(100) with native oxide showed good adhesion to the substrates, passing the Scotch tape test.

A plot of growth rate versus TiCl<sub>4</sub> pulse length showed a growth plateau at  $\geq 0.2$  s pulses, with a saturative growth rate of 0.06 Å/cycle (Figure 16). A similar plot of growth rate versus pulse length of **1** showed saturative behavior at  $\geq 0.2$  s pulses with the same growth rate (Figure 17). As expected, the consumption rate of **1** increased as a function of the pulse length of **1**. Based upon these data, a pulse sequence 0.3 s TiCl<sub>4</sub>/5.0 s N<sub>2</sub> purge/0.2 s **1**/10.0 s N<sub>2</sub> purge was used for all subsequent depositions. Importantly, deposition experiments conducted using only TiCl<sub>4</sub> and a N<sub>2</sub> purge or only **1** and a N<sub>2</sub> purge (3,000 cycles, 180 °C) did not produce any detectable film growth. These experiments demonstrate that growth requires both TiCl<sub>4</sub> and **1** and does not occur by the separate decomposition of either precursor.

**Figure 16.** Saturation plot of TiCl<sub>4</sub> using 0.2 s pulses of **1** at 180 °C.

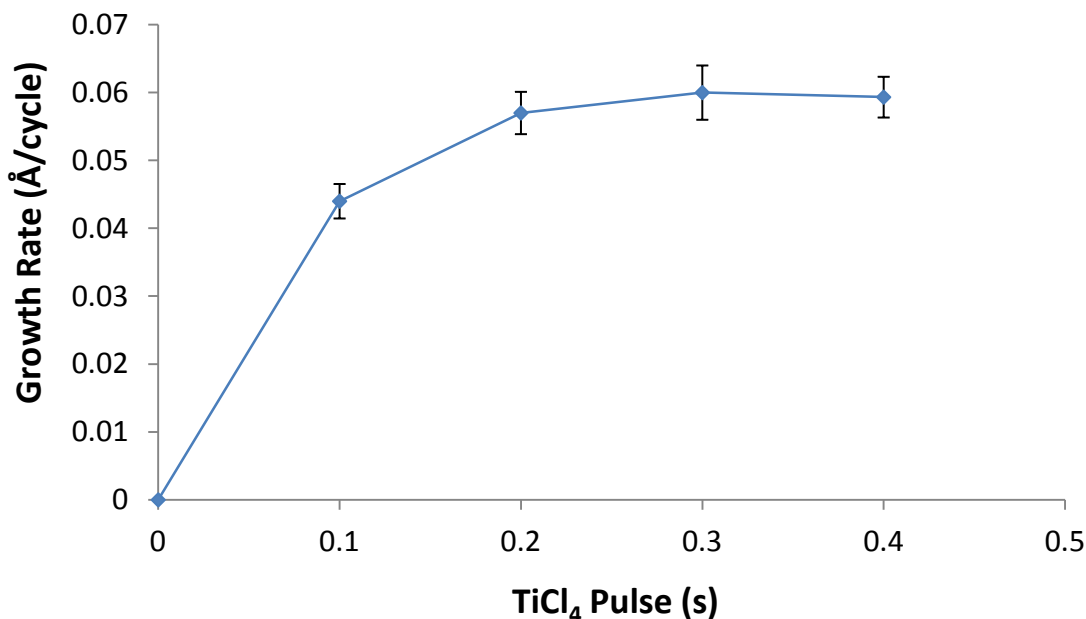


**Figure 17.** Saturation plot of **1** using 0.3 s pulses of  $\text{TiCl}_4$  at 180 °C. The secondary axis shows the consumption rate of **1** as a function of the pulse length of **1**.

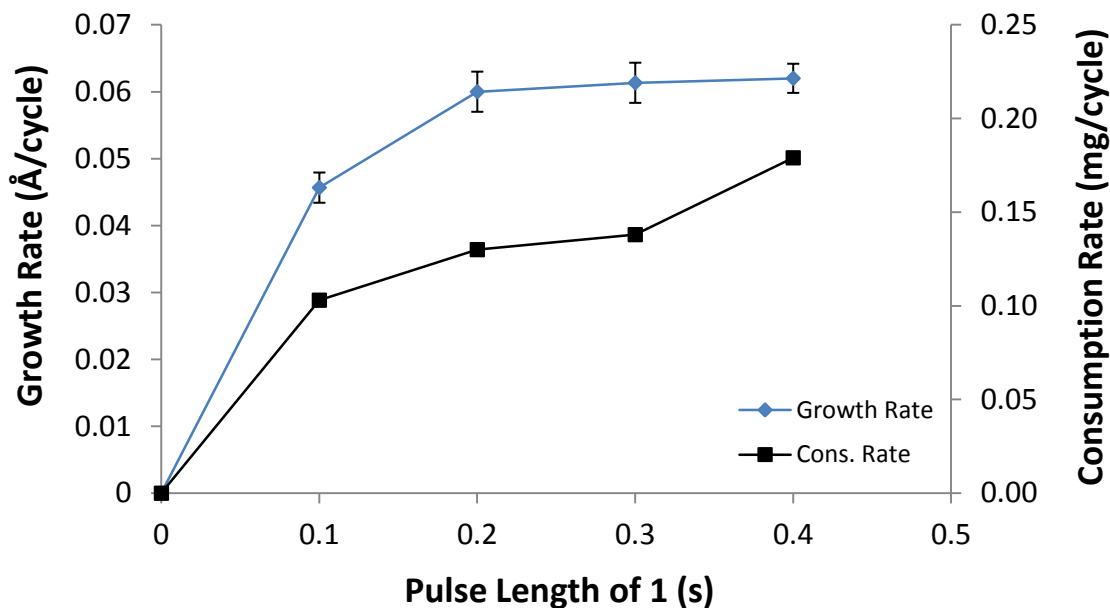


Figure 18 shows a plot of growth rate versus temperature. An ALD window was observed from 110–240 °C, with a growth rate of 0.06 Å/cycle within this range. Temperatures  $\geq 180$  °C afforded increasingly rough films.

**Figure 18.** Plot of growth rate versus temperature using 0.3 s pulses of  $\text{TiCl}_4$  and 0.2 s pulses of **1** for 3,000 cycles.

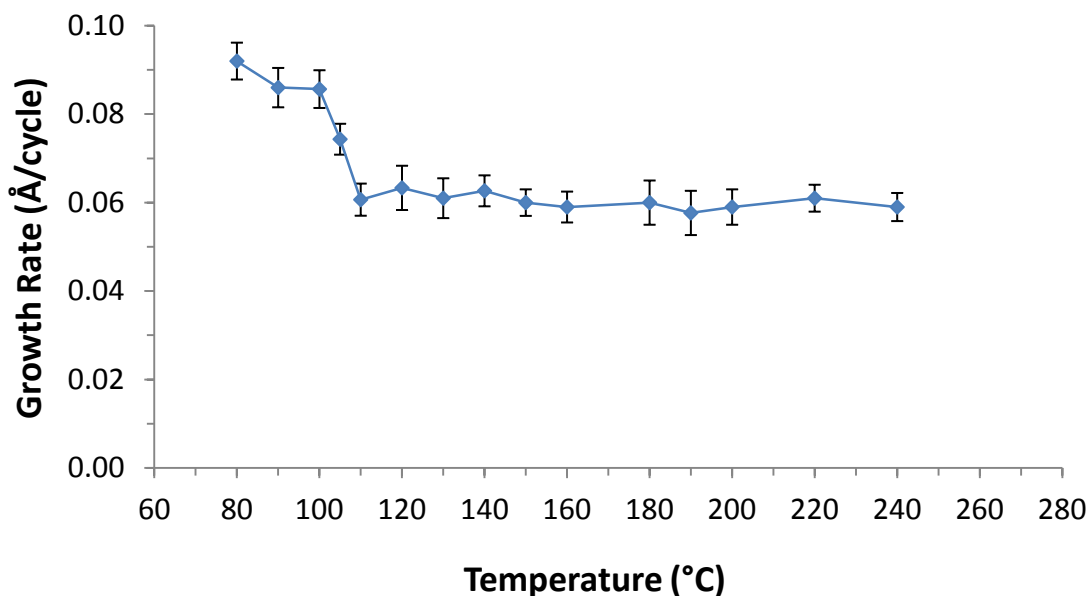
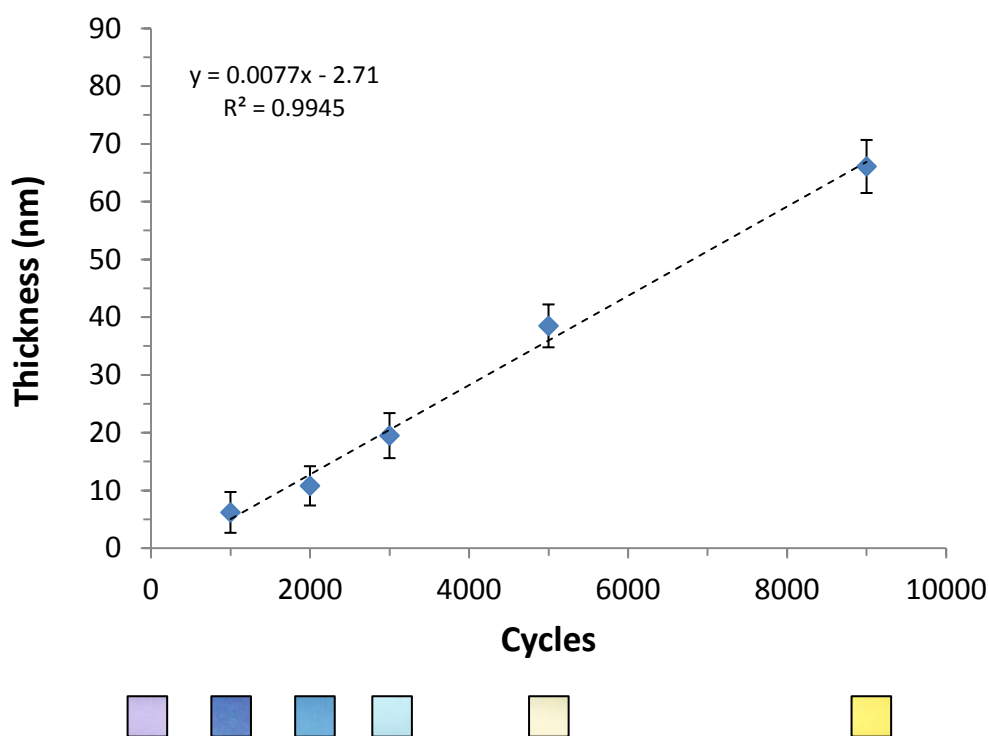


Figure 19 shows a plot of film thickness versus the number of ALD cycles. A trend line constructed by a least squares approach shows a slope of  $0.077 \text{ \AA}/\text{cycle}$ , which is in good agreement with the established growth rate. The y-intercept of  $-2.710 \text{ nm}$  indicates that there is no nucleation delay for this process.

**Figure 19.** Plot of film thickness versus number of ALD cycles using  $\text{TiCl}_4$  and **1** at  $180 \text{ }^\circ\text{C}$ . Images below the x-axis show magnified regions of each film from a single photograph taken of all films.



Figures 20–21 show SEM images of films grown for 3,000 cycles at various substrate temperatures. A constant growth rate is observed up to  $240 \text{ }^\circ\text{C}$ , however, additional particulate growth on top of the film is evident at temperatures  $\geq 180 \text{ }^\circ\text{C}$ . The film becomes indistinguishable from the particulate growth at temperatures  $> 240 \text{ }^\circ\text{C}$ . Figure 22 shows SEM images of smooth, uniform films grown on Si(100) and Pt substrates at  $140 \text{ }^\circ\text{C}$ .

**Figure 20.** Cross-sectional SEM images of films deposited on thermal SiO<sub>2</sub> using TiCl<sub>4</sub> and **1** at 110, 130, 160, and 180 °C.

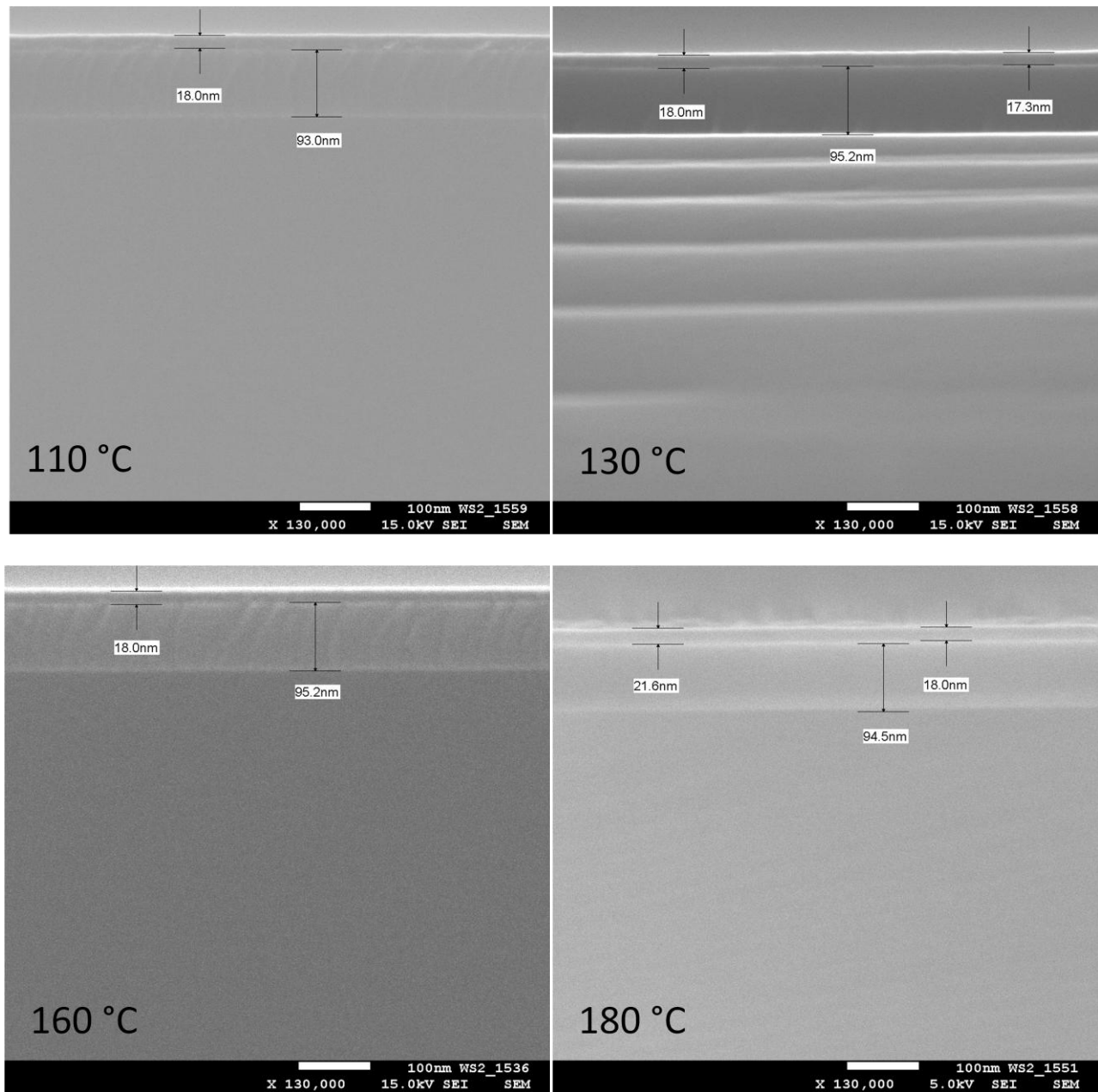


**Figure 21.** Cross-sectional SEM images of films deposited on thermal SiO<sub>2</sub> using TiCl<sub>4</sub> and **1** at 200, 220, 240, and 260 °C.

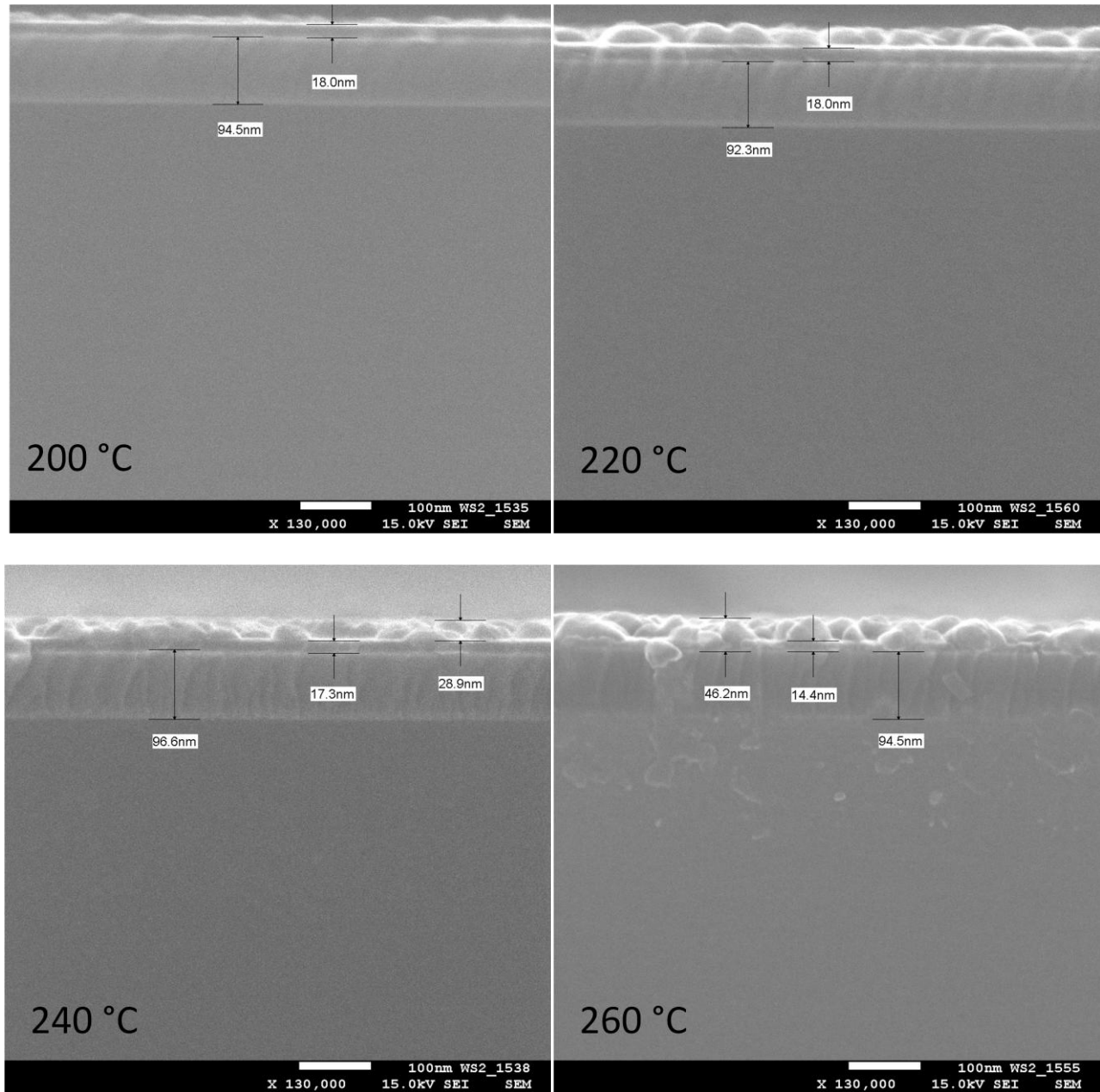
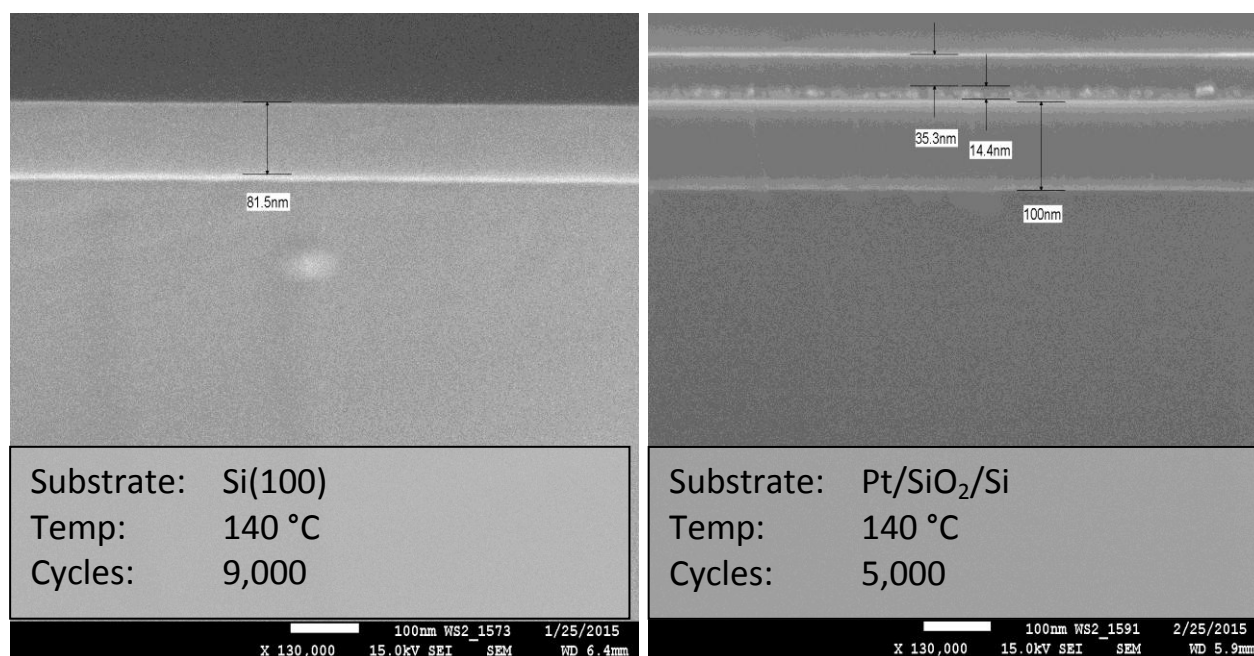




**Figure 22.** Cross-sectional SEM images of films deposited on Si(100) and Pt substrates using  $\text{TiCl}_4$  and **1** at 140 °C.



AFM images of 74–82 nm thick films grown at 140 °C had RMS surface roughnesses of  $\leq 8.8$  nm, indicating smooth surfaces (Table 4, Figures 23–24). AFM images of 69–71 nm thick films grown at 180 °C were notably rougher, coinciding with the additional nanoparticulate growth observed by SEM (Table 4, Figures 25–26).

**Table 4.** Surface roughnesses measured by AFM of films grown using  $\text{TiCl}_4$  and **1** at 140 and 180 °C on Si(100) and  $\text{SiO}_2$  substrates.

140 °C

<u>RMS Roughness (nm)</u>		
Film/Substrate	2 $\mu\text{m}^2$	5 $\mu\text{m}^2$
82 nm Ti/Si(100)	8.8	0.1
74 nm Ti/SiO <sub>2</sub>	1.3	4.9

180 °C

<u>RMS Roughness (nm)</u>		
Film/Substrate	2 $\mu\text{m}^2$	5 $\mu\text{m}^2$
71 nm Ti/Si(100)	17.4	161.7
69 nm Ti/SiO <sub>2</sub>	12.8	13.5

**Figure 23.** AFM image of a  $2 \mu\text{m}^2$  region of a film grown using  $\text{TiCl}_4$  and **1**. The film was deposited on Si(100) with native oxide at  $140^\circ\text{C}$ . The RMS surface roughness of the 82 nm thick film was 8.8 nm.

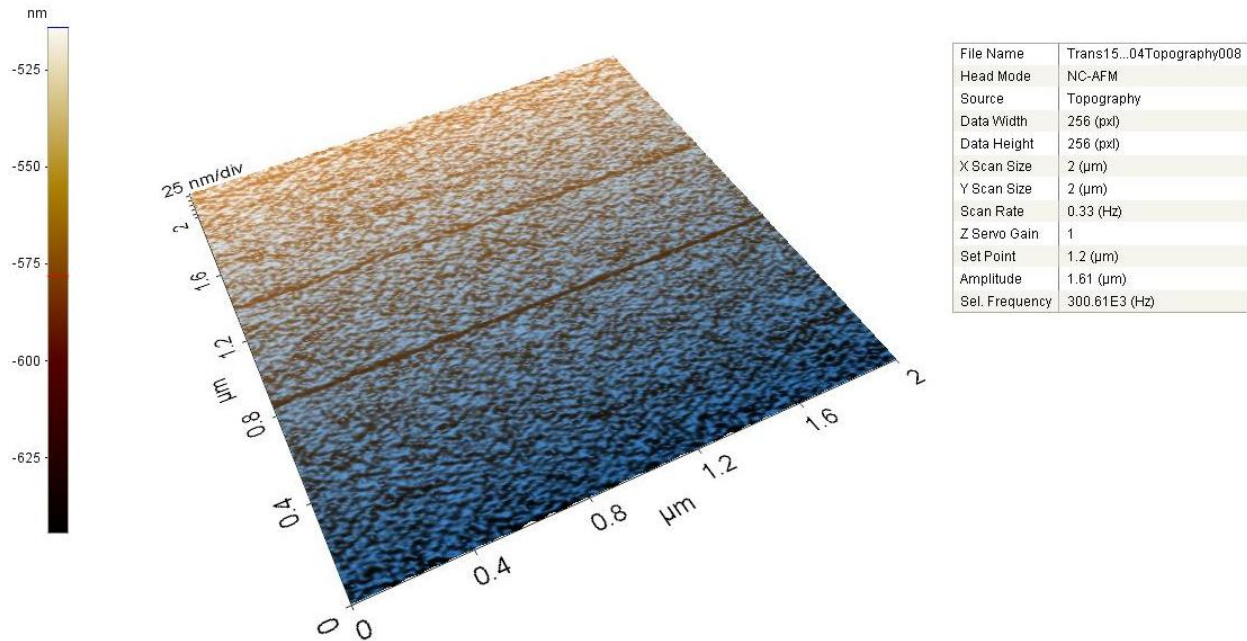


**Figure 24.** AFM image of a  $5 \mu\text{m}^2$  region of a film grown using  $\text{TiCl}_4$  and **1**. The film was deposited on Si(100) with native oxide at  $140^\circ\text{C}$ . The RMS surface roughness of the 82 nm thick film was 0.1 nm.

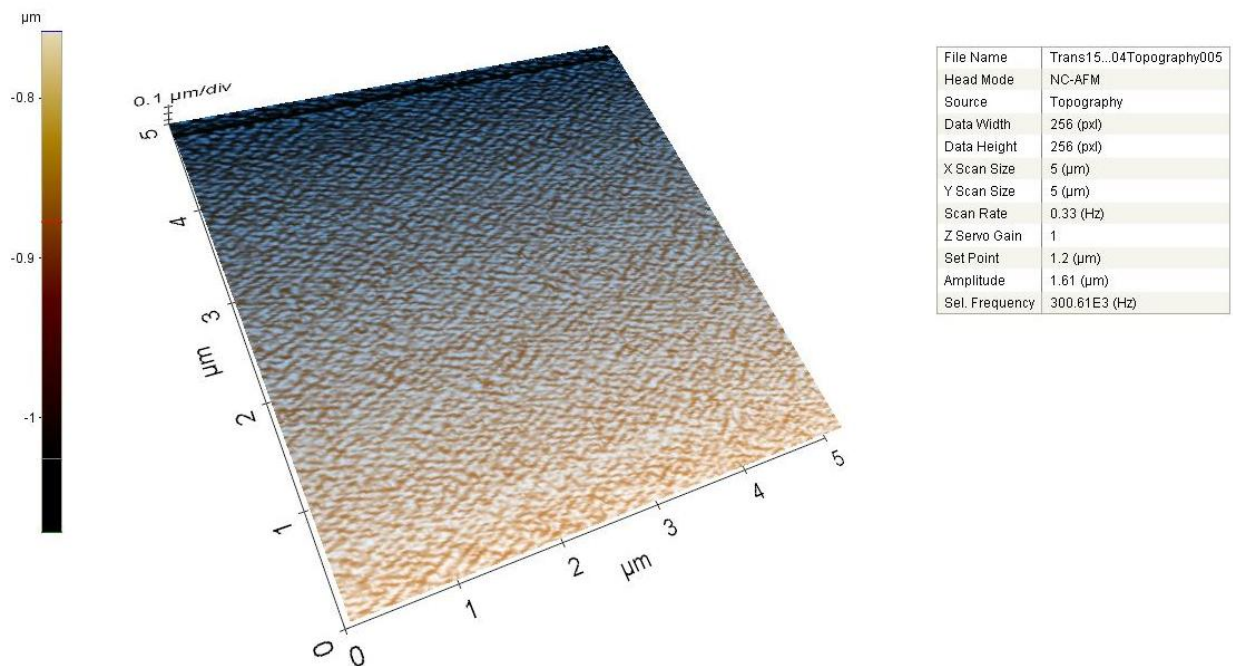


**Figure 25.** AFM image of a  $2 \mu\text{m}^2$  region of a film grown using  $\text{TiCl}_4$  and **1**. The film was deposited on Si(100) with native oxide at  $180^\circ\text{C}$ . The RMS surface roughness of the 71 nm thick film was 17.4 nm.

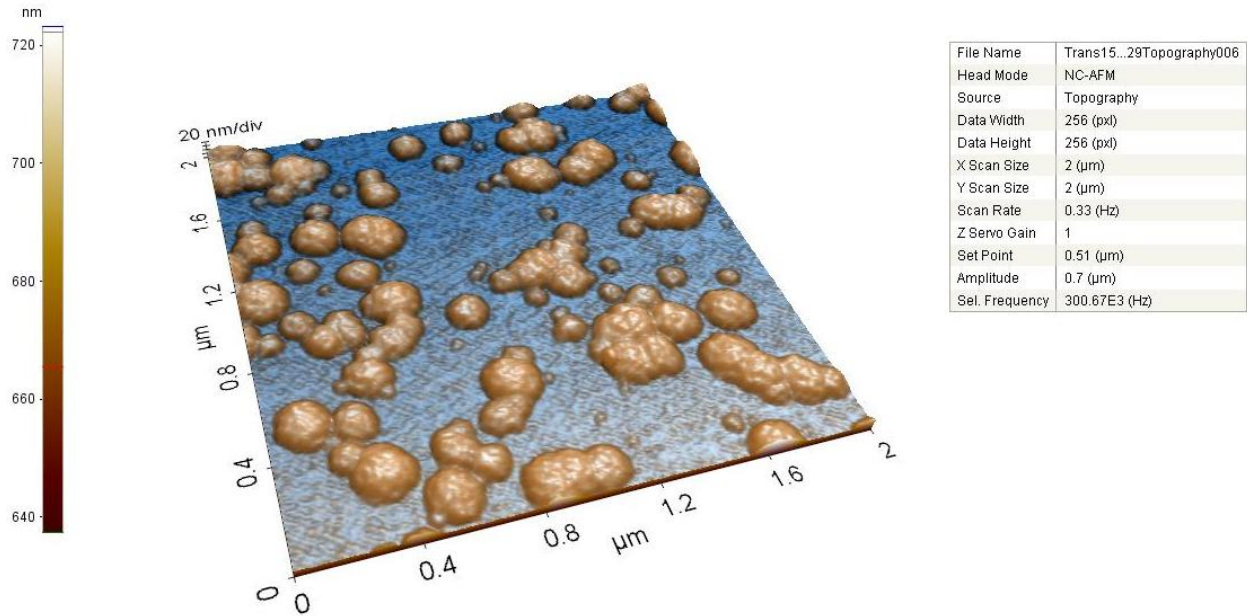
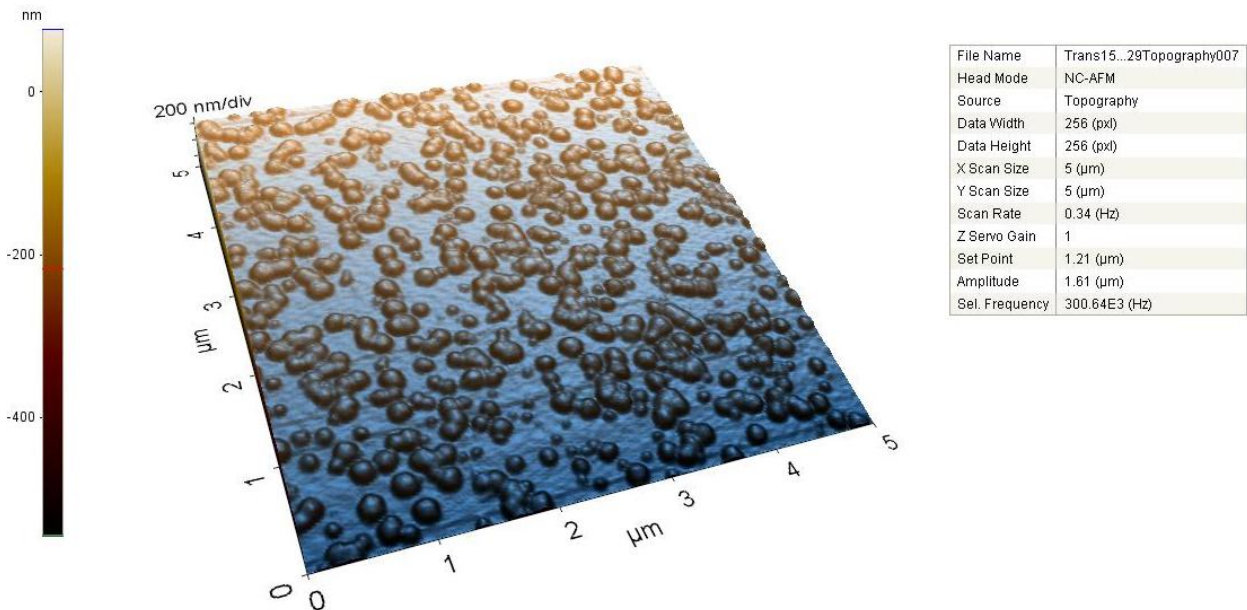


**Figure 26.** AFM image of a  $5 \mu\text{m}^2$  region of a film grown using  $\text{TiCl}_4$  and **1**. The film was deposited on Si(100) with native oxide at  $180^\circ\text{C}$ . The RMS surface roughness of the 71 nm thick film was 161.7 nm.



Energy-dispersive X-ray spectroscopic element mapping (EDS) was performed on 68 nm thick films grown on SiO<sub>2</sub> and Si(100) substrates at 180 °C using 2 kV at -78 °C. Regions with and without nanoparticulate growth showed similar results, independent of the underlying substrate. Detection of C K<sub>α</sub> electrons consistently showed 5–6% carbon content. However, given the negligible carbon detected by XPS upon sputtering, this was likely due to contamination of the chamber. Ti L<sub>α</sub> and O K<sub>α</sub> electrons were detected to determine the composition of the nanoparticles and the underlying film. Ti/O ratios were slightly higher than 2:1, suggesting a primarily TiO<sub>2</sub> composition with sub-oxides present within the penetration depth of the X-rays.

**Figure 27.** Top-down SEM images of films grown on Si(100) (a, b) and SiO<sub>2</sub> (c, d) substrates from TiCl<sub>4</sub> and **1** at 180 °C. EDS analyses were performed in tandem on areas with and without nanoparticulate growth.

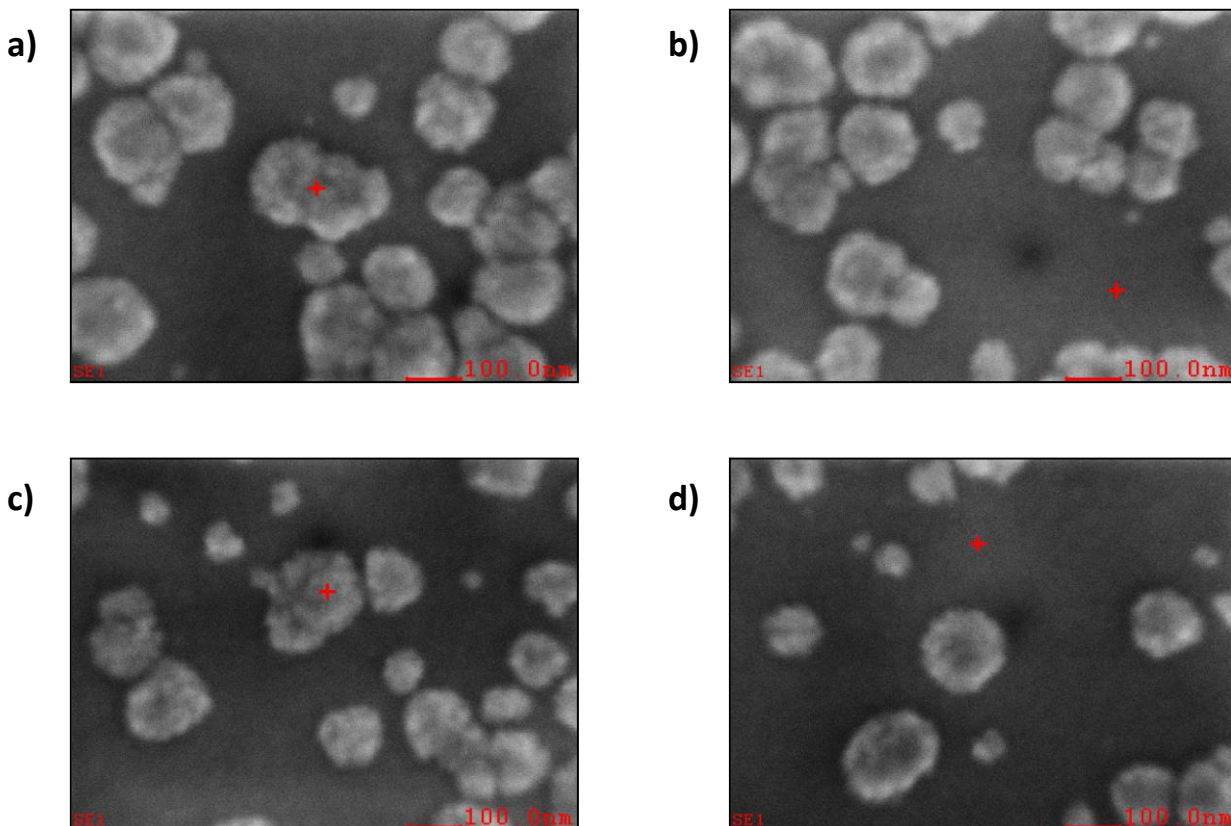


**Table 5.** EDS element mapping of films grown on Si(100) and SiO<sub>2</sub> substrates from TiCl<sub>4</sub> and **1** at 180 °C. The wt.% and at.% were calculated on areas with and without nanoparticulate growth.

Ti/Si(100)	<i>Element</i>	<b>Nanoparticle region</b>		<b>Bare film region</b>	
		<i>Wt%</i>	<i>At%</i>	<i>Wt%</i>	<i>At%</i>
	<i>CK</i>	2.83	6.14	2.68	5.97
	<i>TiL</i>	59.41	32.34	61.63	34.39
	<i>OK</i>	37.76	61.52	35.69	59.64

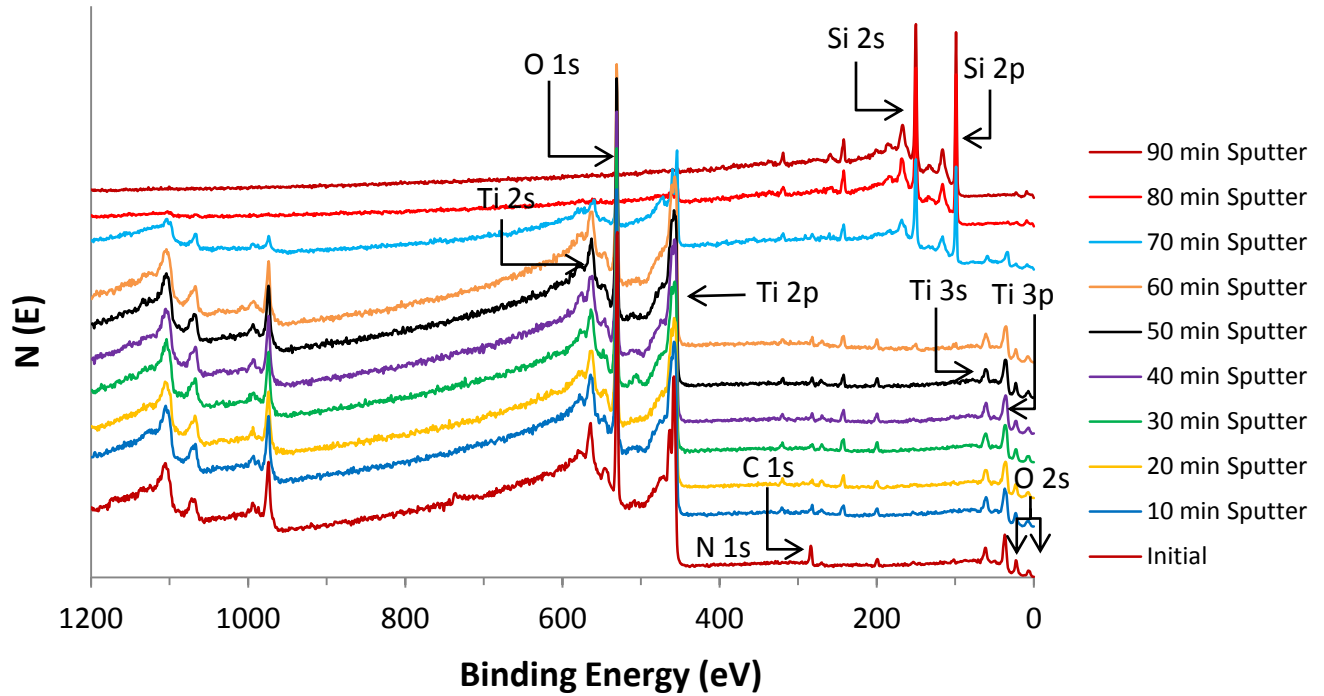
  

Ti/SiO <sub>2</sub>	<i>Element</i>	<b>Nanoparticle region</b>		<b>Bare film region</b>	
		<i>Wt%</i>	<i>At%</i>	<i>Wt%</i>	<i>At%</i>
	<i>CK</i>	2.49	5.66	2.49	5.6
	<i>TiL</i>	63.52	36.26	62.59	35.35
	<i>OK</i>	33.99	58.08	34.93	59.06

Several films were carefully analyzed by XPS. Figures 28–33 show spectra for an 82 nm thick film grown on Si(100) from TiCl<sub>4</sub> and **1** at 140 °C. Figure 30 shows the Ti 2p ionization region, where the as-deposited film (red trace) revealed major ionizations for TiO<sub>2</sub> (2p<sub>3/2</sub> 458.5 eV<sup>305</sup>) and minor ionizations consistent with Ti<sub>2</sub>O<sub>3</sub> (2p<sub>3/2</sub> 457.4 eV) and TiO (2p<sub>3/2</sub> 455.4 eV).<sup>300–304</sup> No Ti metal was observed (2p<sub>3/2</sub> 453.8 eV<sup>305</sup>), demonstrating full oxidation of the surface. Upon sputtering with 3 keV argon ions, the Ti 2p ionizations moved to progressively lower binding energies. A previous XPS study of an 8 nm thick TiO<sub>2</sub> layer formed upon air exposure of a pristine Ti surface demonstrated that 3 keV argon ion sputtering progressively reduces TiO<sub>2</sub> to Ti<sub>2</sub>O<sub>3</sub> and then TiO, but does not lead to Ti metal.<sup>300</sup> The Ti 2p binding energies between 10 and 60 min of argon ion sputtering are consistent with those reported for TiO<sub>2</sub>, Ti<sub>2</sub>O<sub>3</sub>, TiO, and Ti metal.<sup>301</sup> After sputtering for ≥ 70 min, the Ti 2p<sub>3/2</sub> ionizations exactly matched metal (453.8 eV<sup>305</sup>) and were not consistent with TiC (454.8 eV<sup>305</sup>), TiN (454.9 eV<sup>305</sup>), or TiSi<sub>2</sub> (453.2 eV<sup>306</sup>). Figure 31 shows the Si 2p ionization region, suggesting that elemental Si (99.15 eV<sup>305</sup>), not TiSi<sub>2</sub> (98.3 eV<sup>306</sup>), is present at the film/substrate interface. Figure 32 shows an XPS depth profile

indicating low C (2.9–3.0%), N (< 0.5%), Si (0.8–2.2%), and Cl (1.8–2.3%) concentrations between 10 and 50 min of sputtering. The Ti  $2p_{3/2}$  ionization region was subsequently deconvoluted by Gaussian curve fitting using a least-squares approach. Initial values for Gaussian peak centers and full width at half maximum (FWHM) values were obtained from the literature for all stable oxidation states of titanium.<sup>300–305</sup> The Gaussian peak centers and FWHM values were not fixed during the optimization procedure, as impurities in the film can cause small shifts relative to these reference values. Integration was subsequently performed on the Gaussian curves used to model the ionization intensities arising from the presence of Ti(IV), Ti(III), Ti(II), and Ti(0) species. Figure 33 shows a plot of the relative abundance of these oxidation states versus argon ion sputter time. The data show the rapid emergence of Ti(0) after 50 min of sputtering, suggesting the presence of Ti(0) near the film/substrate interface. Figures 34–38 show analogous XPS plots for a 76 nm thick film grown on Si(100) from  $TiCl_4$  and **1** at 180 °C. Results were very similar to the film grown at 140 °C, except that the impurity levels were slightly lower.

**Figure 28.** XPS survey scans of an 82 nm thick film grown on Si(100) from  $\text{TiCl}_4$  and **1** at  $140^\circ\text{C}$ .



**Figure 29.** XPS O 1s ionization region of an 82 nm thick film grown on Si(100) from  $\text{TiCl}_4$  and **1** at  $140^\circ\text{C}$ .

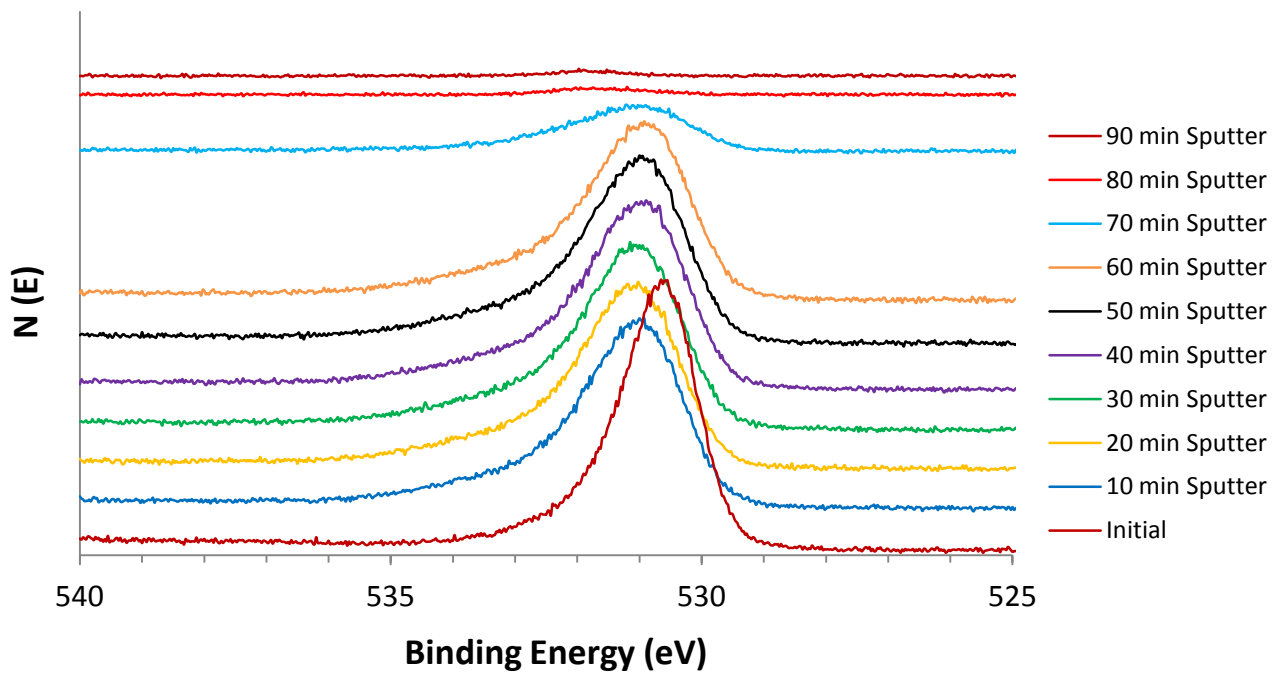


**Figure 30.** XPS Ti 2p ionization region of an 82 nm thick film grown on Si(100) from  $\text{TiCl}_4$  and **1** at 140 °C. Reference 2p binding energies for Ti metal: 453.8 and 459.95 eV;  $\text{TiO}_2$ : 458.5 and 464.2 eV; TiN: 455.7 and 461.3 eV.<sup>305</sup>

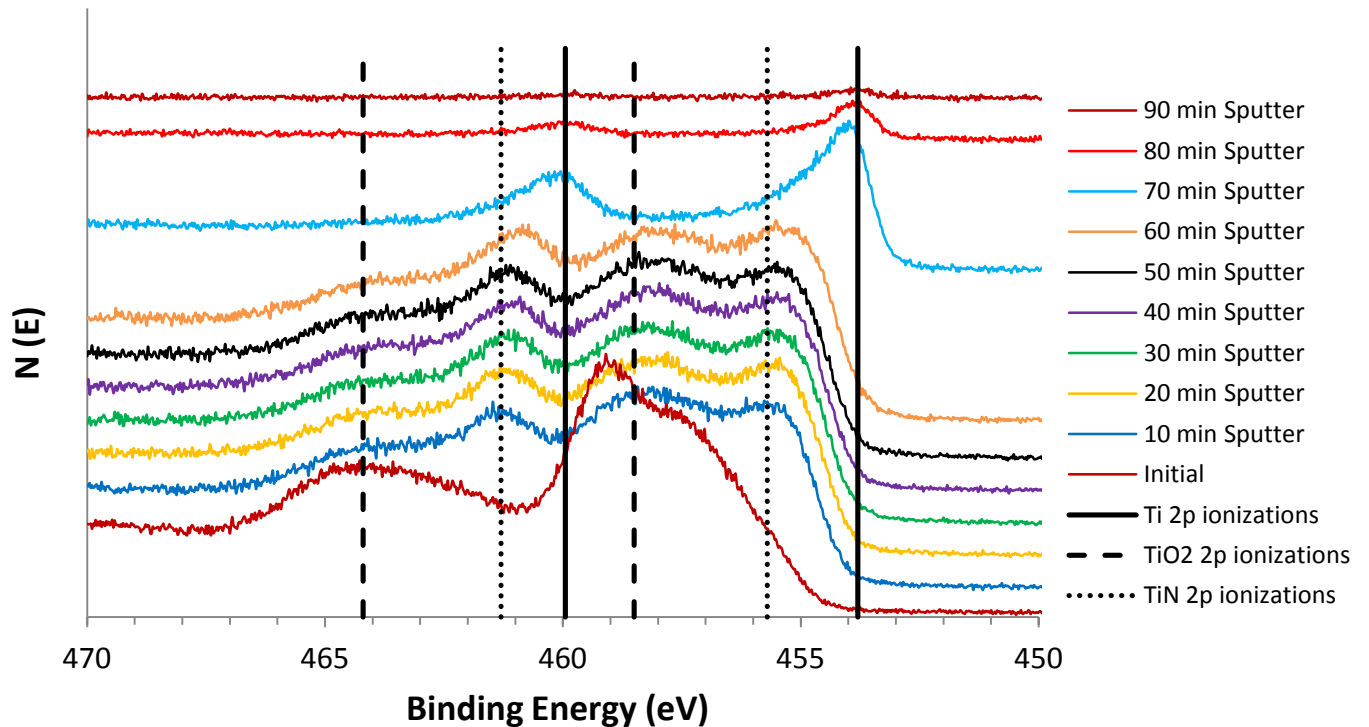


**Figure 31.** XPS Si 2p ionization region of an 82 nm thick film grown on Si(100) from  $\text{TiCl}_4$  and **1** at 140 °C. Reference 2p binding energy for Si: 99.15 eV;  $\text{SiO}_2$ : 103.40 eV.<sup>305</sup>

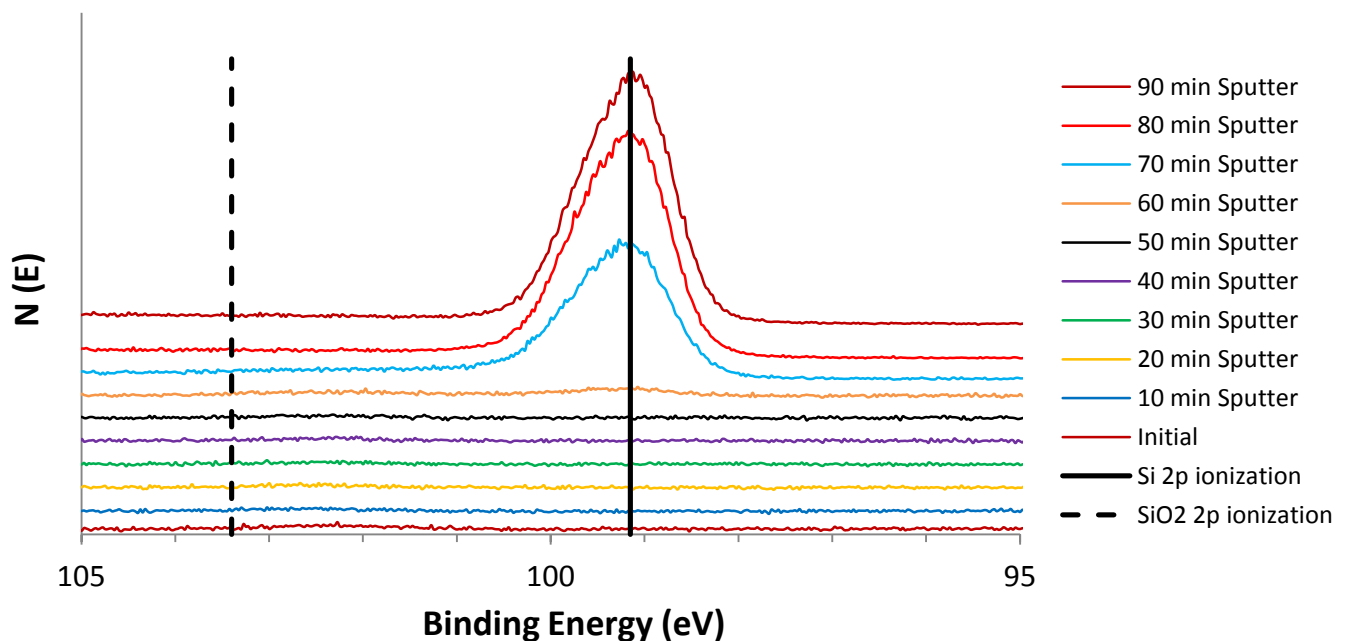




**Figure 32.** XPS depth profile of an 82 nm thick film grown from  $\text{TiCl}_4$  and **1** on Si(100) at  $140^\circ\text{C}$ .

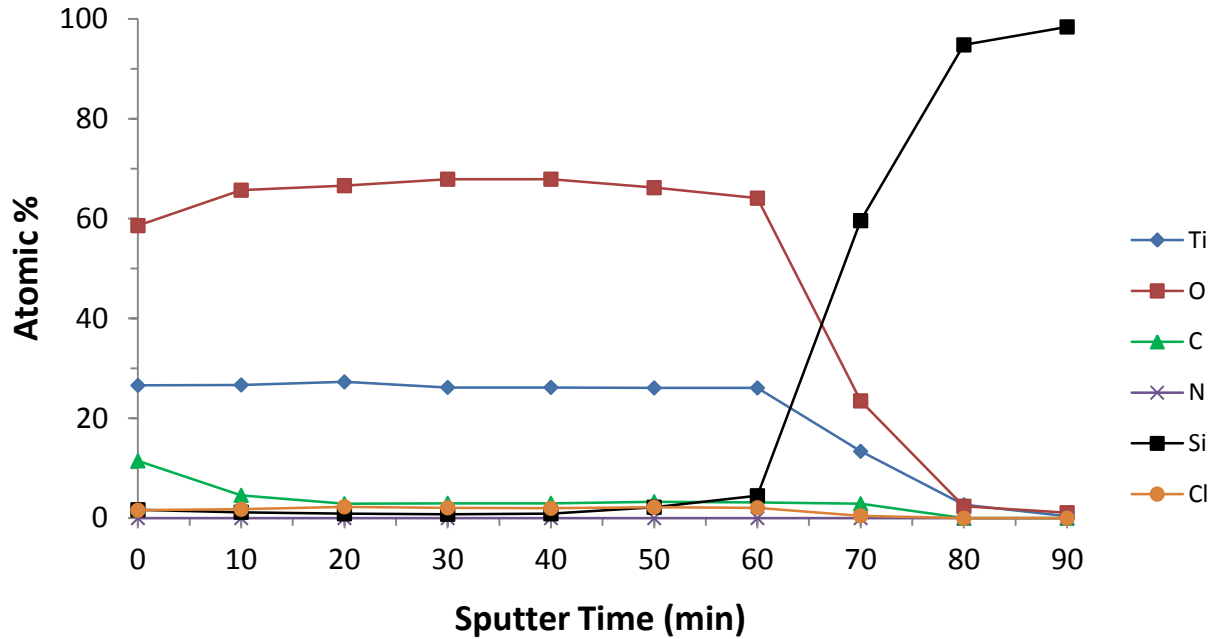


**Figure 33.** Relative abundance of Ti(IV), Ti(III), Ti(II), and Ti(0) oxidation states versus sputter time for an 82 nm thick film grown from  $\text{TiCl}_4$  and **1** on Si(100) at  $140^\circ\text{C}$ .

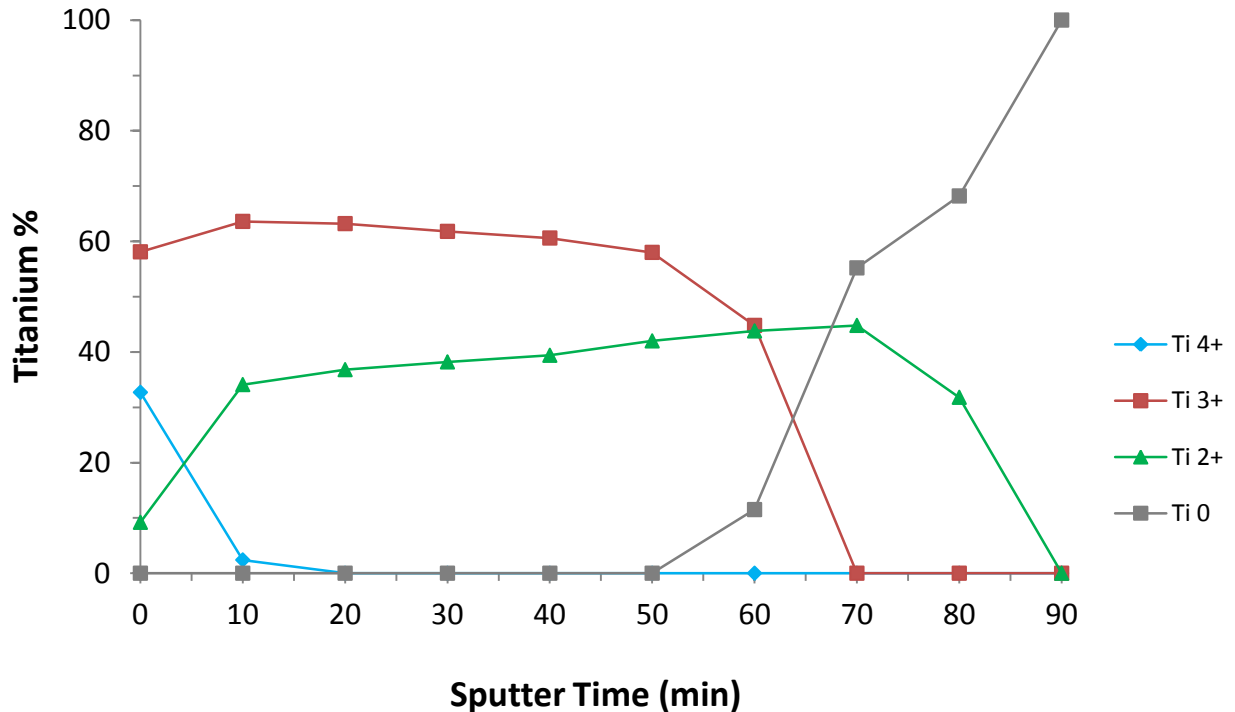


**Figure 34.** XPS survey scans of a 76 nm thick film grown from  $\text{TiCl}_4$  and **1** on Si(100) at  $180^\circ\text{C}$ .

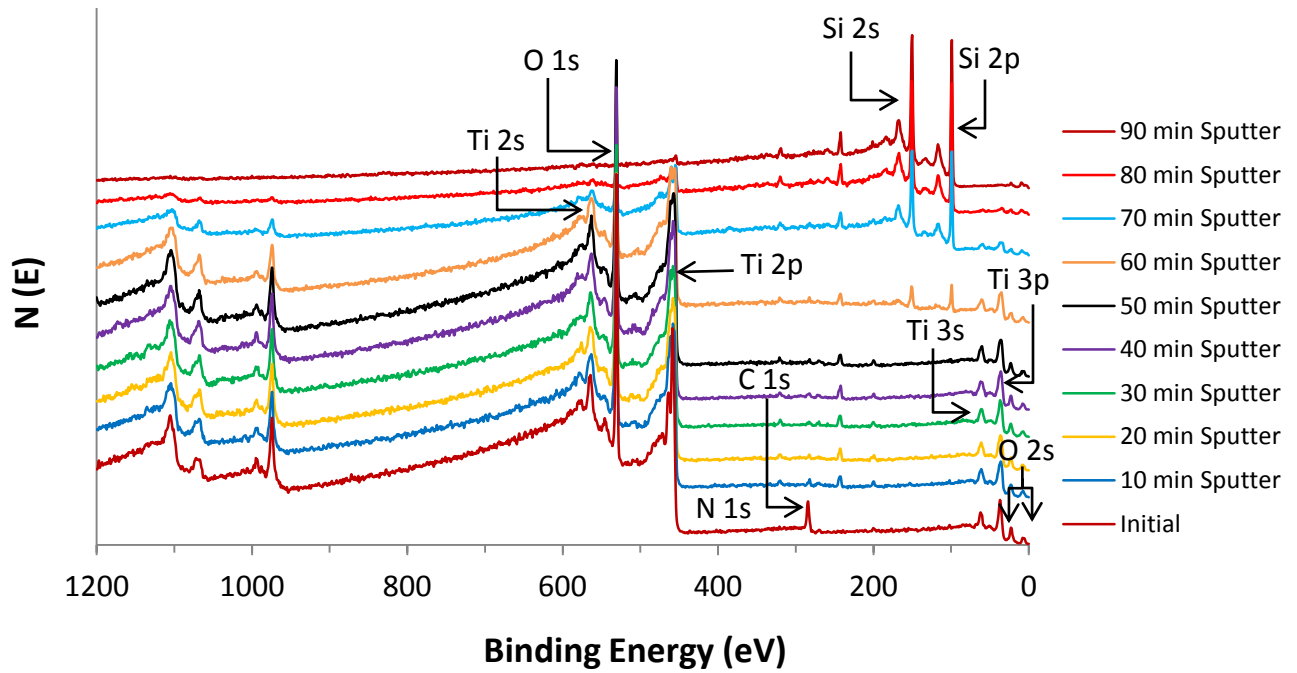


**Figure 35.** XPS O 1s ionization region of a 76 nm thick film grown from  $\text{TiCl}_4$  and **1** on Si(100) at  $180^\circ\text{C}$ .

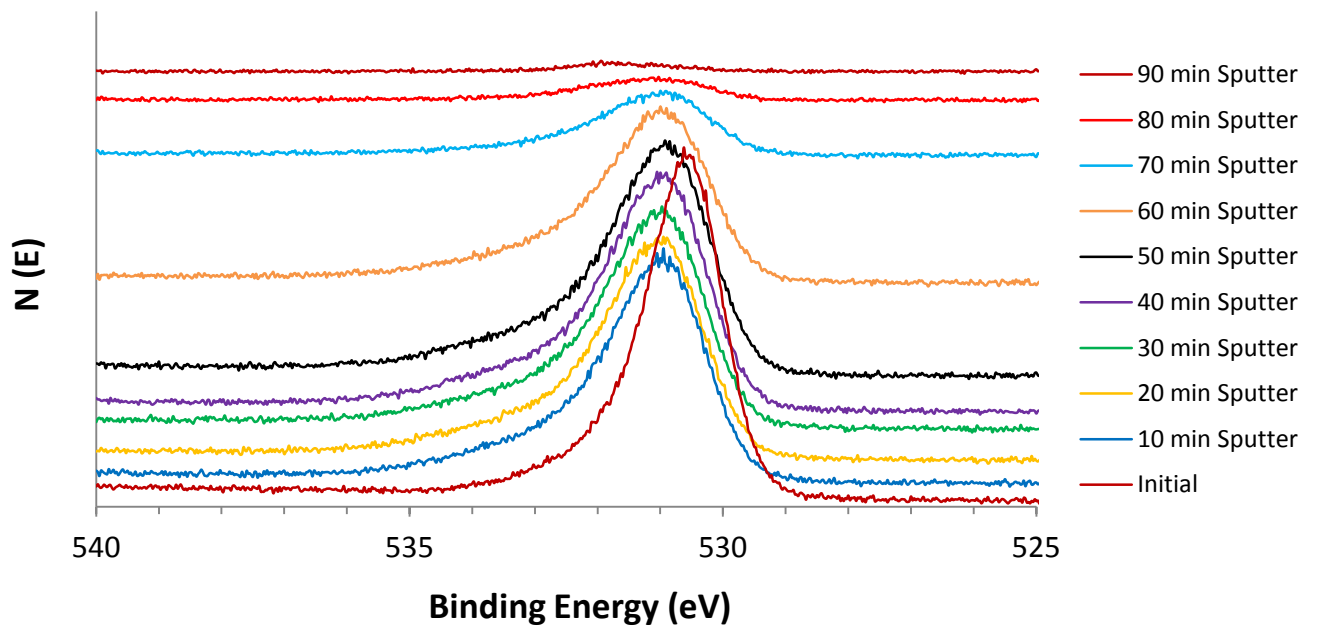


**Figure 36.** XPS Si 2p ionization region of a 76 nm thick film grown from  $\text{TiCl}_4$  and **1** on Si(100) at 180 °C. Reference 2p binding energy for Si: 99.15 eV;  $\text{SiO}_2$ : 103.40 eV.<sup>305</sup>

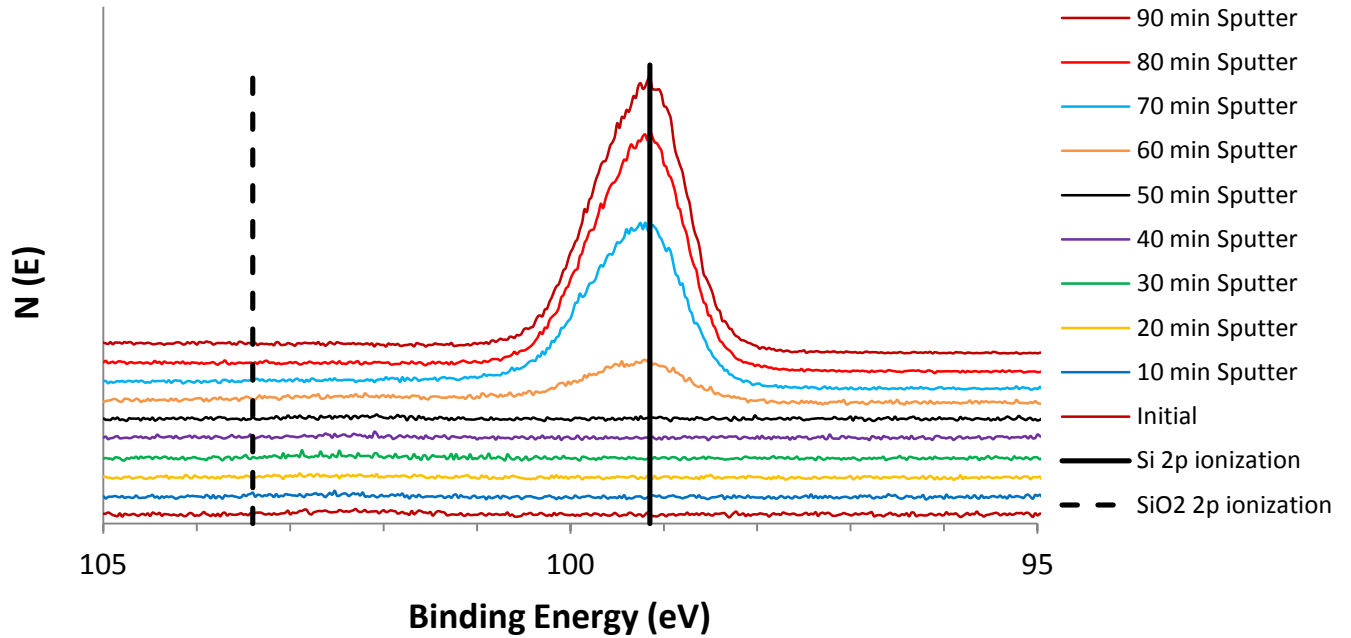


**Figure 37.** XPS Ti 2p ionization region of a 76 nm thick film grown from  $\text{TiCl}_4$  and **1** on Si(100) at 180 °C. Reference 2p binding energies for Ti metal: 453.8 and 459.95 eV;  $\text{TiO}_2$ : 458.5 and 464.2 eV; TiN: 455.7 and 461.3 eV.<sup>305</sup>

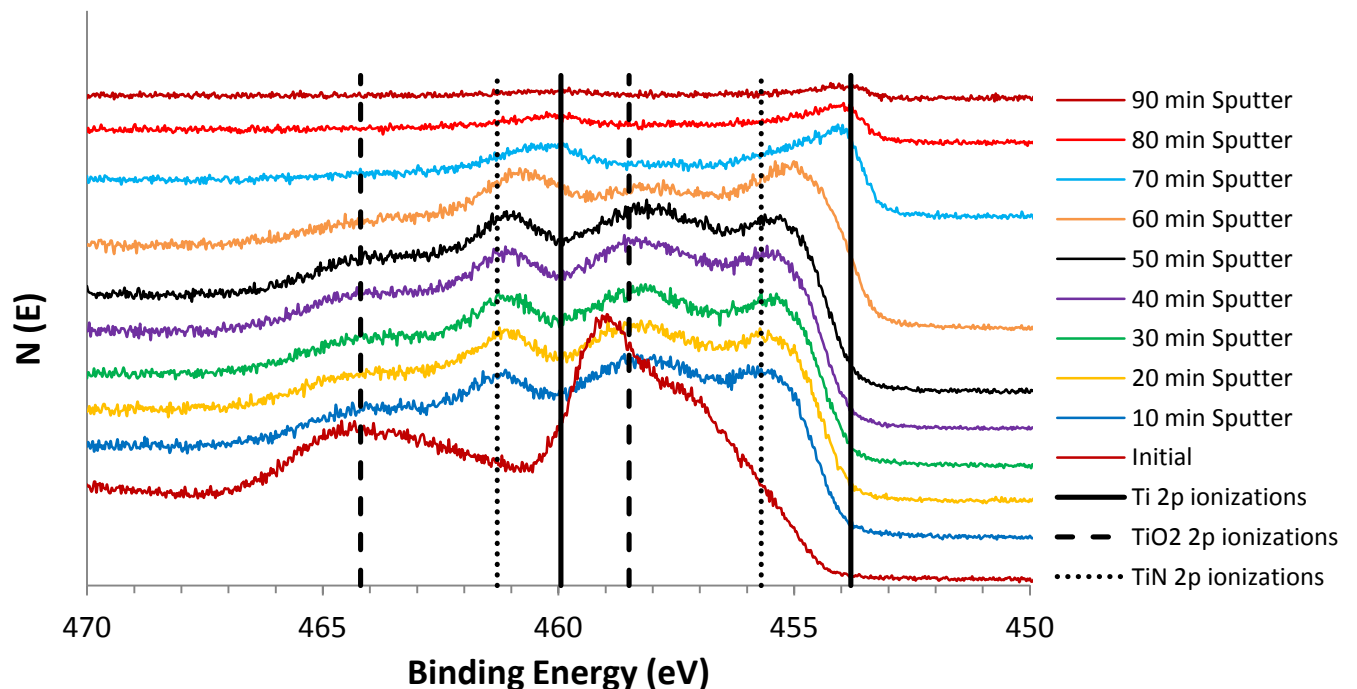
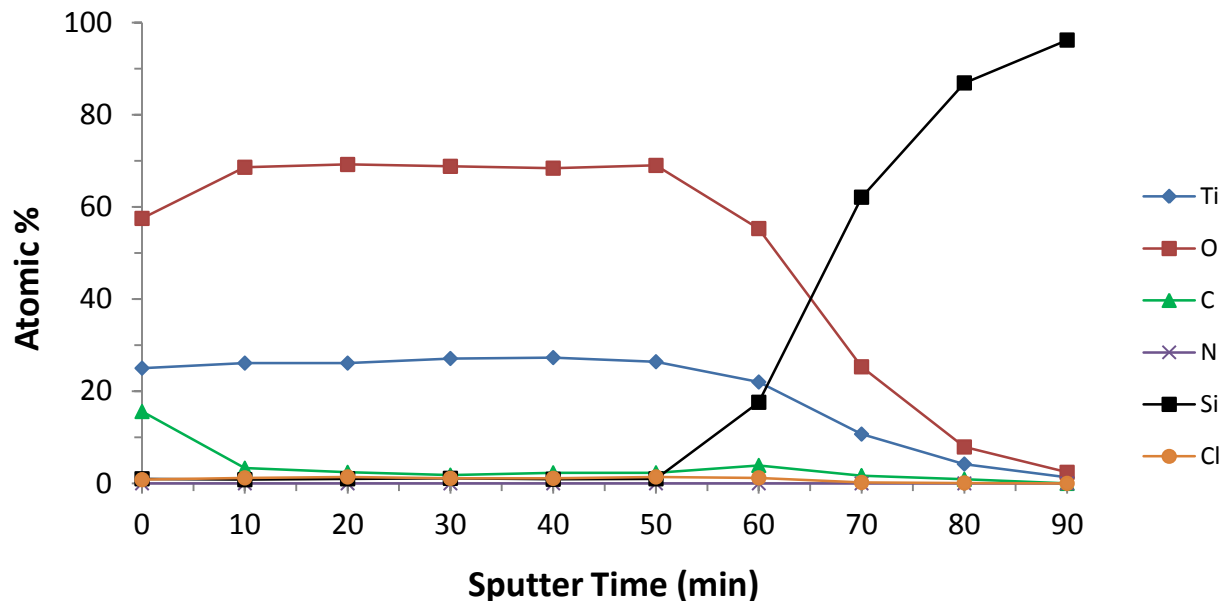


**Figure 38.** XPS depth profile of a 76 nm thick film grown from  $\text{TiCl}_4$  and **1** on Si(100) at  $180^\circ\text{C}$ .



A similar XPS analysis was performed on a 35 nm thick film grown from  $\text{TiCl}_4$  and **1** on Pt/SiO<sub>2</sub>/Si at  $140^\circ\text{C}$ . Figure 39 shows the XPS survey scans, where the emergence of the Pt layer occurs after 40 min of sputtering. Figure 40 shows the O 2p ionization region. The as-deposited film (red trace) shows an ionization centered at  $\sim 530.5$  eV, likely originating from TiO<sub>2</sub>. The intensity of this ionization is very small after sputtering into the Pt layer ( $\sim 30$  min of sputtering) and shifts to  $\sim 532.5$  eV upon penetration through the Pt layer, likely due to the underlying SiO<sub>2</sub> layer. Figures 41–42 show the Pt 4f and Si 2p ionization regions, with the emergence of Pt and SiO<sub>2</sub> observed after 30 and 40 min of sputtering, respectively. Figure 43 shows the Ti 2p ionization region, which differs significantly from the analogous data for films grown on Si(100). In this case, continued sputtering does not result in the Ti 2p ionization signal matching Ti metal. Rather, after sputtering for 10–30 min, the Ti 2p<sub>3/2</sub> ionization is consistent with the presence of TiPt<sub>3</sub> ( $455.1$  eV<sup>307</sup>). The XPS depth profile, shown in Figure 44, also suggests a Ti/Pt alloy, as Ti and Pt are both detected after 25–40 min of sputtering. Interestingly, the presence of oxygen never drops below 40 at.%, even in the Pt layer.

**Figure 39.** XPS survey scans of a 35 nm thick film grown from  $\text{TiCl}_4$  and **1** on  $\text{Pt}/\text{SiO}_2/\text{Si}$  at  $140^\circ\text{C}$ .

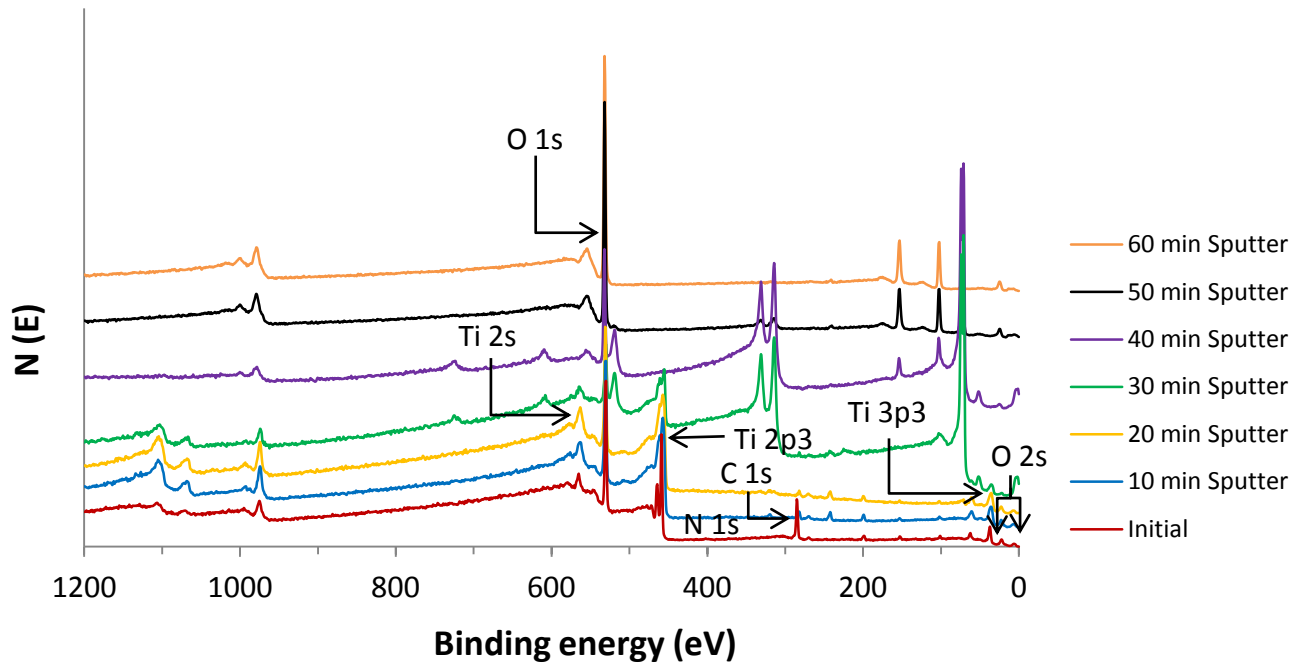


**Figure 40.** XPS O 2p ionization region of a 35 nm thick film grown from  $\text{TiCl}_4$  and **1** on  $\text{Pt}/\text{SiO}_2/\text{Si}$  at  $140^\circ\text{C}$ .

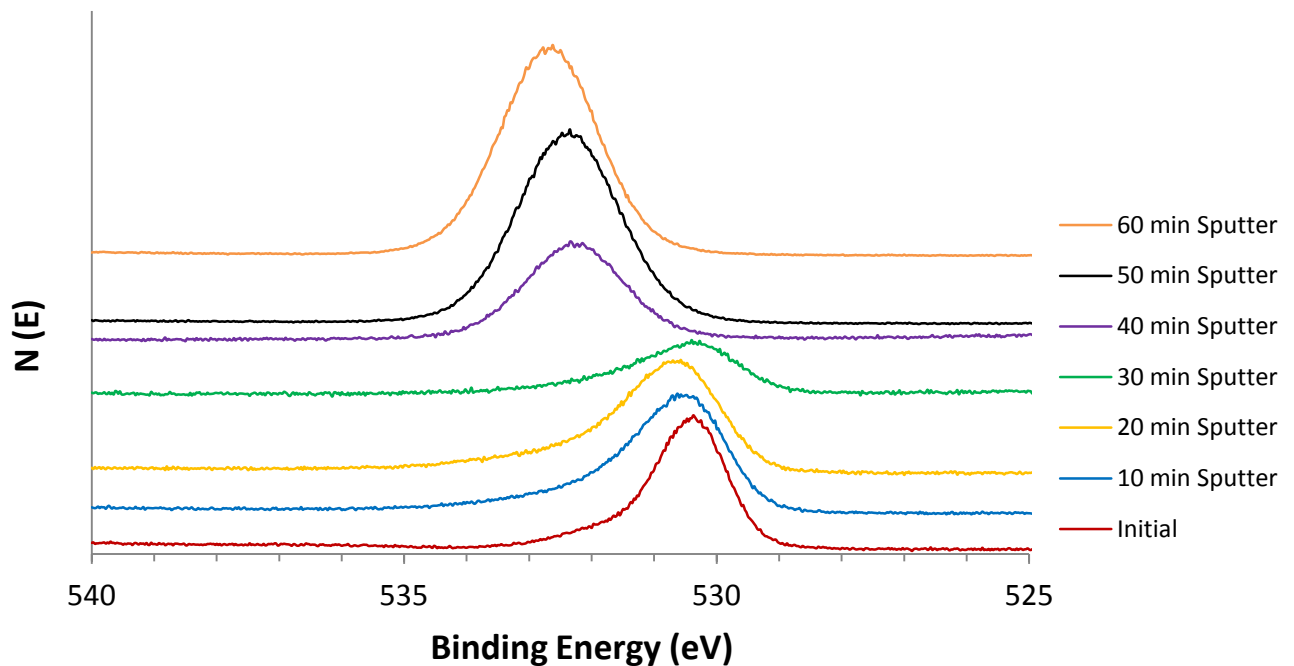


**Figure 41.** XPS Pt 4f ionization region of a 35 nm thick film grown from  $\text{TiCl}_4$  and **1** on Pt/SiO<sub>2</sub>/Si at 140 °C. Reference 4f binding energies for Pt: 70.9 and 74.25 eV.<sup>305</sup>

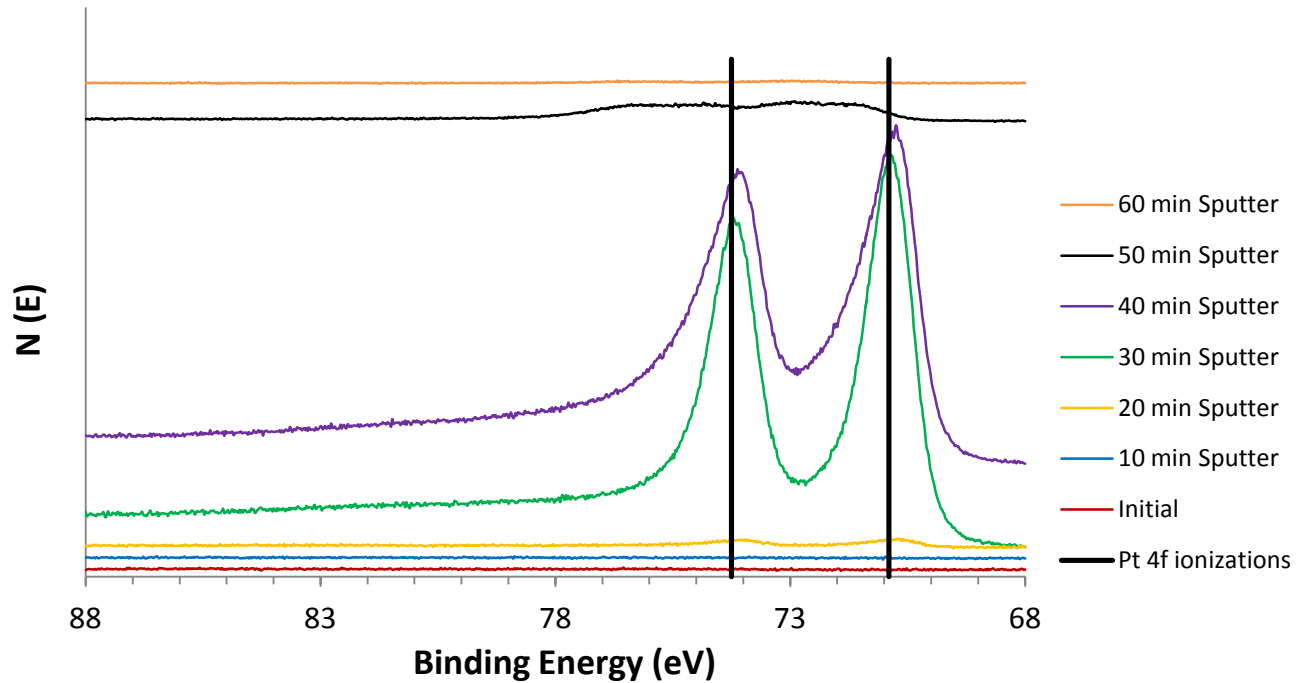


**Figure 42.** XPS Si 2p ionization region of a 35 nm thick film grown from  $\text{TiCl}_4$  and **1** on Pt/SiO<sub>2</sub>/Si at 140 °C. Reference 2p binding energy for Si: 99.15 eV; SiO<sub>2</sub>: 103.40 eV.<sup>305</sup>

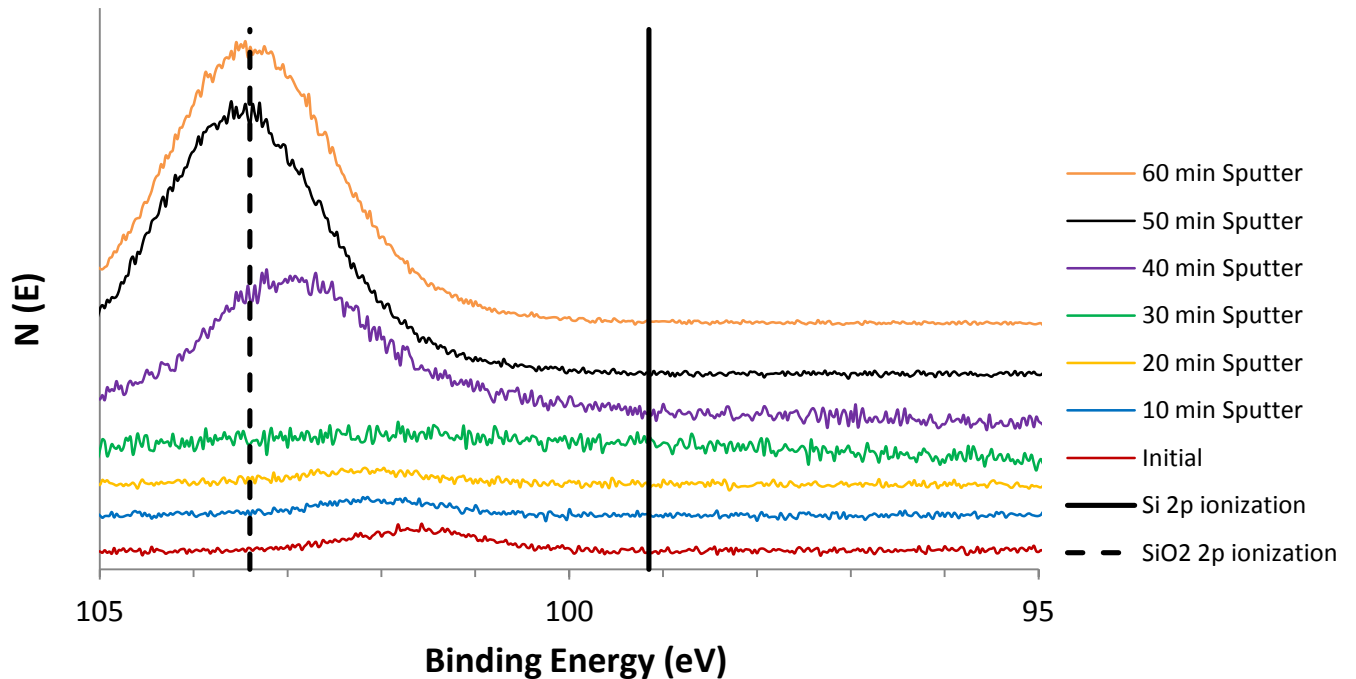


**Figure 43.** XPS Ti 2p ionization region of a 35 nm thick film grown from  $\text{TiCl}_4$  and **1** on Pt/SiO<sub>2</sub>/Si at 140 °C. Reference 2p binding energies for Ti metal: 453.8 and 459.95 eV; TiO<sub>2</sub>: 458.5 and 464.2 eV; TiN: 455.7 and 461.3 eV.<sup>305</sup>

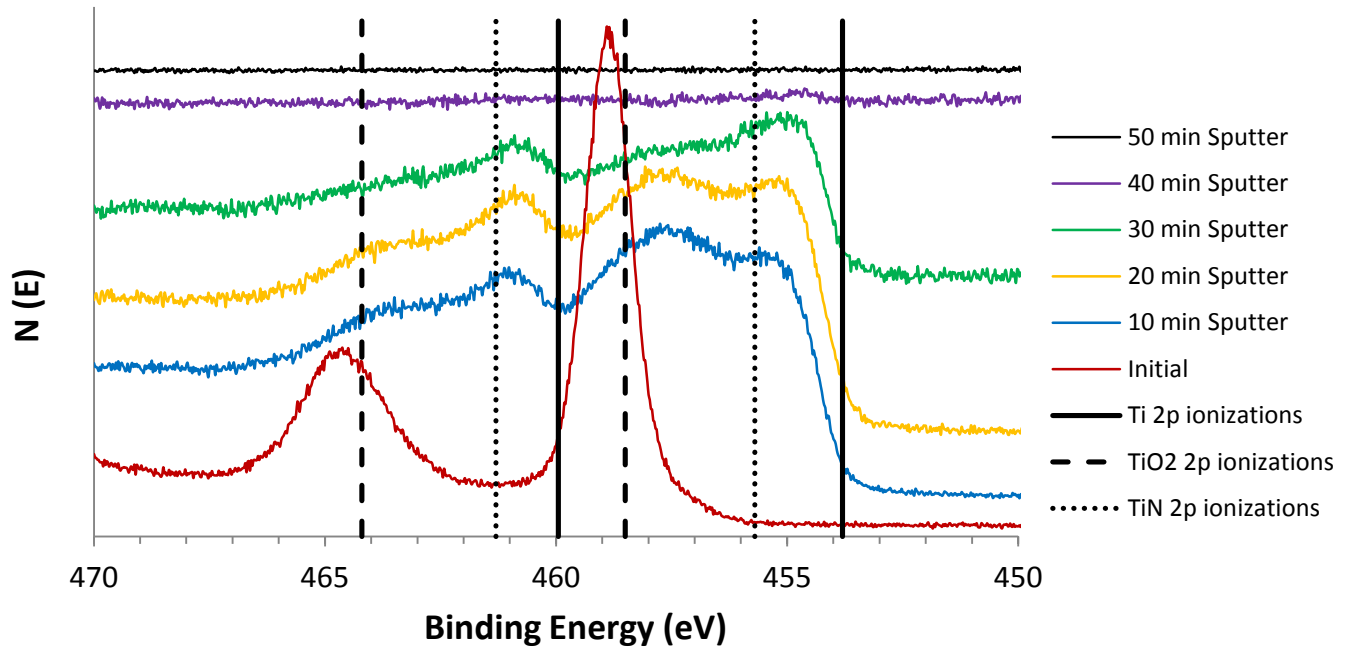
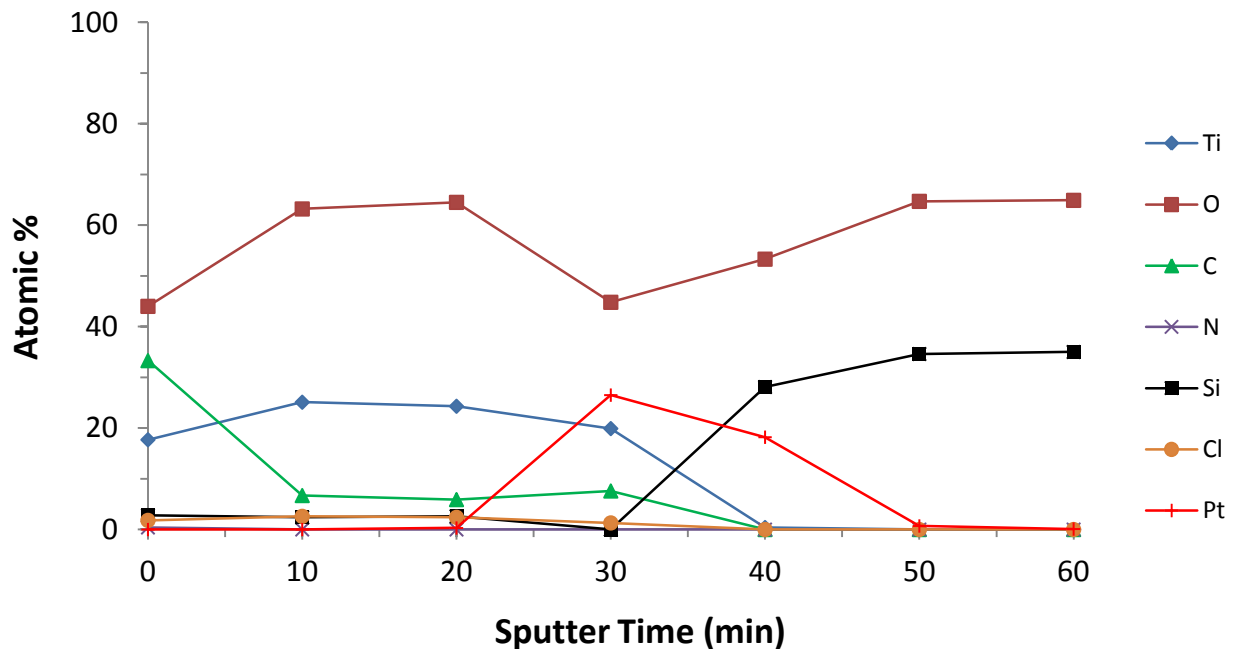


**Figure 44.** XPS depth profile of a 35 nm thick film grown from  $\text{TiCl}_4$  and **1** on Pt/SiO<sub>2</sub>/Si at 140 °C.



For comparison, a 99.7% pure 0.127 mm thick Ti foil was analyzed by XPS. The foil was polished prior to analysis to reduce surface roughness. Continued sputtering with 3 keV argon ions resulted in the Ti 2p ionizations matching the known values for Ti metal (Figures 45–46).<sup>305</sup>

**Figure 45.** XPS survey scans of a 99.7% pure 0.127 mm thick titanium foil.

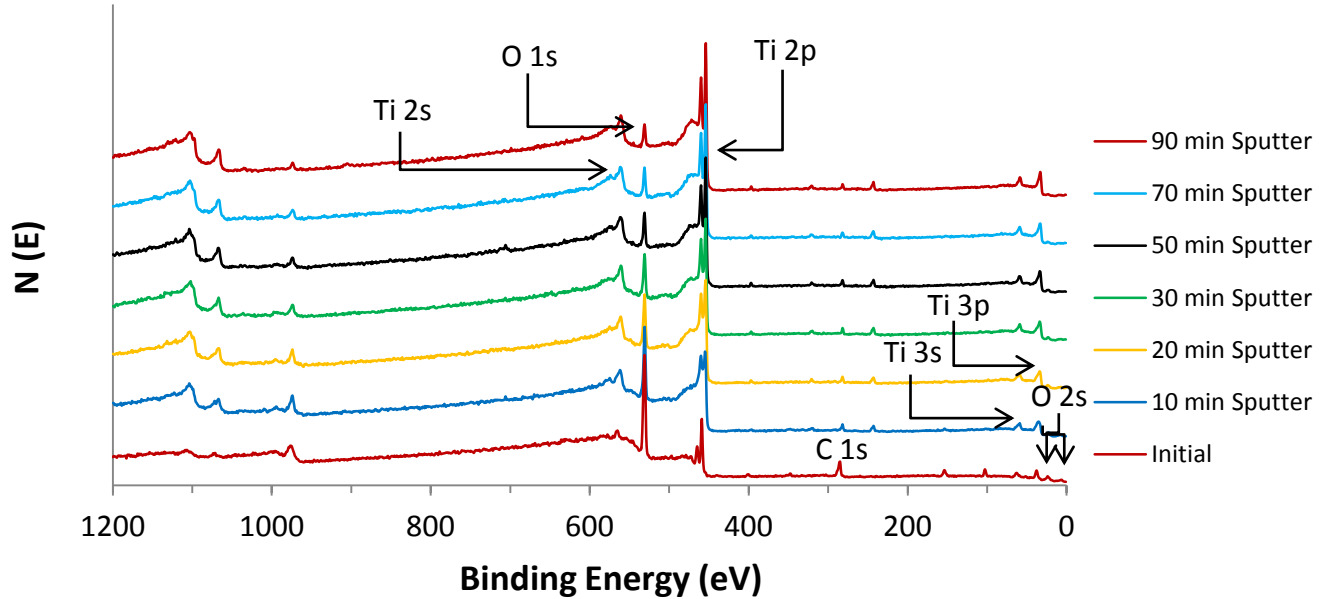
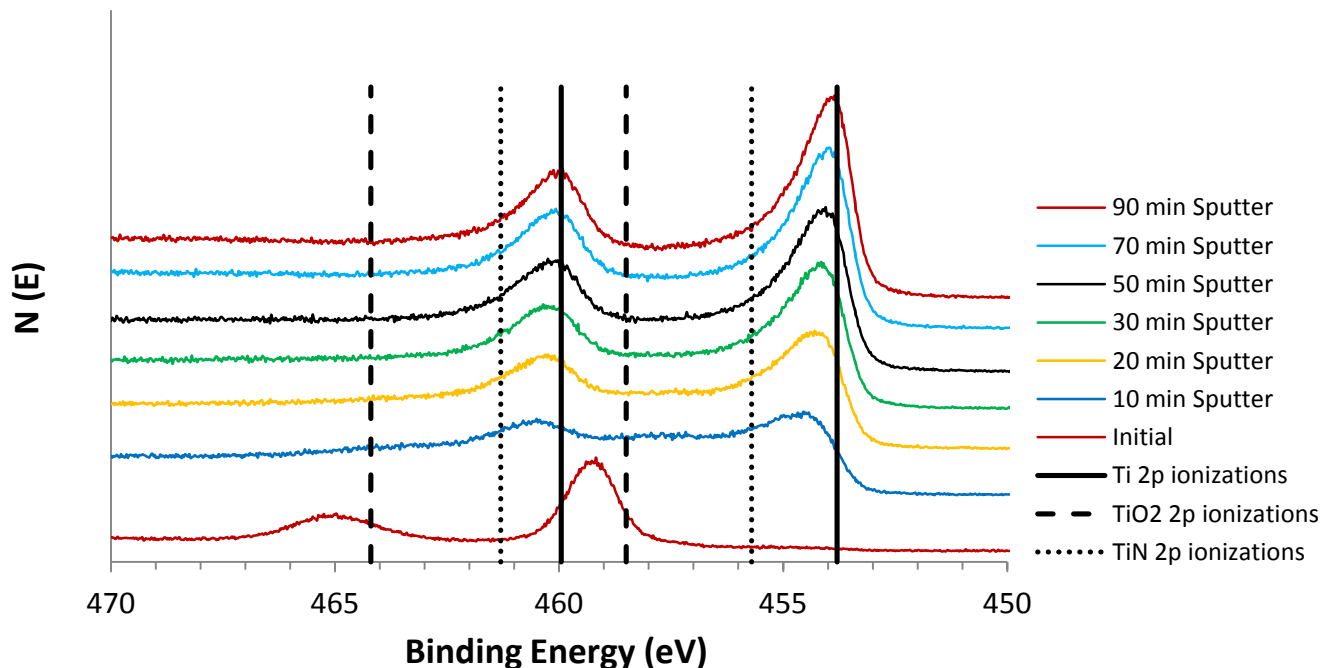


**Figure 46.** XPS Ti 2p ionization region of a 99.7% pure 0.127 mm thick titanium foil. Reference 2p binding energies for Ti metal: 453.8 and 459.95 eV; TiO<sub>2</sub>: 458.5 and 464.2 eV; TiN: 455.7 and 461.3 eV.<sup>305</sup>

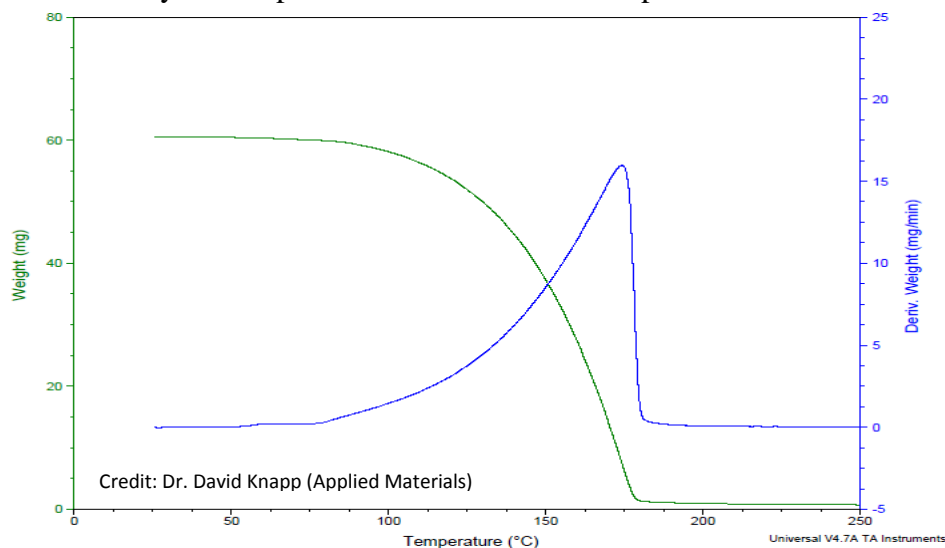




### 2.2.3 Titanium Films from $\text{TiCl}_4$ and 1,4-Bis(trimethylsilyl)-1,4-dihydropyrazine

**Synthesis.** 1,4-Bis(trimethylsilyl)-1,4-dihydropyrazine (**2**) is an  $8\pi$  electron, antiaromatic heterocycle with a very low first vertical ionization potential,<sup>298</sup> previously crystallized as a planar structure.<sup>308</sup> Compound **2** was synthesized by the reductive silylation of pyrazine with lithium and  $\text{ClMe}_3\text{Si}$ .<sup>309</sup> The crude material melted at  $63\text{ }^\circ\text{C}$  and sublimed without residue at  $80\text{ }^\circ\text{C}/0.05\text{ Torr}$ , affording a yellow crystalline product that was pure by  $^1\text{H}$  NMR analysis. The thermal decomposition point of **2** is  $> 265\text{ }^\circ\text{C}$ . Exposure to air at  $23\text{ }^\circ\text{C}$  resulted in its rapid exothermic decomposition to a dark orange liquid. As depicted in Figure 47, TGA analysis performed under inert atmosphere showed a single-step weight loss over a temperature range of approximately  $90\text{--}178\text{ }^\circ\text{C}$ .

**Figure 47.** TGA analysis of **2** performed under inert atmosphere.



**Solution Reactivity.** Solution reductions were attempted using a variety of metal complexes and five molar equivalents of **2** (Table 6). Reactions were visually observed with all metal complexes except  $\text{MnCl}_2$ .

**Table 6.** Solution reactions of metal complexes with **2**.

Metal Source	Solv	Reaction		Reflux		Solution Reaction
		Temp (°C)	Time (min)	Temp (°C)	Time (min)	
Cu(dmap) <sub>2</sub>	THF	rt	15	66	60	copper-colored flakes; green residue & Cu on flask
Cu(tmhd) <sub>2</sub>	THF	rt	30	66	95	copper-colored & dark green flakes; Cu on flask
NiCl <sub>2</sub>	THF	rt	15	66	70	tan powder
CoCl <sub>2</sub>	THF	rt	35	66	60	dark green powder at rt (sticks to stir bar)
FeCl <sub>2</sub>	THF	rt	35	66	60	film on flask; black powder (sticks to stir bar)
ZnCl <sub>2</sub>	THF	rt	15	66	60	few metallic flakes → white precipitate after ~3 days
CrCl <sub>2</sub>	THF	rt	23	66	60	silver-colored flakes → grey suspension
MnCl <sub>2</sub>	THF	rt	15	66	60	none after 1 day
SbCl <sub>3</sub>	CH <sub>2</sub> Cl <sub>2</sub>	rt	30	40	-----	immediately turned opaque purple/brown; grey precipitate after ~10 min
TiCl <sub>4</sub>	CH <sub>2</sub> Cl <sub>2</sub>	rt	< 1	-----	-----	immediately turned black; grey precipitate upon removal of solvent
TiCl <sub>4</sub>	toluene	rt	< 1	-----	-----	immediately turned black; black precipitate turned Prussian blue upon air exposure
SiCl <sub>4</sub>	toluene	rt	< 10	-----	-----	white precipitate that turned dark brown upon air exposure

Reduction of Cu(tmhd)<sub>2</sub> produced a purple precipitate and flecks of Cu on the flask that were confirmed as Cu metal by powder XRD analysis, with a crystallite size of 15.0 ± 0.5 nm (Figures 48–49). Reductions of CoCl<sub>2</sub> and FeCl<sub>2</sub> resulted in materials that stuck to the stir bar, diagnostic

of the ferromagnetic metals (Figure 48). Reduction of  $\text{TiCl}_4$  yielded the immediate formation of a black precipitate, while reduction of  $\text{SiCl}_4$  yielded and a white precipitate that turned dark brown upon air exposure (Figure 48); powder XRD analyses of these products did not show any identifiable reflections.

**Figure 48.** Solution reduction products of  $\text{Cu}(\text{tmhd})_2$ ,  $\text{CoCl}_2$ ,  $\text{FeCl}_2$ , and  $\text{SiCl}_4$  from **2**.

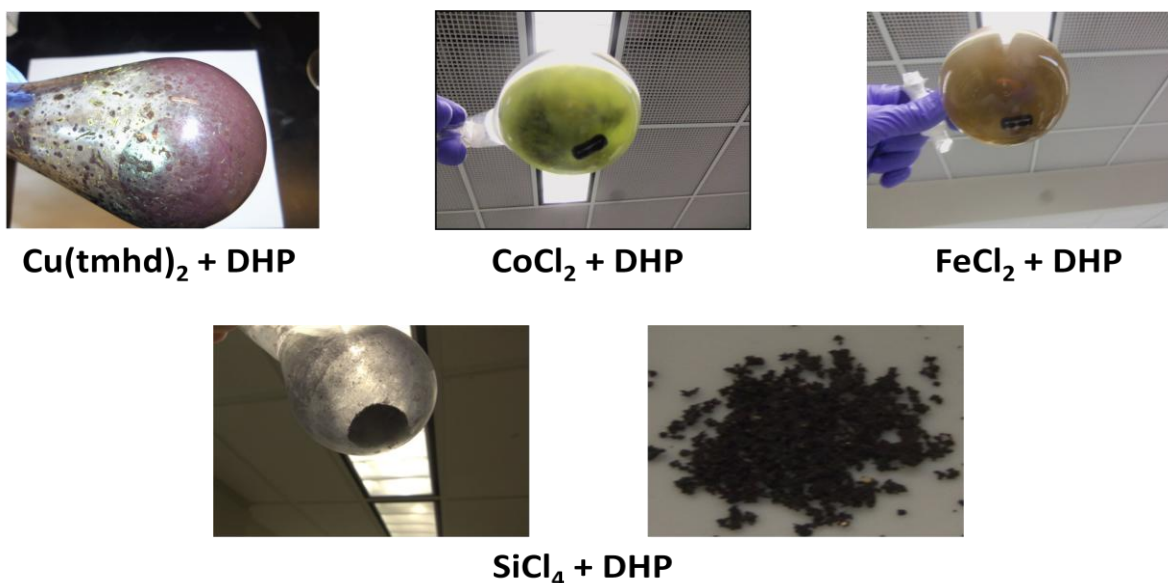
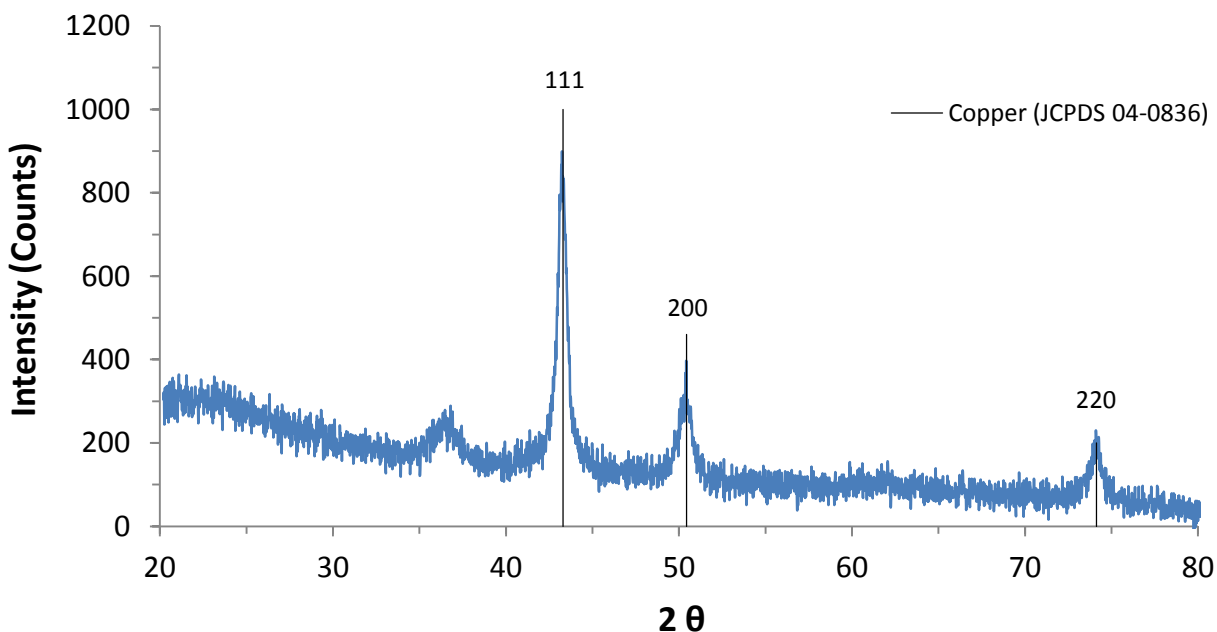
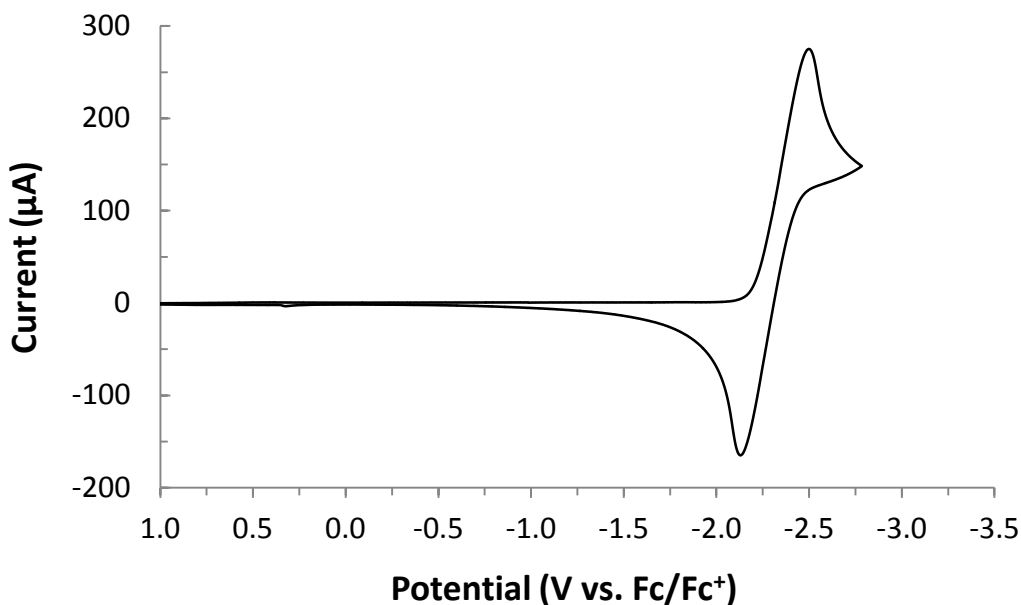


**Figure 49.** Powder XRD spectrum showing Cu metal; reduction of  $\text{Cu}(\text{tmhd})_2$  by **2** in THF.



**Cyclic Voltammetry.** To quantify the reducing power of the pyrazine dianion, CV experiments were performed in DMF, using 0.1 M  $\text{NBu}_4\text{ClO}_4$  as the supporting electrolyte. Reported data are relative to ferrocene (referenced to 0.31 V), using  $\text{Ag}/\text{AgNO}_3$  as the reference electrode. Pyrazine showed a reduction at  $E_{1/2} = -2.32$  V (Figure 50).

**Figure 50.** Cyclic voltammogram of pyrazine relative to ferrocene ( $\text{Fc}/\text{Fc}^+$ ,  $E^\circ = 0.31$  V).



**Film Deposition Data.** Encouraged by the reducing capability of **2**, film depositions were explored using  $\text{TiCl}_4$  and **2** as precursors. Similar growth rates were observed on Si(100) with native oxide and 100 nm thermal  $\text{SiO}_2/\text{Si}$ . The ALD study was conducted using  $\text{SiO}_2$  substrates, while XPS and AES analyses were performed on films grown on Si(100) substrates. All films were exposed to ambient atmosphere prior to analyses, which led to rapid oxidation. X-ray diffraction spectra of all films showed no reflections, suggesting either amorphous films or oxidation of the Ti before the analyses could be conducted. Films measured within 30 s of removal from the reactor were electrically nonconductive by four-point probe analysis,

consistent with the rapid oxidation of the surface. All films showed good adhesion to the substrates, passing the Scotch tape test.

Saturative growth behavior was observed for both  $\text{TiCl}_4$  and **2** at 0.2 and 0.1 s, respectively, with a growth rate of 0.10–0.12 Å/cycle observed at 100 °C (Figures 51–52). As expected, the consumption rate of **2** increased as a function of the pulse length of **2**. Figure 53 shows a plot of growth rate versus  $\text{TiCl}_4$  purge length, suggesting that a  $\geq 5.0$  s  $\text{N}_2$  purge is required to remove unreacted  $\text{TiCl}_4$  from the deposition chamber. Accordingly, a pulse sequence of 0.3 s  $\text{TiCl}_4$ /5.0 s  $\text{N}_2$  purge/0.1 s **1**/10.0 s  $\text{N}_2$  purge was used for all subsequent depositions. Importantly, experiments conducted using only  $\text{TiCl}_4$  and a  $\text{N}_2$  purge or only **2** and a  $\text{N}_2$  purge (3,000 cycles, 100 °C) did not produce any detectable film growth. Thus, growth requires both  $\text{TiCl}_4$  and **2** and does not occur by the separate decomposition of either precursor. Figure 54 shows a plot of growth rate versus temperature, indicating an ALD window of 90–100 °C. Finally, Figure 55 shows a plot of film thickness versus the number of ALD cycles. The trend line indicates a growth rate of 0.118 Å/cycle and the y-intercept of 0.597 nm suggests that there is no nucleation delay for this process.

**Figure 51.** Saturation plot of  $\text{TiCl}_4$  using 0.1 s pulses of **2** at 100 °C.

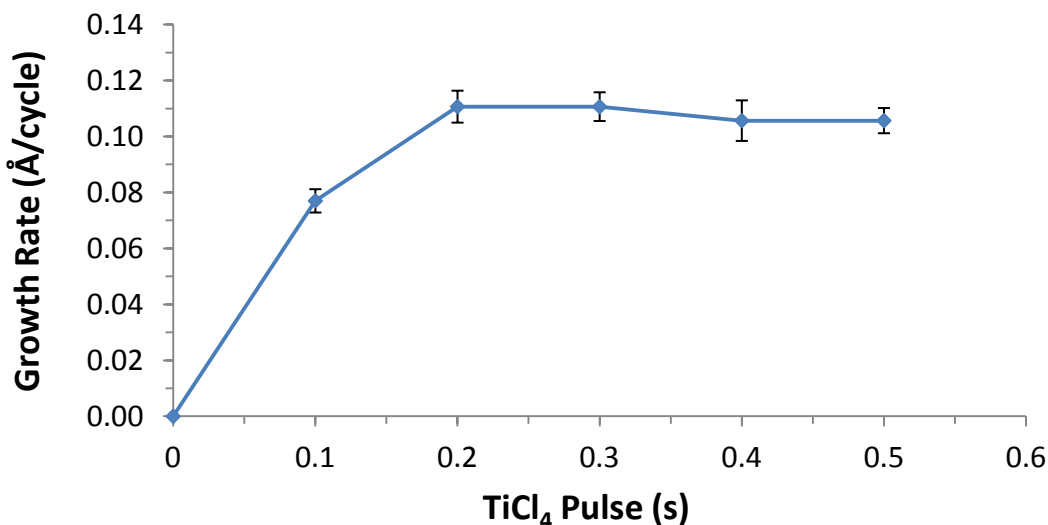


**Figure 52.** Saturation plot of **2** using 0.3 s pulses of  $\text{TiCl}_4$  at 100 °C. The secondary axis shows the consumption rate of **2** as a function of the pulse length of **2**.

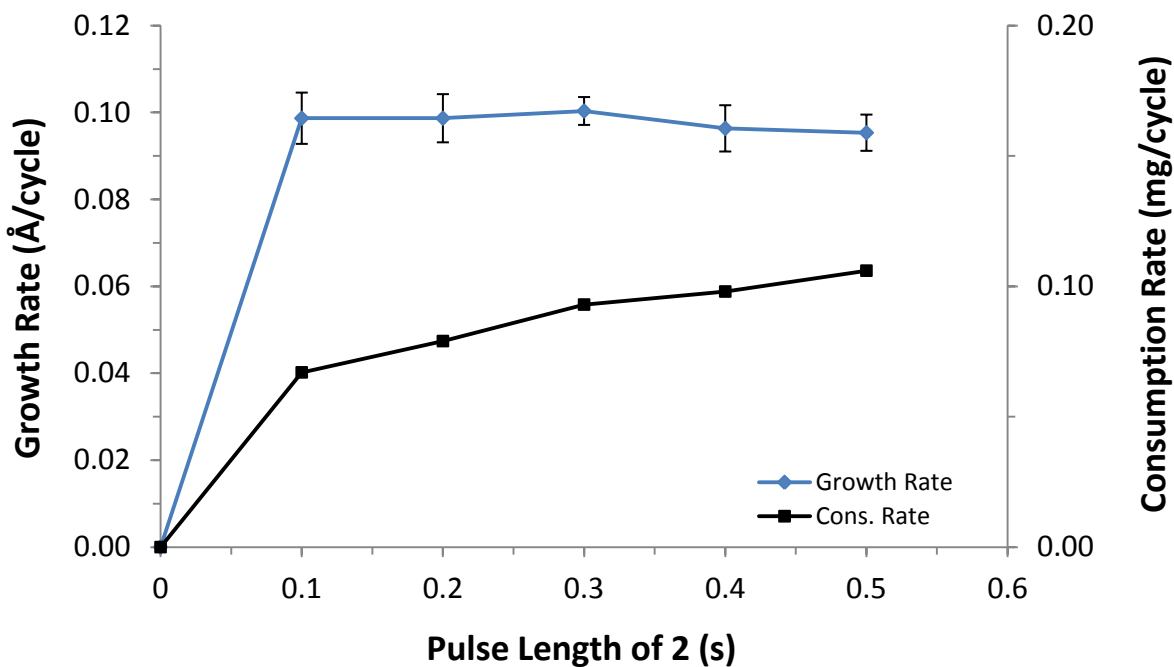


**Figure 53.** Plot of growth rate versus  $\text{TiCl}_4$  purge length using 0.3 s pulses of  $\text{TiCl}_4$  and 0.2 s pulses of **2** at 100 °C.

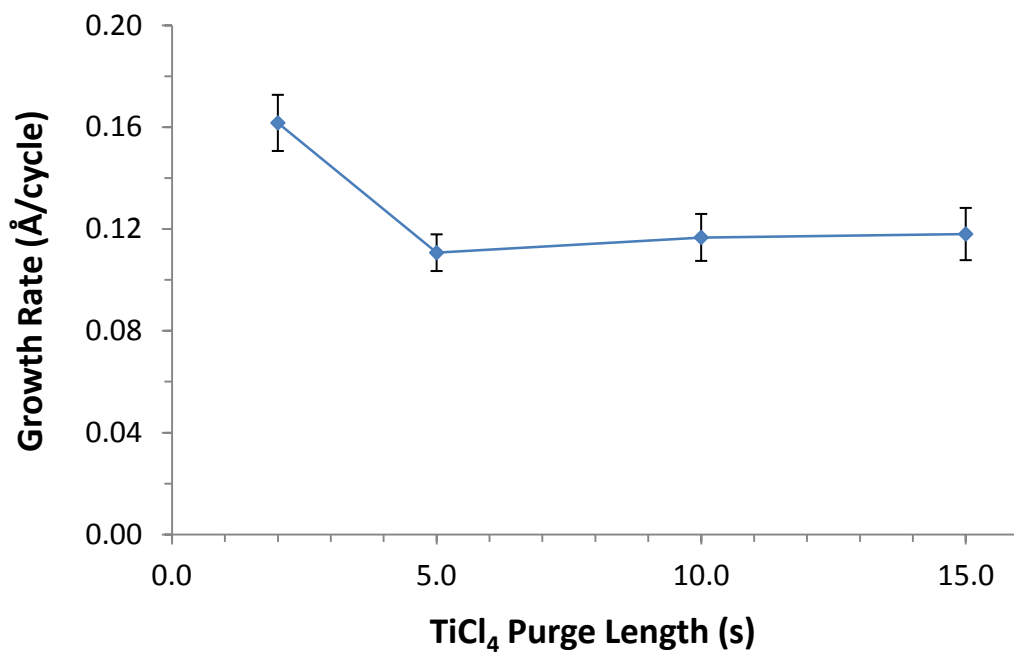


**Figure 54.** Plot of growth rate versus temperature using 0.3 s pulses of  $\text{TiCl}_4$  and 0.1 s pulses of **2** for 3,000 cycles.

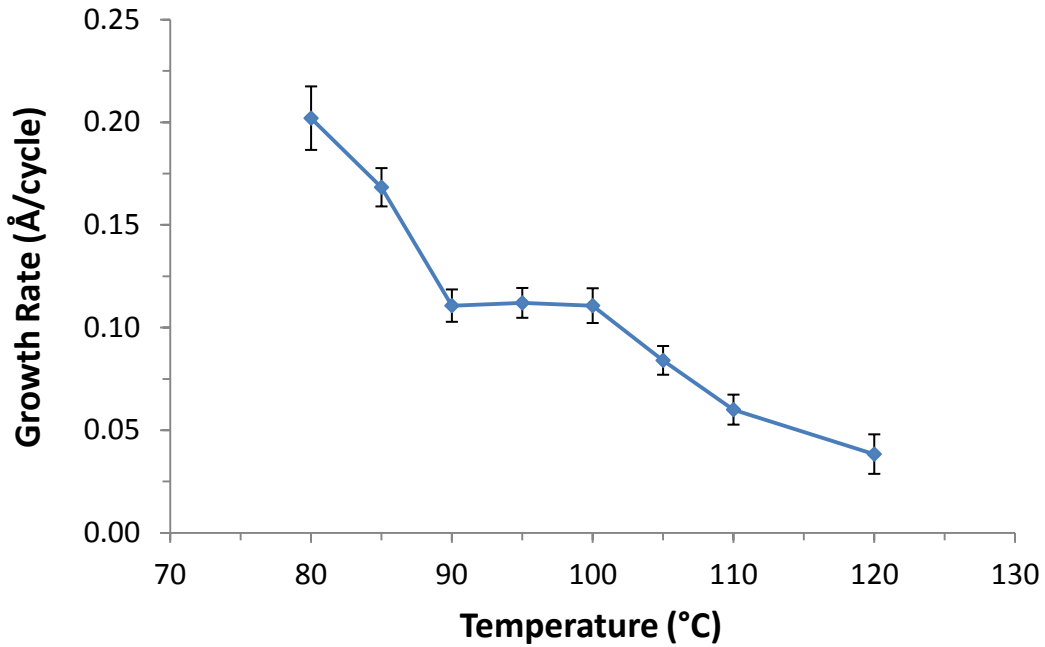


**Figure 55.** Plot of film thickness versus number of ALD cycles using  $\text{TiCl}_4$  and **2** at 100 °C. Images below the x-axis show magnified regions of each film from a single photograph taken of all films.

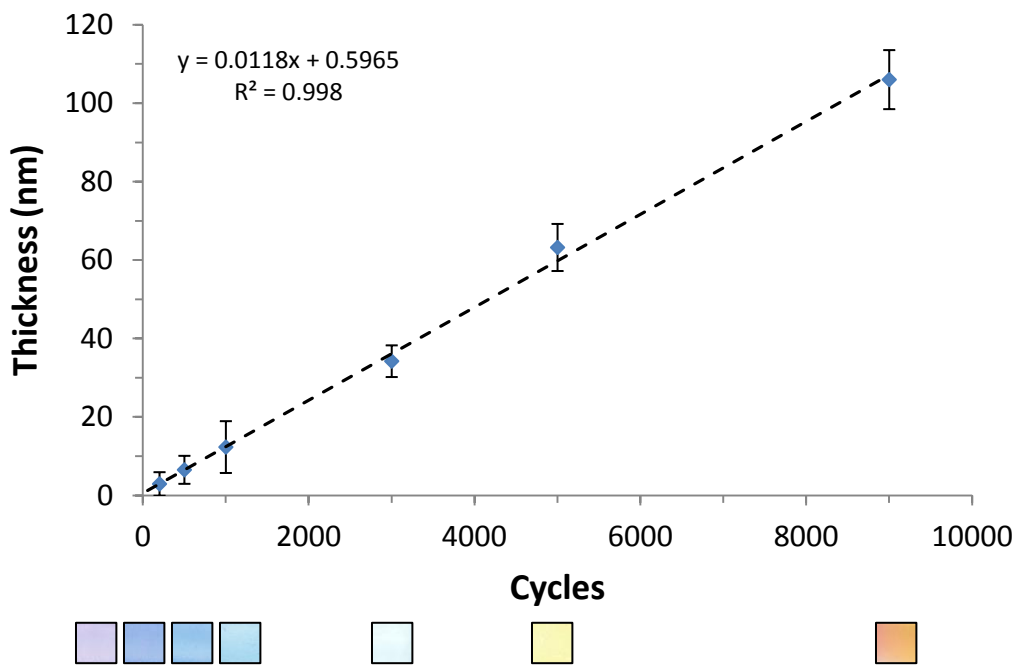
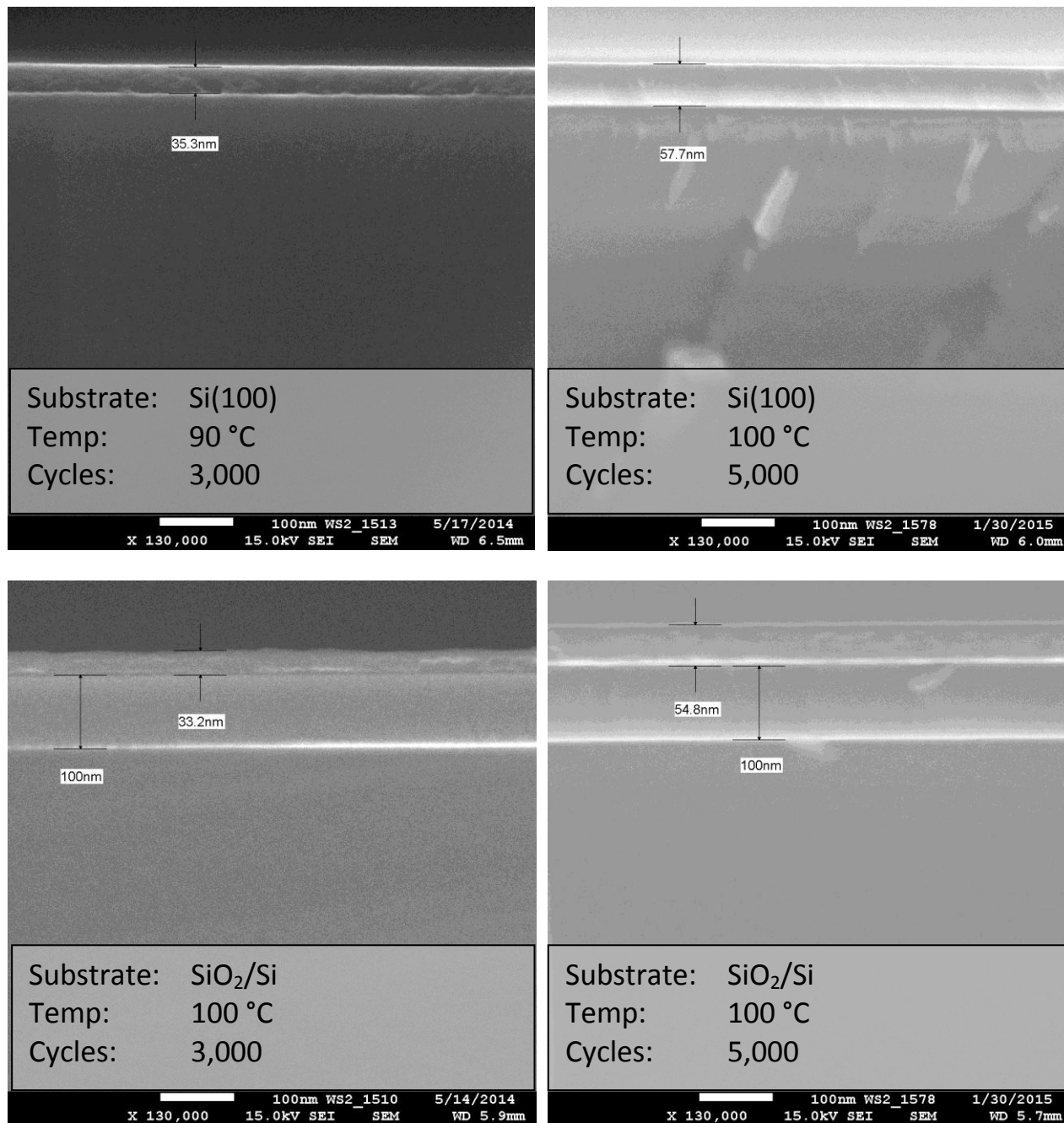


Figure 56 shows SEM images of films grown for 3,000 cycles on Si(100) and SiO<sub>2</sub> substrates. AFM analyses of 55–58 nm thick films grown at 100 °C revealed RMS surface roughnesses of  $\leq 7.0$  nm, indicating smooth surfaces (Figures 57–60, Table 7).

**Figure 56.** Cross-sectional SEM images of films deposited on Si(100) and SiO<sub>2</sub> substrates using TiCl<sub>4</sub> and **2** within the 90–100 °C ALD window.





**Figure 57.** AFM image of a  $2 \mu\text{m}^2$  region of a film grown using  $\text{TiCl}_4$  and **2**. The film was deposited on Si(100) with native oxide at  $100^\circ\text{C}$ . The RMS surface roughness of the 58 nm thick film was 7.0 nm.

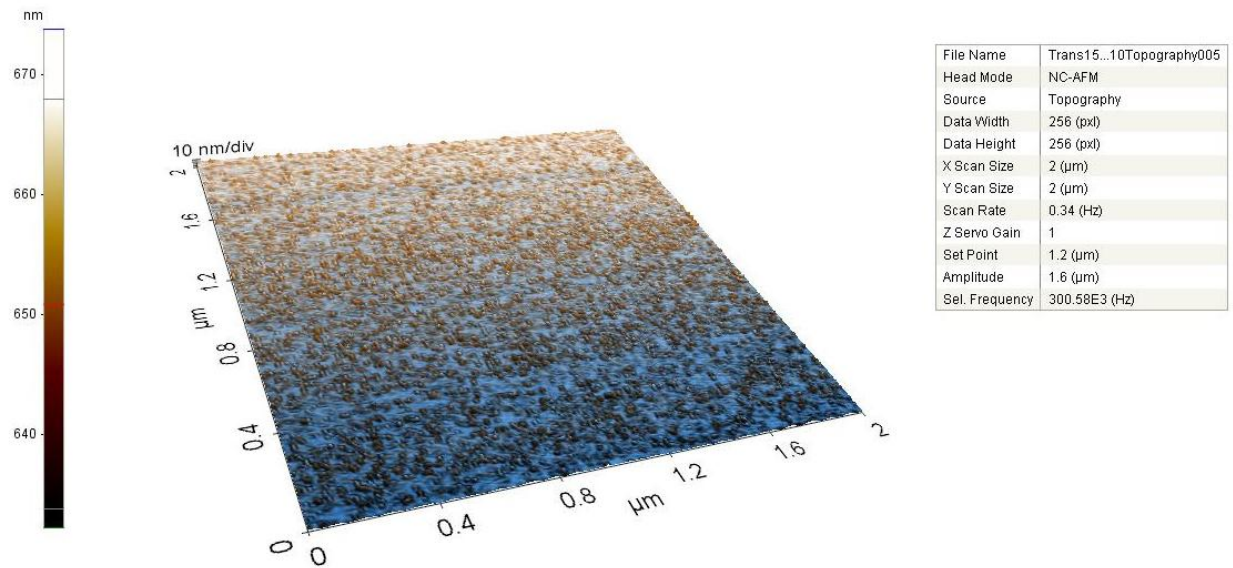


**Figure 58.** AFM image of a  $5 \mu\text{m}^2$  region of a film grown using  $\text{TiCl}_4$  and **2**. The film was deposited on Si(100) with native oxide at  $100^\circ\text{C}$ . The RMS surface roughness of the 58 nm thick film was 3.5 nm.

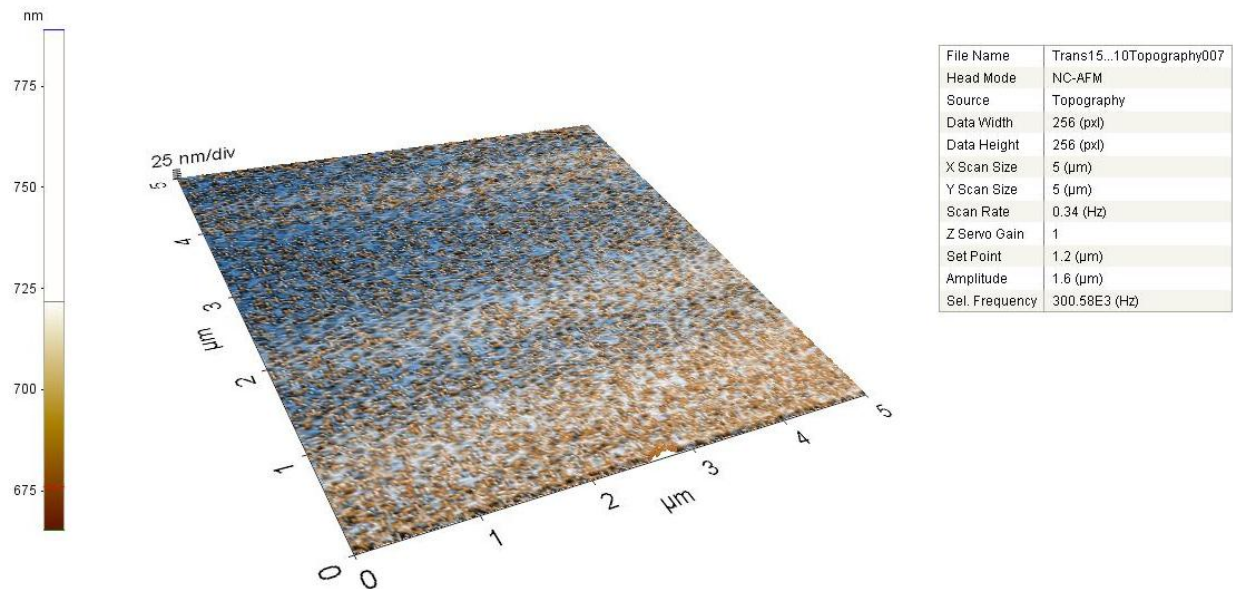


**Figure 59.** AFM image of a  $2 \mu\text{m}^2$  region of a film grown using  $\text{TiCl}_4$  and **2**. The film was deposited on thermal  $\text{SiO}_2$  at  $100 \text{ }^\circ\text{C}$ . The RMS surface roughness of the 55 nm thick film was 2.8 nm.

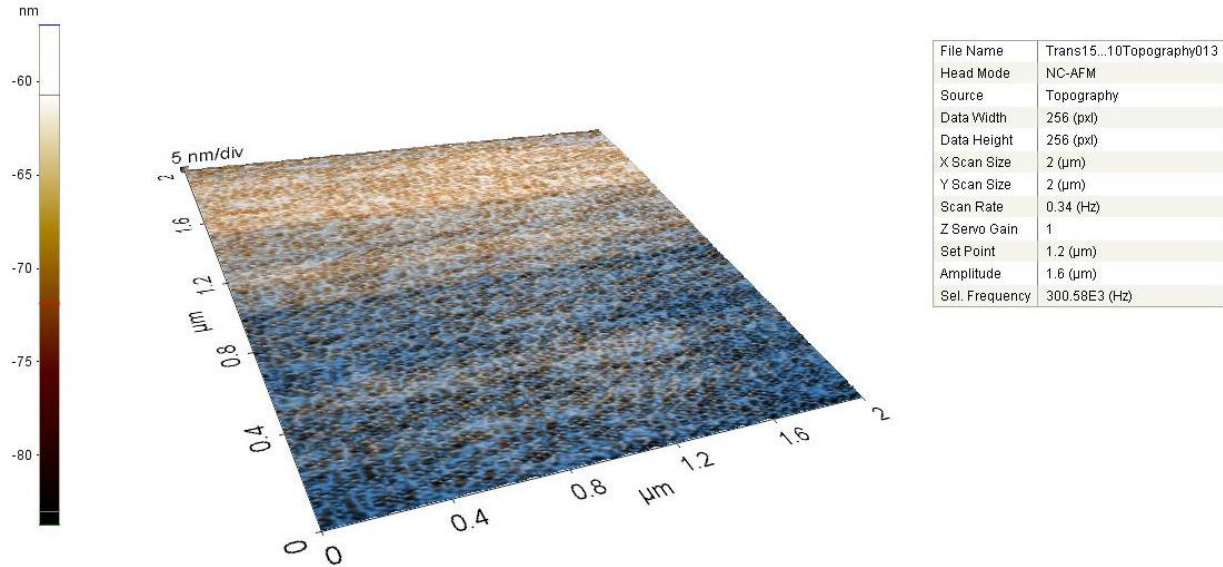


**Figure 60.** AFM image of a  $5 \mu\text{m}^2$  region of a film grown using  $\text{TiCl}_4$  and **2**. The film was deposited on thermal  $\text{SiO}_2$   $100 \text{ }^\circ\text{C}$ . The RMS surface roughness of the 55 nm thick film was 3.1 nm.

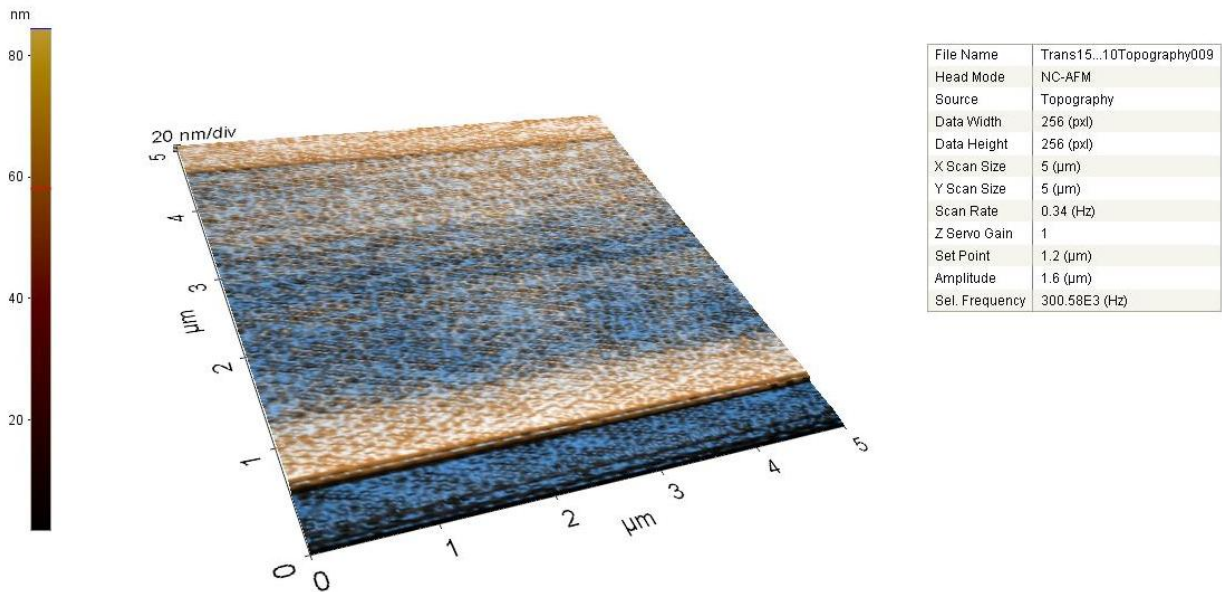


**Table 7.** Surface roughnesses measured by AFM of films grown using  $\text{TiCl}_4$  and **2** at  $100\text{ }^\circ\text{C}$  on Si(100) and  $\text{SiO}_2$  substrates.

$100\text{ }^\circ\text{C}$

RMS Roughness (nm)		
Film/Substrate	$2\ \mu\text{m}^2$	$5\ \mu\text{m}^2$
58 nm Ti/Si(100)	7.0	3.5
55 nm Ti/ $\text{SiO}_2$	2.8	3.1

A 95 nm thick film grown using  $\text{TiCl}_4$  and **2** on Si(100) with native oxide at  $100\text{ }^\circ\text{C}$  was carefully analyzed by XPS. Figure 61 shows the XPS survey scans, where Ti is observed until 60 min of sputtering. Figure 62 shows the O 2p ionization region, where the center of the ionization peak gradually increases to higher binding energies with sputtering, likely due to a shift in concentration from  $\text{TiO}_2$  to  $\text{SiO}_2$ . Figure 63 shows the Si 2p ionization region, with Si observed after ~40 min of sputtering. Figure 64 depicts the Ti 2p ionization region. In contrast to the analogous data for Ti films grown using **1**, the Ti 2p ionizations of the as-deposited film (red trace) of do not possess shoulder regions tapering toward lower binding energies. However, similar to the films grown using **1**, continued sputtering with 3 keV argon ions results in the gradual migration of these ionization peaks to the known values for Ti metal.<sup>305</sup> Sputtering with 3 keV argon ions is not capable of reducing  $\text{TiO}_2$  to Ti metal,<sup>300</sup> thus demonstrating that the reduction occurs by a chemical process. Figure 65 shows the relative atomic concentrations as a function of sputter time. In contrast to data for the analogous process using **1**, persisting C (9–16% ) and N (5–7%) impurities were detected between 10 and 50 min of sputtering, possibly due to the incorporation of pyrazine into the growing film. Accordingly, films grown from **2** are not as pure as those grown from **1**. Finally, Figure 66 shows a plot of Ti(IV), Ti(III), Ti(II), and Ti(0) ionization intensities versus argon ion sputtering time, suggesting the presence of Ti(0) after only 10 min of sputtering.

**Figure 61.** XPS survey scans of a 95 nm thick film grown from  $\text{TiCl}_4$  and **2** on Si(100) at  $100^\circ\text{C}$ .

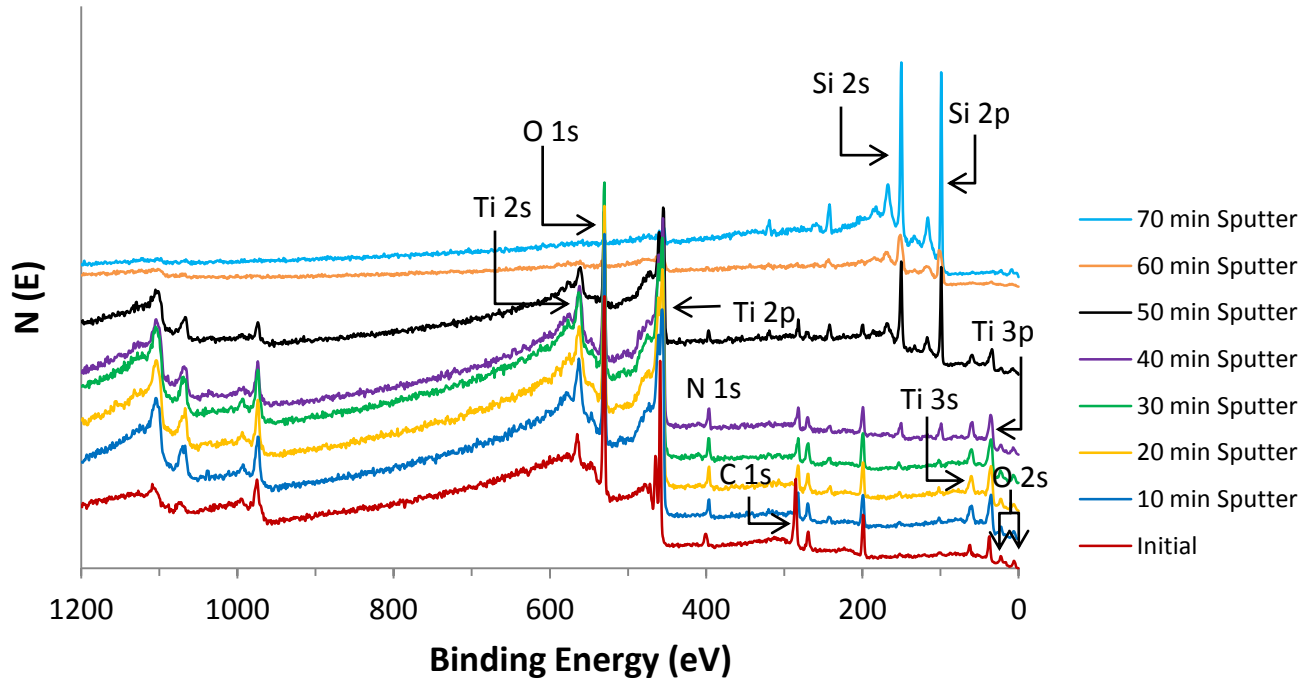


**Figure 62.** XPS O 1s ionization region of a 95 nm thick film grown from  $\text{TiCl}_4$  and **2** on Si(100) at  $100^\circ\text{C}$ .

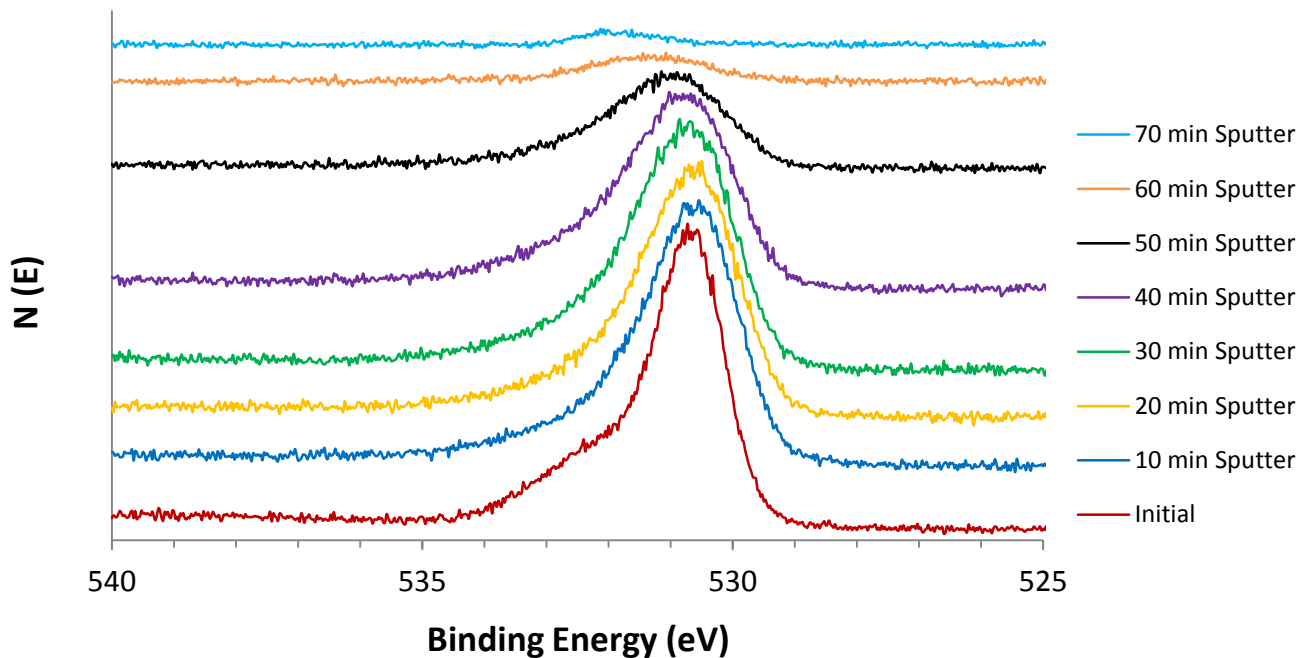


**Figure 63.** XPS Si 2p ionization region of a 95 nm thick film grown from  $\text{TiCl}_4$  and **2** on Si(100) at 100 °C. Reference 2p binding energy for Si: 99.15 eV;  $\text{SiO}_2$ : 103.40 eV.<sup>305</sup>

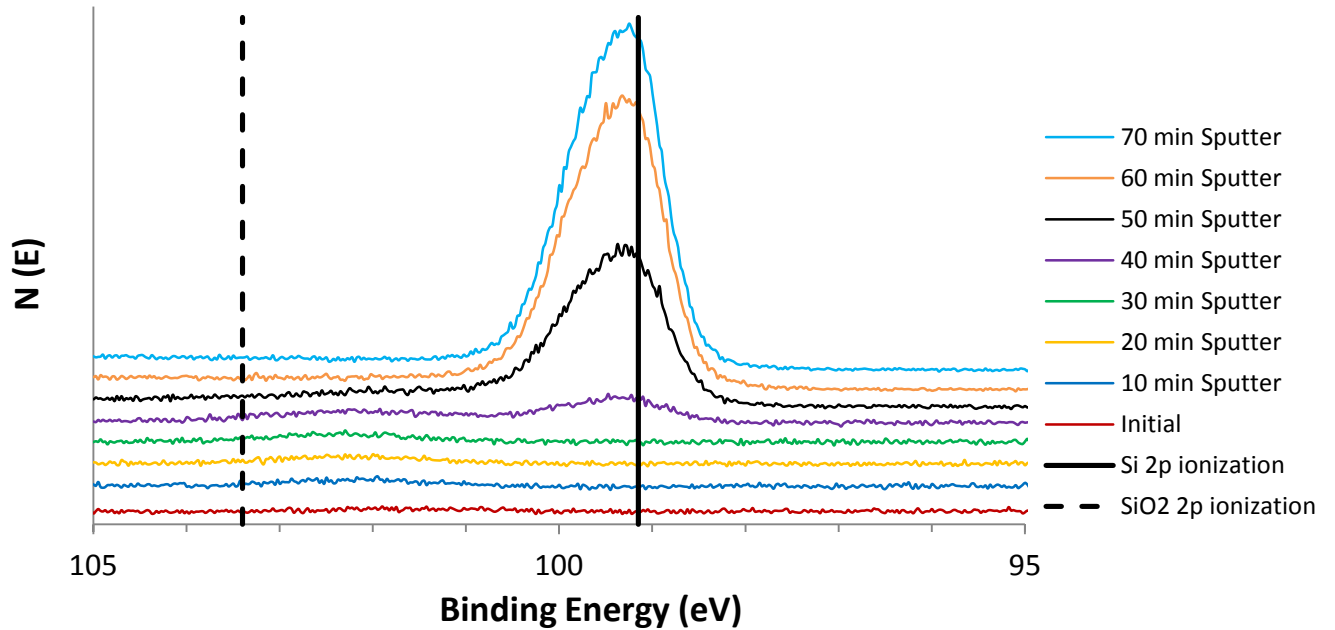


**Figure 64.** XPS Ti 2p ionization region of a 95 nm thick film grown from  $\text{TiCl}_4$  and **2** on Si(100) at 100 °C. Reference 2p binding energies for Ti metal: 453.8 and 459.95 eV;  $\text{TiO}_2$ : 458.5 and 464.2 eV; TiN: 455.7 and 461.3 eV.<sup>305</sup>

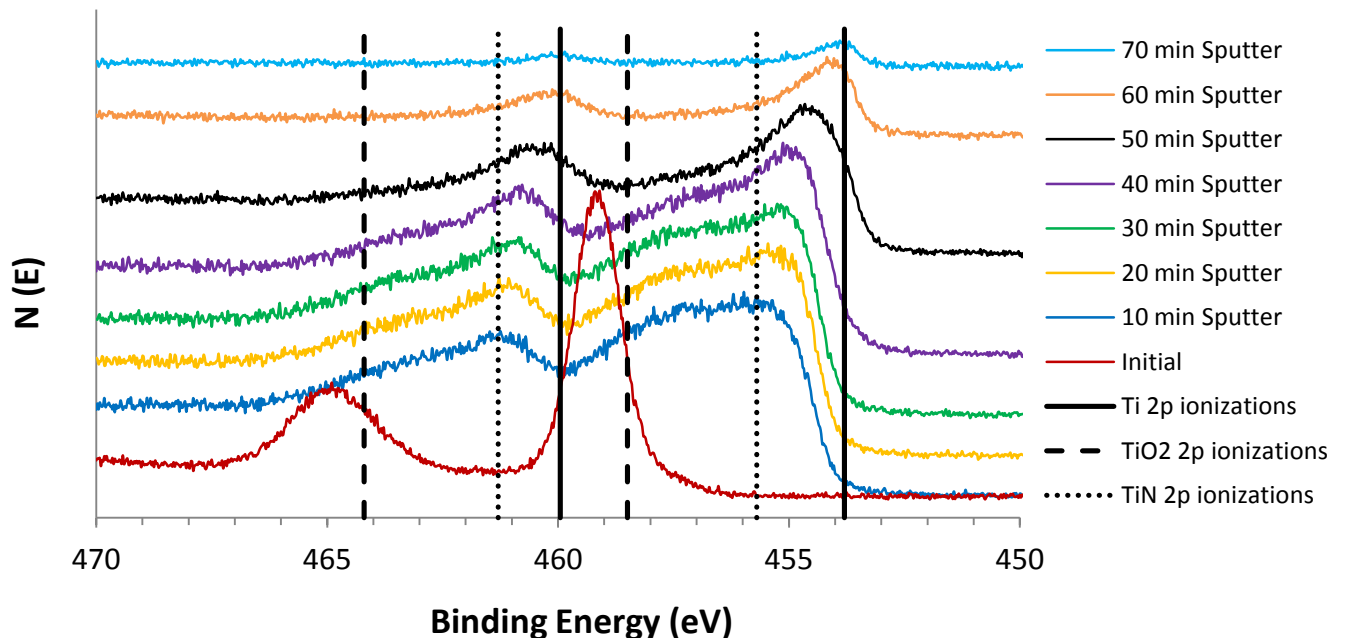


**Figure 65.** XPS depth profile of a 95 nm thick film grown from  $\text{TiCl}_4$  and **2** on Si(100) at  $100^\circ\text{C}$ .

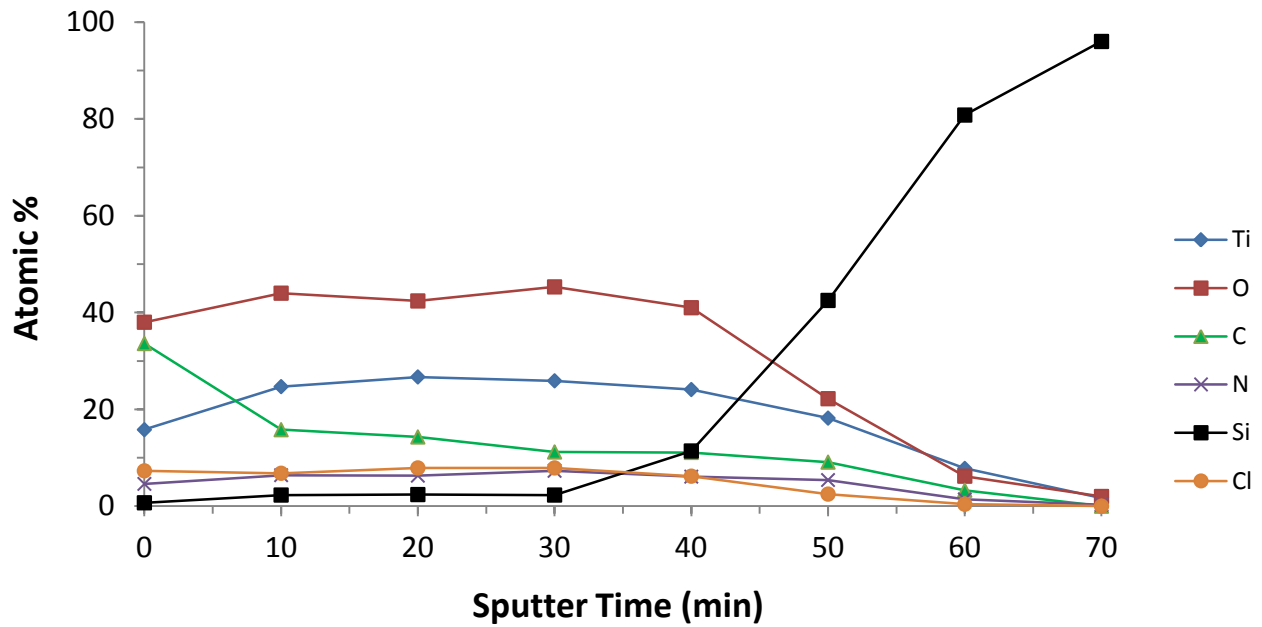
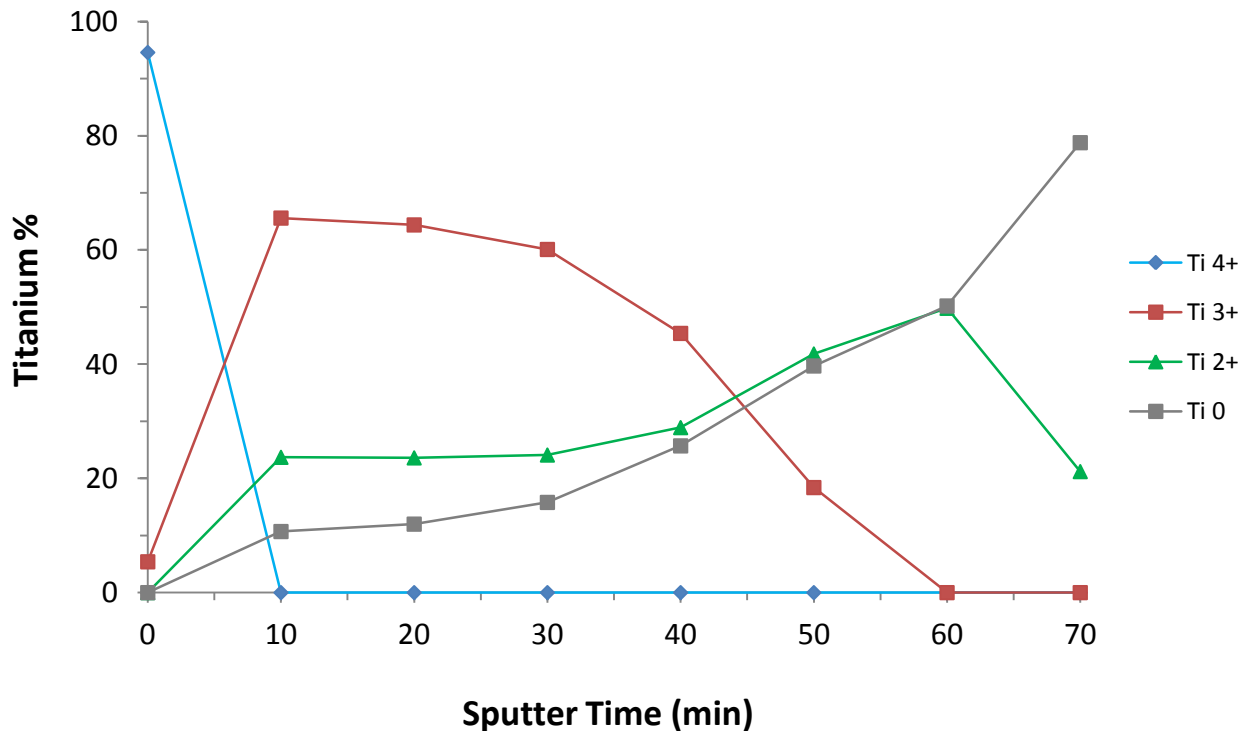
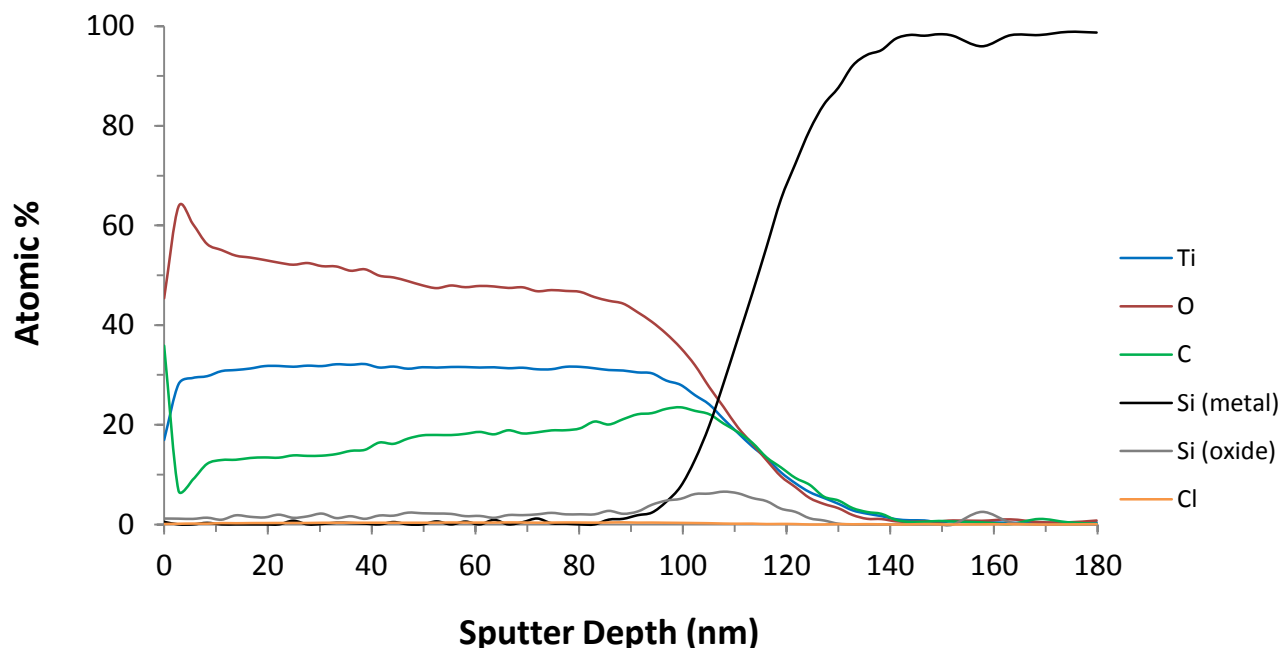


**Figure 66.** Relative abundance of Ti(IV), Ti(III), Ti(II), and Ti(0) oxidation states versus sputter time for a 95 nm thick film grown from  $\text{TiCl}_4$  and **2** on Si(100) at  $100^\circ\text{C}$ .



AES analysis confirmed the persistent C impurity throughout the interior of the film and suggested an O concentration of ~50 at.% until the Si substrate was detected (Figure 67). The presence of N could not be confirmed by AES, since one of the two primary Ti ionizations overlaps the only N ionization. Trace levels of Cl and SiO<sub>2</sub> were also detected throughout the film, with the concentration of the latter peaking at the film/substrate interface.

**Figure 67.** AES depth profile of a 95 nm thick film grown from TiCl<sub>4</sub> and **2** on Si(100) at 100 °C.



An attempt was made to overcoat the Ti film with Co metal to prevent its oxidation upon exposure to ambient atmosphere. Bis(1,4-di-*tert*-butyl-1,3-diazabutadienyl)cobalt(II), **3**, is an ALD precursor with a solid state decomposition temperature of 235 °C.<sup>42</sup> A 97 nm thick Ti film was grown using TiCl<sub>4</sub> and **2** at 100 °C. The film was then transferred to the antechamber of the load-lock on the reactor without breaking vacuum. The solid state booster was loaded with 0.428 g of **3** and vacuum pressure was reestablished at the booster. The Ti film was subsequently

transferred back to the reaction chamber. The “capping” experiment consisted of 200 cycles of 3.0 s pulses of **3** with 10.0 s purges of  $N_2$  at 240 °C. The Co metal deposited as discontinuous nanoparticles (Figure 68). Figures 69–70 show XPS survey scans and the Co 2p ionization region, with the Co concentration ranging from 26.3% (10 min) to 2.9% (70 min) upon sputtering with 3 keV argon ions. Comparison of the Ti 2p ionization region for films with and without the Co overcoat revealed a similar conversion of Ti metal to Ti oxides upon exposure to air, indicating that the Co treatment did not protect the Ti film from oxidation (Figure 71). XPS depth profiling confirmed an O concentration ranging from 29.2–40.8% until the underlying Si substrate was detected after 40 min of sputtering (Figure 72). C and N impurities detected from 10–50 min of sputtering ranged from 9.7–10.9% and 3.6–4.9%, respectively. Elemental mapping by AES indicated that the as-deposited surface exhibited submicron particles that were confirmed to be Co metal on the  $TiO_2$  surface. AES also showed a steady O concentration of ~50 at.% from the surface to the film/substrate interface, which was nearly identical to that of the untreated film.

**Figure 68.** Cross-sectional SEM image of a film deposited on thermal  $SiO_2$  using  $TiCl_4$  and **2**, then overcoated with Co metal by a CVD process.

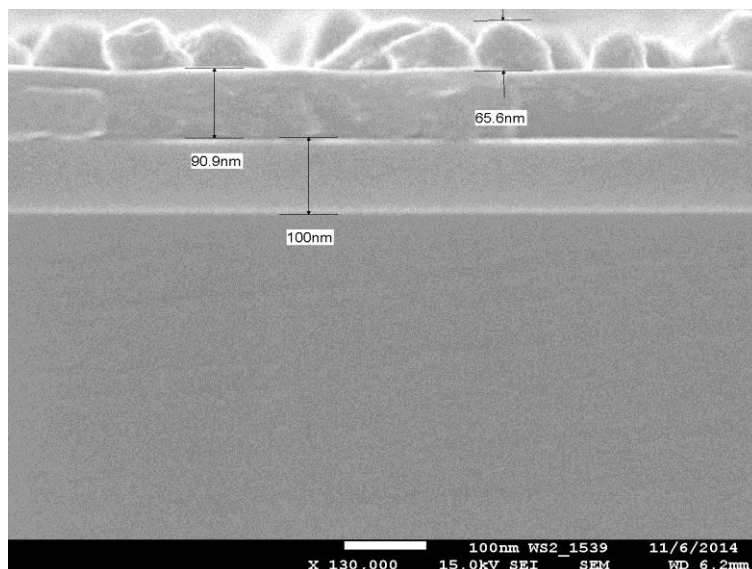




**Figure 69.** XPS survey scans of a 97 nm thick film grown from  $\text{TiCl}_4$  and **2** on Si(100) at  $100^\circ\text{C}$  and overcoated with Co by a CVD process.

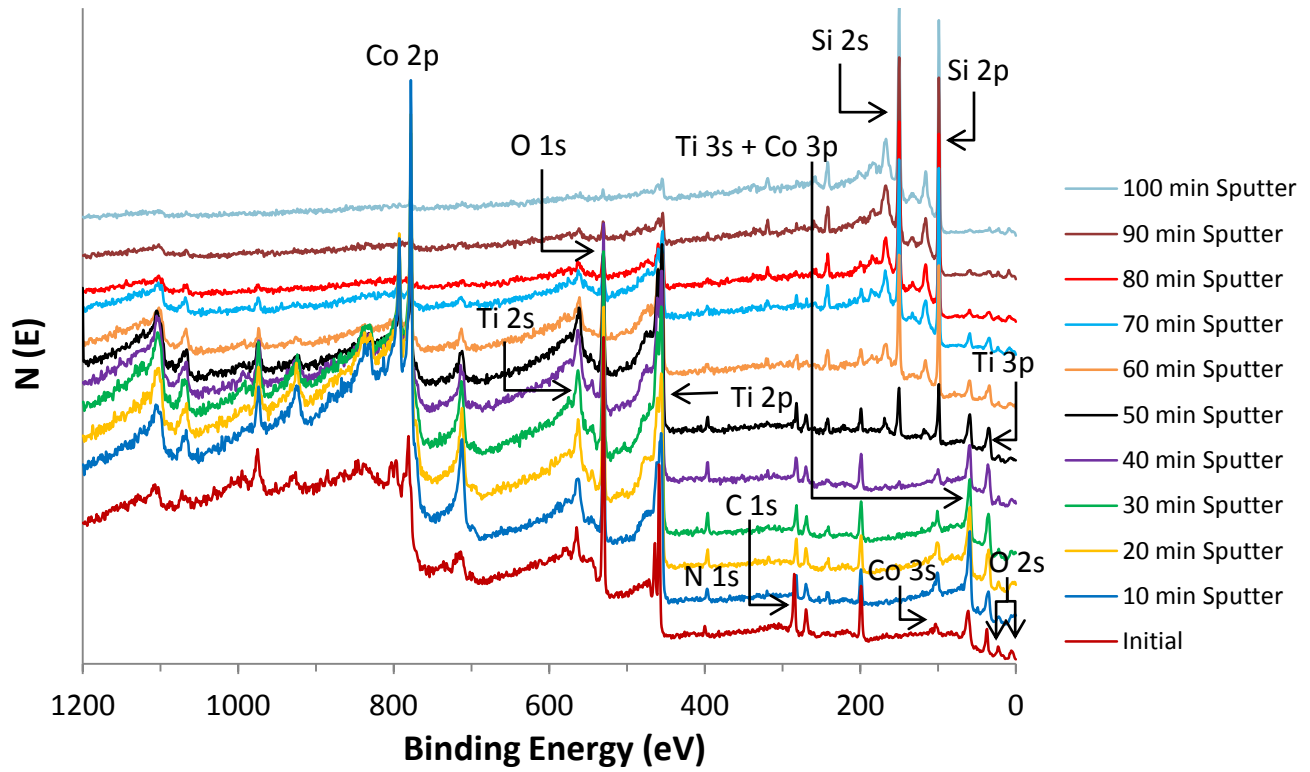


**Figure 70.** XPS Co 2p ionization region of a 97 nm thick film grown from  $\text{TiCl}_4$  and **2** on Si(100) at  $100^\circ\text{C}$  and overcoated with Co by a CVD process. Reference 2p binding energies for Co metal: 777.9 and 792.95 eV; CoO: 780.0 and 795.50 eV.<sup>305</sup>

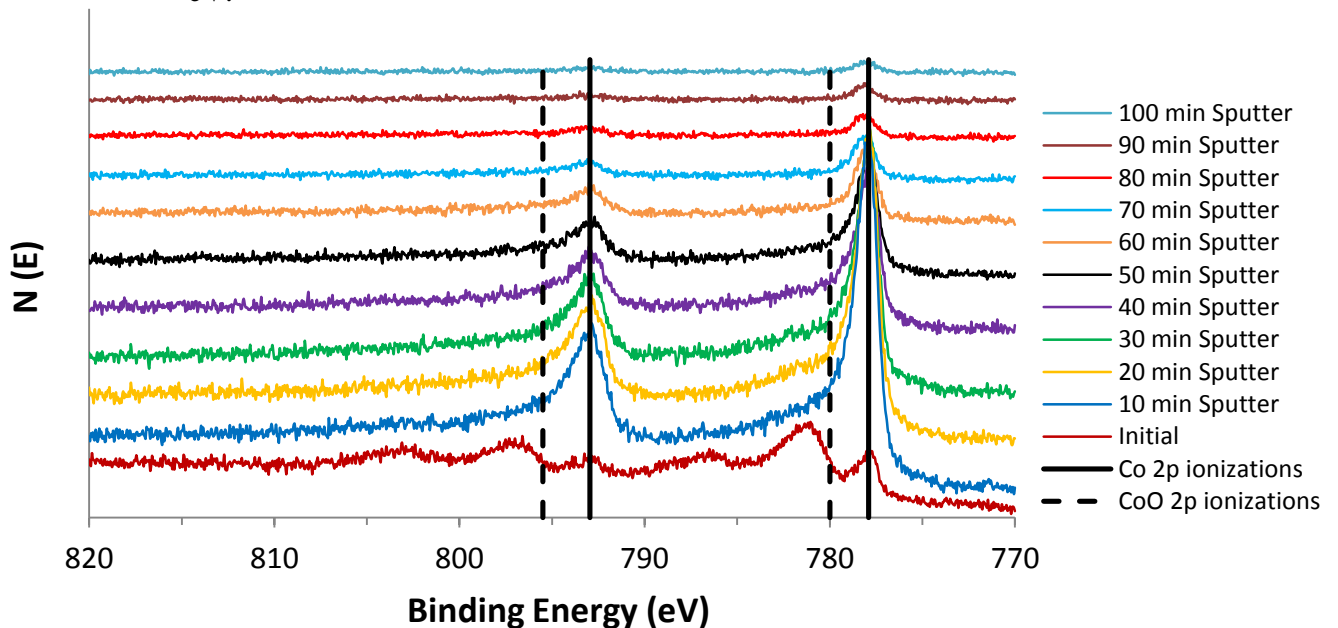


**Figure 71.** XPS Ti 2p ionization region of a 97 nm thick film grown from  $\text{TiCl}_4$  and **2** on Si(100) at 100 °C and overcoated with Co by a CVD process. Reference 2p binding energies for Ti metal: 453.8 and 459.95 eV;  $\text{TiO}_2$ : 458.5 and 464.2 eV; TiN: 455.7 and 461.3 eV.<sup>305</sup>

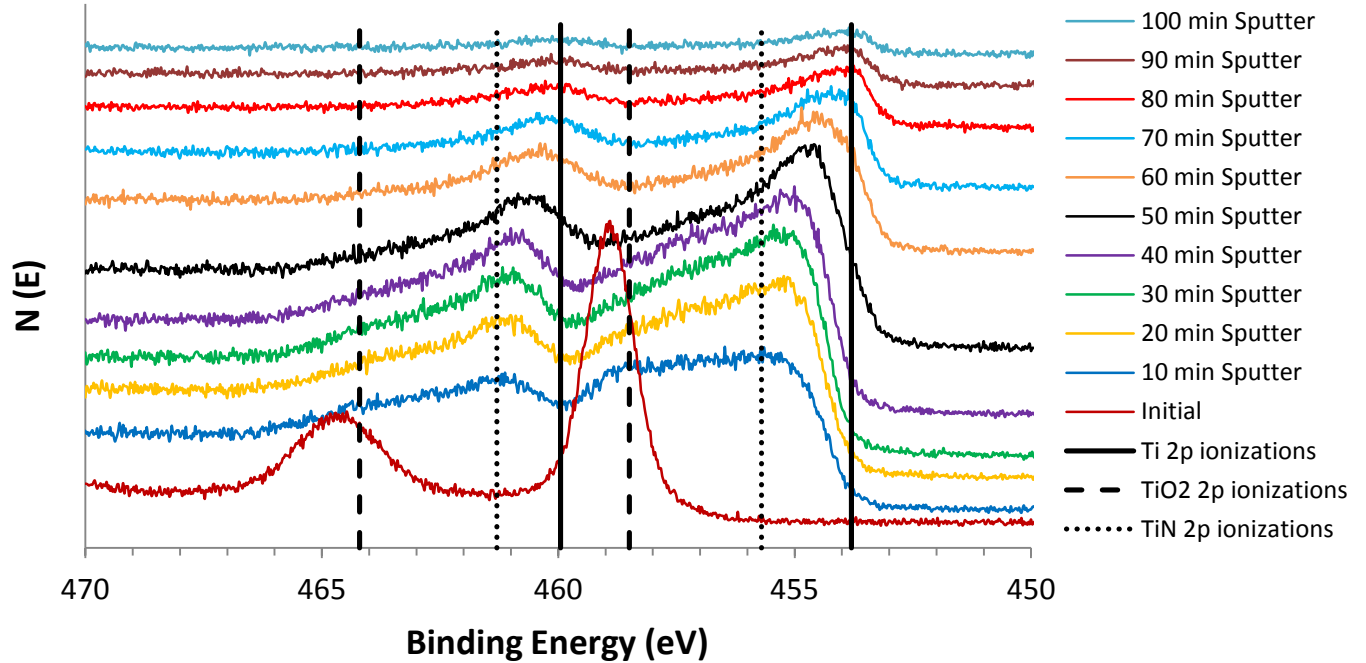


**Figure 72.** XPS depth profile of a 97 nm thick film grown from  $\text{TiCl}_4$  and **2** on Si(100) at 100 °C and overcoated with Co by a CVD process.

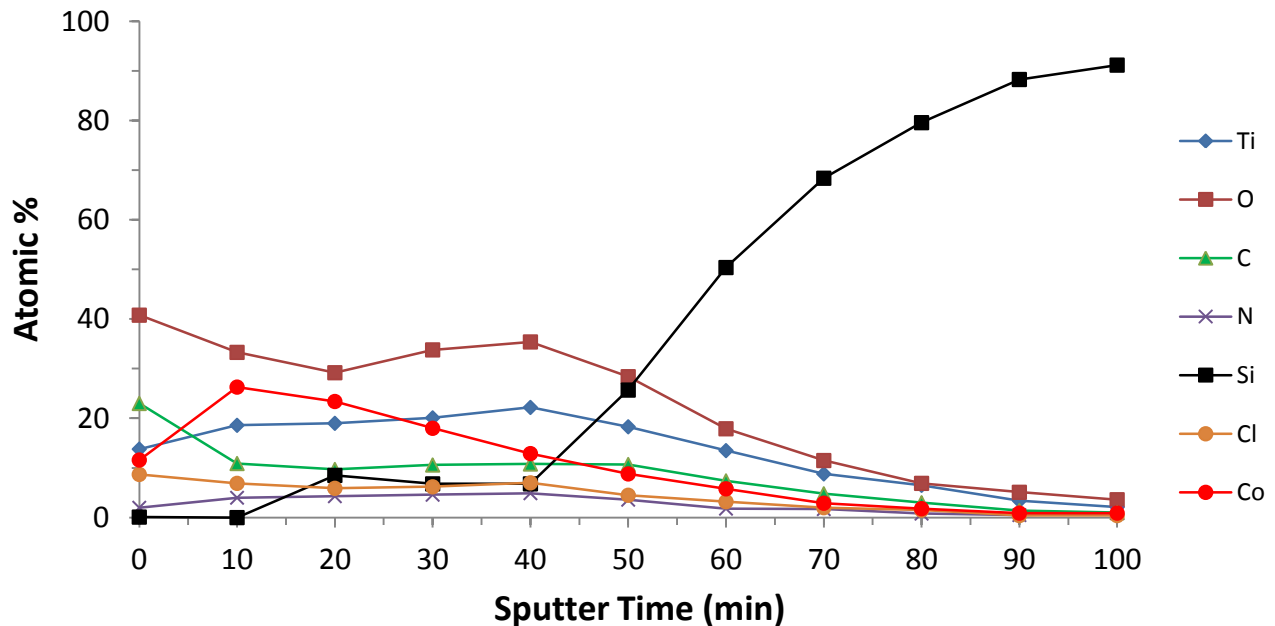
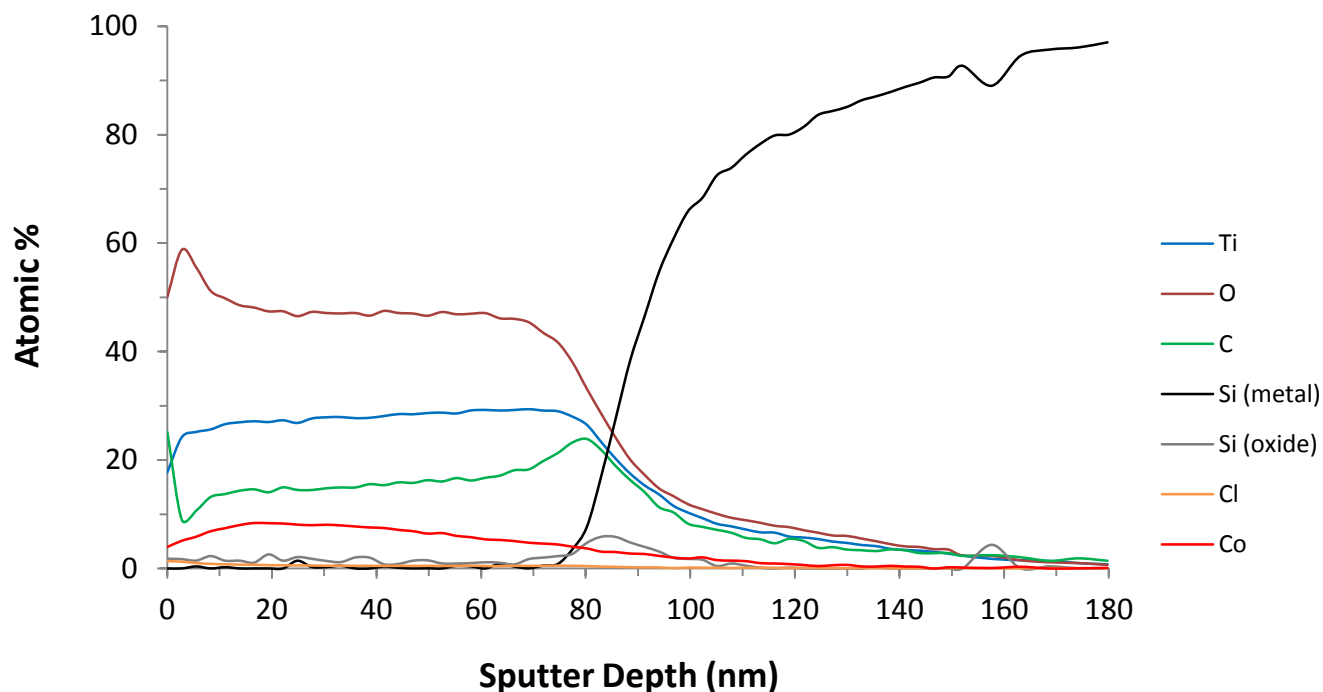


**Figure 73.** AES depth profile of a 97 nm thick film grown from  $\text{TiCl}_4$  and **2** on Si(100) at 100 °C and overcoated with Co by a CVD process.



#### 2.2.4 Antimony Films from $\text{SbCl}_3$ and 1,4-Bis(trimethylsilyl)-1,4-dihydropyrazine

Compound **2** was subsequently used with  $\text{SbCl}_3$  for the growth of Sb metal films. A pulsing sequence of 5.0 s  $\text{SbCl}_3$ /15.0 s  $\text{N}_2$  purge/1.0 s **2**/10.0 s  $\text{N}_2$  purge was applied with the reactor temperature set to 180 °C.  $\text{SbCl}_3$  was delivered by solid state booster, with a constant source temperature of  $38.5 \pm 1.0$  °C, while **2** was delivered by bubbler at 70 °C. After 1,000 cycles, cross-sectional SEM analysis revealed a continuous, 20 nm thick film on a 15 nm thick Pt substrate (Figure 74). The top-down perspective showed a dense granular morphology characteristic of a metallic film (Figure 75). Non-uniform growth was observed on Pd and Cu substrates (Figures 76–77).

**Figure 74.** Cross-sectional SEM image of a 20 nm thick film grown on Pt from  $\text{SbCl}_3$  and **2** for 1,000 cycles at 180 °C.

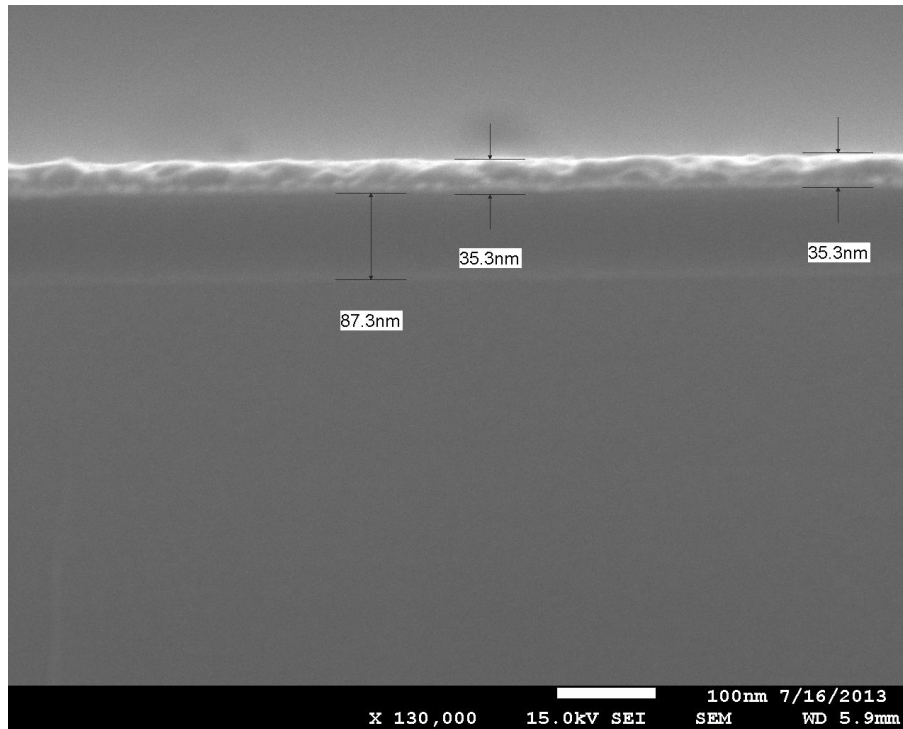


**Figure 75.** Top-down SEM image of a 20 nm thick film grown on Pt from  $\text{SbCl}_3$  and **2** for 1,000 cycles at 180 °C.

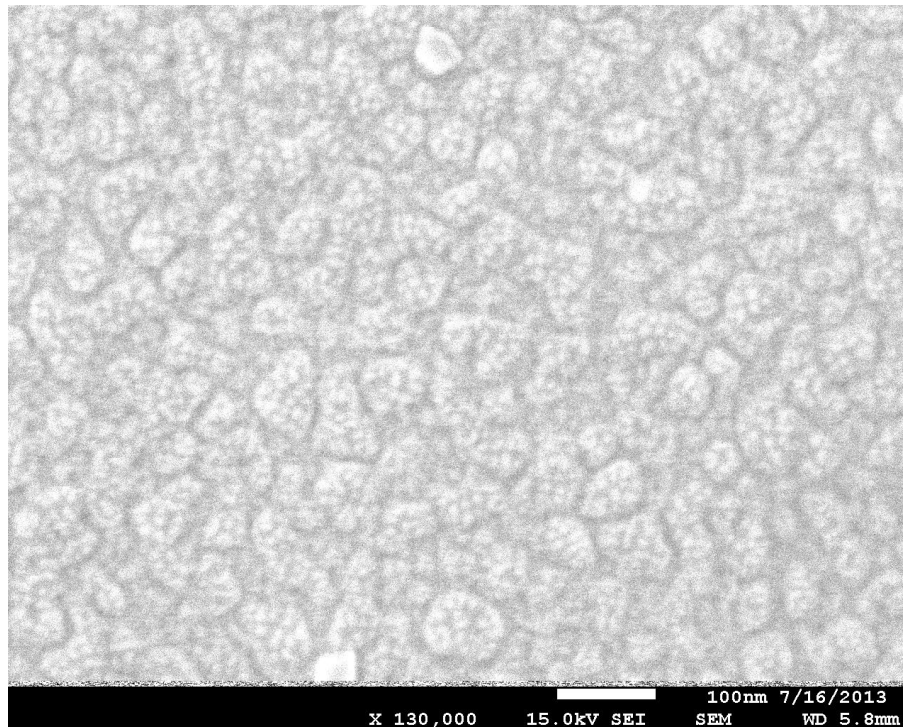


**Figure 76.** Cross-sectional SEM image of material grown on Pd from  $\text{SbCl}_3$  and **2** for 1,000 cycles at 180 °C.

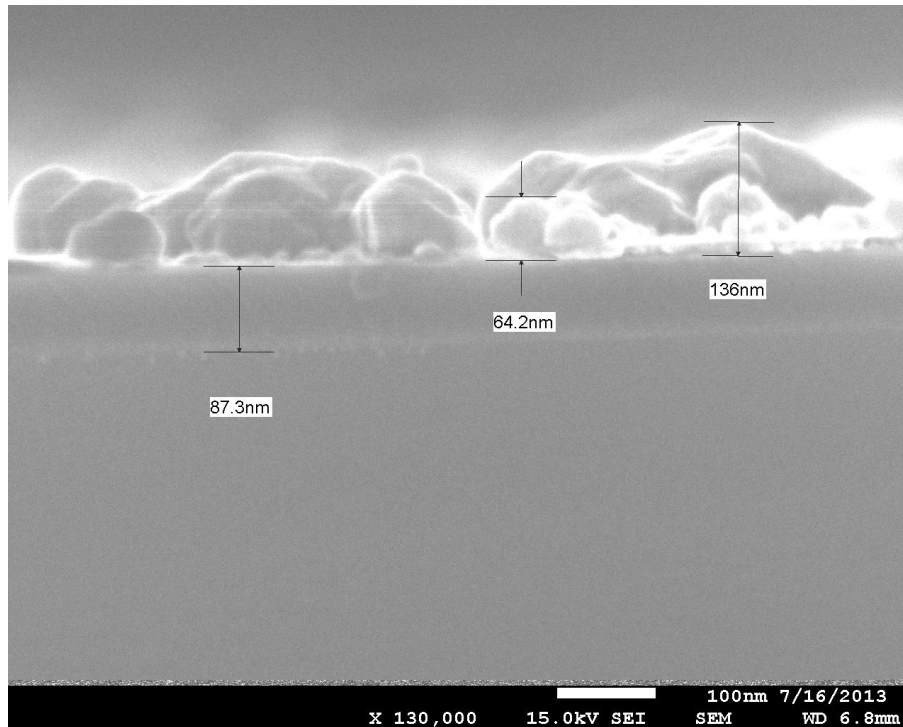
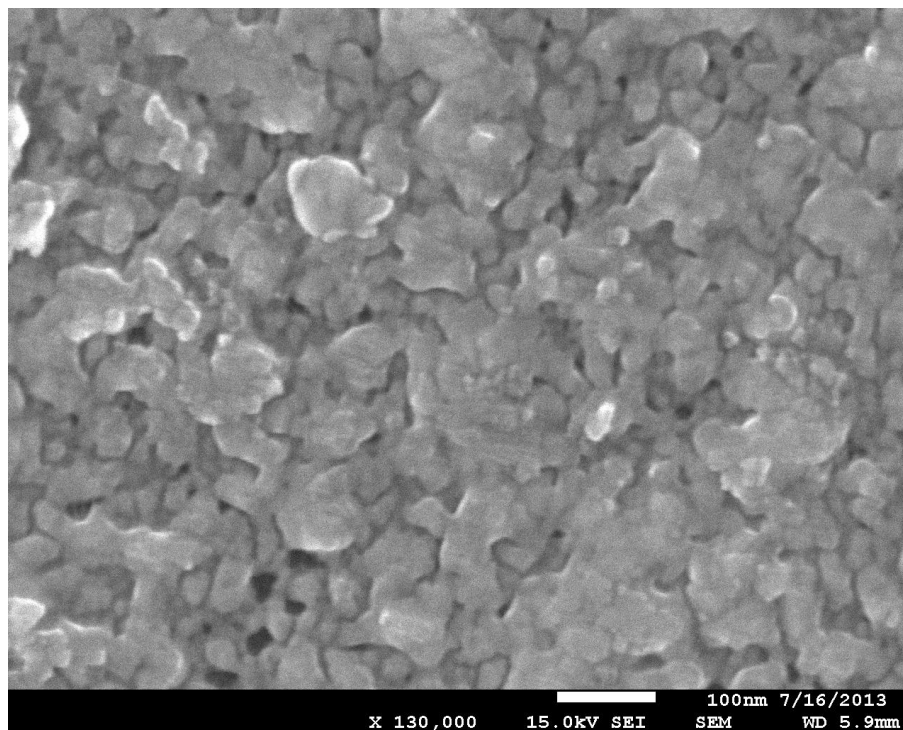


**Figure 77.** Top-down SEM image of material grown on Pd from  $\text{SbCl}_3$  and **2** for 1,000 cycles at 180 °C.



XPS survey scans of a 20 nm thick film deposited on Pt at 180 °C showed the disappearance of the C signal after 1 min of sputtering (Figure 78). It was difficult to quantify the Sb and O concentrations, as the Sb 3d<sub>5/2</sub> and O 1s signals overlap. The Sb 2p region of the as-deposited film showed the presence of Sb<sub>2</sub>O<sub>3</sub> only, while a mixture of Sb and Sb<sub>2</sub>O<sub>3</sub> was observed after 1 min of sputtering (Figure 79). Analysis by powder XRD (performed several months after the deposition) failed to show the presence of any known reflections for Sb or Sb<sub>2</sub>O<sub>3</sub>.

**Figure 78.** XPS survey scans of a 20 nm thick film grown from SbCl<sub>3</sub> and **2** on Pt at 180 °C.

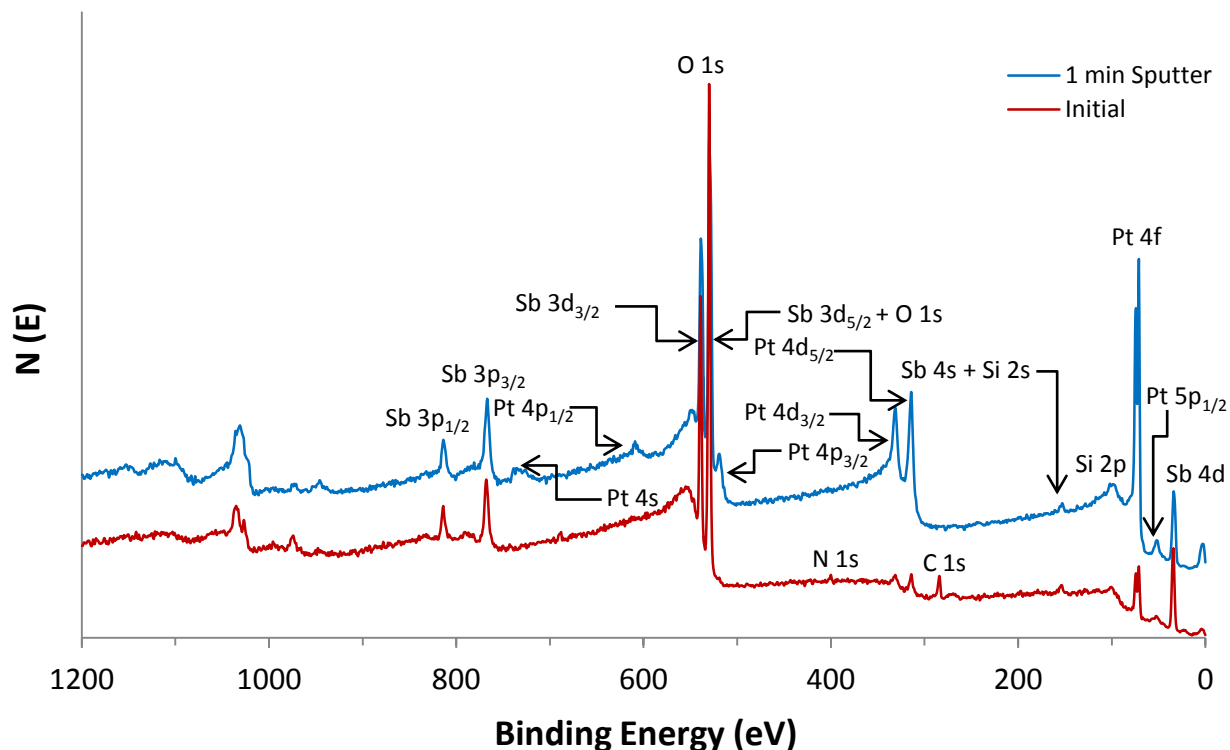
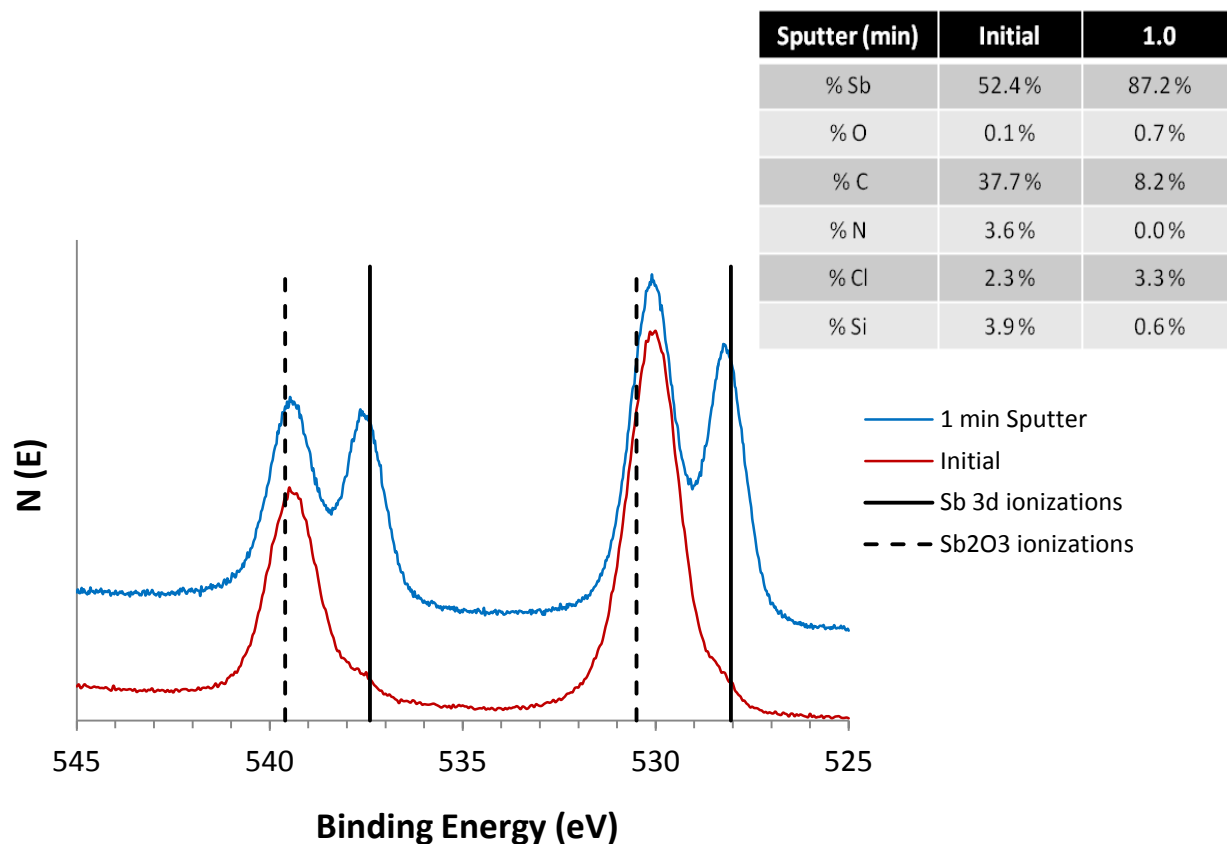


**Figure 79.** XPS Sb 3d ionization region of a 20 nm thick film grown from  $\text{SbCl}_3$  and **2** on Pt at 180 °C. Reference values for Sb metal: 528.05 and 537.40 eV;  $\text{Sb}_2\text{O}_3$ : 530.5 and 539.60 eV.<sup>305</sup>



### 2.3 Conclusions

The growth of Ti metal films has been demonstrated from  $\text{TiCl}_4$  and **1** or **2** as the reducing coreagents. The films oxidized within seconds upon exposure to air. By comparison, plasma ALD-grown 2–15 nm thick Ti films were reported to oxidize within a few seconds upon exposure to air.<sup>11</sup> Sputtered Ti films also oxidize extensively upon exposure to air.<sup>301-304</sup> Previously-reported angular resolved XPS spectra suggest that the natural oxide film exhibits a gradual change in oxidation state, from  $\text{TiO}_2$  to Ti metal,<sup>300,304,310</sup> while RBS analysis of a polished commercially-prepared Ti sample showed a  $\text{TiO}_2$  layer of 4.5 nm, with the entire interfacial layer measuring  $39 \pm 2$  nm.<sup>304</sup>

XPS studies herein of films grown on Si(100) with native oxide revealed Ti 2p ionizations consistent with Ti metal upon sputtering into the film. This region is likely protected from oxidation by limited diffusion of oxygen through the film. Since the 3 keV argon ions used in the sputtering experiments cannot reduce  $\text{TiO}_2$  to Ti metal,<sup>300</sup> the observed Ti metal must arise from the reduction of  $\text{TiCl}_4$  by **1** or **2**. Air-exposed sputtered Ti films on clean Si(100) surfaces showed very similar XPS spectra to those obtained herein,<sup>301</sup> supporting the claim of Ti metal growth from  $\text{TiCl}_4$  and **1** or **2**. XPS analyses demonstrate that films obtained with **1** as the reducing coreagent have low C and Cl levels, with no N observed. These data rule out the formation of TiC, TiN, or low valent  $\text{TiCl}_x$  species. The C and N contamination detected in films grown using **2** may be due to the incorporation of pyrazine into the film. Finally, upon sputtering to the film/substrate interface, the Ti 2p<sub>3/2</sub> and Si 2p binding energies matched those of Ti metal and elemental Si and were not consistent with those of  $\text{TiSi}_2$ .<sup>306</sup> Sputtered Ti metal grown on a clean Si(100) surface at room temperature afforded a very thin (~four monolayers)  $\text{TiSi}_2$  interface, upon which Ti metal then grew.<sup>301</sup> Formation of thicker  $\text{TiSi}_2$  films is carried out by the annealing of Ti metal layers on Si substrates at  $> 700\text{ }^\circ\text{C}$ .<sup>311</sup> The low temperatures of the Ti ALD processes demonstrated herein imply at most very thin  $\text{TiSi}_2$  interfacial layers.

This is the first report of a thermal Ti ALD process. Upon the basis of the reduction potential of toluene ( $E_{1/2} = -2.46\text{ V}$ ), most metal ions in the periodic table should be reduced by the 2-methyl-1,4-cyclohexadienyl dianion,<sup>41</sup> which results upon double desilylation of **1**. A similar argument can be made for **2**. Accordingly, **1** and **2** should be powerful reducing coreagents for the ALD of metal films. A preliminary experiment for the reduction of  $\text{SbCl}_3$  by **2** afforded a smooth, continuous film with a granular morphology on a Pt substrate. XPS analysis showed a mixed composition of Sb metal and  $\text{Sb}_2\text{O}_3$  after only 1 min of sputtering. Further



extension of this work should lead to significant advances in the ALD of electropositive metal and element films that have been previously difficult or impossible to grow by low-temperature thermal processes.

## 2.4 Experimental

**General Considerations.** All manipulations were carried out under argon using either Schlenk or glove box techniques. All glassware was oven-dried at  $\geq 150$  °C prior to use. Tetrahydrofuran was distilled from sodium benzophenone ketyl and sodium metal. Toluene was distilled from sodium metal. Dichloromethane was distilled from calcium hydride. Anhydrous  $\text{TiCl}_4$  was obtained from Alpha Aesar. Anhydrous metal salts and a 99.7% pure Ti foil were obtained from Sigma-Aldrich. Compounds **1**,<sup>299</sup> **2**,<sup>309</sup> and **3**<sup>42</sup> were synthesized according to published procedures.  $^1\text{H}$  and  $^{13}\text{C}\{^1\text{H}\}$  NMR spectra were obtained at 400 and 100 MHz in benzene- $d_6$  and were referenced to the residual proton and the  $^{13}\text{C}$  resonances of the solvent. Sublimations were performed using either a Büchi B-580 or Büchi B-585 sublimation oven.

**Preparation of 2-Methyl-1,4-bis(trimethylsilyl)-2,5-cyclohexadiene (1).** A 200 mL Schlenk flask, equipped with a magnetic stir bar and a rubber septum, was charged with toluene (9.21 g, 0.10 mol) and THF (75 mL). A second 500 mL Schlenk flask, equipped with a magnetic stir bar and a rubber septum, was charged with chlorotrimethylsilane (40.00 g, 0.37 mol), lithium pellets (2.00 g, 0.29 mol), and THF (75 mL). Both flasks were cooled to 0 °C. The toluene solution was added dropwise by cannula to the 500 mL flask. The resultant solution was stirred for 8 h at 5–10 °C. THF along with unreacted chlorotrimethylsilane and toluene were removed under reduced pressure, leaving a clear liquid. The crude product was distilled at 90–100 °C/0.05 Torr as a mixture of two diastereomers: bp 96 °C/0.05 Torr;  $^1\text{H}$  NMR (400 MHz,  $\text{C}_6\text{D}_6$ , 23 °C,  $\delta$ ) 5.62 (m, 1H, CH (ring)), 5.53 (m, 1H, CH (ring)), 5.27 (s, 1H, CH (ring)), 2.22 (m, 1H, SiCH

(ring)), 2.10 (m, 1H, SiCH (ring)), 1.65 (s, 3H, CH<sub>3</sub>), 0.11 (s, 9H, Si(CH<sub>3</sub>)<sub>3</sub>), 0.05 (s, 9H, Si(CH<sub>3</sub>)<sub>3</sub>); <sup>13</sup>C{<sup>1</sup>H} NMR (400 MHz, C<sub>6</sub>D<sub>6</sub>, 23 °C, ppm) 132.87 (s, CHCH<sub>3</sub> (ring)), 126.34 (s, CH (ring)), 122.90 (s, CH (ring)), 118.20 (s, CH (ring)), 36.31 (s, CHSi (ring)), 31.40 (s, CHSi (ring)), 25.10 (s, CH<sub>3</sub>), -1.41 (s, Si(CH<sub>3</sub>)<sub>3</sub>), -3.01 (s, Si(CH<sub>3</sub>)<sub>3</sub>).

**Preparation of 1,4-Bis(trimethylsilyl)-1,4-dihydropyrazine (2).** A 100 mL Schlenk flask, equipped with a magnetic stir bar and a rubber septum, was charged with pyrazine (8.00 g, 0.10 mol) and tetrahydrofuran (30 mL). A second 200 mL Schlenk flask, equipped with a magnetic stir bar and a rubber septum, was charged with chlorotrimethylsilane (32.59 g, 0.30 mol), lithium pellets (2.08 g, 0.30 mol), and THF (30 mL). Both flasks were cooled to 0 °C. The dissolved pyrazine solution was added dropwise by cannula over a 17 min period to the 200 mL flask. The resulting melon-orange solution was stirred for 2 h at 0 °C, then filtered through a 1-inch pad of Celite on a medium glass frit. THF and unreacted chlorotrimethylsilane were removed under reduced pressure, affording a yellow solid. Yellow crystals were obtained by sublimation at 80 °C/0.05 Torr (13.82 g, 61%): mp 62–66 °C; <sup>1</sup>H NMR (C<sub>6</sub>D<sub>6</sub>, 23 °C, δ) 4.70 (s, 4H, CH (ring)), -0.04 (s, 18H, Si(CH<sub>3</sub>)<sub>3</sub>); <sup>13</sup>C{<sup>1</sup>H} NMR (400 MHz, C<sub>6</sub>D<sub>6</sub>, 23 °C, ppm) 115.11 (s, CH (ring)), -2.12 (s, Si(CH<sub>3</sub>)<sub>3</sub>).

**Sublimation Study.** The preparative sublimation of **2** employed a 30 cm long, 2.5 cm diameter glass tube. One end of this tube was sealed, while the other end was fitted with a 24/40 glass joint (male). In an argon-filled dry box, 1.0 g of **2** was loaded into a 1.0 × 3.0 cm glass tube, which was placed inside of the glass sublimation tube at the sealed end. The sublimation tube was subsequently fitted with a 24/40 vacuum adapter and placed into a horizontal Büchi Kugelrohr oven. Approximately 20 cm of the sublimation tube was situated inside of the oven. A pressure of 0.05 Torr was maintained throughout the experiment. The oven temperature was set

to 80 °C. Compound **2** sublimed to the cool zone outside of the oven. The percent recovery was determined by weighing the sublimed product. The percent nonvolatile residue was obtained by weighing the 1.0 × 3.0 cm glass tube upon completion of the sublimation experiment.

**Melting Point and Thermal Decomposition Studies.** The melting point and thermal decomposition temperature of **2** were assessed using a Thermo Scientific Mel-Temp 3.0 digital melting point apparatus and are uncorrected. In an argon-filled dry box, a melting point capillary tube was charged with 1–2 mg of **2**, and the end of the tube was sealed with a small amount of stopcock grease. The capillary tube was then removed from the dry box and the end was flame-sealed. The capillary tube was transferred to the melting point apparatus and was heated at a 5 °C/min gradient starting at 25 °C. A more precise experiment was subsequently performed whereby a sample of **2** was heated at a 0.5 °C/min gradient starting at 57 °C. Additional experiments to determine the decomposition of **2** used a gradient of 10 °C/min. In all cases, the sample evaporated to the top of the capillary tube at ~265 °C. No discoloration of the sample was observed, suggesting that **2** evaporated intact with no decomposition.

In a similar fashion, heating a sample of **1** in a sealed capillary tube resulted in the evaporation of **1** to the top of the tube prior to the onset of decomposition. A subsequent approach employed a 2-dram screw cap vial charged with 2 mL of **1** under argon. The cap of the vial was sealed with Teflon tape prior to removal from the dry box. The vial was placed in a crucible, which was then placed in a ThermoLyne 48000 furnace. The temperature was slowly increased while periodically inspecting the sample for any visual changes. No visual changes were observed at ≤ 450 °C, which was the upper temperature limit of the experiment.

**Cyclic Voltammetry.** CV experiments were performed using a BASi potentiostat in an argon-filled dry box. Experiments were conducted in DMF, using NBu<sub>4</sub>ClO<sub>4</sub> as the supporting

electrolyte. Reported data are relative to ferrocene (referenced to 0.31 V), using Ag/AgNO<sub>3</sub> as the reference electrode.

**Film Growth Studies.** A Picosun Oy R-75BE ALD reactor was used for thin film deposition experiments. A Texol GeniSys N<sub>2</sub> generator supplied 99.9995% N<sub>2</sub> as both the carrier and purge gas. An Ebara ESA25-D multi-stage dry pump was used to maintain a pressure of 6–10 mbar in the reactor while under a constant N<sub>2</sub> flow. A SAES MC1-902FV gas purifier was used to purify the N<sub>2</sub> to 99.99999% for all films grown using **1** and for films grown using **2** for which compositional analyses were performed.

TiCl<sub>4</sub> and **1** or **2** were used as precursors to grow films on Si(100) with native oxide, thermal SiO<sub>2</sub>, and Pt/SiO<sub>2</sub>/Si. These substrates were provided by Applied Materials. Data for the ALD studies were obtained from films grown on 1 cm<sup>2</sup> thermal SiO<sub>2</sub> substrates. TiCl<sub>4</sub> was delivered by bubbler at 23 °C at the reactor pressure. Compounds **1** and **2** were delivered by solid state booster at 64.0 ± 1.0 °C and 56.5 ± 0.5 °C, respectively. Precursor pulse lengths were varied to determine the degree of surface saturation. The substrate temperature was subsequently varied using saturative doses of the precursors.

TGA/DTA analysis of **2** was performed by Dr. David Knapp at Applied Materials (Sunnyvale, CA). Thicknesses of deposited films were measured by cross-sectional SEM using a JEOL-6510LV electron microscope. Growth rates were calculated by dividing the measured film thicknesses by the number of deposition cycles. Film thicknesses were measured at a minimum of three points on each substrate to evaluate the uniformity. For EDS experiments performed in conjunction with this system, the anti-contamination device was cooled with liquid N<sub>2</sub> to minimize carbon contamination. Powder XRD experiments were performed with a Rigaku R200B 12 kW rotating anode diffractometer, using Cu K<sub>α</sub> radiation (1.54056 Å) at 40 kV and

150 mA. Crystalline phases were identified by comparison of the experimental patterns with the powder diffraction files of the International Center of Diffraction Data using the Jade 5.0 software package. Crystallite sizes were calculated from the most intense reflection, using the Scherrer equation with the Jade 5.0 software package. XPS analyses were performed with a Perkin-Elmer ESCA 5500 system using monochromatized ( $\text{SiO}_2$  crystal) Al  $K_\alpha$  radiation (15 kV at 15 mA) and a 90-degree Omni-Focus lens. The typical background pressure during analysis was  $1 \times 10^{-9}$  Torr. An argon ion sputter was used for depth profiling using a 3.0 keV, 25 mA emission current and  $10 \times 10^{-3}$  Pa. The spectrometer was calibrated to the Au  $4f_{7/2}$  peak at 83.80 eV, the Cu  $3p_{3/2}$  peak at 74.9 eV, and the Cu  $2p_{3/2}$  peak at 932.40 eV. A low-energy electron flood gun was used to neutralize the charge by aligning the adventitious carbon (C 1s) peak to 284.6 eV. For all samples, a survey spectrum was recorded over a binding energy range of 0 to 1200 eV using a pass energy of 117.4 eV with a scan step of 1.0 eV. High-resolution multiplex spectra were obtained using a pass energy of 23.5 eV with a scan step of 0.025 eV. AFM micrographs were obtained using a Park Systems XE\_NSOM atomic force microscope. The samples were measured using the tapping mode in air at a frequency of 0.34 Hz. An ACTA tip was used, with a resonance frequency of 300 kHz and a force constant of  $40 \text{ Nm}^{-1}$ . Surface roughnesses were calculated as RMS values by Park Systems XEI software (Rq). For all measurements, the noise was on the order of 3 nm. Sheet resistivity measurements were obtained using a Jandel 4-point probe in combination with a Keithley 2400 SourceMeter and a Keithley 2182A Nanovoltmeter. AES depth profiling was performed by Evans Analytical Group (Sunnyvale, CA).

## CHAPTER 3

### Low Temperature Thermal Atomic Layer Deposition of Cobalt and Other Metal Films Using Formic Acid

#### 3.1 Introduction

Cobalt metal films have important applications as magnetic materials, precursors to  $\text{CoSi}_2$  contact materials, and liners and caps of copper features in microelectronics devices.<sup>122</sup> Numerous PEALD processes for Co metal have been reported,<sup>43–44,129–134</sup> however, plasma can cause substrate damage from highly reactive species and can result in poor conformal coverage of high aspect ratio features due to surface recombination of H atoms.<sup>31,49</sup> Thermal ALD is the preferred technique for depositing conformal films with nanoscale precision on structured and high aspect ratio surfaces. However, reports of thermal ALD processes for Co metal are extremely limited.  $\text{Co}(\text{iPrNC}(\text{Me})\text{N}^{\text{iPr}})_2$  was used with and  $\text{H}_2$  gas at 350 °C for the growth of Co metal at a rate of 0.12 Å/cycle.<sup>36</sup> This precursor was subsequently used at 300–340 °C ( $\text{H}_2$  gas)<sup>136</sup> and 350 °C ( $\text{H}_2$  gas,<sup>137</sup>  $\text{NH}_3$  gas,<sup>137–138</sup> and  $\text{NH}_3$  plasma).<sup>138</sup> Although self-limited behavior was demonstrated,<sup>36</sup> the temperatures used for these studies were significantly higher than the decomposition temperature of  $\text{Co}(\text{iPrNC}(\text{Me})\text{N}^{\text{iPr}})_2$  (215–225 °C),<sup>139</sup> suggesting a likely CVD component toward film growth. A subsequent process using (2-*tert*-butylallyl)Co(CO)<sub>3</sub> and 1,1-dimethylhydrazine was used for the selective ALD of Co metal at 140 °C, however, self-limited growth was not demonstrated.<sup>143</sup> Additionally, thermal decomposition of this precursor appears to commence at ~90 °C (Appendix A), implying a probable CVD component to the film growth process. Finally, a recently-reported process for Co metal ALD used a Co  $\alpha$ -imino alkoxide precursor and  $\text{BH}_3(\text{NHMe}_2)$ .<sup>39</sup> Growth only occurred on Ru substrates (0.07 Å/cycle at 180 °C), and only after a nucleation step consisting of 50 cycles of 20 s pulses of the Co precursor.<sup>39</sup> Film

thickness plateaued after 1,000 ALD cycles, suggesting a catalytic role of the Ru substrate in activating  $\text{BH}_3(\text{NHMe}_2)$ .<sup>39</sup> These methods all demonstrate low growth rates or have otherwise significant drawbacks, highlighting the need for an improved low-temperature Co ALD process.

Recently, a three-step process was reported for the ALD of high-purity Cu films using Cu bis(1-dimethylamino-2-propoxide) ( $\text{Cu}(\text{dmap})_2$ ), formic acid, and hydrazine.<sup>231</sup> Although  $\text{Cu}(\text{dmap})_2$  cannot be reduced by hydrazine, Cu formate is readily reduced by hydrazine to Cu metal.<sup>231</sup> Accordingly, similar three-step processes were considered for Co metal ALD. Winter and coworkers recently developed a series of transition metal diazadienyl complexes of the form  $\text{M}(\text{tBu}_2\text{DAD})_2$  ( $\text{M} = \text{Co}$  (**3**), Ni (**4**), Fe (**5**), Cr (**6**), Mn (**7**)) as ALD precursors.<sup>42</sup> These compounds sublime at low temperatures and demonstrate high thermal stabilities (Table 8).

**Table 8.** Reported thermal properties of  $\text{M}(\text{tBu}_2\text{DAD})_2$  complexes.<sup>42</sup>

Complex		Sublimation		Solid State		Nonvolatile
		Temp (°C/0.05 Torr)	mp (°C)	Decomp. Temp. (°C)	Recovery (%)	Residue (%)
<b>3</b>	Co	115	174–175	235	94.7	5.2
<b>4</b>	Ni	115	184–185	230	92.3	6.9
<b>5</b>	Fe	115	132–134	260	96.1	3.4
<b>6</b>	Cr	85	95–97	295	96.7	3.2
<b>7</b>	Mn	120	155–157	325	95.0	4.3

Chapter 2 described the use of bis(trimethylsilyl) six-membered rings as strongly-reducing coreagents for ALD, where **1** and **2** were used for the reduction of  $\text{TiCl}_4$  to Ti metal. Thus, the envisioned approach for a novel Co ALD process entailed the use of **3**, formic acid, and **2** in a three-step sequence. The discovery that high-purity Co films could be grown using only **3** and formic acid is described in a full deposition study herein. The original three-step approach was subsequently applied to the growth of other transition metal and metal oxide films.

### 3.2 Results and Discussion

**Cyclic Voltammetry.** Compounds **3** and **4** were analyzed by CV in DMF, using 0.1 M  $\text{NBu}_4\text{ClO}_4$  as the supporting electrolyte. Reported data are relative to ferrocene (referenced to 0.31 V), using  $\text{Ag}/\text{AgNO}_3$  as the reference electrode. Reversible redox couples were observed for **3** at  $E_{1/2} = -0.065$  and  $-0.538$  V and for **4** at  $E_{1/2} = 0.191$  and  $-0.487$  V (Figures 80–81).

**Figure 80.** Cyclic voltammogram of **3** relative to ferrocene ( $\text{Fc}/\text{Fc}^+$ ,  $E^\circ = 0.31$  V).

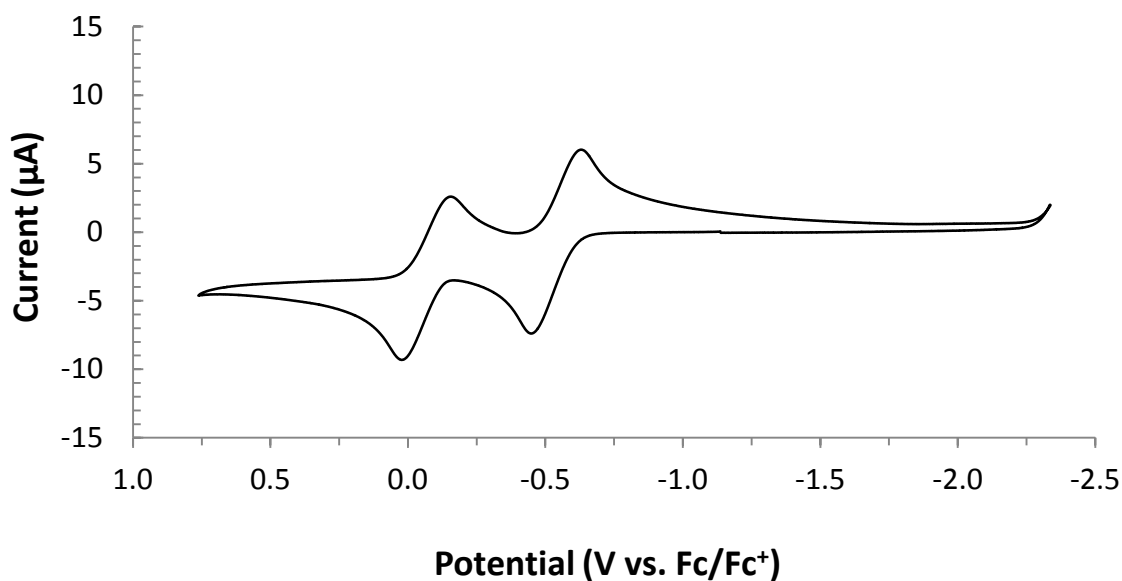
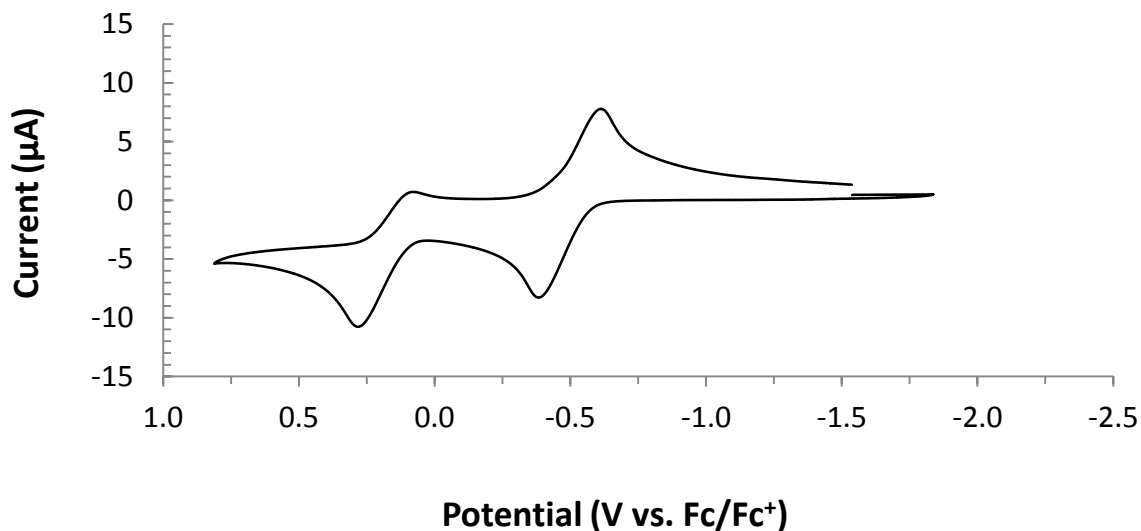


**Figure 81.** Cyclic voltammogram of **4** relative to ferrocene ( $\text{Fc}/\text{Fc}^+$ ,  $E^\circ = 0.31$  V).





**Solution Reactivity.** Compound **3** (1 equivalent) was dissolved in dry THF, yielding a dark green solution, to which formic acid (53 equivalents) was added. After stirring for 45 min at 23 °C, a purple precipitate was observed. After refluxing for 1 hr, the purple precipitate turned pink/red. After sitting overnight, the solution turned brown; none of the precipitate adhered to the stir bar. The powder XRD spectrum of the precipitate was complex, possibly showing the presence of  $\text{Co}(\text{OCHO})_2 \cdot 2\text{H}_2\text{O}$ , Co metal,  $\text{Co}_3\text{O}_4$ , or CoO (Figures 82–84). This experiment was repeated, with **3** (1 equivalent) and formic acid (19 equivalents) each dissolved in dry THF. After adding the formic acid solution to **3** and allowing the mixture to stand without stirring for 20 min, a lighter green solution resulted with a significant amount of precipitate. Stirring this solution at 23 °C for 30 minutes resulted in its changing color from light green to pink to dull purple to light brown. After refluxing for 30 min, the solution was olive green with a pink precipitate. After standing under argon for 20 hrs, the solution turned dark brown; none of the precipitate adhered to the stir bar.

**Figure 82.** Powder XRD spectrum of the product obtained by reacting **3** and formic acid. Major reflections for  $\text{Co}(\text{OCHO})_2 \cdot 2\text{H}_2\text{O}$  <21–0257> are shown by vertical lines.

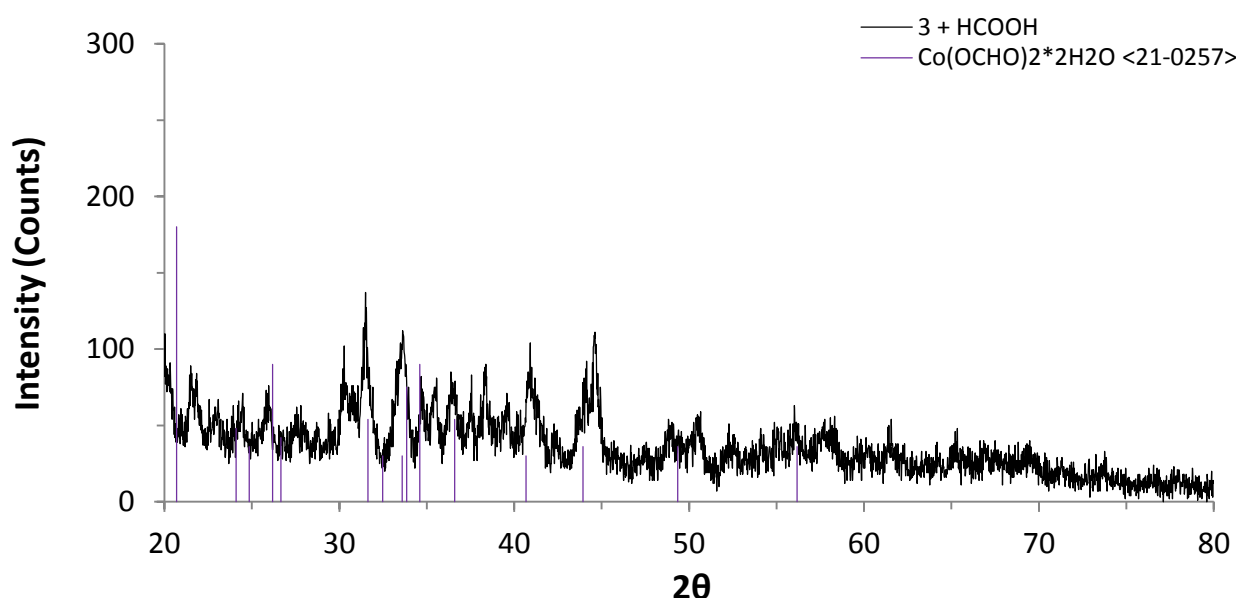


**Figure 83.** Powder XRD spectrum of the product obtained by reacting **3** and formic acid. Known reflections for the hexagonal <05-0727> and cubic <15-0806> phases of cobalt metal are shown by vertical lines. The crystallographic plane associated with each reflection is indicated above each vertical line.

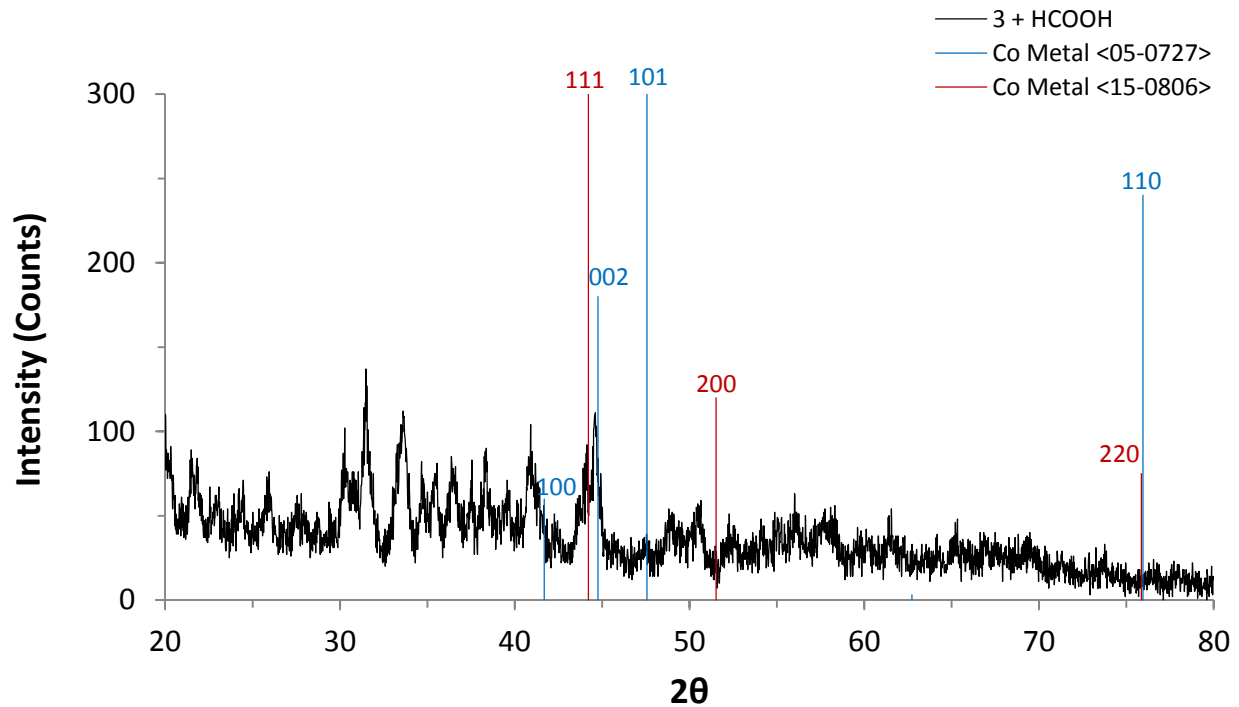
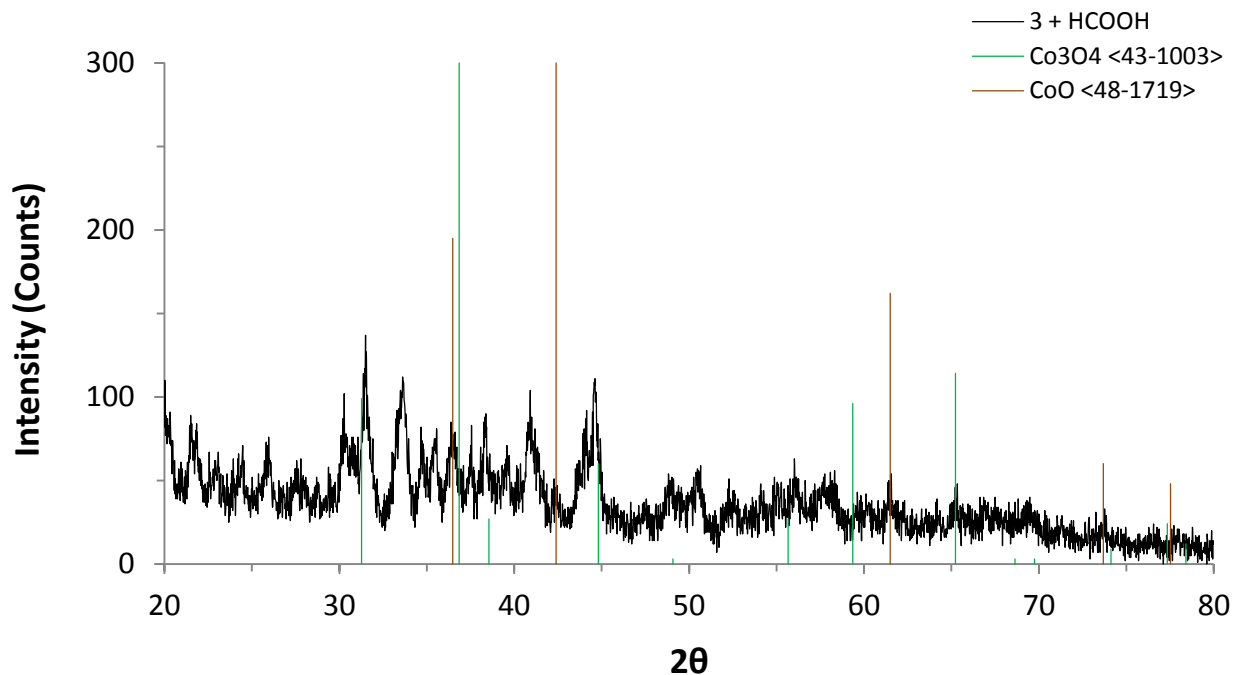


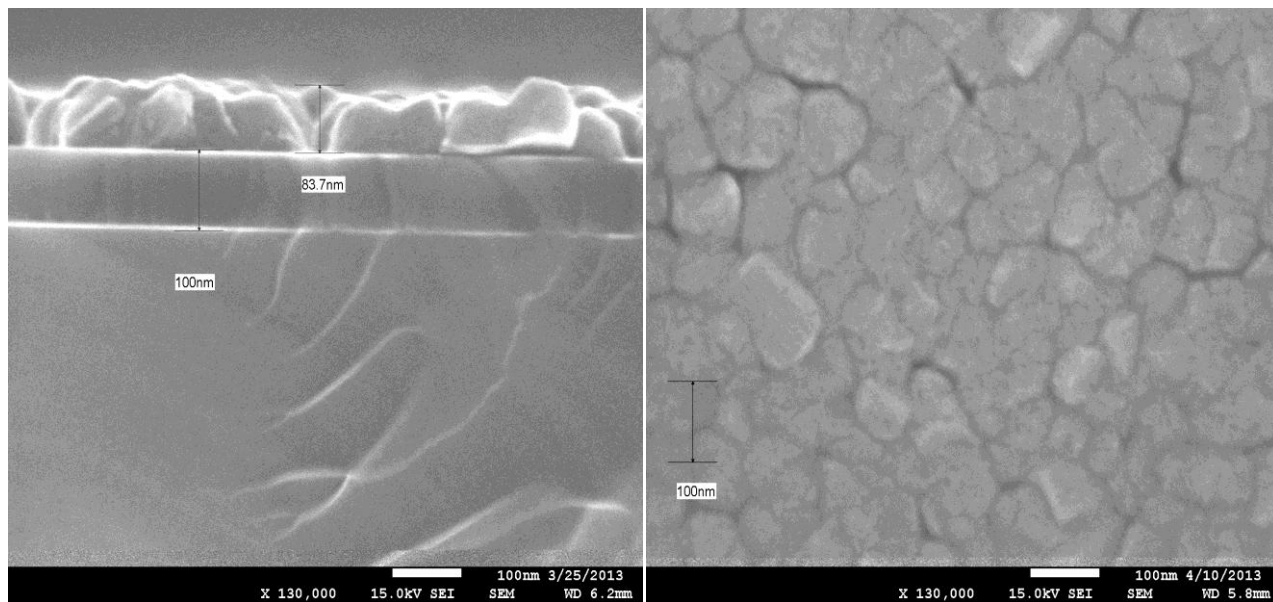
**Figure 84.** Powder XRD spectrum of the product obtained by reacting **3** and formic acid. Known reflections for the cubic cobalt oxide phases  $\text{Co}_3\text{O}_4$  <43-1003> and  $\text{CoO}$  <48-1719> are shown by vertical lines.



### 3.2.1 Cobalt Films by a Three-step Process

An initial deposition experiment was performed for 1,000 cycles at 180 °C. A pulsing sequence of 6.0 s **3**/5.0 s N<sub>2</sub> purge/0.2 s formic acid/5.0 s N<sub>2</sub> purge/1.0 s **2**/10.0 s N<sub>2</sub> purge was applied. Cross-sectional SEM analyses revealed a smooth, continuous film on Ru (24 nm), discontinuous rough films on Si(100) (32 nm) and SiO<sub>2</sub> (84 nm), and nanoparticulate growth on Al<sub>2</sub>O<sub>3</sub>. Top-down SEM analyses showed island-type growth on Si(100) and Al<sub>2</sub>O<sub>3</sub>, with particles measuring 40–56 and 20–34 nm in diameter, respectively. However, a top-down perspective of a film grown on SiO<sub>2</sub> showed a granular morphology consistent with metallic film growth (Figure 85). Visually-uniform films were also observed on Pt and Pd substrates.

**Figure 85.** Cross-sectional and top-down SEM images of an 84 nm thick film grown on SiO<sub>2</sub> from **3**, formic acid, and **2** for 1,000 cycles at 180 °C.



XPS survey scans of a 24 nm thick Co film deposited on Ru at 180 °C showed no N in the as-deposited film and a significant reduction of O and C contamination after 1 min of sputtering. After 2 min of sputtering, the film contained 97.1% Co, and the Co 2p ionizations were an exact match to Co metal (Figures 86–87).

**Figure 86.** XPS survey scans of a 24 nm thick film grown from **3**, formic acid, and **2** on a 5 nm thick Ru substrate at 180 °C.

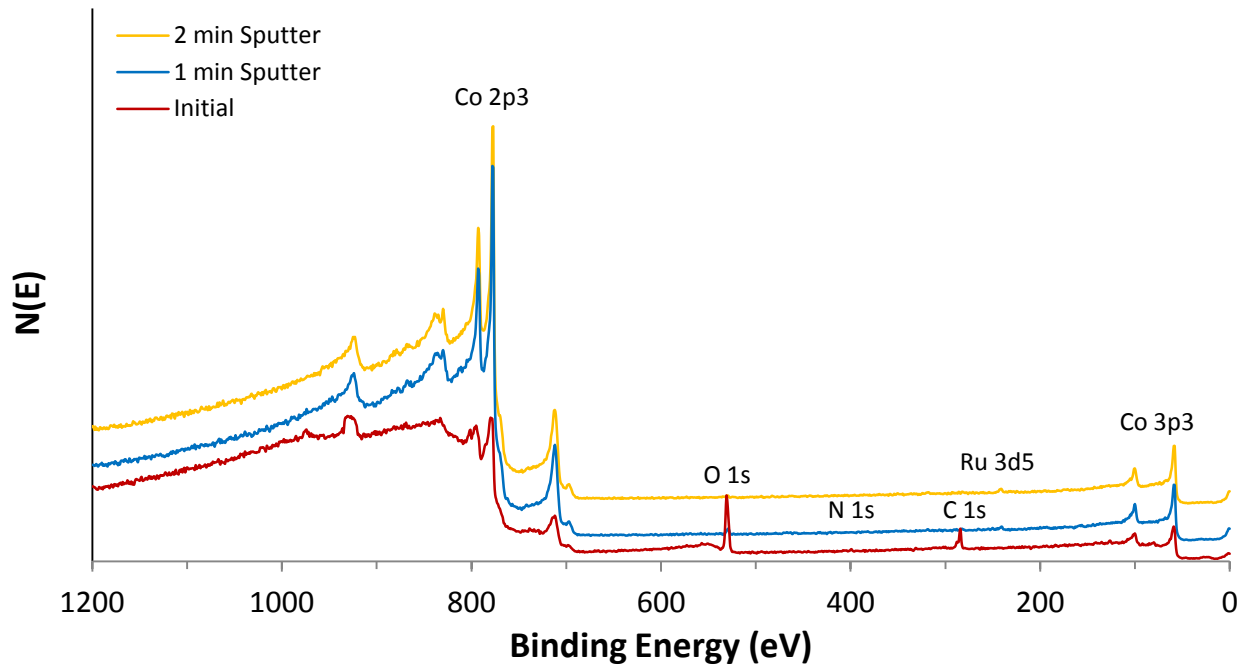
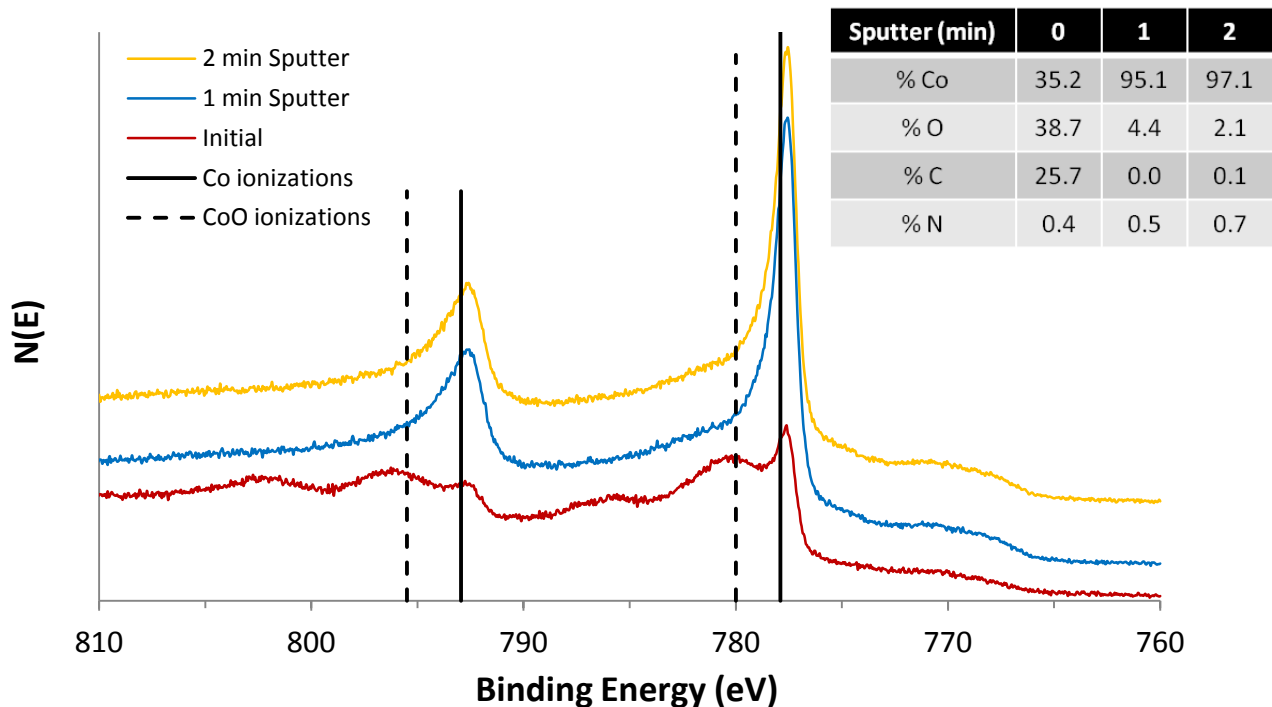
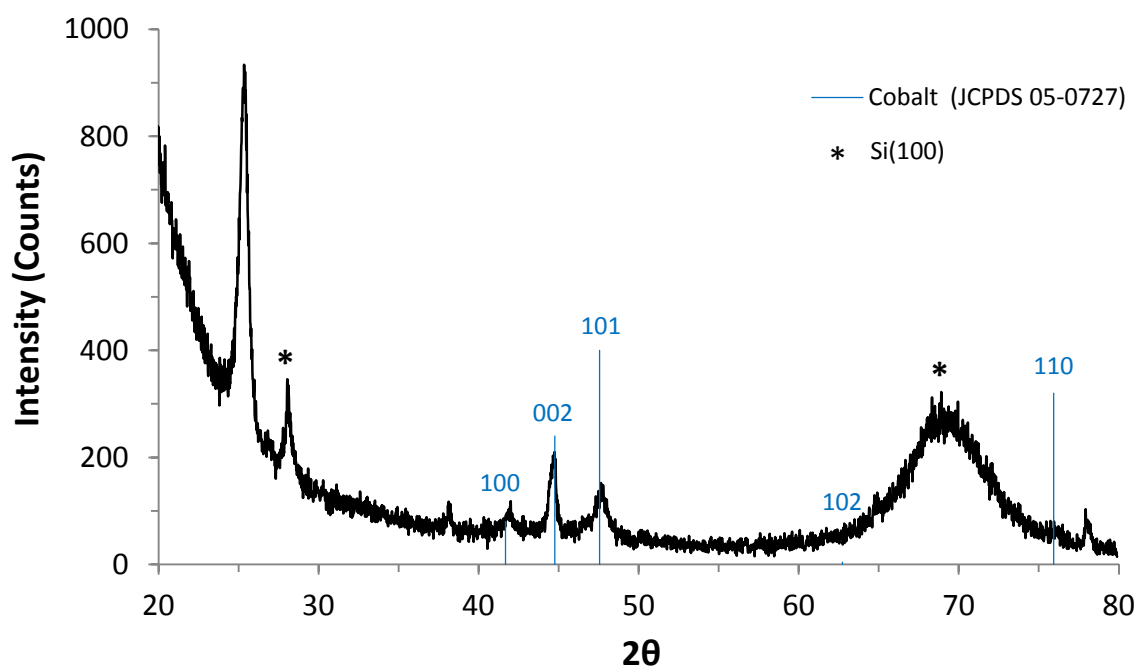


**Figure 87.** XPS Co 2p ionization region of a 24 nm thick film grown from **3**, formic acid, and **2** on a 5 nm thick Ru substrate at 180 °C. Reference 2p binding energies for cobalt metal: 777.9 and 792.95 eV; CoO: 780.0 and 795.50 eV.<sup>305</sup>



A powder XRD spectrum of the film deposited on SiO<sub>2</sub> showed reflections corresponding to lattice planes 100, 200, and 101 of Co metal (Figure 88). The average crystallite size was 20.0 ± 1.3 nm.

**Figure 88.** Powder XRD spectrum of an 84 nm thick Co film grown on SiO<sub>2</sub> from **3**, formic acid, and **2** for 1,000 cycles at 180 °C. Reflections for the hexagonal <05-0727> phase of cobalt metal are shown by vertical lines. The associated crystallographic plane is indicated above each vertical line. Reflections due to the underlying Si(100) substrate are indicated.



### 3.2.2 Cobalt Films by a Two-step Process

A binary process using **3** and **2** did not produce any films at 180 °C. However, a binary process using **3** and formic acid afforded low-resistivity films, and thus, was further investigated. Precursor pulse lengths, substrate temperatures, and the number of ALD cycles were varied to assess the growth behavior. The growth rate was probed as a function of the pulse lengths of **3** and formic acid at 180 °C, using 1,000 cycles and 10.0 s N<sub>2</sub> purges after each precursor pulse. Films were grown on Ru, Pt, Pd, and Cu substrates. The ALD study reported herein was

conducted on Ru substrates. Figure 89 shows a plot of growth rate versus pulse length of **3**, indicating a growth plateau at  $\geq 3.0$  s pulses, with a saturative growth rate of  $0.95 \text{ \AA/cycle}$ . The secondary axis of Figure 89 illustrates that the consumption rate of **3** was proportional to the pulse length of **3**. A similar plot of growth rate versus pulse length of formic acid shows saturative behavior at  $\geq 0.1$  s pulses with the same growth rate (Figure 90). An increase in chamber pressure of  $1.2 \pm 0.2$  mbar was consistently observed during the formic acid pulses, ensuring constant vapor pressure throughout the study. Based upon these data, a pulsing sequence of 5.0 s **3**/10.0 s  $\text{N}_2$  purge/0.2 s formic acid/10.0 s  $\text{N}_2$  purge was used for all subsequent depositions. Figure 91 shows a plot of growth rate versus temperature. An ALD window was observed from 170–180 °C, with a growth rate of approximately  $1.00 \text{ \AA/cycle}$  within this range. The growth rate significantly decreases at  $\geq 200$  °C, likely due to the partial decomposition of **3**. The secondary axis of Figure 91 shows a plot of the bulk resistivity versus temperature. Films grown within the 165–220 °C range had resistivity values of 13–19  $\mu\Omega\cdot\text{cm}$ , approaching that of bulk cobalt ( $6.24 \mu\Omega\cdot\text{cm}$  at 20 °C).<sup>312</sup> Films grown at 240 °C had an average resistivity of 33  $\mu\Omega\cdot\text{cm}$  and a notably different morphology by SEM analysis, likely due to the complete decomposition of **3**. Figure 92 shows a plot of film thickness versus the number of ALD cycles, confirming a growth rate of  $0.95 \text{ \AA/cycle}$ . A deposition experiment using 100 ALD cycles did not produce a continuous film, but rather nanoparticulate growth on the surface with a sheet resistivity identical to that of the untreated Ru substrate ( $59 \pm 4 \Omega/\square$ ). Finally, although self-limiting behavior was observed, experiments conducted without formic acid using a pulsing sequence of 5.0 s **3**/10.0 s  $\text{N}_2$  purge for 1,000 cycles at 180 °C resulted in 13–15 nm thick films. Thus, a minor CVD component may be operant in the growth of these films at 180 °C. Metal surfaces may enhance the decomposition of **3** at temperatures below its solid state decomposition

temperature. It is also possible that the ALD growth mode is kinetically favored over the CVD growth mode and does not affect the saturative behavior of this process at 180 °C.

**Figure 89.** Saturation plot of **3** using 0.2 s pulses of formic acid at 180 °C. The secondary axis shows the consumption rate of **3** as a function of the pulse length of **3**.

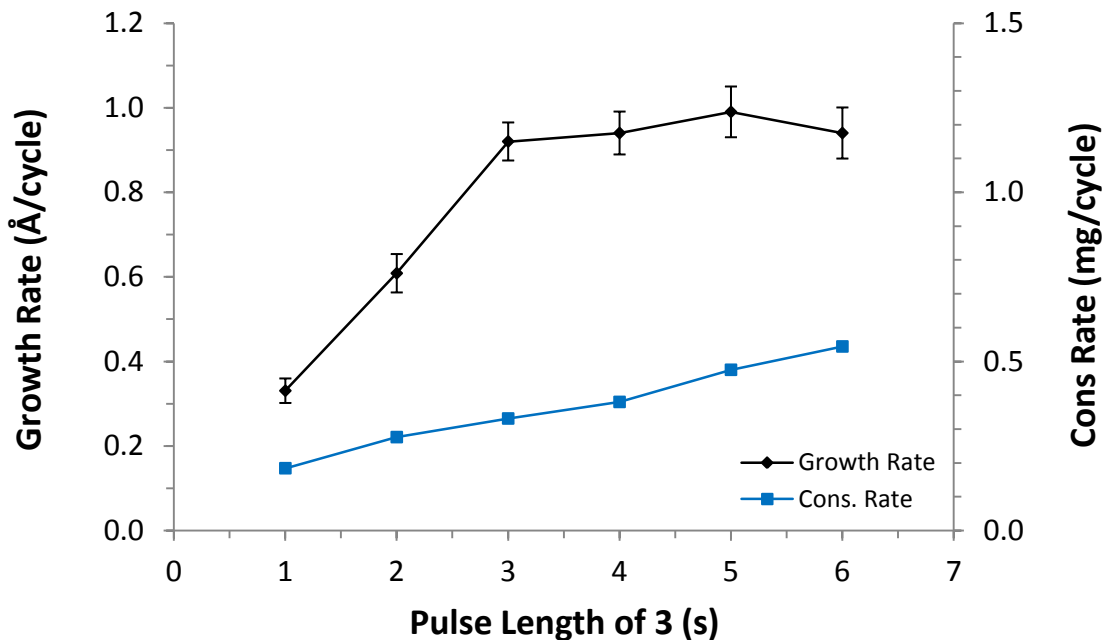


**Figure 90.** Saturation plot of formic acid using 5.0 s pulses of **3** at 180 °C.

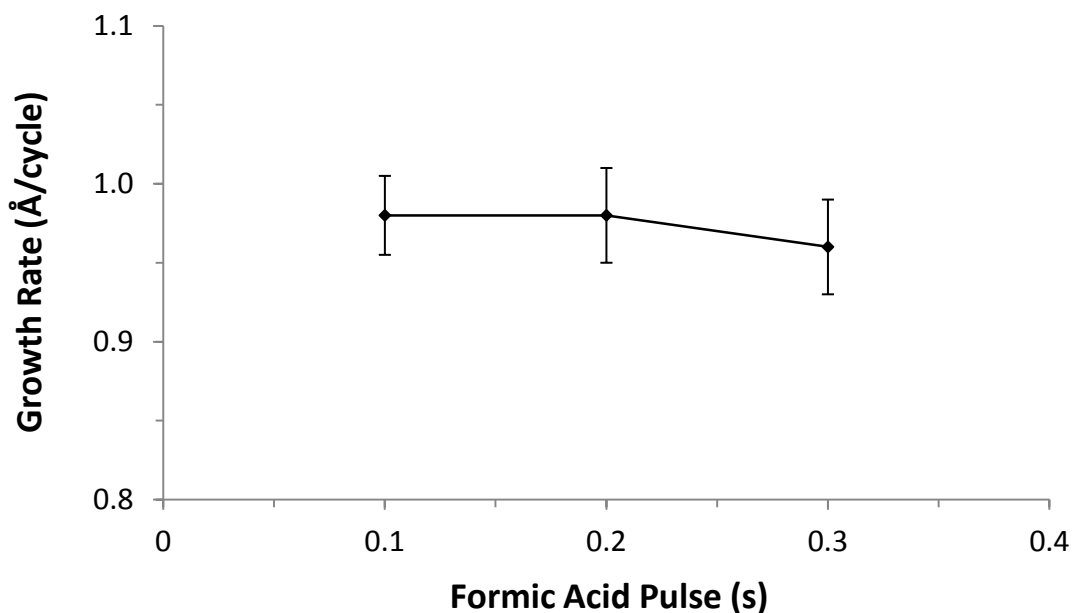


**Figure 91.** Plot of growth rate versus temperature using 5.0 s pulses of 3 and 0.2 s pulses of formic acid for 1,000 cycles. The secondary axis shows the bulk resistivity of the film as a function of temperature.

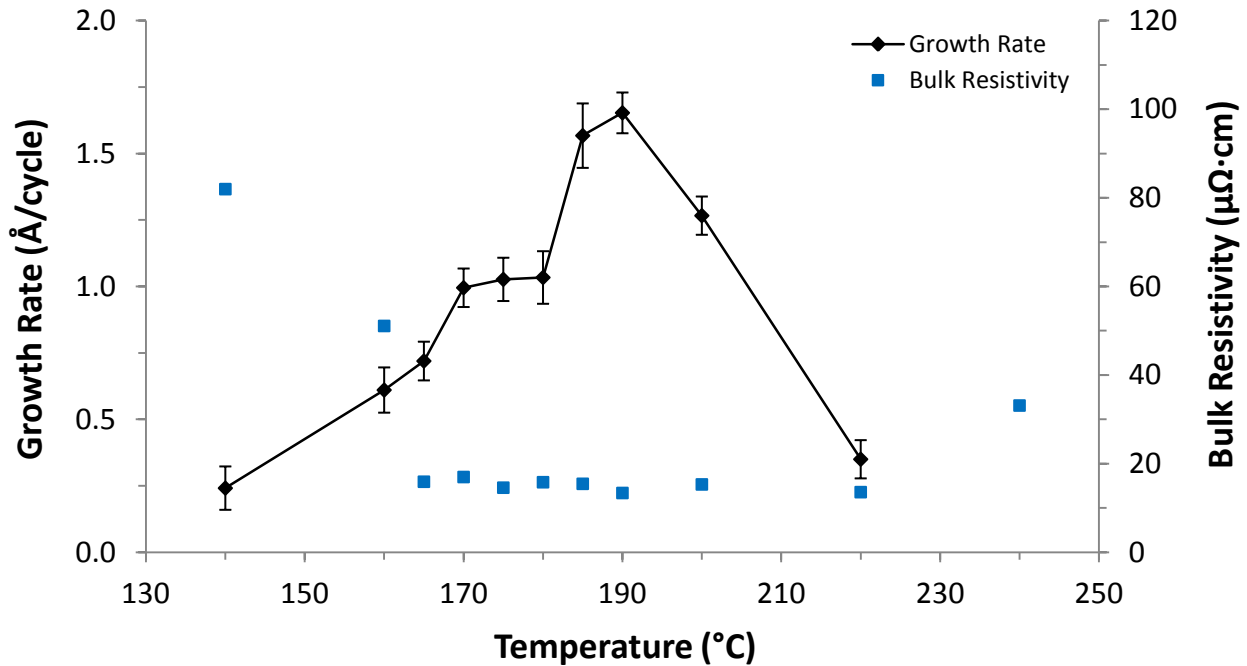
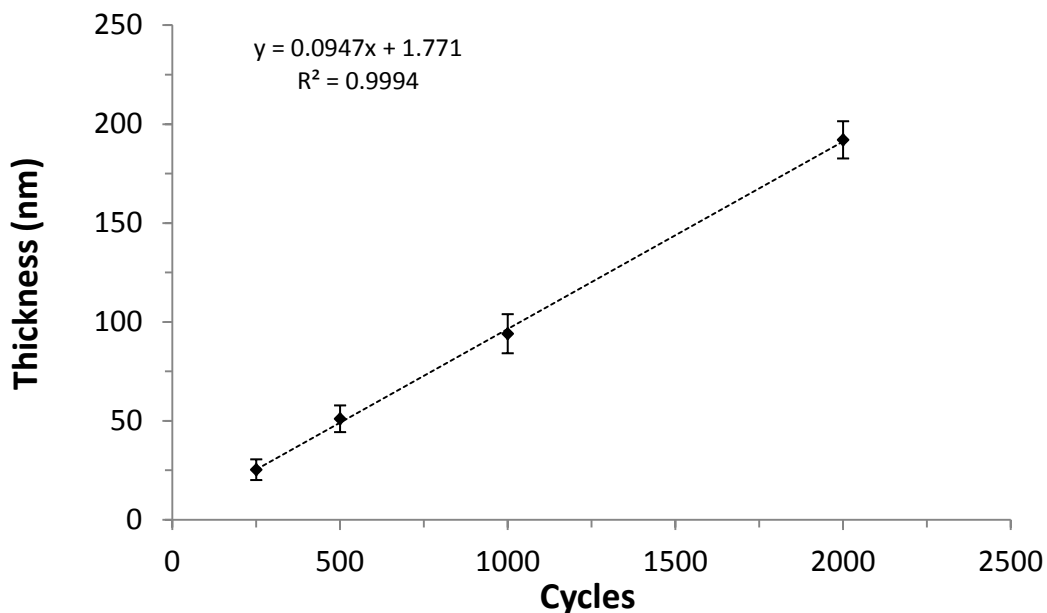


**Figure 92.** Plot of film thickness versus number of ALD cycles using 3 and formic acid at 180 °C.





Cobalt films grown on Ru substrates were carefully analyzed after exposure to ambient atmosphere. Figures 93–102 show SEM images of films grown from 140–240 °C for 1,000 ALD cycles. Uniform, continuous films were deposited on Ru at  $\leq 220$  °C. Top-down perspectives show granular morphologies consistent with metallic films at  $\geq 160$  °C. Films deposited at 140 °C were smooth, with no observed microstructure by cross-sectional or top-down SEM analyses. Films deposited at 240 °C were very rough with nanorods emerging from the surface. The solid state thermal decomposition temperatures of  $\text{Co}^{42}$  and anhydrous  $\text{Co}(\text{OCHO})_2^{313}$  are 235 and 237 °C, respectively. Thus, films grown at  $\geq 235$  °C are expected to be very rough. Figures 103–113 show SEM images of films grown for a differing number of ALD cycles at 180 °C. After 100 cycles, widely spaced nanoparticles were observed with diameters of  $\sim 25\text{--}40$  nm. These particles appear to coalesce to a continuous film at  $\leq 250$  cycles. After 250 cycles, a smooth, continuous 24 nm thick layer was observed (0.96 Å/cycle). Thus, there is a nucleation process that occurs between 100 and 250 cycles with normal ALD growth occurring at or before 250 cycles. After 500 cycles, a granular morphology consistent with a metallic film was apparent by top-down SEM analysis. The same microstructure was observed after 1,000 cycles, however, films grown for 2,000 cycles had a much smaller average grain size. Figures 114–116 show cross-sectional SEM images of continuous films grown on Cu, Pd, and Pt substrates, respectively, for 1,000 cycles at 180 °C.

**Figure 93.** Cross-sectional SEM image of a 24 nm thick film grown on Ru from **3** and formic acid for 1,000 cycles at 140 °C.

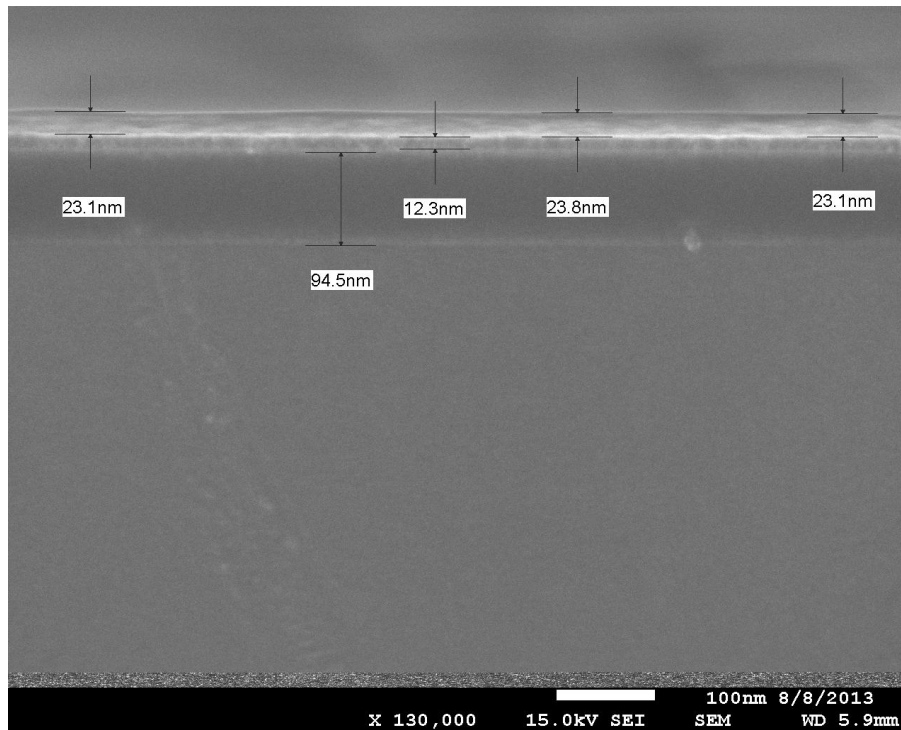


**Figure 94.** Top-down SEM image of a 24 nm thick film grown on Ru from **3** and formic acid for 1,000 cycles at 140 °C.

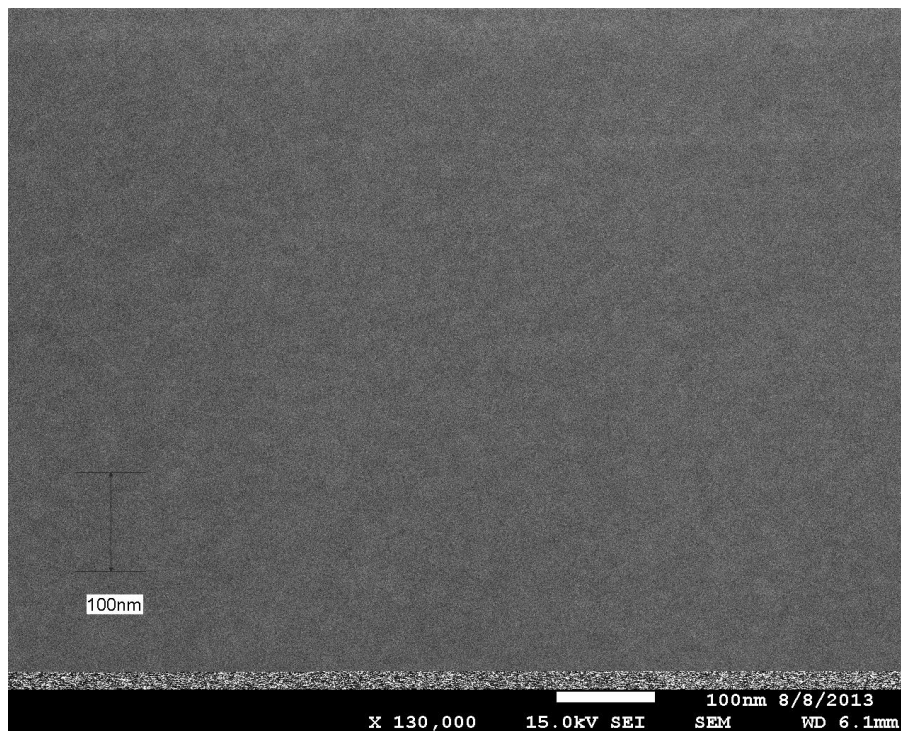


**Figure 95.** Cross-sectional SEM image of a 57 nm thick film grown on Ru from **3** and formic acid for 1,000 cycles at 160 °C.

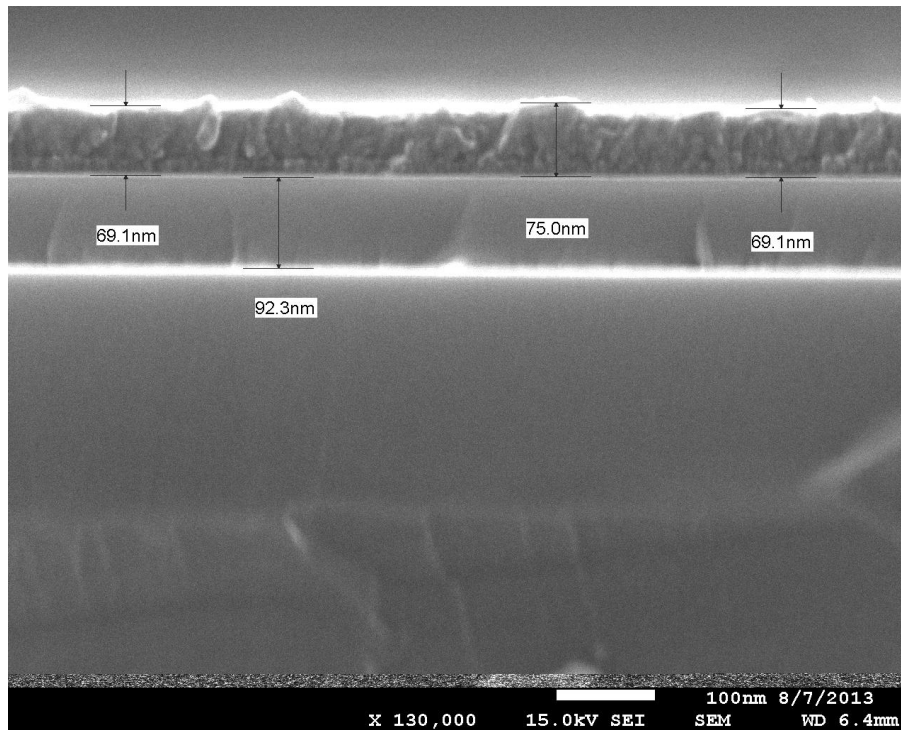


**Figure 96.** Top-down SEM image of a 57 nm thick film grown on Ru from **3** and formic acid for 1,000 cycles at 160 °C.

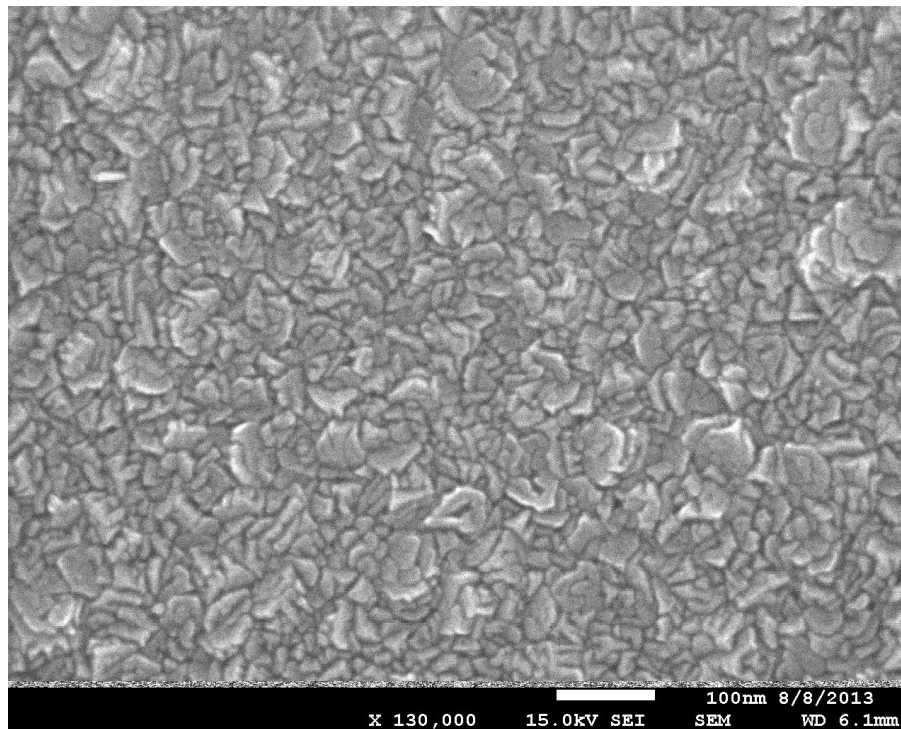


**Figure 97.** Cross-sectional SEM image of a 98 nm thick film grown on Ru from **3** and formic acid for 1,000 cycles at 170 °C.

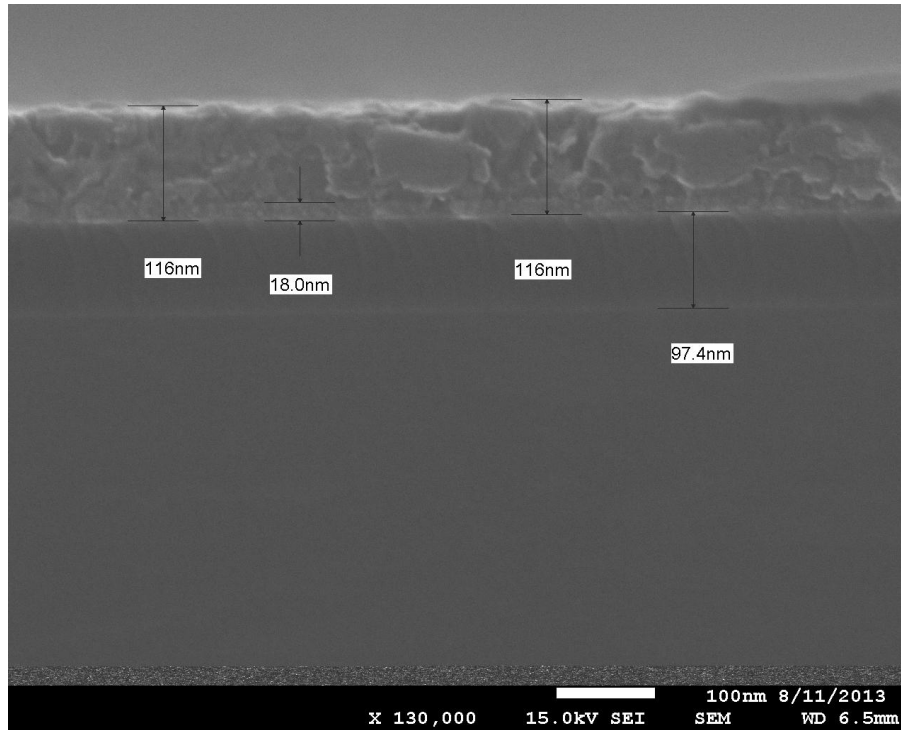


**Figure 98.** Top-down SEM image of a 98 nm thick film grown on Ru from **3** and formic acid for 1,000 cycles at 170 °C.

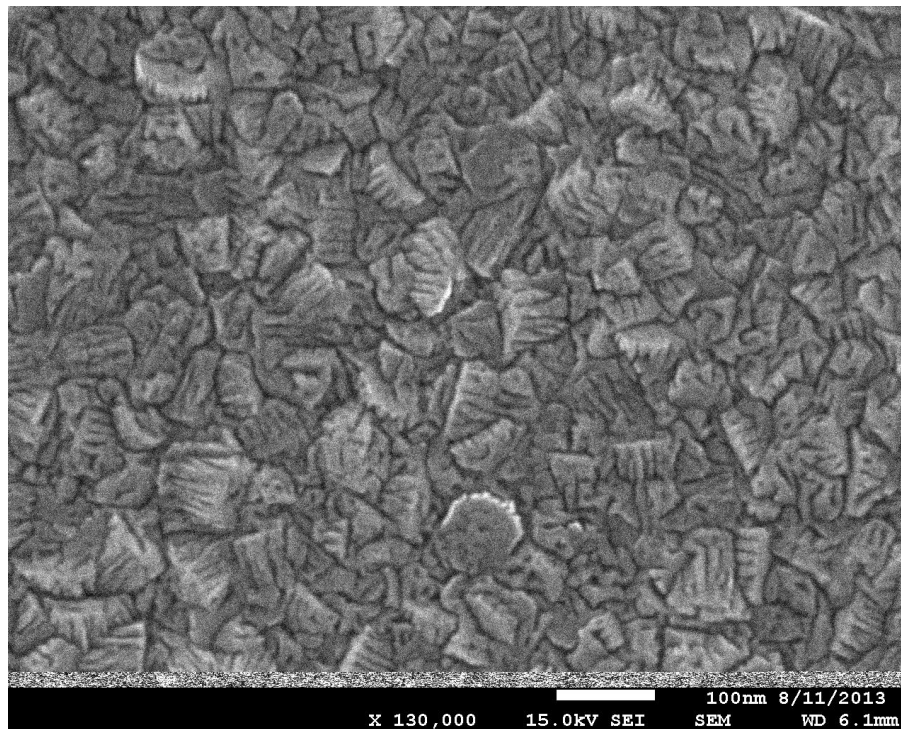


**Figure 99.** Cross-sectional SEM image of a 132 nm thick film grown on Ru from **3** and formic acid for 1,000 cycles at 200 °C.

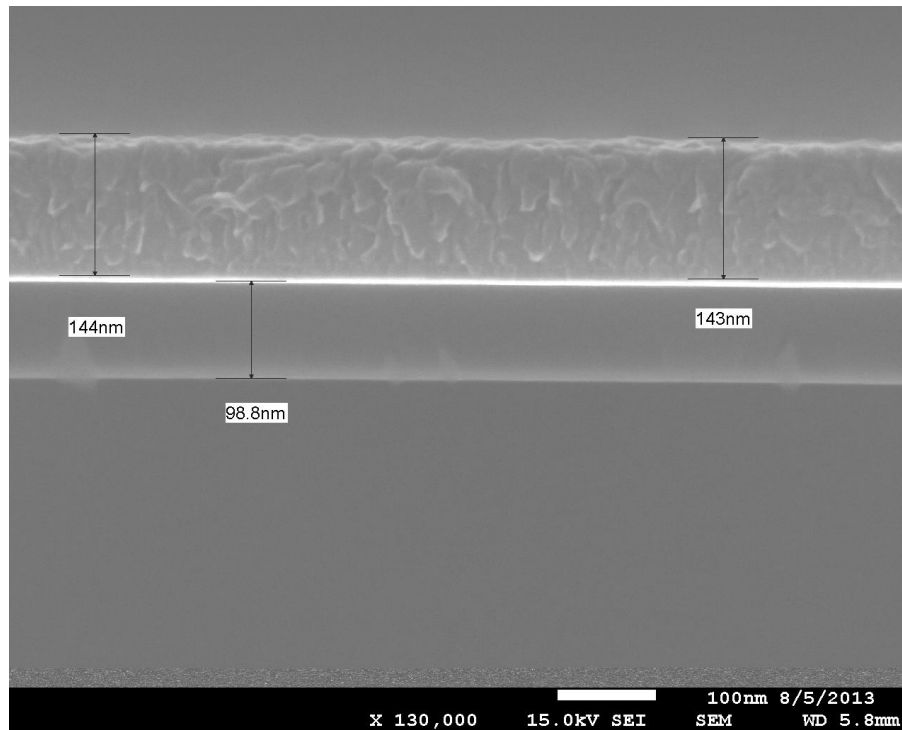


**Figure 100.** Top-down SEM image of a 132 nm thick film grown on Ru from **3** and formic acid for 1,000 cycles at 200 °C.

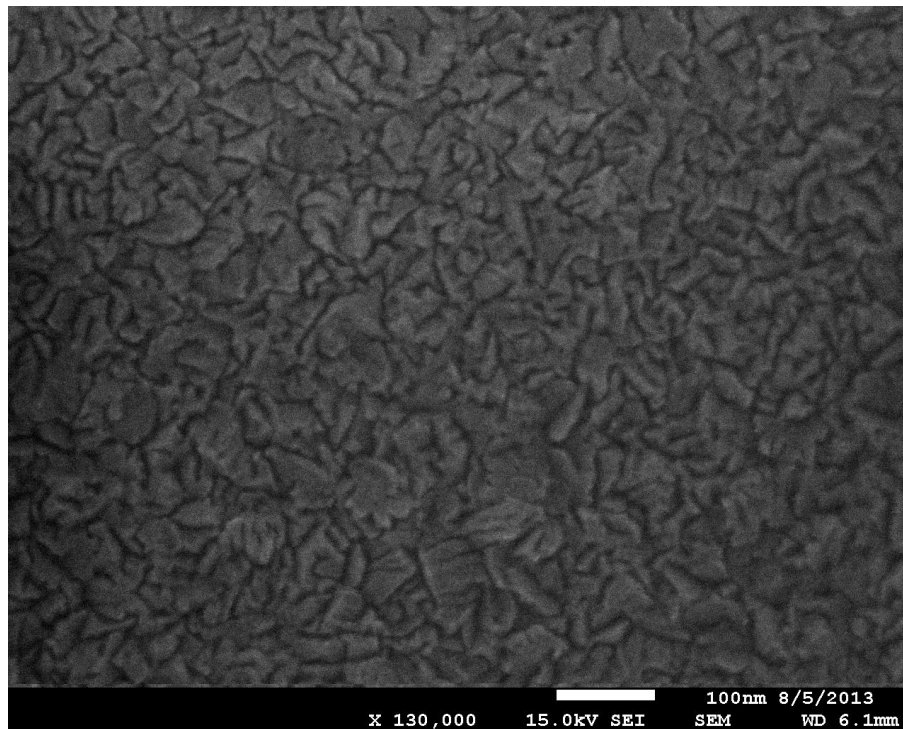


**Figure 101.** Cross-sectional SEM image of a film grown on Ru from **3** and formic acid for 1,000 cycles at 240 °C.

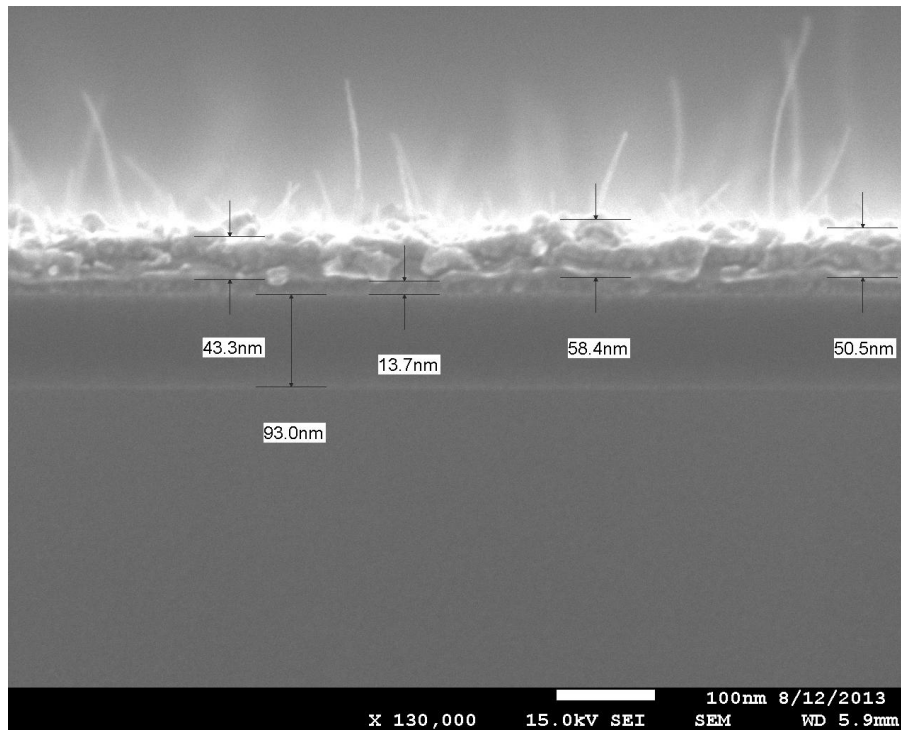


**Figure 102.** Top-down SEM image of a film grown on Ru from **3** and formic acid for 1,000 cycles at 240 °C.

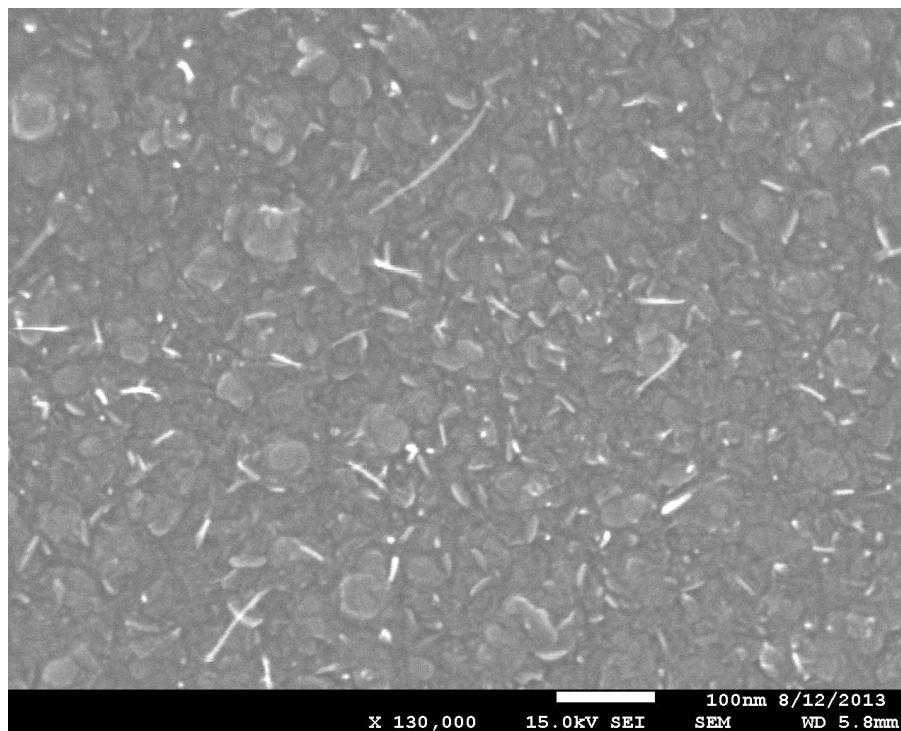


**Figure 103.** SEM image at a 5-degree tilt showing nanoparticulate growth on Ru from **3** and formic acid for 100 cycles at 180 °C.

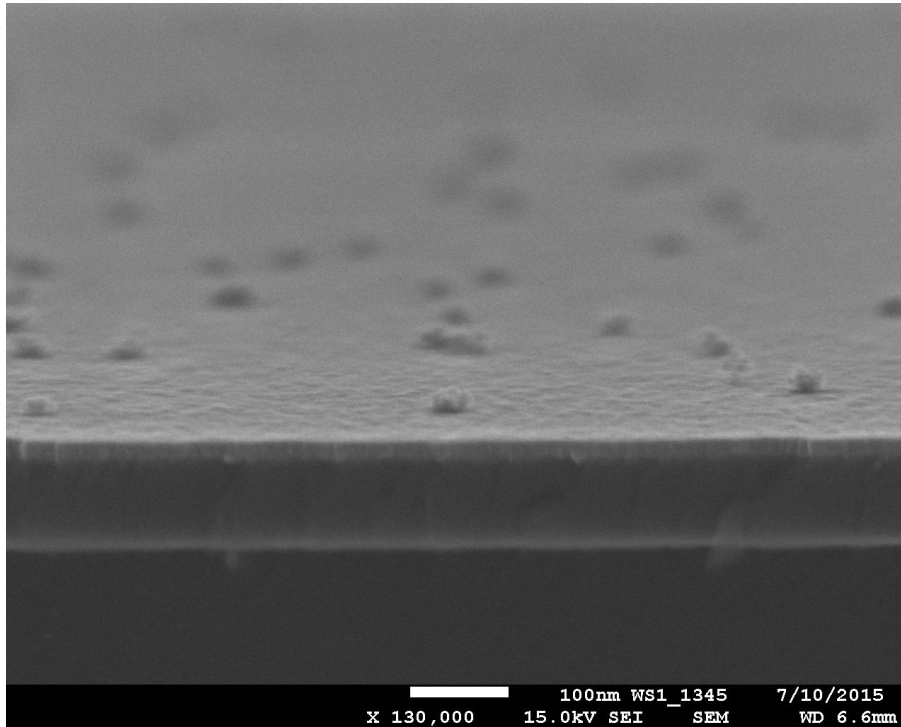


**Figure 104.** SEM image at a 5-degree tilt showing a continuous 24 nm thick film grown on Ru from **3** and formic acid for 250 cycles at 180 °C.

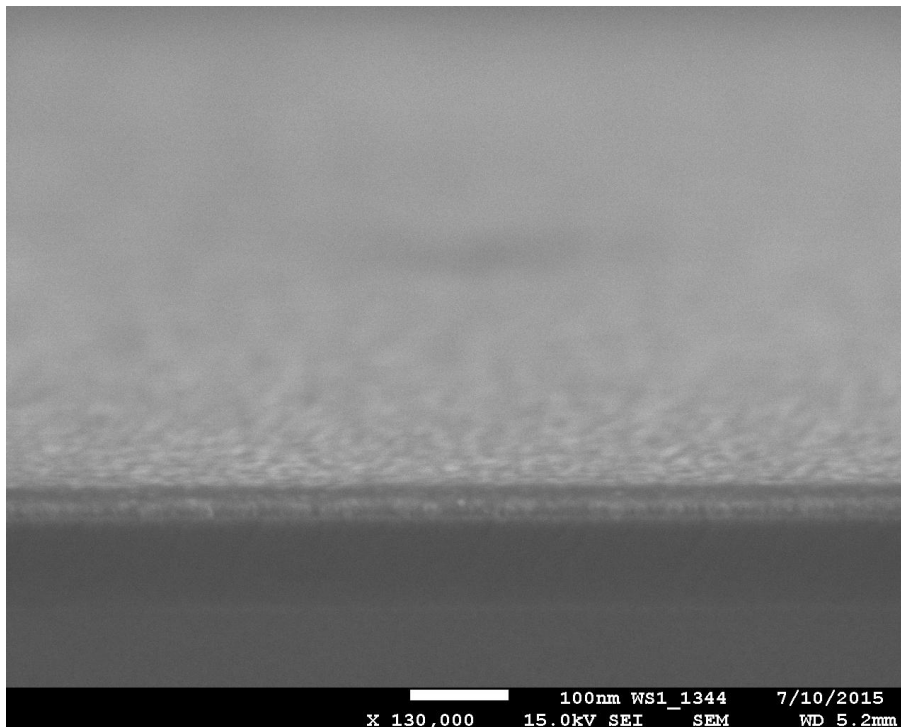


**Figure 105.** Cross-sectional SEM image of a 24 nm thick film grown on Ru from **3** and formic acid for 250 cycles at 180 °C.

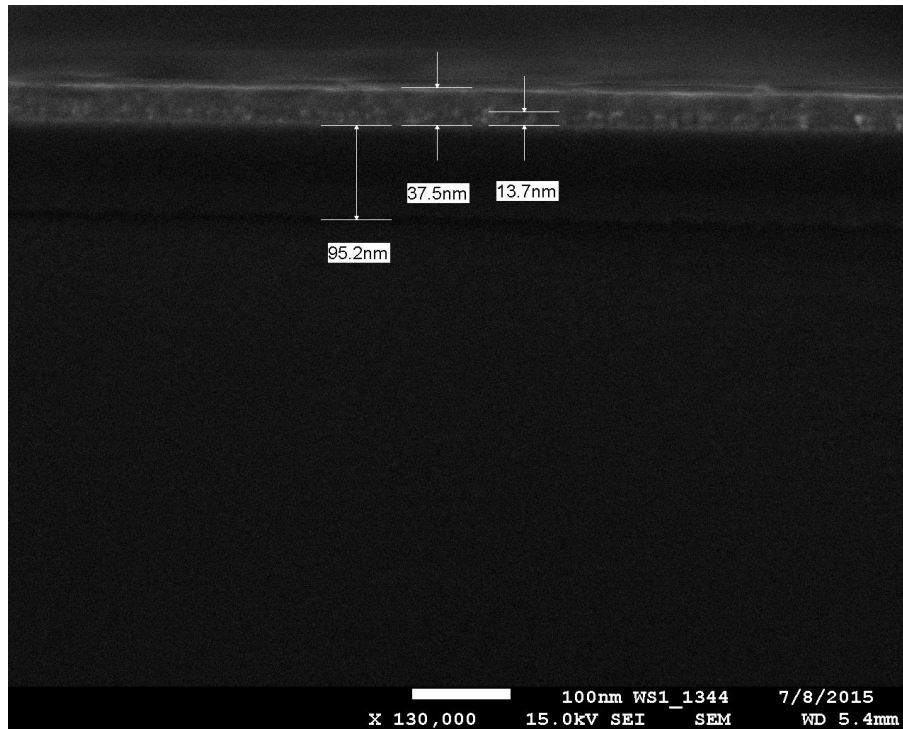


**Figure 106.** Top-down SEM image of a 24 nm thick film grown on Ru from **3** and formic acid for 250 cycles at 180 °C.

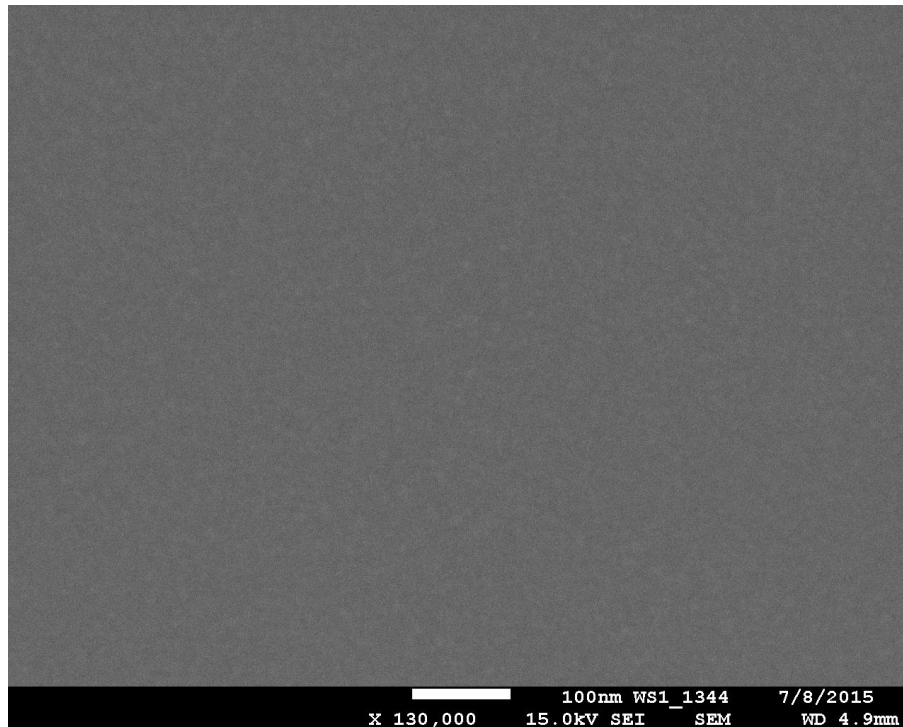




**Figure 107.** Cross-sectional SEM image of a 50 nm thick film grown on Ru from **3** and formic acid for 500 cycles at 180 °C.

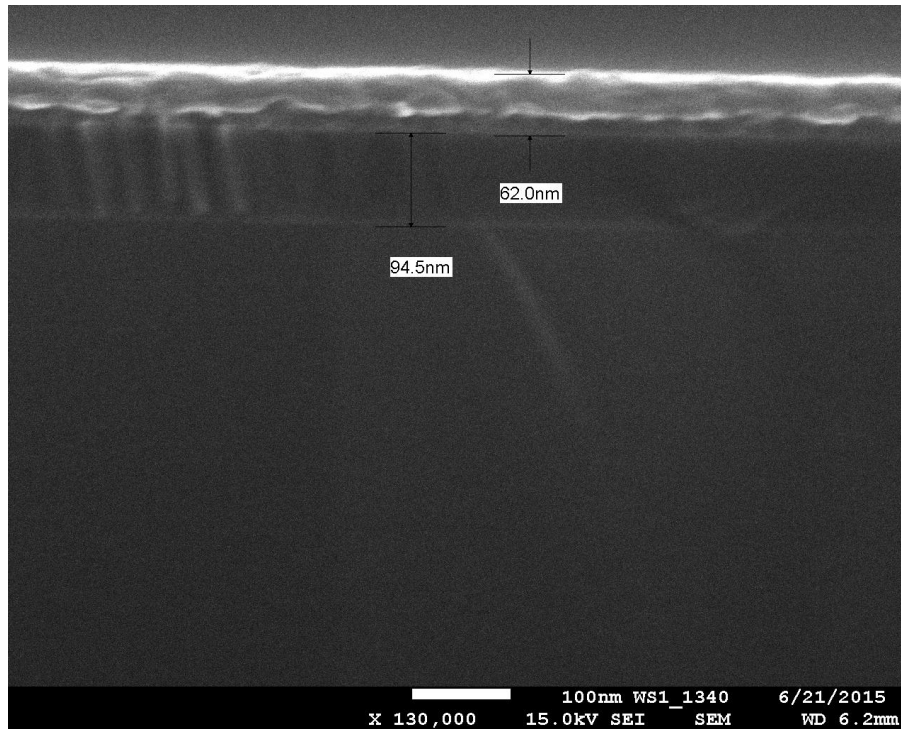


**Figure 108.** Top-down SEM image of a 50 nm thick film grown on Ru from **3** and formic acid for 500 cycles at 180 °C.

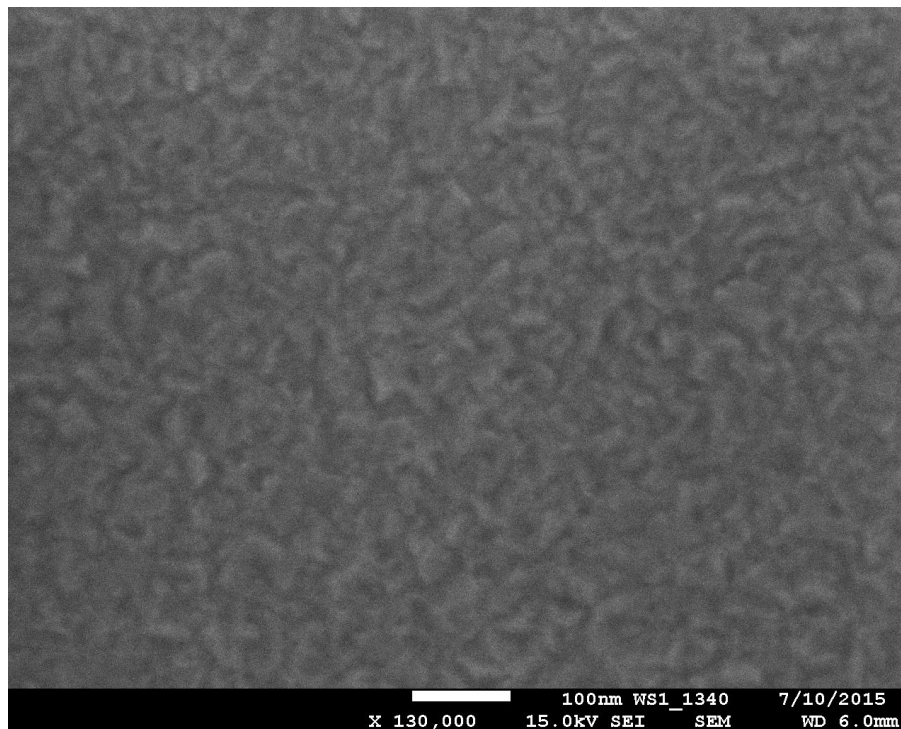


**Figure 109.** Cross-sectional SEM image of a 93 nm thick film grown on Ru from **3** and formic acid for 1,000 cycles at 180 °C.

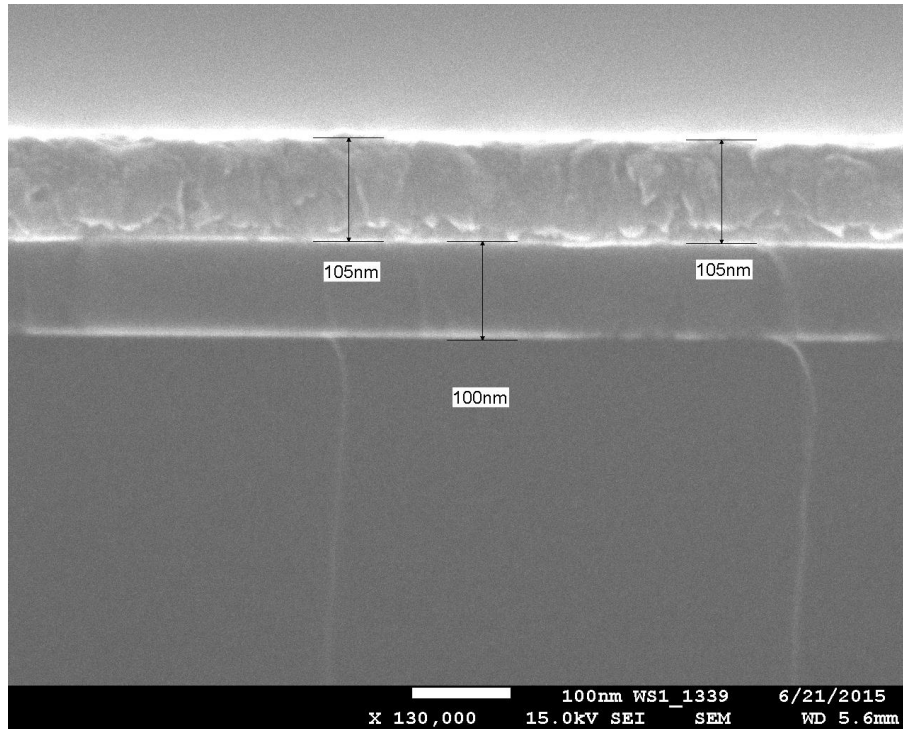


**Figure 110.** Top-down SEM image of a 93 nm thick film grown on Ru from **3** and formic acid for 1,000 cycles at 180 °C.

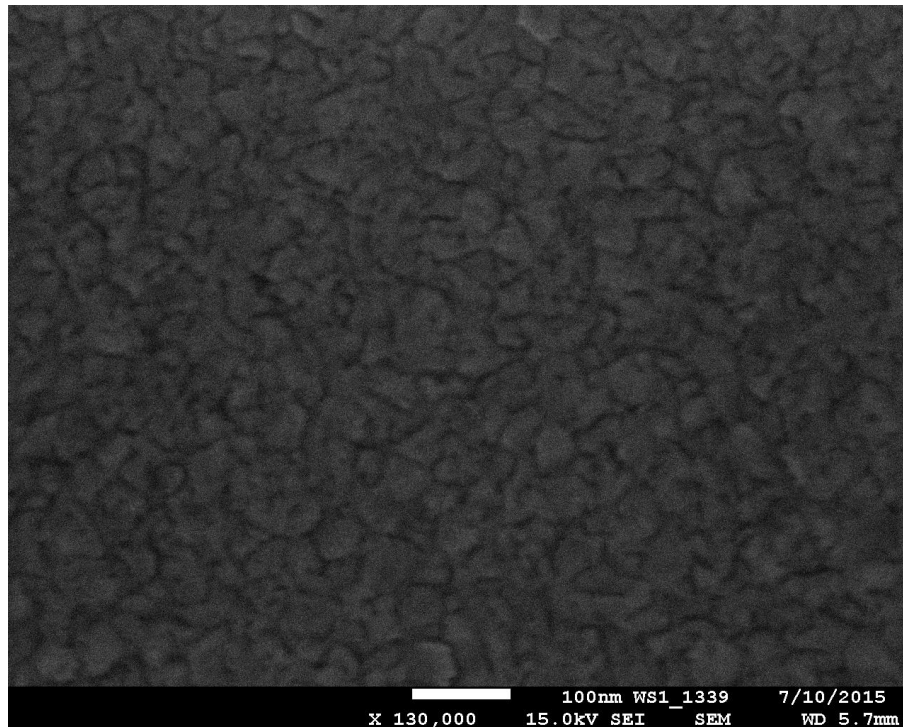


**Figure 111.** Cross-sectional SEM image of a 196 nm thick film grown on Ru from **3** and formic acid for 2,000 cycles at 180 °C.

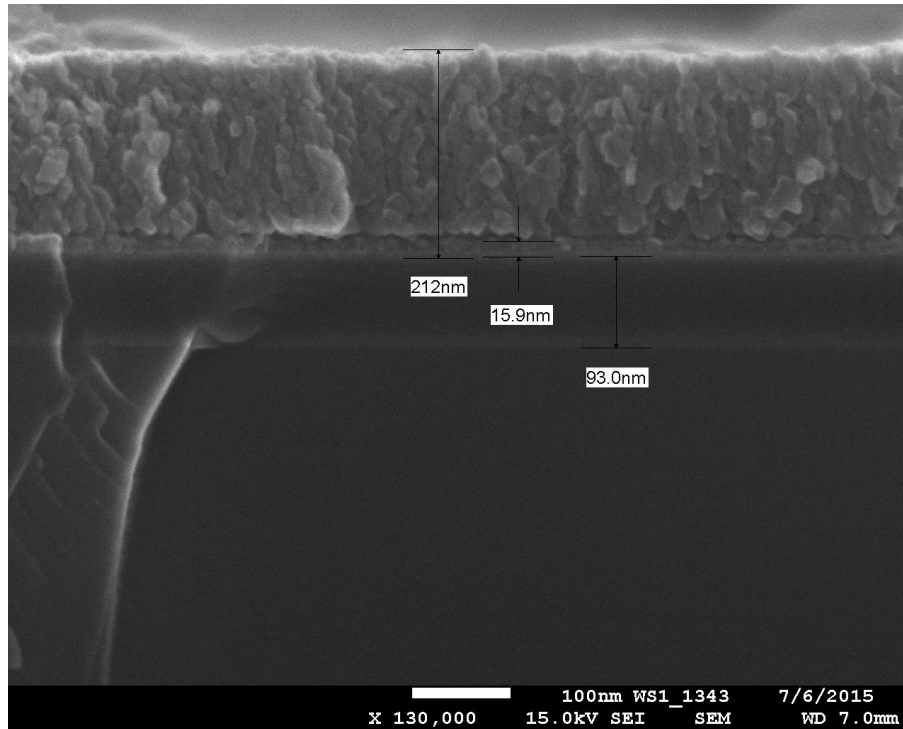


**Figure 112.** Top-down SEM image of a 196 nm thick film grown on Ru from **3** and formic acid for 2,000 cycles at 180 °C; 130,000X magnification.

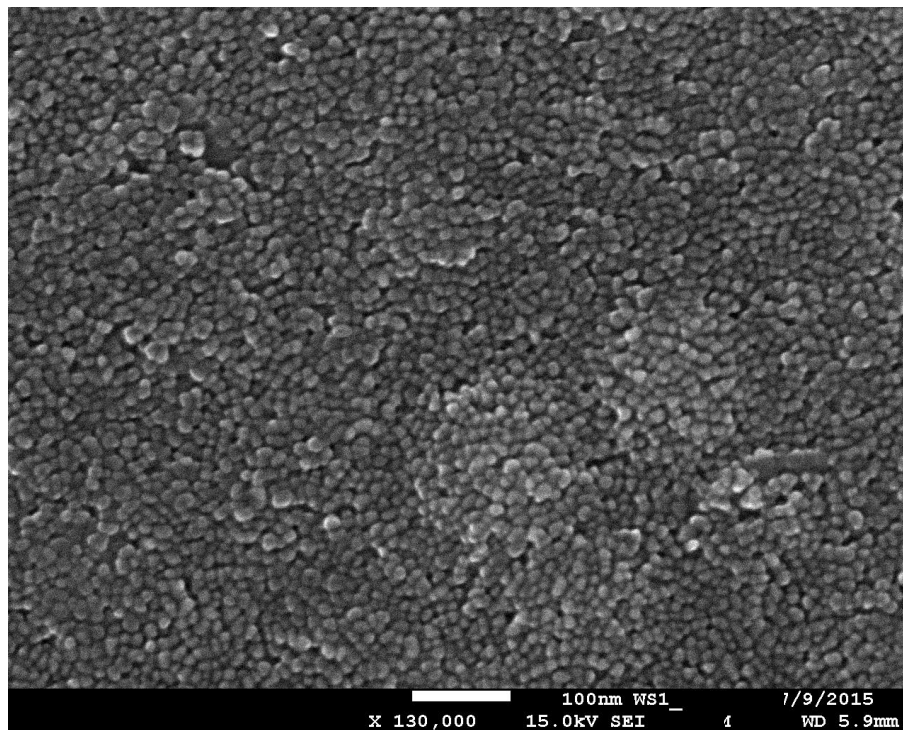


**Figure 113.** Top-down SEM image of a 196 nm thick film grown on Ru from **3** and formic acid for 2,000 cycles at 180 °C; 90,000X magnification.

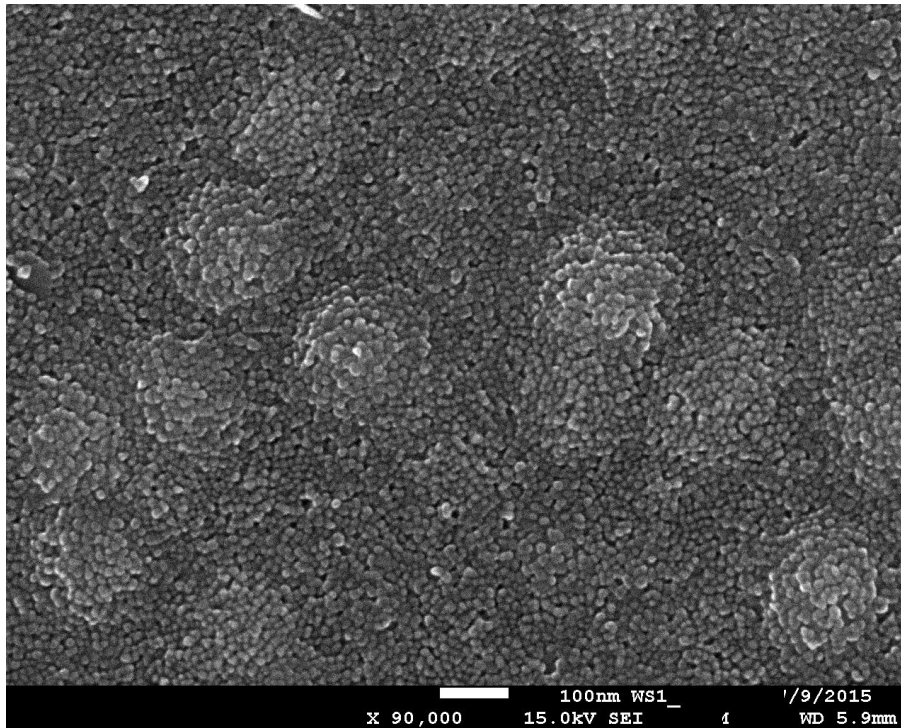


**Figure 114.** Cross-sectional SEM image of a 92 nm thick film grown on Cu from **3** and formic acid for 1,000 cycles at 180 °C.

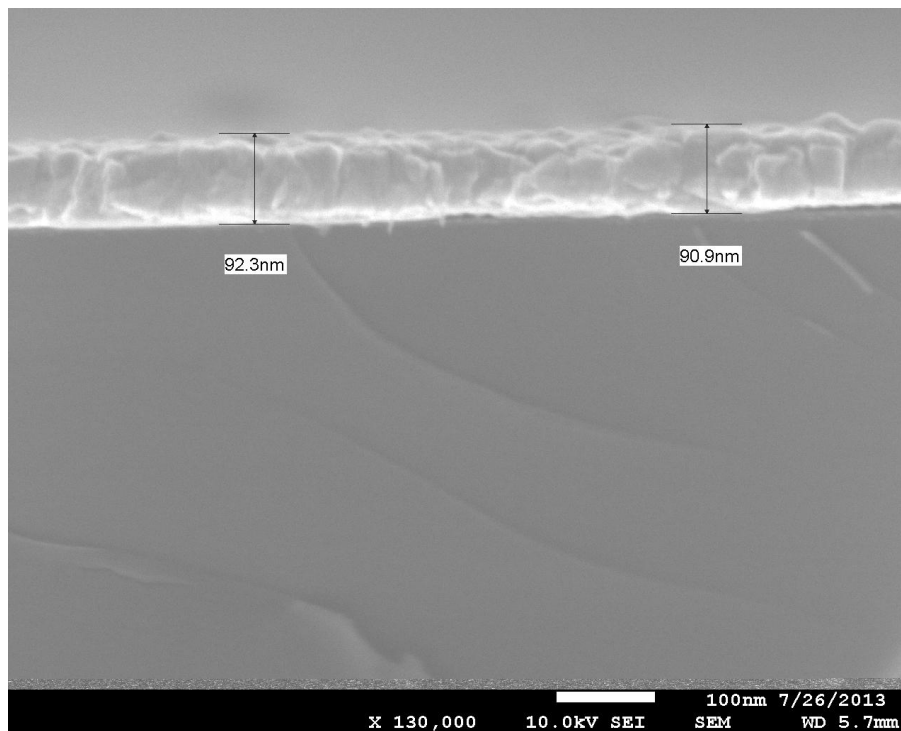


**Figure 115.** Cross-sectional SEM image of a 122 nm thick film grown on Pd from **3** and formic acid for 1,000 cycles at 180 °C.

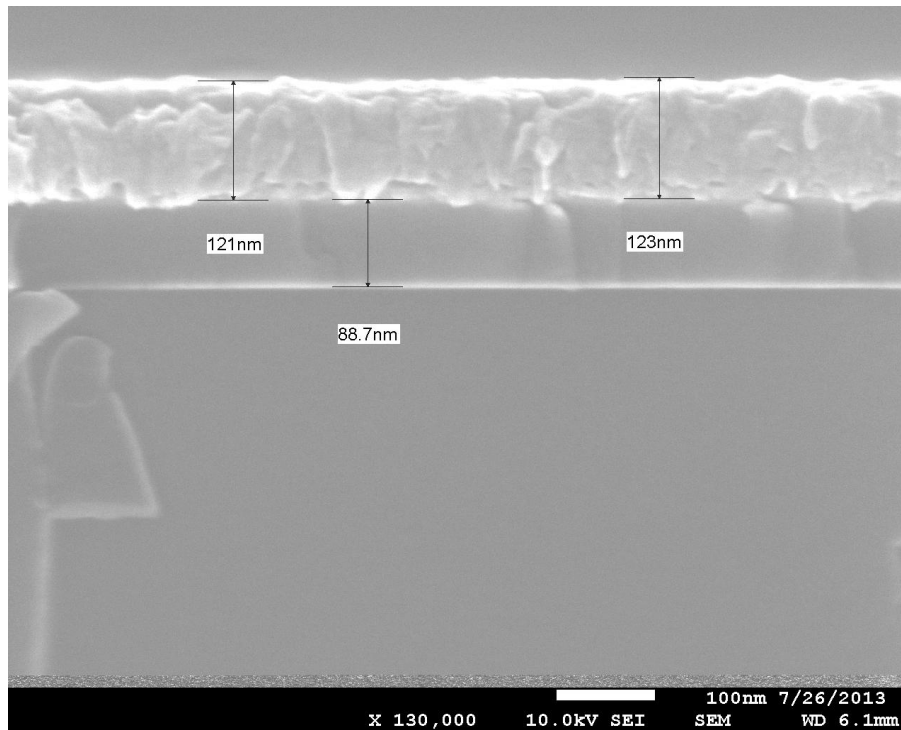
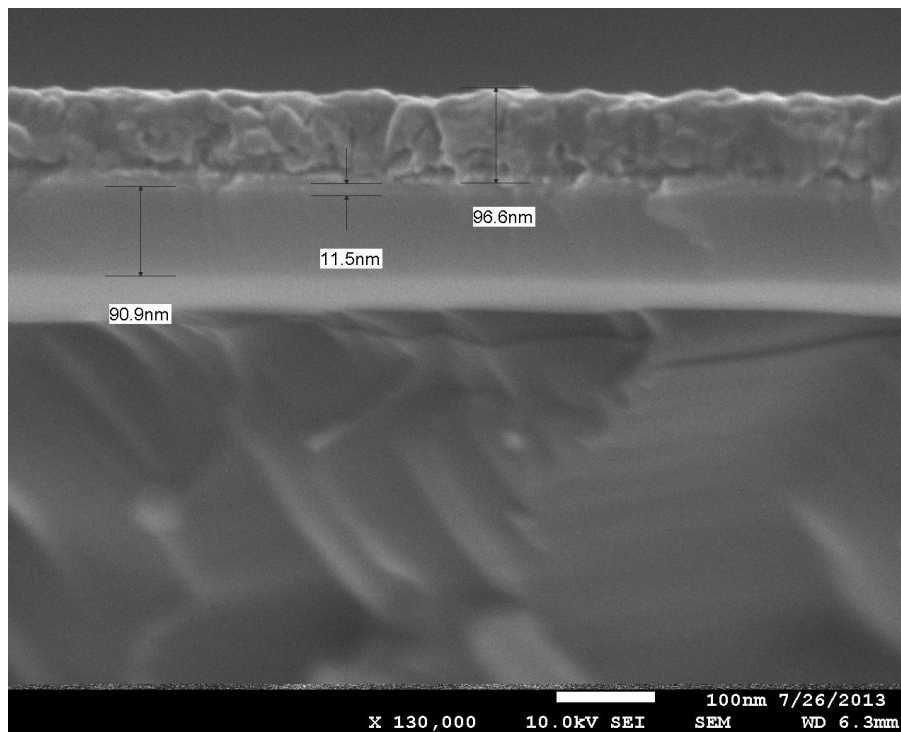


**Figure 116.** Cross-sectional SEM image of a 97 nm thick film grown on Pt from **3** and formic acid for 1,000 cycles at 180 °C.



The surface morphology of these films was examined by AFM. A 105 nm thick film grown on Ru at 180 °C had RMS roughness values of  $\leq 1.245$  nm, indicating an extremely smooth surface (Figure 117, Table 9). For comparison, the RMS surface roughness of the underlying Ru substrate was  $\leq 0.418$  nm.

**Figure 117.** AFM images of a 105 nm thick film grown on Ru from **3** and formic acid at 180 °C: (a) 2  $\mu\text{m}^2$  region, (b) 5  $\mu\text{m}^2$  region.

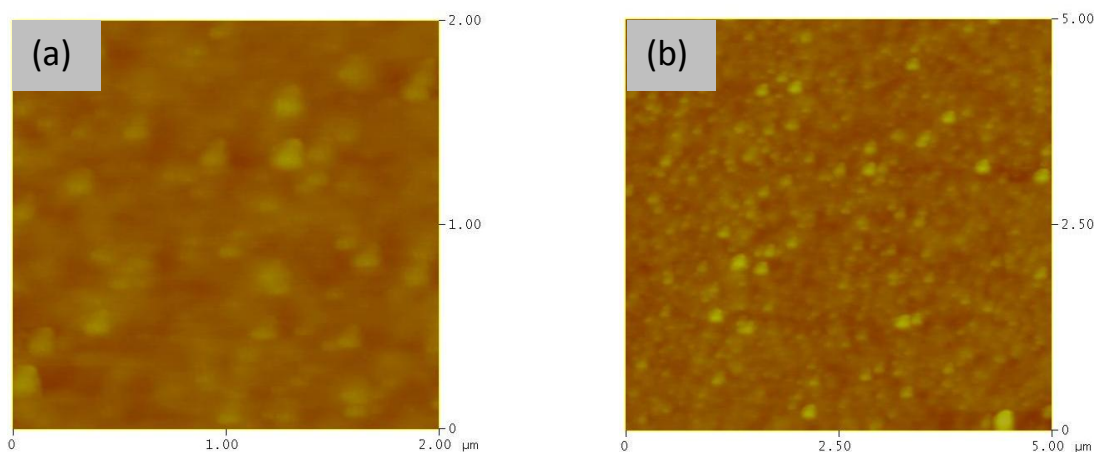


**Table 9.** Surface roughnesses measured by AFM of a 105 nm thick film grown on Ru from **3** and formic acid at 180 °C. Measurements were taken from 2 and 5  $\mu\text{m}^2$  areas.

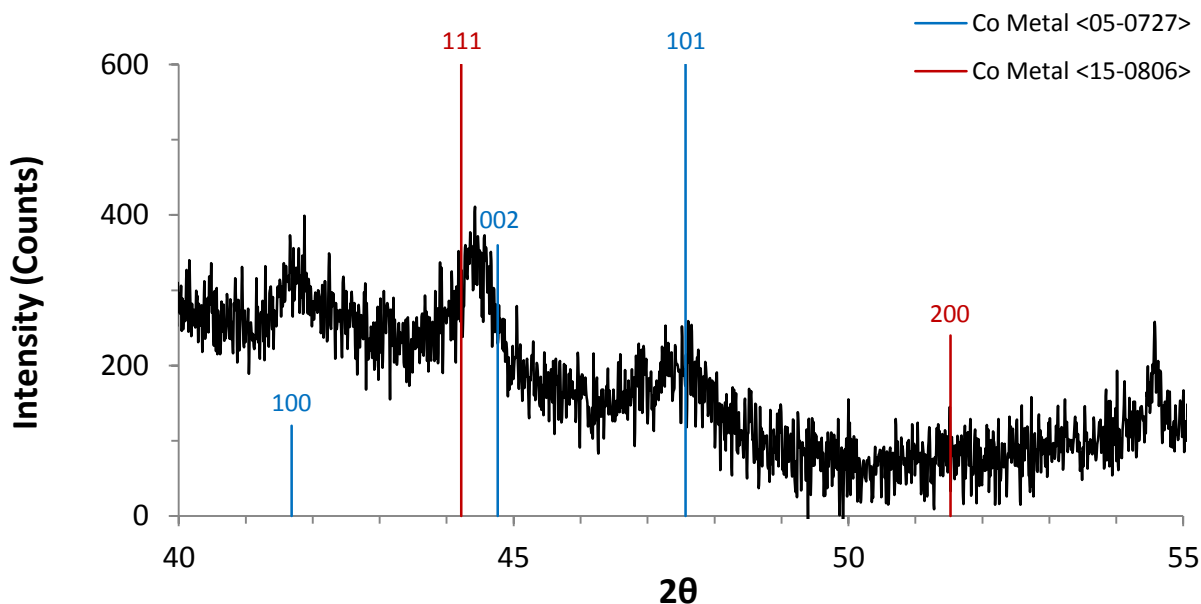
Film/Substrate	Film Thickness (nm)	RMS Roughness (nm)	
		2 $\mu\text{m}^2$	5 $\mu\text{m}^2$
Co/Ru/SiO <sub>2</sub> /Si	105	0.984	1.245
Bare Ru/SiO <sub>2</sub> /Si	-----	0.418	0.357

The presence of crystalline cobalt metal was confirmed by TEM and powder XRD analyses. Figure 118 shows a TEM image of Co metal grown on the carbon film of a Cu TEM grid for 2,000 cycles at 180 °C. The presence of lattice fringes is diagnostic of crystalline material. Figure 119 shows a powder XRD spectrum of a film grown on Ru at 180 °C. Reflections confirm the presence of crystalline Co metal. The average crystallite size was  $13.4 \pm 3.0$  nm, as calculated from the Scherrer equation.

**Figure 118.** TEM image of Co metal grown from **3** and formic acid on a TEM grid at 180 °C.



**Figure 119.** Powder XRD spectrum of a 93 nm thick film grown from **3** and formic acid on Ru for 1,000 cycles at 180 °C. Reflections for the hexagonal <05-0727> and cubic <15-0806> phases of cobalt metal are shown by vertical lines. The associated crystallographic plane is indicated above each vertical line.



Four-point probe resistivity measurements were also performed on these films. In an initial experiment at 180 °C using 1,000 ALD cycles, growth was attempted on a variety of substrates, including Ru, Pd, Pt, Cu, Si(100), Si-H, SiO<sub>2</sub>, and TiN. Films grown on Ru, Pd, Pt, and Cu showed sheet resistivity values significantly lower than those of the bare substrates (Table 10). Bulk resistivity values for these films ranged from 19.2–25.7 μΩ·cm. Films were not visually observed on Si(100), SiO<sub>2</sub>, Si-H, or TiN substrates, and sheet resistivity values for these materials were outside of the range of the four-point probe.

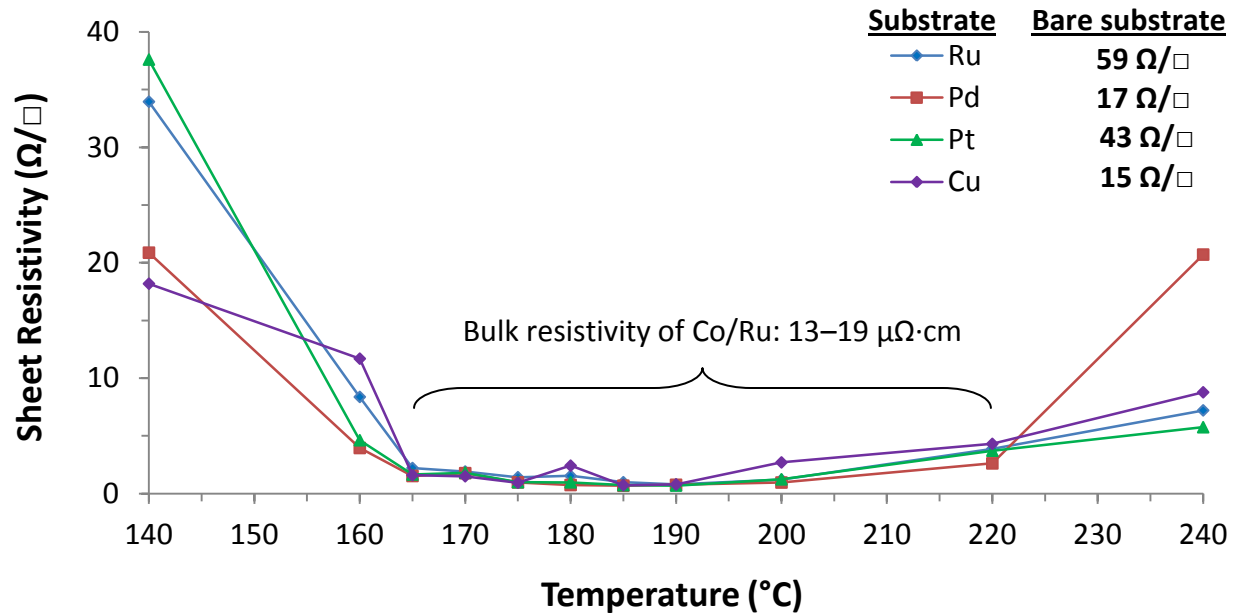
**Table 10.** Resistivity data for substrates and cobalt films grown from **3** and formic acid for 1,000 cycles at 180 °C.

Substrate	Substrate Res. (Ω/□)	Film Thickness (nm)	Film Sheet Res. (Ω/□)	Film Bulk Res. (μΩ·cm)
Ru/TaN/SiO <sub>2</sub> /Si	59.0 ± 0.4	98.9 ± 4.0	2.6 ± 0.7	25.7 ± 0.1
Pd/Ta/SiO <sub>2</sub> /Si	19.8 ± 1.2	120.0 ± 2.9	1.6 ± 0.3	19.2 ± 0.1
Pt/Ta/SiO <sub>2</sub> /Si	42.6 ± 3.0	101.3 ± 6.6	2.1 ± 0.1	21.3 ± 0.1
Cu/Ta/Si	11.9 ± 0.7	82.9 ± 9.6	2.6 ± 0.3	21.6 ± 0.3
Si(100)	-----	No visual film	-----	n/a
Si-H	-----	No visual film	-----	n/a
100 nm SiO <sub>2</sub> /Si	-----	No visual film	-----	n/a
20 nm TiN/Si	185.2 ± 8.5	No visual film	192.1 ± 8.6	n/a

A second resistivity analysis was performed for films grown on Ru, Pd, Pt, and Cu within the 140–240 °C range for 1,000 cycles. Films deposited on Ru within the 165–220 °C range showed sheet resistivities of 0.8–3.9 Ω/□, corresponding to bulk resistivities of 13.4–19.0 μΩ·cm, approaching that of bulk Co metal (6.24 μΩ·cm at 20 °C).<sup>312</sup>



**Figure 120.** Sheet resistivity data for cobalt films grown from **3** and formic acid for 1,000 cycles.



XPS survey scans of a 95 nm thick Co film deposited on Ru at 180 °C showed no N in the as-deposited film and the elimination of all C contamination after 1 min of sputtering (Figure 121). The O content in the film steadily decreased, plateauing at 8.3% after 8 min of sputtering. The Co 2p ionization region showed the presence of CoO in the as-deposited film (red trace, Figure 122). After 1 min of sputtering with 3 keV argon ions, only Co (58.3%) and O (41.7%) were detected. Continued sputtering resulted in ionizations which exactly matched the known values for Co metal after 2 min and a film composition consisting of 91.6% Co metal after 8 min.

**Figure 121.** XPS survey scans of a 95 nm thick film grown from **3** and formic acid on Ru at 180 °C.

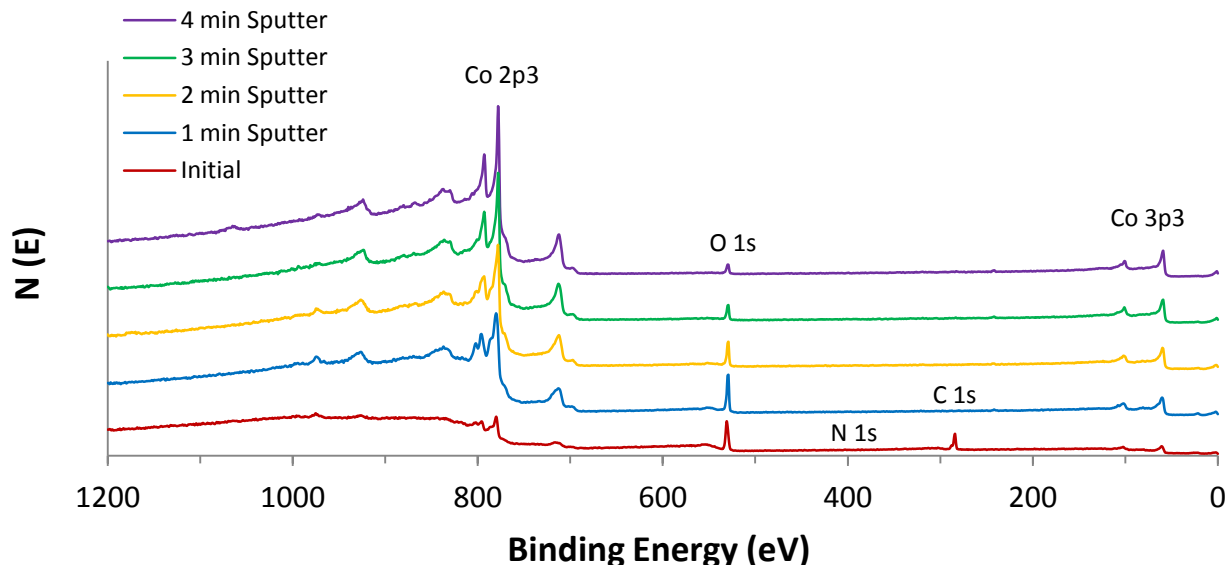
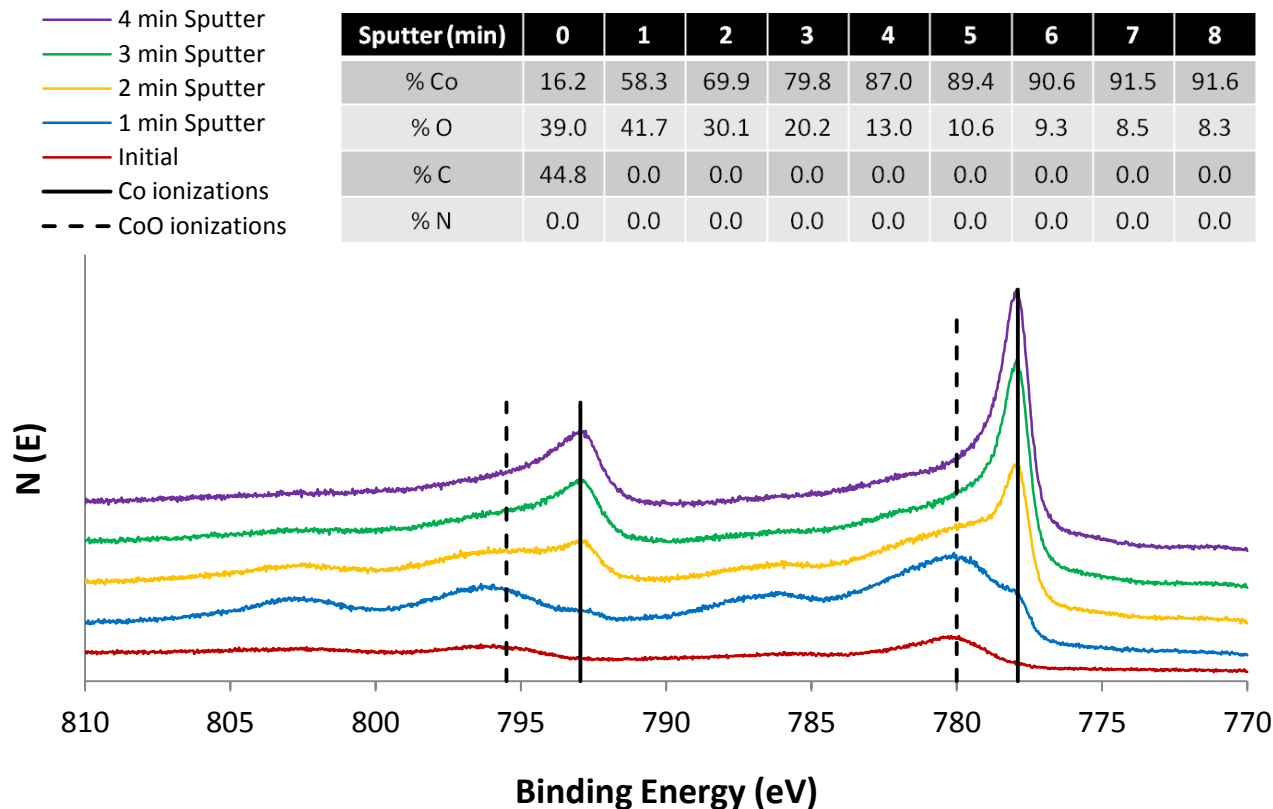


**Figure 122.** XPS Co 2p ionization region of a 95 nm thick film grown from **3** and formic acid on Ru at 180 °C. Reference 2p binding energies for Co metal: 777.9 and 792.95 eV; CoO: 780.0 and 795.50 eV.<sup>305</sup>



Two other precursors were subsequently considered for a Co metal ALD process using formic acid. A three-step approach was attempted at 125 °C using (2-*tert*-butylallyl)Co(CO)<sub>3</sub>,<sup>143</sup> formic acid, and **2**. The onset of thermal decomposition for this Co precursor appears to be ~90 °C (Appendix A), however, it was previously used for the ALD of Co metal and CoSi<sub>2</sub>.<sup>143–144</sup> A pulsing sequence of 2.0 s Co allyl/15.0 s N<sub>2</sub> purge/0.2 s formic acid/5.0 s N<sub>2</sub> purge/1.0 s **2**/10.0 s N<sub>2</sub> purge was applied for 300 cycles. No films were detected on any of the substrates used, including Al<sub>2</sub>O<sub>3</sub>, TiN, Ru, Pd, Pt, Co, Cu, SiO<sub>2</sub>, Si(100), and Si-H. Subsequently, a binary process was attempted at 175 °C using a Co hydrazonate complex<sup>98</sup> and formic acid. A pulsing sequence of 3.0 s Co hydrazonate/10.0 s N<sub>2</sub> purge/0.2 s formic acid/10.0 s N<sub>2</sub> purge was applied for 1,000 cycles. No film growth was detected on the Ru substrates used for this experiment.

First-row transition metals can catalyze the decomposition of formic acid to H<sub>2</sub>, CO<sub>2</sub>, and other products, and Co and Ru are very reactive catalysts.<sup>314</sup> Since no Ru was observed in the XPS spectra of the Co films grown from **3** and formic acid, Co metal likely catalyzes the decomposition of formic acid once a continuous Co layer is grown. Based on the solution experiments previously described, this process may proceed via protonation of the <sup>t</sup>Bu<sub>2</sub>DAD ligands by formic acid (pK<sub>a</sub> = 3.7)<sup>315</sup> toward the formation of an intermediate Co(II) formate layer and other possible products. The underlying Co or Ru layer may catalyze the decomposition of formic acid to H<sub>2</sub> and other species that could reduce these surface-derived layers to Co metal. Data herein suggest a 10–15% CVD component to the growth at 180 °C and a nucleation period of ≤ 250 cycles before normal ALD growth ensues. This small CVD component due to the self-decomposition of **3** may provide a Co seed layer, as **3** has been shown to thermally decompose to Co metal in the solid state.<sup>42</sup> This Co seed layer may be operant in facilitating normal ALD growth at 180 °C. The lack of film growth using the Co hydrazonate

precursor could arise from its higher thermal stability (dec. 260 °C)<sup>98</sup> compared to **3** (dec. 235 °C)<sup>42</sup> and the lack of cobalt metal formation upon its thermal decomposition. Still, the process using **3** and formic acid shows self-limiting behavior and a linear relationship between film thickness and the number of cycles. Accordingly, the ALD growth mode may be kinetically favored over the CVD growth mode upon formation of a continuous Co seed layer. Thus, CVD growth may only occur during the initial formation of the Co seed layer by the self-decomposition of **3**. The mechanistic aspects of this process are speculative and require further investigation.

### 3.2.3 Other Metal-containing Films by Three-step Processes

Encouraged by the effectiveness of **3** as an ALD precursor, other three-step processes were considered using **4-7**, Cu(dmap)<sub>2</sub>, and Ni(dmamp)<sub>2</sub> with formic acid and **2** as coreagents.

#### Nickel

Nickel films were grown using two different precursors, Ni(dmamp)<sub>2</sub> and **4**, at 150 and 180 °C, respectively. Both Ni(dmamp)<sub>2</sub><sup>176</sup> and **4**<sup>42</sup> decompose thermally to nickel metal. However, in the solid state, Ni(dmamp)<sub>2</sub>,<sup>176</sup> **4**,<sup>42</sup> and Ni(OCHO)<sub>2</sub><sup>313</sup> are thermally stable to 180, 230, and 262 °C, respectively.

First, films were grown using a pulsing sequence of 3.0 s Ni(dmamp)<sub>2</sub>/5.0 s N<sub>2</sub> purge/0.2 s formic acid/5.0 s N<sub>2</sub> purge/1.0 s **2**/10.0 s N<sub>2</sub> purge. Source temperatures for Ni(dmamp)<sub>2</sub>, formic acid, and **2** were held constant at 95, 23, and 70 °C, respectively. The temperature of the reactor was 150 °C. After 1,000 cycles, continuous films were measured on Si(100) (42 nm), Si-H (24 nm), Ru (30 nm, Figure 123), Pd (32 nm), Co (20 nm, Figure 124), and SiO<sub>2</sub> (24 nm).

**Figure 123.** Cross-sectional SEM image of a 30 nm thick film grown on a 5 nm thick Ru substrate from Ni(dmamp)<sub>2</sub>, formic acid, and **2** for 1,000 cycles at 150 °C.

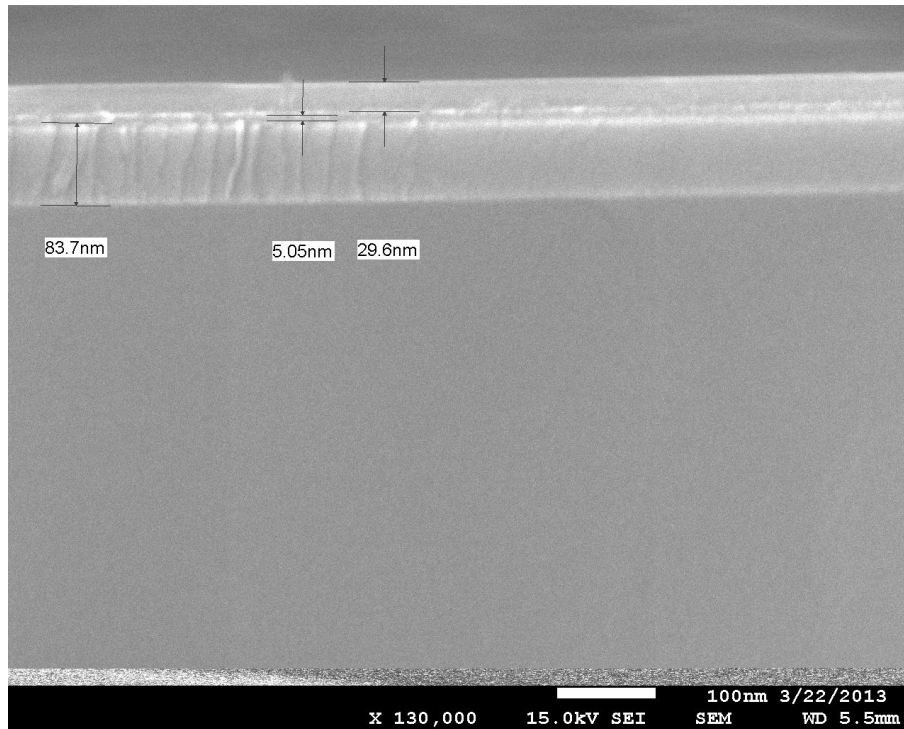
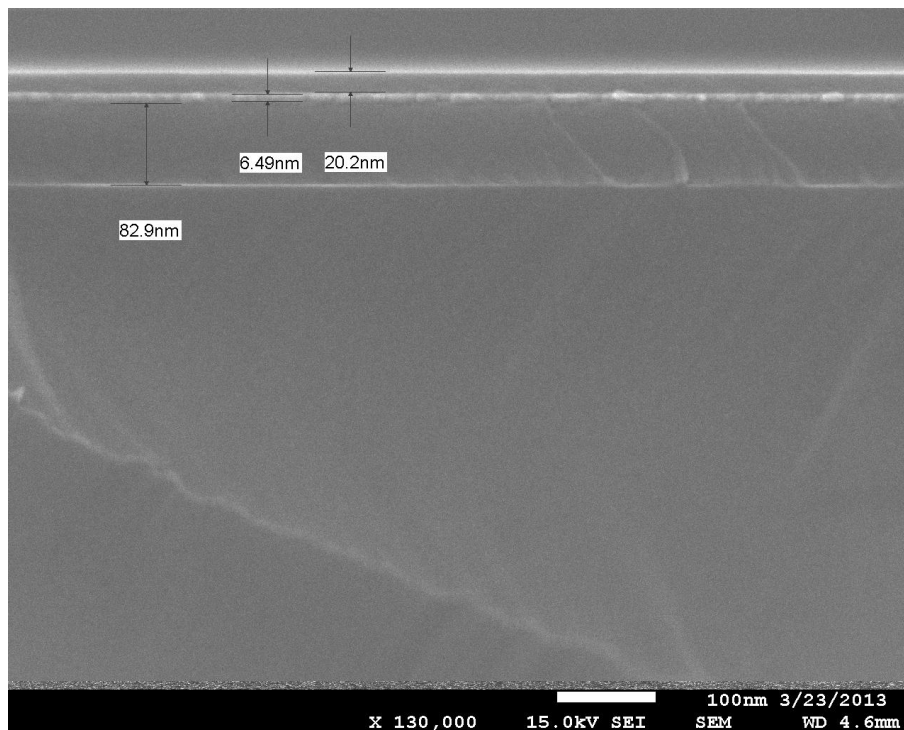


**Figure 124.** Cross-sectional SEM image of a 20 nm thick film grown on a 5 nm thick Co substrate from Ni(dmamp)<sub>2</sub>, formic acid, and **2** for 1,000 cycles at 150 °C.



XPS survey scans of a 32 nm thick film deposited on Pd showed a significant reduction in C content with sputtering (Figure 125). After 1 min of sputtering, the Ni content was 51.3% with 5.2% Pd detected, suggesting incomplete surface coverage by the Ni film. Further sputtering reduced the Ni concentration and increased the Pd/O ratio, due to the increased detection of the underlying Pd substrate. Still, after 1 min of sputtering, the Ni 2p ionization region showed the exclusive presence of Ni metal (Figure 126).

**Figure 125.** XPS survey scans of a 32 nm thick film grown from  $\text{Ni}(\text{dmamp})_2$ , formic acid, and **2** on Pd at 150 °C.

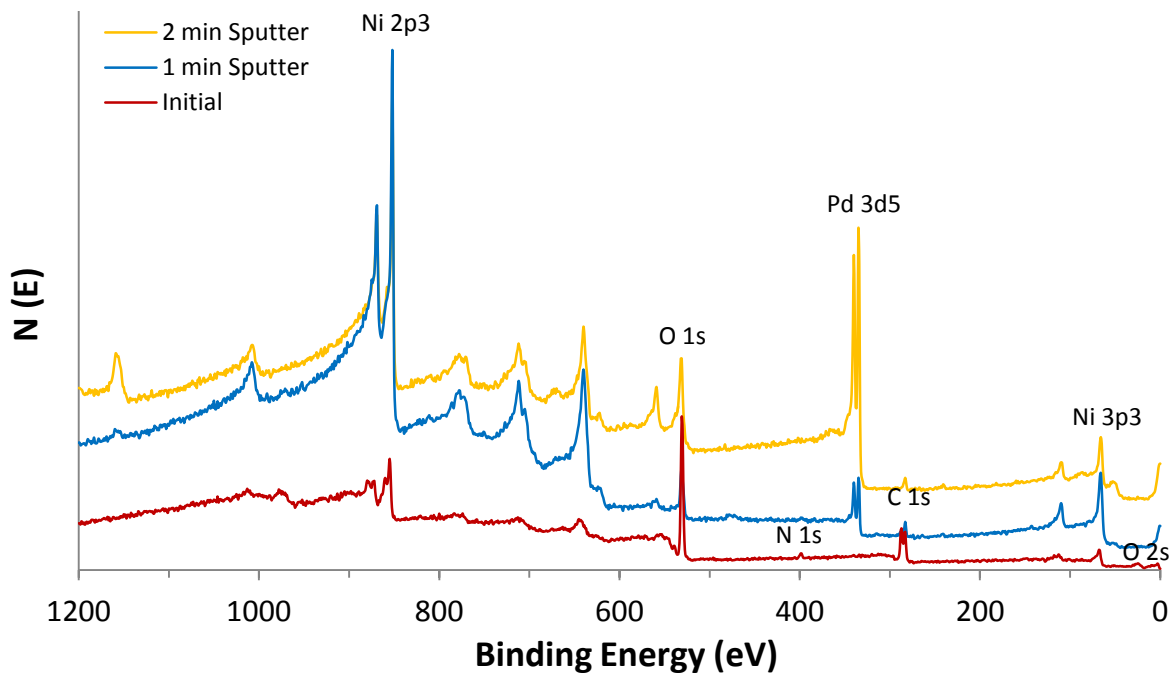
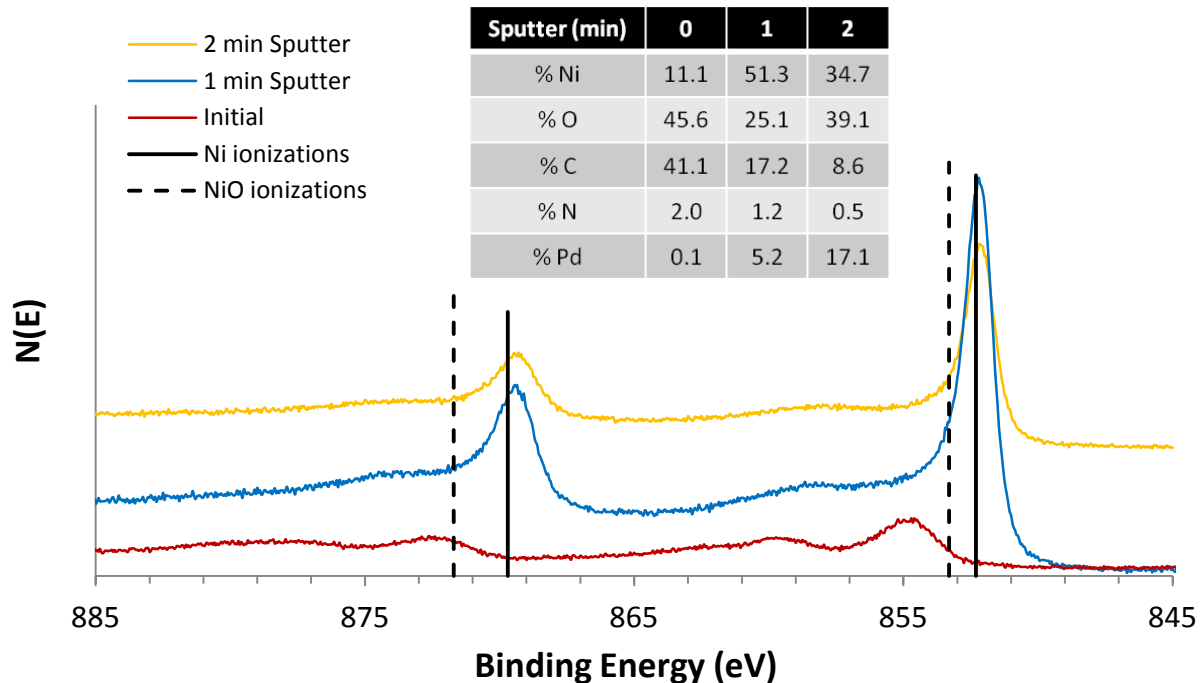


**Figure 126.** XPS Ni 2p ionization region of a 32 nm thick film grown from Ni(dmamp)<sub>2</sub>, formic acid, and **2** on Pd at 150 °C. Reference values for Ni metal: 852.3 and 869.7 eV; NiO: 853.3 and 871.7 eV.<sup>305</sup>



Nickel films were also grown using a pulsing sequence of 6.0 s **4**/5.0 s N<sub>2</sub> purge/0.2 s formic acid/5.0 s N<sub>2</sub> purge/1.0 s **2**/10.0 s N<sub>2</sub> purge. Source temperatures for **4**, formic acid, and **2** were held constant at 128, 23, and 70 °C, respectively. The temperature of the reactor was 180 °C. After 1,000 cycles, cross-sectional SEM analyses showed rough films on Ru (32 nm, Figure 127) and Cu (38 nm), with nanoparticulate growth on Si(100). A top-down perspective showed nanoparticulate growth on Cu, with most of the nanoparticles measuring 10–40 nm in diameter (Figure 128). XPS analysis showed that the film grown on Ru contained 94.0% Ni, and the Ni 2p ionizations were an exact match to Ni metal after 1 min of sputtering (Figures 129–130). However, a significant reduction in sheet resistivity was only observed for the film deposited on a 5 nm Ru/SiO<sub>2</sub> substrate ( $185 \pm 24 \Omega/\square$ ) versus the bare substrate ( $591 \pm 52 \Omega/\square$ ). The powder XRD spectrum of the film deposited on a Cu substrate did not show any reflections corresponding to Ni metal, NiO, or Ni<sub>2</sub>O<sub>3</sub>.

**Figure 127.** Cross-sectional SEM image of a 32 nm thick film grown on a 5 nm thick Ru substrate from **4**, formic acid, and **2** for 1,000 cycles at 180 °C.

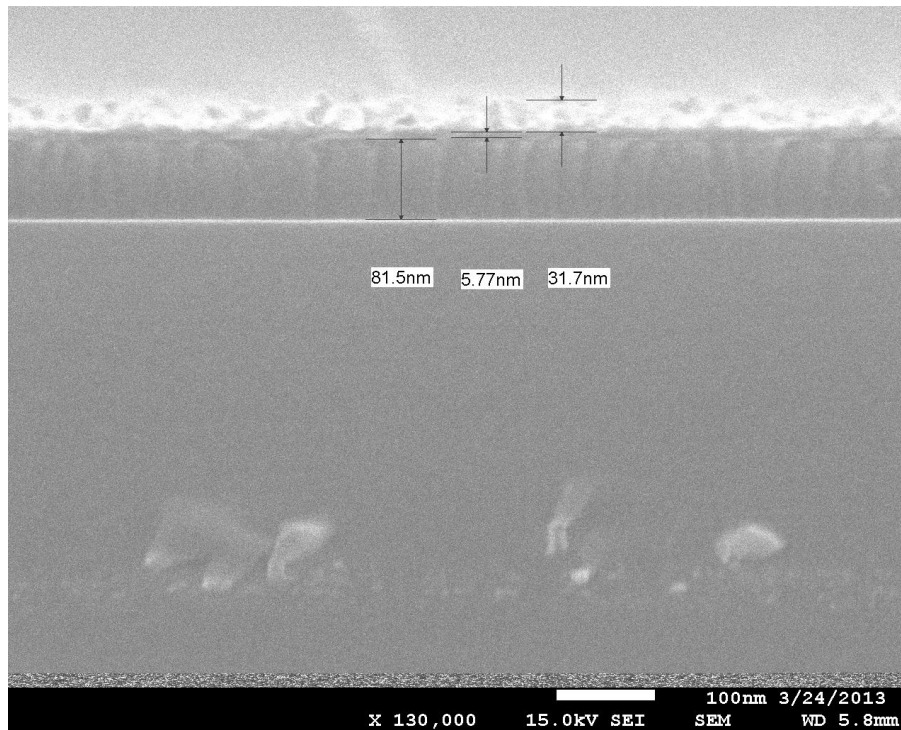


**Figure 128.** Top-down SEM image of nanoparticulate growth on Cu from **4**, formic acid, and **2** for 1,000 cycles at 180 °C.

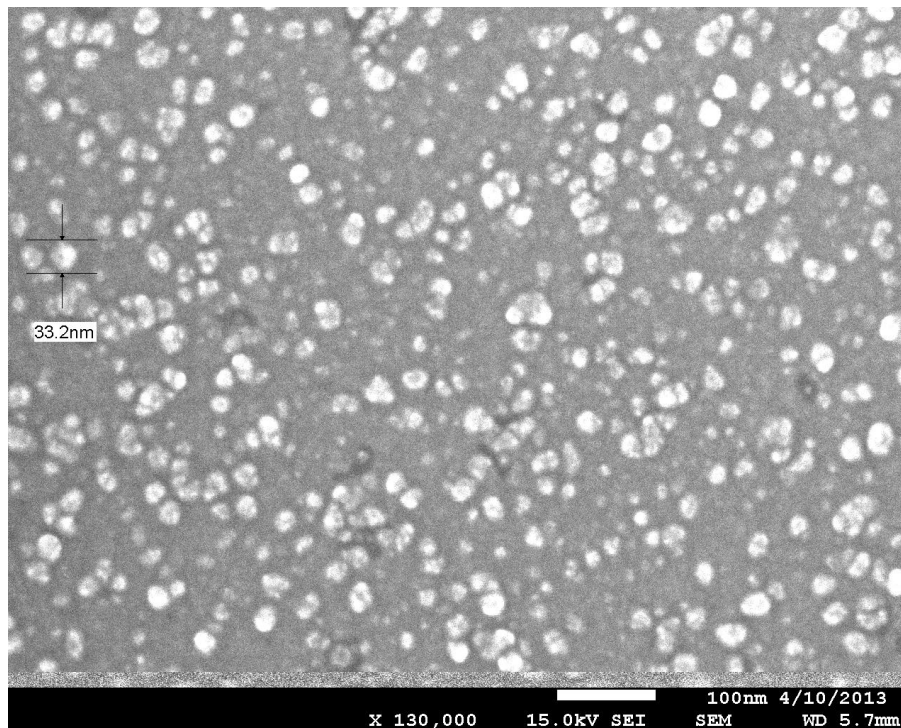




**Figure 129.** XPS survey scans of a 32 nm thick film grown from **4**, formic acid, and **2** on Ru at 180 °C.

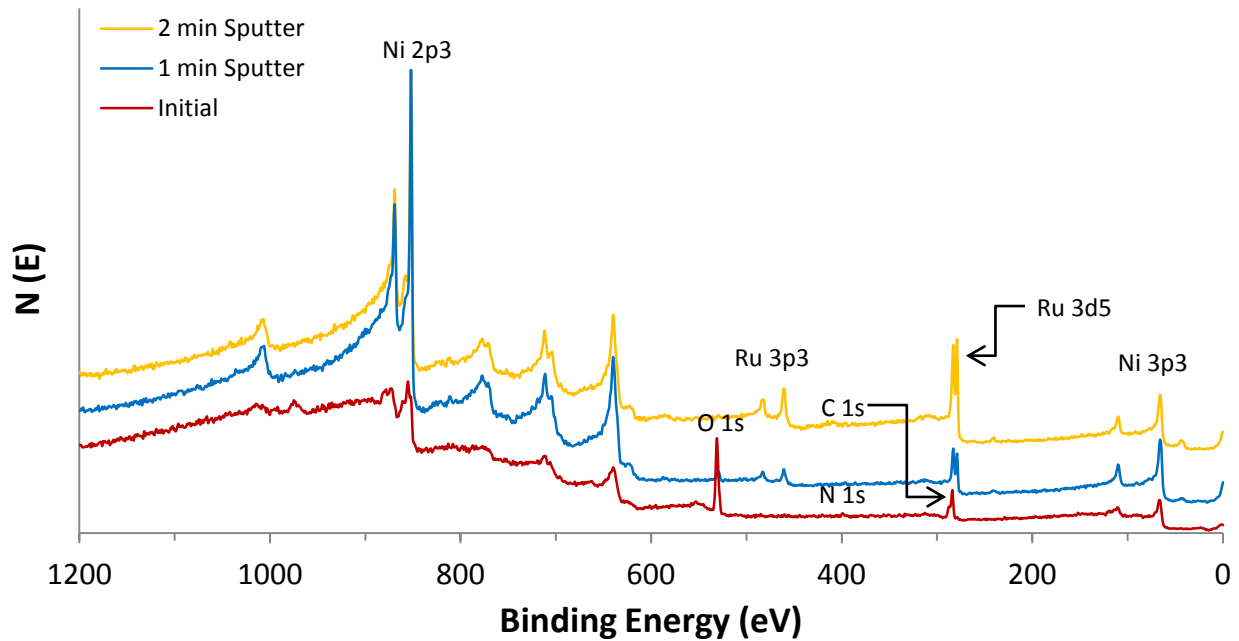
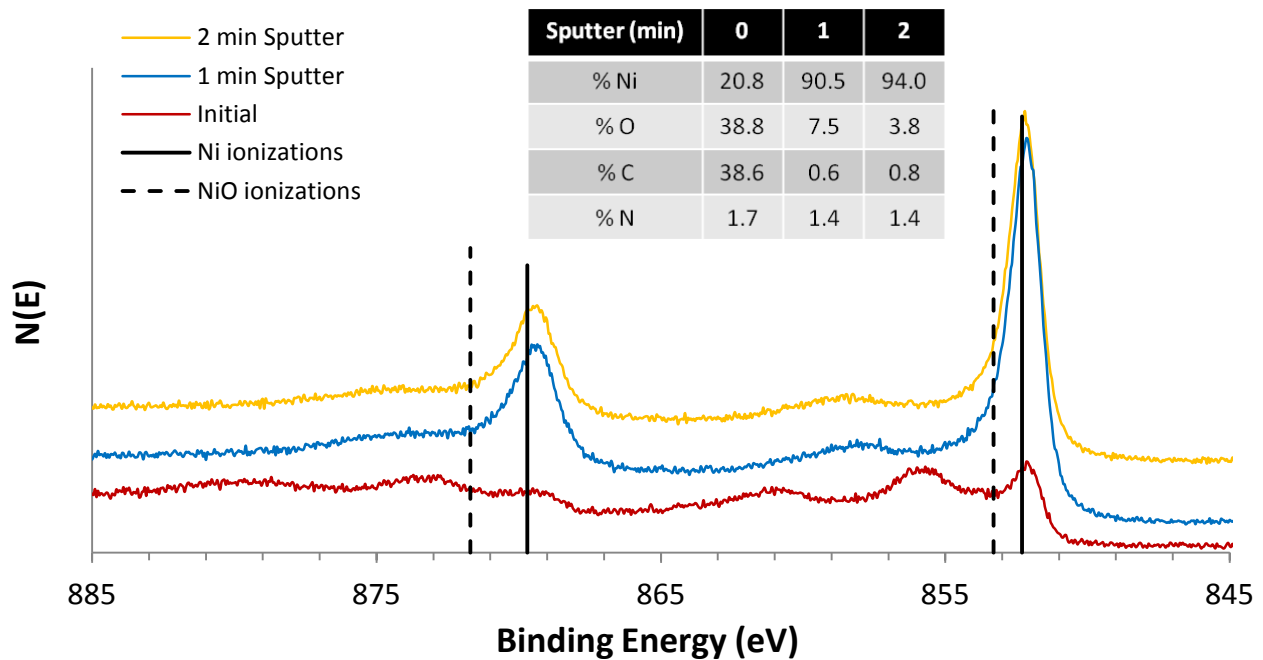


**Figure 130.** XPS Ni 2p ionization region of a 32 nm thick film grown from **4**, formic acid, and **2** on Ru at 180 °C. Reference 2p binding energies for nickel metal: 852.3 and 869.7 eV; NiO: 853.3 and 871.7 eV.<sup>305</sup>



## Iron

Films were grown using a pulsing sequence of 6.0 s **5**/5.0 s N<sub>2</sub> purge/0.2 s formic acid/5.0 s N<sub>2</sub> purge/1.0 s **2**/10.0 s N<sub>2</sub> purge. The temperature of the reactor was 225 °C. After 1,000 cycles, cross-sectional SEM analyses revealed continuous films on Si(100) (24 nm), Ru (30 nm, Figure 131), Co (25 nm), and SiO<sub>2</sub> (32 nm, Figure 132). Top-down SEM analyses revealed a granular morphology on the SiO<sub>2</sub> substrates. XPS survey scans of the 30 nm thick film grown on Ru showed no N in the as-deposited film and a disappearance of C after 1 min of sputtering (Figure 133). After 2 min of sputtering, the Fe/O ratio was 0.85 and the Fe 2p ionization region showed peaks between those for Fe metal and Fe<sub>2</sub>O<sub>3</sub>, indicating the presence of both species (Figure 134).

**Figure 131.** Cross-sectional SEM image of a 30 nm thick film grown on a 5 nm thick Ru substrate from **5**, formic acid, and **2** for 1,000 cycles at 225 °C.

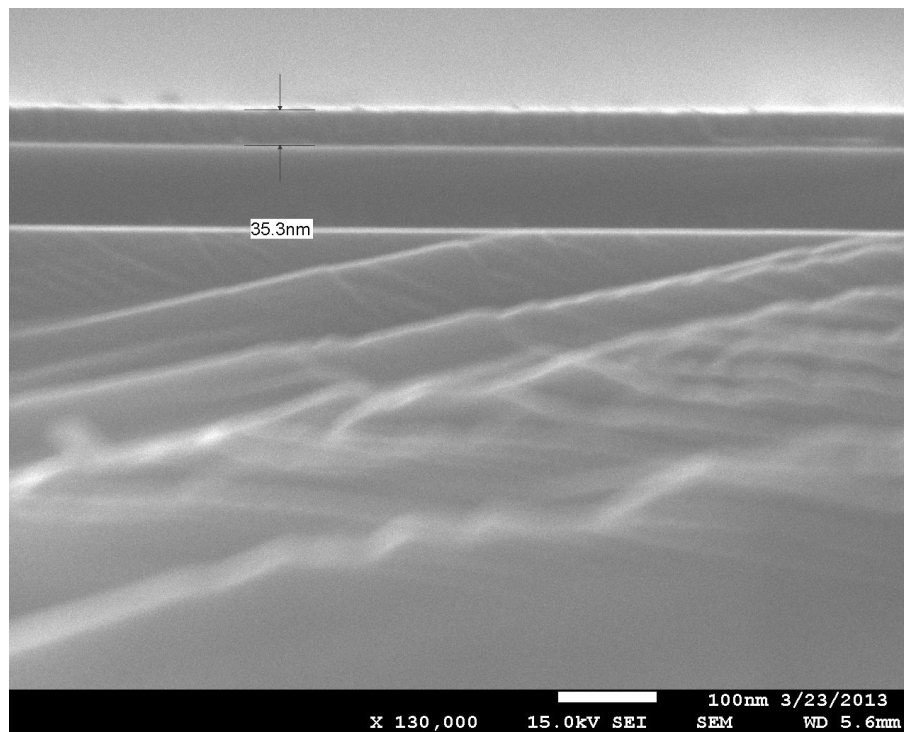


**Figure 132.** Cross-sectional SEM image of a 32 nm thick film grown on SiO<sub>2</sub> from **5**, formic acid, and **2** for 1,000 cycles at 225 °C.

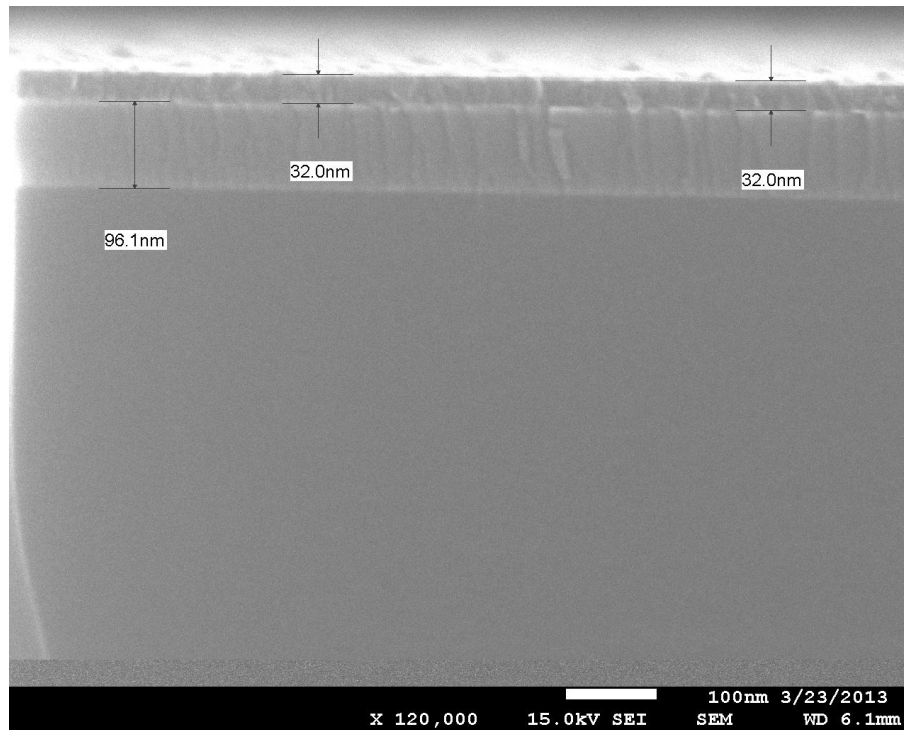


**Figure 133.** XPS survey scans of a 30 nm thick film grown from **5**, formic acid, and **2** on Ru at 225 °C.

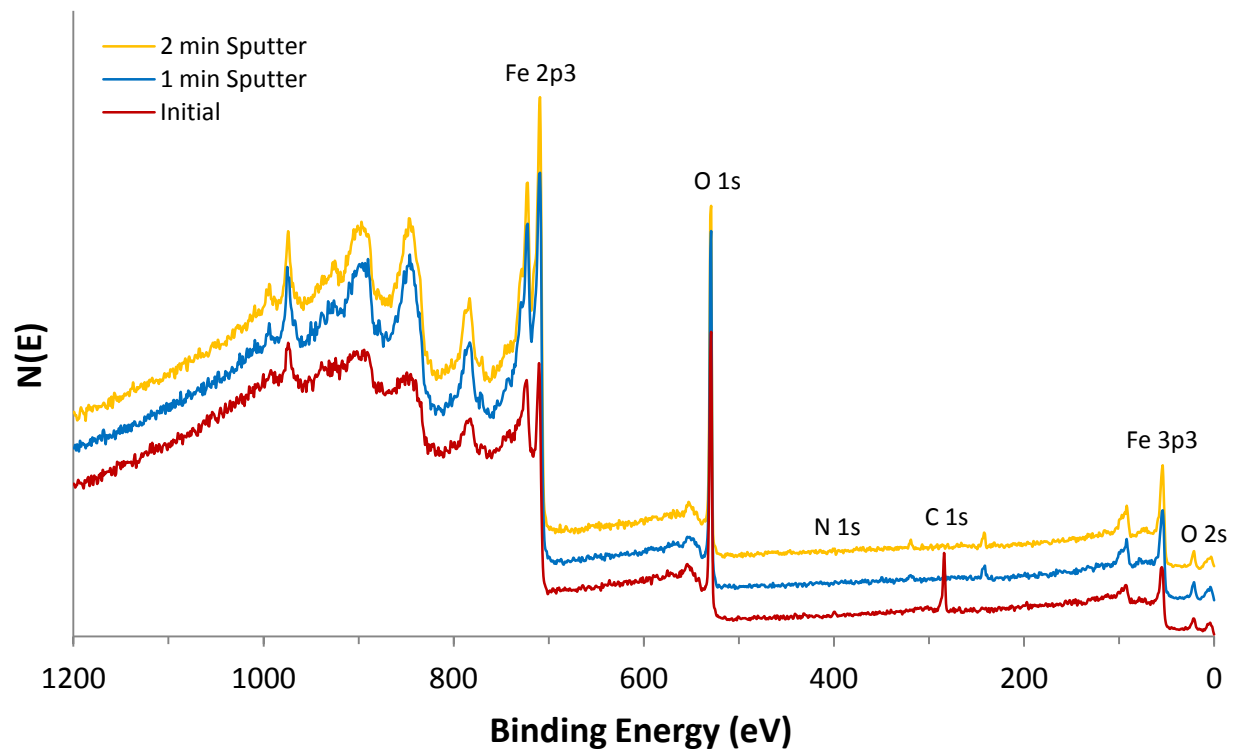
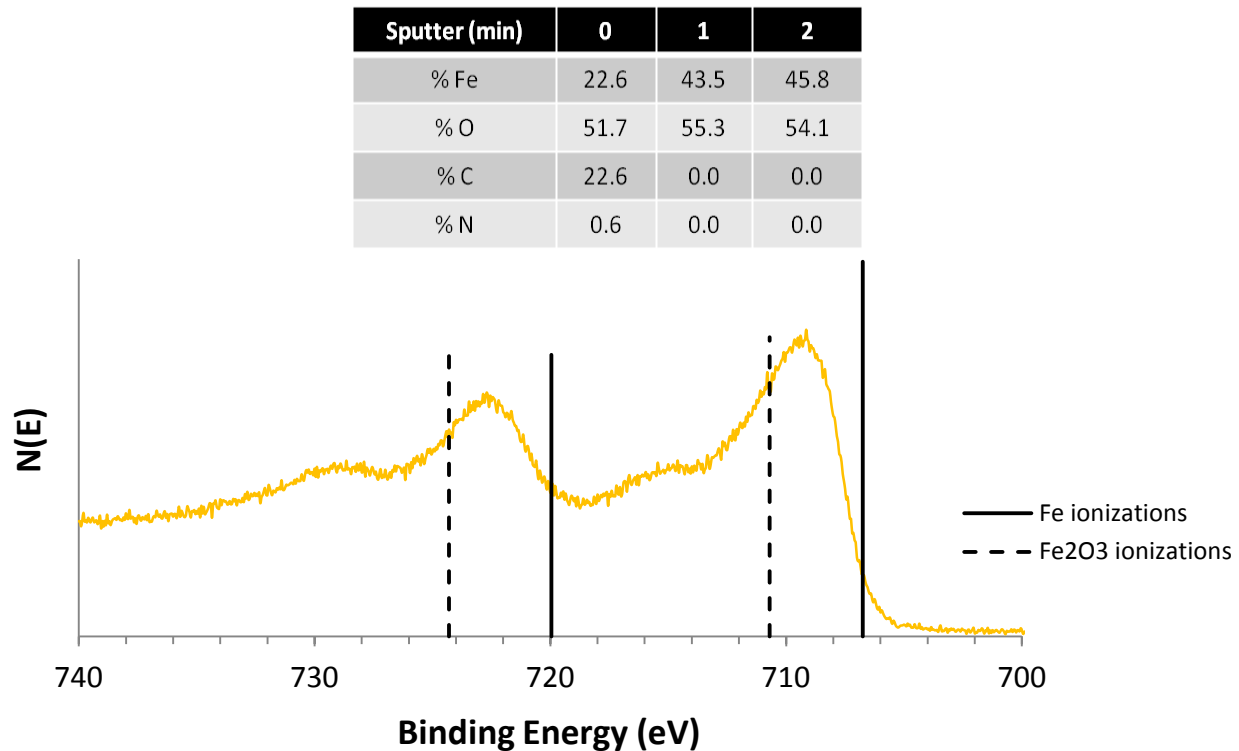


**Figure 134.** XPS Fe 2p ionization region of a 30 nm thick film grown from **5**, formic acid, and **2** on Ru at 225 °C after 2 min of sputtering. Reference values for Fe metal: 706.75 and 719.95 eV; Fe<sub>2</sub>O<sub>3</sub>: 710.70 and 724.30 eV.<sup>305</sup>



### Chromium

Films were grown using a pulsing sequence of 6.0 s **6**/5.0 s N<sub>2</sub> purge/0.2 s formic acid/5.0 s N<sub>2</sub> purge/1.0 s **2**/10.0 s N<sub>2</sub> purge. The temperature of the reactor was 225 °C. After 1,000 cycles, cross-sectional SEM analyses revealed continuous films on Si(100) (55 nm), Ru (38 nm, Figure 135), Co (106 nm), and SiO<sub>2</sub> (129 nm, Figure 136). Additionally, films were visually observed on Si-H, Pd, Pt, Cu, and TiN substrates. XPS survey scans of the 129 nm thick film deposited on SiO<sub>2</sub> showed a significant reduction in C content with sputtering (Figure 137). After 2 min of sputtering, the Cr/O ratio was 2:3, with the Cr 2p ionizations matching those for Cr<sub>2</sub>O<sub>3</sub> (Figure 138). However, these peaks were broad, with shoulders overlapping the known ionizations for Cr metal.

**Figure 135.** Cross-sectional SEM image of a 38 nm thick film grown on a 5 nm thick Ru substrate from **6**, formic acid, and **2** for 1,000 cycles at 225 °C.

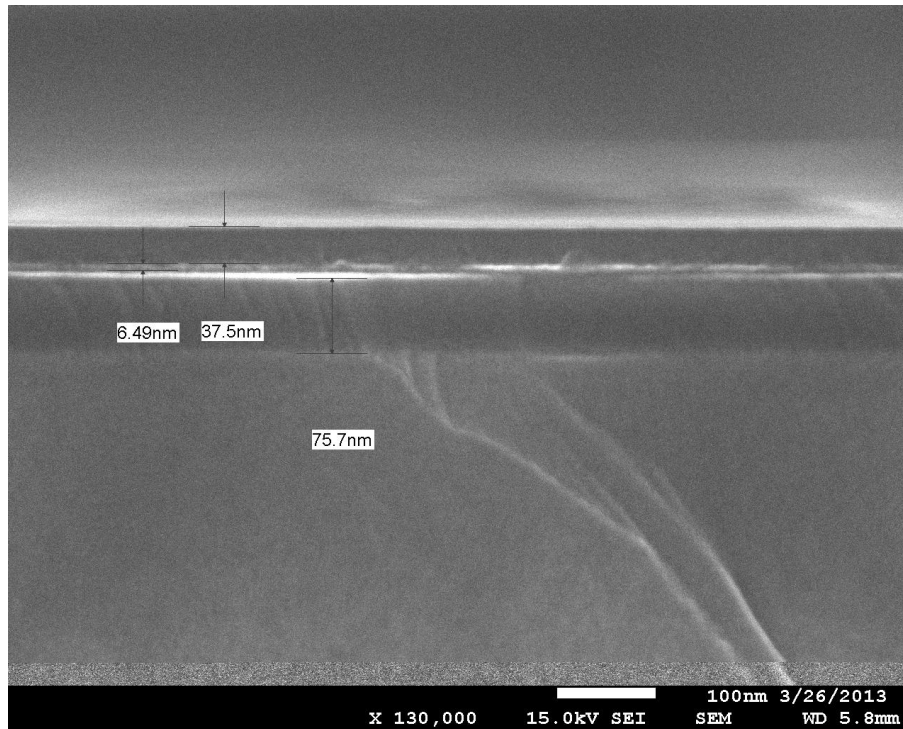


**Figure 136.** Cross-sectional SEM image of a 129 nm thick film grown on SiO<sub>2</sub> from **6**, formic acid, and **2** for 1,000 cycles at 225 °C.

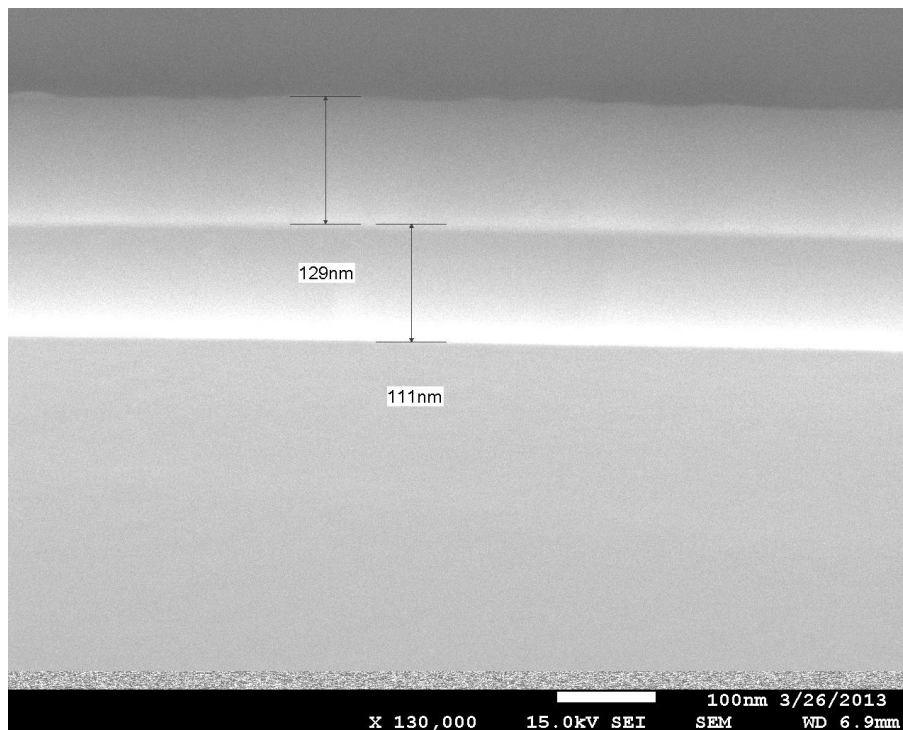


**Figure 137.** XPS survey scans of a 129 nm thick film grown from **6**, formic acid, and **2** on SiO<sub>2</sub> at 225 °C.

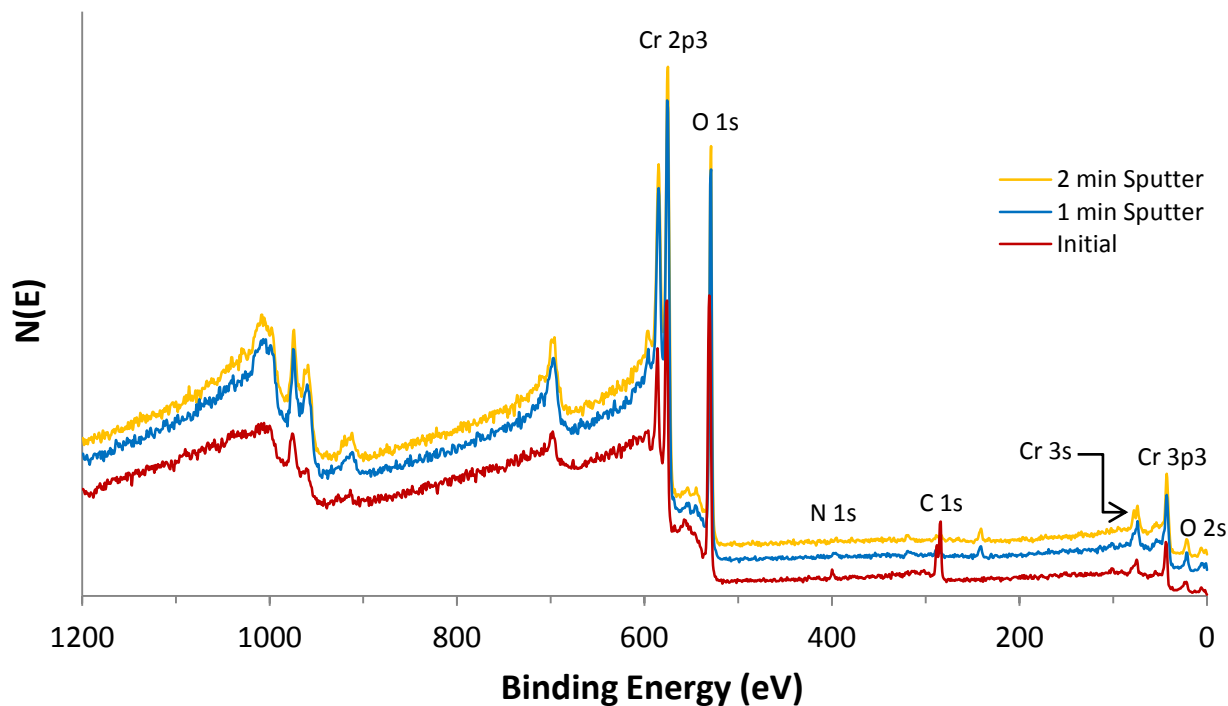
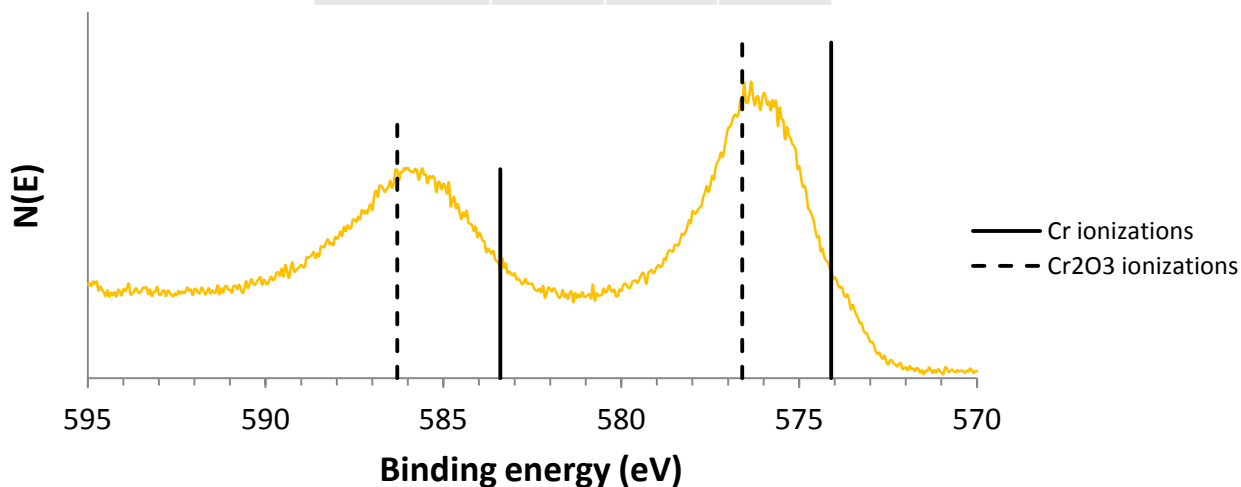


**Figure 138.** XPS Cr 2p ionization region of a 129 nm thick film grown from **6**, formic acid, and **2** on SiO<sub>2</sub> at 225 °C after 2 min of sputtering. Reference values for Cr metal: 574.1 and 583.4 eV; Cr<sub>2</sub>O<sub>3</sub>: 576.6 and 586.3 eV.<sup>305</sup>

Sputter (min)	0	1	2
% Cr	18.1	35.2	37.2
% O	51.4	60.9	58.1
% C	28.8	3.6	4.0
% N	1.1	0.3	0.7



## Manganese

Films were grown using a pulsing sequence of 6.0 s **7**/5.0 s N<sub>2</sub> purge/0.2 s formic acid/5.0 s N<sub>2</sub> purge/1.0 s **2**/10.0 s N<sub>2</sub> purge. The temperature of the reactor was 225 °C. After 1,000 cycles, cross-sectional SEM analyses revealed nanoparticulate growth on Ru, Co, and SiO<sub>2</sub> (Figure 139). Top-down perspectives of films grown on Ru and Co showed nanoparticles measuring 48–74 and 35–48 nm in diameter, respectively (Figure 140). XPS survey scans of material grown on SiO<sub>2</sub> showed no N in the as-deposited film and a disappearance of C with sputtering (Figure 141). After 2 min of sputtering, the Mn 2p ionization region showed peaks between those for Mn metal and MnO<sub>2</sub>, indicating the presence of both species (Figure 142). However, the Mn content never exceeded 10% of the total atomic concentration.

**Figure 139.** Cross-sectional SEM image of nanoparticulate growth on SiO<sub>2</sub> from **7**, formic acid, and **2** for 1,000 cycles at 225 °C.

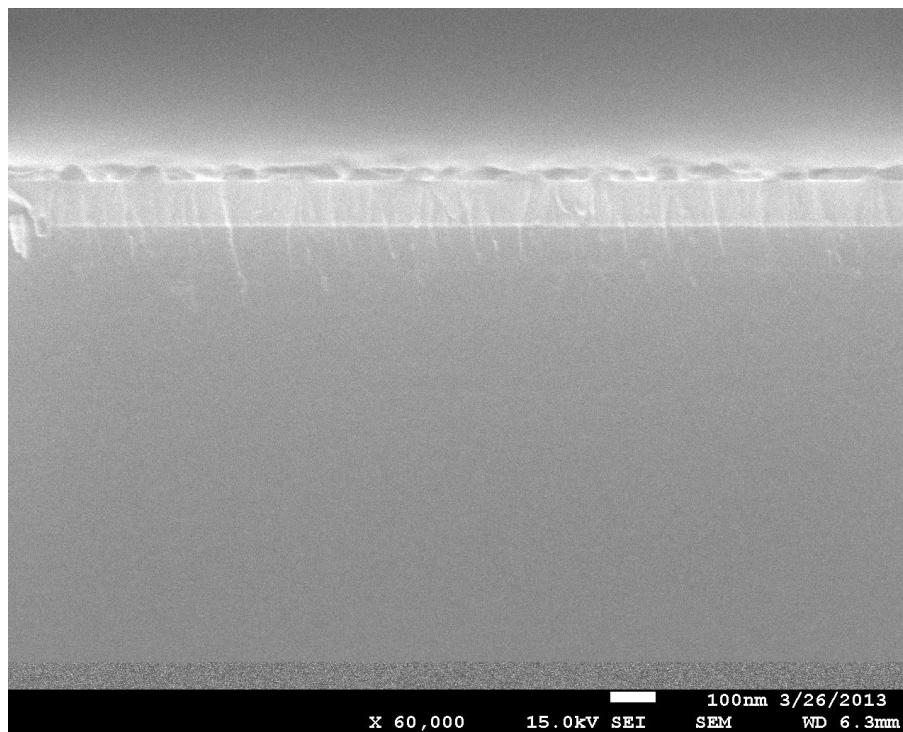


**Figure 140.** Top-down SEM image of nanoparticulate growth on a 5 nm thick Ru substrate from **7**, formic acid, and **2** for 1,000 cycles at 225 °C.

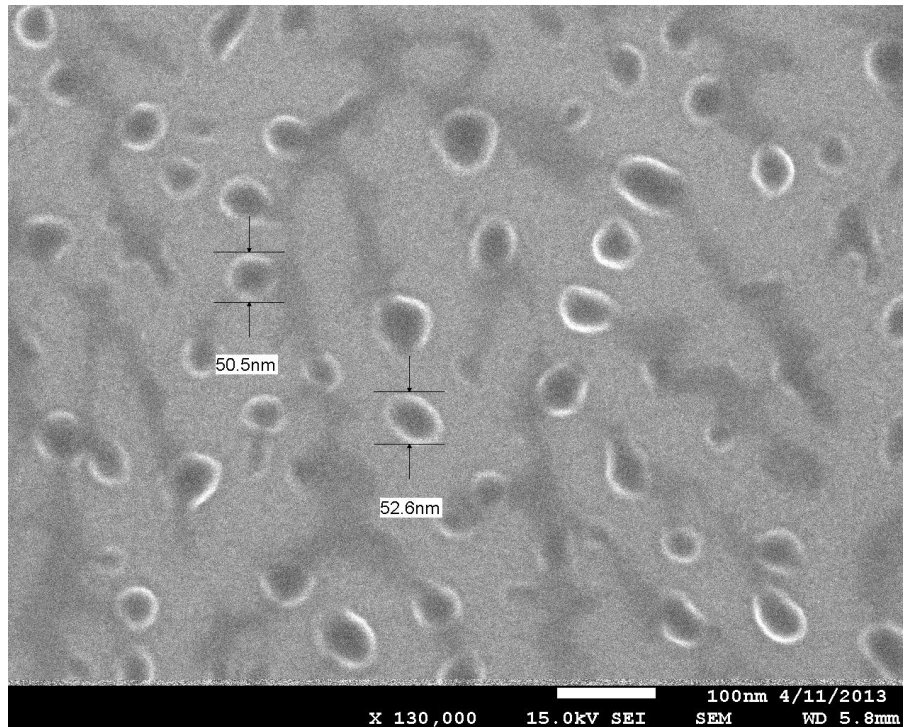


**Figure 141.** XPS survey scans of nanoparticulate growth from **7**, formic acid, and **2** on SiO<sub>2</sub> at 225 °C.

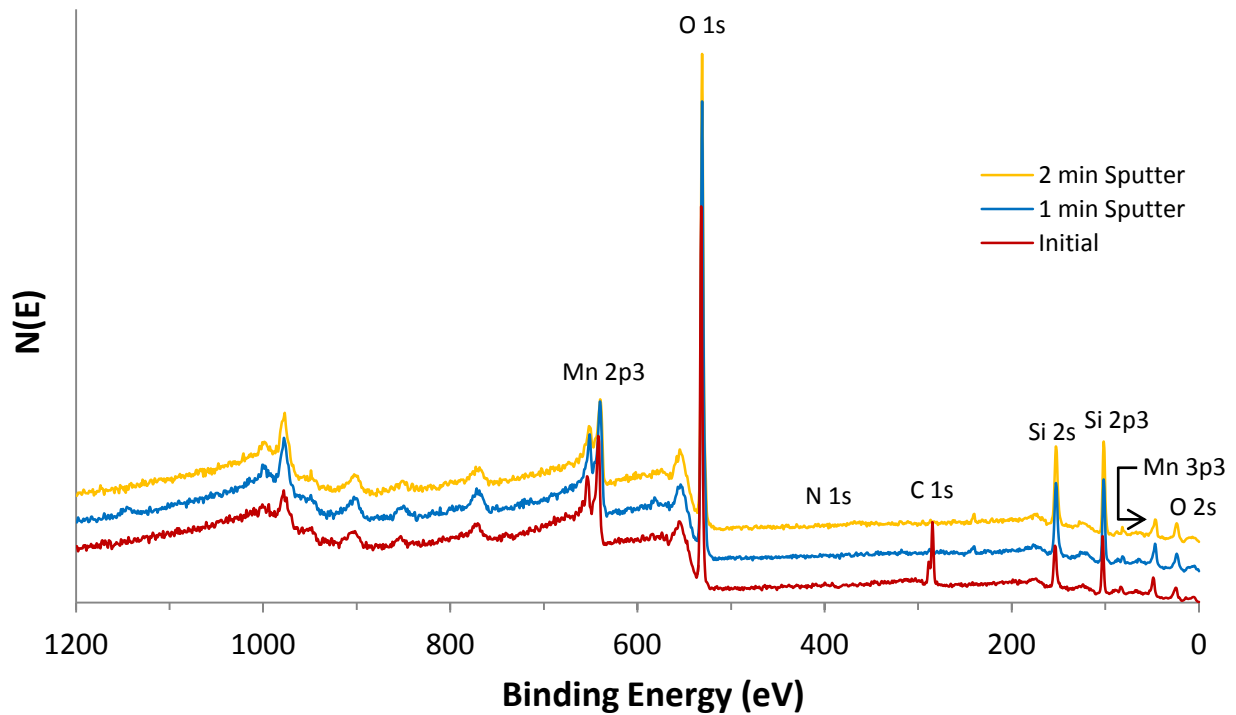
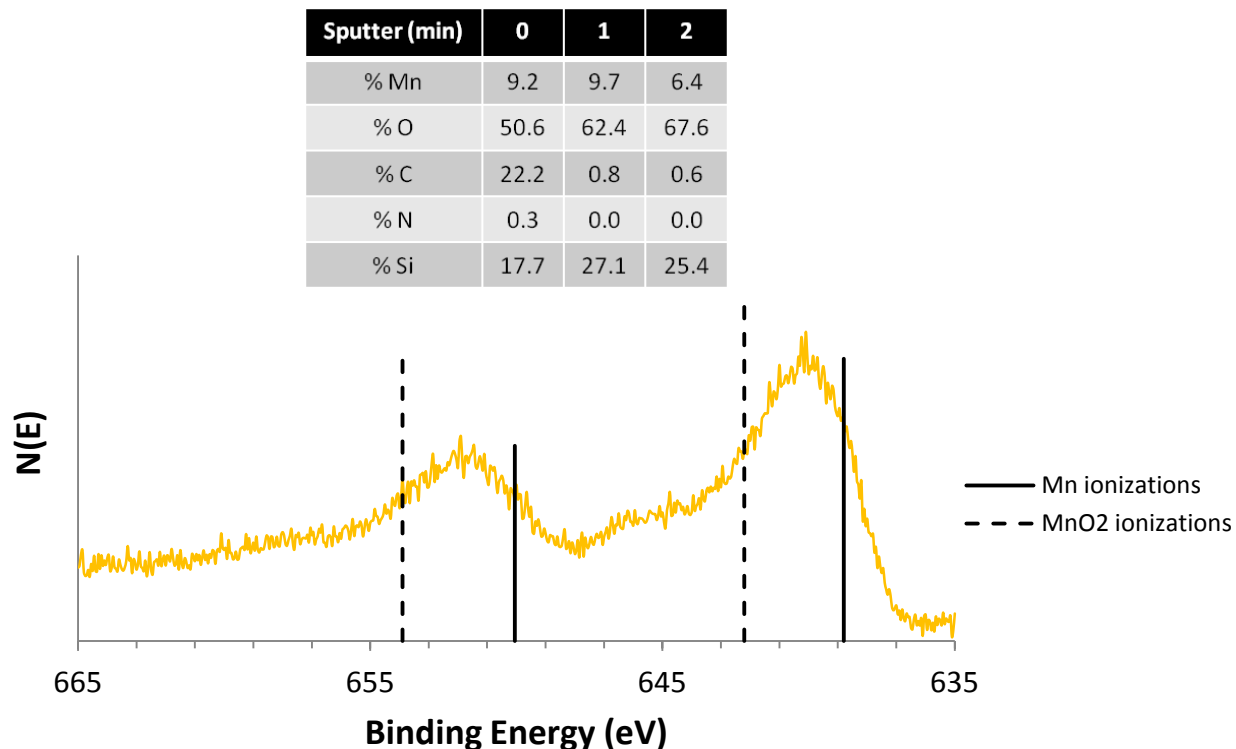




**Figure 142.** XPS Mn 2p ionization region of nanoparticulate growth from **7**, formic acid, and **2** on SiO<sub>2</sub> at 225 °C after 2 min of sputtering. Reference values for Mn metal: 638.8 and 650.05 eV; MnO: 642.2 and 653.9 eV.<sup>305</sup>



### Copper

An initial attempt toward a binary process using Cu(dmap)<sub>2</sub> and **2** did not produce any film growth. A three-step pulsing sequence was subsequently applied, consisting of 3.0 s Cu(dmap)<sub>2</sub>/5.0 s N<sub>2</sub> purge/0.2 s formic acid/5.0 s N<sub>2</sub> purge/1.0 s **2**/10.0 s N<sub>2</sub> purge. The temperature of the reactor was 150 °C. After 1,000 cycles, cross-sectional SEM analyses revealed nanoparticulate growth on Si(100), Si-H, Ru, Pd, Cu, Co, SiO<sub>2</sub>, and TiN substrates. Sheet resistivities were not significantly reduced relative to the bare substrates. XPS analysis was performed on material grown on the Si-H substrate (Figures 145–146). The Cu 2p ionization region showed the presence of Cu metal, with a concentration of 54.9% after 2 min of sputtering. In the solid state, Cu(dmap)<sub>2</sub> and Cu(OCHO)<sub>2</sub> decompose thermally at approximately 175 and 200 °C,<sup>157</sup> respectively, setting the upper temperature limit for this process.

**Figure 143.** Cross-sectional SEM image of nanoparticles grown on a 5 nm thick Co substrate from  $\text{Cu}(\text{dmap})_2$ , formic acid, and **2** for 1,000 cycles at 150 °C.

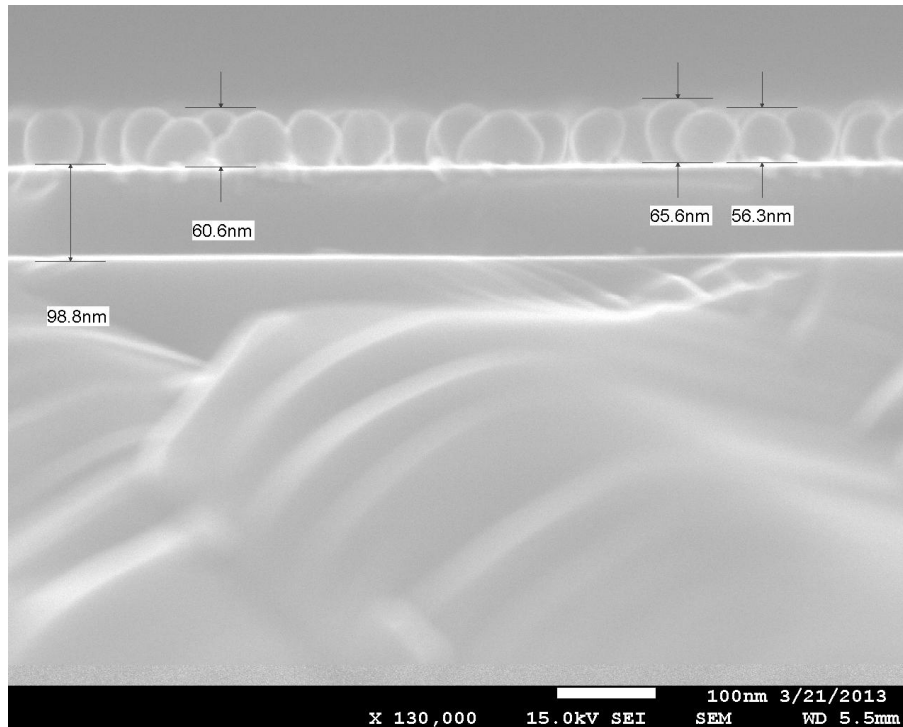


**Figure 144.** Top-down SEM image of nanoparticles grown on a 5 nm thick Co substrate from  $\text{Cu}(\text{dmap})_2$ , formic acid, and **2** for 1,000 cycles at 150 °C.

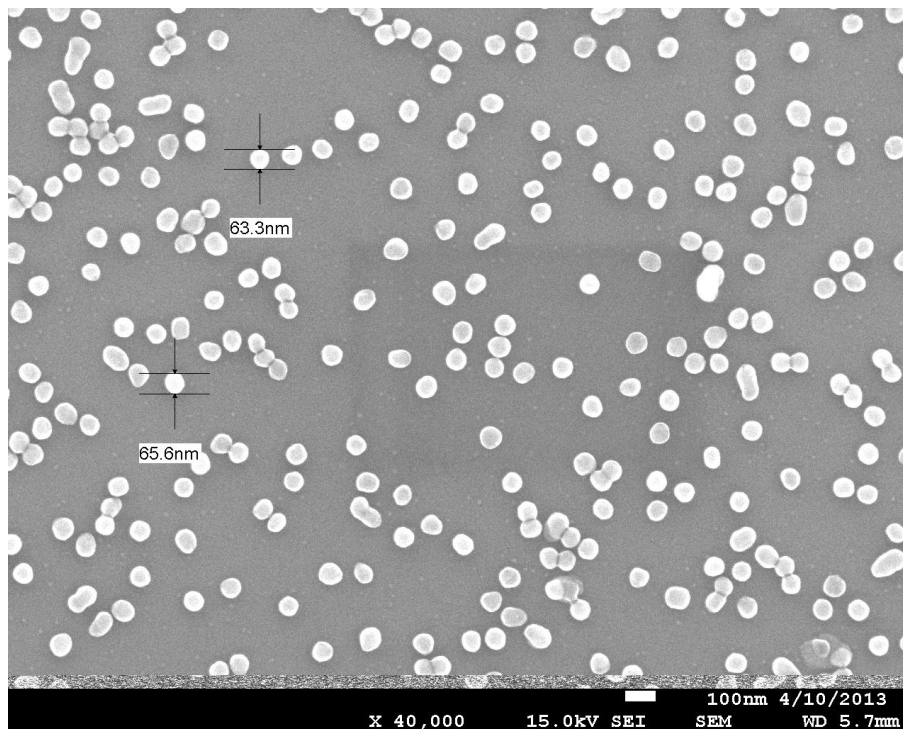


**Figure 145.** XPS survey scans of nanoparticulate growth from  $\text{Cu}(\text{dmap})_2$ , formic acid, and **2** on Si-H at 150 °C.

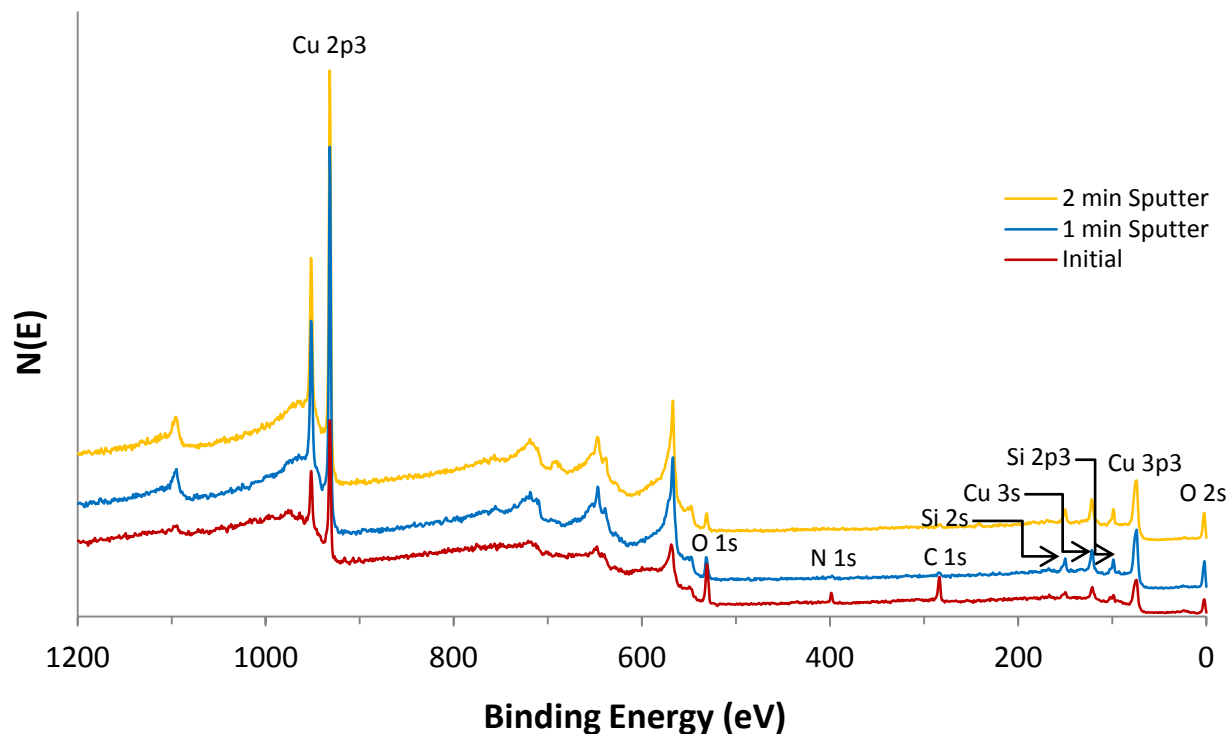
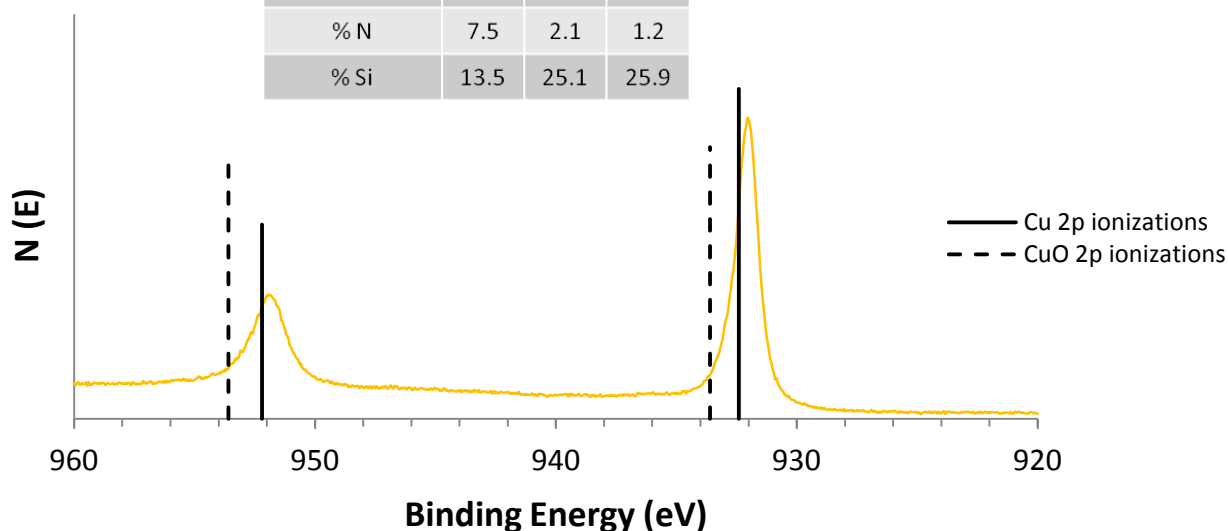


**Figure 146.** XPS Cu 2p ionization region of nanoparticulate growth from  $\text{Cu}(\text{dmap})_2$ , formic acid, and **2** on Si-H at 150 °C after 2 min of sputtering. Reference values for Cu metal: 932.4 and 952.2 eV; CuO: 933.6 and 953.6 eV.<sup>305</sup>

Sputter (min)	0	1	2
% Cu	16.7	48.9	54.9
% O	25.3	14.9	12.4
% C	37.0	9.0	5.5
% N	7.5	2.1	1.2
% Si	13.5	25.1	25.9



### 3.3 Conclusions

Herein, the ALD of cobalt metal films has been demonstrated using **3**, formic acid, and **2** as precursors. Subsequently, a full deposition study was performed for the binary process employing only **3** and formic acid. A growth rate of 0.95 Å/cycle was observed within a 170–180 °C window on Ru substrates. Although self-limiting behavior was evident for films grown at 180 °C, 15–16% of the growth appears to arise from a CVD component due to the partial decomposition of **3**. The growth rate significantly decreases at  $\geq 200$  °C, likely due to the accelerated thermal self-decomposition of **3**.

Several of these films were carefully analyzed after exposure to air. Films grown on Ru, Pt, Pd, and Cu substrates showed very low sheet resistivities within the 165–220 °C temperature range, with bulk resistivities of films grown on Ru substrates approaching that of bulk cobalt metal.<sup>312</sup> Microscopic analyses showed granular morphologies with very smooth surfaces. Lattice fringes were observed for a Co film deposited on a TEM grid at 180 °C, diagnostic of crystalline material. Reflections consistent with Co metal were observed by powder XRD, while XPS analysis showed the exclusive presence of Co metal after 2 min of sputtering and 91.6% Co content after 8 min of sputtering. This approach demonstrates the ALD of high-quality Co metal films that overcomes the limitations of previously-reported Co ALD processes, including low growth rates,<sup>36,39</sup> growth temperatures that are well above the precursor decomposition temperatures,<sup>31,36,38,136–138</sup> no demonstration of self-limited ALD growth,<sup>143</sup> and variable, high resistivities of the Co films.<sup>136–138</sup> Application of the initial three-step approach using a variety of first-row transition metal diazabutadienyl and alkoxide complexes with formic acid and **2** as coreagents afforded films of Ni metal, Fe/Fe<sub>2</sub>O<sub>3</sub>, and Cr<sub>2</sub>O<sub>3</sub>, along with particulate growth of Mn/MnO and Cu metal.

### 3.4 Experimental

**General Considerations.** All manipulations were carried out under Ar using either Schlenk or glove box techniques. All glassware was oven-dried at  $\geq 150$  °C prior to use. Tetrahydrofuran was distilled from sodium benzophenone ketyl and sodium metal. Toluene was distilled from sodium metal. Hexanes was distilled from  $P_2O_5$ . All chemicals were obtained from Sigma Aldrich.  $NiCl_2 \cdot MeCN$ ,<sup>316</sup>  $tBu_2DAD$ ,<sup>317</sup> **2**,<sup>309</sup> **3-7**,<sup>42</sup>  $Cu(dmap)_2$ ,<sup>318-319</sup> and  $Ni(dmamp)_2$ <sup>169,320</sup> were synthesized according to published procedures.  $^1H$  and  $^{13}C\{^1H\}$  NMR spectra were obtained at 400 and 100 MHz respectively, and were referenced to the residual proton and the  $^{13}C$  resonances of the solvent. Sublimations were performed using either a Büchi B-580 or Büchi B-585 sublimation oven. CV experiments were performed as described in Chapter 2.

**Film Growth Studies.** A Picosun Oy R-75BE ALD reactor was used for thin film deposition experiments. A Texol GeniSys  $N_2$  generator supplied 99.9995%  $N_2$  as both the carrier and purge gas. An Adixen 2033 C2 oil pump was used to maintain a pressure of 6–10 mbar in the reactor while under a constant  $N_2$  flow. Films were grown on 10 nm Ru/2 nm TaN/100 nm  $SiO_2/Si$ , 5 nm Ru/85 nm  $SiO_2/Si$ , 5 nm Co/85 nm  $SiO_2/Si$ , 15 nm Pt/2 nm Ta/100 nm  $SiO_2/Si$ , 10 nm Pd/2 nm Ta/100 nm  $SiO_2/Si$ , 10 nm Cu/3 nm Ta/Si, 100 nm  $SiO_2/Si$ . All substrates were provided by Applied Materials (Sunnyvale, CA). Data for the ALD study using **3** and formic acid were obtained from films grown on  $1\text{ cm}^2$  Ru/TaN/ $SiO_2/Si$  substrates. This substrate had a Ru/TaN layer of  $12 \pm 4$  nm with an underlying  $SiO_2$  layer of  $93 \pm 7$  nm. Formic acid was delivered by bubbler at 23 °C at the reactor pressure. Compounds **3-7** were delivered by solid state booster at  $128.0 \pm 1.0$  °C.  $Cu(dmap)_2$  and  $Ni(dmamp)_2$  were delivered by booster at  $95.0 \pm 1.0$  °C. Compound **2** was delivered by bubbler at 70 °C at the reactor pressure. Precursor pulse

lengths were varied to determine the degree of surface saturation. The substrate temperature was subsequently varied using saturative doses of the precursors. Films were cooled to  $\leq 30$  °C prior to removal from the reactor and exposure to ambient atmosphere.

Powder XRD analyses of chemical samples along with SEM and XPS analyses of films were performed as described in Chapter 2. Powder XRD analyses of films were performed with a Bruker D8 ADVANCE DAVINCI diffractometer, using copper  $K_{\alpha}$  radiation (1.54056 Å) at 40 kV and 40 mA. Crystalline phases were identified by comparing the experimental spectrum with the powder diffraction files of the International Center of Diffraction Data using the Jade 5.0 software package. Crystallite sizes were calculated from the most intense reflection, using the Scherrer equation with the Jade 5.0 software package. AFM micrographs were obtained with a MultiMode Nanoscope IIIa atomic force microscope (Digital Instruments, VEECO). The samples were measured using the tapping mode in air with an E scanner with a maximum scanning size of 12  $\mu\text{m}$  at a frequency of 1 or 2 Hz. A Tap150AI-G tip was used, with a resonance frequency of 150 kHz and a force constant of 5  $\text{Nm}^{-1}$ . Surface roughnesses were calculated as RMS values. TEM analysis was performed using a JEOL 2010 transmission electron microscope at 200 keV accelerating voltage. Sheet resistivity measurements were obtained using a Jandel 4-point probe in combination with a Keithley 2400 SourceMeter and a Keithley 2182A Nanovoltmeter. Bulk resistivity was calculated as the product of sheet resistivity and film thickness. All reported resistivity values are the average of 6 or more measurements  $\pm$  the standard deviation. All films passed the Scotch tape test.

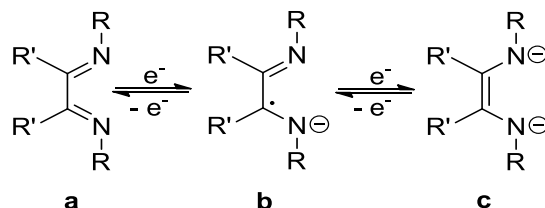
## CHAPTER 4

Evaluation of Mg(II), Al(III), Ti(IV), Zn(II), and Zr(IV) Bis(1,4-di-*tert*-butyl-1,3-diazabutadienyl) Complexes as Precursors for Atomic Layer Deposition

## 4.1 Introduction

The redox non-innocent nature of the  $\alpha$ -diimine ligand enables a neutral, monoanion, or dianion form (Chart 12), depending on the charge of the coordinated cation.<sup>42,321</sup> Complexes of this class are well-documented for the Cr(II),<sup>322</sup> Mn(II),<sup>323</sup> Fe(II),<sup>324</sup> Co(II),<sup>80</sup> and Ni(II)<sup>325</sup> cations. Recently, Winter reported a set of complexes using the 1,4-di-*tert*-butyl-1,3-diazabutadienyl ligand as precursors for CVD and ALD.<sup>42</sup> These M(*t*Bu<sub>2</sub>DAD)<sub>2</sub> complexes (M = Co (3), Ni (4), Fe (5), Cr (6), Mn (7)) self-decompose to metal and present a linear relationship between the thermal decomposition temperature and the reduction potential of the respective cation.<sup>42</sup> Such a ligand-to-metal electron transfer process suggests the utility of these compounds as CVD precursors. Also, as proposed in Chapter 3, this decomposition pathway may be useful in providing a seed layer for ALD growth. Consequently, further attention is warranted toward similar compounds as potential ALD precursors. Herein, the electronic structure and thermal properties are described for previously-reported M(*t*Bu<sub>2</sub>DAD)<sub>2</sub> complexes (M = Mg (8),<sup>326</sup> Ti (9),<sup>327</sup> Zn (10),<sup>326</sup> Zr (11),<sup>328</sup> Al (12)),<sup>329</sup> along with the novel Al(*t*Bu<sub>2</sub>DAD)Cl<sub>2</sub> (13).

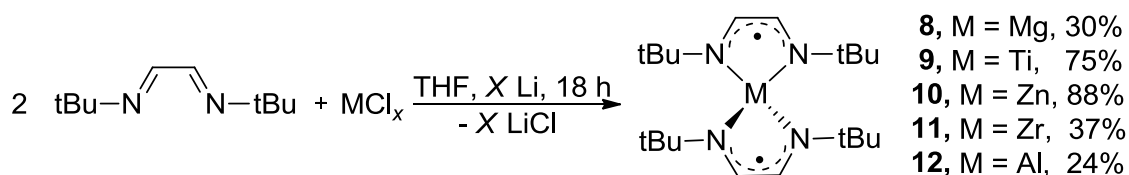
**Chart 12.** Three forms of the redox non-innocent  $\alpha$ -diimine ligand: (a) neutral ligand, (b) radical monoanion, (c) dianion.



## 4.2 Results and Discussion

**Synthesis.** Treatment of anhydrous metal chlorides ( $MCl_x$ ,  $M = Mg, Ti, Zn, Zr$ ) with two equivalents of  $tBu_2DAD$  and  $X$  equivalents of lithium metal afforded complexes of the formula  $M(tBu_2DAD)_2$  as black-red (**8**), black-red (**9**), brown-green (**10**), and orange (**11**) powders (Figure 147). The attempted synthesis of a novel five-coordinate  $Al(tBu_2DAD)_2Cl$  compound employed the treatment of anhydrous  $AlCl_3$  with two equivalents of  $tBu_2DAD$  and two equivalents of lithium metal. Instead, a mixture of  $Al(tBu_2DAD)_2$  as green (**12**) and  $Al(tBu_2DAD)Cl_2$  as black-orange (**13**) powders were produced. Sublimation of the crude materials yielded air-sensitive crystalline products. Compound **13** is a monomer, as are the related monomeric complexes  $FeCl_3(tBu_2DAD)$ ,<sup>330a</sup>  $CoCl_2(tBu_2DAD)$ ,<sup>330b</sup> and  $NiBr_2(tBu_2DAD)$ ,<sup>330c</sup> which differ from the dimer  $Ti(tBu_2DAD)Cl_2$ .<sup>327</sup> The formation of **12** by this method requires the reduction of one equivalent of the  $tBu_2DAD$  monoanion to a dianionic state, highlighting the ability of this ligand to participate in electron transfer processes. It is not possible to prepare  $Cu(II)$  or  $Cu(I)$  complexes containing  $tBu_2DAD$  ligands, as the reduction potentials for these ions ( $Cu(II)$ : 0.342 V,  $Cu(I)$ : 0.521 V)<sup>41</sup> result in the spontaneous self-reduction to  $Cu$  metal.<sup>42</sup> By contrast, the attempted synthesis of  $Ti(II)(tBu_2DAD)_2$  from  $TiCl_2$  resulted in the self-oxidation of  $Ti(II)$  to  $Ti(IV)$  and the concurrent reduction of the  $tBu_2DAD$  ligands from monoanions to dianions, as determined from bond length measurements of a low-resolution crystal structure.

**Figure 147.** Synthesis of metal diazadienyl complexes.





The effect of the ligand oxidation state on electron shielding can be observed by comparing the proton shifts of the  ${}^t\text{Bu}_2\text{DAD}$  ligand with the diamagnetic complexes **4**, **9**, and **11**. The signals for the imine proton of **9** and **11** are shifted to higher field relative to the neutral ligand (Figure 148), and are in good agreement with NMR data from other dianionic diimine ligands.<sup>293</sup> By contrast, the imine proton of **4** shows a downfield shift due to proton deshielding. Figure 149 shows the deshielding of the *tert*-butyl protons of **4**, **9**, and **11** relative to the  ${}^t\text{Bu}_2\text{DAD}$  ligand.

**Figure 148.**  ${}^1\text{H}$  NMR spectra of the ligand backbone (imine) proton for diamagnetic  ${}^t\text{Bu}_2\text{DAD}$  complexes.

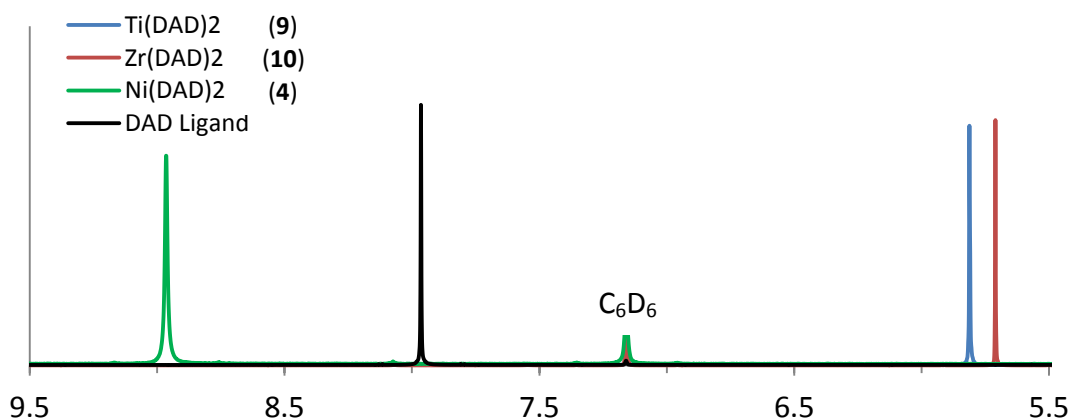
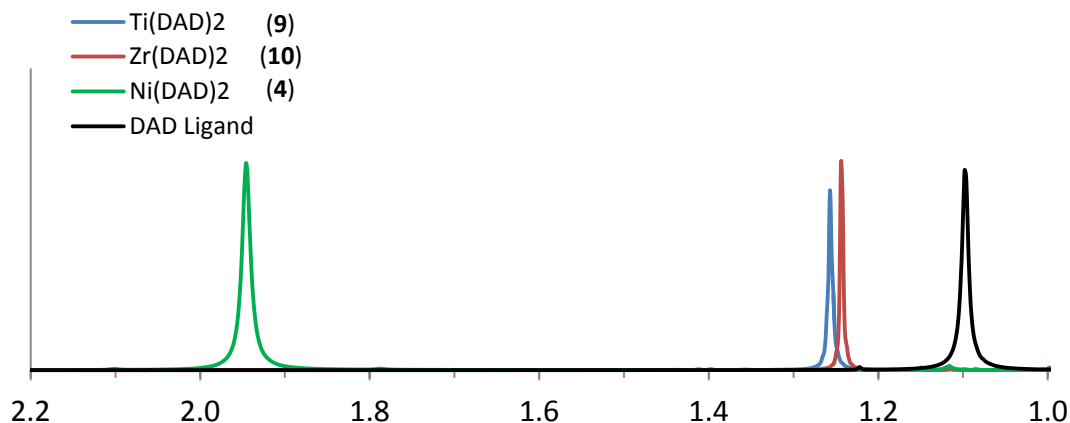


**Figure 149.**  ${}^1\text{H}$  NMR spectra of the *tert*-butyl proton for diamagnetic  ${}^t\text{Bu}_2\text{DAD}$  complexes.



**Structural Aspects.** An X-ray crystal structure was determined for the novel compound **13** (Figure 150). The ligand framework contains a carbon-carbon bond of 1.395 Å and nitrogen-carbon bonds of 1.334–1.345 Å (Table 11). These lengths are intermediate to those expected for single or double bonds, and are thus diagnostic of the radical anion form of the 'Bu<sub>2</sub>DAD ligand. The calculated density of **13** was 1.227 g/cm<sup>3</sup>. X-ray crystal structures were previously reported for **8**,<sup>326</sup> **10**,<sup>326</sup> and **12**.<sup>329</sup> Herein, structures were determined for **8**, **9**, and **12**, with calculated crystalline densities of 1.020, 1.535, and 1.188 g/cm<sup>3</sup>, respectively. Analysis of **9** revealed metallic dark black-red coxcomb crystals, however, the structure was of very low resolution. The structure of **11** has not been previously reported, and attempts to solve it herein were unsuccessful.

**Figure 150.** Perspective view of **13** with thermal ellipsoids at the 50% probability level.

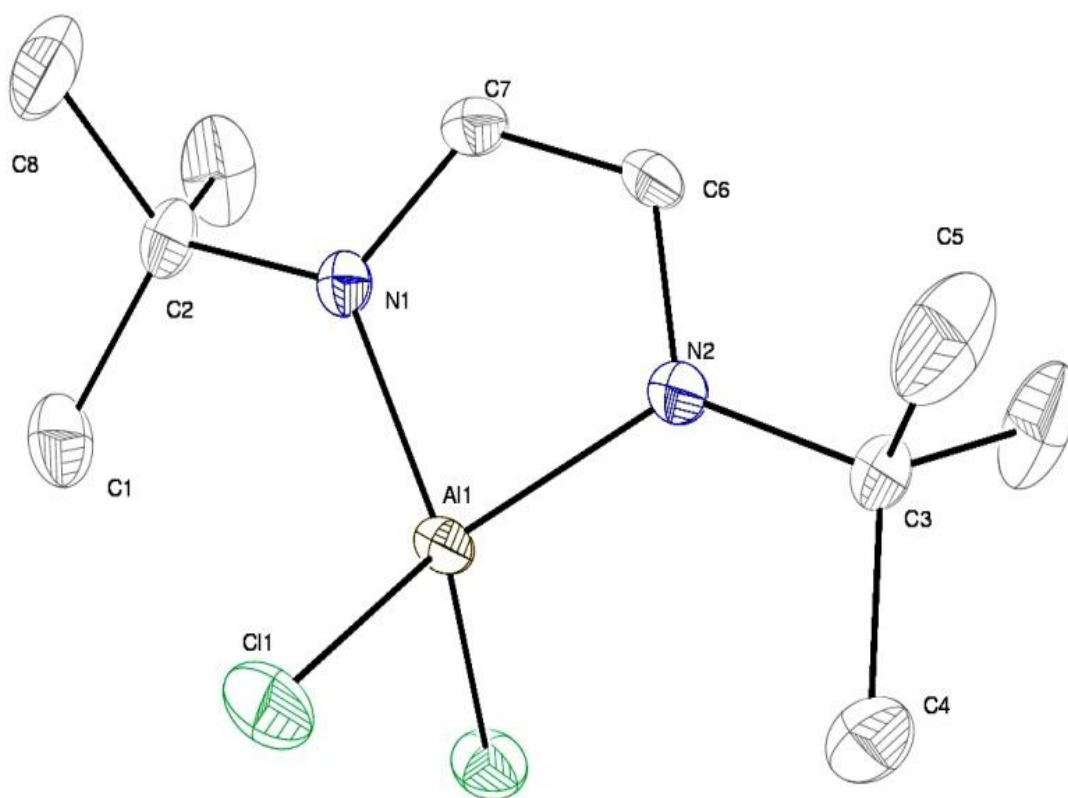


**Table 11.** Crystal data, collection parameters, bond lengths (Å) and angles (°) for **13**.

Chemical formula	$C_{10}H_{20}AlCl_2N_2$	Al1-N1	1.8712(15)
Formula weight	266.16	Al1-N2	1.8748(16)
Crystal size (mm)	$0.111 \times 0.263 \times 0.374$	Al1-Cl1	2.1284(4)
Crystal habit	clear dark black-orange prism	N1-C2	1.482(2)
Crystal system	monoclinic	N1-C7	1.345(2)
Space group	P 1 21 1	N2-C3	1.489(2)
a (Å)	7.0771(3)	N2-C6	1.334(2)
b (Å)	10.0638(5)	C1-C2	1.523(3)
c (Å)	10.4824(4)	C2-C8	1.5262(18)
$\alpha$ (°)	90	C3-C4	1.521(3)
$\beta$ (°)	105.220(2)	C3-C5	1.5157(19)
$\gamma$ (°)	90	C6-C7	1.395(3)
V (Å <sup>3</sup> )	720.40(5)		
Z	2	N1-Al1-N2	89.20(7)
T (K)	100(2)	N1-Al1-Cl1	114.03(3)
$\lambda$ (Å)	0.71073	N2-Al1-Cl1	113.87(3)
$\rho_{\text{calcd}}$ (g·cm <sup>-3</sup> )	1.227	Cl1-Al1-Cl1	110.49(3)
$\mu$ (mm <sup>-1</sup> )	0.486	C2-N1-Al1	131.61(12)
R1 (%)	3.29	C7-N1-Al1	107.75(12)
wR2	7.56	C3-N2-Al1	131.82(12)
		C6-N2-Al1	108.12(12)
R(F) = $\Sigma  F_o  -  F_c   / \Sigma F_o $			
$R_w(F)^2 = [\Sigma w(F_o^2 - F_c^2)^2 / \Sigma w(F_o^2)^2]^{1/2}$ for I > 2 $\sigma$ (I)			

**Volatility, Thermal Stability, and Electronic Structure.** The physical properties of **8–13** were studied by preparative sublimation experiments, melting point/solid state thermal decomposition measurements, and magnetic moment measurements. Sublimed recoveries of **8–13** were 82.0–92.3%, with nonvolatile residues  $\leq 5.6\%$ . The air-sensitive nature of **8–13** required the use of an argon-filled glove box, hampering attempts to maximize product isolation. Melting points were in reasonable agreement with the literature for **8** (143 °C reported) and **10** (140 °C reported).<sup>326</sup> By contrast, melting points were found to be considerably higher than literature values for **11** (148 °C reported)<sup>328</sup> and **12** (187 °C reported).<sup>329</sup> Attempts were made to determine the solid state decomposition temperatures of **8–13**. Winter demonstrated a linear relationship

between the thermal decomposition temperature and the  $M(\text{II}) \rightarrow M(0)$  reduction potential for **3–7**.<sup>42</sup> Surprisingly, **10** was observed to commence decomposition at 235 °C, well below the 286 °C proposed by this model for  $\text{Zn}(\text{II}) \rightarrow \text{Zn}(0)$  ( $E^\circ = -0.7926 \text{ V}$ ).<sup>41</sup> The remaining compounds exhibit a very gradual color change upon heating, preventing an accurate determination of their decomposition temperatures. The silver-grey decomposition products obtained by heating **9** and **10** in sealed capillary tubes were mounted in a single crystal diffractometer; no evidence of metal was found for either sample. The lack of metal upon thermal decomposition of **9** and **10** coupled with the lack of well-defined decomposition temperatures for **8–9** and **11–13** suggest that decomposition may occur by a pathway other than reduction from ligand-to-metal electron transfer. This is may be due to the lack of d-electrons in complexes containing  $\text{Mg}(\text{II})$ ,  $\text{Ti}(\text{IV})$ ,  $\text{Zn}(\text{II})$ ,  $\text{Zr}(\text{IV})$ , and  $\text{Al}(\text{III})$  cations. By contrast, the  ${}^t\text{Bu}_2\text{DAD}$  radical anions exhibit antiferromagnetic coupling to d-electrons in the mid-to-late first-row transition metal complexes **3–7**. Additionally, the reduction potentials of Mg, Ti, Zr, and Al are extremely negative (Table 12), thus, other decomposition pathways may be more energetically favorable.

**Table 12.** Electrochemical potentials of metals used in **8–13**.<sup>41</sup>

Reaction	$E^\circ(\text{V})$
$\text{Mg}(\text{II}) + 2e^- \leftrightarrow \text{Mg}(0)$	-2.372
$\text{Ti}(\text{II}) + 2e^- \leftrightarrow \text{Ti}(0)$	-1.631
$\text{Zn}(\text{II}) + 2e^- \leftrightarrow \text{Zn}(0)$	-0.7926
$\text{Zr}(\text{IV}) + 4e^- \leftrightarrow \text{Zr}(0)$	-1.45
$\text{Al}(\text{III}) + 3e^- \leftrightarrow \text{Al}(0)$	-1.676

Solid state magnetic moment data suggest two radical anion ligands in **8** and **10**. Compound **12** contains one radical anion ligand and one dianion ligand, while **13** contains a single radical anion ligand, in good agreement with crystal structure bond length measurements. Compounds **9** and **11** each possess two dianion ligands, with no unpaired electrons for detection.

**Table 13.** Preparative sublimation data, melting point, solid state decomposition temperature, and magnetic moment data for **8–13**.

	Prep. Subl. (°C/0.05 Torr)	Recovered (%)	Non-volatile Residue (%)	Melting Point (°C)	Decomp. (°C)	Solid State Magnetic Moment ( $\mu_B$ )	
						Observed	Expected
<b>8</b>	110	82.0	1.1	143–144	-----	2.83	2.83
<b>9</b>	120	88.6	2.0	129–132	-----	n/a	n/a
<b>10</b>	115	91.1	0.4	135–137	235–245	2.81	2.83
<b>11</b>	110	89.7	1.0	175–178	-----	n/a	n/a
<b>12</b>	125	92.3	2.9	196–201	-----	1.74	1.73
<b>13</b>	105	88.9	5.6	157–158	-----	1.75	1.73

### 4.3 Conclusions

Compounds **8–13** were evaluated as potential ALD precursors. These compounds were synthesized by a salt metathesis approach as a convenient alternative to previously-described methods using metal vapor<sup>329</sup> or Rieke metals.<sup>326</sup> All sublime at low temperatures ( $\leq 125$  °C/0.05 Torr) with little non-volatile residue remaining. Complex **10** is a promising ALD precursor, as it sublimes without residue and is thermally stability to  $\sim 235$  °C. By contrast to their mid-to-late transition metal analogues,<sup>42</sup> **8–13** appear to decompose by a pathway other than reduction from ligand-to-metal electron transfer. The novel compound **13** is a monomer in the solid state. Magnetic moment data confirm the expected forms of the <sup>t</sup>Bu<sub>2</sub>DAD ligand for paramagnetic complexes **8**, **10**, **12**, and **13**.

## 4.4 Experimental

**General Considerations.** All manipulations were carried out under argon using either Schlenk or glove box techniques. All glassware was oven-dried at  $\geq 150$  °C prior to use. Tetrahydrofuran and diethyl ether were distilled from sodium benzophenone ketyl and sodium metal. Hexanes was distilled from  $P_2O_5$ . All chemicals were obtained from Sigma Aldrich or Alpha Aesar and used as received. 1,4-di-*tert*-butyl-1,3-diazabutadiene was prepared according to a literature procedure.<sup>317</sup>

$^1H$  and  $^{13}C\{^1H\}$  NMR spectra were obtained at 400 and 100 MHz respectively, and were referenced to the residual proton and the  $^{13}C$  resonances of the solvent. Melting points and decomposition temperatures were determined using an Electrothermal (45 W) melting point apparatus and are uncorrected; each sample was prepared as described in Chapter 2. Data are reported as the average of a minimum of 3 measurements. Infrared spectra were obtained on a Shimadzu IRAffinity-1 spectrometer with a MIRacle 10 single reflection ATR accessory, using mineral oil as the medium. Magnetic moments were determined in the solid state using a Johnson Mathey MSB-1 magnetic susceptibility balance. Sublimations were performed using either a Büchi B-580 or Büchi B-585 sublimation oven. Preparative sublimation experiments used 0.5–1.0 g samples at 0.05 Torr and were performed as described in Chapter 2. The temperature was adjusted such that each sublimation experiment was completed in less than three hours. Single-crystal X-ray structures were obtained using a Bruker D8 single crystal diffractometer. The frames were integrated with the Bruker SAINT software package using a narrow-frame algorithm. The structures were solved and refined using the Bruker SHELXL-2013 (Sheldrick, 2013) software package.

**Preparation of Bis(1,4-di-*tert*-butyl-1,3-diazabutadienyl)magnesium (II) (8).**

A 100 mL Schlenk flask, equipped with a magnetic stir bar and a rubber septum, was charged with <sup>t</sup>Bu<sub>2</sub>DAD (2.037 g, 12.111 mmol) and THF (40 mL). Lithium metal pellets (0.085 g, 12.248 mmol) were slowly added at ambient temperature, and the resultant dark red-brown solution was stirred for 18 h. This solution was then added by cannula over a period of 10 min to a stirred suspension of anhydrous MgCl<sub>2</sub> (0.567 g, 5.955 mmol) in THF (40 mL) at -78 °C. The resultant dark brown solution was stirred for 72 hr at ambient temperature, turning dark green after 15 min. The volatile components were removed under reduced pressure. Dark black-red crystals of **8** were obtained by sublimation at 110 °C/0.05 Torr (0.658 g, 30%): mp 143–144 °C (reported: 143 °C);<sup>326</sup> IR (mineral oil, cm<sup>-1</sup>) 2121 (w), 2054 (w), 1835 (w), 1742 (m), 1691 (m), 1645 (m), 1544 (m), 1529 (m), 1514 (m), 1463 (m), 1423 (m), 1392 (m), 1361 (m), 1255 (m), 1209 (s), 1023 (w), 931 (w), 771 (m);  $\mu_{\text{eff}} = 2.83 \mu_{\text{B}}$  in the solid state.

**Preparation of Bis(1,4-di-*tert*-butyl-1,3-diazabutadienyl)titanium(IV) (9).**

A 100 mL Schlenk flask, equipped with a magnetic stir bar and a rubber septum, was charged with <sup>t</sup>Bu<sub>2</sub>DAD (5.470 g, 32.521 mmol) and THF (70 mL). Lithium metal pellets (0.465 g, 67.003 mmol) were slowly added at ambient temperature, and the resultant solution was stirred for 18 h. This solution was then added by cannula to a stirred solution of anhydrous TiCl<sub>4</sub> (2.820 g, 14.867 mmol) in hexanes (30 mL). The resultant solution was stirred for 24 h at ambient temperature. The volatile components were removed under reduced pressure and the resultant crude material was dissolved in hexanes (70 mL). The solution was filtered through a 1-inch pad of Celite on a coarse glass frit, followed by removal of hexanes under reduced pressure. Dark black-red crystals of **9** were obtained by sublimation at 120 °C/0.05 Torr (4.305 g, 75%): mp 129–132 °C; IR (mineral oil, cm<sup>-1</sup>) 1474 (w), 1392 (m), 1359 (m), 1217 (s), 1151 (m), 1102 (w),

1060 (w), 1021 (w), 939 (w), 864 (m), 812 (m), 777 (m);  $^1\text{H}$  NMR (400 MHz,  $\text{C}_6\text{D}_6$ , 23 °C,  $\delta$ ) 5.81 (s, 4H, CH), 1.26 (s, 36H,  $\text{C}(\text{CH}_3)_3$ );  $^{13}\text{C}\{^1\text{H}\}$  NMR (400 MHz,  $\text{C}_6\text{D}_6$ , 23 °C, ppm) 102.29 (s, CH), 58.40 (s,  $\text{C}(\text{CH}_3)_3$ ), 32.05 (s,  $\text{C}(\text{CH}_3)_3$ ).

**Preparation of Bis(1,4-di-*tert*-butyl-1,3-diazabutadienyl)zinc(II) (10).**

A 100 mL Schlenk flask, equipped with a magnetic stir bar and a rubber septum, was charged with  $^t\text{Bu}_2\text{DAD}$  (5.000 g, 29.727 mmol) and THF (30 mL). Lithium metal pellets (0.207 g, 29.827 mmol) were slowly added at ambient temperature, and the resultant solution was stirred for 18 h. This solution was then added by cannula to a stirred suspension of  $\text{ZnCl}_2$  (2.030 g, 14.892 mmol) in THF (20 mL). The resultant dark green solution was stirred for 24 h at ambient temperature. The volatile components were removed under reduced pressure. Dark brown-green crystals of **10** were obtained by sublimation at 115 °C/0.05 Torr (5.264 g, 88%): mp 135–137 °C (reported: 140 °C);<sup>326</sup> IR (mineral oil,  $\text{cm}^{-1}$ ) 2124 (w), 1699 (m), 1681 (m), 1651 (m), 1558 (m), 1539 (m), 1521 (m), 1508 (m), 1473 (m), 1454 (m), 1361 (m), 1255 (m), 1211 (s), 1041 (w), 1016 (w), 936 (w), 767 (m);  $\mu_{\text{eff}} = 2.81 \mu_{\text{B}}$  in the solid state.

**Preparation of Bis(1,4-di-*tert*-butyl-1,3-diazabutadienyl)zirconium(IV) (11).**

A 100 mL Schlenk flask, equipped with a magnetic stir bar and a rubber septum, was charged with  $^t\text{Bu}_2\text{DAD}$  (3.061 g, 18.199 mmol) and diethyl ether (30 mL). Lithium metal pellets (0.297 g, 42.795 mmol) were slowly added at ambient temperature, and the resultant solution was stirred for 18 h. This solution was then added by cannula to a stirred suspension of anhydrous  $\text{ZrCl}_4$  (1.638 g, 7.029 mmol) in diethyl ether (20 mL). The resultant rust-brown solution was stirred for 72 h at ambient temperature. The volatile components were removed under reduced pressure. Dark orange crystals of **10** were obtained by sublimation at 110 °C/0.05 Torr (1.094 g, 37%): mp 175–178 °C (reported: 148 °C);<sup>328</sup> IR (mineral oil,  $\text{cm}^{-1}$ ) 1560 (w), 1518 (w), 1457 (w), 1386 (m),



1357 (m), 1244 (m), 1215 (s), 1130 (s), 1088 (w), 1059 (w), 1014 (w), 974 (w), 941 (m), 866 (s), 807 (w), 763 (s);  $^1\text{H}$  NMR (400 MHz,  $\text{C}_6\text{D}_6$ , 23 °C,  $\delta$ ) 5.71 (s, 4H, CH), 1.24 (s, 36H, C(CH<sub>3</sub>)<sub>3</sub>);  $^{13}\text{C}\{^1\text{H}\}$  NMR (400 MHz,  $\text{C}_6\text{D}_6$ , 23 °C, ppm) 104.21 (s, CH), 56.42 (s, C(CH<sub>3</sub>)<sub>3</sub>), 32.11 (s, C(CH<sub>3</sub>)<sub>3</sub>).

**Preparation of Bis(1,4-di-*tert*-butyl-1,3-diazabutadienyl)aluminum(III) (12) and 1,4-Di-*tert*-butyl-1,3-diazabutadienyl-dichloroaluminum(III) (13).**

A 100 mL Schlenk flask, equipped with a magnetic stir bar and a rubber septum, was charged with  $^t\text{Bu}_2\text{DAD}$  (4.973 g, 29.566 mmol) and diethyl ether (40 mL). Lithium metal pellets (0.221 g, 31.844 mmol) were slowly added at ambient temperature, and the resultant dark brown solution was stirred for 18 h. This solution was then added by cannula to a stirred suspension of anhydrous  $\text{AlCl}_3$  (1.987 g, 14.902 mmol) in diethyl ether (20 mL). The resultant dark green solution was stirred for 18 h at ambient temperature. The volatile components were removed under reduced pressure. Dark black-orange crystals of **13** were obtained by sublimation at 105 °C/0.05 Torr (1.282 g, 32%): mp 157–158 °C; IR (mineral oil,  $\text{cm}^{-1}$ ) 1527 (w), 1469 (m), 1454 (m), 1392 (w), 1369 (s), 1330 (m), 1263 (w), 1197 (s), 1062 (w), 964 (m), 840 (w), 781 (s);  $\mu_{\text{eff}} = 1.75 \mu_{\text{B}}$  in the solid state. Green crystals of **12** were obtained by sublimation at 125 °C/0.05 Torr (1.300 g, 24%): mp 196–201 °C (reported: 187 °C);<sup>329</sup> IR (mineral oil,  $\text{cm}^{-1}$ ) 1739 (w), 1699 (m), 1678 (m), 1651 (m), 1558 (m), 1539 (m), 1514 (m), 1473 (m), 1454 (m), 1361 (m), 1253 (m), 1220 (s), 1197 (s), 1095 (s), 1035 (w), 985 (m), 952 (w), 785 (m);  $\mu_{\text{eff}} = 1.74 \mu_{\text{B}}$  in the solid state.

## CHAPTER 5

### Unusual Stoichiometry Control in the Atomic Layer Deposition of Manganese Borate Films from Manganese Bis(tris(pyrazolyl)borate) and Ozone

#### 5.1 Introduction

Metal borates are constituents in nonlinear optical crystals.<sup>331</sup> The bonding structure of the boron atoms has a strong effect on nonlinear (second-order) optical behavior.<sup>332</sup>  $\beta$ -BaB<sub>2</sub>O<sub>4</sub> is a frequency-doubling, second harmonic generating (SHG) material of visible and near IR laser light.<sup>333</sup> It is one of only a few SHG materials for use below 500 nm.<sup>333</sup> Thin films of  $\beta$ -BaB<sub>2</sub>O<sub>4</sub> are used in optical devices such as frequency converters, waveguides, and switches.<sup>333</sup> Recently, first-row transition metal borates have emerged as oxygen evolution catalysts,<sup>334</sup> cathode materials in lithium ion batteries,<sup>288</sup> catalysts for H<sub>2</sub> production by hydrolysis of sodium borohydride,<sup>335</sup> and superhydrophilic films.<sup>336</sup>

For many applications, metal borates need to be grown as thin films on various substrates. Thin films of cobalt borate and nickel borate were electrodeposited from solutions of the metal ions in the presence of borate buffers,<sup>334</sup> while nanowhiskers of Ni<sub>3</sub>(BO<sub>3</sub>)<sub>2</sub> were grown on nickel substrates by a molten salt method.<sup>336</sup> Metal borate thin film growth by gas phase processes is complicated by the high vapor pressure of B<sub>2</sub>O<sub>3</sub>, which often makes it difficult to control the metal/boron ratios in the thin films. As an example, BaB<sub>2</sub>O<sub>4</sub> films were grown by DLI-CVD from an organic solution containing Ba(tmhd)<sub>2</sub>(tetraglyme) and Ba(O<sup>i</sup>Pr)<sub>3</sub>, with O<sub>2</sub> and N<sub>2</sub>O as the oxidizer gases.<sup>337</sup> Film growth was achieved between 640 and 840 °C, but a 1.0:2.5 Ba:B precursor stoichiometry was required to obtain BaB<sub>2</sub>O<sub>4</sub> films. Thin films of Mg<sub>2</sub>B<sub>2</sub>O<sub>5</sub><sup>338a</sup> and  $\beta$ -BaB<sub>2</sub>O<sub>4</sub><sup>338b</sup> were grown by CVD using MgTp<sub>2</sub> and [BaTp<sub>2</sub>]<sub>2</sub><sup>339a</sup> (Tp = tris(pyrazolyl)borate), respectively, at 750–900 °C with O<sub>2</sub> as the coreagent. The Tp ligands provided the boron atoms,

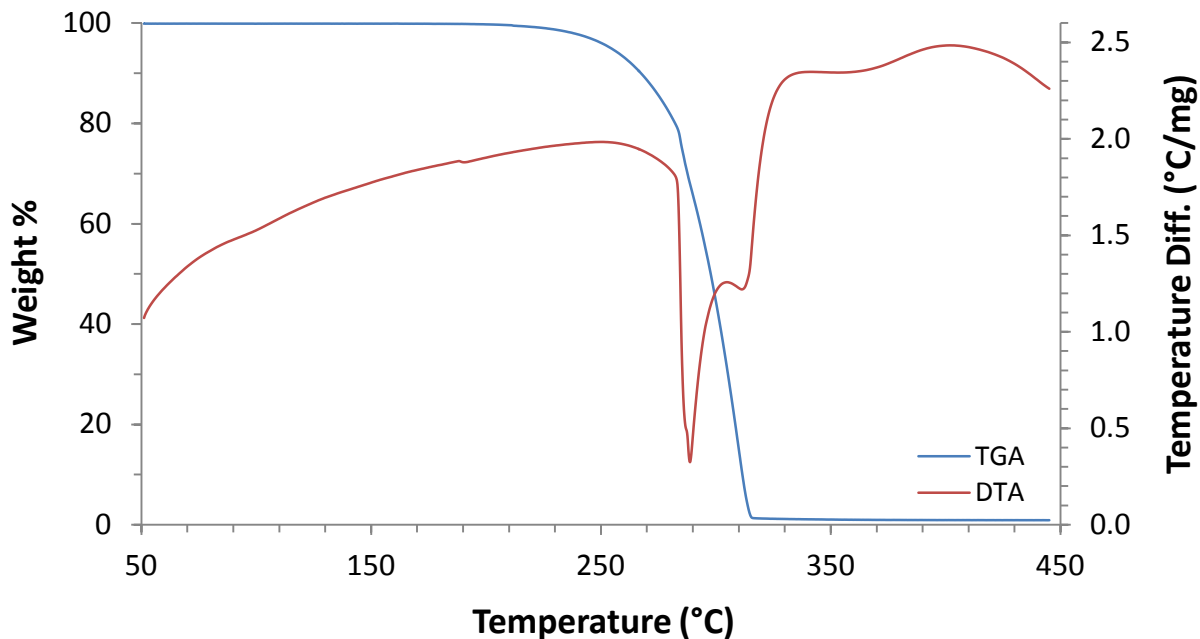
however, the 2:1 boron:metal stoichiometry in  $\text{MgTp}_2$  was not retained in the  $\text{Mg}_2\text{B}_2\text{O}_5$  film.<sup>338a</sup>  $\text{B}_2\text{O}_3$  is known to volatilize from borate films at  $\sim 400$  °C, above which it is postulated that the film favors the composition of greatest thermodynamic stability.<sup>339b-d</sup> The ALD of  $\text{MB}_2\text{O}_4$  films (M = Ca, Sr, Ba) was subsequently reported between 250 and 400 °C using  $\text{CaTp}_2$ ,  $\text{SrTp}_2$ , and  $\text{BaTp}^{\text{Et}_2}_2$  as the metal and boron precursors and water as the oxygen source.<sup>339b-d</sup> Very significantly, the 2:1 boron/metal ratio in the precursors was retained in the  $\text{MB}_2\text{O}_4$  films, thereby providing a potentially general method for controlling the stoichiometry in borate thin films.<sup>339b-d</sup> ALD growth from bimetallic precursors does not typically replicate the exact precursor stoichiometries in the resultant films.<sup>340</sup> Thus, given the increasing importance of first-row transition metal borates,<sup>288,334-336</sup> the application of transition metal  $\text{MTP}_2$  precursors for the ALD of thin films warrants further exploration.

The thermal properties of  $\text{MTP}_2$  (M = Mn (**14**), Fe (**15**), Co (**16**), Ni (**17**), Cu (**18**), Zn (**19**)) were recently investigated.<sup>341</sup> These compounds are thermally-stable to 290–370 °C. Preparative sublimations (200–210 °C/0.05 Torr) showed  $\geq 98.8\%$  recovery with no residue for **14–17** and **19**, and 86.5% recovery with 7.3% residue for **18**.<sup>341</sup> Compounds **14** and **16** have solid state decomposition temperatures of 370 and 340 °C,<sup>341</sup> respectively, and are promising candidates for ALD precursors.

## 5.2 Results and Discussion

### 5.2.1 $\text{Mn}_3(\text{BO}_3)_2$ Films from Bis(tris(pyrazolyl)borate)Mn(II) and Ozone

TGA/DTA analyses of **14** showed a single-step weight loss (blue) overlapping the sole endotherm (red) from 240–315 °C (Figure 151). Consistent with the reported preparative sublimation data,<sup>341</sup> no remaining residue was detected.

**Figure 151.** TGA/DTA analyses of **14**.

Films were grown on Si(100) substrates with a native oxide layer. Saturation was determined by varying the length of one precursor pulse while keeping the other fixed at a saturative dose for 2,000 cycles. Figure 152 shows the dependence of growth rate (blue) and consumption rate of **14** (black) on the pulse length of **14**, using 5.0 s ozone pulses. Figure 153 shows the dependence of growth rate on ozone pulse length, using 5.0 s pulses of **14**. Self-limited growth was achieved using a pulsing sequence of 5.0 s **14**/5.0 s N<sub>2</sub> purge/5.0 s ozone/5.0 s N<sub>2</sub> purge, with a measured growth rate of 0.18 Å/cycle at 325 °C. The effect of substrate temperature on film growth was subsequently investigated. A constant growth rate of 0.18 Å/cycle was observed between 300–350 °C. A plot of thickness versus number of cycles was linear, with a growth rate of 0.194 Å/cycle. The y-intercept was –3.827 nm, suggesting efficient nucleation. Films deposited within the 300–350 °C window were non-conductive and showed good adhesion to the Si(100) substrate, passing the Scotch tape test.

**Figure 152.** Saturation plot of **14** using 5.0 s pulses of ozone at 325 °C. The secondary axis shows the consumption rate of **14** as a function of the pulse length of **14**.

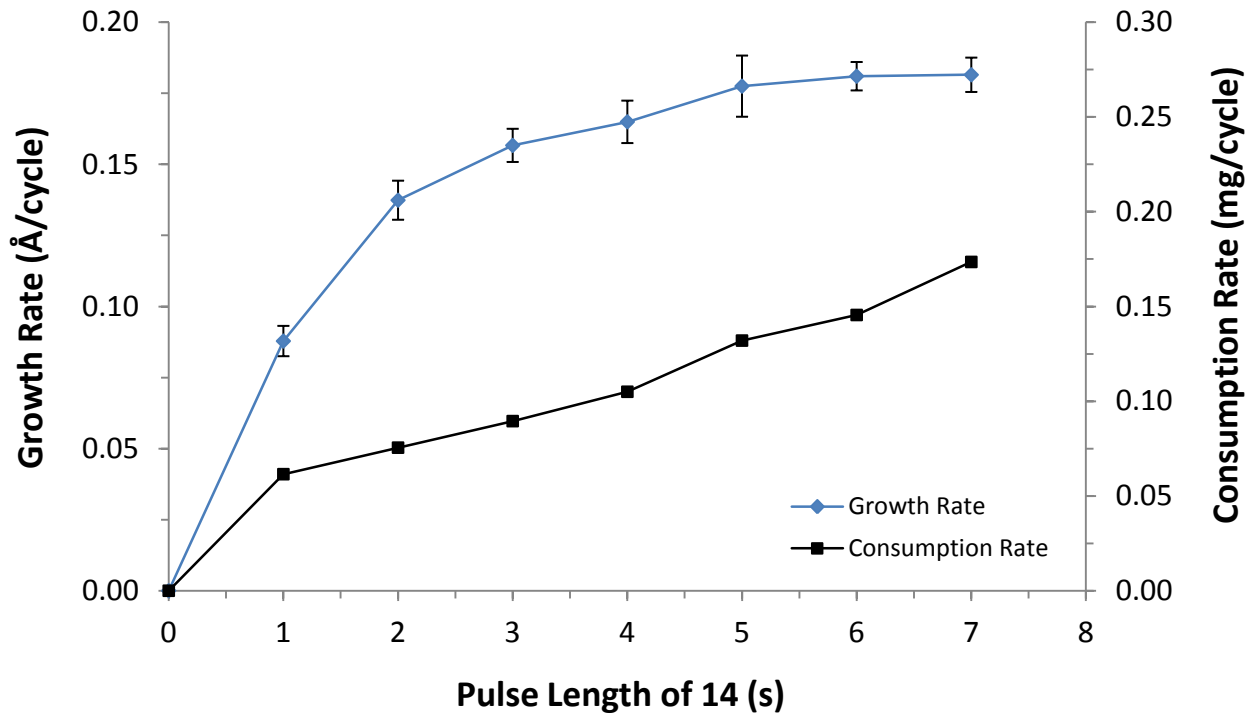


**Figure 153.** Saturation plot of ozone using 5.0 s pulses of **14** at 325 °C.

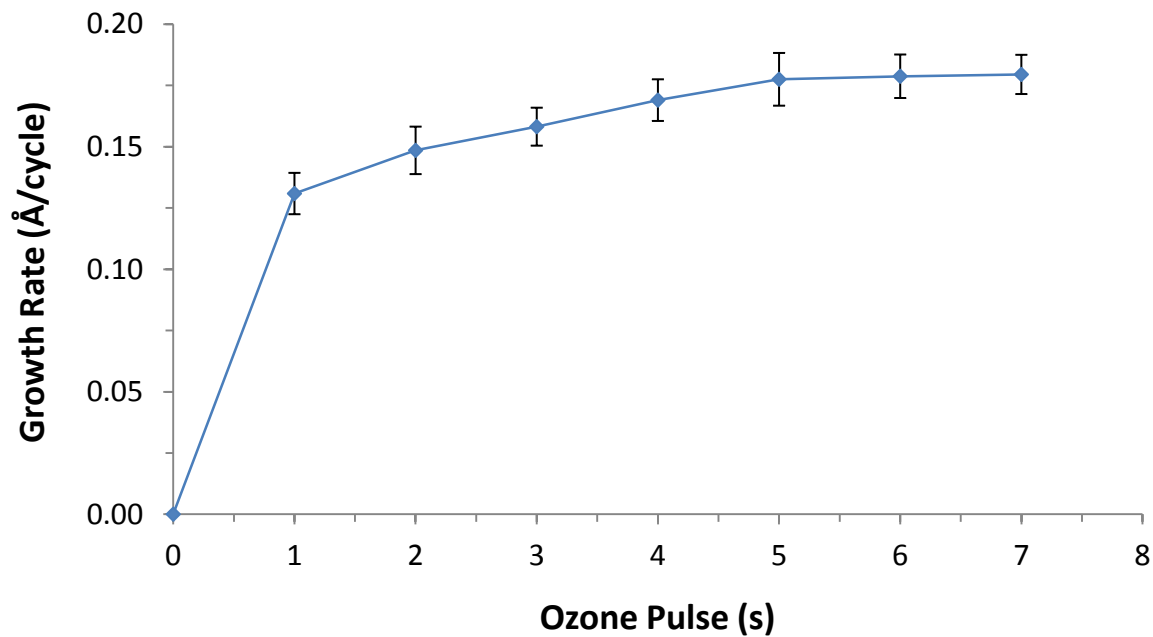


**Figure 154.** Plot of growth rate versus temperature using 5.0 s pulses of **14** and 5.0 s pulses of ozone for 2,000 cycles.

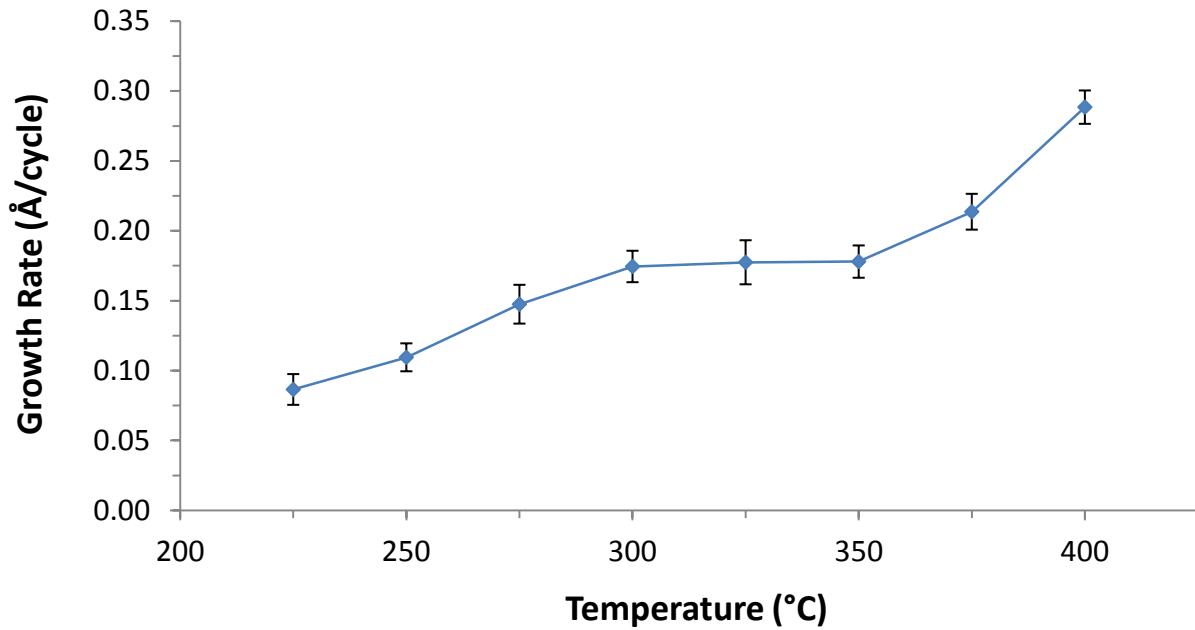
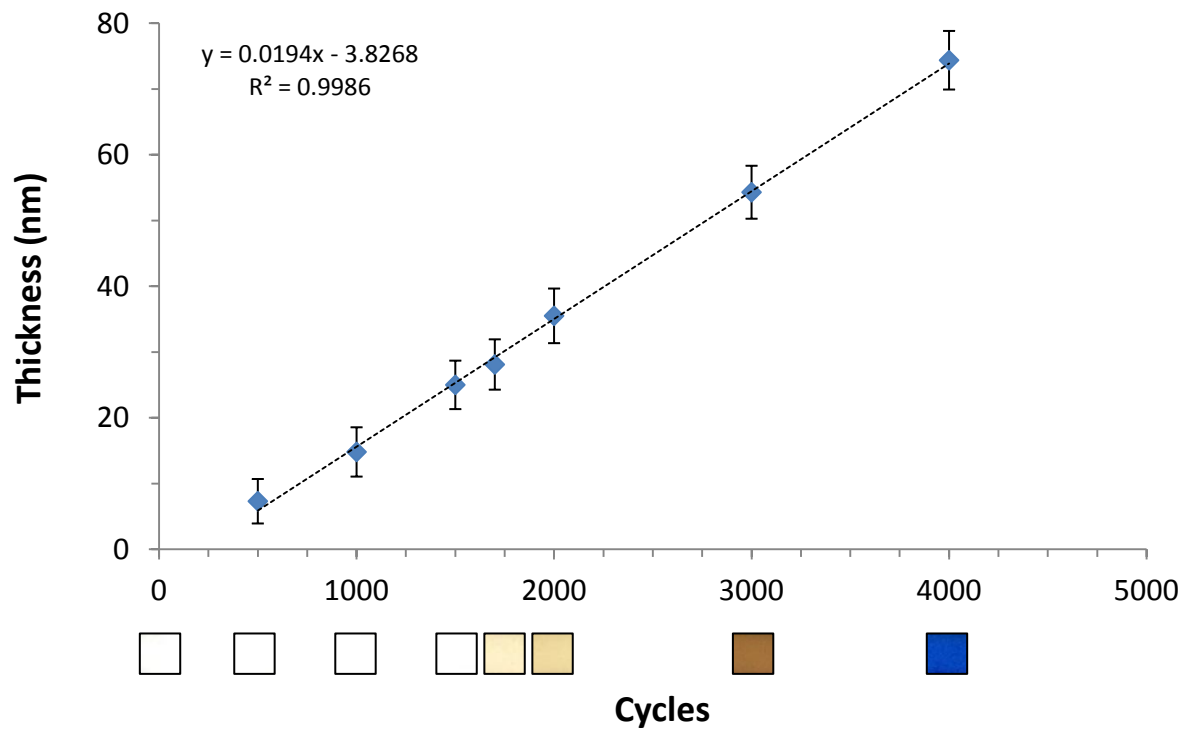


**Figure 155.** Plot of film thickness versus number of ALD cycles using **14** and ozone at 325 °C. Images below the x-axis show magnified regions of each film from a single photograph taken of all films.



Microscopic techniques were used to analyze the films. Cross-sectional measurements by SEM revealed uniform films on the Si(100) substrates (Figure 156). The surface morphology was then quantified by AFM (Figure 157). Films grown at 300 and 325 °C showed RMS surface roughnesses of 0.417–0.463 nm, while the film grown at 350 °C was slightly rougher, with RMS values of 0.561 and 0.534 nm for the 3 and 5  $\mu\text{m}^2$  regions, respectively (Table 14). Accordingly, the film surfaces are very smooth.

**Figure 156.** Cross-sectional SEM image of a 56 nm thick film grown on Si(100) from **14** and ozone for 3,000 cycles at 325 °C.

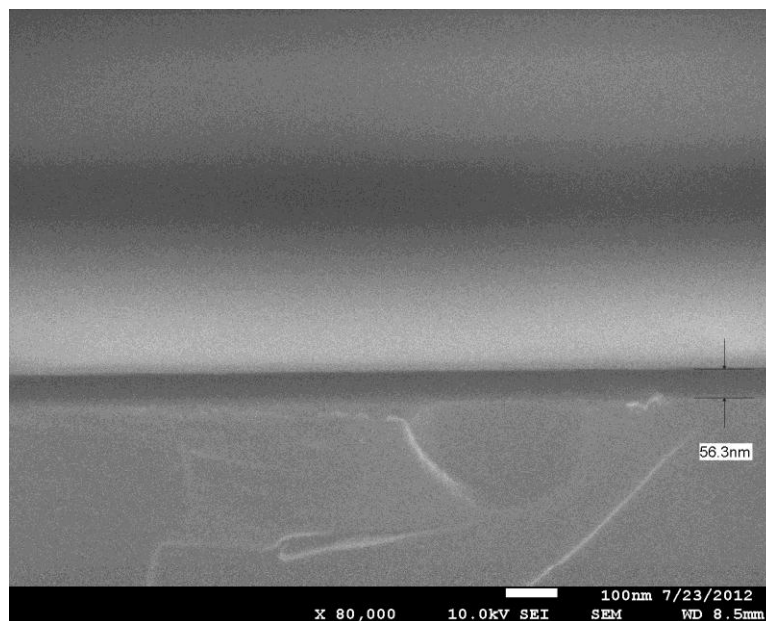


**Figure 157.** AFM images of 3  $\mu\text{m}^2$  regions of films grown from **14** and ozone on Si(100) for 2,000 cycles: (a) 300 °C, (b) 325 °C, (c) 350 °C.

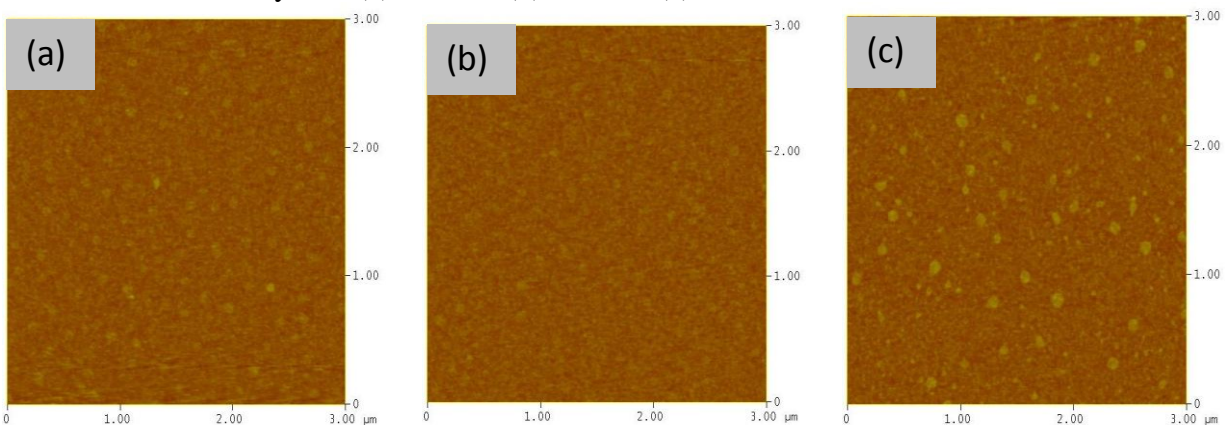


**Table 14.** Surface roughnesses measured by AFM of films grown from **14** and ozone at 300, 325, and 350 °C for 2,000 cycles. Measurements were taken from 3 and 5  $\mu\text{m}^2$  areas.

Deposition Temperature (°C)	Film Thickness (nm)	RMS Roughness (nm)	
		3 $\mu\text{m}^2$	5 $\mu\text{m}^2$
300	35 $\pm$ 2.2	0.463	0.417
325	36 $\pm$ 3.2	0.441	0.428
350	36 $\pm$ 2.4	0.561	0.534

A 36 nm thick film deposited at 325 °C showed no reflections by powder XRD, indicating amorphous material. Identical films grown at 325 °C were annealed under either N<sub>2</sub> or O<sub>2</sub> atmospheres at 100 °C increments from 400–1100 °C for one hour at each temperature. Films remained amorphous after annealing, not matching any known phases for Mn<sub>x</sub>B<sub>y</sub>O<sub>z</sub> compositions. Figures 158–159 show the powder XRD spectrum of the as-deposited film (purple trace), along with the spectra of the films after annealing under either N<sub>2</sub> or O<sub>2</sub> atmospheres at 500, 800, and 1100 °C.

**Figure 158.** Powder XRD spectra of a 36 nm thick film grown from **14** and ozone on Si(100) for 2,000 cycles at 325 °C. The film was annealed under an N<sub>2</sub> atmosphere.

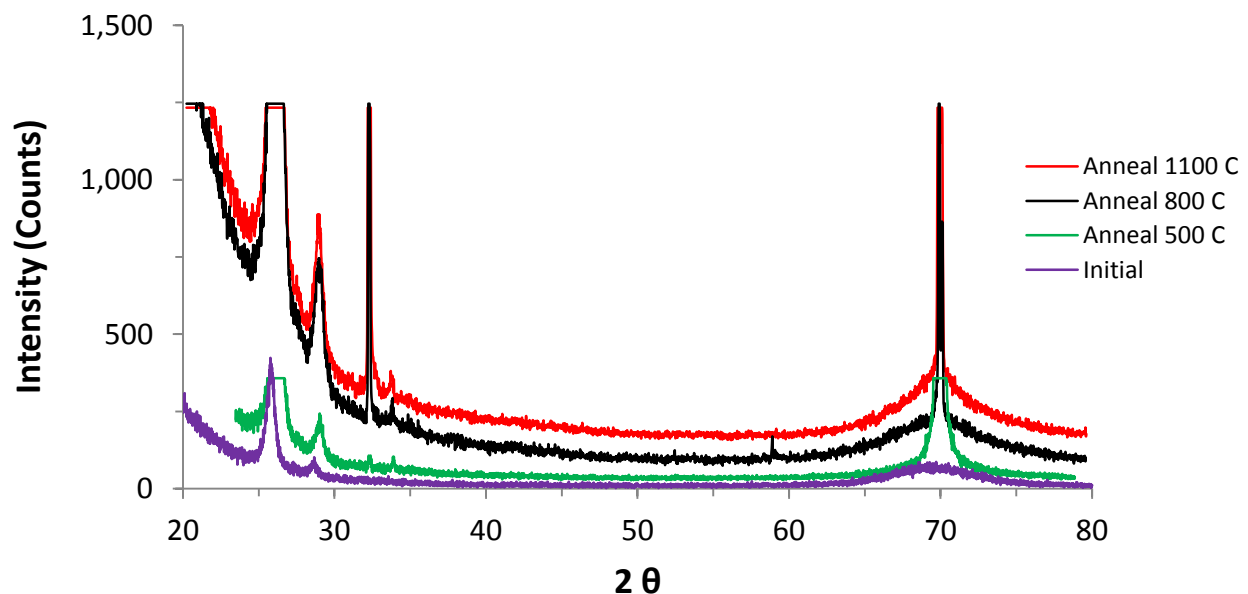
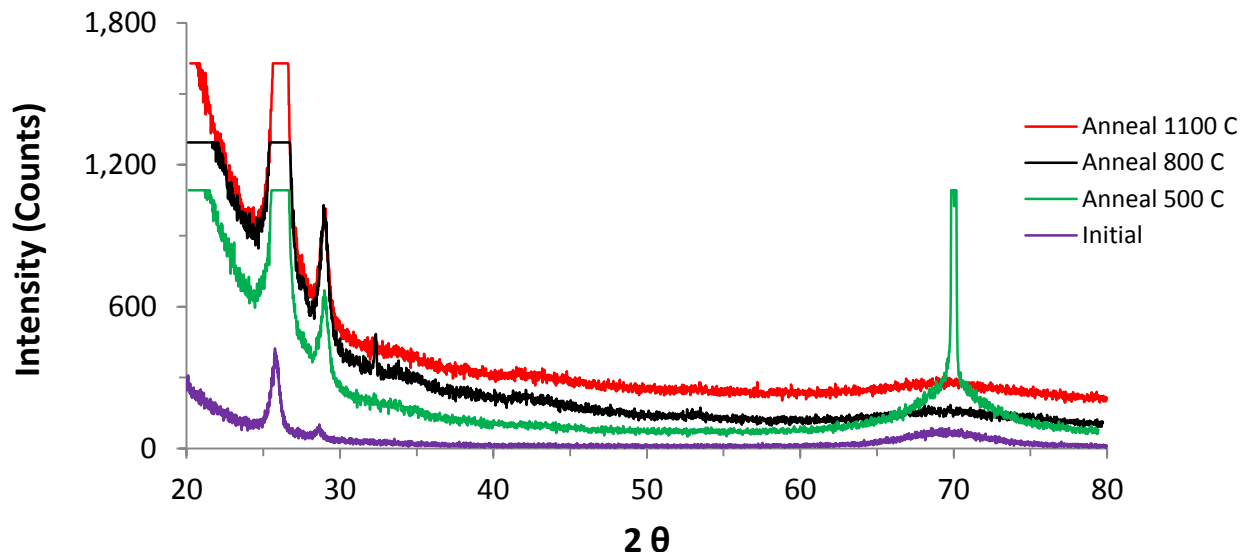




**Figure 159.** Powder XRD spectra of a 36 nm thick film grown from **14** and ozone on Si(100) for 2,000 cycles at 325 °C. The film was annealed under an O<sub>2</sub> atmosphere.



Compositional analyses were performed on 35–36 nm thick films grown within the 300–350 °C ALD window. XPS survey scans revealed carbon and nitrogen contamination in the as-deposited films which were below the detection limits (< 0.5%) after 1 min of argon ion sputtering. After 2 min of sputtering, films grown at 300, 325, and 350 °C showed atomic compositions of Mn<sub>1.87</sub>B<sub>2</sub>O<sub>4.24</sub>, Mn<sub>1.76</sub>B<sub>2</sub>O<sub>4.35</sub>, and Mn<sub>1.82</sub>B<sub>2</sub>O<sub>4.47</sub>, respectively. However, these data likely have high uncertainties due to the small ionization cross sections of boron and oxygen. The high-resolution spectra of the B 1s and Mn 2p ionization regions were identical for all films after 2 min of sputtering, implying that the oxidation states of boron and manganese do not change within the ALD window.

TOF-ERDA was performed to obtain more precise stoichiometries. Films grown at 300, 325, and 350 °C afforded compositions of Mn<sub>2.58</sub>B<sub>2</sub>O<sub>6.75</sub>, Mn<sub>3.02</sub>B<sub>2</sub>O<sub>7.75</sub>, and Mn<sub>2.65</sub>B<sub>2</sub>O<sub>6.98</sub>, respectively (Figures 165–167). Among various known borates, these values are closest to Mn<sub>3</sub>(BO<sub>3</sub>)<sub>2</sub>.<sup>288c</sup> The films contained significant carbon (C<sub>0.21–0.26</sub> versus B<sub>1.00</sub>) and hydrogen (H<sub>0.90–1.09</sub> versus B<sub>1.00</sub>), however, the concentrations of these elements decreased deeper in the

films. Consistent with the XPS data, these impurities likely correspond to weakly-bound surface hydrocarbon species. Additionally, TOF-ERDA data show that the surfaces of the films have greater manganese content, with similar surface densities observed for all films ( $\sim 300 \times 10^{15}$  at./cm<sup>2</sup>).

**Table 15.** XPS atomic concentrations (at.%) of 35–36 nm thick films grown from **14** and ozone on Si(100) after 2 minutes of sputtering.

Deposition Temperature (°C)	% Mn	% B	% O	% C	% N
300	22.9	24.5	52.0	0.3	0.3
325	21.5	24.5	53.4	0.3	0.3
350	21.8	23.9	53.4	0.4	0.5

**Figure 160.** XPS survey scans of a 35 nm thick film grown from **14** and ozone on Si(100) at 300 °C.

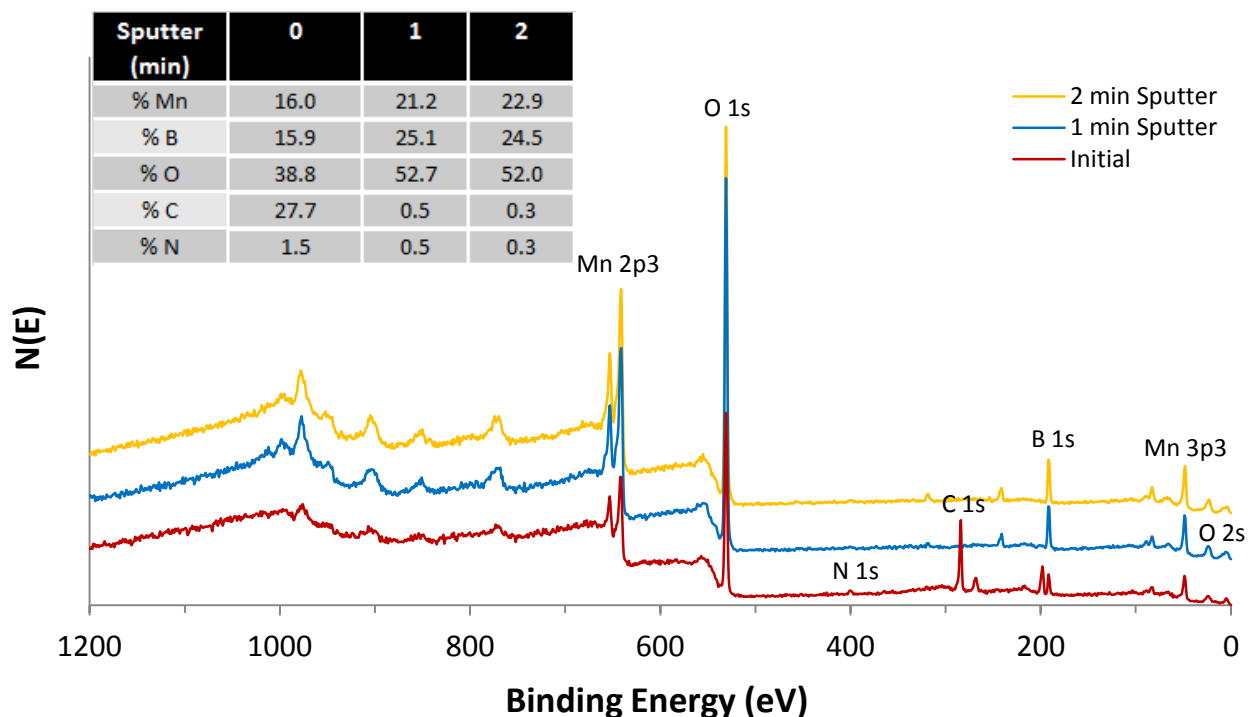


**Figure 161.** XPS survey scans of a 36 nm thick film grown from **14** and ozone on Si(100) at 325 °C.

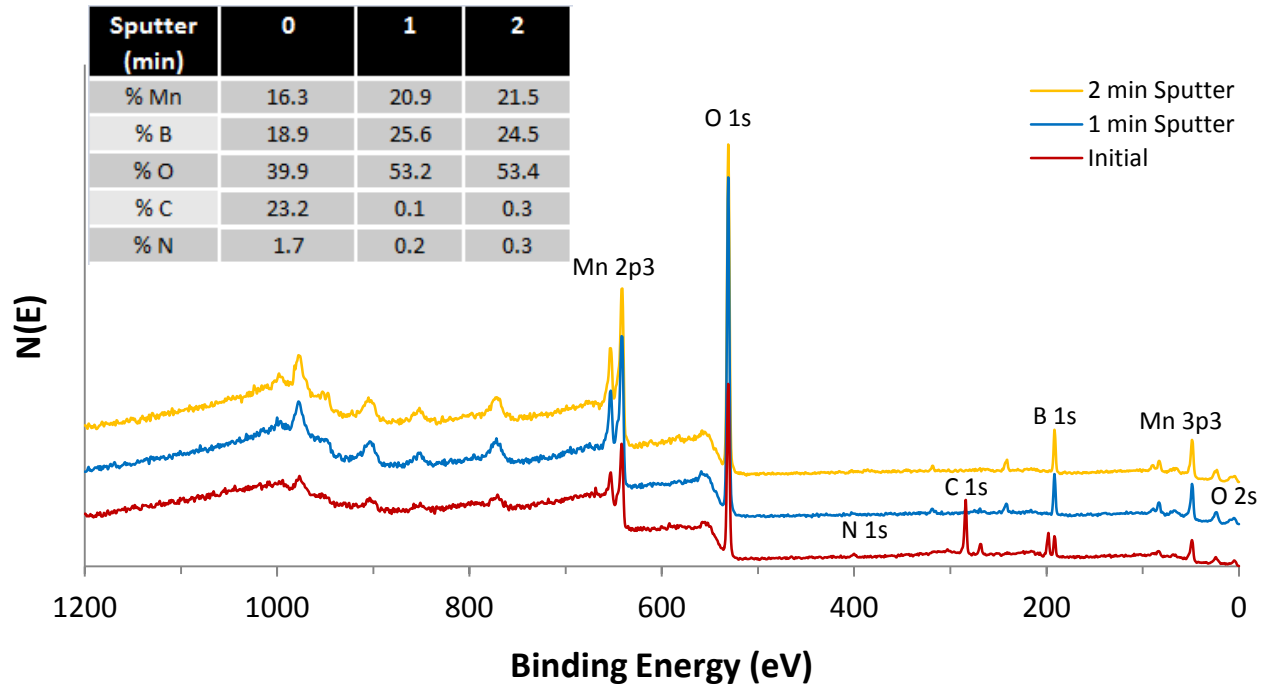


**Figure 162.** XPS survey scans of a 36 nm thick film grown from **14** and ozone on Si(100) at 350 °C.

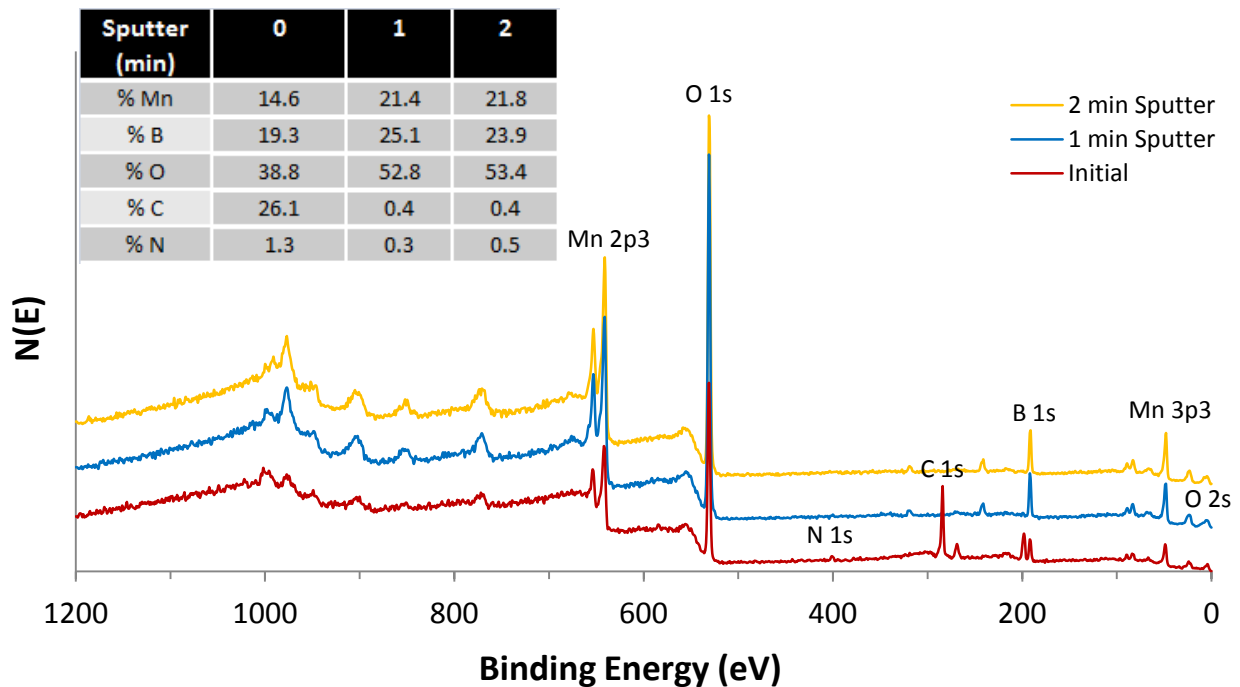


**Figure 163.** XPS B 1s ionization region of 35–36 nm thick films grown from **14** and ozone on Si(100) after 2 min of sputtering.

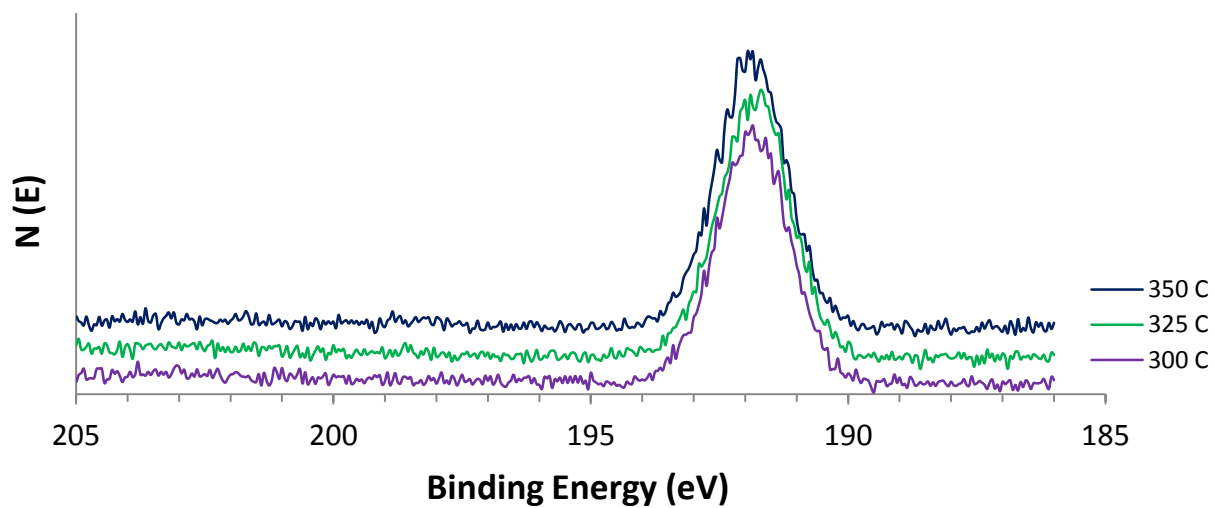


**Figure 164.** XPS Mn 2p ionization region of 35–36 nm thick films grown from **14** and ozone on Si(100) after 2 min of sputtering. Reference 2p binding energies for Mn metal: 638.8 and 650.05 eV; MnO: 642.2 and 653.9 eV.<sup>305</sup>

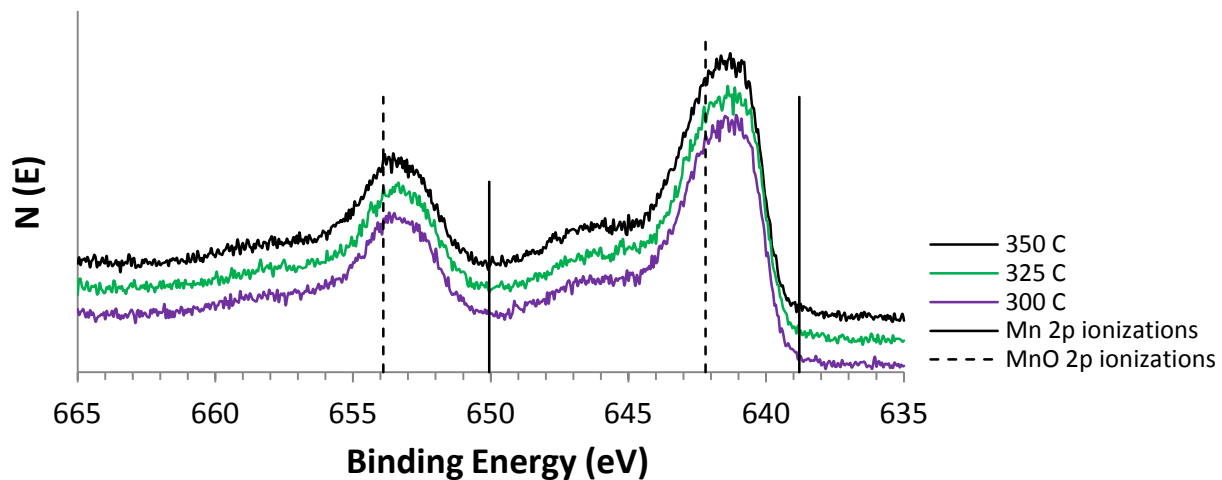


**Table 16.** TOF-ERDA atomic concentrations (at.%) of 35–36 nm thick films grown from **14** and ozone on Si(100).

Deposition Temperature (°C)	% Mn	% B	% O	% C	% H
300	18.8 ± 0.6	14.6 ± 0.4	49.3 ± 0.7	3.8 ± 0.7	13.6 ± 2
325	19.5 ± 0.6	12.9 ± 0.4	50.0 ± 0.7	3.4 ± 0.7	14.3 ± 2
350	19.2 ± 0.6	14.5 ± 0.4	50.6 ± 0.7	3.1 ± 0.7	12.7 ± 2

**Figure 165.** TOF-ERDA depth profile of a 35 nm thick film grown from **14** and ozone on Si(100) at 300 °C.

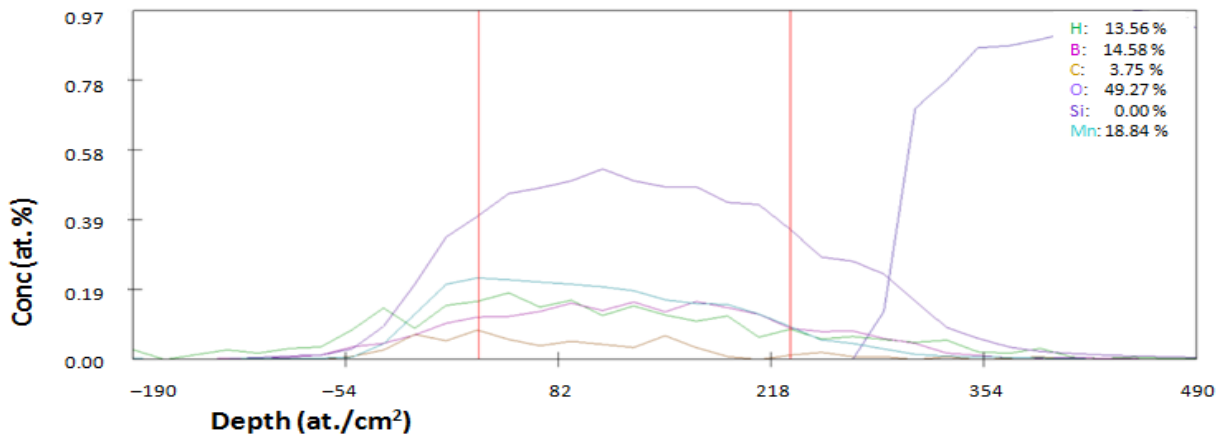


**Figure 166.** TOF-ERDA depth profile of a 35 nm thick film grown from **14** and ozone on Si(100) at 325 °C.

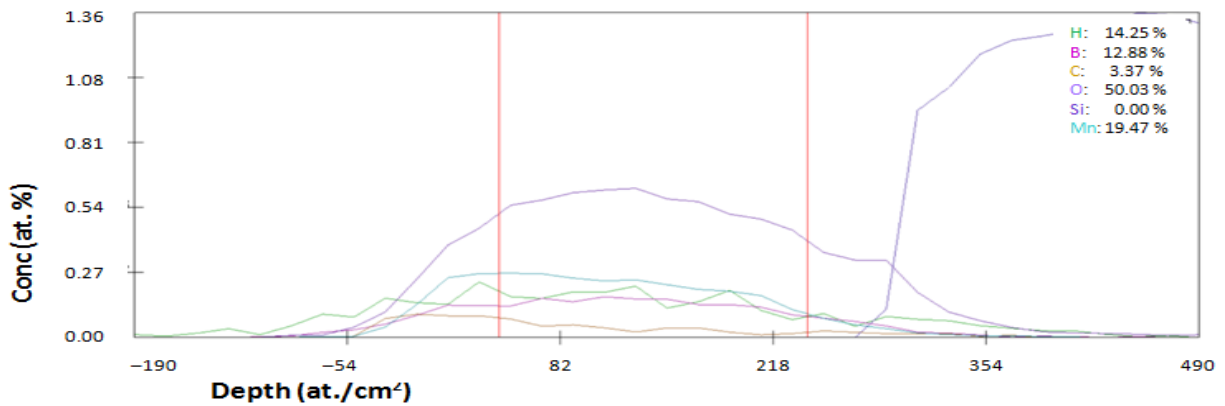
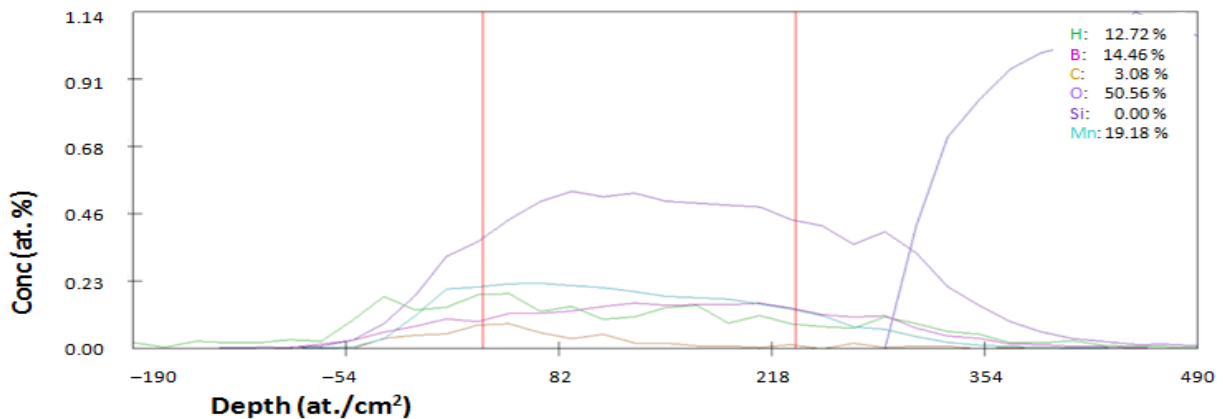


**Figure 167.** TOF-ERDA depth profile of a 35 nm thick film grown from **14** and ozone on Si(100) at 350 °C.



UV-Vis analysis was performed on the films used for saturative dose determination. Figure 168 shows a plot of reflectance versus wavelength for films of varying thickness due to incremental changes in the applied pulse length of **14**. Figure 169 shows analogous data for films grown using incremental changes in the pulse length of ozone. In both cases, the film thickness most strongly affects reflectance at  $\sim 370$  nm. The influence of film thickness on reflectance is reduced at longer wavelengths. At a wavelength of 1,100 nm, reflectance was 27–29% for all films within the 17.6–36.6 nm thickness range.

**Figure 168.** Plot of reflectance versus wavelength of films grown from **14** and ozone on Si(100) at 325 °C. The pulse of **14** was varied with a constant 5.0 s pulse of ozone.

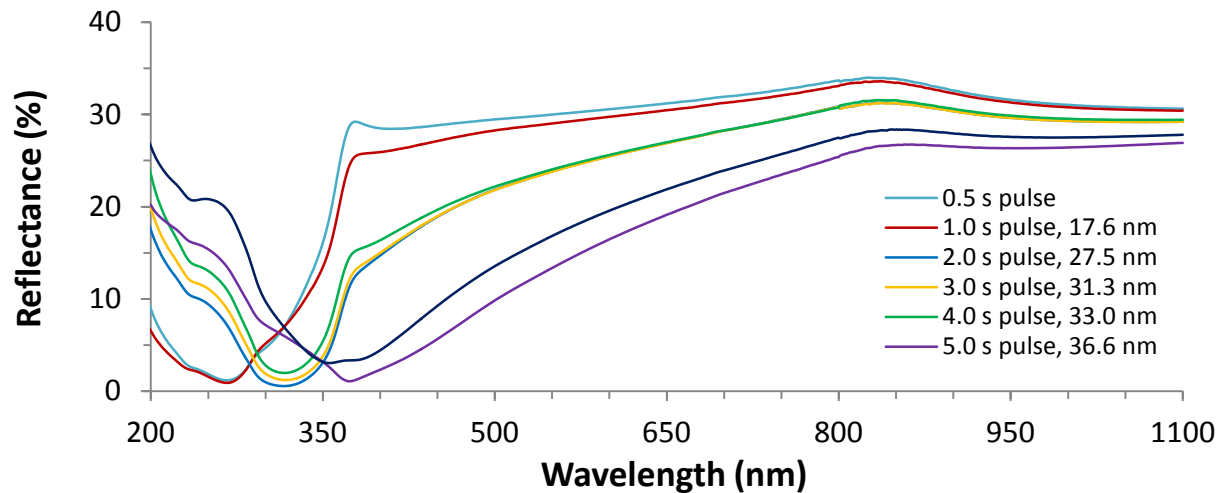
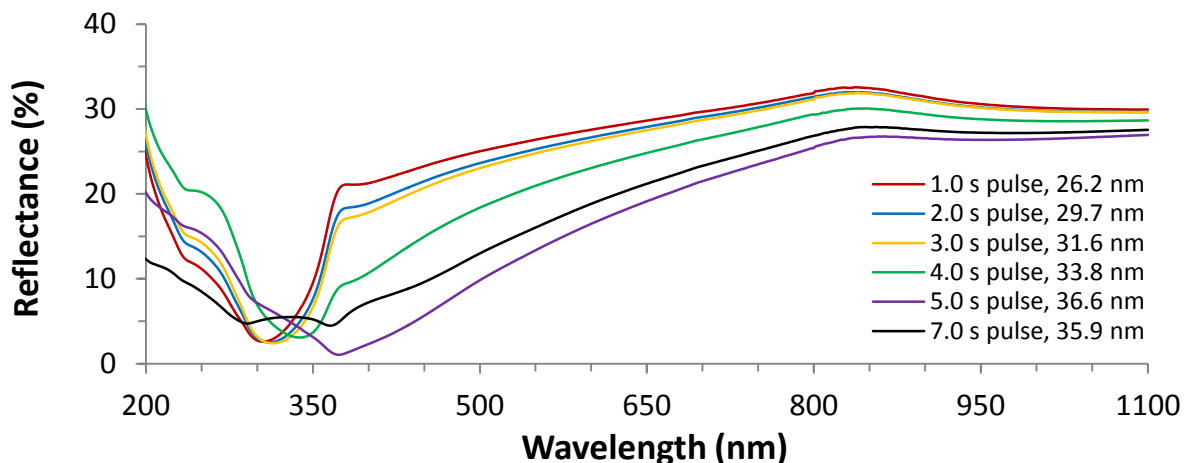


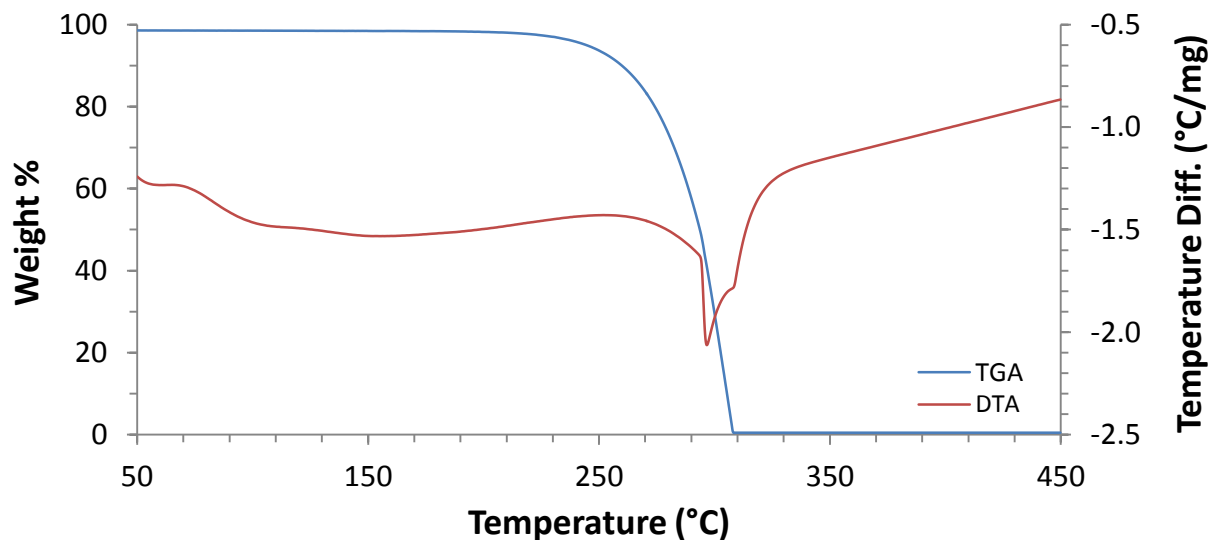
**Figure 169.** Plot of reflectance versus wavelength of films grown from **14** and ozone on Si(100) at 325 °C. The pulse of ozone was varied with a constant 5.0 s pulse of **14**.



### 5.2.2 CoB<sub>2</sub>O<sub>4</sub> Films from Bis(tris(pyrazolyl)borate)Co(II) and Ozone

TGA/DTA analyses of **16** showed a single-step weight loss (blue) overlapping the sole endotherm (red) from 250–310 °C (Figure 170). Consistent with the reported preparative sublimation data,<sup>341</sup> no remaining residue was detected.

**Figure 170.** TGA/DTA analyses of **16**.



Films were grown on Si(100) substrates with a native oxide layer using **16** as the precursor, by a method analogous to that described for films grown using **14**. Figure 171 shows the dependence of growth rate (blue) and consumption rate of **16** (black) on the pulse length of **16**, using 5.0 s pulses of ozone. Figure 172 shows the dependence of growth rate on ozone pulse length, using 6.0 s pulses of **16**. Considering these data, a pulsing sequence of 6.0 s **16**/5.0 s N<sub>2</sub> purge/5.0 s ozone/5.0 s N<sub>2</sub> purge was applied for all subsequent depositions, with a measured growth rate of 0.39 Å/cycle at 325 °C. A plot of thickness versus number of cycles was linear, with a growth rate of 0.42 Å/cycle. A trend line constructed by a least-squares approach had a y-intercept of -9.846 nm, suggesting a small nucleation period of ~240 cycles. All films were non-conductive and passed the Scotch tape test. Films grown at 325 °C were smooth and of uniform thickness by SEM analysis (Figure 174).

**Figure 171.** Saturation plot of **16** using 5.0 s pulses of ozone at 325 °C. The secondary axis shows the consumption rate of **16** as a function of the pulse length of **16**.

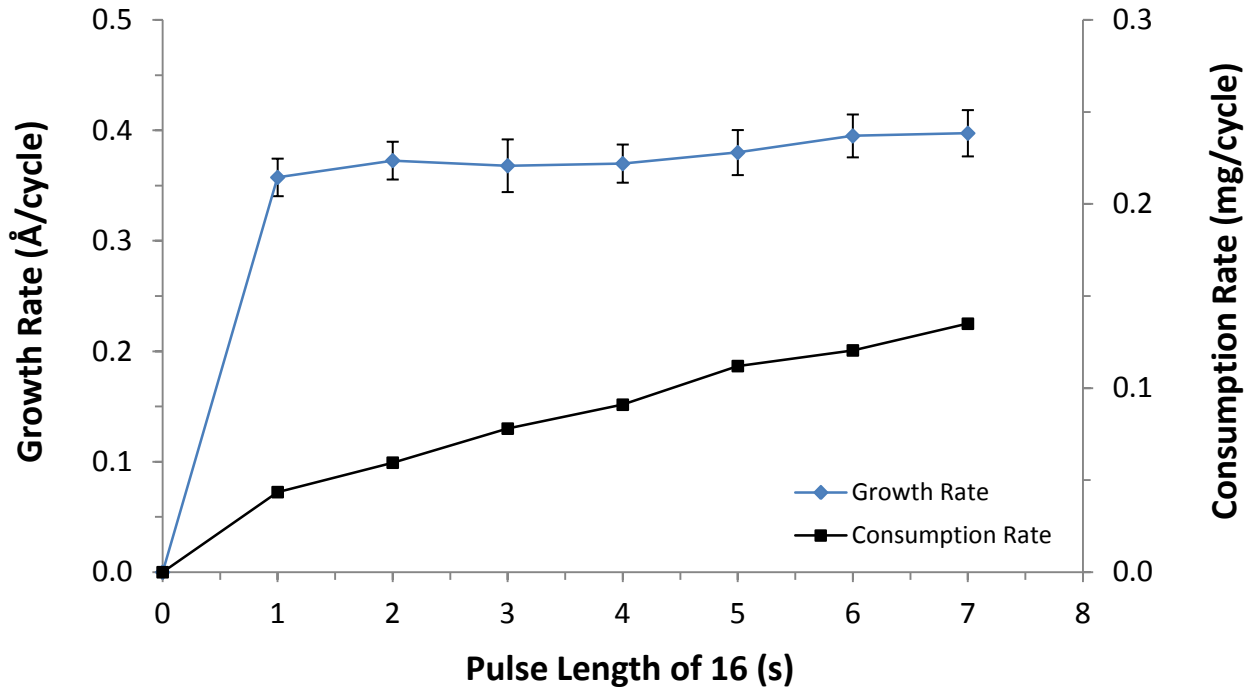


**Figure 172.** Saturation plot of ozone using 6.0 s pulses of **16** at 325 °C.

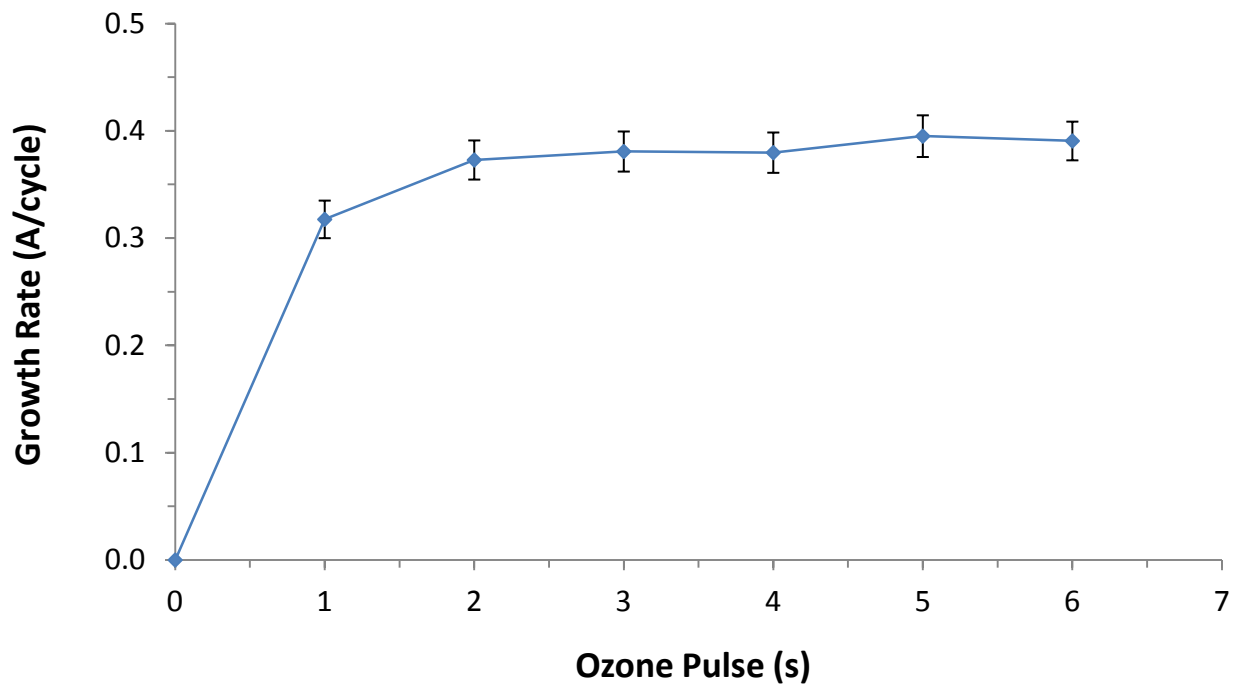




**Figure 173.** Plot of film thickness versus number of ALD cycles using **16** and ozone at 325 °C. Images below the x-axis show magnified regions of each film from a single photograph taken of all films.

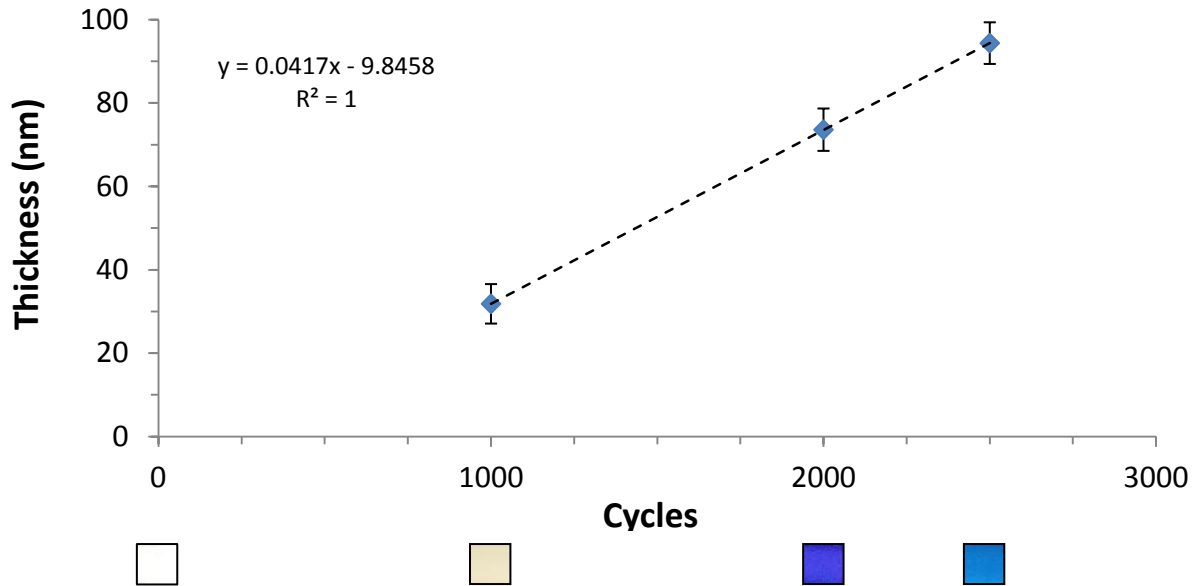
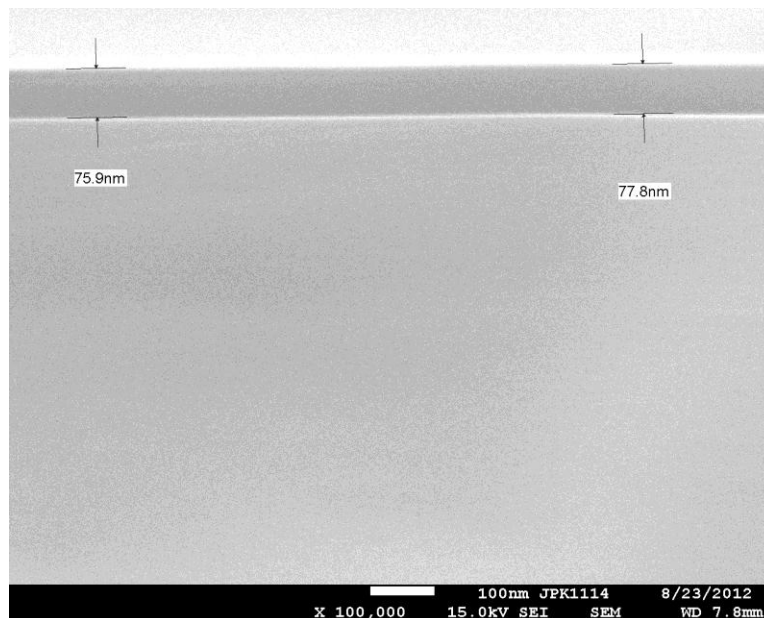


**Figure 174.** Cross-sectional SEM image of a 78 nm thick film grown on Si(100) from **16** and ozone for 2,000 cycles at 325 °C.



Compositional analyses were performed on 78 nm thick films deposited at 325 °C. XPS analysis showed a composition of  $\text{Co}_{1.35}\text{B}_2\text{O}_{4.50}$  after 2 min of argon ion sputtering, whereas TOF-ERDA afforded a composition of  $\text{Co}_{1.08}\text{B}_2\text{O}_{4.06}$ . Unlike the manganese borate films, the B/Co ratios were constant throughout the film. Carbon, nitrogen, and hydrogen levels were below the detection limits of XPS (C, N < 0.5%) and TOF-ERDA (C, N < 0.1%; H < 0.3%). Based upon these analyses, films of the approximate composition  $\text{CoB}_2\text{O}_4$  are deposited from **16** and ozone at 325 °C. XPS analysis of the B 1s region showed the ionization centered at 191.85 eV, identical to the B 1s ionizations of the manganese borate films. XPS analysis of the Co 2p region revealed shoulders on both the  $2p_{3/2}$  and  $2p_{1/2}$  ionizations that are consistent with a Co(II) oxidation state.<sup>342</sup> A film grown at 325 °C had a surface density of  $\sim 750 \times 10^{15}$  at./cm<sup>2</sup>, as measured by TOF-ERDA. UV-Vis analysis of a 78 nm thick film showed maximum reflectance (59%) at 375 nm.

**Figure 175.** XPS survey scans of a 78 nm thick film grown from **16** and ozone on Si(100) at 325 °C.

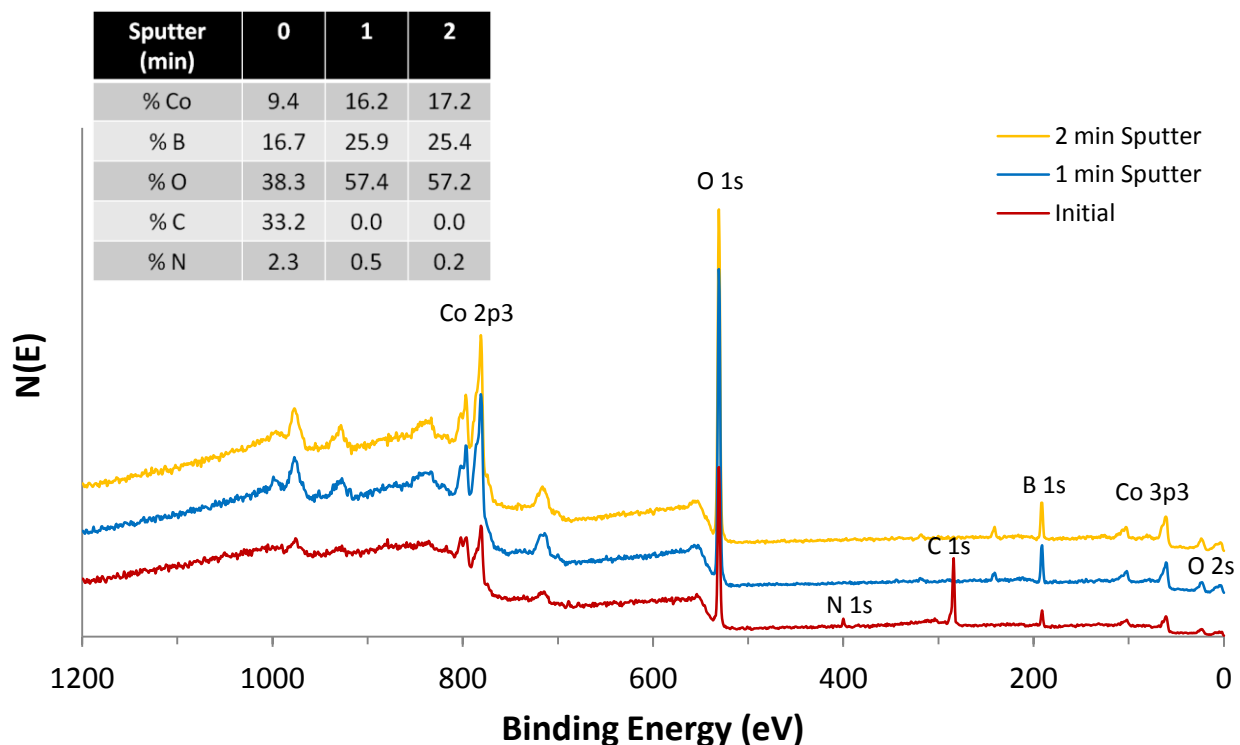


**Figure 176.** XPS B 1s ionization region of a 78 nm thick film grown from **16** and ozone on Si(100) at 325 °C after 2 min of sputtering.

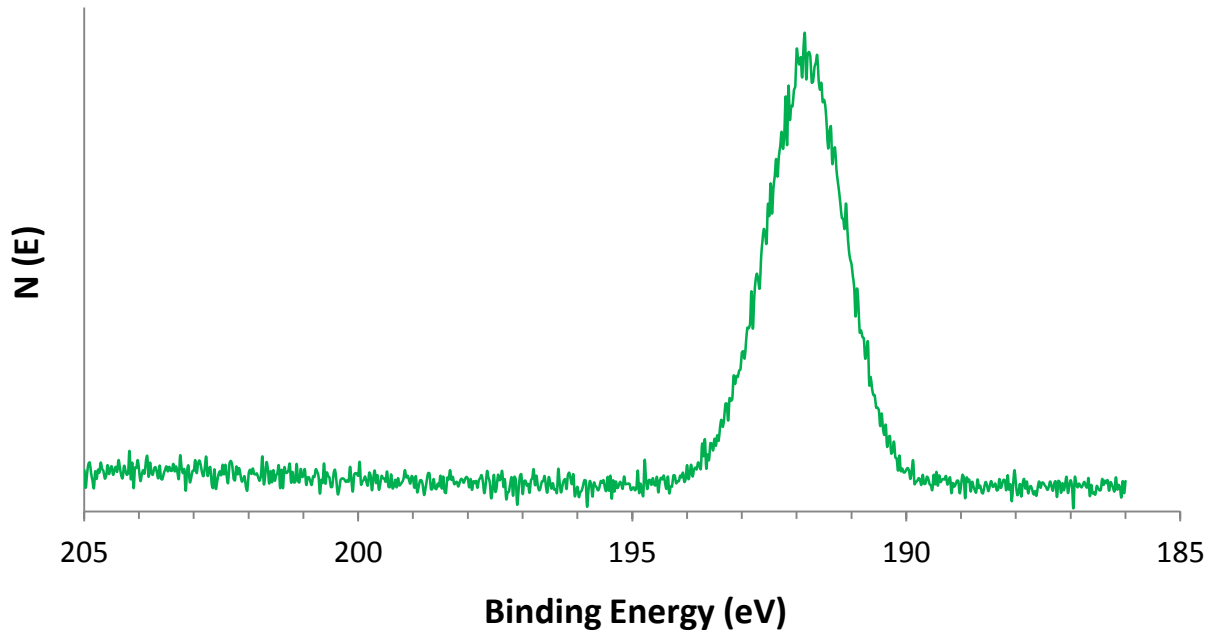


**Figure 177.** XPS Co 2p ionization region of a 78 nm thick film grown from **16** and ozone on Si(100) at 325 °C after 2 min of sputtering. Reference 2p binding energies for Co metal: 777.9 and 792.95 eV; CoO: 780.0 and 795.50 eV.<sup>305</sup>

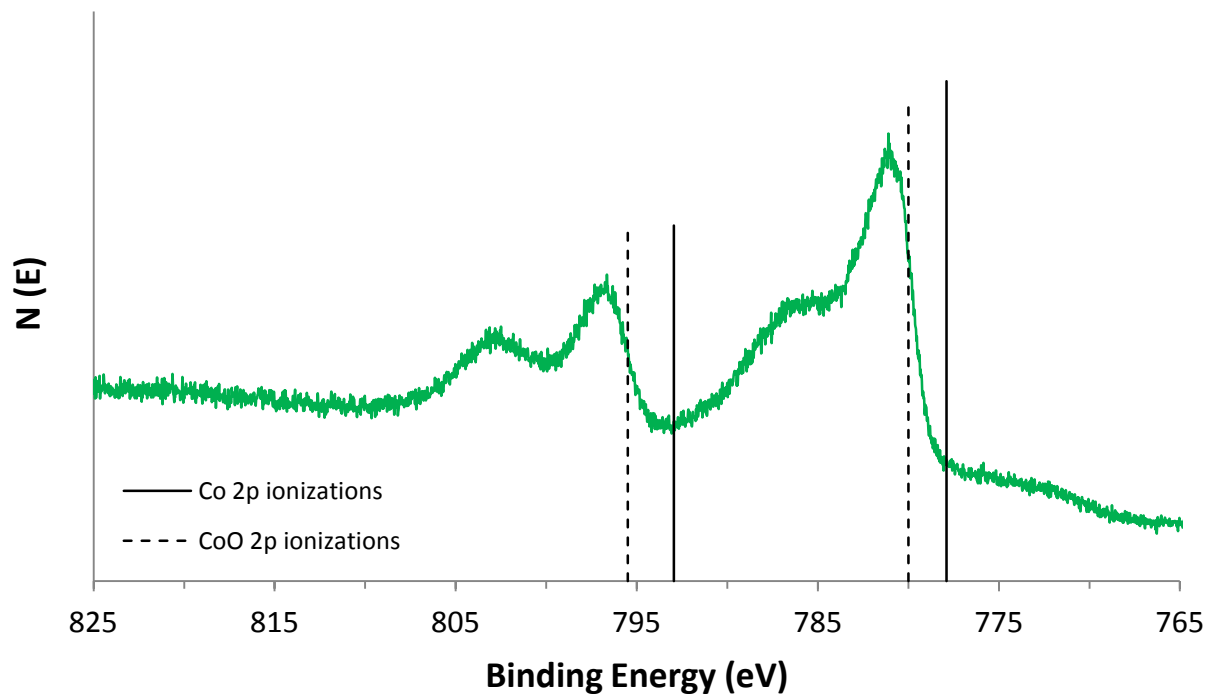


**Figure 178.** TOF-ERDA depth profile of a 78 nm thick film grown from **16** and ozone on Si(100) at 325 °C.

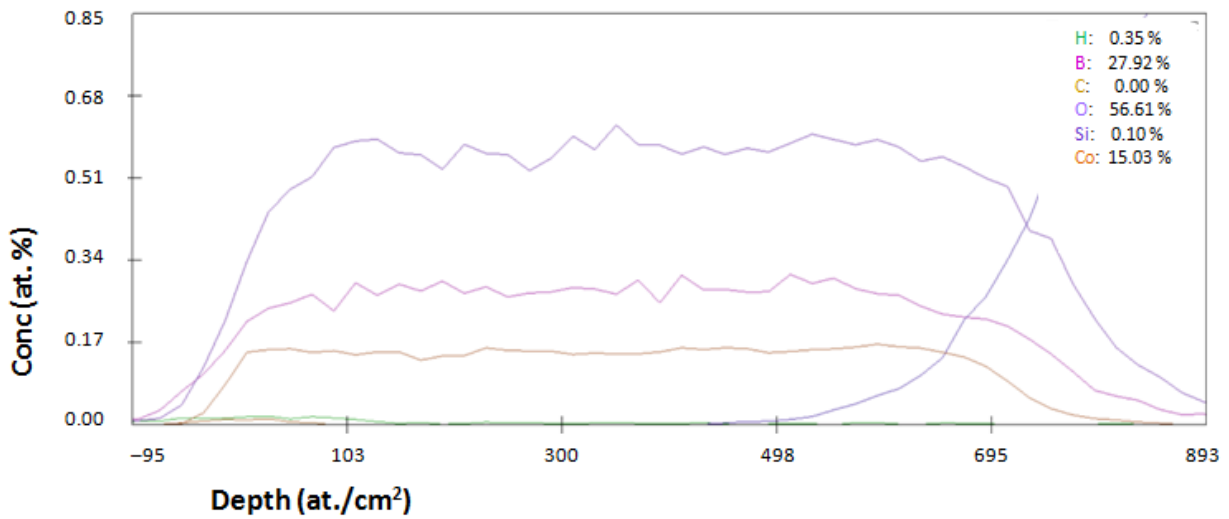
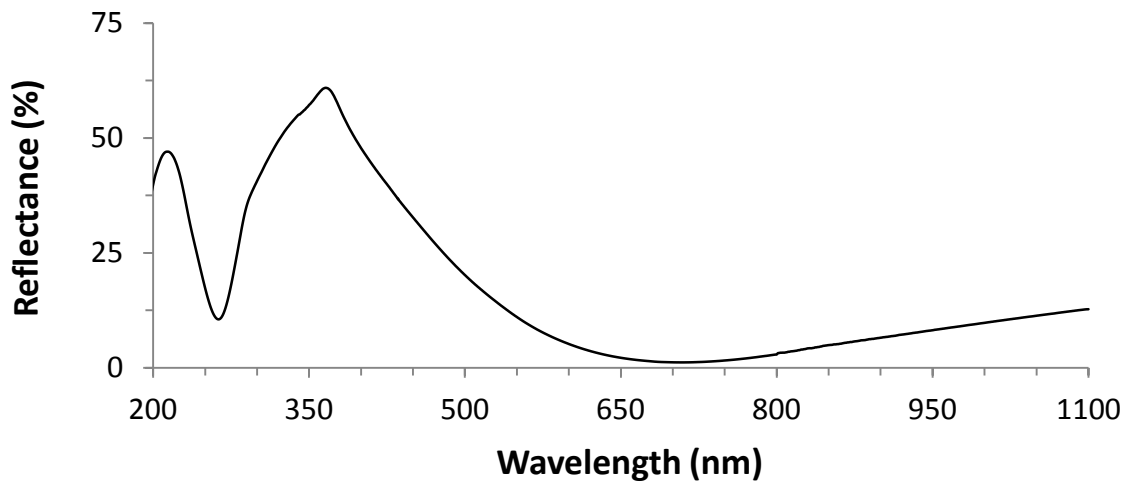


**Figure 179.** Plot of reflectance versus wavelength of a 78 nm thick film grown from **16** and ozone on Si(100) at 325 °C. The applied pulses of **16** and ozone were 6.0 and 5.0 s, respectively.



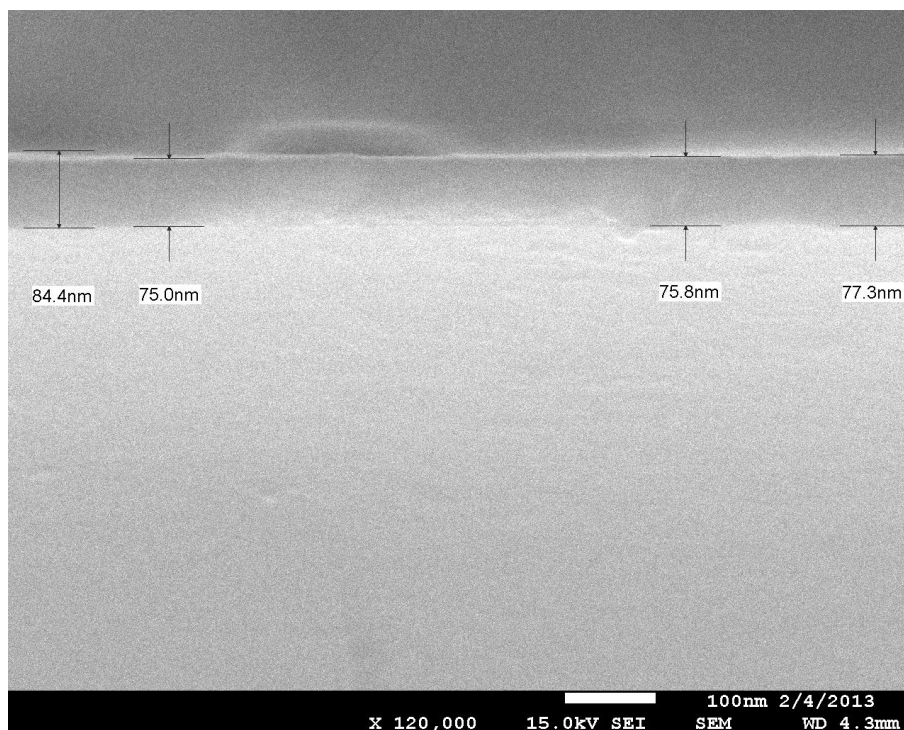
### 5.2.3 Other Films from Bis(tris(pyrazolyl)borate) Precursors and Ozone

Encouraged by the utility of **14** and **16** as ALD precursors, analogous processes using **15** and **17–19** were investigated. Depositions were performed at 325 °C on Si(100) substrates with a native oxide layer. The thermal properties of **20–21** were subsequently evaluated.

#### Iron

Films were initially grown using a pulsing sequence of 5.0 s **15**/5.0 s N<sub>2</sub> purge/5.0 s ozone/5.0 s N<sub>2</sub> purge. A consumption rate of 0.121 mg/cycle was calculated for **15**. After 2,000 cycles, very pale yellow films 20 ± 3 nm thick were measured by SEM (0.10 Å/cycle). A subsequent experiment used a pulsing sequence of 4.0 s **15**/10.0 s N<sub>2</sub> purge/5.0 s ozone/5.0 s N<sub>2</sub> purge. Compound **15** was delivered at an elevated source temperature of 205 ± 2 °C, yielding a consumption rate of 0.328 mg/cycle, with the ozone generator set to 75% power. After 4,000 cycles, deep blue films 76 ± 3 nm thick were measured by SEM (0.19 Å/cycle).

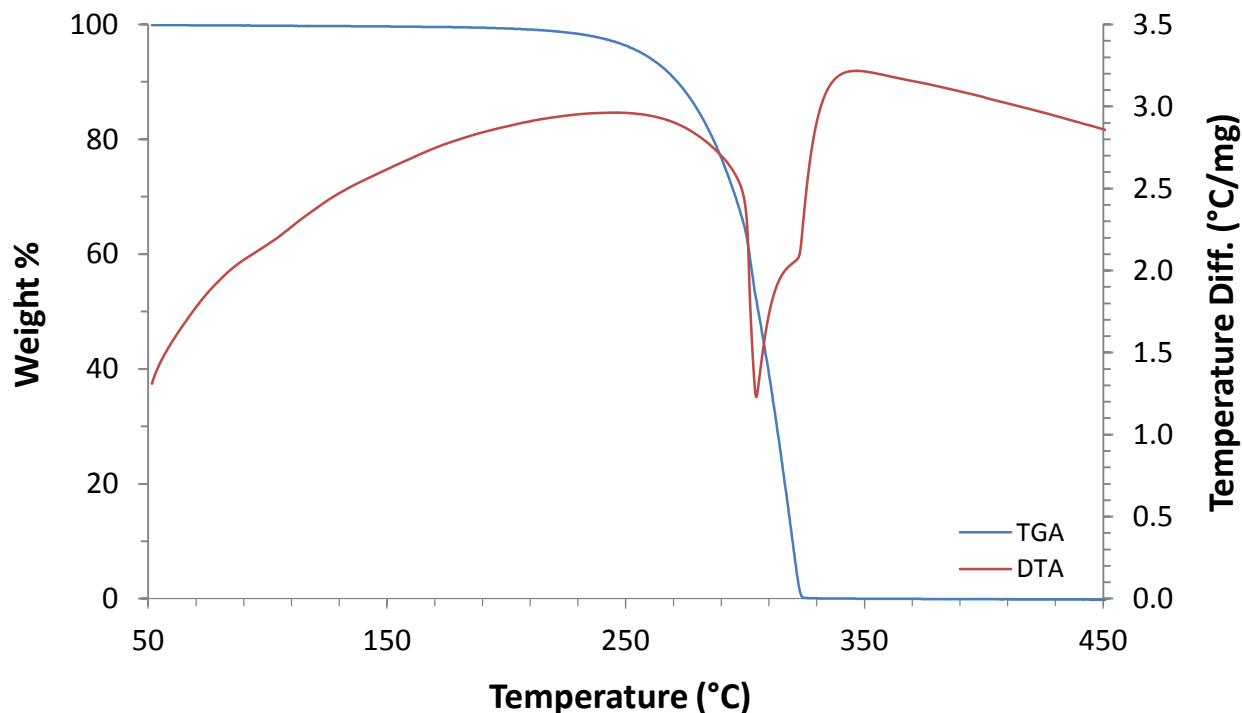
**Figure 180.** Cross-sectional SEM image of a 76 nm thick film grown on Si(100) from **15** and ozone for 4,000 cycles at 325 °C.



## Nickel

As depicted in Figure 181, TGA/DTA analyses of **17** showed a single-step weight loss (blue) overlapping the sole endotherm (red) from 240–325 °C. Consistent with the reported preparative sublimation data,<sup>341</sup> no remaining residue was detected.

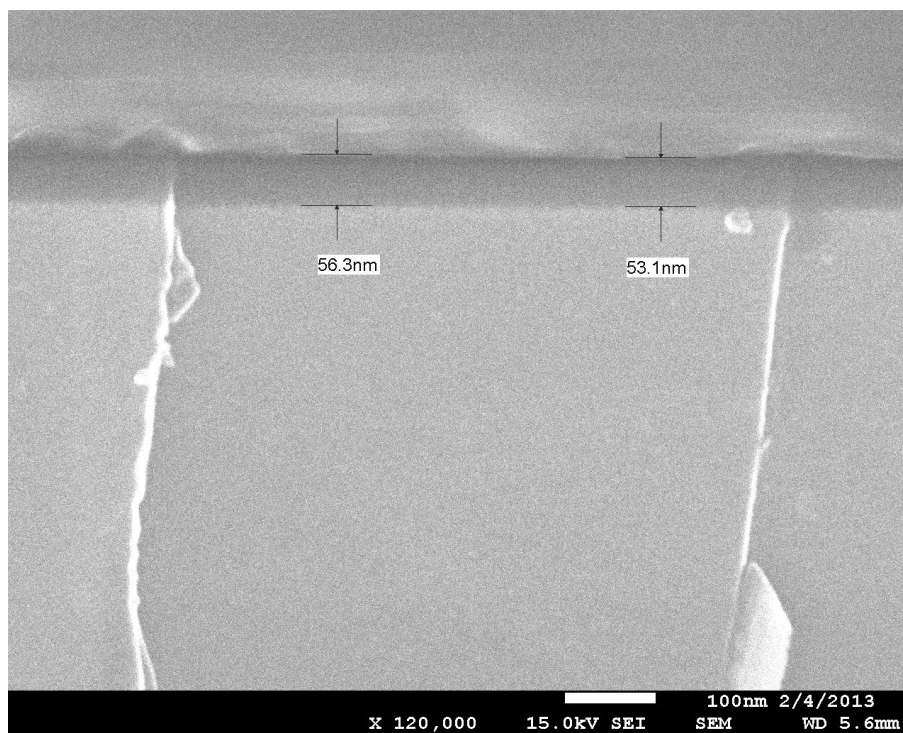
**Figure 181.** TGA/DTA analyses of **17**.



Films were initially grown using a pulsing sequence of 5.0 s **17**/5.0 s N<sub>2</sub> purge/5.0 s ozone/5.0 s N<sub>2</sub> purge. A consumption rate of 0.119 mg/cycle was calculated for **17**. After 3,000 cycles, very pale yellow films 12 ± 3 nm thick were measured by SEM (0.04 Å/cycle). The ozone generator was increased to 75% power for subsequent experiments. A pulsing sequence of 4.0 s **17**/5.0 s N<sub>2</sub> purge/5.0 s ozone/5.0 s N<sub>2</sub> purge was applied. An elevated source temperature for **17** of 205 ± 2 °C resulted in a consumption rate of 0.411 mg/cycle. After 2,000 cycles, very pale yellow films 9 ± 2 nm thick were measured by SEM (0.05 Å/cycle). A final experiment used a pulsing sequence of 4.0 s **17**/10.0 s N<sub>2</sub> purge/5.0 s ozone/5.0 s N<sub>2</sub> purge with the same

delivery conditions for **17** (0.361 mg/cycle). After 4,000 cycles, pale orange films  $56 \pm 3$  nm thick were measured by SEM (0.14 Å/cycle).

**Figure 182.** Cross-sectional SEM image of a 56 nm thick film grown on Si(100) from **17** and ozone for 4,000 cycles at 325 °C.



### Copper

Film growth was attempted using a pulsing sequence of 5.0 s **18**/5.0 s N<sub>2</sub> purge/5.0 s ozone/5.0 s N<sub>2</sub> purge. Consumption rates of 0.069 and 0.073 mg/cycle were calculated for **18** after 1,600 and 2,500 ALD cycles, respectively. No films were observed visually or by SEM. A subsequent experiment used a pulsing sequence of 4.0 s **18**/10.0 s N<sub>2</sub> purge/5.0 s ozone/5.0 s N<sub>2</sub> purge. Compound **18** was delivered at an elevated source temperature of  $203 \pm 2$  °C, yielding a consumption rate of 0.254 mg/cycle. No films were visually observed after 2,000 cycles.

## Zinc

Film growth was attempted using a pulsing sequence of 5.0 s **19**/5.0 s N<sub>2</sub> purge/5.0 s ozone/5.0 s N<sub>2</sub> purge. Consumption rates of 0.095 and 0.087 mg/cycle were calculated for **19** after 800 and 3,000 ALD cycles, respectively. No films were observed visually or by SEM.

## Vanadium and Chromium

Bis(tris(pyrazolyl)borate)vanadium(II) (**20**) and chromium(II) (**21**) complexes have been previously reported,<sup>343</sup> however, they have yet to be studied as ALD precursors. Herein, these compounds were synthesized in a manner analogous to **14–19**. Compound **20** (deep red crystals) melts within the 294–304 °C range. It appears to be fully decomposed by 309 °C, and may decompose upon melting. Preparative sublimation of **20** at 210 °C/0.05 Torr yielded 86.8% recovered material with no residue. Figure 183 shows a crystal structure of **20**; a crystalline density of 1.443 g/cm<sup>3</sup> was determined for this octahedral complex (Table 17). Compound **21** (deep red/orange crystals) melts within the 275–285 °C range and appears to decompose at ≤ 365 °C. Preparative sublimation of **21** at 210 °C/0.05 Torr yielded 94.6% recovered material with no residue. Figure 184 shows a crystal structure of **21**; a crystalline density of 1.490 g/cm<sup>3</sup> was determined (Table 18). The asymmetric unit contains two independent half-molecules that both show Jahn-Teller distortion, consistent with high-spin  $d^4$  complexes. Each represents half of the distorted octahedral complex, with elongated Cr1-N1 (2.4218 Å) and Cr2-N11 (2.519 Å) bonds. The Cr2-N11 distance is greater than the default value required for the refinement software to show a bond between these two atoms.



**Figure 183.** Perspective view of **20** with thermal ellipsoids at the 50% probability level.

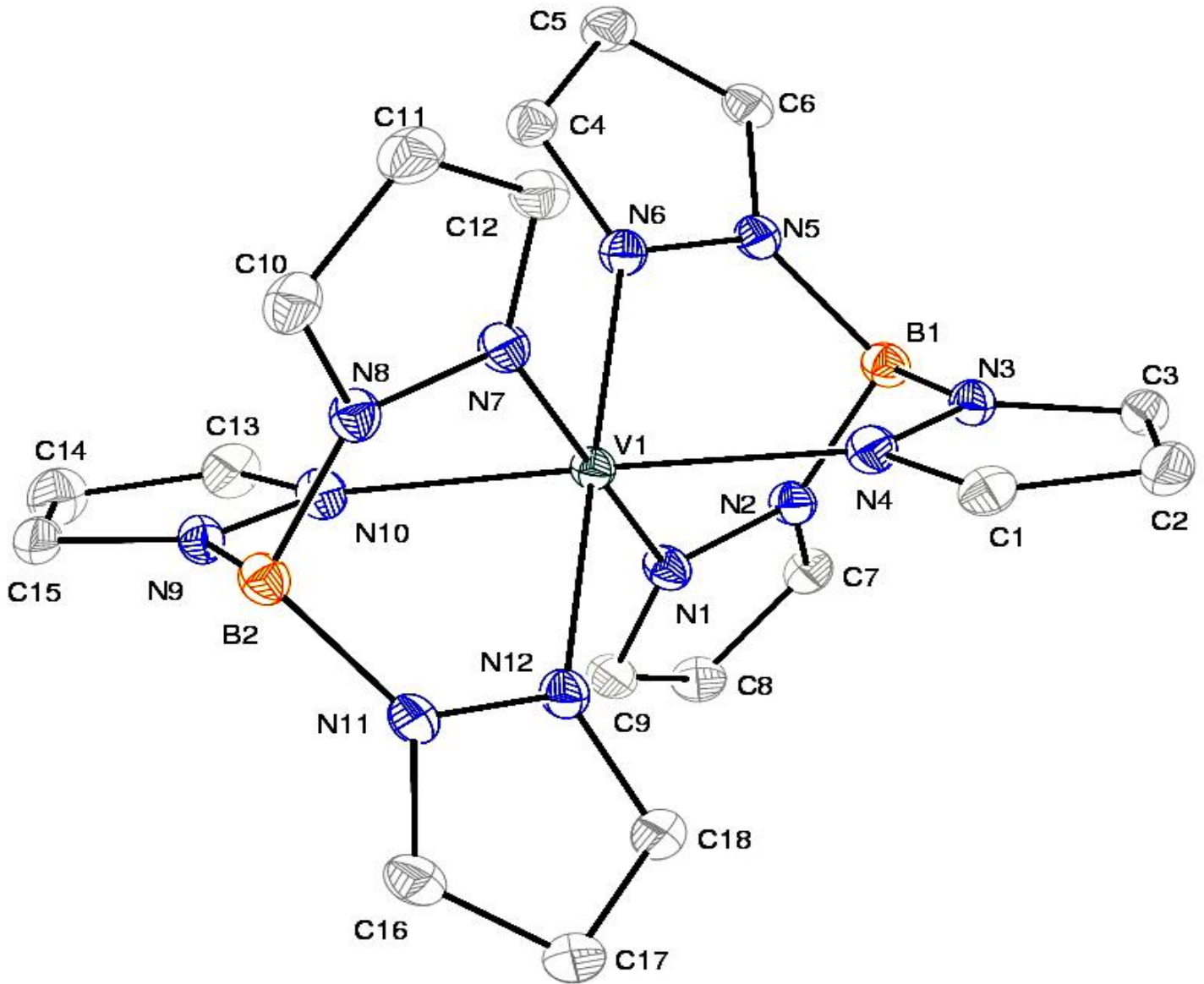


**Table 17.** Crystal data, collection parameters, bond lengths (Å) and angles (°) for **20**.

Chemical formula	C <sub>19</sub> H <sub>21</sub> B <sub>2</sub> VN <sub>12</sub>	V1-N1	2.1422(14)
Formula weight	477.02	V1-N4	2.1318(14)
Crystal size (mm)	0.100 × 0.200 × 0.300	V1-N6	2.1371(14)
Crystal habit	deep red columnar	V1-N7	2.1428(14)
Crystal system	monoclinic	V1-N10	2.1378(14)
Space group	P 1 21/n 1	V1-N12	2.1328(14)
a (Å)	9.6121(8)	N2-B1	1.542(2)
b (Å)	17.5031(15)	N3-B1	1.545(2)
c (Å)	13.1586(12)	N5-B1	1.544(2)
α (°)	90	N8-B2	1.543(2)
β (°)	97.386(5)	N9-B2	1.538(2)
γ (°)	90	N11-B2	1.545(2)
V (Å <sup>3</sup> )	2195.5(3)	B1-H7	1.0
Z	4	B2-H20	1.0
T (K)	100(2)		
λ (Å)	0.71073	N1-V1-N4	85.60(5)
ρ <sub>calcd</sub> (g·cm <sup>-3</sup> )	1.443	N1-V1-N6	85.72(5)
μ (mm <sup>-1</sup> )	0.486	N1-V1-N7	177.20(5)
R1 (%)	0.0331	N1-V1-N10	93.47(5)
wR2	0.0942	N1-V1-N12	95.72(5)
		N4-V1-N6	85.26(5)
		N4-V1-N7	95.72(5)
		N4-V1-N10	178.24(6)
		N4-V1-N12	93.71(5)
		N6-V1-N7	91.92(5)
		N6-V1-N10	96.16(5)
		N6-V1-N12	178.17(5)
		N7-V1-N10	85.28(5)
		N7-V1-N12	86.67(5)
		N10-V1-N12	84.90(5)

$$R(F) = \frac{\sum ||F_o| - |F_c||}{\sum |F_o|}$$

$$R_w(F)^2 = \frac{[\sum w(F_o^2 - F_c^2)^2]}{\sum w(F_o^2)^2}]^{1/2} \text{ for } I > 2\sigma(I)$$

**Figure 184.** Perspective views of the two half-molecules comprising the asymmetric unit of **21** with thermal ellipsoids at the 50% probability level.

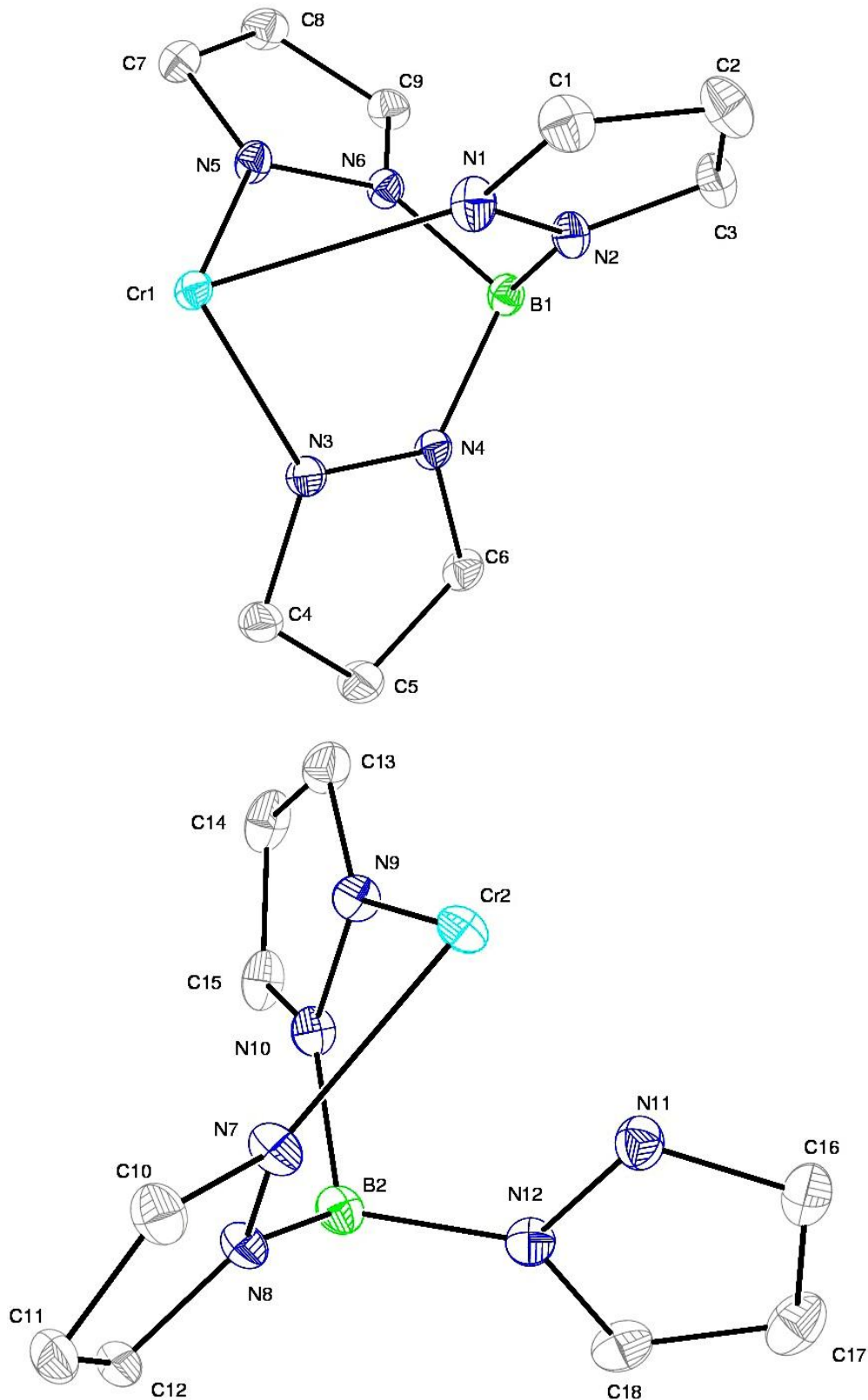


**Table 18.** Crystal data, collection parameters, bond lengths (Å) and angles (°) for **21**.

Chemical formula	C <sub>19</sub> H <sub>21</sub> B <sub>2</sub> CrN <sub>12</sub>	Cr1-N1	2.4218(7)
Formula weight	491.10	Cr1-N3	2.0871(6)
Crystal size (mm)	0.100 × 0.200 × 0.300	Cr1-N5	2.1311(7)
Crystal habit	deep red/orange columnar	Cr2-N7	2.0900(7)
Crystal system	triclinic	Cr2-N9	2.1123(7)
Space group	P -1	Cr2-N11	2.519
a (Å)	10.3872(10)	N2-B1	1.5418(10)
b (Å)	10.8041(10)	N4-B1	1.5436(10)
c (Å)	11.6208(10)	N6-B1	1.5457(10)
α (°)	70.051(4)	N8-B2	1.5458(11)
β (°)	89.416(4)	N10-B2	1.5448(11)
γ (°)	64.752(4)	N12-B2	1.5323(11)
V (Å <sup>3</sup> )	1094.64(18)	B1-H1A	1.0
Z	2	B2-H2A	1.0
T (K)	100(2)		
λ (Å)	0.71073	N1-Cr1-N3	85.33(2)
ρ <sub>calcd</sub> (g·cm <sup>-3</sup> )	1.490	N1-Cr1-N5	79.86(2)
μ (mm <sup>-1</sup> )	0.559	N3-Cr1-N5	86.62(2)
R1 (%)	2.95	N7-Cr2-N9	87.35(3)
wR2	8.61	N7-Cr2-N11	84.36
		N9-Cr2-N11	78.78

$$R(F) = \frac{\sum ||F_o| - |F_c||}{\sum |F_o|}$$

$$R_w(F)^2 = \frac{[\sum w(F_o^2 - F_c^2)^2]}{\sum w(F_o^2)^2}]^{1/2} \text{ for } I > 2\sigma(I)$$

### 5.3 Conclusions

Compounds **14** and **16** were used with ozone for the ALD of metal borate films with distinct stoichiometries. The **14**/ozone process gave a growth rate of 0.18 Å/cycle within an ALD window of 300–350 °C. Increased thicknesses for films grown at  $\geq 375$  °C are likely due to the thermal decomposition of **14**. Films grown at 325 °C were non-conductive and remained amorphous after annealing to 1100 °C under either an N<sub>2</sub> or O<sub>2</sub> atmosphere. While XPS analyses suggested a stoichiometry of MnBO<sub>2</sub>, TOF-ERDA implied a more oxygen-rich composition approximating Mn<sub>3</sub>(BO<sub>3</sub>)<sub>2</sub>. A similar ALD process using **16**/ozone afforded a growth rate of 0.39 Å/cycle at 325 °C. XPS and TOF-ERDA suggested a film stoichiometry of CoB<sub>2</sub>O<sub>4</sub> that matched the 2:1 B/Co ratio of **16**. This stoichiometry has been previously observed in CoB<sub>2</sub>O<sub>4</sub> crystals grown at high temperature and high pressure,<sup>344</sup> and is analogous to those observed in ALD-grown MB<sub>2</sub>O<sub>4</sub> films (M = Ca, Sr, Ba) from CaTp<sub>2</sub>, SrTp<sub>2</sub>, or BaTp<sup>Et<sub>2</sub></sup><sub>2</sub> with water.<sup>339b-d</sup> This approach was subsequently applied for film growth using **15** or **17** with ozone at 325 °C.

Replication of the 2:1 B/Co ratio of **16** in the CoB<sub>2</sub>O<sub>4</sub> films implies that **16** physisorbs in a molecular fashion to the surface of the growing film, and is then efficiently transformed by ozone to CoB<sub>2</sub>O<sub>4</sub>. By contrast, Mn<sub>3</sub>(BO<sub>3</sub>)<sub>2</sub> films obtained by **14** and ozone suggest that **14** chemisorbs on the surface of the growing film with an average loss of one Tp ligand per molecule of **14**. Subsequent treatment with ozone leads to Mn<sub>3</sub>(BO<sub>3</sub>)<sub>2</sub> films. For comparison, an ALD process using Mn(tmhd)<sub>3</sub> and ozone afforded MnO<sub>2</sub> films between 140 and 230 °C.<sup>99,104</sup> In the manganese borate process demonstrated herein, the ozone pulses likely oxidize surface-bound MnTp species to Mn(IV) borates that also contain oxo ligands. Since high-valent manganese(IV) oxides are strong oxidants,<sup>99,104</sup> the subsequent pulse of **14** likely leads to the oxidation of one Tp ligand by the surface oxo groups and loss of volatile products that remove an

average of one boron atom per molecule of **14**. In contrast to the range of higher oxidation state manganese oxides, cobalt oxides are limited to CoO and Co<sub>3</sub>O<sub>4</sub>,<sup>345</sup> neither of which is a strong oxidant. Thus, **16** likely physisorbs molecularly to the surface of the growing film, and is subsequently transformed to CoB<sub>2</sub>O<sub>4</sub> upon treatment with ozone. The large difference in growth rate between the Mn<sub>3</sub>(BO<sub>3</sub>)<sub>2</sub> (0.18–0.19 Å/cycle) and CoB<sub>2</sub>O<sub>4</sub> (0.39–0.42 Å/cycle) processes may arise because multiple higher-valent manganese-oxygen bonds are required to oxidize the Tp ligand in **14**, thereby reducing the surface coverage of MnTp fragments. By contrast, **16** appears to physisorb molecularly, providing greater surface coverage in the monolayer.

The processes described herein demonstrate the rare control of thin film stoichiometries in ALD that is governed by the elements present in a single precursor. In particular, deposition of Mn<sub>3</sub>(BO<sub>3</sub>)<sub>2</sub> films from **14** demonstrates that intermediate oxidizing surfaces obtained with ozone can lead to a borate film stoichiometry that differs from that of the precursor. Bimetallic precursors have been previously used in ALD in attempts to control the concentrations of two elements in thin films, but afforded poor stoichiometric control. Single precursors containing 1:2 Sr/Ta ratios were employed for the ALD of Sr-Ta-O films,<sup>340a,b</sup> but Sr/Ta ratios ranging from 0.5 to 1.5 were obtained under various deposition conditions. The lack of stoichiometric control could arise from formation of volatile tantalum oxides.<sup>340b</sup> Films of PrAlO<sub>x</sub> and NdAlO<sub>x</sub> were grown by ALD from 1:1 Nd/Al or Pr/Al bimetallic isopropoxide precursors, but nonstoichiometric Pr/Al and Nd/Al ratios (0.30–0.71) resulted.<sup>340c</sup> Bi(CH<sub>2</sub>SiMe<sub>3</sub>)<sub>3</sub> and ozone were used for the ALD of Bi-Si-O films,<sup>340d</sup> but the Si/Bi ratio increased from 1.5 to 5.0 between 200 and 450 °C.

The processes demonstrated herein enable the ALD of conformal transition metal borates with precise thickness control and well-defined stoichiometries. They are the first examples of

the vapor phase growth of first-row transition metal borate films. Results from this study should allow these materials to be explored in catalysis, lithium ion batteries, and other applications.

## 5.4 Experimental

**General Considerations.** Manipulations were carried out under argon using either Schlenk or glove box techniques in the handling of  $\text{KBH}_4$  for the synthesis of KTp. Metathesis reactions were run under ambient atmosphere. KTp and **14–19** were synthesized according to literature procedures.<sup>346</sup> All chemicals were obtained from Sigma Aldrich. Sublimations were performed as described in Chapter 2. TGA/DTA analyses were conducted on a Perkin-Elmer Pyris 1 TGA system between 50 and 450 °C using  $\text{N}_2$  as the flow gas with a heating rate of 10 °C/min. Single-crystal X-ray structures were obtained as described in Chapter 4 and were solved and refined using the SHELXL-2014/7 (Sheldrick, 2014) software package. Some of the reported bond lengths and bond angles were measured using the Mercury 3.6 (Build RC6) crystal structure visualization program.

**Deposition Experiments.** A Picosun Oy R-75BE ALD reactor was used for thin film deposition experiments. A Texol GeniSys nitrogen generator supplied 99.9995%  $\text{N}_2$  as both the carrier and purge gas. An Adixen 2033 C2 oil pump was used to maintain a pressure of 6–10 mbar in the reactor while under a constant  $\text{N}_2$  flow. Compounds **14–19** were delivered by solid state booster, with a source temperature of  $194 \pm 2$  °C unless otherwise noted. Ozone was delivered at 500 sccm by an IN USA AC-Series ozone generator operating at 50% power unless otherwise noted. Powder XRD, SEM, XPS, and resistivity analyses were performed as described in Chapter 2. AFM analyses were performed as described in Chapter 3. TOF-ERDA analyses were performed at the University of Jyväskylä, Finland. Mn-containing films were analyzed

using a 6.8 MeV  $^{35}\text{Cl}$  beam in mirror geometry (20.5 + 20.5) with a  $41^\circ$  recoil angle time-of-flight ERD. The Co-containing film was measured with an 8.5 MeV  $^{35}\text{Cl}$  beam. UV-Vis analyses were performed with a JASCO V-570 UV/VIS/NIR Spectrophotometer (Rev. 1.00); reported data are an average of 3 measurements. All films passed the Scotch tape test.



## CHAPTER 6

### Conclusions

The stringent demands of microelectronic device fabrication favor the use of ALD for applications requiring conformal film growth with sub-nm thickness control. However, many existing ALD processes require high deposition temperatures, hazardous coreagents, or the use of plasma to facilitate film growth. These limitations can lead to the incorporation of contaminating elements, safety concerns for HVM, and loss of thickness control during the film growth process. Consequently, the research presented herein demonstrates new chemistry for the low-temperature thermal ALD of first-row transition metal films which meets the requisite criteria for integration into future microelectronic device fabrication processes.

Chapter 1 offers a motivation for the research herein by outlining the challenges facing the continued miniaturization of microelectronic devices. Relevant examples of materials containing transition metal thin films are presented. Next, common techniques for vapor-phase film growth are introduced, including PVD, CVD, and ALD. Finally, the present status of first-row transition metal precursors and vapor deposition processes is reviewed in detail.

Chapter 2 introduces a class of bis(trimethylsilyl) six-membered rings as strongly-reducing coreagents for ALD.<sup>347</sup> Compounds **1** and **2** were used with  $\text{TiCl}_4$  for the growth of Ti metal films. The reaction is driven by the formation of strong Si-Cl bonds, affording  $\text{ClMe}_3\text{Si}$  as a volatile byproduct with two equivalents of the resulting  $8 \pi$  electron dianionic intermediate species coordinated to a Ti(IV) cation. Subsequent aromatization of these dianionic rings facilitates the reduction of Ti(IV) to Ti(0) by reducing the metal center by two electrons per ligand. Compound **2** was especially useful, supporting a growth rate of  $0.06 \text{ \AA/cycle}$  within a temperature range of  $110\text{--}240 \text{ }^\circ\text{C}$ . Films grown at  $< 180 \text{ }^\circ\text{C}$  were smooth by SEM and AFM

analyses, while films grown at  $\geq 180$  °C were increasingly rough, with additional nanoparticulate growth on top of the films. All films readily oxidized upon exposure to air, producing a surface of  $\text{TiO}_2$  and a gradient layer of Ti suboxides.<sup>300,304,310</sup> However, XPS analyses showed the definitive presence of Ti metal at the film/substrate interface. Importantly, the 3 keV argon ions used for sputtering are incapable of reducing Ti oxides to Ti metal, thus confirming reduction by a chemical process.<sup>300</sup> Upon the basis of the reduction potential of toluene ( $E_{1/2} = -2.46$  V), most metal ions in the periodic table should be reduced by the 2-methyl-1,4-cyclohexadienyl dianion,<sup>41</sup> which results upon double desilylation of **1**. This work constitutes the first report of a thermal Ti ALD process. Compound **2** was also used for the reduction of  $\text{SbCl}_3$  to Sb metal at 180 °C. After 1 min of sputtering, XPS analysis showed a film composition of 87.2% Sb as a mixture of  $\text{Sb}_2\text{O}_3$  and Sb metal.

Chapter 3 describes novel processes using **3** and formic acid for the ALD of high-purity Co metal films. Initially, a three-step approach, including **2** as a reducing coreagent, afforded 97.1% pure Co metal films at 180 °C. The discovery that **2** was unnecessary led to the development of a binary process with a growth rate of 0.95 Å/cycle within a 170–180 °C window. These films were very smooth by SEM and AFM analyses. Powder XRD confirmed the presence of Co metal, with an average crystallite size of  $13.4 \pm 3.0$  nm. XPS analysis with continued sputtering resulted in ionizations that exactly matched the known values for Co metal after 2 min and a film composition consisting of 91.6% Co metal after 8 min. Films grown on Ru, Pd, Pt, and Cu substrates showed notably lower sheet resistivities compared to the bare substrates. Bulk resistivities of films grown on Ru from 165–220 °C were 13.4–19.0  $\mu\Omega\cdot\text{cm}$ , approaching that of bulk Co metal.<sup>312</sup> Deposition data demonstrate that there is a small (15–16%) CVD component to the growth at 180 °C and also a nucleation period of  $\leq 250$  cycles for the initial

nanoparticulate growth to coalesce into a continuous film. This CVD growth from the self-decomposition of **3** may provide a seed layer for the ALD of Co metal. The approach described herein overcomes the limitations of previously-reported Co ALD processes, including low growth rates,<sup>36,39</sup> growth temperatures that are well above the precursor decomposition temperatures,<sup>31,36,38,136–138</sup> no demonstration of self-limited ALD growth,<sup>143</sup> and variable, high resistivities of the Co films.<sup>136–138</sup> Accordingly, three-step processes were subsequently explored for the growth of other first-row transition metal films using diazabutadienyl and alkoxide complexes with formic acid and **2** as coreagents.

Chapter 4 explores the utility of **8–13** as ALD precursors that contain the redox non-innocent 1,4-di-*tert*-butyl-1,3-diazabutadienyl ligand. The syntheses of these compounds employed a convenient metathesis approach, analogous to that reported for **3–7**.<sup>42</sup> Proton NMR or magnetic moment data show the oxidation state of the ligand, and are reported for diamagnetic (**9, 11**) and paramagnetic (**8, 10, 12–13**) complexes, respectively. These compounds sublime at  $\leq 125$  °C/0.05 Torr with little or no residue. Compound **10** may be especially useful for ALD, as it has a fairly low melting point (135–137 °C) and a high thermal decomposition temperature (235 °C). A crystal structure for the novel **13** is also reported.

Chapter 5 outlines processes for the ALD of Mn and Co borate films from **14** and **16**, respectively, with ozone as the coreagent. These processes give distinct borate stoichiometries, demonstrating rare compositional control in ALD growth that is governed by the elements present in a single precursor. The **14**/ozone process affords a growth rate of 0.18 Å/cycle within an ALD window of 300–350 °C. Films remained amorphous after annealing to 1100 °C under either an N<sub>2</sub> or O<sub>2</sub> atmosphere. While XPS analyses suggested a stoichiometry of MnBO<sub>2</sub>, TOF-ERDA implied a more complex, oxygen-rich composition approximating Mn<sub>3</sub>(BO<sub>3</sub>)<sub>2</sub>. The data

suggest that **14** chemisorbs on the surface of the growing film with an average loss of one Tp ligand per molecule of **14**. Subsequent treatment with ozone then leads to  $\text{Mn}_3(\text{BO}_3)_2$  films. The analogous ALD process using **16**/ozone affords a growth rate of 0.39 Å/cycle. XPS and TOF-ERDA suggested a film stoichiometry of  $\text{CoB}_2\text{O}_4$  that matched the 2:1 B/Co ratio of **16**. The data imply that **16** physisorbs in a molecular fashion to the surface of the growing film, and is then efficiently transformed by ozone to  $\text{CoB}_2\text{O}_4$ . Films grown using **14** or **16** were non-conductive, and smooth by SEM and AFM analyses. These processes are the first examples of vapor-phase growth of first-row transition metal borate films. Film growth was also achieved using **15** or **17** with ozone at 325 °C. Finally, the thermal properties of **20–21** suggest that these compounds may be useful for ALD; crystal structures of both compounds are reported.

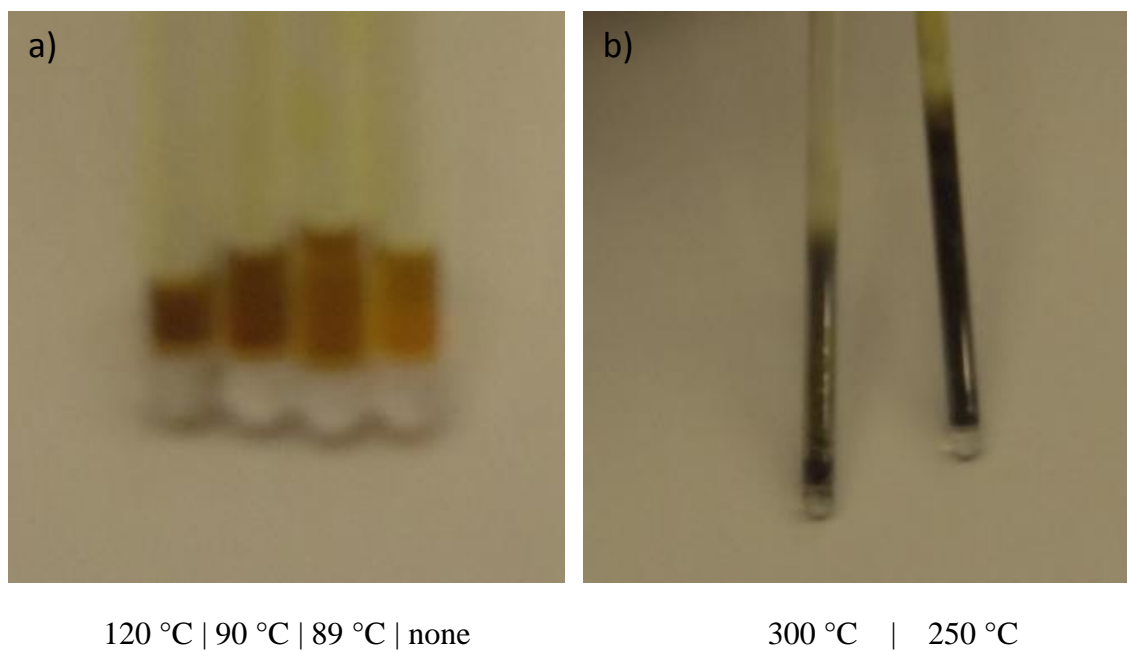
## APPENDIX A

### Thermal Analysis of (2-*tert*-Butylallyl)Co(CO)<sub>3</sub>

As referenced in Chapter 1 (pgs. 27–28) and Chapter 3 (pgs. 103, 132), the onset of thermal decomposition of (2-*tert*-butylallyl)Co(CO)<sub>3</sub> appears to commence at ~90 °C in the bulk liquid state. Herein, the thermal analysis of this compound is described in detail.

Samples of (2-*tert*-butylallyl)Co(CO)<sub>3</sub> were loaded into capillary tubes in an argon-filled dry box. A small amount of vacuum grease was used to plug the open end of the capillary tubes. The tubes were then removed from the box and quickly flame sealed. Experiments employed an Electrothermal (45 W) melting point apparatus. Initially, a starting temperature of 60 °C was used. After 2 min, the temperature was increased to 70 °C, held for 5 min, increased to 80 °C, held for 5 min, increased to 90 °C, and held for 5 min. The sample was observed after each 5 min interval. After holding the sample at 90 °C for 5 min, it appeared notably darker than the other samples that had not been heated. In a more precise experiment, a sample was heated to 78 °C and held for 5 min prior to observation. This process was repeated at 2 °C steps up to 88 °C, after which a very slight change in color was observed. This stepwise heating was continued to 89, 90, and 120 °C, using a 5 min holding time prior to observation at each temperature. After being heated at 120 °C for 5 min, the sample was visually darker than the sample that had not been heated (Figure A1-a). Other samples were then separately heated to 89 and 90 °C, held for 5 min each, and observed (Figure A1-a). A slight darkening was observed for the sample heated to 89 °C, while the sample heated to 90 °C was the same color as the sample that was heated to 120 °C. Samples heated to 250 and 300 °C were very dark grey/black in color (Figure A1-b).

**Figure A1.** Thermal analysis of (2-*tert*-butylallyl)Co(CO)<sub>3</sub> after heating to various temperatures.



## APPENDIX B

## Permissions

## Republication/Electronic Request Form



Wiley Global Permissions &lt;permissions@wiley.com&gt;

To: Joseph Peter Klesko;

Reply all |

Tue 10/6/2015 7:01 AM

Dear Joe,

Im happy to confirm again that in respect of the reuse in your thesis of the article Metallic Materials Deposition: Metal-Organic Precursors *ENCYCLOPEDIA OF INORGANIC AND BIOINORGANIC CHEMISTRY* 2012, DOI: 10.1002/9781119951438.eibc0128.pub2, Permission is hereby granted for the use requested subject to the usual acknowledgements (author, title of material, title of book/journal, ourselves as publisher). You should also duplicate the copyright notice that appears in the Wiley publication; this can be found on the copyright page if the material is a book or within the article if it is a journal.

Any third party material is expressly excluded from this permission. If any of the material you wish to use appears within our work with credit to another source, authorisation from that source must be obtained.

This permission does not include the right to grant others permission to photocopy or otherwise reproduce this material except for accessible versions made by non-profit organisations serving the blind, visually impaired and other persons with print disabilities (VIPs).

Best wishes,

Rebecca Cook  
Permissions Assistant  
John Wiley & Sons Ltd  
The Atrium  
Southern Gate, Chichester  
West Sussex, PO19 8SQ  
UK

---

Update based on the original article by Charles H. Winter, Wenjun Zheng and Hani M. El-Kaderi, *Encyclopedia of Inorganic Chemistry* Second Edition, © 2005, John Wiley & Sons, Ltd.

---

*Encyclopedia of Inorganic and Bioinorganic Chemistry*, Online © 2011–2012 John Wiley & Sons, Ltd.

This article is © 2012 John Wiley & Sons, Ltd.

This article is published in the *Encyclopedia of Inorganic and Bioinorganic Chemistry* in 2012 by John Wiley & Sons, Ltd.  
DOI: 10.1002/9781119951438.eibc0128.pub2



Title:

Thermal Atomic Layer Deposition of Titanium Films Using Titanium Tetrachloride and 2-Methyl-1,4-bis(trimethylsilyl)-2,5-cyclohexadiene or 1,4-Bis(trimethylsilyl)-1,4-dihydropyrazine

Logged in as:

Joseph Klesko

[LOGOUT](#)

**Author:** Joseph P. Klesko, Christopher M. Thrush, Charles H. Winter

**Publication:** Chemistry of Materials

**Publisher:** American Chemical Society

**Date:** Jul 1, 2015

Copyright © 2015, American Chemical Society

### PERMISSION/LICENSE IS GRANTED FOR YOUR ORDER AT NO CHARGE

This type of permission/license, instead of the standard Terms & Conditions, is sent to you because no fee is being charged for your order. Please note the following:

- Permission is granted for your request in both print and electronic formats, and translations.
- If figures and/or tables were requested, they may be adapted or used in part.
- Please print this page for your records and send a copy of it to your publisher/graduate school.
- Appropriate credit for the requested material should be given as follows: "Reprinted (adapted) with permission from (COMPLETE REFERENCE CITATION). Copyright (YEAR) American Chemical Society." Insert appropriate information in place of the capitalized words.
- One-time permission is granted only for the use specified in your request. No additional uses are granted (such as derivative works or other editions). For any other uses, please submit a new request.

[BACK](#)
[CLOSE WINDOW](#)

Copyright © 2015 [Copyright Clearance Center, Inc.](#) All Rights Reserved. [Privacy statement](#). [Terms and Conditions](#).  
Comments? We would like to hear from you. E-mail us at [customer@copyright.com](mailto:customer@copyright.com)



## REFERENCES

1. Moore, G. E. *Electronics* **1965**, 114–117.
2. Tullo, A. H.; McCoy, M.; Tremblay, J.-F. *C&EN* **2015**, 93, 31–37.
3. *International Technology Roadmap for Semiconductors*; 2015. <http://www.itrs.net>.
4. (a) Brunner, T. A. *J. Vac. Sci. Technology B* **2003**, 21, 2632–2637. (b) Brunner, T. A. *J. Microlith., Microfab., Microsyst.* **2002**, 188.
5. *Boron and Refractory Borides*; Matkovich, V. I., Ed.; Springer-Verlag: New York, 1977.
6. Xue, D.; Betzler, K.; Hesse, H.; Lammers, D. S. *Solid State Commun.* **2000**, 114, 21–25.
7. Maia, L. J. Q.; Bernardi, M. I. B.; Feitosa, C. A. C.; Mastelaro, V. R.; Zanatta, A. R.; Hernandez, A. C. *Thin Solid Films* **2004**, 457, 246–252.
8. Wilk, G. D.; Wallace, R. M.; Anthony, J. M. *J. Appl. Phys.* **2001**, 89, 5243–5275.
9. (a) Kim, H. *Surf. Coat. Technol.* **2006**, 200, 3104–3111. (b) Kim, H. *J. Vac. Sci. Technol. B* **2003**, 21, 2231–2261. (c) Merchant, S.M.; Kang, S.H.; Sanganeria, M.; van Schravendijk, B.; Mountsier, T. *JOM-J. Min. Met. Mater. Soc.* **2001**, 52, 43–48. (d) Wang, S.-Q. *MRS Bull.* **1994**, 19, 30–40.
10. Roule, A.; Amuntencei, M.; Deronzier, E.; Haumesser, P. H.; Da Silva, S.; Avale, X.; Pollet, O.; Baskaran, R.; Passemard, G. *Microelectron. Eng.* **2007**, 84, 2610–2614.
11. (a) Rossnagel, S. M.; Sherman, A.; Turner, F. *J. Vac. Sci. Technol. B* **2000**, 18, 2016–2020. (b) Kim, H.; Rossnagel, S. M. *J. Vac. Sci. Technol. A* **2002**, 20, 802–808.
12. Usui, T.; Nasu, H.; Takahashi, S.; Shimizu, N.; Nishikawa, T.; Yoshimaru, M.; Shibata, H.; Wada, M.; Koike, J. *IEEE T. Electron Dev.* **2006**, 53, 2492–2499.

13. (a) Winter, C. H. *Aldrichimica Acta* **2000**, 3–8. (b) Won, Y. S.; Kim, Y. S.; Anderson, T. J.; Reitfort, L. L.; Ghiviriga, I.; McElwee-White, L. *J. Am. Chem. Soc.* **2006**, *128*, 13781–13788. (c) McElwee-White, L. *Dalton Trans.* **2006**, 5327–5333. (d) Koh, W.; Kumar, D.; Li, W.-M.; Sprey, H.; Raaijmakers, I. J. *Solid St. Technol.* **2005**, *48*, 54–58. (e) Sim, H. S.; Kim, S.-I.; Kim, Y. T. *J. Vac. Sci. Technol. B* **2003**, *21*, 1411–1414. (f) Lee, B. H.; Yong, K. *J. Vac. Sci. Technol. B* **2004**, *22*, 2375–2379. (g) Kelsey, J. E.; Goldberg, C.; Nuesca, G.; Peterson, G.; Kaloyeros, A. E.; Arkles, B. *J. Vac. Sci. Technol. B* **1999**, *17*, 1101–1104.
14. Koike, J.; Wada, M. *Appl. Phys. Lett.* **2005**, *87*, 041911.
15. Bruynseraede, C.; Fischer, A. H.; Ungar, F.; Schumacher, J.; Sutcliffe, V.; Michelon, J.; Maex, K. Proceedings of the IEEE Int. Interconnect Technol. Conf., Burlingame, CA, June 7–9, 2004; IEEE: 2004; pp. 12–14.
16. Haneda, M.; Iijima, J.; Koike, J. *Appl. Phys. Lett.* **2007**, *90*, 252107.
17. Chu, J. P.; Lin, C. H.; John, V. S. *Appl. Phys. Lett.* **2007**, *91*, 132109.
18. Barmak, K.; Cabral, C., Jr.; Rodbell, K. P.; Harper, J. M. E. *J. Vac. Sci. Technol. B* **2006**, *24*, 2485–2498.
19. (a) Frederick, M. J.; Goswami, R.; Ramanath, G. *J. Appl. Phys.* **2003**, *93*, 5966–5972. (b) Frederick, M. J.; Ramanath, G. *J. Appl. Phys.* **2004**, *95*, 363–366. (c) Frederick, M. J.; Ramanath, G. *J. Appl. Phys.* **2004**, *95*, 3202–3205.
20. Moon, D.-Y.; Han, D.-S.; Park, J.-H.; Shin, S.-Y.; Park, J.-W.; Kim, B. M.; Cho, J. Y. *Thin Solid Films* **2012**, *521*, 146–149.
21. Kalutarage, L. C.; Clendenning, S. B.; Winter, C. H. *ECS Trans.* **2014**, *64*, 147–157.
22. Rossnagel, S. M. *J. Vac. Sci. Technol. A* **2003**, *21*, S74–S87.

23. (a) Pierson, H. O. *Handbook of Chemical Vapor Deposition (CVD)*; Noyes Publications/William Andrew Publishing: Norwich, NY, 1999. (b) Gladfelter, W. L. *Chem. Mater.* **1993**, *5*, 1372–1388. (c) Gates, S. M. *Chem. Rev.* **1996**, *96*, 1519–1532. (d) Doppelt, P. *Coord. Chem. Rev.* **1998**, *180*, 1785–1809.
24. (a) Leskelä, M.; Ritala, M. *Angew. Chem. Int. Ed.* **2003**, *42*, 5548–5554. (b) Niinistö, L.; Päiväsaari, J.; Niinistö, J.; Putkonen, M.; Nieminen, M. *Phys. Stat. Sol. A.* **2004**, *201*, 1443–1452. (c) Putkonen, M.; Niinistö, L. *Top. Organomet. Chem.* **2005**, *9*, 125–145. (d) Puurunen, R. L. *J. Appl. Phys.* **2005**, *97*, 121301. (e) George, S. M. *Chem. Rev.* **2010**, *110*, 111–131. (f) Knez, M.; Nielsch, K.; Niinistö, L. *Adv. Mater.* **2007**, *19*, 3425–3438. (g) Leskelä, M.; Ritala, M.; Nilsen, O. *MRS Bull.* **2011**, *36*, 877–884.
25. Norman, J. A. T.; Muratore, B. A.; Dyer, P. N.; Roberts, D. A.; Hochberg, A. K.; Dubois, L. H. *Mater. Sci. Eng., B* **1993**, *17*, 87–92.
26. (a) Aleskovskii, V. B. *Zh. Prikl. Khim.* **1974**, *47*, 2145. (b) Puurunen, R. L. *J. Appl. Phys.* **2005**, *97*, 121301. (c) Malygin, A. A. *J. Ind. Eng. Chem.* **2006**, *12*, 1–11.
27. (a) Solehmainen, K.; Kapulainen, M.; Heimala, P.; Polamo, K. *IEEE Photonic Tech L.* **2004**, *16*, 194–196. (b) Graugnard, E.; Gaillot, D. P.; Dunham, S. N.; Neff, C. W.; Yamashita, T.; Summers, C. J. *Appl. Phys. Lett.* **2006**, *89*, 181108. (c) Gaillot, D. P.; Graugnard, E.; Blair, J.; Summers, C. J. *Appl. Phys. Lett.* **2007**, *91*, 181123. (d) Tan, L. K.; Gao, H.; Zong, Y.; Knoll, W. *J. Phys. Chem. C.* **2008**, *112*, 17576–17580. (e) Kumar, P.; Wiedmann, M. K.; Winter, C. H.; Avrutsky, I. *Appl. Optics* **2009**, *48*, 5407–5412.
28. (a) Yen, W. M., Weber, M. J. *Inorganic Phosphors: Compositions, Preparation, and Optical Properties*; CRC Press: 2004. (b) Leskelä, M.; Koskentalo, T.; Blasse, G. *J. Solid State Chem.* **1985**, *89*, 272–279. (c) Schipper, W. J.; van der Voort, D.; van der Berg, P.;

- Vroon, Z. A. E. P.; Blasse, G. *Mater. Chem. Phys.* **1993**, *33*, 311–317. (d) Peterson, J. R.; Xu, W.; Dai, S. *Chem. Mater.* **1995**, *7*, 1686–1689. (e) Seo, H. J.; Moon, B. K.; Kim, B. J.; Kim, J. B.; Tsuboi, T. *J. Phys. Condens. Mater.* **1999**, *11*, 7635–7644. (f) Pir, P. V.; Dotsenko, V. P.; Efryushina, N. P.; Berezovskaya, I. V. *Inorg. Mater.* **2006**, *42*, 901–907. (g) Chang, C.-K.; Chen, T.-M. *Appl. Phys. Lett.* **2007**, *91*, 081902. (h) Song, W.-S.; Kim, Y.-S.; Yang, H. *Mater. Chem. Phys.* **2009**, *117*, 500–503. (i) Pekgözlü, İ.; Karabulut, H. *Inorg. Mater.* **2009**, *45*, 61–64.
29. Parsons, G. N.; Elam, J. W.; George, S. M.; Haukka, S.; Jeon, H.; Kessels, W. M. M.; Leskelä, M.; Poodt, P.; Ritala, M.; Rossnagel, S. M. *J. Vac. Sci. Technol. A* **2013**, *31*, 050818.
30. Miikkulainen, V.; Leskelä, M.; Ritala, M.; Puurunen, R. L. *J. Appl. Phys.* **2013**, *113*, 021301.
31. Knisley, T. J.; Kalutarage, L. C.; Winter, C. H. *Coord. Chem. Rev.* **2013**, *257*, 3222–3231.
32. Kalutarage, L. C.; Heeg, M. J.; Martin, P. D.; Saly, M. J.; Kuiper, D. S.; Winter, C. H. *Inorg. Chem.* **2013**, *52*, 1182–1184.
33. Park, K.-H.; Bradley, A. Z.; Thompson, J. S.; Marshall, W. J. *Inorg. Chem.* **2006**, *45*, 8480–8482.
34. Thompson, J. S.; Zhang, L.; Wyre, J. P.; Brill, D. J.; Lloyd, K. G. *Thin Solid Films* **2009**, *517*, 2845–2850.
35. Sadique, A. R.; Heeg, M. J.; Winter, C. H. *Inorg. Chem.* **2001**, *40*, 6349–6355.
36. Lim, B. S.; Rahtu, A.; Gordon, R. G. *Nat. Mater.* **2003**, *2*, 748–754.
37. Lim, B. S.; Rahtu, A.; Park, J.-S.; Gordon, R. G. *Inorg. Chem.* **2003**, *42*, 7951–7958.

38. Li, Z.; Lee, D. K.; Coulter, M.; Rodriguez, L. N. J.; Gordon, R. G. *Dalton Trans.* **2008**, 2592–2597.
39. Kalutarage, L. C.; Martin, P. D.; Heeg, M. J.; Winter, C. H. *J. Am. Chem. Soc.* **2013**, *135*, 12588–12591.
40. Zaera, F. *J. Phys. Chem. Lett.*, **2012**, *3*, 1301–1309.
41. *Handbook of Chemistry and Physics*, 92<sup>nd</sup> Ed.; CRC Press: Boca Raton, FL, 2011–2012; pp 5–80–5–89, <http://www.hbcnetbase.com/>.
42. Knisley, T. J.; Saly, M. J.; Heeg, M. J.; Roberts, J. L.; Winter, C. H. *Organometallics* **2011**, *30*, 5010–5017.
43. Kim, K.; Lee, K.; Han, S.; Jeong, W.; Jeon, H. *J. Electrochem. Soc.* **2007**, *154*, H177–H181.
44. Kim, J.-M.; Lee, H.-B.-R.; Lansalot, L.; Dussarrat, C.; Gatineau, J.; Kim, H. *Jpn. J. Appl. Phys.* **2010**, *49*, 05FA10.
45. Lee, H.-B.-R.; Gu, G. H.; Son, J. Y.; Park, C. G.; Kim, H. *Small* **2008**, *4*, 2247–2254.
46. Lee, H.-B.-R.; Bang, S.-H.; Kim, W.-H.; Gu, G. H.; Lee, Y. K.; Chung, T.-M.; Kim, C. G.; Park, C. G.; Kim, H. *Jpn. J. Appl. Phys.* **2010**, *49*, 05FA11.
47. Chae, J.; Park, H.-S.; Kang, S.-w. *Electrochem. Solid-State Lett.* **2002**, *5*, C64–C66.
48. Coyle, J. P.; Dey, G.; Sirianni, E. R.; Kemell, M. L.; Yap, G. P. A.; Ritala, M.; Leskelä, M.; Elliott, S. D.; Barry, S. T. *Chem. Mater.* **2013**, *25*, 1132–1138.
49. Profijt, H. B.; Potts, S. E.; van de Sanden, M. C. M.; Kessels, W. M. M. *J. Vac. Sci. Technol. A* **2011**, *29*, 050801.
50. Patel, S.; Butt, A.; Tao, Q.; Rossero A., J. I.; Royhman, D.; Sukotjo, C.; Takoudis, C. G. *Colloid Surface B* **2014**, *115*, 280–285.

51. Kumar, N.; Yang, Y.; Noh, W.; Girolami, G. S.; Abelson, J. R. *Chem. Mater.* **2007**, *19*, 3802–3807.
52. Yoshida, N.; Han, K.; Beach, M.; Lu, X.; Hung, R.; Chen, H.; Tang, W.; Lei, Y.; Zhou, J.; Jin, M.; Xu, K.; Phatak, A.; Sun, S.; Hassan, S.; Gandikota, S.; Chang, C.-P.; Brand, A. *Solid State Technol.* **2014**, <http://electroiq.com/blog/2014/10/threshold-voltage-tuning-for-10nm-and-beyond-cmos-integration/>.
53. Huang, R. P.; Tsai, T. C.; Lin, W.; Huang, H. F.; Tsai, M. C.; Hsu, H. K.; Hsu, C. M.; Lin, J. F.; Wu, J. Y. *Microelectron. Eng.* **2013**, *106*, 56–62.
54. Veloso, A.; Chew, S. A.; Higuchi, Y.; Ragnarsson, L.-A.; Simoen, E.; Schram, T.; Witters, T.; Van Ammel, A.; Dekkers, H.; Tielens, H.; Devriendt, K.; Heylen, N.; Sebaai, F.; Brus, S.; Favia, P.; Geypen, J.; Bender, H.; Phatak, A.; Chen, M. S.; Lu, X.; Ganguli, S.; Lei, Y.; Tang, W.; Fu, X.; Gandikota, S.; Noori, A.; Brand, A.; Yoshida, N.; Thean, A.; Horiguchi, N. *Jpn. J. Appl. Phys.* **2013**, *52*, 04CA02.
55. (a) Karlsson, P. G.; Richter, J. H.; Andersson, M. P.; Johansson, M. K.-J.; Blomquist, J.; Uvdal, P.; Sandell, A. *Surf. Sci.* **2011**, *605*, 1147–1156. (b) Edusi, C.; Hyett, G.; Sankar, G.; Parkin, I. P. *Chem. Vap. Deposition* **2011**, *17*, 30–36.
56. Kariniemi, M.; Niinistö, J.; Vahkamäki, M.; Kemell, M.; Ritala, M.; Leskelä, M. *J. Vac. Sci. Technol., A* **2012**, *30*, 01A115.
57. Kim, S. J.; Dang, V.-S.; Xu, K.; Barreca, D.; Maccato, C.; Carraro, G.; Bhakta, R. K.; Winter, M.; Becker, H.-W.; Rogalla, D.; Sada, C.; Fischer, R. A.; Devi, A. *Phys. Status Solidi A* **2015**, 1–8.
58. (a) Aarik, L.; Arroval, T.; Rammula, R.; Mändar, H.; Sammelseg, V.; Aarik, J. *Thin Solid Films* **2013**, *542*, 100–107. (b) Aarik, J.; Arroval, T.; Aarik, L.; Rammula, R.;

- Kasikov, A.; Mändar, H.; Hudec, B.; Hušeková, K.; Fröhlich, K. *J. Cryst. Growth* **2013**, *382*, 61–66.
59. Pore, V.; Rahtu, A.; Leskelä, M.; Ritala, M.; Sajavaara, T.; Keinonen, J. *Chem. Vap. Deposition* **2004**, *10*, 143–148.
60. Pore, V.; Dimri, M.; Khanduri, H.; Stern, R.; Lu, J.; Hultman, L.; Kukli, K.; Ritala, M.; Leskelä, M. *Thin Solid Films* **2011**, *519*, 3318–3324.
61. Alekhin, A. P.; Lapushkin, G. I.; Markeev, A. M.; Sigarev, A. A.; Toknova, V. F. *Russ. J. Gen. Chem.* **2010**, *80*, 1091–1096.
62. (a) Avril, L.; Reymond-Laruinaz, S.; Decams, J. M.; Bruyère, S.; Potin, V.; Marco de Lucas, M. C.; Imhoff, L. *Appl. Surf. Sci.* **2014**, *288*, 201–207. (b) Kukli, K.; Lu, J.; Link, J.; Kemell, M.; Puukilainen, E.; Heikkilä, M.; Hoxha, R.; Tamm, A.; Hultman, L.; Stern, R.; Ritala, M.; Leskelä, M. *Thin Solid Films* **2014**, *565*, 165–171.
63. Katamreddy, R.; Omarjee, V.; Feist, B.; Dussarrat, C. *ECS Trans.* **2008**, *16*, 113–122.
64. Nam, T.; Kim, J.-M.; Kim, M.-K.; Kim, H.; Kim, W.-H. *J. Korean Phys. Soc.* **2011**, *59*, 452–457.
65. Kukli, K.; Kemell, M.; Dimri, M. C.; Puukilainen, E.; Tamm, A.; Stern, R.; Ritala, M.; Leskelä, M. *Thin Solid Films*, **2014**, *565*, 261–266.
66. Shimada, S.; Takada, Y.; Tsujino, J. *Surf. Coat. Technol.* **2005**, *199*, 72–76.
67. Heo, S. C.; Choi, C. *Microelectron. Eng.* **2012**, *94*, 11–13.
68. Fainer, N. I.; Golubenko, A. N.; Rumyantsev, Y. M.; Kesler, V. G.; Maksimovskii, E. A.; Kuznetsov, F. A. *Glass Phys. Chem.* **2011**, *37*, 322–329.
69. Wasslen, Y. A.; Tois, E.; Haukka, S.; Kreisel, K. A.; Yap, G. P. A.; Halls, M. D.; Barry, S. T. *Inorg. Chem.* **2010**, *49*, 1976–1982.

70. Ludviksson, A.; Nooney, M.; Bruno, R.; Bailey, A.; Kodas, T. T.; Hampden-Smith, M. J. *Chem. Vap. Deposition* **1998**, *4*, 129–132.
71. Hendricks, J. H.; Aquino, M. I.; Maslar, J. E.; Zachariah, M. R. *Chem. Mater.* **1998**, *10*, 2221–2229.
72. (a) Kritikos, L.; Zambelis, L.; Papadimitropoulos, G.; Davazoglou, D. *Surf. Coat. Technol.* **2007**, *201*, 9334–9339. (b) Mathur, S.; Ruegamar, T.; Grobelsek, I. *Chem. Vap. Deposition* **2007**, *13*, 42–47. (c) Menezes, W. G.; Reis, D. M.; Oliveira, M. M.; Soares, J. F.; Zarbin, A. J. G. *Chem. Phys. Lett.* **2007**, *445*, 293–296. (d) Granqvist, C. G. *Int. J. Nanotechnol.* **2009**, *6*, 785–798.
73. Granqvist, C. G. *Adv. Mater.* **2003**, *15*, 1789–1803.
74. Granqvist, C. G. *Thin Solid Films* **1990**, *193–194*, 730–741.
75. Rogers, K. D. *Powder Diffr.* **1993**, *8*, 240–244.
76. Piccirillo, C.; Binions, R.; Parkin, I. P. *Chem. Vap. Deposition* **2007**, *13*, 145–151.
77. (a) Ibris, N.; Salvi, A. M.; Liberatore, M.; Decker, F.; Surca, A. *Surf. Interface Anal.* **2005**, *37*, 1092–1104. (b) Deki, S.; Aoi, S.; Kajinami, Y. *J. Mater. Sci.* **1997**, *32*, 4269–4273. (c) Navone, C.; Pereira-Ramos, J. P.; Baddour-Hadjean, R.; Salot, R. *J. Power Sources* **2005**, *146*, 327–330. (d) Guan, Z. S.; Yao, J. N.; Yang, Y. A.; Loo, B. H. *J. Electroanal. Chem.* **1998**, *443*, 175–179. (e) Field, M. N.; Parkin, I. P. *J. Mater. Chem.* **2000**, *10*, 1863–1866. (f) Saitzek, S.; Guinneton, F.; Guirleo, G.; Sauques, L.; Aguir, K.; Gavarrí, J.-R. *Thin Solid Films* **2008**, *516*, 891–897. (g) Lee, J. W.; Min, S. R.; Cho, H. N.; Chung, C. W. *Thin Solid Films* **2007**, *515*, 7740–7743. (h) Mantoux, A.; Groult, H.; Balnois, E.; Doppelt, P.; Gueroudji, L. *J. Electrochem. Soc.* **2004**, *151*, A368–A373. (i) Światowska-Mrowiecka, J.; Maurice, V.; Zanna, S.; Klein, L.; Marcus, P. *Electrochim.*



- Acta* **2007**, 52, 5644–5653. (j) Parkin, I. P.; Binions, R.; Piccirillo, C.; Blackman, C. S.; Manning, T. D. *J. Nano Res.* **2008**, 2, 1–20. (k) Shimizu, Y.; Nagase, K.; Miura, N.; Yamazoe, N. *Jpn. J. Appl. Phys.* **1990**, 9, L1708. (l) Abo El Soud, A. M.; Mansour, B.; Soliman, L. I. *Thin Solid Films* **1994**, 247, 140–143. (m) Maruyama, T.; Ikuta, Y. *J. Mater. Sci.* **1993**, 28, 5073–5078. (n) Dachuan, Y.; Niankan, X.; Jingyu, Z.; Xiulin, Z. *Mater. Res. Bull.* **1996**, 31, 335–340.
78. Manning, T. D.; Parkin, I. P.; Clark, R. J. H.; Sheel, D.; Pemble, M. E.; Vernadou, D. J. *Mater. Chem.* **2002**, 12, 2936–2939.
79. Mendialdua, J.; Casanova, R.; Barbaux, Y. *J. Electron Spectrosc. Relat. Phenom.* **1995**, 71, 249–261.
80. Beardslee, J. A.; Mebust, A. K.; Chaimowitz, A. S.; Davis-VanAtta, C. R.; Leonard, H.; Moersch, T. L.; Afridi, M. Y.; Taylor, C. J. *Chem. Vap. Deposition* **2010**, 16, 206–210.
81. (a) Chang, H. L. M.; Gao, Y.; Zhang, T. J.; Lam, D. J. *Thin Solid Films* **1992**, 216, 4–7. (b) Zhang, H.; Chang, H. L. M.; Guo, J.; Zhang, T. J. *J. Mater. Res.* **1994**, 9, 2264–2271.
82. Crociani, L.; Carta, G.; Natali, M.; Rigato, V.; Rossetto, G. *Chem. Vap. Deposition* **2011**, 17, 6–8.
83. (a) Saeli, M.; Binions, R.; Piccirillo, C.; Parkin, I. P. *Appl. Surf. Sci.* **2009**, 255, 7291–7295. (b) Sahana, M. B.; Dharmaprasanth, M. S.; Shivashankar, S. A. *J. Mater. Chem.* **2002**, 12, 333–338.
84. Barreca, D.; Depero, L. E.; Franzato, E. Rizzi, G. A. Sangaletti, L.; Tondello, E. Vettoria, U. *J. Electrochem. Soc.* **1999**, 146, 551–558.
85. Boscher, N. D.; Blackman, C. S.; Carmalt, C. J.; Parkin, I. P.; Prieto, A. G. *Appl. Surf. Sci.* **2007**, 253, 6041–6046.

86. Piccirillo, C.; Binions, R.; Parkin, I. P. *Thin Solid Films* **2008**, *516*, 1992–1997.
87. Kiri, P.; Warwick, M. E. A.; Ridley, I.; Binions, R. *Thin Solid Films* **2011**, *520*, 1363–1366.
88. (a) Rampelberg, G.; Schaekers, M.; Martens, K.; Xie, Q.; Deduytsche, D.; De Schutter, B.; Blasco, N.; Kittl, J.; Detavernier, C. *Appl. Phys. Lett.* **2011**, *98*, 162902. (b) Rampelberg, G.; Deduytsche, D.; De Schutter, B.; Premkumar, P. A.; Toeller, M.; Schaekers, M.; Martens, K.; Radu, I.; Detavernier, C. *Thin Solid Films* **2014**, *550*, 59–64.
89. Kim, D. Y.; Girolami, G. S. *J. Am. Chem. Soc.* **2006**, *128*, 10969–10977.
90. Boldyrev, Y. I.; Ivanova, N. D.; Sokolsky, G. V.; Ivanov, S. V.; Stadnik, O. A. *J Solid State Electrochem.* **2013**, *17*, 2213–2221.
91. Siddiqi, M.A.; Siddiqui, R.A.; Atakan, B. *J. Chem. Eng. Data* **2010**, *55*, 2149–2154.
92. (a) Carta, G.; Natali, M.; Rossetto, G.; Zanella, P.; Salmaso, G.; Restello, S.; Rigato, V.; Kaciulis, S.; Mezzi, A. *Chem. Vap. Deposition* **2005**, *11*, 375–380. (b) Douard, A.; Maury, F. *Surf. Coat. Technol.* **2005**, *200*, 1407–1412. (c) Bullen, H. A.; Garrett, S. J. *Chem. Mater.* **2002**, *14*, 243–248. (d) Ivanov, P. G.; Watts, S. M.; Lind, D. M. *J. Appl. Phys.*, **2001**, *89*, 1035–1040. (e) DeSisto, W. J.; Broussard, P. R.; Ambrose, T. F.; Nadgorny, B. E.; Osofsky, M. S. *Appl. Phys. Lett.*, **2000**, *76*, 3789–3791. (f) Maruyama, T.; Akagi, H. *J. Electrochem. Soc.*, **1996**, *143*, 1955–1958.
93. (a) Lippitz, A.; Hübert, T. *Surf. Coat. Technol.* **2005**, *200*, 250–253. (b) Dasgupta, A.; Kuppasami, P.; Lawrence, F.; Raghunathan, V. S.; Premkumar, P. A.; Nagaraja, K. S. *Mater. Sci. Eng. A* **2004**, *374*, 362–368. (c) Hones, P.; Martin, N.; Regula, M.; Levy, F. *J. Phys. D: Appl. Phys.* **2003**, *36*, 1023–1029. (d) Barata, A.; Cunha, L.; Moura, C. *Thin Solid Films* **2001**, *398–399*, 501–506.

94. El-Kadri, O. M.; Heeg, M. J.; Winter, C. H. *Dalton Trans.* **2006**, 4506–4513.
95. Sousa, P. M.; Silvestre, A. J.; Conde, O. *Thin Solid Films* **2011**, *519*, 3653–3657.
96. Lin, H.-T.; Nayak, P. K.; Wang, S.-C.; Chang, S.-Y.; Huang, J.-L. *J. Eur. Ceram. Soc.* **2011**, *31*, 2481–2487.
97. (a) Goedde, D. M.; Girolami, G. S. *J. Am. Chem. Soc.* **2004**, *126*, 12230–12231. (b) Goedde, D. M.; Windler, G. K.; Girolami, G. S. *Inorg. Chem.* **2007**, *46*, 2814–2823. (c) Jayaraman, S.; Klein, E. J.; Yang, Y.; Kim, D. Y.; Girolami, G. S.; Abelson, J. R. *J. Vac. Sci. Technol. A* **2005**, *23*, 631–633.
98. Kalutarage, L. C.; Martin, P. D.; Heeg, M. J.; Winter, C. H. *Inorg. Chem.* **2013**, *52*, 5385–5394.
99. Nilsen, O.; Fjellvåg, H.; Kjekshus, A. *Thin Solid Films* **2003**, *444*, 44–51.
100. (a) Chen, L.; Schoonman, J. *Solid State Ionics* **1993**, *60*, 227–231. (b) Yu, X. Q.; He, Y.; Sun, J. P.; Tang, K.; Li, H.; Chen, L. Q.; Huang, X. J. *Electrochem. Commun.* **2009**, *11*, 791–794.
101. Rizzi, G. A.; Zannoni, R.; Di Siro, S.; Perriello, L.; Granozzi, G. *Surf. Sci.* **2000**, *462*, 187–194.
102. Qin, X.; Sun, H.; Zaera, F. *J. Vac. Sci. Technol. A* **2012**, *30*, 01A112.
103. Nakamura, T.; Tai, R.; Nishi, T.; Tachibara, K. *J. Electrochem. Soc.* **2005**, *152*, C584–C587.
104. Nilsen, O.; Foss, S.; Fjellvåg, H.; Kjekshus, A. *Thin Solid Films* **2004**, *468*, 65–74.
105. Burton, B. B.; Fabreguette, F. H.; George, S. M.; *Thin Solid Films* **2009**, *517*, 5658–5665.
106. Sun, H.; Qin, X.; Zaera, F. *J. Phys. Chem. Lett.* **2011**, *2*, 2525–2530.

107. Sun, H.; Qin, X.; Zaera, F. *J. Phys. Chem. Lett.* **2012**, *3*, 2523–2527.
108. Au, Y.; Lin, Y.; Kim, H.; Beh, E.; Liu, Y.; Gordon, R. G. *J. Electrochem. Soc.* **2010**, *157*, D341–D345.
109. Smith, G. B.; Gentle, A.; Swift, P. D.; Earp, A.; Mronga, N. *Sol. Energy Mater. Sol. Cells* **2003**, *79*, 179–197.
110. Yazdi, M. B.; Goyallon, M.-L.; Bitsch, T.; Kastner, A.; Schlott, M.; Alff, L. *Thin Solid Films* **2011**, *519*, 2531–2533.
111. Mathur, S.; Sivakov, V.; Shen, H.; Barth, S.; Cavelius, C.; Nilsson, A.; Kuhn, P. *Thin Solid Films* **2006**, *502*, 88–93.
112. (a) Kang, S. H. *JOM* **2008**, *60*, 28–33. (b) Vaz, C. A. F.; Bland, J. A. C.; Lauhoff, G. *Rep. Prog. Phys.* **2008**, *71*, 056501. (c) Shiratsuchi, Y.; Yamamoto, M.; Bader, S. D. *Progr. Surf. Sci.* **2007**, *82*, 121–160.
113. Lin, Y.; Xu, Y.; Mayer, M. T.; Simpson, Z. I.; McMahon, G.; Zhou, S.; Wang, D. *J. Am. Chem. Soc.* **2012**, *134*, 5508–5511.
114. Bachmann, J.; Jing J.; Knez, M.; Barth, S.; Shen, H.; Mathur, S.; Gösele, U.; Nielsch, K. *J. Am. Chem. Soc.* **2007**, *129*, 9554–9555.
115. Lie, M.; Klepper, K. B.; Nilsen, O.; Fjellvåg, H.; Kjekshus, A. *Dalton Trans.* **2008**, 253–259.
116. Scheffe, J. R.; Francés, A.; King, D. M.; Liang, X.; Branch, B. A.; Cavanagh, A. S.; George, S. M.; Weimer, A. W. *Thin Solid Films* **2009**, *517*, 1874–1879.
117. Martinson, A. B. F.; DeVries, M. J.; Libera, J. A.; Christensen, S. T.; Hupp, J. T.; Pellin, M. J.; Elam, J. W. *J. Phys. Chem. C* **2011**, *115*, 4333–4339.

118. Tamm, A.; Dimri, M. C.; Kozlova, J.; Aidla, A.; Tätte, T.; Arroval, T.; Mäeorg, U.; Mändar, H.; Stern, R.; Kukli, K. *J. Cryst. Growth* **2012**, *343*, 21–27.
119. Zandi, O.; Klahr, B. M.; Hamann, T. W. *Energy Environ. Sci.* **2013**, *6*, 634–642.
120. Stauf, G. T.; Driscoll, D. C.; Dowben, P. A. *Thin Solid Films* **1987**, *153*, 421–430.
121. Low, Y. H.; Bain, M. F.; Bien, D. C. S.; Montgomery, J. H.; Armstrong, B. M.; Gamble, H. S. *Microelectron. Eng.* **2006**, *83*, 2229–2233.
122. (a) Lutzev, L. V.; Stognij, A. I.; Novitskii, N. N. *Phys. Rev. B* **2009**, *80*, 184423. (b) Vo-Van, C.; Kassir-Bodon, Z.; Yang, H.; Coraux, J.; Vogel, J.; Pizzini, S.; Bayle-Guillemaud, P.; Chshiev, M.; Ranno, L.; Guisset, V.; David, P.; Salvador, V.; Fruchart, O. *New J. Phys.* **2010**, *12*, 103040. (c) Zhu, S.; Van Meirhaeghe, R. L.; Detavernier, C.; Cardon, F.; Ru, G.-P.; Qu, X.-P.; Li, B.-Z. *Solid-St. Electronics* **2000**, *44*, 663–671. (d) He, M.; Zhang, X.; Nogami, T.; Lin, X.; Kelly, J.; Kim, H.; Spooner, T.; Edelstein, D.; Zhao, L. *J. Electrochem. Soc.* **2013**, *160*, D3040–D3044. (e) Yang, C.-C.; Flaitz, P.; Wang, P. C.; Chen, F.; Edelstein, D. *IEEE Electr. Device Lett.* **2010**, *31*, 728–730. (f) McCoy, M. *C&EN* **2014**, *92*, 16–17.
123. (a) Barreca, D.; Devi, A.; Fischer, R. A.; Bekermann, D.; Gasparotto, A.; Gavagnin, M.; Maccato, C.; Tondello, E.; Bontempi, E.; Depero, L. E.; Sada, C. *CrystEngComm* **2011**, *13*, 3670–3673. (b) Burriel, M.; Garcia, G.; Santiso, J.; Abrutis, A.; Saltyte, Z.; Figueras, A. *Chem. Vap. Deposition* **2005**, *11*, 106–111.
124. Donders, M. E.; Knoops, H. C. M.; Kessels, W. M. M.; Notten, P. H. L. *J. Power Sources* **2012**, *203*, 72–77.
125. Han, B.; Park, J.-M.; Choi, K. H.; Lim, W.-K.; Mayangsari, T. R.; Koh, W.; Lee, W.-J. *Thin Solid Films* **2015**, *589*, 718–722.

126. Klepper, K. B.; Nilsen, O.; Fjellvåg, H. *Thin Solid Films* **2007**, *515*, 7772–7781.
127. Lybeck, J.; Valkeapaa, M.; Shibasaki, S.; Terasaki, I.; Yamauchi, H.; Karppinen, M. *Chem. Mater.* **2010**, *22*, 5900–5904.
128. Lee, K.; Park, T.; Lee, J.; Kim, J.; Kim, J.; Kwak, N.; Yeom, S.; Jeon, H. *Jap. J. Appl. Phys.* **2008**, *47*, 5396–5399.
129. Park, J.-H.; Moon, D.-Y.; Han, D.-S.; Kang, Y.-J.; Shin, S.-R.; Jeon, H.-T.; Park, J.-W. *Surf. Coat. Technol.* **2014**, *259*, 98–101.
130. (a) Lee, H.-B.-R.; Kim, H. *Electrochem. Solid State Lett.* **2006**, *9*, G323–G325. (b) Lee, K.; Kim, K.; Park, T.; Jeon, H.; Lee, Y.; Kim, J.; Yeom, S. *J. Electrochem. Soc.* **2007**, *154*, H899–H903.
131. Kim, K.; Lee, K.; Han, S.; Park, T.; Lee, Y.; Kim, J.; Yeom, S.; Jeon, H. *Jpn. J. Appl. Phys.* **2007**, *46*, L173–L176.
132. Lee, H.-B.-R.; Son, J. Y.; Kima, H. *Appl. Phys. Lett.* **2007**, *90*, 213509.
133. (a) Yoon, J.; Lee, H.-B.-R.; Kim, D.; Cheon, T.; Kim, S.-H.; Kim, H. *J. Electrochem. Soc.* **2011**, *158*, H1179–H1182. (b) Lee, H.-B.-R.; Park, Y. J.; Baik, S.; Kim, H. *Chem. Vap. Deposition* **2012**, *18*, 41–45.
134. Park, J.; Lee, H.-B.-R.; Kim, D.; Yoon, J.; Lansalot, C.; Gatineau, J.; Chevrel, H.; Kim, H. *J. Energy Chem.* **2013**, *22*, 403–407.
135. Daub, M.; Knez, M.; Goesele, U.; Nielsch, K. *J. Appl. Phys.* **2007**, *101*, 09J111.
136. Lee, H.-B.-R.; Kim, H. *ECS Trans.* **2008**, *16*, 219–225.
137. Lee, H.-B.-R.; Kim, W.-H.; Lee, J. W.; Kim, J.-M.; Heo, K.; Hwang, I. C.; Park, Y.; Hong, S.; Kim, H. *J. Electrochem. Soc.* **2010**, *157*, D10–D15.

138. Lee, H.-B.-R.; Kim, J.; Kim, H.; Kim, W.-H.; Lee, J. W.; Hwang, I. *J. Korean Phys. Soc.* **2010**, *56*, 104–107.
139. Raudzus, A. W.; Winter, C. H. unpublished results, Wayne State University.
140. Li, J.; Wu, J.; Zhou, C.; Han, B.; Lei, X.; Gordon, R.; Cheng, H. *Int. J. Quantum Chem.* **2009**, *109*, 756–763.
141. Wu, J.; Li, J.; Zhou, C.; Lei, X.; Gaffney, T.; Norman, J. A. T.; Li, Z.; Gordon, R.; Cheng, H. *Organometallics* **2007**, *26*, 2803–2805.
142. Kwon, J.; Saly, M.; Kanjolia, R. K.; Chabal, Y. J. *Chem. Mater.* **2011**, *23*, 2068–2074.
143. Kwon, J.; Saly, M.; Halls, M. D.; Kanjolia, R. K.; Chabal, Y. J. *Chem. Mater.* **2012**, *24*, 1025–1030.
144. Bernal-Ramos, K.; Saly, M. J.; Kanjolia, R. K.; Chabal, Y. J. *Chem. Mater.* **2015**, *27*, 4943–4949.
145. Karunaratne, M. C.; Knisley, T. J.; Tunstull, G. S.; Heeg, M. J.; Winter, C. H. *Polyhedron* **2013**, *52*, 820–830.
146. (a) Gillot, F.; Oró-Solé, J.; Palacín, M. R. *J. Mater. Chem.* **2011**, *21*, 9997–10002. (b) Wang, Y.; Fu, Z.-S.; Yue, X.-L.; Qin, W.-Z. *J. Electrochem. Soc.* **2004**, *151*, E162–E167.
147. Li, Z.; Gordon, R. G.; Li, H.; Shenai, D. V.; Lavoie, C. *J. Electrochem. Soc.* **2010**, *157*, H679–H683.
148. West, A. R. *Basic Solid State Chemistry*, 2<sup>nd</sup> ed.; Wiley: New York, 1999; p. 319.
149. Min, K.-C.; Kim, M.; You, Y.-H.; Lee, S. S.; Lee, Y. K.; Chung, T.-M.; Kim, C. G.; Hwang, J.-H.; An, K.-S.; Lee, N.-S.; Kim, Y. *Surf. Coat. Technol.* **2007**, *201*, 9252–9255.

150. Lee, M.-J.; Seo, S.; Kim, D.-C.; Ahn, S.-E.; Seo, D. H.; Yoo, I.-K.; Baek, I.-G.; Kim, D.-S.; Byun, I.-S.; Kim, S.-H. *Adv. Mater.* **2007**, *19*, 73–76.
151. Chung, T.-M.; Lee, S. S.; Cho, W.; Lee, Y. K.; Hwang, J.-H.; An, K.-S.; Kim, C. G. *Bull. Korean Chem. Soc.* **2011**, *32*, 783–784.
152. Sun, K.; Saadi, F. H.; Lichterman, M. F.; Hale, W. G.; Wang, H.-P.; Zhou, X.; Plymale, N. T.; Omelchenko, S. T.; He, J.-H.; Papadantonakis, K. M.; Brunshwig, B. S.; Lewis, N. S. *Proc. Natl. Acad. Sci. U.S.A.* **2015**, *112*, 3612–3617.
153. Hu, C.-C.; Teng, H. *J. Catal.* **2010**, *272*, 1–8.
154. Ishikawa, M.; Kada, T.; Machida, H.; Ohshita, Y.; Ogura, A. *Jpn. J. Appl. Phys.* **2004**, *43*, 1833–1836.
155. Lindahl, E.; Ottosson, M.; Carlsson, J.-O. *Surf. Coat. Technol.* **2010**, *205*, 710–716.
156. Lindahl, E.; Ottosson, M.; Carlsson, J.-O. *ECS Trans.* **2009**, *25*, 365–372.
157. Knisley, T. J. New Precursors and Chemistry for the Growth of Transition Metal Films By Atomic Layer Deposition. Ph.D. Dissertation, Wayne State University, Detroit, MI, 2012.
158. Yeh, W.-C.; Matsumura, M. *Jpn. J. Appl. Phys.* **1997**, *36*, 6884–6887.
159. Kang, J.-K.; Rhee, S.-W. *Thin Solid Films* **2001**, *391*, 57–61.
160. Malandrino, G.; Perdicaro, L. M. S.; Condorelli, G.; Fragalà, I. L.; Rossi, P.; Dapporto, P. *Dalton Trans.* **2006**, 1101–1106.
161. Fujii, E.; Tomozawa, A.; Torii, H.; Takayama, R. *Jpn. J. Appl. Phys.* **1996**, *35*, L328–L330.
162. Lu, H. L.; Wiemer, C.; Perego, M.; Spiga, S.; Fanciulli, M.; Pavia, G. *J. Electrochem. Soc.* **2008**, *155*, H807–H811.



163. Bachmann, J.; Zolotaryov, A.; Albrecht, O.; Goetze, S.; Berger, A.; Hesse, D.; Novikov, D.; Nielsch, K. *Chem. Vap. Deposition* **2011**, *17*, 177–180.
164. Lindahl, E.; Ottosson, M.; Carlsson, J.-O. *Chem. Vap. Deposition* **2009**, *15*, 186–191.
165. Yang, T. S.; Cho, W.; Kim, M.; An, K.-S.; Chung, T.-M.; Kim, C. S.; Kim, Y. *J. Vac. Sci. Technol. A* **2005**, *23*, 1238–1243.
166. Premkumar, P. A.; Toeller, M.; Adelman, C.; Meersschat, J.; Franquet, A.; Richard, O.; Tielens, H.; Brijs, B.; Moussa, A.; Conard, T.; Bender, H.; Schaekers, M.; Kittl, J. A.; Jurczak, M.; Elshocht, S. V. *Chem. Vap. Deposition* **2012**, *18*, 61–69.
167. You, Y.-H.; So, B.-S.; Hwang, J.-H.; Cho, W.; Lee, S. S.; Chung, T.-M.; Kim, C. G.; An, K.-S. *Appl. Phys. Lett.* **2006**, *89*, 222105.
168. (a) So, B. S.; Cho, W.; You, Y.-H.; Hwang, J.-H.; Lee, S. S.; Chung, T.-M.; Lee, Y. K.; Kim, C. G.; An, K.-S. *ECS Trans.* **2007**, *3*, 279–282. (b) So, B.-S.; You, Y.-H.; Kim, K.-H.; Hwang, J.; Cho, W.; Lee, S. S.; Chung, T.-M.; Lee, Y. K.; Kim, C. G.; An, K.-S.; Kim, Y.-C.; Lee, Y.-H.; Seo, W.-S. *Electrochem. Solid-State Lett.* **2007**, *10*, J61–J64.
169. Yoo, S. H.; Choi, H.; Kim, H.-S.; Park, B. K.; Lee, S. S.; An, K.-S.; Lee, Y. K.; Chung, T.-M.; Kim, C. G. *Eur. J. Inorg. Chem.* **2011**, 1833–1839.
170. Kada, T.; Ishikawa, M.; Machida, H.; Ogura, A.; Ohshita, Y.; Soai, K. *J. Cryst. Growth* **2005**, *275*, E1115–E1119.
171. Kada, T.; Ishikawaa, M.; Machidaa, H.; Ogurac, A.; Ohshitad, Y.; Soai, K. *J. Cryst. Growth* **2005**, *275*, e1115–e1119.
172. (a) Bakovets, V. V.; Mitkin, V. N.; Gelfond, N. V. *Chem. Vap. Deposition* **2005**, *11*, 112–117. (b) Bakovets, V. V.; Mitkin, V. N.; Gelfond, N. V. *Chem. Vap. Deposition* **2005**, *11*, 368–374.

173. Ishikawa, M.; Kada, T.; Machida, H.; Ohshita, Y.; Ogura, A. *Jpn. J. Appl. Phys.* **2004**, *43*, 1833–1836.
174. Baiker, A.; Maciejewski, M. *J. Chem. Soc., Faraday Trans.* **1984**, *80*, 2331–2341.
175. Lee, K-M.; Kim, C. Y.; Choi, C. K.; Yun, S-W.; Ha, J-B.; Lee, J-H.; Lee, J. Y. *J. Korean Phys. Soc.* **2009**, *55*, 1153–1157.
176. Knisley, T. J.; Winter, C. H. unpublished results, Wayne State University.
177. Do, K.-W.; Yang, C.-M.; Kang, I.-S.; Kim, K.-M.; Back, K.-H.; Cho, H.-I.; Lee, H.-B.; Kong, S.-H.; Hahm, S.-H.; Kwon, D.-H.; Lee, J.-H.; Lee, J.-H. *Jpn. J. Appl. Phys.* **2006**, *45*, 2975–2979.
178. Kim, W.-H.; Lee, H.-B.-R.; Heo, K.; Lee, Y. K.; Chung, T.-M.; Kim, C. G.; Hong, S.; Heo, J.; Kim, H. *J. Electrochem. Soc.* **2011**, *158*, D1–D5.
179. (a) Yang, C.-M.; Yun, S.-W.; Ha, J.-B.; Na, K.-I.; Cho, H.-I.; Lee, H.-B.; Jeong, J.-H.; Kong, S.-H.; Hahm, S.-H.; Lee, J.-H. *Jpn. J. Appl. Phys.* **2007**, *46*, 1981–1983. (b) Ha, J.-B.; Yun, S.-W.; Lee, J.-H. *Curr. Appl. Phys.* **2010**, *10*, 41–46.
180. Arockiasamy, S.; Mallika, C.; Sreetharan, O. M.; Raghunathan, V. S.; Nagaraja, K. S. *Inorg. Chim. Acta.* **2009**, *362*, 1977–1983.
181. (a) Li, Z.; Gordon, R. G. *Chem. Vap. Deposition* **2006**, *12*, 435–441.
182. (a) Liu, Z. Q.; Wang, W. J.; Wang, T. M.; Chao, S.; Zheng, S. K. *Thin Solid Films* **1998**, *325*, 55–59. (b) Maya, L. *J. Vac. Sci. Technol. A* **1993**, *11*, 604–608.
183. (a) Cremer, R.; Witthaut, M.; Neuschütz, D.; Trappe, C.; Laurenzis, M.; Winkler, O.; Kurz, H. *Mikrochim. Acta* **2000**, *133*, 299–302. (b) Maruyama, T.; Morishita, T. *Appl. Phys. Lett.* **1996**, *69*, 890–891.

184. (a) Kwon, J.-D.; Kwon, S.-H.; Jung, T.-H.; Nam, K.-S.; Chung, K.-B.; Kim, D.-H.; Park, J.-S. *Appl. Surf. Sci.* **2013**, *285P*, 373–379. (b) Wadia, C.; Alivisatos, A. P.; Kammen, D. M. *Environ. Sci. Technol.* **2009**, *43*, 2072–2077. (c) Olsen, L. C.; Bohara, R. C.; Urie, M. W. *Appl. Phys. Lett.* **1979**, *34*, 47–49. (d) Fernando, C.A.N.; Wetthasinghe, S.K. *Sol. Energ. Mat. Sol. Cells* **2000**, *63*, 299–308. (e) Kosugi, T.; Kaneko, S. *J. Am. Ceram. Soc.* **1998**, *81*, 3117–3124.
185. (a) Murarka, S. P. *Mater. Sci. Eng.* **1997**, *R19*, 87–151. (b) Chae, Y. K.; Shimogaki, Y.; Komiyama, H. J. *J. Electrochem. Soc.* **1998**, *145*, 4226–4233. (c) Rickerby, J.; Steinke, J. H. G. *Chem. Rev.* **2002**, *102*, 1525–1550.
186. Rosenberg, R.; Edelstein, D. C.; Hu, C. K.; Rodbell, K. P. *Annu. Rev. Mater. Sci.* **2000**, *30*, 229–262.
187. (a) Ramasamy, K.; Malik, M. A.; O'Brien, P. *Chem. Sci.* **2011**, *2*, 1170–1172. (b) Abdelhady, A. L.; Malik, M. A.; O'Brien, P. *J. Mater. Chem.* **2012**, *22*, 3781–3785. (c) Ramasamy, K.; Malik, M. A.; O'Brien, P. *Chem. Commun.* **2012**, *48*, 5703–5714.
188. Winter, C. H.; Knisley, T. J.; Kalutarage, L. C.; Zavada, M. A.; Klesko, J. P.; Perera, T. H. *Encyclopedia of Inorganic and Bioinorganic Chemistry*; Wiley: Chichester, 2012.
189. Gordon, P. G.; Kurek, A.; Barry, S. T. *ECS J. Solid State Sc.* **2015**, *4*, N3188–N3197.
190. Cavallotti, C.; Gupta, V.; Sieber, C.; Jensen, K. F. *Phys. Chem. Chem. Phys.* **2003**, *5*, 2818–2827.
191. Choi, K.-K.; Rhee, S.-W. *Thin Solid Films* **2002**, *409*, 147–152.
192. Powell, R. A.; Fair, J. A. Copper atomic layer chemical vapor deposition. U. S. Patent 6464779, October 15, 2002.

193. Joulaud, M.; Angekort, C.; Doppelt, P.; Mourier, T.; Mayer, D. *Microelectronic Eng.* **2002**, *64*, 107–115.
194. Joulaud, M.; Omnes, L.; Mourier, T.; Mayer, D.; Doppelt, P. Proceedings from the 203<sup>rd</sup> Meeting of the Electrochemical Society, Paris, France, April 28, 2003; Electrochemical Society: 2003.
195. Semaltianos, N. G.; Pastol, J.-L.; Doppelt, P. *Surf. Sci.* **2004**, *562*, 157–169.
196. Tran, P. D.; Allavena-Valette, A.; Kamous, F.; Doppelt, P. *Polyhedron* **2009**, *28*, 4091–4095.
197. Tran, P. D.; Doppelt, P. *Surf. Coat. Technol.* **2007**, *201*, 9066–9070.
198. Mothes, R.; Rüffer, T.; Shen, Y.; Jakob, A.; Walfort, B.; Petzold, H.; Schulz, S. E.; Ecke, R.; Gessnerb, T.; Lang, H. *Dalton Trans.* **2010**, *39*, 11235–11247.
199. Norman, J. A. T.; Perez, M.; Schulz, S. E.; Waechtler, T. *Microelectron. Eng.* **2008**, *85*, 2159–2163.
200. Song, H.; Norman, J. A. T.; Shimogaki, Y. *Microelectronic Eng.* **2010**, *87*, 249–253.
201. Ma, Q.; Zaera, F. *J. Vac. Sci. Technol. A* **2015**, *33*, 01A108.
202. Kang, S. W.; Seong, D. J.; Yun, J. Y.; Rhee, S. W. *Electrochem. Solid-State Lett.* **2006**, *9*, C161–C163.
203. Park, K.-H.; Marshall, W. J. *J. Org. Chem.* **2005**, *70*, 2075–2081.
204. Li, Z.; Barry, S. T.; Gordon, R. G. *Inorg. Chem.* **2005**, *44*, 1728–1735.
205. Ma, Q.; Guo, H.; Gordon, R. G.; Zaera, F. *Chem. Mater.* **2011**, *23*, 3325–3334.
206. Ma, Q.; Guo, H.; Gordon, R. G.; Zaera, F. *Chem. Mater.* **2010**, *22*, 352–359.
207. Ma, Q.; Zaera, F.; Gordon, R. G. *J. Vac. Sci. Technol. A* **2012**, *30*, 01A114.
208. Yao, Y.; Zaera, F. *J. Vac. Sci. Technol. A* **2016**, *34*, 01A101.

209. Willcocks, A. M.; Robinson, T. P.; Roche, C.; Pugh, T.; Richards, S. P.; Kingsley, A. J.; Lowe, J. P.; Johnson, A. L. *Inorg. Chem.* **2012**, *51*, 246–257.
210. (a) Coyle, J. P.; Monillas, W. H.; Yap, G. P. A.; Barry, S. T. *Inorg. Chem.* **2008**, *47*, 683–689. (b) Coyle, J. P.; Johnson, P. A.; DiLabio, G. A.; Barry, S. T.; Müller, J. *Inorg. Chem.* **2010**, *49*, 2844–2850. (c) Whitehorne, T. J. J.; Coyle, J. P.; Mahmood, A.; Monillas, W. H.; Yap, G. P. A.; Barry, S. T. *Eur. J. Inorg. Chem.* **2011**, 3240–3247.
211. (a) Coyle, J. P.; Kurek, A.; Pallister, P. J.; Sirianni, E. R.; Yap, G.P. A.; Barry, S. T. *Chem. Commun.* **2012**, *48*, 10440–10442. (b) Coyle, J. P.; Pallister, P. J.; Kurek, A.; Sirianni, E. R.; Yap, G. P. A.; Barry, S. T. *Inorg. Chem.* **2013**, *52*, 910–917.
212. Kim, T.; Yao, Y.; Coyle, J. P.; Barry, S. T.; Zaera, F. *Chem. Mater.* **2013**, *25*, 3630–3639.
213. Willcocks, A. M.; Pugh, T.; Hamilton, J. A.; Johnson, A. L.; Richards, S. P.; Kingsley, A. J. *Dalton Trans.* **2013**, *42*, 5554–5565.
214. Kang, S.-W.; Yun, J.-Y.; Chang, Y. H. *Chem. Mater.* **2010**, *22*, 1607–1609.
215. (a) Liu, X.; Zhu, C.; Eller, B. S.; Sun, T.; Jezewski, C. J.; King, S. W.; Nemanich, R. J. *J. Vac. Sci. Technol. B* **2012**, *30*, 052203. (b) Haidu, F.; Gordan, O. D.; Zahn, D. R. T. *Thin Solid Films* **2012**, *520*, 4410–4417. (c) Brona, J.; Wasielewski, R.; Ciszewski, A. *Appl. Surf. Sci.* **2012**, *258*, 9623–9628.
216. Choi, J. M.; Lee, D.; Park, J. H.; Kim, C. G.; Chung, T.-M.; Kim, B.-M.; Byun, D. *Microelectronic Eng.* **2012**, *89*, 109–115.
217. Becker, R.; Devi, A.; Weiß, J.; Weckenmann, U.; Winter, M.; Kiener, C.; Becker, H.-W.; Fischer, R. A. *Chem. Vap. Deposition* **2003**, *9*, 149–156.

218. Niskanen, A.; Rahtu, A.; Sajavaara, T.; Arstila, K.; Ritala, M.; Leskelä, M. *J. Electrochem. Soc.* **2005**, *152*, G25–G28.
219. Wu, L.; Zeng, W.; Eisenbraun, E. *ECS Trans.* **2007**, *11*, 67–78.
220. Jezewski, C.; Lanford, W. A.; Wiegand, C. J.; Singh, J. P.; Wang, P.-I.; Senkevich, J. J.; Lu, T.-M. *J. Electrochem. Soc.* **2005**, *152*, C60–C64.
221. Moon, D.-Y.; Han, D.-S.; Shin, S.-Y.; Park, J.-W.; Kim, B. M.; Kim, J. H. *Thin Solid Films* **2011**, *519*, 3636–3640.
222. (a) Mao, J.; Eisenbraun, E.; Omarjee, V.; Korolev, A.; Dussarat, C. *IEEE Trans. Semicond. Manuf.* **2013**, *26*, 17–22. (b) Mao, J.; Eisenbraun, E.; Omarjee, V.; Korolev, A.; Dussarat, C. *ECS Trans.* **2011**, *41*, 33–39. (c) Mao, J.; Eisenbraun, E.; Omarjee, V.; Korolev, A.; Lansalot, C.; Dussarat, C. *ECS Trans.* **2010**, *33*, 125–135.
223. Hagen, D. J.; Connolly, J.; Nagle, R.; Povey, I. M.; Rushworth, S.; Carolan, P.; Ma, P.; Pemble, M. E. *Surf. Coat. Technol.* **2013**, *230*, 3–12.
224. Ma, Q.; Zaera, F. *J. Vac. Sci. Technol. A* **2013**, *31*, 01A112.
225. Huo, J.; Solanki, R. *J. Mater. Res.* **2002**, *17*, 2394–2398.
226. Waechtler, T.; Oswald, S.; Roth, N.; Jakob, A.; Lang, H.; Ecke, R.; Schulz, S. E.; Gessner, T.; Moskvina, A.; Schulze, S.; Hietschold, M. *J. Electrochem. Soc.* **2009**, *156*, H453–H459.
227. Waechtler, T.; Ding, S.-F.; Hofmann, L.; Mothes, R.; Xie, Q.; Oswald, S.; Detavernier, C.; Schulz, S. E.; Qu, X.-P.; Lang, H.; Gessner, T. *Microelectron. Eng.* **2011**, *88*, 684–689.

228. Melzer, M.; Waechtler, T.; Müller, S.; Fiedler, H.; Hermann, S.; Rodriguez, R. D.; Villabona, A.; Sendzik, A.; Mothes, R.; Schulz, S. E.; Zahn, D. R. T.; Hietschold, M.; Lang, H.; Gessner, T. *Microelectronic Eng.* **2013**, *107*, 223–228.
229. Dhakal, D.; Waechtler, T.; Schulz, S. E.; Gessner, T.; Lang, H.; Mothes, R.; Tuchscherer, A. *J. Vac. Sci. Technol. A* **2014**, *32*, 041505.
230. Park, J.-M.; Jin, K.; Han, B.; Kim, M. J.; Jung, J.; Kim, J. J.; Lee, W.-J. *Thin Solid Films* **2014**, *556*, 434–439.
231. Knisley, T. J.; Ariyasena, T. C.; Sajavaara, T.; Saly, M. J.; Winter, C. H. *Chem. Mater.* **2011**, *23*, 4417–4419.
232. Mårtensson, P.; Carlsson, J.-O. *Chem. Vap. Deposition* **1997**, *3*, 45–50.
233. Juppo, M.; Ritala, M.; Leskelä, M. *J. Vac. Sci. Technol. A* **1997**, *15*, 2330–2333.
234. Solanki, R.; Pathangey, B. *Electrochem. Solid St. Lett.* **2000**, *3*, 479–480.
235. Mane, A. U.; Shivashankar, S. A. *Mat. Sci. Semicon. Proc.* **2004**, *7*, 343–347.
236. Mane, A. U.; Shivashankar, S. A. *J. Cryst. Growth* **2005**, *275*, e1253–e1257.
237. (a) Mårtensson, P.; Carlsson, J.-O. *J. Electrochem. Soc.* **1998**, *145*, 2926–2931. (b) Gupta, R.; Willis, B. G. *Appl. Phys. Lett.* **2007**, *90*, 253102. (c) Hsu, I. J.; McCandless, B. E.; Weiland, C.; Willis, B. G. *J. Vac. Sci. Technol. A* **2009**, *27*, 660–667.
238. Norman, J. A. T.; Perez, M.; Lei, X.; Cheng, H. *ECS Trans.* **2007**, *3*, 161–170.
239. Park, K.-M.; Kim, J.-K.; Han, B.; Lee, W.-J.; Kim, J.; Shin, H.-K. *Microelectron. Eng.* **2012**, *89*, 27–30.
240. Hagen, D. J.; Povey, I. M.; Rushworth, S.; Wrench, J. S.; Keeney, L.; Schmidt, M.; Petkov, N.; Barry, S. T.; Coyle, J. P.; Pemble, M. E. *J. Mater Chem, C* **2014**, *2*, 9205–9214.

241. Dey, G.; Elliott, S. *Theor. Chem. Acc.* **2014**, *133*, 1416.
242. Li, Z.; Gordon, R. G.; Farmer, D. B.; Lin, Y.; Vlassak, J. *Electrochem. Solid St. Lett.* **2005**, *8*, G182–G185.
243. (a) Dai, M.; Kwon, J.; Langereis, E.; Wielunski, L.; Chabal, Y. J.; Li, Z.; Gordon, R. G. *ECS Trans.* **2007**, *11*, 91–101. (b) Dai, M.; Kwon, J.; Halls, M. D.; Gordon, R. G.; Chabal, Y. J. *Langmuir* **2010**, *26*, 3911–3917.
244. Seitz, O.; Dai, M.; Aguirre-Tostado, F. S.; Wallace, R. M.; Chabal, Y. J. *J. Am. Chem. Soc.* **2009**, *131*, 18159–18167.
245. Kucheyev, S. O.; Biener, J.; Baumann, T. F.; Wang, Y. M.; Hamza, A. V.; Li, Z.; Lee, D. K.; Gordon, R. G. *Langmuir* **2008**, *24*, 943–948.
246. Lee, B. H.; Hwang, J. K.; Nam, J. W.; Lee, S. U.; Kim, J. T.; Koo, S.-M.; Baunemann, A.; Fischer, R. A.; Sung, M. M. *Angew. Chem. Int. Ed.* **2009**, *48*, 4536–4539.
247. Dey, G.; Elliott, S. D. *J. Phys. Chem. A* **2012**, *116*, 8893–8901.
248. Vidjayacoumar, B.; Emslie, D. J. H.; Clendenning, S. B.; Blackwell, J. M.; Britten, J. F.; Rheingold, A. *Chem. Mater.* **2010**, *22*, 4844–4853.
249. Vidjayacoumar, B.; Emslie, D. J. H.; Blackwell, J. M.; Clendenning, S. B.; Britten, J. F. *Chem. Mater.* **2010**, *22*, 4854–4866.
250. Kalutarage, L. C.; Clendenning, S. B.; Winter, C. H. *Chem. Mater.* **2014**, *26*, 3731–3738.
251. Guillon, H.; Daniele, S.; Hubert-Pfalzgraf, L. G.; Bavoux, C. *Inorg. Chim. Acta* **2000**, *304*, 99–107.
252. Domide, D.; Walter, O.; Behrens, S.; Kaifer, E.; Himmel, H.-J. *Eur. J. Inorg. Chem.* **2011**, 860–867.



253. Oo, T. Z.; Chandra, R. D.; Yantara, N.; Prabhakar, R. R.; Wonga, L. H.; Mathews, N.; Mhaisalkar, S. G. *Org. Electron.* **2012**, *13*, 870–874.
254. Dutta, S.; Dodabalapur, A. *Sens. Actuators, B* **2009**, *143*, 50–55.
255. Lee, E. Y. M.; Tran, N. H.; Lamb, R. N. *Appl. Surf. Sci.* **2005**, *241*, 493–496.
256. Short, A.; Jewell, L.; Doshay, S.; Church, C.; Keiber, T.; Bridges, F.; Carter, S.; Alersa, G. *J. Vac. Sci. Technol. A* **2013**, *31*, 01A138.
257. Chopra, K. L.; Major, S.; Pandya, D. K. *Thin Solid Films* **1983**, *102*, 1–46.
258. Minami, T.; Nanto, H.; Tanaka, S. *Jpn. J. Appl. Phys.* **1984**, *24*, L605–L607.
259. Iwata, K.; Sakemi, T.; Yamada, A.; Fons, P.; Awai, K.; Yamamoto, T.; Shirakata, S.; Matsubara, K.; Tambo, H.; Sakurai, K.; Ishizuka, S.; Niki, S. *Thin Solid Films* **2005**, *480–481*, 199–203.
260. Wenas, W. W.; Yamada, A.; Konagai, M.; Takahashi, K. *Jpn. J. Appl. Phys.* **1991**, *30*, L441–L443.
261. (a) Iwata, K.; Fons, P.; Niki, S.; Yamada, A.; Matsubara, K. *Phys. Status Solidi A* **2000**, *180*, 287–292. (b) Iwata, K.; Fons, P.; Niki, S.; Yamada, A.; Matsubara, K. *J. Cryst. Growth* **2000**, *209*, 526–531. (c) Iwata, K.; Fons, P.; Niki, S.; Yamada, A.; Matsubara, K. *J. Cryst. Growth* **2000**, *214*, 50–54. (d) Iwata, K.; Fons, P.; Niki, S.; Yamada, A.; Matsubara, K. *Phys. Status Solidi B* **2001**, *229*, 887–890.
262. Alam, M. J.; Cameron, D. C. *J. Vac. Sci. Technol. A* **2001**, *19*, 1642–1646.
263. Saraf, L. V.; Engelhard, M. H.; Wang, C. M.; Lea, A. S.; McCready, D. E.; Shutthanandan, V.; Baer, D. R.; Chambers, S. A. *J. Mater. Res.* **2007**, *22*, 1230–1234.
264. Hlaing Oo, W. M.; Saraf, L. V.; Engelhard, M. H.; Shutthanandan, V.; Bergman, L.; Huso, J.; McCluskey, M. D. *J. Appl. Phys.* **2009**, *105*, 013715.

265. Garcia, J. M. J.; Adame, J. A.; Alvarez, R. C.; López, F. J. *Electrochem. Solid-State Lett.* **2012**, *15*, H167–H172.
266. Losurdo, M.; Giangregorio, M. M.; Sacchetti, A.; Capezzuto, P.; Bruno, G.; Malandrino, G.; Fragalà, I. L. *J. Mater. Res.* **2006**, *21*, 1632–1637.
267. Hill, M. R.; Jones, A. W.; Russell, J. J.; Roberts, N. K.; Lamb, R. N. *Inorg. Chim. Acta* **2005**, *358*, 201–206.
268. Bekermann, D.; Rogalla, D.; Becker, H.-W.; Winter, M.; Fischer, R. A.; Devi, A. *Eur. J. Inorg. Chem.* **2010**, 1366–1372.
269. Kim, D.; Kang, H.; Kim, J.-M.; Kim, H. *Appl Surf Sci.* **2011**, *257*, 3776–3779.
270. Park, H. K.; Yang, B. S.; Park, S.; Kim, M. S.; Shin, J. C.; Heo, J. *J. Alloys Compd.* **2014**, *605*, 124–130.
271. Yuan, H.; Luo, B.; Yu, D.; Cheng, A.; Campbell, S. A. *J. Vac. Sci. Technol. A* **2012**, *30*, 01A138.
272. Pourret, A.; Guyot-Sionnest, P.; Elam, J. W. *Adv. Mater.* **2008**, *20*, 1–4.
273. (a) Jones, P. L.; Cotton, D. R.; Moore, D.; *Thin Solid Films* **1982**, *88*, 163–174. (b) Emma, T.; McDonough, M. *J. Vac. Sci. Technol. A* **1984**, *2*, 362–364.
274. Tanninen, V. P.; Oikkonen, M.; Tuomi, T. *Thin Solid Films* **1983**, *109*, 283–291.
275. (a) Smith, P. B. *J. Vac. Sci. Technol. A* **1989**, *7*, 1451–1455. (b) Li, J. W.; Su, Y. K.; Yokoyama, M. *Appl. Surf. Sci.* **1993**, *65*, 433–436.
276. Shen, X.-P.; Han, M.; Hong, J.-M.; Xue, Z.; Xu, Z. *Chem. Vap. Deposition* **2005**, *11*, 250–253.
277. Barreca, D.; Gasparotto, A.; Maragno, C.; Tondello, E. *J. Electrochem. Soc.* **2004**, *151*, G428–G435.

278. Barreca, D.; Gasparotto, A.; Maragno, C.; Tondello, E.; Sada, C. *Chem. Vap. Deposition* **2004**, *10*, 229–236.
279. Afzaal, M.; Crouch, D.; Malik, M. A.; Motevalli, M.; O'Brien, P.; Park, J.-H.; Woollins, J. D. *Eur. J. Inorg. Chem.* **2004**, 171–177.
280. Seo, K. W.; Yoon, S. H.; Lee, S. S.; Shim, I.-W. *Bull. Korean Chem. Soc.* **2005**, *26*, 1582–1584.
281. Short, A.; Jewell, L.; Bielecki, A.; Keiber, T.; Bridges, F.; Carter, S.; Alers, G. *Vac. Sci. Technol. A* **2014**, *32*, 01A125.
282. Zheng, Z.-H.; Fan, P.; Liu, P.-J.; Luo, J.-T.; Liang, G.-X.; Zhang, D.-P. *J. Alloys Compd.* **2014**, *594*, 122–126.
283. Suh, S.; Hoffman, D. M.; Atagi, L. M.; Smith, D. C. *Chem. Vap. Deposition* **2001**, *7*, 81–84.
284. Hill, M. R.; Jensen, P.; Russell, J. J.; Lamb, R. N. *Dalton Trans.* **2008**, 2751–2758.
285. (a) Chang, M.-C.; Otten, E. *Chem. Commun.* **2014**, *50*, 7431–7433. (b) Chang, M.-C.; Dann, T.; Day, D. P.; Lutz, M.; Wildgoose, G. G.; Otten, E. *Angew. Chem. Int. Ed.* **2014**, *53*, 4118–4122. (c) Chang, M.-C.; Roewen, P.; Travieso-Puente, R.; Lutz, M.; Otten, E. *Inorg. Chem.* **2015**, *54*, 379–388. (d) Travieso-Puente, R.; Chang, M.-C.; Otten, E. *Dalton Trans.* **2014**, *43*, 18035–18041.
286. (a) Rollison, C. L. In *Comprehensive Inorganic Chemistry*, vol. 3; Bailar Jr., J. C., Emeleus, H. J., Nyholm, R., Trotman-Dickenson, A. F., Eds.; PergamonPress: Oxford, 1973; pp. 623–769. (b) Kemmitt, R. D. W. In *Comprehensive Inorganic Chemistry*, vol. 3; Bailar Jr., J. C., Emeleus, H. J., Nyholm, R., Trotman-Dickenson, A. F., Eds.; PergamonPress: Oxford, 1973; pp. 771–876.

287. Sanyal, U.; Jagirdar, B. R. *Inorg. Chem.* **2012**, *51*, 13023–13033.
288. (a) Barpanda, P.; Dwibedi, D.; Ghosh, S.; Kee, Y.; Okada, S. *Ionics* **2015**, *21*, 1801–1812. (b) Mun, J.; Lee, J.; Hwang, T.; Lee, J.; Noh, H.; Choi, W. *J. Electroanal. Chem.* **2015**, *745*, 8–13. (c) Le Roux, B.; Bourbon, C.; Lebedev, O. I.; Colin, J.-F.; Pralong, V. *Inorg. Chem.* **2015**, *54*, 5273–5279. (d) Afuon, S.; Kundu, D.; Darbandi, A. J.; Hahn, H.; Krumeich, F.; Nesper, R. *J. Mater. Chem. A* **2014**, *2*, 18946–18951. (e) Afyon, S.; Wörle, M.; Nesper, R. *Angew. Chem. Int. Ed.* **2013**, *52*, 12541–12544. (f) Lee, K.-J.; Kang, L.-S.; Uhm, S.; Yoon, J. S.; Kim, D.-W.; Hong, H. S. *Curr. Appl. Phys.* **2013**, *13*, 1440–1443.
289. Bernal Ramos, K.; Saly, M. J.; Chabal, Y. J. *Coord. Chem. Rev.* **2013**, *257*, 3271–3281.
290. Emslie, D. J. H.; Chadha, P.; Price, J. S. *Coord. Chem. Rev.* **2013**, *257*, 3282–3296.
291. Saito, T.; Nishiyama, H.; Tanahashi, H.; Kawakita, K.; Tsurugi, H.; Mashima, K. *J. Am. Chem. Soc.* **2014**, *136*, 5161–5170.
292. Tsurugi, H.; Tanahashi, H.; Nishiyama, H.; Fegler, W.; Saito, T.; Sauer, A.; Okuda, J.; Mashima, K. *J. Am. Chem. Soc.* **2013**, *135*, 5986–5989.
293. Tsurugi, H.; Saito, T.; Tanahashi, H.; Arnold, J.; Mashima, K. *J. Am. Chem. Soc.* **2011**, *133*, 18673–18683.
294. Arteaga-Müller, R.; Tsurugi, H.; Saito, T.; Yanagawa, M.; Oda, S.; Mashima, K. *J. Am. Chem. Soc.* **2009**, *131*, 5370–5371.
295. Popoff, N.; Espinas, J.; Gouré, E.; Boyron, O.; Le Roux, E.; Basset, J.-M.; Gauvin, R. M.; De Mallmann, A.; Taoufik, M. *Macromol. Rapid Commun.* **2011**, *32*, 1921–1924.
296. Vashchenko, A. V.; Pavlova, T. O.; Chuvashhev, N. F. *Russ. J. Gen. Chem.* **2013**, *83*, 1094–1097.

297. (a) Schleyer, P. v. R.; Maerker, C.; Dransfeld, A.; Jiao, H.; Hommes, N. J. R. v. E. *J. Am. Chem. Soc.* **1996**, *118*, 6317–6318. (b) Chen, Z.; Wannere, C. S.; Corminboeuf, C.; Puchta, R.; Schleyer, P. v. R. *Chem. Rev.* **2005**, *105*, 3842–3888. (c) Fallah-Bagher-Shaidaei, H.; Wannere, C. S.; Corminboeuf, C.; Puchta, R.; Schleyer, P. v. R. *Org. Lett.* **2006**, *8*, 863–866. (d) Psciuk, B. T.; Lord, R. L.; Winter, C. H.; Schlegel, H. B. *J. Chem. Theory Comput.* **2012**, *8*, 4950–4959.
298. Kaim, W. *J. Am. Chem. Soc.* **1983**, *105*, 707–713.
299. Laguerre, M.; Dunogues, J.; Calas, R.; Duffaut, N. *J. Organomet. Chem.* **1976**, *112*, 49–59.
300. McCafferty, E.; Wightman, J. P. *Appl. Surf. Sci.* **1999**, *143*, 92–100.
301. Benito, N.; Palacio, C. *Appl. Surf. Sci.* **2014**, *301*, 436–441.
302. Xia, J.; Masaki, N.; Jiang, K.; Yanagida, S. *J. Phys. Chem. B* **2006**, *110*, 25222–25228.
303. Godfroid, T.; Gouttebaron, R.; Dauchot, J. P.; Leclère, P.; Lazzaroni, R.; Hecq, M. *Thin Solid Films* **2003**, *437*, 57–62.
304. Pouilleau, J.; Devilliers, D.; Garrido, F.; Durand-Vidal, S.; Mahé, E. *Mater. Sci. Eng. B* **1997**, *B47*, 235–243.
305. *Handbook of X-ray Photoelectron Spectroscopy*; Wagner, C. D., Riggs, W. M., Davis, L. E., Moulder, J. F., Murlenberg, G. E., Eds.; Perkin-Elmer Corporation: Eden Prairie, MN, 1979.
306. Yang, W. Y.; Iwakuro, H.; Yagi, H.; Kuroda, T.; Nakamura, S. *Jpn. J. Appl. Phys.* **1984**, *23*, 1560–1567.
307. Beard, B. C.; Ross, P. N. *J. Phys. Chem.* **1986**, *90*, 6811–6817.
308. Hausen, H. D.; Mundt, O.; Kaim, W. *J. Organomet. Chem.* **1985**, *296*, 321–337.

309. Sulzbach, R. A.; Iqbal, A. F. M. *Angew. Chem., Int. Ed.* **1971**, *10*, 127.
310. Sittig, C. E. Ph.D. Dissertation, Nr. 12657, Swiss Federal Institute of Technology (ETH), 1998.
311. Tam, P. L.; Cao, Y.; Nyborg, L. *Surf. Sci.* **2012**, *606*, 329–336.
312. *Cobalt*; 2015. <https://en.wikipedia.org/wiki/Cobalt>.
313. Vecher, A. A.; Dalidovich, S. V.; Gusev, E. A. *Thermochim Acta* **1985**, *89*, 383–386.
314. (a) Columbia, M. R.; Thiel, P. A. *J. Electroanalyt. Chem.* **1994**, *369*, 1–14. (b) Inglis, H. S.; Taylor, D. *J. Chem. Soc. (A)* **1969**, 2985–2987. (c) Waechtler, T.; Ding, S.-F.; Hofmann, L.; Mothes, R.; Xie, Q.; Oswald, S.; Detavernier, D.; Schulz, S. E.; Qu, X.-P.; Lang, H.; Gessner, T. *Microelectron. Eng.* **2011**, *88*, 684–689.
315. Ravindranathan, P.; Patil, K. C. *Thermochim. Acta* **1983**, *71*, 53–57.
316. Reedijk, J.; Groeneveld, W. L. *Recl. Trav. Chim. Pays-Bas.* **1968**, *87*, 552–558.
317. Kliegman, J. M.; Barnes, R. K. *Tetrahedron* **1970**, *26*, 2555–2560.
318. Singh, J. V.; Baranwal, B. P.; Mehrotra, R. C. *Z. Anorg. Allg. Chem.* **1981**, *477*, 235–240.
319. Goel, S. C.; Kramer, K. S.; Chiang, M. Y.; Buhro, W. E. *Polyhedron* **1990**, *9*, 611–613.
320. (a) Heydari, A.; Mehrdad, M.; Maleki, A.; Ahmadi, N. *Synthesis* **2004**, *10*, 1563–1565.  
(b) Anwander, R.; Munck, F. C.; Priermeier, T.; Scherer, W.; Runte, O.; Herrmann, W. *A. Inorg. Chem.* **1997**, *36*, 3545–3552.
321. (a) Rojas-Sáenz, H.; Suárez-Moreno, G. V.; Ramos-García, I.; Duarte-Hernández, A. M.; Mijangos, E.; Peña-Hueso, A.; Contreras, R.; Flores-Parra, A. *New J. Chem.* **2014**, *38*, 391–405.

322. (a) Ghosh, M.; Sproules, S.; Weyhermüller, T.; Wieghardt, K. *Inorg. Chem.* **2008**, *47*, 5963–5970. (b) Kreisel, K. A.; Yap, G. P. A.; Theopold, K. H. *Inorg. Chem.* **2008**, *47*, 5293–5303. (c) Kreisel, K. A.; Yap, G. P. A.; Dmitrenko, O.; Landis, C. R.; Theopold, K. H. *J. Am. Chem. Soc.* **2007**, *129*, 14162–14163.
323. Ghosh, M.; Weyhermüller, T.; Wieghardt, K. *Dalton Trans.* **2008**, 5149–5151.
324. (a) Khusnivarov, M. M.; Weyhermüller, T.; Bill, E.; Wieghardt, K. *J. Am. Chem. Soc.* **2009**, *131*, 1208–1221. (b) Khusnivarov, M. M.; Weyhermüller, T.; Bill, E.; Wieghardt, K. *Angew. Chem. Int. Ed.* **2008**, *47*, 1228–1231. (c) Muresan, N.; Lu, C. C.; Ghosh, M.; Peters, J. C.; Abe, M.; Henling, L. M.; Weyhermüller, T.; Bill, E.; Wieghardt, K. *Inorg. Chem.* **2008**, *47*, 4579–4590. (d) Bart, S. C.; Hawrelak, E. J.; Lobkovsky, E.; Chirik, P. *Organometallics* **2005**, *24*, 5518–5527. (e) tom Dieck, H.; Diercks, R.; Stamp, L.; Bruder, H.; Schuld, T. *Chem. Ber.* **1987**, *120*, 1943–1950. (f) tom Dieck, H.; Bruder, H. *J. Chem. Soc., Chem. Commun.* **1977**, 24–25.
325. (a) Muresan, N.; Weyhermüller, T.; Wieghardt, K. *Dalton Trans.* **2007**, 4390–4398. (b) Muresan, N.; Chlopek, K.; Weyhermüller, T.; Neese, F.; Wieghardt, K. *Inorg. Chem.* **2007**, *46*, 5327–5337. (c) Khusnivarov, M. M.; Harms, K.; Burghaus, O.; Sundermeyer, J. *Eur. J. Inorg. Chem.* **2006**, 2985–2996. (d) Gorls, H.; Walther, D.; Sieler, J. *Cryst. Res. Technol.* **1987**, *22*, 1145–1151. (e) Svoboda, M.; tom Dieck, H.; Kruger, C.; Tsay, Y.-H. *Z. Naturforsch.* **1981**, *36b*, 814–822. (f) Robinson, M. A.; Curry, J. D.; Busch, D. H. *Inorg. Chem.* **1963**, *2*, 1178–1181. (g) Kaltsoyannis, N. *J. Chem. Soc., Dalton Trans.* **1996**, 1583–1589.
326. Gardiner, M. G.; Hanson, G. R.; Henderson, M. J.; Lee, F. C.; Raston, C. L. *Inorg. Chem.* **1994**, *33*, 2456–2461.

327. tom Dieck, H.; Rieger, H. J.; Fendesak, G. *Inorg. Chim. Acta* **1990**, *177*, 191–197.
328. Scholz, J.; Görls, H. *Inorg. Chem.* **1996**, *35*, 4378–4382.
329. Geoffrey, F.; Cloke, N.; Dalby, C. I.; Henderson, M. J.; Hitchcock, P. B.; Kennard, C. H. L.; Lamb, R. N.; Raston, C. L. *J. Chem. Soc., Chem. Commun.* **1990**, 1394–1396.
330. (a) Allan, L. E. N.; Shaver, M. P.; White, A. J. P.; Gibson, V. C. *Inorg. Chem.* **2007**, *46*, 8963–8970. (b) Barral, M. C.; Delgado, E.; Gutiérrez-Puebla, E.; Jimenez-Aparicio, R.; Monge, A.; del Pino, C.; Santos, A. *Inorg. Chim. Acta* **1983**, *74*, 101–107. (c) Jameson, G. B.; Oswald, H. R.; Beer, H. R. *J. Am. Chem. Soc.* **1984**, *106*, 1669–1675.
331. (a) Nikogosyan, D. N. *Nonlinear Optical Crystals: A Complete Survey*; Springer: New York, 2005. (b) Chen, C.; Lin, Z.; Wang, Z. *Appl. Phys. B* **2005**, *80*, 1–25. (c) Keszler, D. A. *Curr. Opin. Sol. State Mater. Sci.* **1996**, *1*, 204–208. (d) Becker, P. *Adv. Mater.* **1998**, *10*, 979–992.
332. Xue, D.; Betzler, K.; Hesse, H.; Lammers, D. S. *Solid State Commun.* **2000**, *114*, 21–25.
333. Maia, L. J. Q.; Bernardi, M. I. B.; Feitosa, C. A. C.; Mastelaro, V. R.; Zanatta, A. R.; Hernandez, A. C. *Thin Solid Films* **2004**, *457*, 246–252.
334. (a) Smith, A. M.; Trotochaud, L.; Burke, M. S.; Boettcher, S. W. *Chem. Commun.* **2015**, *51*, 5261–5263. (b) Farrow, C. L.; Bediako, D. K.; Surendranath, Y.; Nocera, D. G.; Billinge, S. J. L. *J. Am. Chem. Soc.* **2013**, *135*, 6403–6406. (c) Choi, S. K.; Choi, W.; Park, H. *Phys. Chem. Chem. Phys.* **2013**, *15*, 6499–6507. (d) Jin, T.; Diao, P.; Xu, D.; Wu, Q. *Electrochim. Acta* **2013**, *114*, 271–277. (e) Bediako, D. K.; Surendranath, Y.; Nocera, D. G. *J. Am. Chem. Soc.* **2013**, *135*, 3662–3674. (f) Winkler, M. T.; Cox, C. R.; Nocera, D. G.; Buonassisi, T. *PNAS* **2013**, *110*, E1076–E1082. (g) Bediako, D. K.; Lassalle-Kaiser, B.; Surendranath, Y.; Yano, J.; Yachandra, V. K.; Nocera, D. G. *J. Am.*



- Chem. Soc.* **2012**, *134*, 6801–6809. (h) Surendranath, Y.; Bediako, D. K.; Nocera, D. G. *PNAS* **2012**, *109*, 15617–15621. (i) Esswein, A. J.; Surendranath, Y.; Reece, S. Y.; Nocera, D. G. *Energy Environ. Sci.* **2011**, *4*, 499–504. (j) Reece, S. Y.; Hamel, J. A.; Sung, K.; Jarvi, T. D.; Esswein, A. J.; Pijpers, J. J. H.; Nocera, D. G. *Science* **2011**, *334*, 645–648. (k) Dinča, M.; Surendranath, Y.; Nocera, D. G. *PNAS* **2010**, *107*, 10337–10341. (l) Surendranath, Y.; Dinča, M.; Nocera, D. G. *J. Am. Chem. Soc.* **2009**, *131*, 2615–2620.
335. Ozera, A. M.; Simagina, V. I.; Komova, O. V.; Netskina, O. V.; Odegova, G. V.; Bulavchenko, O. A.; Rudina, O. A.; Rudina, N. A. *J. Alloys Compounds* **2012**, *513*, 266–272.
336. Wang, Y.; Feng, J.; Feng, B.; Song, X.; Cao, J. *RSC Adv.* **2015**, *5*, 28950–28957.
337. Studebaker, D. B.; Stauf, G. T.; Baum, T. H.; Marks, T. J.; Zhou, H.; Wong, G. K. *Appl. Phys. Lett.* **1997**, *70*, 565–567.
338. (a) Malandrino, G.; Lo Nigro, R.; Fragalà, I. L. *Inorg. Chim. Acta* **2006**, *360*, 1138–1142. (b) Malandrino, G.; Lo Nigro, R.; Fragalà, I. L. *Chem. Vap. Deposition* **2007**, *13*, 651–655.
339. (a) Saly, M. J.; Heeg, M. J.; Winter, C. H. *Inorg. Chem.* **2009**, *48*, 5303–5312. (b) Saly, M. J.; Munnik, F.; Winter, C. H. *J. Mater. Chem.* **2010**, *20*, 9995–10000. (c) Saly, M. J.; Munnik, F.; Winter, C. H. *Chem. Vap. Deposition*, **2011**, *17*, 128–134. (d) Saly, M. J.; Munnik, F.; Baird, R. J.; Winter, C. H. *Chem. Mater.* **2009**, *21*, 3742–3744.
340. (a) Likosius, M.; Wenger, C.; Pasko, S.; Costina, I.; Dabrowski, J.; Sorge, R.; Müssig, H.-J.; Lohe, C. *IEEE Trans. Electron Dev.* **2008**, *55*, 2273–2377. (b)

- Vehkamäki, M.; Ritala, M.; Leskelä, M.; Jones, A. C.; Davies, H. O.; Sajavaara, T.; Rauhala, T.; Rauhala, E. *J. Electrochem. Soc.* **2004**, *151*, F69–F72. (c) Gaskell, J. M.; Przybylak, S.; Jones, A. C.; Aspinall, H.; Chalker, P. R.; Black, K.; Potter, R. J.; Taechakumput, P.; Taylor, S. *Chem. Mater.* **2007**, *19*, 4796–4803. (d) Harjuoja, J.; Hatanpää, T.; Vehkamäki, M.; Väyrynen, S.; Putkonen, M.; Niinistö, L.; Ritala, M.; Leskelä, M.; Rauhala, E. *Chem. Vap. Deposition* **2005**, *11*, 362–367.
341. Bellow, J. A.; Winter, C. H. unpublished results, Wayne State University.
342. McIntyre, N. S.; Cook, M. G. *Anal. Chem.* **1975**, *47*, 2208–2213.
343. Dapporto, P.; Mani, F.; Mealli, C. *Inorg. Chem.* **1978**, *17*, 1323–1329.
344. Neumaira, S. C.; Kaindlb, R.; Huppertz, H. *Z. Naturforsch.* **2010**, *65b*, 1311–1317.
345. Greenwood, N. N., Earnshaw, A. *Chemistry of the Elements*, 2<sup>nd</sup> Ed.; Elsevier: Amsterdam, 1997; pp 1119–1120.
346. Trofimenko, S. *J. Am. Chem. Soc.* **1967**, *89*, 3170–3177.
347. Klesko, J. P.; Thrush, C. M.; Winter, C. H. *Chem. Mater.* **2015**, *27*, 4918–4921.

**ABSTRACT****NEW CHEMISTRY FOR THE GROWTH OF FIRST-ROW TRANSITION METAL FILMS BY ATOMIC LAYER DEPOSITION**

by

**JOSEPH PETER KLESKO****December 2015**

**Advisor:** Prof. Charles H. Winter  
**Major:** Chemistry (Physical)  
**Degree:** Doctor of Philosophy

Thin films containing first-row transition metals are widely used in microelectronic, photovoltaic, catalytic, and surface-coating applications. In particular, metallic films are essential for interconnects and seed, barrier, and capping layers in integrated circuitry. Traditional vapor deposition methods for film growth include PVD, CVD, or the use of plasma. However, these techniques lack the requisite precision for film growth at the nanoscale, and thus, are increasingly inadequate for many current and future applications. By contrast, ALD is the favored approach for depositing films with absolute surface conformality and thickness control on 3D architectures and in high aspect ratio features. However, the low-temperature chemical reduction of most first-row transition metal cations to their zero-valent state is very challenging due to their negative electrochemical potentials. A lack of strongly-reducing coreagents has rendered the thermal ALD of metallic films an intractable problem for many elements. Additionally, several established ALD processes for metal films are plagued by low growth rates, impurity incorporation, poor nucleation, high surface roughness, or the need for hazardous coreagents. Finally, stoichiometric control of ternary films grown by ALD is rare, but

increasingly important, with emerging applications for metal borate films in catalysis and lithium ion batteries.

The research herein is focused toward the development of new ALD processes for the broader application of metal, metal oxide, and metal borate thin films to future nanoscale technologies. These processes display self-limited growth and support the facile nucleation of smooth, continuous, high-purity films. Bis(trimethylsilyl) six-membered rings are employed as strongly-reducing organic coreagents for the ALD of titanium and antimony metal films. Additionally, new processes are developed for the growth of high-purity, low-resistivity cobalt and nickel metal films by exploiting the redox non-innocent nature of a series of recently-reported 1,4-di-*tert*-butyl-1,3-diazabutadienyl complexes. Other metal complexes using the same ligand system are subsequently evaluated for use as ALD precursors. Finally, a novel approach is described for the stoichiometric control of first-row transition metal manganese and cobalt borate films, whereby the film composition is governed by the elements present in a single precursor.

Computational techniques such as density functional theory (DFT) using nucleus-independent chemical shift (NICS) are used to determine the electronic structure and predict the relative reducing power of organic coreagents. Potential ALD precursors are analyzed by  $^1\text{H}$  and  $^{13}\text{C}$  NMR, IR, thermogravimetric and differential thermal analyses (TGA/DTA), melting point and solid state decomposition measurements, magnetic susceptibility measurements, preparative sublimation studies, and solution-screening reactions. Deposition parameters are optimized for successful ALD processes. The composition and surface morphology of the resultant films are studied by scanning electron microscopy (SEM), transmission electron microscopy (TEM), atomic force microscopy (AFM), X-ray photoelectron spectroscopy (XPS), auger electron spectroscopy (AES), X-ray diffractometry (XRD), time-of-flight elastic recoil detection analysis

(TOF-ERDA), ultraviolet-visible spectroscopy (UV-Vis), and four-point probe resistivity measurements.

## AUTOBIOGRAPHICAL STATEMENT

JOSEPH PETER KLESKO

### Education

- 2015 Ph.D., Chemistry (Physical), Wayne State University, Detroit, MI  
Research Advisor: Prof. Charles H. Winter
- 2009 M.A., Physics, Wayne State University, Detroit, MI
- 2005 M.S., Chemistry, University of Detroit Mercy, Detroit, MI
- 2003 B.S., Chemical Engineering, University of Detroit Mercy, Detroit, MI  
Magna Cum Laude

### Patents

“Bis(trimethylsilyl) Six-membered Ring Systems and Related Compounds as Reducing Agents for Forming Layers on a Substrate” **Klesko, J. P.**; Winter, C. H. US 9157149 (issued 10/13/2015); WO 2014/210512 (filed 06/27/2014); TWN 103122314 (filed 07/27/2014).

### Publications

“Unusual Stoichiometry Control in the Atomic Layer Deposition of Manganese Borate Films from Manganese Bis(tris(pyrazolyl)borate) and Ozone,” **Klesko, J. P.**; Bellow, J. A.; Saly, M. J.; Julin, J.; Sajavaara, T.; Winter, C. H. *Submitted*.

“Low Temperature Thermal Atomic Layer Deposition of Cobalt Metal Films,” **Klesko, J. P.**; Winter, C. H. *Submitted*.

“Thermal Atomic Layer Deposition of Titanium Films Using Titanium Tetrachloride and 2-Methyl-1,4-bis(trimethylsilyl)-2,5-cyclohexadiene or 1,4-Bis(trimethylsilyl)-1,4-dihydropyrazine,” **Klesko, J. P.**; Thrush, C. M.; Winter, C. H. *Chem. Mater.* **2015**, *27*, 4918–4921. DOI: 10.1021/acs.chemmater.5b01707.

“Metallic Materials Deposition: Metal-Organic Precursors,” Winter, C. H.; Knisley, T. J.; Kalutarage, L. C.; Zavada, M. A.; **Klesko, J. P.**; Perera, T. H. *Encyclopedia of Inorganic and Bioinorganic Chemistry*; Wiley: Chichester, **2012**. DOI: 10.1002/9781119951438.eibc0128.pub2.